UNIVERSIDADE DE LISBOA

INSTITUTO SUPERIOR TÉCNICO

UNIVERSITÉ DE BORDEAUX

UNDER ERASMUS MUNDUS PROGRAMME

Advanced Metal Graphene Composite Electrodes for a new Generation of Electrochemical Energy Storage Devices

Alberto Adan Mas

Supervisors: Doctor Maria de Fátima Grilo da Costa Montemor
Doctor Liliane Guerlou-Demourgues

Thesis approved in public session to obtain the PhD Degree in Materials Engineering

Jury final Classification: Pass with distinction

2018

UNIVERSIDADE DE LISBOA
INSTITUTO SUPERIOR TÉCNICO

UNIVERSITÉ DE BORDEAUX

UNDER ERASMUS MUNDUS PROGRAMME

Advanced Metal Graphene Composite Electrodes for a new Generation of Electrochemical Energy Storage Devices

Alberto Adan Mas

Supervisors: Doctor Maria de Fátima Grilo da Costa Montemor
Doctor Liliane Guerlou-Demourgues

Thesis approved in public session to obtain the PhD Degree in Materials Engineering

Jury final Classification: Pass with distinction

Jury

Chairperson: Doctor Rogério Anacleto Cordeiro Colaço, Instituto Superior Técnico, Universidade de Lisboa

Members of the commitee:

Doctor Liliane Guerlou-Demourgues, Institut de Chimie de la Matière Condensée de Bordeaux, Université de Bordeaux, France

Doctor Adélio Miguel Magalhães Mendes, Faculdade de Engenharia, Universidade de Porto

Doctor Margarida Maria Portela Correia dos Santos Romão, Instituto Superior Técnico, Universidade de Lisboa

Doctor Filipe Miguel Henriques Lebre Ramos Figueiredo, Universidade de Aveiro

Doctor Raquel Alexandra Galamba Duarte, Escola Superior do Tecnologia do Barreiro, Instituto Politécnico de Setúbal

Funding Institution
International Doctoral School in Functional Materials

2018

I. Abstracts

Resumo

A procura crescente de energia em setores distintos, como residencial, transporte e industrial, bem como a proliferação de fontes renováveis de produção de energia, exigem novos e mais eficientes dispositivos de armazenamento de energia. Consequentemente, tem-se observado um interesse crescente na produção e engenharia de materiais para armazenamento de energia. Muito dos esforços de R&D estão centrados no desenvolvimento de materiais nanoestruturados que possam responder aos requisitos da aplicação, tais como densidade de energia, densidade de potência e estabilidade face à ciclagem do dispositivo. Presentemente são muitos os materiais investigados como potenciais candidatos para elétrodos para dispositivos de armazenamento de energia por via eletroquímia, nomeadamente baterias, condensadores, pseudocondensadores ou supercondensadores. O objetivo do presente trabalho é produzir e estudar novos materiais com uma resposta eletroquímica intermédia entre um elétrodo típico de supercondensador e um elétrodo típico de bateria, também conhecidos como elétrodos híbridos. Por essa razão, selecionaram-se hidróxidos e óxidos de níquel e cobalto devido à sua elevada atividade eletroquímica e baixo custo. Estes materiais foram combinados com derivados de grafeno, que exibem alta condutividade e elevada área superficial ativa. Portanto, este trabalho foca a síntese e caracterização fisico química e eletroquímica de hidróxidos e óxidos de níquel-cobalto nanoestruturados e sua combinação com óxido de grafeno reduzido para aplicações de armazenamento de energia. A síntese foi efectuada por duas vias distintas: eletrodeposição e exfoliação.

A eletrodeposição é usada para obter hidróxidos e óxidos de níquel-cobalto em combinação com óxido de grafeno reduzido. Os resultados evidenciam um efeito sinérgico quando o óxido de grafeno reduzido é combinado com o (hidr)óxido de níquel-cobalto, isto é, um aumento na capacidade, condutividade e estabilidade do compósito quando comparado com o (hidr)óxido de níquel-cobalto. Neste trabalho é dada especial atenção à espectroscopia de impedância eletroquímica que foi utilizada para avaliar os fenômenos que ocorrem durante a carga e descarga contínua e compreender os processos que ocorrem no material ativo e que resultam na sua degradação.

O hidróxido de níquel-cobalto é também preparado por exfoliação, em meio aquoso, por meio da intercalação de lactato, enquanto o tetra-butilamónio é utilizado na exfoliação do

óxido de níquel-cobalto. A resposta eletroquímica é avaliada em diferentes eletrólitos após reconstrução. Os resultados revelam a influência das espécies intercaladas durante o processo de exfoliação: quando a exfoliação é realizada para fins de armazenamento de energia, as espécies intercaladas e a força da interação com o material ativo devem ser consideradas de antemão para evitar o bloqueio superficial ou inibição da interação elétrodo-eletrólito. Os resultados mostraram que a exfoliação é uma rota promissora para aumentar a área de superfície ativa dos materiais, um parâmetro crítico no desempenho eletroquímico dos materiais dos eletrodos.

Nesta dissertação é também estudado o mecanismo de carga-descarga do hidróxido de níquel-cobalto, que ainda não está completamente entendido. Assim, compreender esse mecanismo é um passo crítico para otimizar a morfologia e o desempenho do material e para projetar futuros dispositivos de armazenamento de energia. Para esclarecer os processos que ocorrem durante a carga, aplica-se o modelo de Mott-Schottky foi aplicado parade modo a avaliar a variação da conductividade do material e da sua capacidade na interface elétrodo-eletrólito. Utiliza-se a micropotenciometria local para conhecer as variações locais de pH, pNa e O_2 dissolvido nas proximidades da interface. Os resultados evidenciam as variações na condutividade durante o processo de carga do material, enfatizam a importância do potencial aplicado durante a aquisição dos dados de espectroscopia de impedância eletroquímica para correta interpretação dos resultados e sugerem que a via mais viável durante a descarga de hidróxido de níquel-cobalto é um modelo de transporte de protões.

Palavras-chave: Hidróxido de níquel-cobalto, óxido de níquel-cobalto, grafeno, electrodeposição, exfoliação, armazenamento de energia.

Abstract

The increasing demand of energy in transportation, residential sector and industry, as well as the proliferation of more efficient renewable sources of energy require novel and more efficient energy storage devices. Consequently, recent efforts in material engineering are focused towards the development of nanostructured materials that can cope with said needs, ultimately related to the energy density, power density and cycling stability of the device. Many materials are currently being investigated as potential candidates for energy storage, which are classified in materials for batteries, capacitors, pseudocapacitors or supercapacitors. The aim of the present work is to generate materials with an intermediate electrochemical response between a supercapacitor and a battery, also known as hybrid electrodes. For that reason, nickel and cobalt hydroxides have been selected due to their high electrochemical activity and low cost and have been combined with graphene derivatives, which exhibit high conductivity and active surface area. Therefore, this work concerns the synthesis as well as the physicochemical and electrochemical characterization of nanostructured nickel-cobalt hydroxides and oxides and their combination with reduced graphene oxide for energy storage applications by means of two routes, electrodeposition and exfoliation.

On the one hand, electrodeposition is used to obtain nickel-cobalt hydroxides and oxides in combination with electrochemically reduced graphene oxide. Results evidence a synergistic effect when reduced graphene oxide is combined with nickel-cobalt (hydr)oxide, this is, an increase in capacity, conductivity and cycling stability of the material when compared to the parent nickel-cobalt (hydr)oxide. Moreover, special emphasis is done in the interpretation of electrochemical impedance spectroscopy to evaluate the phenomena occurring during continuous charge-discharge and discern the processes occurring within the active material that result in its degradation.

On the other hand, nickel-cobalt hydroxide is exfoliated in aqueous media by means of lactate intercalation while tetrabutylammonium cations are used in the exfoliation of nickel-cobalt oxyhydroxide; the electrochemical responses of both material types are evaluated in different electrolytes after re-stacking. Results reveal the influence of the intercalated species during the exfoliation process: when exfoliation is performed for energy storage purposes, the intercalated species and the strength of the interaction with the active material must be considered beforehand to avoid surface blockage or inhibited electrode-electrolyte interaction. Nonetheless, results corroborate that exfoliation is a

promising route to increase active surface area of the materials, a critical parameter in the electrochemical performance of electrode materials.

Finally, the charge-discharge mechanism of nickel-cobalt hydroxide is not completely understood yet. Thus, unveiling this mechanism is a critical step to morphology and performance optimization and design of future energy storage devices based on this material. To throw some light into the processes occurring during charge, the Mott-Schottky model has been applied to evaluate the variance of its capacitance at the electrode-electrolyte interface while local-micropotentiometry has been used to evaluate the pH, pNa and dissolved O_2 variations at the nearby of the interface. Results evidence the changes in conductivity during the charging process of the material, emphasize the importance of applied potential during the electrochemical impedance spectroscopy data acquisition for its correct interpretation and suggest that the most feasible route during charge-discharge of nickel-cobalt hydroxide is a proton transport model.

Key-words: Nickel-cobalt hydroxide, nickel-cobalt oxide, graphene, electrodeposition, exfoliation, energy storage.

- Résumé

La demande croissante d'énergie dans le transport, le secteur résidentiel et l'industrie, ainsi que la prolifération de sources d'énergie renouvelable nécessitent des dispositifs plus efficaces de stockage de l'énergie. Les récents efforts en ingénierie des matériaux sont axés sur le développement de matériaux nanostructurés susceptibles de faire face à ces besoins, tant en termes de densité énergétique (quantité totale d'énergie stockée par unité de masse ou de volume), de densité de puissance (puissance qui peut être transférée par unité de temps,de masse ou de volume), que de stabilité en cyclage, qui correspond à la dégradation des dispositifs en utilisation continue. De nombreux matériaux sont actuellement étudiés en tant que candidats potentiels pour le stockage d'énergie au sein des batteries, condensateurs, supercondensateurs (dispositifs pouvant stocker beaucoup plus d'énergie que les condensateurs tout en conservant une densité de puissance élevée) ou pseudocondensateurs. L'objectif de ce travail est d'élaborer des matériaux destinés à être utilisés dans des électrodes hybrides avec une réponse électrochimique intermédiaire par rapport à celles observées dans un supercondensateur et une batterie. Dans ce contexte, les (hydr)oxydes de nickel et de cobalt ont été choisis en raison de leur activité électrochimique élevée et de leur faible coût et ont été combinés avec des dérivés de graphène, qui présentent une conductivité et une surface active élevées. Ce travail concerne plus précisément la synthèse par deux voies, l'électrodéposition et l'exfoliation, d' hydroxydes et oxydes de nickel-cobalt nanostructurés, et leur combinaison avec l'oxyde de graphène réduit. L'accent a été mis sur la caractérisation physico-chimique et électrochimique pour les applications de stockage de l'énergie.

L''électrodéposition est utilisée pour obtenir des hydroxydes et oxydes de nickel-cobalt en combinaison avec de l'oxyde de graphène réduit électrochimiquement. Les résultats mettent en évidence un effet synergique qui se traduit par une augmentation de la capacité, de la conductivité ainsi que de la stabilité en cyclage du matériau comparativement à l'(hydr)oxyde nickel-cobalt parent. De plus, l'accent a été mis sur l'interprétation des phénomènes de dégradation survenant lors de la charge-décharge et sur l'identification des processus se produisant dans l'électrode et entraînant sa dégradation.

En ce qui concerne la deuxième voie de synthèse, l'(hydr)oxyde de nickel-cobalt est exfolié dans des milieux aqueux. Ceci est réalisé via l'intercalation d'entités lactate pour les hydroxydes et de cations tétrabutylammonium pour l'exfoliation des oxyhydroxydes. Les hydroxydes et les oxyhydroxydes de nickel-cobalt sont des matériaux lamellaires et,

par conséquent, peuvent être en feuillets par intercalation de molécules volumineuses dans un solvant dans des conditions adéquates. Ensuite, les réponses électrochimiques des deux matériaux sont évaluées dans différents électrolytes après délamination et ré-empilement. Les résultats révèlent l'influence primordiale des espèces intercalées lors du processus d'exfoliation, lactate et tétrabutylammonium,: la nature des espèces intercalées ainsi que les forces d''interaction avec le matériau actif doivent être considérées préalablement pour éviter le blocage de la surface et l'inhibition de l'interaction électrode-électrolyte. Les résultats corroborent que l'exfoliation est une voie prometteuse pour augmenter la surface active des matériaux, mais constitue néanmoins un paramètre critique dans la performance électrochimique des matériaux d'électrode.

Enfin, la dernière partie s'inscrit dans l'investigation du mécanisme de charge-décharge de l'hydroxyde de nickel-cobalt, qui n'était pas encore complètement compris à ce jour. L'appréhension de ce mécanisme est une étape critique pour l'optimisation des performances et la conception de futurs dispositifs de stockage de l'énergie basés sur ce matériau. Afin d'éclairer les processus de charge, le modèle de Mott-Schottky a été utilisé tandis que la micropotentiométrie locale a été mise en œuvre pour évaluer les variations de pH, de pNa et d'oxygène dissous à la proximité de l'interface. Les résultats mettent en évidence les changements de conductivité pendant l'oxydation (charge) du matériau, et soulignent l'importance du potentiel appliqué lors de l'acquisition des données de spectroscopie d'impédance électrochimique dans l'optique d'une interprétation correcte. Le modèle le plus probable lors de la charge-décharge de l'hydroxyde de nickel-cobalt s'avère être celui d'un transport de proton.

Mots clés: Hydroxyde de nickel-cobalt, oxyde de nickel-cobalt, graphène, électrodéposition, exfoliation, stockage de l'énergie.

II. Acknowledgements

A mi padre y a mi madre.

"Life is not about waiting for the storm to pass. Is about learning to dance in the rain."

- Viviane Green

Mi vida ha cambiado mucho durante estos cuatro años, llena de retos y obstáculos a superar. Tengo que agradecérselo a mucha gente, cuyo apoyo ha sido imprescindible para poder continuar sin perder el rumbo. En primer lugar, tengo que agradecerle esta tesis a mi padre, que siempre vivirá en mi corazón, y a mi madre, cuya fuerza de voluntad, esfuerzo y superación no deja de asombrarme. Esta tesis no habría sido posible sin vosotros dos. Gracias.

A mis abuelos, por darme tanto amor cuando era niño. No sería quien soy sin vosotros.

Tengo que agradecérselo también a mi familia de corazón, a mis amigos. Lore, Lau, Lucy, Ana Epistaxis y Ana Beni, gracias por visitarme en cada lugar que estoy y por ser tan grandes amigas. Gracias Jose, por estar desde los 4 años. Gracias a todos esos amigos que, no importa cuánto tiempo pase fuera, siempre me recogen con los brazos abiertos, amor y planes de lujo: Juan, Marc, Pepelu, Víctor, Mary, Ferran, Erik, Fer, Didac, Nacho, Pablito, Heresy, L'Època, Adewello, Anih, Diana, Alfonso, Juanito, Miguel, Itachi, Jefa, Jordi, Juan Palomo, Ana Lluch, Laurita, Molina, Saúl, Robin y Esther, Tamara, Paula… Espero no dejarme a nadie! Tengo mucha suerte y jamás podría haber sobrevivido estos años sin vuestro apoyo. También a mis compis de carrera, que ya son amigos para toda la vida, Bea, Ángel, Marta, Sandra, Driss, Noe, Jorge y Jesús.

I would like to express my most sincerely gratitude to Prof. Fátima Montemor and Prof. Liliane Guerlou-Demourgues, they have not only guided me during my scientific growth but have also supported and helped me in the times I needed it most. I have learned a lot from you.

I would also like to thank the International Doctoral School in Functional Materials (IDS-FunMat) for giving me this excellent opportunity to research in a field I have deeply enjoyed and discover two beautiful cultures in the meantime. I would also like to thank all the people I have met during our one-week spiritual retirments, from colleagues to professors, and all the people dealing with administrative issues (Carla Carvalho, Ana Pipio, Marianne Delmas, Audrey Sidobre and Christopher Niesen). This wonderful experience has brought some new friends into my life!

I would also like to thank all the people I have had the pleasure to work with, both in IST and ICMCB (counting PLACAMAT and the Centre de MicroCaractérisation Raimond Castaing). Some of you have been great support. Thanks to Maria João Carmezim, Raquel Duarte, Sonia Eugénio, Cathy, Sabine, Philippe Dagault, Philippe Legros, Marion Gayot, Christine Labrugere, Philippe Dagault, Stephane Le Blond de Plouy, François Weill, Patrizia Paradiso, Maria Julio, Sonia Buffière, Eric Labraud, Isabel Nogueira, Laura Ilharco, Auguste Fernandes. I would especially like show gratitude to Prof. Teresa Silva, with whom I have really enjoyed correcting articles.

To all the friends I made during my stay in France, Miguel, nos lo hemos pasado demasiado bien, Chris, Teba, Ángel, Marina, Amelia, Mingming, JB, Clem, Marion, Marie, Marine, Angela, Celine… I will always remember some of our awesome moments!

To my colleagues and friends in Lisbon, Maryna (qué sería de mi sin nuestros cafés), Tuyen, Alejandra (que suerte haberte tenido cerca en mis primeras andadas en Lisboa), Kevin, Kush, Rodrigo, Kasia, Miguel (o melhor parceiro de mesa), Lénia, Mafalda, Mario, Teixiera, Joana, Marta, Yegor, Roma, Olesya, Bernat, Laura, Andreia, Natalia, Quico, Darya, Jay, Wilson, Simone, Etienne, Ramzi, Ivan, Tiago… you have all been great. Gracias Raquel por tu apoyo durante estos últimos meses.

My most sincere **thank you** to all of you.

III. Table of Contents

IV. List of figures

V. List of tables

VI. Abbreviations and Acronyms

AFM	Atomic force microscopy
BET	Brunauer-Emmett-Teller
CP	Conductive polymer
CPE	Constant phase element
CQD	Carbon quantum dots
CTAB	Cetrimonium bromide
CV	Cyclic voltammetry
CVD	Chemical vapour deposition
ED	Electrodeposition
EDS	Energy Dispersive X-Ray Spectroscopy
E_{FB}	Flatband potential
EIS	Electrochemical impedance spectroscopy
EQCM	Electrochemical quartz cristal microbalance
Er-GO	Electrochemically reduced graphene oxide
ESD	Energy storage devices
FEG-SEM	Field-emission gun scanning electron microscopy
FTIR	Fourier-transform infrared spectroscopy
GCD	Galvanostatic charge-discharge
GIXD	Grazing-Incidence X-Ray Diffraction
GO	Graphene Oxide
HOPG	Highly-oriented pyrolytic graphite
HER	Hydrogen evolution reaction
HMT	Hexamethylenetetramine
HOPG	Highly oriented pyrolytic graphite
HR-TEM	High-resolution transmission electron microscopy
LDH	Layered double hydroxide
MWCNT	Multi-wall carbon nanotube
OER	Oxygen evolution reaction
PANI	Polyaniline
PEDOT	Poly(3,4-ethylenedioxythiophene)
PPy	Polypyrrol
PS	Polystirene
PTFE	Polytetrafluoroethylene
rGO	Reduced graphene oxide
SAED	Selected area electron diffraction
SCE	Saturated calomel electrode
SDS	Sodium dodecyl sulphate
SIET	Selective ion electrode technique
SSD	Solid-state diffusion
TBAOH	Tetrabutyl ammonium hydroxide
TMAOH	Tetramethyl ammonium hydroxide
XPS	X-ray photoelectron spectroscopy
XRD	X-ray diffraction

State of the art

1. Materials for Electrochemical Energy Storage

The United Nations has pin-pointed climate change as one of the eighteen global issues of biggest concern in the world, and energy as one of humanity top problems for the next century. As a consequence, more than 3000 international environmental agreements have been developed to raise awareness and shift towards a more sustainable growth [1]. Our lifestyle is sustained by energy production and consumption. However, up to an 80% of the energy production derives from the combustion of fossil fuels, which leads to the formation of CO_2, the main driver of climate change [2]. Another big concern is the depletion of those fossil fuels. According to the U.S. Energy Information Administration, there has been an overconsumption of energy during approximately the last 60 years, as seen in Fig. 1.1. In fact, the main sources used to produce energy are coal, natural gas and crude oil [3], all non-renewable sources.

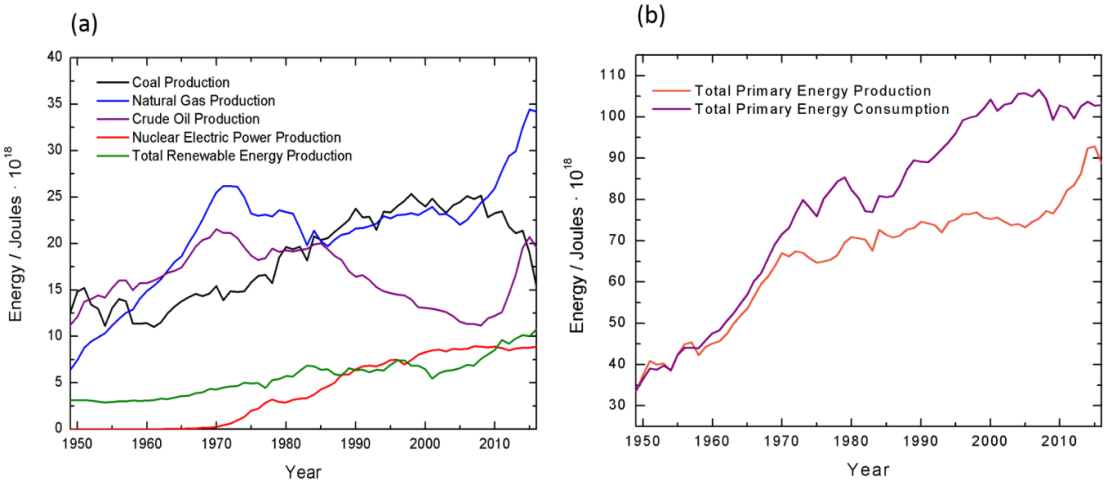

Fig.1.1. (a) World Energy Consumption and Production and (b) Source of Energy production overview from 1949 to 2016. Data extracted with copyright permission of the U.S. Energy Information Administration [3].

Thus, to ensure a sustainable development, an energy transition is required. Humanity shall reduce their petroleum, natural gas and coal energy consumption and transition into renewable sources of energy, including geothermal, solar, wind, biomass and hydroelectric. However, there is a major issue concerning renewable energy sources and their production intermittency [4]. Nonetheless, there are three more aspects to sustainable energy usage that shall be optimized apart from production, namely; transport, conversion and storage.

In particular, energy storage plays a key role in the transition to low-carbon economies. Fully-functional energy storage reservoirs that can deliver reliable power to an ever-growing society (Fig. 1b) are crucial [5].To comply with the European Union policy goals for 2030, an increase in the electrification of the energy system is expected. In the past, due to the existence of daily consumption cycles of electricity, mainly based on fossil fuels, nuclear energy and hydrothermal production, the need of variability in the energy production was not relevant. As a consequence, the necessity for energy storage was limited. It is reported that in 2014 the total amount of electricity stored was estimated to 171 GW, a 2% of the total generation. However, energy consumption patterns have been changing relatively fast; nowadays there is an increased demand of energy in electric form and energy for operative off-grid technologies [6].

Regarding the delivery of electricity, smart grids and flexible generation are required for a successful societal development. Smart grids are electrical grids in which appliances and metrics are employed, such as renewable and efficient energy resources; being *conditioning and control of the production* and *distribution of the electric power* two of their most important characteristics [7,8]. An adequate amount of energy can only be efficiently supplied if the corresponding energy storage system has the properties to satisfactory perform that task. For that reason, optimized energy storage systems shall be developed.

Moreover, it is well known that many recent technologic developments rely on mobile energy storage suppliers. Devices such as laptops or mobile phones need to be transported. Most of the devices are not designed to require a constant supply of electricity but to be independent from the general grid. Thus, another risen challenge to consider is how to tailor the properties of an energy storage device so it can comply with the energetic demand of a particular application. Therefore, there is an increasing need to improve the current ability to store energy. If we are unable to capture, manage and store energy efficiently, the only alternative, but unlikely solution, would be to reduce energy consumption [9].

For that reason, different energy storage systems have been developed and are under constant improvement. All the energy storage systems developed so far can be classified in five different groups: mechanical, thermal, chemical, electrochemical and electrical. Fig. 1.2 demonstrates a more accurate categorization of energy storage systems.

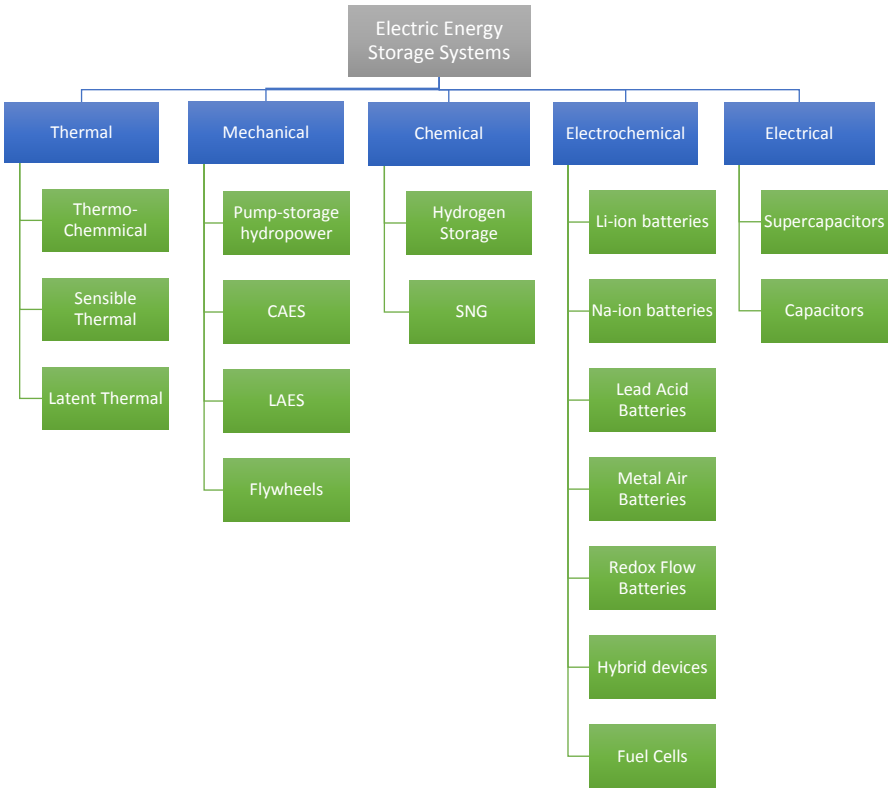

Fig. 1.2. Scientific categorization of Electrical Energy storage systems. CAES stands for Compressed Air Energy Storage; LAES for Liquid Air Energy Storage; SNG for Synthetic Natural Gas. Note that this list is representative of the major electrical energy storage systems and may not include all of them. Diagram extracted and modified with copyright permission of the E-Storage report on World Energy Resources by the World Energy Council [10].

Depending on the duration and the frequency of the power supply required by an application, different energy storage systems may be used. For example, in applications that require seconds to minutes of power supplies, batteries, supercapacitors or flywheels may be used; whereas for slightly longer periods of times, this is daily usage, batteries, pump hydropower, CAES/LAES, thermochemical or redox flow batteries would be used [10]. This is exemplified in Fig. 1.3.

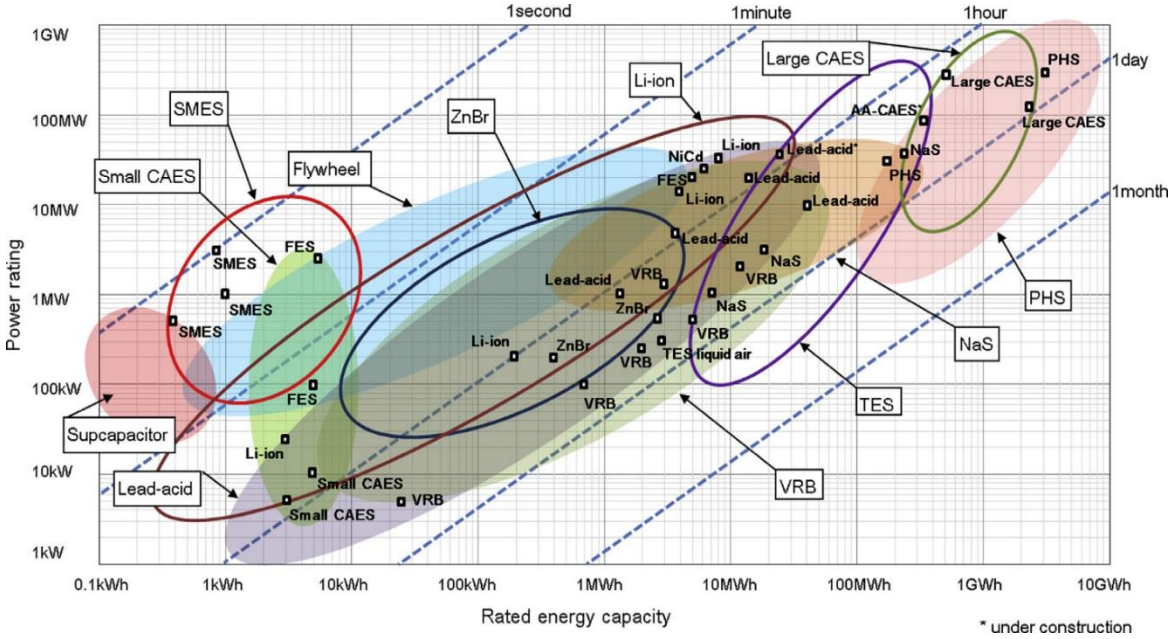

Fig.1.3. Diagram exemplifying the type of suitable applications for an energy storage device according to the power and energy required. Reprinted with Copyright permission from Clarke et al. [11]

Regarding mechanical systems, pumped hydro-energy storage has been dominating the energy storage market for over a century. It simply consists on generating electricity by moving water between two water tanks at different levels. Compressed air energy storage uses off-peak electricity to compress air in geological structures that is released to drive a turbine when energy is required. Liquid air energy storage is similar, but the air is compressed and cooled in refrigeration plants. Finally, flywheels store kinetic energy in rotating discs that are suspended on magnetic bearings [10]. However, although mechanical systems are able to bridge short imbalances in energy demand, they are quickly depleted [12].

Thermal systems are classified in three different groups depending on their fundamental principles. Thermochemical are based on reversible temperature-dependent chemical reactions such as sorption-based reactions. Latent thermal storage is based on phase transitions. Sensible thermal storage is based on materials with very high thermal capacities. Thermal storage applications are, unfortunately, very limited [10].

Concerning chemical energy storage, energy can be stored in the form of hydrogen or synthetic natural gas, also called “power gas” technologies, which consist of water splitting followed by the reaction of carbon dioxide with hydrogen by means of an electrolyser to produce synthetic methane [13].

This suite of diverse technologies is constantly evolving, and new energy storage systems are continuously being developed. In fact, exhaustive research is being done on all of the different energy storage systems presented. Nonetheless, it is of particular interest to further develop electrochemical and chemical energy storage devices. Although it is an

outdated non-environmentally-friendly technology, lead-acid batteries dominated the market from 1990 to 2015, accounting for a 90% of the total market [14]. Storage in commercial batteries currently fail to reach the required energy storage densities required for the energy reservoirs to supply the whole economy [12]. For that reason, a great focus of research is being done in the field of electrochemical energy storage, impulsed by the tremendous growth of the battery demand during the last decade, as shown in fig. 1.4 [15].

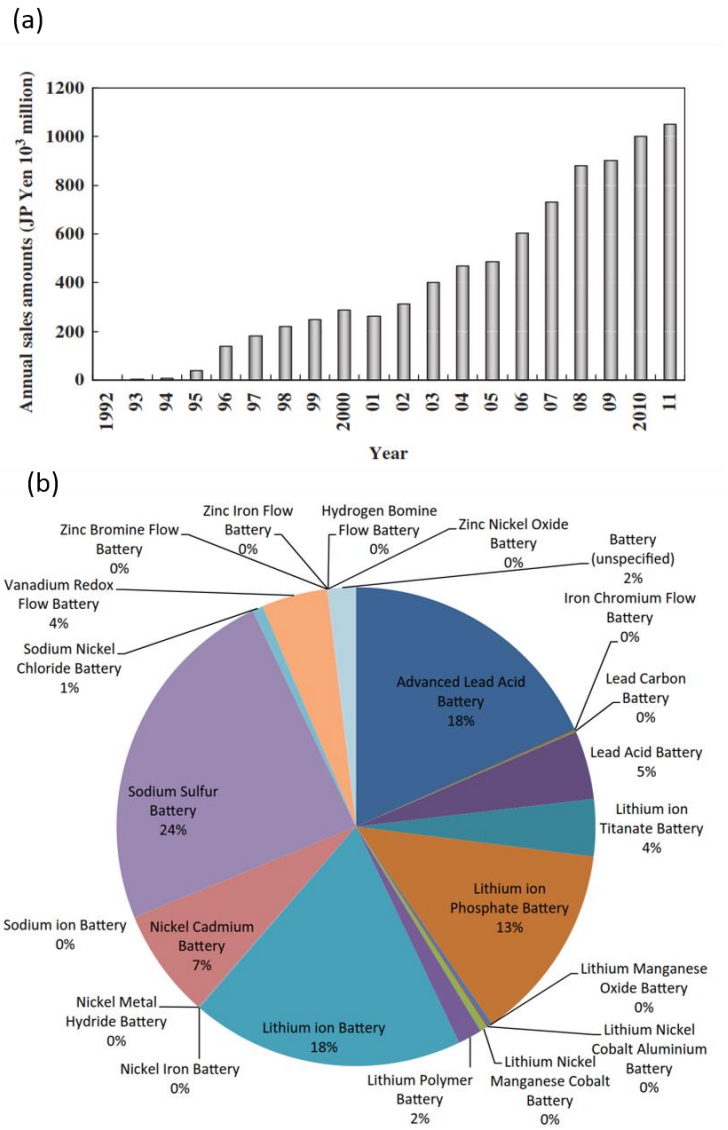

Fig. 1.4. (a) Growth of the market demand for Lithium-ion batteries, reproduced from Lithium-Ion batteries: Advances and applications, edited by Gianfranco Pistoia [15]. (b) Partition of the technology share that each energy system has exemplifying the diversity of different battery research being conducted. Image obtained with copyright permission from Aneke et al. [16].

In the pursuit of refined and efficient energy storage systems with tailored properties, many different electrochemical and electrical energy storage systems and combinations thereof have been developed. The fundamental principles of electrochemical energy storage systems and electrical systems shall be understood and are discussed and compared in the following section.

Electrochemical Energy Storage

As aforementioned, there is an increased interest in tailoring the properties of energy storage devices (ESD) for specific applications. Among the different energy storage devices, a possible approach towards optimised energy usage is the study of electrochemical and electrical systems.

On one hand, electrical energy storage devices are divided into two main groups, capacitors and supercapacitors. On the other hand, fuel cells and batteries integrate the group of electrochemical ESDs. However, in the development of new energetic solutions, novel electrochemical responses and device configurations are achieved that have intermediate outcomes. For that reason, the division between the two, although clear in their fundamental principles, is not always straightforward when a system response is evaluated. For that reason, an overview to the different ESDs configurations is here introduced.

Furthermore, any given technology has some features that makes it suitable for a specific application. These features determine the best technology to be adopted and shall also be evaluated to understand the extent to which the commercially available devices are different. The properties that determine the functional units of an energy storage system are: energy density and power density, life time, capital and operating costs, storage capacity and duration, round trip efficiency (defined as the "ratio of electricity output from the storage device to the electricity input to the device during one charge/discharge cycle") and response time [16].

Nowadays, given the different electrochemical responses, this type of energy storage systems can be classified in four groups, as shown in figure 1.5, namely; capacitors, supercapacitors, pseudocapacitors or redox supercapacitors and batteries. Note that fuel-cells are not considered since they are out of the scope of the present work. Moreover, because of the extensive work performed in this topic, only an overview of the main materials and not an in-depth review of all the materials involved in electrochemical energy storage is provided.

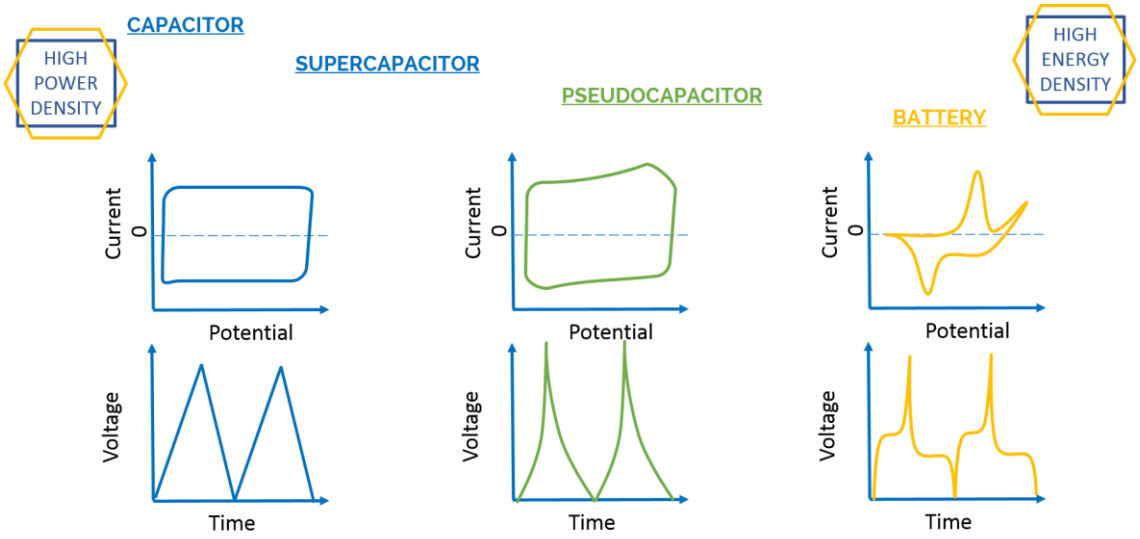

Fig. 1.5. Classification of the different electrochemical energy storage devices depending on the electrochemical response of the electrode materials.

It is worth delimiting the scope of the present work. Many aspects of electrochemical energy storage devices have not been included, such as some less explored materials and

composites, different current collectors, an exhaustive review on electrolytes used or an exhaustive study of different synthesis techniques. For example, metal-organic frameworks, quantum dots, nitride-based composites and composites based on organic active materials, beyond conductive polymers, are fascinating fields of study in the field of super- and pseudocapacitive energy storage that have not been included. Some information can be found in the appropriate literature such as the review of Aurback et al. [17] or the review by Wu et al., which summarizes the latest developments in electrode materials for super- and pseudocapacitors [18]. In the same manner, there are appropriate reviews in most of the major components of energy storage devices. This chapter is only intended to provide a review on the state-of-the-art and major developments in the field of materials for energy storage with emphasis in nickel oxides and hydroxide, cobalt oxide and hydroxide, graphene-based materials and combination thereof.

1.1 Capacitors

Capacitors, also known as electrostatic capacitors, store electricity by means of charge separation. They are usually made of two parallel metal electrodes that are separated by a dielectric material. The dielectric material acts as an insulator preventing the recombination of both charges. This configuration is shown in Fig. 1.6.

The accumulated charge at the electrode interface comes from two different possible sources. It is either the result of an excess or deficit of conduction-band electrons at the surface (or near-surface) regions of the active material or from the counterbalancing of charge densities accumulated on the electrode-electrolyte interface [19].

The unit for the energy stored in a capacitor is capacitance. Capacitance is mathematically described by the ratio between the positive, or negative, charge stored at each plate and the voltage applied between them, as expressed by equation 1.1:

$$C = \frac{Q}{V} \qquad (eq.\,1.1)$$

The dielectric plays a key role in the performance of the capacitor since the operating voltage greatly depends upon its strength. Then, the dielectric strength is defined as the maximum electric field that can exist in the dielectric without electrical breakdown. Capacitance is measured in Farads (F), which is the ratio between coulombs (Q) and volts per metre (V/m) [20] and traditional capacitors are at the order of microfarads.

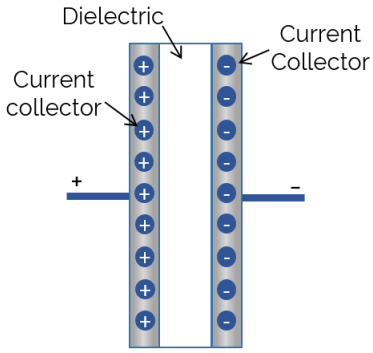

Fig. 1.6. Schematic representation of a capacitor configuration.

The application of capacitors goes from backup circuits of microcomputers to smoothing circuits in power supplies and DC blocking in signal filtering. These applications do not require much energy but depend on fast charge-discharge [21].

Traditional capacitors are usually composed of two metallic plates, traditionally based on aluminium, tantalum or ceramic materials, with a solid electrolyte used to separate two identical electrodes [21]. The non-conductive dielectric is usually glass, ceramic, plastic film, paper, mica or oxide layers. Electrolytic capacitors are a form of capacitors in which the construction is similar to that of a battery, with a conductive electrolyte salt, but with the same electrode materials as regular capacitors [20]. However, traditional capacitors cannot store enough energy in the volume/weight available and research is more focused towards developing electrochemical double layer capacitors, which are of much higher energy density.

1.2 Electrochemical double layer capacitors

Electrochemical double layer capacitors, also known as ultracapacitors or supercapacitors, utilize high-surface area electrode materials and thin electrolytic dielectrics to achieve capacitances that can be orders of magnitude higher than traditional capacitors. The porous nature of the electrode material enables a much higher energy density of these devices as compared to traditional capacitors. As suggested by its name, a double layer capacitor must employ two double-layers of counter-ions, one at each electrode interface, with counterbalancing charge densities on the electrode surface. The capacitance is associated with the electrode-potential-dependent accumulation of electrostatic charge at the interface by means of surface dissociation and ion adsorption as the only accumulation of surface charge. During the charging process, the electrons travel from the negative electrode to the positive through an external load. Simultaneously, cations in the electrolyte move towards the negative electrode while anions move to the positive electrode with no variation of the electrolyte composition or concentration [22].

Their behaviour is explained by equation 1.2.

$$C = \varepsilon_o \frac{A}{d} \qquad (eq.\,1.2)$$

where A represents the electrode surface area, d is the separation between the electronic and ionic charge and ε_o is the medium permittivity. Electrodes with optimized surface area can reach up to 1000-2000 $m^{2} \cdot g^{-1}$. Thus, although they have a similar structure to electrolytic capacitors, as seen in Fig. 1.7, they can store much more charge. As evidenced by equation 1.2., capacitance depends on the distance between the ionic charge and the electronic charge and, in this case, it is determined by the electrode-electrolyte interface, at the order of Ångström. Thus, the capacitance is severely increased.

Since each interface generates a capacitor on its own but two electrodes are required, a complete cell can be considered as two capacitors in series. Thus, the cell capacitance will be described as [23]:

$$\frac{1}{C_{cell}} = \frac{1}{C_1} + \frac{1}{C_2} \qquad (eq.\,1.3)$$

Electrochemical capacitors can consequently be classified into two main groups, symmetrical and asymmetric. The former group uses the same electrode material for both electrodes while the latter uses different materials for the cathode and the anode. It is worth mentioning that the electrolyte can either be organic (acetonitrile or propylene carbonate for example) or aqueous (potassium hydroxide or sulphuric acid for instance) in nature [20].

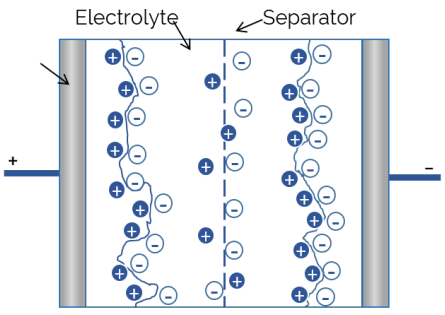

Fig. 1.7. Schematic representation of an electrochemical capacitor.

Supercapacitors are mainly evaluated by four parameters, energy density, power density, charge-discharge cycling and operational voltage window. The energy density (E) and power density (P_{max}) are calculated according to:

$$E = \frac{1}{2} CV^2 \qquad (eq. 1.4)$$

$$P_{max} = \frac{V^2}{4R} \qquad (eq. 1.5)$$

Where V is the nominal voltage and R the equivalent series resistance (ESR) in ohms [24]. In general, supercapacitors have a specific energy comprised between 1-10 $W \cdot h \cdot kg^{-1}$ with a specific power in the range of 500-10.000 $W \cdot kg^{-1}$, which corresponds from seconds to minutes of charge-discharge time. They are greatly dependent on the capacitance of the device, based on the electrode material characteristics, mainly, surface area and pore-size distribution. Moreover, due to their lack of chemical reactions, they can be cycled up to 500.000-1.000.000 times without losing capacitance. Due to the highly reversible nature of electrostatic storage, no changes are produced in electrode volume, eliminating swelling, mechanical degradation or other phenomena associated to chemical reactivity [23,25].

On the other hand, the operational voltage window is greatly dependent on the solvent used in the electrolyte. Aqueous electrolytes, either acidic or alkaline, have high ionic conductivity, low cost and are widely accepted, especially due to their low environmental impact. However, they are limited by water decomposition potential range, which is approximately 1.23V [26]. Aqueous solvents are, nonetheless, interesting due to the higher capacitance than carbonaceous materials exhibit as compared to their non-aqueous counterpart. This is the result of their higher dielectric constant and lower internal resistance [27]. Non-aqueous electrolytes, for instance, propylene carbonate containing quaternary alkyl ammonium salts, have shown expanded operating voltages up to 2.5V [26].

When selecting a material for supercapacitor applications, a unique set of properties is sought [23]:

- High electronic conductivity.
- High active surface area with controlled pore structure.
- Good chemical and thermal stability and corrosion resistance.
- Processability and compatibility in composite materials.
- Low cost.

Among the materials used for supercapacitors, carbon is the most developed and studied form [28]. There is an extensive variety of carbon materials with different properties due to their different physical and chemical characteristics. Currently, the main focus is to develop high-surface area with low matrix resistivity. The role of carbon in supercapacitors has different forms: electro-conductive additive, support for active material, electron transfer catalysis, intercalation hosts, substrates for current leads, and as heat-transfer, porosity surface area or capacitance controllers [23].

Most of commercial carbon-based materials are described as “engineered carbons”. These are amorphous carbons with a more or less disordered microstructure based on graphite [29]. The extent of graphitization is based on thermal treatment in which sections of hexagonal carbon layers regain order between the layers in a stacking process. Between

amorphous carbon and graphite, a wide range of materials with tailored properties can be prepared for specific applications.

Active carbons are usually obtained from carbon-rich organic precursors, such as natural materials (coconut shells, wood, pitch or coal) or synthetic materials (polymers) that are thermally treated in a carbonization process in inert atmosphere. By means of a selective oxidation process, active surface area or pore volume can be increased [28]. Moreover, carbon can be functionalized with surface groups to manipulate their double-layer properties, such as wettability, point of zero charge, electric contact resistance, ion adsorption or self-discharge characteristics [30]. Therefore, by controlling the ratio between edge sites, which are more reactive, basal sites and the degree of disorder, the chemical properties of a carbon-based materials can also be tuned. Functionalization of carbon-based materials can be done with oxygen, hydrogen, nitrogen sulphur and halogens by means of physical or chemical bonding; the most important being surface oxides in acidic, basic or neutral form.

Given the importance of this type of materials in supercapacitor technology, different types of carbon are available, which Pandolfo et al. [23] grouped in: Carbon blacks, carbon aerogels, carbon fibres, glassy carbons, carbon nanotubes and nanofibres and graphene and Brousse et al. [17] recently complemented with carbon quantum dots and onion like carbons, N-doped carbons and carbon-based composites.

Carbon black

Carbon blacks consist of carbon colloids with quasi-spherical shape. They are usually produced by partial combustion/thermal decomposition of hydrocarbons in the gas phase that produce colloidal carbon particles that agglomerate in various morphologies [31]. Given their high conductivity (10^{-1} to 10^{2} $\Omega^{-1}cm^{-1}$), small particle size, structure and large active surface area (>1500 m^2g^{-1}) , porosity and surface chemistry they have been widely applied for energy storage applications as conductive fillers [32]. Supercapacitors using carbon black as electrode material have shown up to 250 $F \cdot g^{-1}$ [33,34]. Nevertheless, carbon blacks suffer from low density and usually require high amount of binders to produce stable electrodes, resulting in poor conductivity and volumetric capacitance [23].

Carbon aerogel

Carbon aerogels are highly porous materials that are generally synthesized by poly-condensation of resorcinol and formaldehyde via sol-gel and subsequent pyrolysis [35]. Sol-gel process enables the tailoring of the macroscopic properties of the aerogel and, when derived from the aforementioned precursors, they can reach active surface areas at the order of 400-1000 $m^2 \cdot g^{-1}$ with 2-50 nm diameter pores and high density. Moreover, after pyrolysis, they are usually more conductive than most activated carbons. This technique enables the production of different morphologies, as diverse as thin-film and powders, without the need of binders, under certain conditions. Regarding, their electrochemical response, studies have shown that carbon aerogels with pore diameters within 3 to 13 nm showed the highest capacitances and capacities up to 18 $\mu F \cdot cm^{-2}$ and 50 $F \cdot cm^{-3}$ have been achieved [23,36].

Carbon fibres

Carbon fibres are produced from thermosetting organic materials. A precursor, such as cellulose or polyacrylonitrile is melt and extruded into a thin fibre. It is then stabilized at 200-400 ºC and carbonized at 800-1500 ºC. It can be further oxidized in a controlled atmosphere or graphitized with a thermal post-treatment. The quality of the precursor materials and the assembly of the aromatic constituents in their entangling will determine

the final properties of the material. In general, they exhibit micro-porosity (<2 nm) with good accessibility to active sites because of the limited fibre dimensions, which results in large exposed surface area. Pore diameter and length can be, in some extent, controlled, resulting in high adsorption capacity and adsorption rates. Carbon fibres can be obtained in many forms. Active carbon foam cloths with surface up to 2500 $m^2 \cdot g^{-1}$ are commercially available with good electrical conductivity and large active surface area [37–39].

Glassy carbons

Glassy carbons are synthesized by thermal degradation of polymer resins and their properties are usually dependent on the maximum heat treatment. Optimum performance has been achieved at 1800ºC. Its accessible surface area is relatively small as compared to other carbon forms, with pores in the 1-5 nm range. Due to its low electrical resistivity, it has been considered for high-power supercapacitor applications with a reported capacitance of approximately $13 \mu F \cdot cm^{-2}$ [40]. In an attempt to enhance this value, electrochemical or thermal oxidation processes have been done, achieving extended active surface areas of 1800 $m^2 \cdot cm^{-3}$ and ~20 $\mu F \cdot cm^{-2}$ [23,41,42].

Carbon quantum dots

Carbon quantum dots (CQD) demonstrate low volumetric capacitance on their own and are hard to synthesize. However, they can be supported on top of a 3D carbon matrix, leading to increased capacitance. Similar results can be found for nanotubes, graphene or other nanomaterials. Moreover, yielding enough quantity is currently unfeasible for practical applications. Most are developed by means of complicated processes that result in low yield. For that reason, they are generally studied as part of a composite material [17]. These zero-dimensional carbon nanomaterials benefit from high specific surface area, low toxicity, chemical stability and biocompatibility that, when combined with macrostructured materials can yield promising results. For instance, Qu et al. prepared a 3D carbon quantum dot aerogel by means of resorcinol and formaldehyde in sol-gel polymerization. After argon pyrolization the electrode had a capacitance of 294 $F \cdot g^{-1}$ at 0.5 $A \cdot g^{-1}$ with a 6% loss after 1000 cycles [43]. Activated carbon was also combined with carbon quantum dots by one simple sonication step by Porat et al. resulting in a 0.185 $F \cdot cm^{-2}$ capacitance and excellent cycling stability [44]. In a similar way, CQD have been combined with graphene but results were less promising, 0.44 $mF \cdot cm^{-2}$ after 1000 cycles. This poor performance was attributed to graphene agglomeration [45].

Carbon nanotubes and nanofibers

Carbon nanotubes (CNTs) and nanofibers are usually produced by catalytic decomposition of hydrocarbons with controlled nanostructures and crystallinity [46]. Both single-walled and multi-walled carbon nanotubes were considered for supercapacitor applications due to their morphology, which confers low electrical resistivity, high porosity and an accessible structure. Studies have been performed in both aqueous and non-aqueous electrolytes, however, they present low gravimetric and volumetric density as compared to activated carbons. Depending on the morphology and purity of CNTs, different values of specific capacitance have been obtained. Thus, purified CNTs, without traces of catalyst from the synthesis procedure or amorphous carbon, have a mesoporous structure with capacitance between 15 and 80 $F \cdot g^{-1}$ [47]. Specific capacitance can be increased to 130 $F \cdot g^{-1}$ by oxidative treatments that induce pseudocapacitance. Activation strategies by means of KOH have been undertaken, resulting in an increased surface area from 430 to 1035 $m^2 g^{-1}$ and a specific capacitance of 90 $F \cdot g^{-1}$. On the other hand, multi-walled carbon nanotubes exhibited microporosity

with enhanced accessible surface with a capacitance of 102 $F \cdot g^{-1}$ in sulphuric acid [48]. Other strategies, such as combining it with polymers, resulted in capacities as high as 265 $F \cdot g^{-1}$, for instance, when combined with polypyrrole [49]. Nonetheless, the specific energies obtained by means of carbon nanotubes have great dependence on their synthesis method and are generally lower than for conventional carbons, which tend to have larger surface areas [23].

CNTs have been combined with activated carbon to enhance their electrochemical response. Noked et al. dissolved CNTs in a mixture of vinyl dichloride monomer before polymerization followed by carbonization and activation, resulting in 200 $mF \cdot cm^{-2}$ and nearly 100% capacitance retention after 50 000 cycles [50]. Hierarchical morphologies may lead to better electrochemical performances, as some results have already suggested (CNTs on top of carbon nanofibers reached 70 $W \cdot h \cdot kg^{-1}$ at 0.5 $A \cdot g^{-1}$ with 3% capacitance fade after 20 000 cycles [51]) although proper material and experimental designing must be undertaken for the material to achieve competitive performances.

Doping carbons with nitrogen induces chemical and physical alterations that are ultimately reflected in their electrochemical activity. Most synthesis rely on nitrogen-containing precursors, although they usually have limited nitrogen content [52,53]. A three step method consisting of carbonisation, nitrogen functionalization and activation was recently developed, leading to 6.8$\mu F \cdot cm^{-2}$ [54]. However, more attempts to improve capacitance must be undertaken. For example, different studied strategies have been reducing the size of mono-dispersed particles, displaying 390 $F \cdot g^{-1}$ at 1$A \cdot g^{-1}$ and 2% capacitance drop after 8000 cycles [55], or introducing nitrogen-enriched carbon particles on top of organic cores, exhibiting 260 $F \cdot g^{-1}$ at 20 $mA \cdot g^{-1}$ [17].

Graphene

Graphene is another promising material for energy storage applications. Given its relevance in the present work, a more in-depth study of the state-of the art is included at the end of this chapter.

Table 1.1
Comparison of the average capacitance values displayed by different carbon forms. Reproduced with copyright permission of [56].

Carbon-based material	Capacitance ($F \cdot g^{-1}$)
Activated carbon	<200
Activated carbon fibre	120 – 370
Templated carbon	100-350
Carbon aerogel	100-125
Carbon nanotube	15-135
Graphene derivatives	14-270

In many cases, optimizing the synthesis of a carbon-based material is merely based on optimizing pore size and distribution and accessible surface area. However, recent findings have revealed a contribution of micro-porosity to the capacitive mechanism. This highlights the lack of fundamental understanding of electrochemical interfaces at the nanoscale and the behaviour of confined ions [28,57,58]. This challenges the conventional theory of the double layer with solvated ions adsorbed on both sides of the pore walls. Current research is being devoted to developing materials in which higher capacitance is achieved by matching pore size with ion size and by eliminating macro- and mesopores. However, experimental results depend upon a great number of variables and, therefore, computational simulation shall be used in the future designing and

understanding of electrical double layer capacitors and re-evaluate the double layer theory to account for solvation and de-solvation effects.

Experimentally, Gogotsi et al. [59] reported carbide-derived carbons with pore sizes smaller than 1 nm that showed enhanced capacitance. Results suggested that capacitance can be increased when the diameter of the pore is smaller than that of the solvated electrolyte ion. If a uniform mesoporous structure is achieved, high-capacity and high-rate capability carbons can be produced. Thus, designing mesoporous channels that enable electrolyte penetration, combined with controlled micro- and mesopore walls with increased number of active sites may result in increased capacitance. This is the case for the ordered hierarchical mesoporous/microporous carbon developed by Liu et al. [60], which achieved 146 $F \cdot g^{-1}$ in organic electrolytes and good scan rates (up to 200 $mV \cdot s^{-1}$) and for resol-derived hierarchical porous carbon developed by Li et al. [61], which showed the high capacitance of 307 $F \cdot g^{-1}$ in 6M KOH.

New applications for supercapacitors are constantly being developed, there is great number of publications in the application of supercapacitors. Nonetheless, Sharma and Bhatti considered [20]:

- Memory back-up: reliable and durable short-term emergency supply.
- Electric vehicles: used when a peak load is required, such as in accelerating or mountain driving. They are also used in regenerative braking to reduce fuel consumption.
- Power quality: Improving the reliability and quality of power distribution.
- Battery monitoring: When short, high-current bursts of energy are required it is extremely demanding for a battery. Supercapacitors relieve the battery by meeting the power requirements extending the battery lifetime.
- Portable power supplies: Adequate for moderate energy-demanding devices.
- Electrochemical actuators: Actuation systems usually demand pulsed currents with high power peak requirements. Supercapacitors are used to manage the peak load in combination with batteries to supply the required energetic amount.
- Adjustable-speed drives: Used in industry, they tend to have power fluctuations. Supercapacitors can adequate their power disturbances and voltage fluctuations and require no maintenance.
- Renewable energy applications: Batteries have a short lifetime because continuous cycling has a detrimental effect on them. Supercapacitors increase this lifetime up to 20 years. It is also noticeable the increase of energy efficiency.

1.3 Pseudocapacitors

Pseudocapacitors are devices that use fast electrochemical surface reactions or pseudo-intercalation in combination with electrostatic mechanisms to store their charge. This principle allows increased energy density while maintaining fast charge-discharge rates [62]. Conway [19] identified three main faradaic processes by which pseudocapacitance is possible, namely, underpotential deposition, redox pseudocapacitance and intercalation pseudocapacitance.

Despite having very similar electrochemical fingerprints, these processes are based on completely different physical mechanisms. Underpotential deposition or reversible adsorption is based on the adsorption of metal ions on top of another metal surface well above their redox potential. This is the case, for instance, for lead on top of a gold surface [63]. Redox pseudocapacitance has a different mechanism. In this case, ions are simultaneously adsorbed on top of a material's surface producing a faradaic charge-transfer. Finally, intercalation pseudocapacitance is founded on the intercalation of ions into tunnels, present at the electrode, producing a charge-transfer faradaic reaction that does not involve a phase transition. Both intercalation and redox pseudocapacitance are exemplified in Fig. 1.8.

Although different in nature, these processes can be equated when evaluating their potential response as a function of the extent to which either adsorption/desorption or intercalation at the electrode-electrolyte interface has occurred (total charge stored). This is exemplified by equation 1.6:

$$E \approx E^0 - \frac{RT}{nF}\ln\left(\frac{\chi}{1-\chi}\right) \qquad (eq.\,1.6)$$

where E is the potential (V), R is the ideal gas constant ($J \cdot mol^{-1}K^{-1}$), T is the temperature (K), n is the number of electrons and F is the Faraday constant ($C \cdot mol^{-1}$). Finally, χ can be the fractional coverage of the surface or the inner structure, the extent of fractional absorption or the extent of conversion of an oxidized species to their reduced form [19,63]. As shown in equation 1.7, capacitance is defined for those regions in which the plot E vs. χ is linear:

$$C = \frac{nF}{m} \cdot \frac{\chi}{E} \qquad (eq.\,1.7)$$

where m is the molecular weight of the active material. It is remarkable that, unlike in electrochemical capacitors, the capacitance response is not always constant and, therefore, it is named as pseudo-capacitor. Pseudo- is a prefix meaning apparent, exemplifying the similar behaviour of these materials to a supercapacitor but with a different physical mechanism [63].

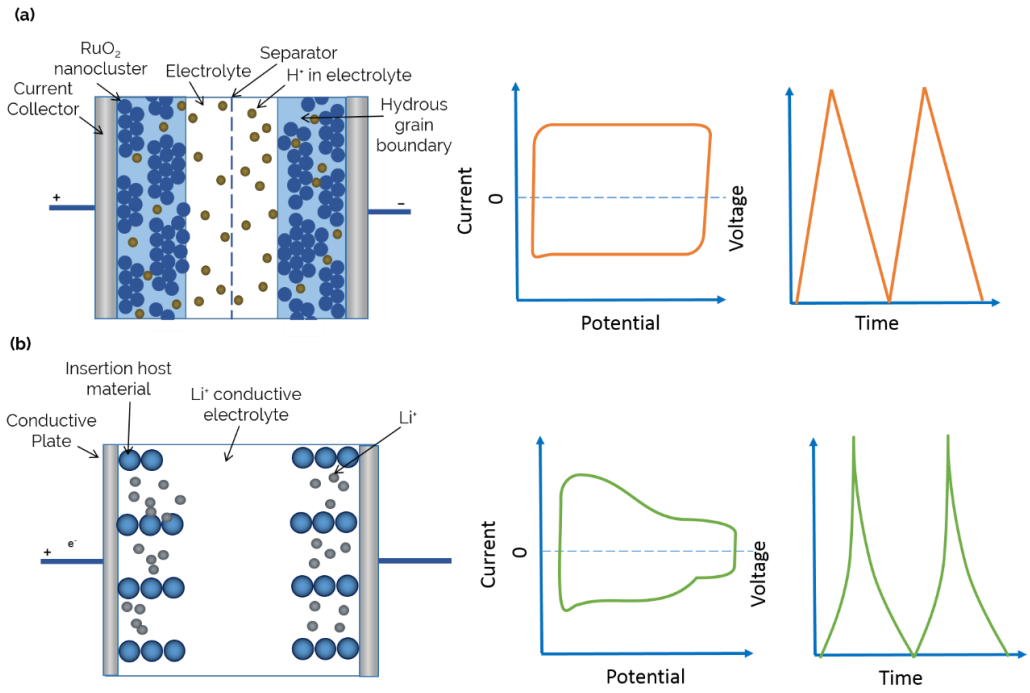

Fig. 1.8. Illustration exemplifying (a) redox pseudocapacitance and (b) intercalation pseudocapacitance with their respective electrochemical fingerprints.

Since pseudocapacitance is faradaic in origin, it involves the passage of charge across the double layer in a similar manner to the mechanism that occurs in batteries. The electrochemical process, therefore, occurs at both the surface and near bulk of the material, inducing far greater capacitances than EDLS, but with far less power density [22]. Capacitance is consequently based on the relation between the charge acceptance of the active material and the change of potential. It is worth noticing that, due to the oxygen functionalities contained on carbon-based supercapacitive materials, there is always a 5-10% contribution of pseudocapacitance in their response. In the case of pseudocapacitor materials, there is always the same amount of contribution arising from electrostatic double-layer capacitance, proportionally to their electrochemically accessible interfacial areas [19].

The three types of faradaic processes, exemplified in Fig. 1.9, are usually associated to different materials. For example, reversible adsorption usually refers to hydrogen on the surface of gold, while redox reactions are, broadly associated to surface reactions of transition metal oxides and intercalation reactions are linked to reversible electrochemical doping-de-doping in conductive polymers or intercalation/de-intercalation in metal oxides [22]. Thus, most pseudocapacitor electrodes are based on either transition metal oxides/hydroxides or polymer-based materials. Moreover, they can be divided into intrinsic or extrinsic pseudocapacitors. Intrinsic pseudocapacitance is assigned to materials that present pseudocapacitance regardless their particle size, for instance, RuO_2 or MnO_2; while extrinsic pseudocapacitance materials are those whose pseudocapacitive behaviour arises because of their nanostructure, which also suppresses phase transformation and enhances surface reactions. This is the case, for example, for $LiCoO_2$ when its dimension is reduced to 17 nm or of V_2O_5 [63,64].

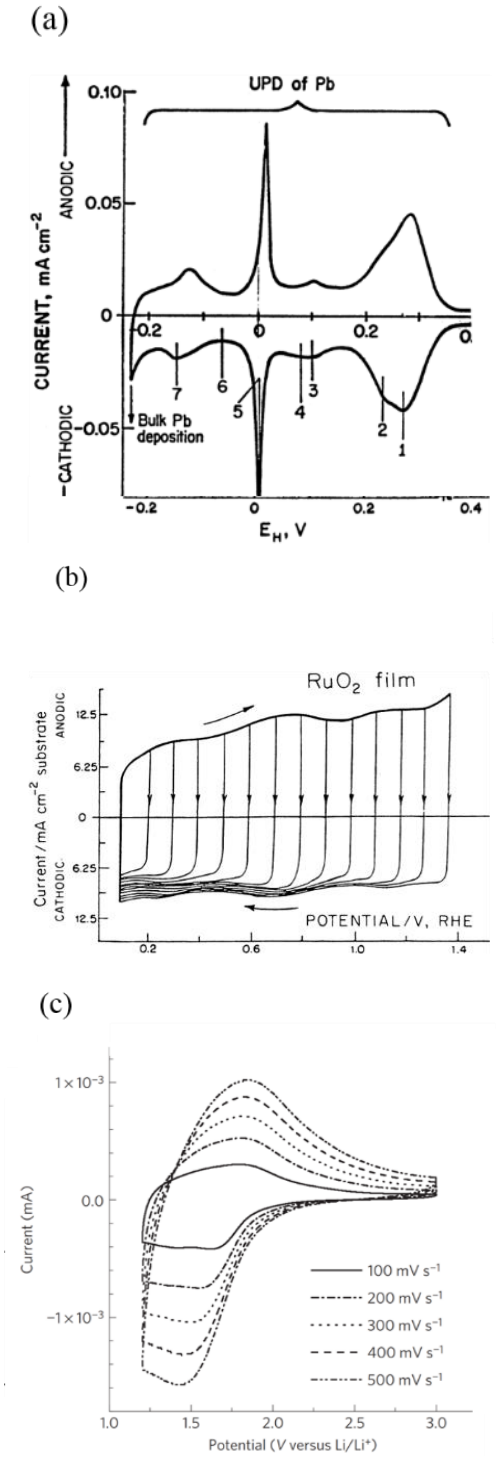

Fig. 1.9. (a) Example of a cyclic voltammetry profile of underpotential deposition of lead adatoms on polycrystalline gold from $HClO_4$ aqueous solution. **(b)** RuO_2 in aqueous 0.1M H_2SO_4 as one of the most common examples of redox pseudocapacitance. Cyclic voltammetry shows a series of positive electrode potentials (vs. RHE) at $50mV \cdot s^{-1}$ exemplifying the squared nature of the pseudocapacitive response. **(c)** Cyclic voltammetry at different scan rates of Nb_2O_5 in 1M $LiClO_4$ demonstrating the high-rate capability of this pseudocapacitive intercalation material Reprinted with copyright permission of [27] and [65].

1.3.1 Metal Oxides

The most studied materials with pseudocapacitance response are MnO_2 and RuO_2. On the other hand, metal oxides such as Nb_2O_5 are examples of good intercalation pseudocapacitance as 70% of its theoretical capacity, based on lithium ion intercalation, can be stored in approximately one minute. Thus, redox reactions do not take place at the surface of the material but by means of redox reactions in the bulk that are not diffusion-controlled, given their fast kinetics. Thus, in order to consider a metal oxide as pseudocapacitive material, four main criteria have to be met [66,67]:

1. Linear dependence of the potential on the state of charge.
2. Charge-storage capacity quasi-independent of rate.
3. Redox peaks with small offsets.
4. No phase transformation during the charge-discharge process.

Consequently, metal oxides are distinguished given their redox or intercalation nature.

Pseudo-capacitance based on surface redox reactions

There are many transition metal oxides and hydroxides that have been studied and have pseudocapacitive properties. Their response will depend upon the structure, hydration and electrolyte. The most studied materials for this purpose are MnO_2, $RuO_2{\cdot}H_2O$, oxides with spinel structure and other transition metal hydroxides.

RuO_2

Hydrous ruthenium oxide was the first discovered material with pseudocapacitive properties. However, it is a scarce, highly-toxic material and, therefore, cannot be used for large-scale applications. For that reason, many methods have been developed to optimize and limit its usage [68].

Ruthenium oxide has a wide potential window, highly reversible redox reactions, three distinct oxidation states, high proton and electron conductivity, high capacitance, good thermal stability, long cycle life and high rate capability and exhibits a rectangular shape at the cyclic voltammetry that is close to that of a carbon electrochemical fingerprint [22]. Moreover, the capacitance obtained, pre-calculated by means of theoretical calculations considering BET active area, demonstrated extremely higher capacitance values than expected for a double-layer [69]. In fact, double-layer only accounts for approximately 10% of the accumulated charge [22]. Moreover, it was demonstrated that this process was not diffusion-controlled as is the case for battery materials. However, impedance results showed a response that was not close to that of an ideal capacitor. As a consequence, Conway et al. [19] suggested that ruthenium's oxide capacitance derived from a series of oxidation/reduction reactions over a potential range. Later, Zheng et al. [70] reported the first specific capacitance value of 720 $F{\cdot}g^{-1}$ for hydrous RuO_2 and proved that the charging mechanism involved the protonation of the oxide.

Pseudocapacitance of RuO_x derives from surface reactions. For that reason, many attempts have been directed towards maximizing active surface area [71]. Many different techniques have been used, such as increasing substrate roughness or area, thin-film preparation, creating micropores, etc. [72–74]. One of the most effective ways to increase capacitance has been to combine water with RuO_x, facilitating proton/cation exchange and electron-hopping. Hydrous ruthenium oxide is a good proton conductor (10^{-8} to 10^{-2} $cm^2\ s^{-1}$) and fast ionic conductor.

Since then, many studies to understand the mechanism and improve the material's capacitance have been performed. Sugimoto et al. [75] expanded layered ruthenic acid ($H_xRuO_{2+y}\cdot zH_2O$) and delaminated it into nanosheets. They studied the electrochemical response at a 2 to 500 $mV\cdot s^{-1}$ scan rate range and observed the much faster reaction kinetics of the oxidation-reduction process as compared to traditional batteries. To date, one of the highest capacitance values achieved is that of hydrated ruthenium oxide reported by Hu et al. [76], in which a capacitance value of 1240 $F\cdot g^{-1}$ was achieved at 25 $mV\cdot s^{-1}$.

Crystallinity and crystal size also play a major role in the pseudocapacitive performance of ruthenium oxide. A good crystalline structure limits volume variation during intercalation processes, limiting diffusion. For that reason, amorphous RuO_x exhibits better performance that its crystalline counterpart, and this crystallinity is greatly dependent on the synthesis procedure. On the other hand, smaller particles shorten diffusion distance, facilitating proton transport, and increase active surface area [77],[78].

In an attempt to lower the quantity of ruthenium oxide utilized, it has been combined with numerous cheaper metal oxides, such as SnO_2, MnO_2, NiO or WO_3, or with other low-cost materials such as carbons or conductive polymers. Additive metals can provide extra pseudocapacitance while facilitating electron and proton transport, reduce aggregation and minimize particle size. Carbon-based materials are usually used as supports to enhance ruthenium oxide dispersion, induce porosity, enable easy ion transport and increase electrical conductivity. Finally, polymer-based composites also exhibit high capacitance and high power, prevent aggregation and distribute uniformly ruthenium oxide particles, increase active surface area, enhance proton conduction and improve adhesion to the current collector. Unfortunately, they suffer from volume changes, being detrimental to the final performance. For more information, the reader is suggested to read Wang et al. [22] review on electrode materials for electrochemical supercapacitors.

MnO_2 / Spinel Mn_3O_4

MnO_2 is the most studied pseudocapacitive material as an alternative to ruthenium oxide since it was first investigated by Lee and Goodenough [79] in KCl aqueous electrolyte because of its low toxicity and cost-effectiveness.

Manganese oxide is usually operated in neutral aqueous electrolytes. Its electrochemical fingerprint, characterized by a squared voltammetry, indicates fast superficial redox reactions that usually correspond to a change in oxidation state of manganese from +4 to +3 [63]:

$$Mn^{IV}O_2 + xA^+ + xe^- \leftrightarrow A_xMn^{III}O_2 \qquad (eq.\,1.8)$$

Where "A" represents an alkali metal ion. Theoretically, the maximum capacitance that could be achieved is 1233 $F\cdot g^{-1}$ in a 0.9 V potential window. However, they have limited capacitance and power density due to the poor conductivity of manganese oxide, and only values around 200-250 $F\cdot g^{-1}$ have been achieved so far. Because of its poor conductivity, only the outer layer of the material is active, introducing inactive mass. Ultrathin layers have also been produced, with capacitance values higher than 1000 $F\cdot g^{-1}$ (1020 $F\cdot g^{-1}$ at 5$mV\cdot s^{-1}$ and 450 $F\cdot g^{-1}$ at 100 $mV\cdot s^{-1}$with an approximately 10% decay after 100 cycles for gold/manganese oxide nanowires [80], and 1380 $F\cdot g^{-1}$ in the 0-0.9 V potential range for Pt-MnO_2 at 5 $mV\cdot s^{-1}$ [81]). This demonstrates that, if more active sites of MnO_2 are accessible by the electrolyte, higher capacitance values can be achieved. This has led to numerous synthesis strategies for this material, such as microemulsion preparation, ethylene glycol reduction, hydrothermal, sol-gel, microwave-assisted emulsion,

coprecipitation or anodic electrodeposition among many others, as described by Ivey et al. in their review [82].

Manganese oxide has numerous allotropes and crystal structure greatly influences the capacitance of MnO_2. Wide intercalation tunnels contribute to high capacitance. Ghodbane et al. [83] and Munichandraiah et al. [84] studied different manganese allotropes, namely, Birnessite (δ-MnO_2), Cryptomelane (α-MnO_2), Ni-todorokite, Pyrolusite (β-MnO_2), Ramsdellite (γ-MnO_2), Spinel (λ-MnO_2) and OMS-5 and reported their specific capacitances in relation to their BET area and ionic conductivity, concluding that the preparation technique is crucial for the surface morphology of the material. 3D structures had the highest capacitance values and, the larger the cavity, the larger the capacitance [83].

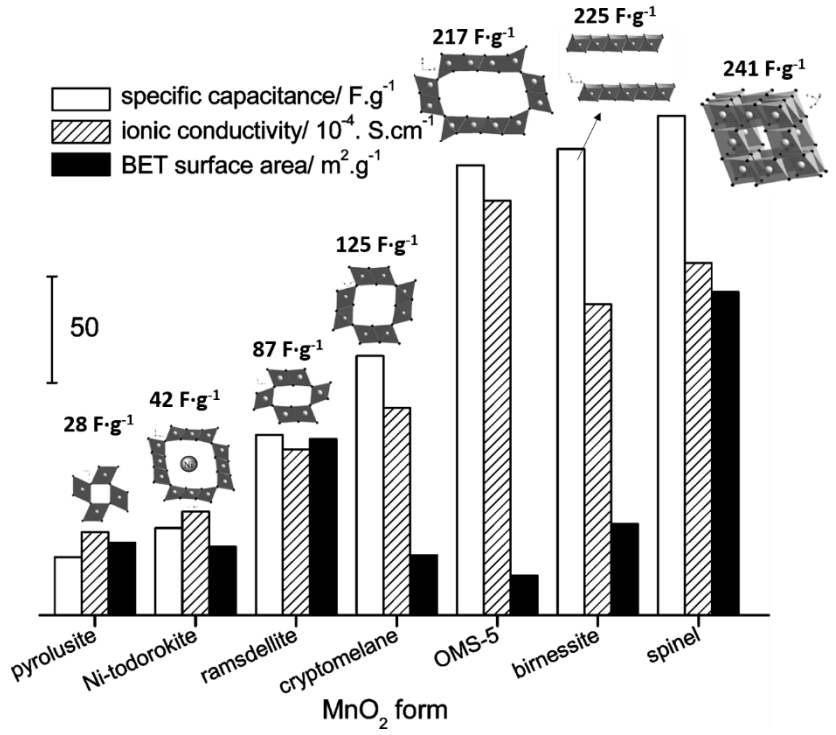

Fig. 1.10. Results obtained for different manganese oxide allotropes in the study performed by Ghodbane et al. Reprinted with copyright permission of [83].

It is also worth mentioning that, in general, different synthesis strategies lead to different types of manganese oxide that have a big difference in capacitance. Amorphous manganese oxide mainly has capacitance contributions from surface reactions while crystalline MnO_2 shows intercalation contribution from bulk to a certain extent [85].

As seen in figure 1.10, spinel manganese oxide and birnessite manganese oxide show the most promising results. Spinel structure is characterized by the general AB_2O_4 formula, which has three-dimensional diffusion channels. Many different materials are gathered under this structure such as Fe_3O_4 and Co_3O_4 or mixed metal spinels such as $MnFe_2O_4$ or $NiCo_2O_4$. Spinel manganese oxide is pseudocapacitive in nature, however, it also has poor electronic conductivity. Studies show a maximum capacitance of 420 $F \cdot g^{-1}$ at 5 $mV \cdot s^{-1}$ in KCl when a carbon nanotube conductive structure was introduced [86], 583 $F \cdot g^{-1}$ at 1$A \cdot g^{-1}$ in 6M KOH [87] and 272 $F \cdot g^{-1}$ at 0.5 $A \cdot g^{-1}$ when doped with chrome in 1M Na_2SO_4 [88].

There are several challenges to overcome regarding manganese oxide such as dissolution in the electrolyte during cycling, low surface area and poor electronic and ionic

conductivity. Therefore, future research based on manganese oxide will try so address these issues by implementing new strategies such as developing new MnO_2 nanostructures, doping it with other transition metal ions such as cobalt to improve stability and conductivity or synthesizing new composite materials [22].

Fe_3O_4

Among the different spinel structures, Fe_3O_4 also exhibits pseudocapacitance while Fe_2O_3 has a battery-like electrochemical response. Given that it is the fourth most abundant element on earth, it would be interesting to exploit iron as energy storage material. Iron is usually oxidized into three kinds of oxides, namely, Fe_2O_3, Fe_3O_4 and FeO [89]. Given that Fe_2O_3 is the most thermodynamically stable form, it is the most used form of iron oxide. Nonetheless, it also has three polymorphs, α with rhombohedral structure, β with orthorhombic structure and γ with cubic structure, depending on the arrangement of the octahedral within the crystalline structure.

Another important iron oxide, given its pseudocapacitive properties, is Fe_3O_4, with face-centred cubic unit cell, with iron in two different oxidation states, II and III. In comparison to other metal oxides, iron oxides have relatively high conductivity, unfortunately, iron oxides do not have very high specific capacitance [90]. For example, Fe_3O_4 prepared by Wang et al. [91] displayed capacitances of 170 $F \cdot g^{-1}$ in aqueous 1M Na_2SO_3, but only 3$F \cdot g^{-1}$ in 1M KOH. Another example is that of Liu and Chen [92], who synthesized cubic nanoparticles of Fe_3O_4 with 118.2 $F \cdot g^{-1}$ when applying 6 mA (no mass specified) in the -1 to 0.1V range with a 11.25% capacitance loss after 500 cycles.

Different synthesis strategies have been developed to produce iron(III) oxide. Hydrothermal and solvothermal (ethanol, ethylene) synthesis are the most common synthesis procedure with nitrates sulphates and chlorates as most common precursors [93–95]. But also anodic electrodeposition (leading to a capacitance of 146 $F \cdot g^{-1}$at 5 $mV \cdot s^{-1}$) [96], cathodic ED [97,98] or chemical precipitation [99,100].

To overcome aggregation, poor electronic conductivity, capacity fading with cycling and low capacitance values, composite materials have been prepared. Overall, magnetite-based Fe_3O_4 composites exhibit capacitance in the 115-220 $F \cdot g^{-1}$ range with a good cycling stability. Within the most explored strategies, using carbon nanotubes as dispersive material for iron oxide nanoparticles has been one of the major strategies. For example, Guan et al. [101] reported a Fe_3O_4/CNT composite with a specific capacitance of 117 $F \cdot g^{-1}$ at a current density of 10 $mA \cdot cm^{-2}$ and a 9% decrease after 500 cycles. Multi-wall carbon nanotubes (MCNTs) have also been proved to improve ion diffusion. MCNTs/Fe_2O_3 thin-films were prepared with 100 $F \cdot g^{-1}$ specific capacitance at 2 $mV \cdot s^{-1}$. Nonetheless, poor electronic conductivity was still detrimental to the overall performance, with a decrease in capacitance to 8 $F \cdot g^{-1}$ when 200 $mV \cdot s^{-1}$ were applied [102].

Unur and Sinan [103] prepared Fe_3O_4 nanoparticles by chemical co-precipitation and subsequently mixed them with hazelnut shell powder and magnesium acetate to produce an iron oxide-carbon composite by means of hydrothermal reaction. The material presented 136.2 $F \cdot g^{-1}$ at 1$A \cdot g^{-1}$ in 1M Na_2SO_4 calculated for the 0 to -1.2V (vs. Ag/AgCl) potential range. Moreover, capacitance was almost completely retained after 1000 cycles. Fe_3O_4 nanoparticles were also grown on reduced graphene oxide by hydrothermal techniques and were compared to an analogous material with carbon nanotubes instead of reduced graphene oxide by Yuan et al. [104]. In their study Fe_3O_4 exhibited 65.4 $F \cdot g^{-1}$ at 0.5 $A \cdot g^{-1}$ while Fe_3O_4/CNTs displayed 110.5 $F \cdot g^{-1}$ and Fe_3O_4/r-GO 220.1 $F \cdot g^{-1}$. This phenomenon was explained but aggregation avoidance and increased active surface area

for the rGO-containing composite. Nonetheless, low capacitance and poor cycling stability are yet to be overcome for iron oxide materials and, therefore, further work has to be done to be suitable for electrochemical pseudocapacitor applications [90].

V_2O_5

Vanadium oxide also exhibits pseudocapacitive behaviour in neutral aqueous electrolyte such as NaCl or KCl and, given its unique electrical, optical and electrochemical properties, it has raised increasing interest during the past years. Many oxide-based compounds can be produced with vanadium, such as vanadium monoxide (VO), vanadium trioxide (V_2O_3), vanadium dioxide (VO_2), vanadium pentoxide (V_2O_5), etc. because of the numerous oxidation states that vanadium can adopt. As expected, different properties can be achieved depending on the stabilized phase [89].

Among the different possibilities, vanadium pentoxide and vanadium dioxide are the most explored phases for energy storage applications given their high capacitance for the former and capacity for the latter (despite its battery-like behaviour, it is described in the present section).

The theoretical capacity of V_2O_5 is 294 $mA \cdot h \cdot g^{-1}$ for lithium ion batteries in the potential range between 2.0 and 4.0V (vs. Li^+/Li) [105,106] while it is 340 $mA \cdot h \cdot g^{-1}$ for VO_2 [107,108]. As in the case of previous metal oxides, it can be produced by solvothermal and hydrothermal [109,110], sol-gel [111] and anodic electrodeposition [112].

Regarding its application for pseudocapacitors, Saravanakumar et al. [109] reported values of 304 $F \cdot g^{-1}$ at 0.1$A \cdot g^{-1}$ in the -0.2 to 0.8V potential range and a capacity loss of 24% after approximately 300 cycles. Goodenough et al. [113] prepared amorphous vanadium penta-oxide that displayed 350 $F \cdot g^{-1}$ in KCl in the 0.0 to 0.8V potential range at 5 $mV \cdot s^{-1}$. It was studied that V_2O_5 response is greatly dependent upon the electrolyte used, with optimum results for 2M KCl electrolyte, with which Wang et al. [114] reported 190 $F \cdot g^{-1}$ for V_2O_5 at 5 $mV \cdot s^{-1}$ in the -0.2 to 0.8V potential range, while 106 $F \cdot g^{-1}$ were obtained in H_2SO_4 1M and 8 $F \cdot g^{-1}$ in KOH 2M. This behaviour is characteristic of extrinsic pseudocapacitors. V_2O_5 aerogels that are pressed into conductive wax display perfectly capacitive CVs (high exposure of surface area, 1300 $F \cdot g^{-1}$) [115] while aerogels with traditional electrode composition exhibits a CV with prominent peaks as a result of the required thermal treatment.

It is known that vanadium oxide has poor electrochemical stability due to chemical dissolution and material pulverization [110] and poor electrical conductivity [22]. For that reason, vanadium-oxide-based composites tend to incorporate materials that stabilize the system and enhance electronic conductivity. To overcome this issue, it has been combined with CNTs displaying 910 $F \cdot g^{-1}$ at 10 $mV \cdot s^{-1}$ in 1M $LiClO_4$ in the 1.5V to 4.0V potential range [116]. It has also been combined with other more conductive metal oxides such as SnO_2. For instance, SnO_2-V_2O_5-CNTs composite displayed 121 $F \cdot g^{-1}$ at 100 $mV \cdot s^{-1}$ in 0.1M KCl in the 0-0.8V potential range [117]. Finally, composites with reduced graphene oxide have also been developed. Given that reduced graphene oxide is an excellent conductive matrix that can serve as support for vanadium oxide nanoparticles, RGO-V_2O_5 electrodes displayed the excellent capacitance of 537 $F \cdot g^{-1}$ at 1 $A \cdot g^{-1}$ in neutral aqueous electrolyte in the -0.3 to 0.7V potential range and a capacitance loss of a 16% after 1000 cycles [118].

Composite materials with vanadium oxide are promising candidates for future electrochemical energy storage devices but poor electrical conductivity and stability still remain as challenges to overcome [63].

SnO_2

Tin oxide is not as explored as other oxides since its specific capacitance is much lower. Nonetheless, given its high electrical conductivity, it has been pin-pointed as potential material for electrochemical energy storage devices. In general, all reported values are smaller than 150 $F \cdot g^{-1}$, such as 66 $F \cdot g^{-1}$ for SnO_2 sol-gel or 69.8 $F \cdot g^{-1}$ at 1 $mV \cdot s^{-1}$ for SnO_2 impregnated on top of carbon aerogel in 1M H_2SO_4 in the -1.0V to 1.0V potential range [119]. Shin et al. [120] synthesized SnO_2 hierarchical nanobranches that exhibited 40.5$\mu F \cdot cm^{-2}$ at 20 $mV \cdot s^{-1}$ in 1M Na_2SO_4 and a nearly 9% of capacitance loss after 1000 cycles. Tyagi and Dhara [121] reported SnO_2 by means of soft chemical method and studied their electrochemical response. In the potential range from -0.2V to 0.5V vs. Ag/AgCl in 0.5M KOH their quantum dots displayed 10 $F \cdot g^{-1}$ at 20 $mV \cdot s^{-1}$. Even when mixed with RuO_2 it only displayed 24 $F \cdot g^{-1}$ at 3$mA \cdot cm^{-2}$ in the -1.0V to 1.0V potential range in 1M H_2SO_4 [122]. One of the few exceptions that can be found was reported by Miura et al. [123], who synthesized amorphous SnO_2 on top of stainless steel by means of potentiodynamic electrodeposition, yielding 285 $F \cdot g^{-1}$ at 10 $mV \cdot s^{-1}$ and 101 $F \cdot g^{-1}$ at 200 $mV \cdot s^{-1}$ in the 0.0V to 1.0V potential range and 0.1M Na_2SO_4 electrolyte. However, the main limitation of SnO_2 apart from its low capacitance is the 200-300% volume change during charge-discharge which leads to pulverization and loss of electrical contact. Introducing carbon structures is intended to buffer volume changes [121], however, results were not as high as expected in many cases. Nevertheless, when combined with reduced graphene oxide hydrogel by means of solvothermal synthesis, Lim et al. [124] reported a value of 363 $F \cdot g^{-1}$ at 10 $mV \cdot s^{-1}$ in 1.0M Na_2SO_4. It is worth mentioning that, despite this result, some other forms of SnO_2/graphene-derivative displayed lower values in the 34-100 $F \cdot g^{-1}$ range [125,126].

Mixed metal oxides with spinel structure

There are not many reports on $MnFe_2O_4$ and $CoFe_2O_4$ given their modest capacitance. For $MnFe_2O_4$ in 1M NaCl and KCl, values of 105 $F \cdot g^{-1}$ and 115 $F \cdot g^{-1}$ [127] were achieved, respectively, in a 1V potential window. In an attempt to improve their electrical conductivity, composites with carbon-based materials have been prepared, such as $MnFe_2O_4$/carbon black (however, results showed poorer capacitance but better cycling stability than $MnFe_2O_4$) [128], reduced graphene oxide/$MnFe_2O_4$ (with an improved capacitance of 271 $F \cdot g^{-1}$ at 0.5 $A \cdot g^{-1}$ in 6M KOH and a 104% capacitance after 5000 cycles) [129] or the ternary nanocomposite PANI/$MnFe_2O_4$/reduced graphene oxide, which displayed 307.2 $F \cdot g^{-1}$ at 0.1 $A \cdot g^{-1}$ [130].

Pseudocapacitors based on pseudo-intercalation

There is an important feature to consider when evaluating an intercalation pseudocapacitive material. No phase transformation shall undergo during the intercalation process. For example, MoO_2 usually undergoes a monoclinic-to-orthorhombic phase transition when charged as bulk material. However, when molybdenum oxide is nanostructured, this phase transition is supressed, and the material complies with the pseudocapacitive requirements (therefore being defined as extrinsic pseudocapacitor). A general approach is to develop nanostructured materials since they tend to show capacitor-like behaviour when their crystallite size is smaller than 20 nm. Currently, this is explained by either a larger number of accessible active sites at the surface or the suppression of phase transitions. Only a few materials have been characterized in their nanosheet 2D form, where, under certain conditions, the entire surface of the sample is exposed, as in the case of TiO_2 [67].

T-Nb_2O_5

Nb_2O_5 is usually used in lithiated non-aqueous media to promote lithium insertion in a <2V potential (vs. Li/Li^+). The lithiation of niobium oxide proceeds up to x=2 in $Li_xNb_2O_5$ corresponding to a theoretical capacity of $200mA{\cdot}h{\cdot}g^{-1}$. Recently, pseudo-hexagonal (TT- Nb_2O_5) and orthorhombic (T- Nb_2O_5) phases were discovered to have a continuous change of potential with state of charge. Therefore, no phase transition occurs in this charging process and the material can be considered as pseudocapacitive [131]. Dunn et al. [132] first reported the pseudocapacitive properties of orthorhombic niobium oxide synthesized by sol-gel processes, which displayed values $>400F{\cdot}g^{-1}$ in non-aqueous electrolyte ($LiClO_4$ 1M) at sweep rates up to $100\ mV{\cdot}s^{-1}$. This indicates that faradaic reactions occur in very short timescales with fast ion [132,133]. Augustyn et al. [66] reported $380\ F{\cdot}g^{-1}$ calculated for a 60 seconds discharge, equivalent to $20\ mV{\cdot}s^{-1}$, in 1M $LiPF_6$ and discussed the pseudocapacitve kinetics of T-Nb_2O_5 synthesized by a sol-gel route. T-Nb_2O_5 is an extrinsic pseudocapacitive material that, when 40-µm or thinner films consisting of approximately 40 nm nanoparticles are prepared, the material exhibits pseudocapacitive material while, for bulk T-Nb_2O_5, clear faradaic peaks are observed.

Moreover, it was reported that the crystalline structure of the material determines the ultimate its electrochemical response. Consequently, when the material is amorphous, lower capacitance values are obtained ($224\ F{\cdot}g^{-1}$) compared to crystallized in its orthorhombic phase ($555\ F{\cdot}g^{-1}$). Computational studies determine that certain exposed planes exhibit lower energy barriers for lithium intercalation despite having lower surface area [134,135]. In general, intrinsic pseudocapacitors are not as dependent on active surface area since they are based on intercalation. Thus, different architecture engineering for these materials is required and is to be expected in future studies [63].

TiO_2

Another promising lithium intercalation pseudocapacitive material is titanium dioxide, as Graetzel et al. demonstrated [136]. Titanium charge storage is based in the +4/+3 redox couple and lithium intercalation occurs below 2V vs. Li/Li^+ [63]. They prepared TiO_2(B), a metastable monoclinic phase of titanium dioxide by means of hydrothermal synthesis and studied its electrochemical properties in $LiN(CF_3SO_2)_2$. They concluded that this phase of titania accommodated lithium ions via surface-confined processes given that the redox peak current of the material varied linearly with sweep rates [68]. Later, Li et al. [137] studied hydrogen titanate tubes and stablished that pseudocapacitance was arising from the open-layered cross section, which had a much larger inter-layer space than normal Li-intercalation materials.

Zhang et al. [138] synthesized $H_2Ti_3O_7$ nanowires via alkaline-hydrothermal synthesis and its lithium-intercalation pseudocapacitance properties was investigated in 1M $LiPF_6$. Results show a reversible capacity of $800\ C{\cdot}g^{-1}$. Wang et al. [139] obtained similar results for $H_2Ti_6O_{13}$ nanowires prepared by hydrothermal method. In their study, hydrogenated titania nanowires displayed $828\ F{\cdot}g^{-1}$ in the potential window from 2.0 to 1.0V (vs. Li/Li^+) in non-aqueous electrolyte. Moreover, they also observed linear variation with sweep rate of the redox peak current. This pseudocapacitive behaviour arises from the low-density crystal structure that these titania phases contain, enabling rapid lithium ion transport from the surface to the sub-surface [136]. Therefore, they can be considered as intrinsic pseudocapacitors with broad redox peaks that overlap in their CVs even in their bulk form. This enables the scalability to thicker electrode materials but, unfortunately, present irreversible capacity loss that needs further understanding for the material to be applicable in future pseudocapacitor devices [63].

Other metal oxides

Many other metal oxides, such as MoO_2, IrO_2, or WO_3 can be considered for future electrochemical energy storage applications. For example, MoO_2 1D nanorods were synthesized by thermal decomposition of tetrabutylammonium hexamolybdate and exhibited 140 $F \cdot g^{-1}$ at 1 $mA \cdot cm^{-2}$. However, the material did not exhibit very good cycling stability performance, with a 14% loss after 50 cycles [140]. Dunn et al. [141] studied the pseudocapacitive properties of the material and concluded that, for nanocrystals smaller than 15 nm, the reversible phase change from monoclinic to orthorhombic that is observed in the bulk material is suppressed. Thus, MoO_2 exhibits extrinsic pseudocapacitive behaviour. Moreover, they created a composite with reduced graphene oxide to increase its capacity. At 10 $mV \cdot s^{-1}$ the composite material presented 615 $F \cdot g^{-1}$ in a 1V potential window versus the 300 $F \cdot g^{-1}$ that the analogous material without reduced graphene oxide had. Other alternative is tungsten oxide (WO_3), which has good electronic conductivity, yielding, for instance, 196 $F \cdot g^{-1}$ at 10 $mV \cdot s^{-1}$ with 58% capacitance retention after 5000 cycles when synthesized as nanoflowers by electrodeposition [142] or iridium oxide, that showed a specific capacitance of 293 $F \cdot g^{-1}$ at 5 $mV \cdot s^{-1}$ and has attractive electrical and electrochemical properties despite the fact that its price is even higher than that of ruthenium [143].

There is a vast range of potential metal oxides that may be used as energy storage electrodes. However, beyond their electrochemical performance, cost and abundance, ease of synthesis and toxicity are also key factors to consider when synthesizing novel materials. This has become evident with ruthenium oxide. Despite the outstanding properties of RuO_2, this material is unlikely to be used in large-scale applications. Thus, when selecting new materials for novel electrodes, a careful selection and evaluation of the different parameters shall be considered.

1.3.2 Conductive polymers

Conductive polymers (CP) benefit from low cost, low environmental impact, high conductivity, high voltage window, high capacitance/capacity and reversibility and adjustable redox reactions. Capacitance behaviour in CPs is based on redox reactions in which, during oxidation, ions are transferred to the polymer backbone while released during reduction. These redox reactions are not limited to surface reactions but affect the bulk material without structural alteration, conferring the process with high reversibility [22].

They are generally formed through either chemical or electrochemical oxidation of the monomer. Consequently, the oxidation reaction of the monomer occurs at the same time as the oxidation of the polymer [144] while the counter ion/dopant is inserted. When ions are inserted into CPs matrix, polymers gain either positive (p-doping) or negative charge (n-doping). Thus, electronic conductivity can be induced by means of redox reactions that delocalize electrons on their polymer chain.

Common polymers are polyacetylene (PA), polyaniline (PANI), polypyrrol (PPy), polythiophene (PTh), poly(3,4-ethylenedioxythiophene) (PEDOT) and their derivatives. All these materials have a dopant ratio of 0.33 except for PEDOT, which has 0.5 [145]. In the case of PANI and PPy, they can only be p-doped and, therefore, are usually used as cathode materials. On the other hand, PTh can be n-doped or p-doped. However, it shows poor conductivity in the reduced state and its capacitance is low. For that reason, they also tend to be only used as cathode material [22,68].

The charge reactions, according to the type of doping are presented in equations 1.9 and 1.10 [145]:

$$CP \rightarrow CP^{n+}(A^-)_n + ne^- \ (p-doping) \qquad (eq.1.9)$$

$$CP + ne^- \rightarrow (C^+)_n CP^{n-} \ (n-doping) \qquad (eq.1.10)$$

Polymers present similar features to metal oxides for battery and pseudocapacitor materials: higher charge storage capabilities, since they are based on redox reactions, but slower kinetics. Moreover, they often degrade under less than a thousand cycles due to changes in physical structure caused by the intercalation/de-intercalation of ions [146].

For example, PANI hydrogels electrodes, synthesised using aniline hydrochloric salt as precursor and oxidizing it with ammonium persulfate, exhibited the high capacitance of 750 $F \cdot g^{-1}$ at $1A \cdot g^{-1}$ [147]; PPy deposited on stretchable stainless steel reached 170 $F \cdot g^{-1}$ at $0.5A \cdot g^{-1}$ in a solid-state supercapacitor [148].

One of the main disadvantages of polymers is that they are restricted to a very narrow potential window and, if exceeded, the material degrades or becomes completely insulating due to the loss of the dopant charge. Moreover, volume changes (swelling and shrinking) during charge and discharge due to intercalated ions affects electrode stability. This usually leads to mechanical degradation and poor cycling capacitance retention. In order to overcome this issue, research is focused on either improve structure and morphology, hybridizing it with carbon-based materials or creating composites with metal oxides [22].

In fact, the properties of the polymers can be greatly improved when combined with other materials. Wang et al. [22] summarized the main results obtained for CP-based electrode materials in their review, and their combination with carbon-based material, inorganic oxides and hydroxides [149,150], and other metal compounds [151–153]. Composite materials are intended to either have better conductivity, better cyclability, more mechanical stability, higher specific capacitance or easier processability [154].

Polyaniline (PAni)

Polyaniline is one of the most studied energy storage materials. Its high electroactivity, doping level, specific capacitance in acidic medium (400-500 $F \cdot g^{-1}$) and stability has promoted polyaniline's usage in research [146]. The major disadvantage is that it requires a protic solvent, acidic solution or protic ionic liquid, this is, it requires a proton to be charged [155]. Many factors affect the capacity that polyaniline yields, such as synthetic route, polymer morphology, the binders and additive used and the thickness of the electrode. For instance, it can display 107 $F \cdot g^{-1}$ when doped with $LiPF_6$ with an approximately 22% capacitance drop after 9000 cycles [156].

Polypyrrole (PPy)

Polypyrrole's flexibility in processing has attracted much interest for electrochemical energy storage applications. However, it cannot be n-doped and, as a consequence, can only be used as cathode material [145]. It present high capacitance per unit volume (400-500 $F \cdot cm^{-3}$) but its doping ratio is limited because of its dense growth. This limits capacitance per gram when thicker coatings are prepared [145,157].

Polythiophene derivatives (Pth)

There are many variations of n-doped thiophene such as poly(3-(4-fluorophenyl)thiophene) [PFPT], poly(ditheno(3,4-b:3',4'd) thiophene) [PDTT] or poly(3-methyl thiophene) [PMeT] [145]. In general, specific capacitance is higher when p-doped and the conductivity of n-doped is usually not very high. PDTT displayed 106.4 $\mu F \cdot cm^{-2}$ when p-doped while 43.2 $\mu F \cdot cm^{-2}$ when n-doped [158]. The main drawbacks of n-dope polythiophene is its self-discharge and low cycle-stability. Many different variations in which electron withdrawing groups are bonded to the previously bonded phenyl, alkyl or alkoxy groups in the third position of the thiophene are made to overcome this limitation. This results in derivatives such as PEDOT, PFPT or poly(3-(3,4-difluorophenyl)thiophene) [MPFT] among others [159]. However, there are still few reports on n-doped polythiophene derivatives because of the strong dependence of the electrochemical behaviour with the size of the counter ion and solvent.

Literature on PEDOT has largely grown due to its properties, namely, electron rich with low oxidation potential and wide potential window with high capacitance [160,161]. It also has good thermal and chemical stability, high charge mobility and high surface area, which results in fast kinetics. The main counterpart for using this material is that it has low specific capacitance. For example, Snook and Chen [162] reported a capacitance of only 92 $F \cdot g^{-1}$, while Lota et al. [154] prepared a PEDOT pellet with a capacitance of 80-100 $F \cdot g^{-1}$.They also achieved a much higher capacitance of 180 $F \cdot g^{-1}$, however, given their thin-film configuration, results were said to not be feasible for energy storage purposes.

1.3.3 Final note on materials for super- and pseudocapacitors

There is a large amount of ongoing work, based on different strategies, to synthesize the next-generation of materials for pseudo- and supercapacitors. Furthermore, the use of these materials is constantly being extended to new applications. Kaner et al. [163] brilliantly summarized in their review the main fields of interest for supercapacitors and pseudocapacitor developments: AC filtering, flexible and stretchable energy storage devices, energy storage devices integrated in wearable electronics, transparent devices, fast-charging, lightweight energy storage devices for ultrathin electronics, supercapacitors with the energy density of batteries, safe energy storage devices achieved by means of perm-selective membranes, longer lifetime energy storage devices, self-healing batteries and binder-free electrode materials. With that in mind, it seems crucial to develop new strategies to increase energy density while maintaining power density. A list of strategies to fulfil that goal are included in Fig. 1.11.

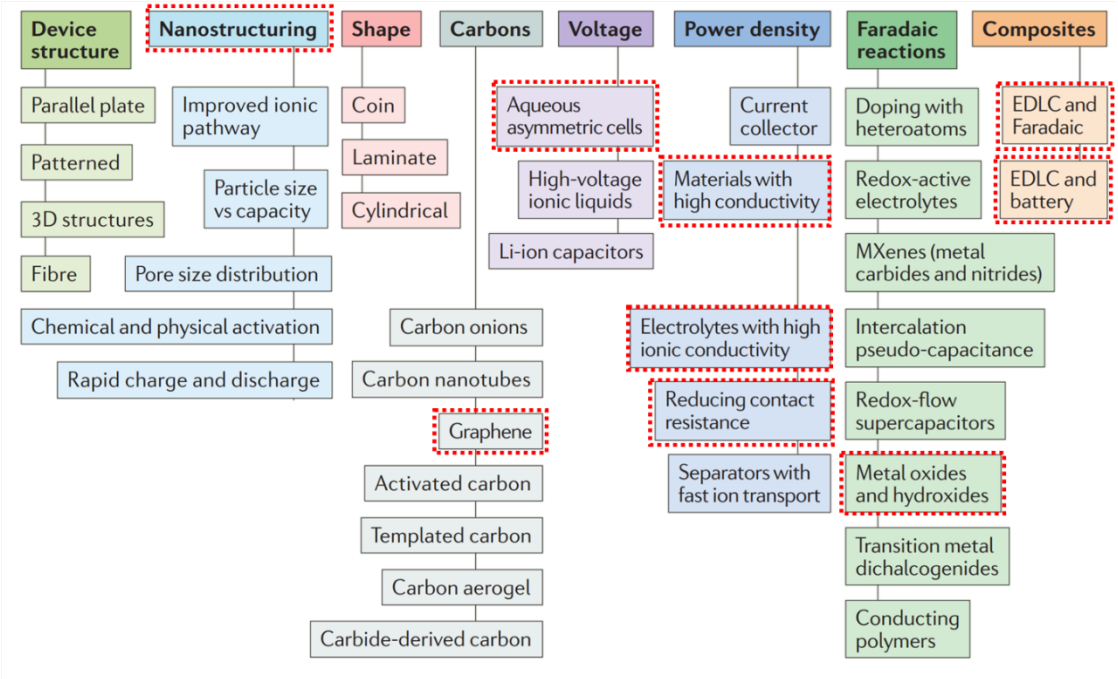

Fig. 1.11. Current strategies implemented in the development of next-generation super- and pseudo-capacitors. Modified version of the image presented in [163] with emphasis, in red, of the strategies that have a direct impact on the present work.

Some of these highlighted strategies to enhance the performance of super- and pseudocapacitors are the core of the present manuscript. In fact, the main goal is to combine *graphene* with metal oxides, oxyhydroxides and hydroxides, which is intended to increase conductivity of the faradaic materials by creating an EDLC-faradaic composite with lowered contact resistance. Moreover, nickel and cobalt oxides, hydroxides and oxyhydroxides are nanostructured when synthesized, leading to improved ionic pathways and enhanced charge-discharge times. All of this investigated in a highly-ionic conductor aqueous electrolyte. This combination of EDLC and battery materials, known as hybrid composites, has been recently studied and differentiated from hybrid devices, where two electrodes, one with a faradaic battery-like response and one with a super- or pseudocapacitive response, are required. Intertwining two materials with electrochemical charge storage mechanisms of different nature entails certain fundamental challenges that require further understanding, which is explained in the following section.

1.4. Pseudocapacitors to batteries: From surface to bulk capacity contribution and hybrid composites.

The underlaying mechanism for the charge-discharge of a rechargeable battery is based on redox reactions that generally consist on the intercalation/de-intercalation of cations (usually H^+, Li^+ or Na^+) within the crystalline structure in a phase transformation of the electrode material that is induced by the change in oxidation state of the metal.

Some confusion arises when comparing batteries and pseudocapacitors. Many reports have already set that the electrochemical response of these devices is different in nature. The issue arises with hybrid composites with intermediate response, since they can exhibit relevant contribution from different processes [68,164,165]. This is well summarized in the article presented by Gogotsi et al. [166] and schematically represented, in terms of electrochemical fingerprint differences, in Fig. 1.12.

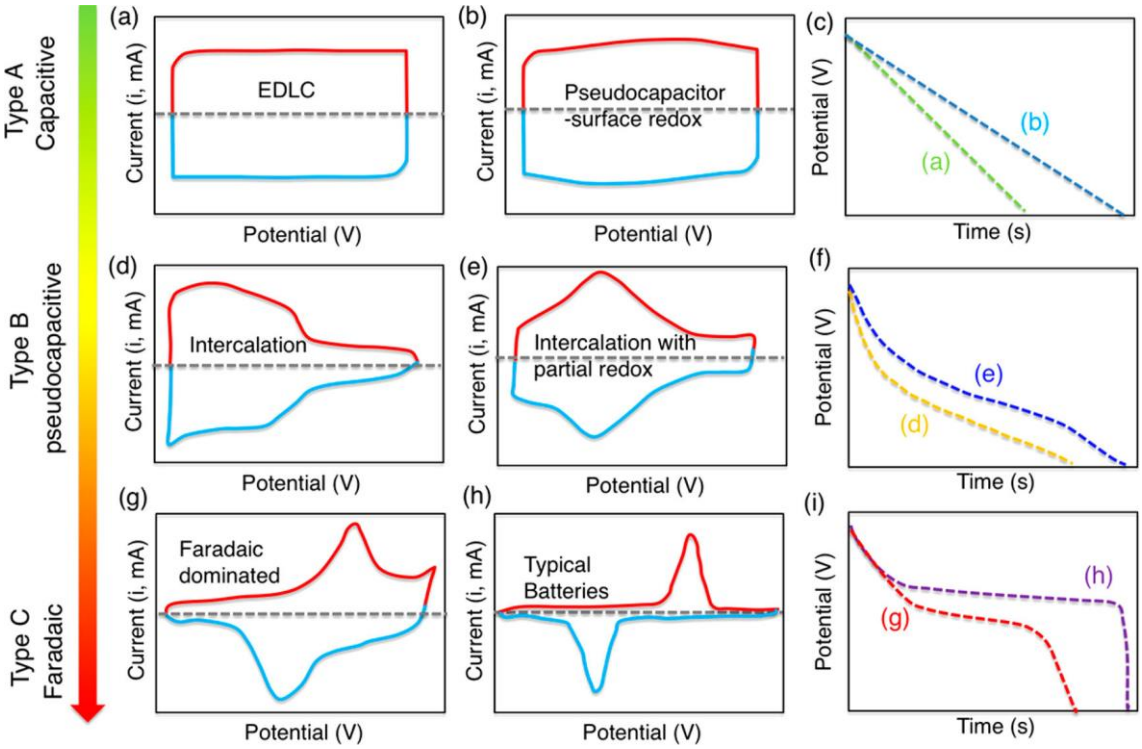

Fig. 1.12. Schematic representation of the representative cyclic voltammograms and galvanostatic charge-discharge for energy storage materials with different charge storage mechanism. They are, therefore, divided in capacitive for EDLC and pseudocapacitors based on surface redox reactions, pseudocapacitive for intercalation and intercalation with partial redox reactions and, finally, faradaic when it is faradaic dominated or purely a battery-like material. Reprinted with copyright permission of [166].

There are several intrinsic differences that are worth mentioning. First, charging of batteries is usually related to a phase transformation while pseudocapacitors do not change their crystalline structure. Another relevant feature is different intrinsic kinetics. While batteries are dominated by diffusion-controlled phenomena within the crystalline framework of the electrode, pseudocapacitors are based on superficial reactions and, therefore, do not present such feature. This can be correlated to a different electrochemical response measured by cyclic voltammetry [68].

The voltammetric response of an active material at various sweep rates is described as [167–169]:

$$i = a \cdot v^b \qquad (eq.1.11)$$

i being measured current at a fixed potential, a and b two constants and v the applied sweep rate. Since battery behaviour is controlled by cation-diffusion in the crystalline structure, the corresponding response has been worked out to be [169]:

$$i = n \cdot F \cdot A \cdot C \cdot D^{1/2} \cdot v^{1/2} \left(\frac{\alpha n F}{RT}\right)^{\frac{1}{2}} \pi^{\frac{1}{2}} \chi(bt) \qquad (eq.1.12)$$

where C is the surface concentration of the electrode material, α is the transfer coefficient, D is the chemical diffusion coefficient, n is the number of electrons involved in the electrode reaction, F is the Faraday constant, A is the surface area of the electrode material, R is the molar gas constant, T is the temperature and $\chi(bt)$ is a function that represents the normalized current.

Given the dependence of the current provided by a battery with diffusion, the relation between peak current and sweep rate can be therefore represented as:

$$i_p = a \cdot v^{1/2} \qquad (eq.1.13)$$

In this case b has the value 0.5. On the other hand, the electrochemical response of a pseudocapacitor is not diffusion-controlled and the resulting equation is:

$$i = C_d \cdot A \cdot v \qquad (eq.1.14)$$

Where C_d is capacitance and A the surface area of the active material. When considering the electrochemical response of a battery, the electrode potential has a defined value. Consequently, there are peaks at the cyclic voltammetry curve and a plateau at the galvanostatic charge-discharge curves (Fig. 1.12h,i), which are defined by the value of Gibbs energy for a well-defined phase transformation and the composition/concentration of solution. Contrastively, pseudocapacitors are based on the electro-adsorption of species in a continuous logarithmic function. Consequently, cyclic voltammetry does not present said peaks and galvanostatic charge-discharge displays a linear voltage-time dependence as displayed in Figure 1.12c [68].

As a remark, it is worth noticing that, for some pseudocapacitive materials, intercalation only contributes partially to the overall response. They present a hybrid charge storage mechanism consisting of capacitive effects and diffusion-controlled insertion [167]:

$$i(v) = k_1 \cdot v + k_2 \cdot v^{1/2} \qquad (eq.1.15)$$

It is, consequently, possible to distinguish the percentage of intercalation contribution from capacitive processes at specific potentials. Trassati et al. stated in their analysis that capacity that occurs due to surface processes is constant with the sweep rate and will always be present whereas capacity that derives from diffusion-limited processes will vary according to $v^{-1/2}$. Thus, the capacitive contribution, calculated at the "infinite-sweep rate" capacity, can be calculated by extrapolation of the capacity obtained as a function of the sweep rate, as shown in Fig. 1.13 [170]:

$$Q = Q_{v=\infty} + constant \cdot v^{-1/2} \qquad (eq.1.16)$$

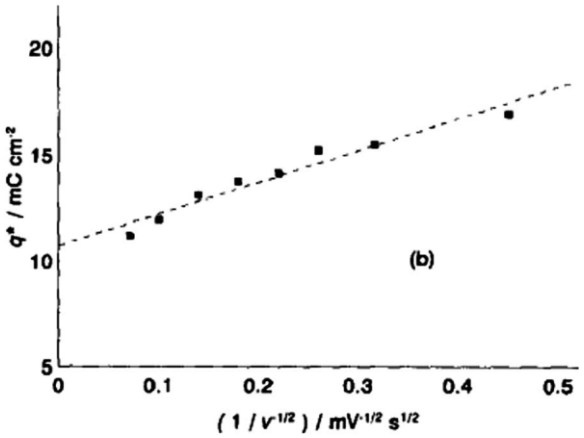

Fig. 1.13. Kinetic analysis of capacity contribution from outer surface response proposed by Trasatti et al. The y-intercept would correspond to the infinite sweep rate capacity. Reprinted with copyright permission from [170].

Recently, materials with hybrid charge storage mechanism have been developed. In the pursuit for high-energy density and high-power density materials, when a faradaic battery-like material is mixed with a high active surface area material, both the contribution of capacitive and faradaic charge storage mechanism are relevant to the displayed electrochemical performance of the material, Fig. 1.12g [171]. In the same way that the combination of capacitors with batteries are used to complement each other, the combination of different materials with different charge storage mechanisms can be used to improve overall performance [172]. This leads to hybrid composites that also known as **internal parallel hybrids, hybrid composites** or **high-rate battery materials** (Fig. 1.14).

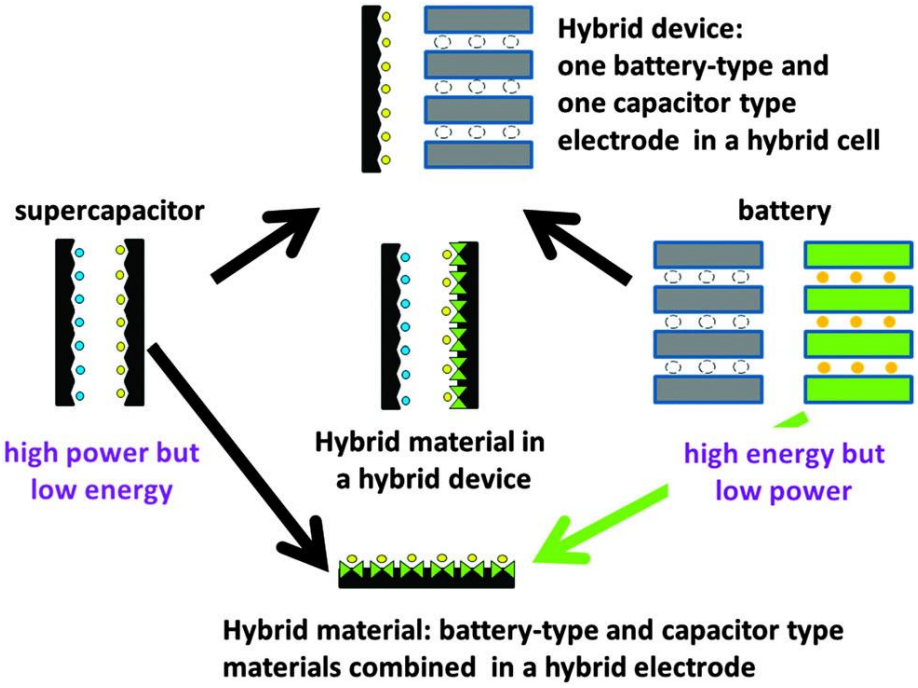

Fig. 1.14. Schematic representation exemplifying the hybridization approaches for the combination of supercapacitor and battery-like responses though device configuration (Hybrid device) or though material engineering (Hybrid material). Re-printed with copyright permission from [172].

The goal for these hybrid composite materials is to display faradaic and capacitive response in parallel. This can be displayed as an extended working potential or as increased kinetics of the reactions associated to the faradaic charge-discharge mechanism. In general, battery-like materials have two limitations: they are confined to a very limited potential range and they are limited by diffusion-controlled phenomena. Regarding the former, an enhanced power response can be achieved if the initial stage of charge is supercapacitive in nature (until the faradaic reaction potential is reached). Regarding the latter, shortened diffusion paths may, eventually, reduce its diffusion-control dependency.

For example, certain materials have traditionally exhibited a battery-like behaviour, such as NiO or Co_3O_4. However, high-power properties, associated to fast redox kinetics, have been achieved by enlarging its active surface area when nano-structuring them. Nonetheless, despite their high cycling stability and high capacity/power performance in aqueous electrolyte, the main drawback of narrow potential window was still present. By means of device and materials engineering, this drawback can be overcome. For example, combining materials with dissimilar properties may create synergistic combinations that palliate the main deficiencies present in the parent materials [171]. The most recurrent combination is that of electroactive and conductive materials that interact at the nano-scale to produce novel phases, or intimate interactions between them, at an atomic/molecular level (and not producing a simple mixture) [172] .

These two strategies, nano-structuring and hybrid composite production, have been the main focus of the present manuscript, where nickel-cobalt (hydr)oxide materials, traditionally used in batteries, have been nanostructured with the initial goal of achieving faradaic reactions confined to the surface of the material (pseudocapacitance) and have been combined with reduced graphene oxide to create hybrid composites that could either benefit from fast kinetics in the faradaic reaction, expanded active potential window or better cycling stability, usually associated to carbon-based material but not to metal hydr(oxides). For that reason, an extensive review of nickel, cobalt, nickel-cobalt oxides and hydroxides and reduced graphene oxide, with special emphasis on electrochemically reduced graphene oxide, is done. It must be noted that most studies provide capacitance values in $F \cdot g^{-1}$ units for nickel and cobalt (hydr)oxides, which is wrong and misleading when a battery-like response is obtained, and units shall be converted to $mA \cdot h \cdot g^{-1}$. Values here reported are expressed in the same original form as the initial work, however, values of voltage range are provided for a more in-sight interpretation of the presented values.

Finally, it is worth mentioning that batteries are, currently, the main field of study in electrochemical energy storage. Because of their mature stage of development and overall hegemony in commercially available energy storage devices, an in-depth discussion of all materials and battery types is unfeasible and out of the scope of the present work. As aforementioned, the scope of the present manuscript is to develop hybrid composites by means of nanostructuring nickel-cobalt oxide, hydroxide and oxyhydroxide to confine their reactions to a superficial level, thus increasing their power capabilities, and to engineer composites with relevant capacitance contribution from graphene derivatives. Nonetheless, there is an obvious battery-like contribution from the metal oxides and hydroxides in the work presented in this manuscript and, therefore, the use of nanostructured nickel and cobalt oxides and hydroxides and graphene for battery applications is considered in the following sections, where the state-of-the-art of these materials for electrochemical energy storage applications is reviewed. Special emphasis is done on nickel hydroxide as electrode material for battery applications, since its use is still relevant in commercially available metal-hydride batteries and the author believes the presented manuscript may be relevant in that field of study.

1.5 Nanostructured nickel and cobalt (hydr)oxides for energy storage applications

NiO

Nickel oxide is used in alkaline electrolytes as material for energy storage due to its easy synthesis and low cost [173–175]. NiO usually behaves as a battery-like material in bulk. However, when nanostructured, its redox reactions can be confined to surface, increasing the pseudocapacitive component of charge storage. There are several considerations when NiO is studied as a potential candidate in energy storage [19,90]: Its electrical conductivity must be maximized, two or more oxidation states shall coexist over a potential range, surface area shall be maximized so high rate capabilities are achieved in combination with the excellent capacity value of nickel oxide and electrolyte shall easily interact with the material favouring the charge-discharge redox reaction.

During charge, nickel oxide transforms into its more conductive oxyhydroxide form as shown in equation 1.17 and 1.18:

$$NiO + OH^- \leftrightarrow NiOOH + e^- \qquad \text{(eq. 1.17)}$$

$$NiO + H_2O \leftrightarrow NiOOH + H^+ + e^- \qquad \text{(eq. 1.18)}$$

It is worth mentioning, however, that there are two main hypotheses regarding the energy storage mechanism for nickel oxide. On one hand, NiO/NiOOH as exemplified is considered. On the other hand, it is assumed that in alkali electrolyte NiO creates a passivation layer of $Ni(OH)_2$ and the charging reaction is that of nickel hydroxide [176–180]. In any case, during the charge reaction of nickel oxide Ni(II) oxidizes to Ni(III) and, the final electrochemical response is greatly dependent on porosity, degree of crystallinity and domain size and surface area [90].

In fact, the synthesis procedures and associated nanostructure have a strong effect on the final properties of nickel oxides [181]. Nickel oxide is usually reduced by heat treatment of nickel hydroxide. Yang et al. studied the effect of the calcination temperature on nickel hydroxide xerogels obtained by sol-gel. Then, they treated at different temperatures, from 110ºC to 450ºC for 1h to produce nickel oxides and measured their electrochemical response. They observed an increase in pore volume until 280ºC. If temperature was further increase, this parameter remained constant. Only when a temperature of at least 280ºC was applied there was a full conversion from the hydroxide to the oxide form and, an increase on temperature produced an increased crystallinity, as expected. Finally, they reported capacitance values obtained in the 0.0V to 0.6V potential range vs. Hg/HgO at 2 $mA \cdot cm^{-2}$ applied current. Results showed that a maximum *capacitance* of 696 $F \cdot g^{-1}$ was obtained at 250ºC and then decreased with increased temperature. This is later explained by a limited ion transport and electrolyte penetration in more crystalline structures which leads to slow electrochemical processes and charge storage delivery [182]. Therefore, when production of nickel oxide is considered, synthesis methods for nickel hydroxide are evaluated with the subsequent calcination process.

Nanomaterials with very different morphology have been prepared, such as nanoplates, nanosheets, nanorings, etc. Yan et al. [183] reported a hydrothermal method to produce nanoplates and nanocolumns (stacking of nanoplates) that, in 1M KOH and in the potential range from -0.25V to 0.65V vs. SCE they exhibited a maximum of *390* $F \cdot g^{-1}$ at 5$A \cdot g^{-1}$. Nanoflakes have also been prepared by precipitation with a maximum *capacitance* reported value of 942 $F \cdot g^{-1}$ in the 0.0V to 0.40V potential range, 2M KOH at an applied current of 5mA [184]. As a matter of fact, the final morphology is usually correlated to the synthesis method used, and many routes have been explored in the production of this material. For example, if NiO is synthesized by chemical bath

deposition by means of an alkaline bath of nickel nitrate followed by thermal treatment, a maximum value of *167 F·g*$^{-1}$ for a NiO honeycomb thin-film on top of stainless steel, obtained at 20 mV·s^{-1} in the -0.8V to 0.4V vs. SCE in 2M KOH has been reported [181]. If porosity is controlled during the synthesis method, as in the case in sol-gel synthesis, an increased *capacitance* can be obtained. For example, Zhang et al. [185] produced nickel oxide aerogels by a citric-acid and formamide assisted sol-gel synthesis, followed by thermal treatment. Aerogels present increased porosity that enhances electrode-electrolyte interactions, leading to much higher capacity values, (*~800 F·g*$^{-1}$) at 10 mV·s^{-1} in the 0.0V to 0.5V potential range and, if temperature treatment is optimized, much higher values are obtained.

Kate et al. [90] summarized and evaluated the pros and cons of the most common synthesis techniques for the production of NiO for energy storage purposes (Fig. 1.15), namely, hydrothermal and solvothermal synthesis, chemical bath deposition, chemical precipitation, electrochemical deposition, microwave and electrophoretic deposition and sol-gel. Some of the different morphologies and synthesis routes to produce nickel oxide are summarized in Table 1.2.

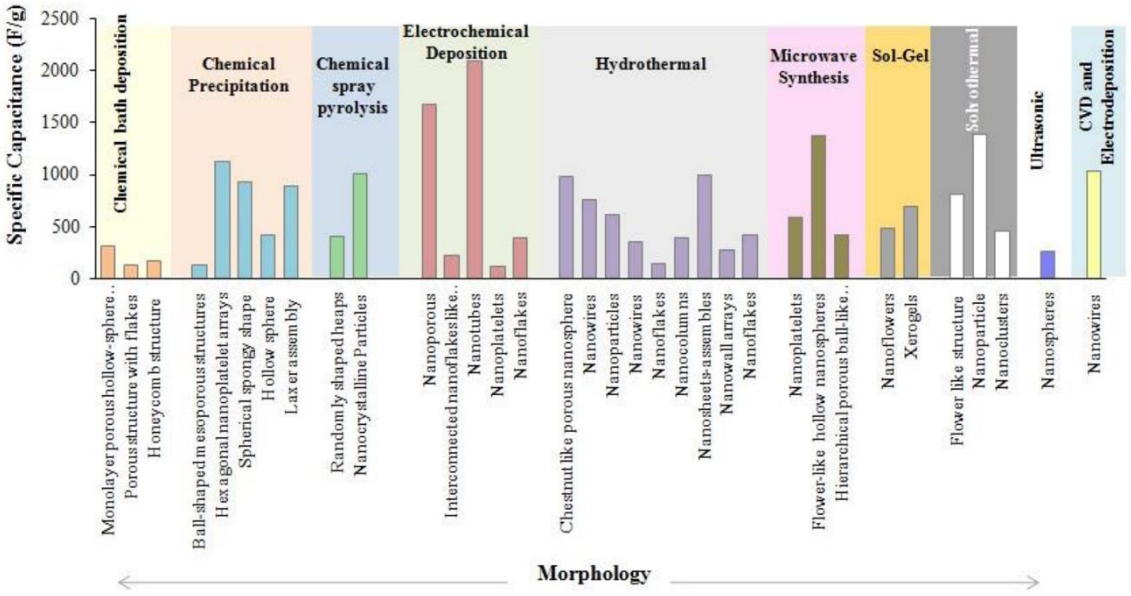

Fig. 1.15. Representation of different morphologies and associated reported specific capacitances for NiO. Extracted with copyright permission from [90].

Table 1.2
Summary of some of the reported morphologies for nickel oxide together with their synthesis route and capacity values.

Material	Morphology	Synthesis	Calcination Temperature (ºC)	*Capacitance* ($F \cdot g^{-1}$)	Current density /Scan rate	Electrolyte	Potential window (V)	Capacity retention (number cycles)	Ref.
Porous NiO	Nanoslices	Chemical bath deposition and hydrothermal treatment	400	*176*	5 $A \cdot g^{-1}$	KOH 1M	-0.3 to 0.7 (vs. SCE)	100% (1000)	[183]
Porous NiO	Nanoplates	Chemical bath deposition and hydrothermal treatment	400	*285*	5 $A \cdot g^{-1}$	KOH 1M	-0.3 to 0.7 (vs. SCE)	>100% (1000)	[183]
Porous NiO	Nanocolumn	Chemical bath deposition and hydrothermal treatment	400	*390*	5 $A \cdot g^{-1}$	KOH 1M	-0.3 to 0.7 (vs. SCE)	>100% (1000)	[183]
NiO	Nanoflakes	Chemical bath deposition	250	*942*	5 mA	KOH 2M	0.0 to 0.5 (vs. SCE)	82% (1000)	[186]
Hierarchical porous NiO	Nanoflowers	Microwave-assisted synthesis	300-400	*277*	2.5 $mV \cdot s^{-1}$	KOH 2M	-0.2 to 0.5 (vs. SCE)	97% (100)	[187]
NiO	Nanospheres	Ostwald-ripening in alkaline solution	300	*710*	1 $A \cdot g^{-1}$	KOH 6M	0.0 to 0.60 (vs. SCE)	98% (2000)	[188]
NiO	Nanowall arrays	Hydrothermal	500	*270*	0.67 $A \cdot g^{-1}$	KOH 1M	0.0 to 0.55 (vs. SCE)	93% (4000)	[189]
NiO	Nanoflakes	Potentiodynamic electrodeposition	300	*222*	10 $mV \cdot s^{-1}$	KOH 1M	-0.2 to 0.4 (vs. SCE)	94% (1000)	[190]
NiO	Thin-film	Galvanostatic electrodeposition	200-400	*277*	5 $mV \cdot s^{-1}$	KOH 1M	0.0 to 0.5 (vs. Ag/AgCl)	-	[191]
NiO	Nanotubes	Ni electroplating and annealing	450	*2076*	12 $A \cdot g^{-1}$	KOH 1M	0.35 to 0.85 (vs. SHE)	~100% (500)	[192]
NiO	Nanorods	Ni electroplating and annealing	450	*1026*	7 $A \cdot g^{-1}$	KOH 1M	0.35 to 0.85 (vs. SHE)	~100% (500)	[192]

Electrodeposition is a simple technique for the preparation of nickel oxide materials. Anodic electrodeposition of porous nickel oxide films on top of a stainless steel foil was performed by using a bath of sodium acetate, nickel sulphate and sodium sulphate at a 0.9V vs. Ag/AgCl potential [174] and subsequent thermal treatment at 300ºC for 1h, displaying a specific capacity of 178 $C \cdot g^{-1}$ at 10 $mV \cdot s^{-1}$ and 130 $C \cdot g^{-1}$ at 200 $mV \cdot s^{-1}$ and a capacity retention of nearly 80% after 4000 cycles. Electrodeposited NiO and $Ni(OH)_2$ materials generally display high-power capabilities. This is attributed to their nanoflake structure that enables faradaic reactions to occur on the grain surface enhancing and electron conduction and shortening proton diffusion paths.

Several groups have reported thin-films with extremely high capacitance values. Wu et al. [193] reported 1478 $F \cdot g^{-1}$ at 0.5$A \cdot g^{-1}$ in KOH 1M at the potential window from 0.05 to 0.45V vs. SCE, with very good rate capability and long cycle stability (87% after 500 cycles). These results were displayed when NiO was deposited from $Ni(NO_3)_2$ 0.08M by applying -0.9V vs. SCE until a total charge of 0.5C passed, and subsequent thermal treatment. In their report, they stated that the charging mechanism was not diffusion controlled but a very fast redox reaction at the interface. Contrastively, Srinivasan [179] reported only 59 $F \cdot g^{-1}$ in the 0.0V to 0.5V vs. Ag/AgCl in KOH 3% for NiO electrodeposited on gold from 1.8M $Ni(NO_3)_2$ and 0.075M $NaNO_3$ at a cathodic current of 5$mA \cdot cm^{-2}$. More intermediate responses have been obtained for NiO prepared by anodic electrodeposition and thermal treatment at 300ºC, for example, *167F·g^{-1}* in 1M KOH at 1$A \cdot g^{-1}$ in the 0.0V-0.45V potential range and *140F·g^{-1}* after 5000 cycles [194]. Again, porosity seems to be a determining factor in electrolyte penetration and performance of nickel oxide, limiting diffusion paths [195].

It is generally reported that two main limitations shall be overcome for its potential use in energy storage devices. These are: poor cycle performance and high resistivity [196]. Many authors compare their performance to supercapacitor and pseudocapacitor electrodes despite the redox activity with phase transformations because of their high rate capabilities and capacitance contribution (expanded active surface area due to their nanostructure). Thus, when compared to supercapacitor electrodes, their degradation is extremely high. However, if compared to battery materials, its capacity value is extremely inferior while it presents excellent capacity retention with cycling. It is worth mentioning that, in many cases, also an activation process during the first 1000 charge/discharge cycles is observed. This is generally attributed to electrolyte penetration to the inner initially-inaccessible pores.

Nonetheless, it is still interesting to avoid degradation of NiO. For that matter, cobalt or carbon-based materials are generally added as stabilizing agents. Nickel-cobalt oxide was also combined with carbon nanotubes to improve electronic conductivity and chemical stability, resulting on *569 F·g^{-1}* at 10 $mA \cdot cm^{-2}$ in 1M KOH in the 0.0V to 0.5V potential range and a 99.8% capacity retention after 1000 cycles. Moreover, the effect of the Ni/Co ratio has been studied and it was determined that the material exhibited a maximum capacity at a 50% cobalt content [197].

In addition, high resistivity, because of the semiconductor nature of nickel oxide, is another of the main limitations of nickel oxide. Again, composite materials with carbon-based materials or introducing cobalt shall overcome this limitation to a certain extent. Carbon-based materials can act as conductive matrix on top of which nickel oxide nanoparticles can undergo redox reactions while shortening diffusion paths. For example, when CNTs are mixed with NiO, results up to *1000 F·g^{-1}* have been reported, three times bigger than NiO thin film [198]. Nonetheless, for such a high capacitance, NiO film on

top of CNT was only about 5nm thick and the mass considered was that of NiO and not the entire composite, leading to an overestimation of the value.

Reduced graphene oxide is also used as support for NiO nanoparticles. For example, Trung et al. [199] synthesized a 3D porous reduced graphene oxide on top of which NiO nanoparticles were deposited via thermal treatment in a 3-step process (Fig. 1.16). The material exhibited excellent capacity (*1328 $F \cdot g^{-1}$* at $1A \cdot g^{-1}$ in the -0.1V to 0.35V vs. SCE in KOH 2M) and cycling stability (87% retention after 2000 cycles). However, it seems crucial to further optimize the synthesis of composite materials and investigate the electrochemical properties that they may yield.

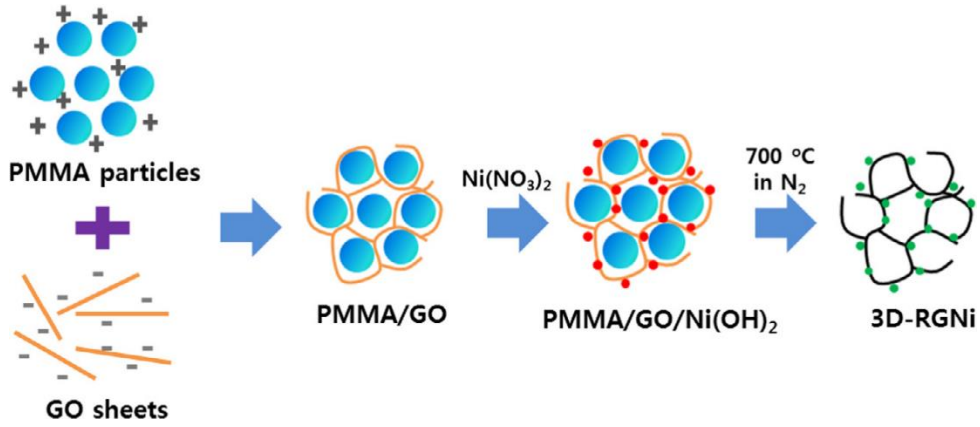

Fig. 1.16. Illustration of a synthesis process of reduced graphene oxide with nickel oxide nanoparticles developed by Trung et al. Reprinted with copyright permission of [199].

Spinel Co_3O_4 and CoO_x as electrode material in alkaline media

The electrochemical fingerprint of bulk spinel cobalt oxide is very different to the analogous spinel manganese oxide or iron oxide: It presents two faradaic peaks that correspond to a battery-like electrochemical response. However, when nanostructured, its increased active surface and surface-confined redox reactions result in noticeable capacitance contribution. Therefore, it has interesting electrochemical and physical features, for instance, its redox reaction is highly reversible, it has long-term stability, large surface area and, when transformed into oxyhydroxide in its charged state, it has good conductivity [22]. Moreover, given the high theoretical capacity of Co_3O_4 (890 $mA \cdot h \cdot g^{-1}$) and of CoO (718 $mA \cdot h \cdot g^{-1}$), these materials have attracted much attention in their potential application for energy storage [90].

Its charging reaction in alkali media is presented in eq. 1.19:

$$Co_3O_4 + H_2O + OH^- \leftrightarrow 3\ CoOOH + e^- \qquad \text{(eq. 1.19)}$$

At the same time, cobalt oxyhydroxide can undergo a second reaction in which the material is transformed into Co(IV) oxide, as depicted by eq. 1.20.

$$CoOOH + OH^- \leftrightarrow CoO_2 + H_2O + e^- \qquad \text{(eq. 1.20)}$$

There are many different strategies to synthesize this material, such as template assisted [200], chemical coating [201], spray pyrolysis [202], sol-gel [203], etc. Furthermore, to increase the active surface of the material, intrinsically related to its electrochemical performance, several microstructures and morphologies have also been developed. For example, microspheres [200], nanosheets, aerogels [204], nanowires [205], nanorods [206], nanoflowers [207], nanotubes [208] or thin films [202]. As in the case for NiO, these nanostructures are greatly dependent upon the synthesis strategy employed, which

greatly influences the final electrochemical response of the material. For example, mesoporous microspheres were prepared by silica-template directed synthesis. Reports showed that a *capacitance* of *102 $F \cdot g^{-1}$* can be achieved [200]. Kim et al. [209] electrodeposited cobalt hydroxide that, by means of a thermal treatment, was transformed into cobalt oxide. Their material in 2M KOH displayed *235 $F \cdot g^{-1}$* in the -0.1V to 0.4V potential range vs. Ag/AgCl. It seems that, in general, cobalt oxide has a lower charge storage capability. This is related to the anhydrous nature of the material [202]. To provide an overview of this material as electrode material, some examples of different nanostructures and synthesis methods employed in the production of cobalt oxide are summarized in Table 1.3.

The preparation of cobalt oxide by means of electrodeposition is usually performed in a two-step process. For example, Yuan et al. [210] synthesized cobalt oxide nanosheets on top of nickel foam by means of electrodeposition from nitrate precursors at -1.0V vs. SCE for 20 minutes followed by a calcination process at 250ºC for 2h. The material showed a capacity of 379.86 $mA \cdot h \cdot g^{-1}$ in the 0.5V potential range at $2A \cdot g^{-1}$, 204.3 $mA \cdot h \cdot g^{-1}$ at $10A \cdot g^{-1}$ and approximately a 5% capacity drop during the first 500 cycles.

Some authors reported that spinel cobalt oxide presents several limitations, such as poor cycling stability and lower potential window. However, it is evidenced by the reported results that, in general, high capacity retention with cycling is observed in alkali media. Anyhow, this effect is more visible in cobalt oxide as electrode material for lithium ion batteries. In that case, later considered, nanoparticles tend to aggregate during charge-discharge cycling and composite materials, surface-modified cobalt oxide and doped cobalt oxides have been produced to overcome this challenge [211].

Carbon is usually used in the production of cobalt oxide composite materials. For example, Co_3O_4 nanowires have been synthesized on top of CVD graphene foam [212]. In this case, the electrochemical response limited to the 0-0.5V potential range had a pseudocapacitor behaviour with a specific capacitance of *768 $F \cdot g^{-1}$* at 10 $A \cdot g^{-1}$ and growing capacitance up to *1100 $F \cdot g^{-1}$* with cycling. The stabilization of capacitance with cycling has been observed in other graphene-based composites [213]. For instance, He et al. [214] prepared Co_3O_4 on top of exfoliated graphene oxide and reported *430$F \cdot g^{-1}$* at 3 $A \cdot g^{-1}$ in 6M KOH in which approximately a 100% of capacitance was retained after 300 cycles.

MWCNT/Co_3O_4 composite was prepared by acid treatment of MWCNTs followed by precipitation and reflux in n-hexanol, displaying a capacitance of 200 $F \cdot g^{-1}$ in the -0.6V to 0.4V potential range vs. $Hg/HgSO_4$ in 1M KOH [215]. It seems that introducing the carbon-based material led to an expanded potential window, which can really benefit the ultimate performance of the device.

García-Gómez et al. [216] studied the potentiostatic electrodeposition of reduced graphene oxide with cobalt oxide. For that purpose, cyclic voltammetry in the -1.5V to 0.5V vs. SCE potential range was applied to a cobalt nitrate/graphene oxide suspension at different scan rates and evaluated their performance in 1M KOH. Best results were obtained when electrodeposition was performed at a 75 $mV \cdot s^{-1}$ scan rate, when the material exhibited *608 $F \cdot g^{-1}$* at $1A \cdot g^{-1}$ and increased reversibility when compared to only CoO_x.

Table 1.3
Summary of some of the reported morphologies for cobalt oxide together with their synthesis route and capacity values.

[1] Results are likely to be associated to cobalt hydroxide given the applied calcination temperature.

[2] No in-depth study of the mechanism by which the potential range may be extended. Furthermore, the reported value is wider than the 1.2V potential window of aqueous electrolytes.

Material	Morphology	Synthesis	Calcination Temperature (ºC)	*Capacitance* ($F \cdot g^{-1}$)	Current density /Scan rate	Electrolyte	Potential window (V)	Capacity retention (number cycles)	Ref.
Mesoporous Co_3O_4	Microspheres	Template assisted precipitation	200-450	*102*	3 $mV \cdot s^{-1}$	KOH 4M	0.1 to 0.6 (Hg/HgO)	74% (500)	[200]
Microporous Co_3O_4	Aerogel	Epoxy addition and supercritical CO_2 drying	200	*623*	25 $mV \cdot s^{-1}$	NaOH 1M	0.2 to 0.53 (Ag/AgCl)	96% (1000)	[204]
MWCNTs/Co_3O_4	Nanotubes	Acid treatment and chemical precipitation in *n*-hexanol	140, reflux	*200*	10 $mV \cdot s^{-1}$	KOH 1M	-0.6 to 0.4 (Hg/Hg_2SO_4)	-	[215]
Co_3O_4	Thin-film	Spry pyrolysis	400	*74*	5 $mV \cdot s^{-1}$	KOH 2M	0.0 to -0.6 (SCE)	-	[202]
Co_3O_4	Xerogel powder	Sol-gel	110-600 (max. 150)[1]	*291*	5 $mV \cdot s^{-1}$	KOH 1M	-0.3 to 0.5 (SCE)	Not quantified	[203]
Co3O4/ Ni foam	Nanowires	Template-free growth method	300	*746*	5 $mA \cdot cm^{-2}$	KOH 6M	-0.05 to 0.38 (SCE)	85% (500)	[205]
Nanoporous Co_3O_4	Nanorods	Hydrothermal	300	*280*	5 $mV \cdot s^{-1}$	KOH 2M	-0.2 to 0.6 (SCE)	-	[206]
Porous Co_3O_4	Microspheres	Solvothermal (ethylene glycol)	300	*1183*	2 $A \cdot g^{-1}$	KOH 2M	0.0 to 0.5 (SCE)	93% (5000)	[208]
Co_3O_4	Thin-film	Electrodeposition	200	*235*	20 $mV \cdot s^{-1}$	KOH 2M	-0.1 to 0.4 (Ag/AgCl)	-	[209]
Co_3O_4	Nanowires	Precipitation	90	*922*	2 $A \cdot g^{-1}$	KOH 1M	-0.4 to 0.4 (SCE)	95% (5000)	[217]
Co_3O_4/Ag	Nanowires	Precipitation and Layered deposition	90	*1006*	2 $A \cdot g^{-1}$	KOH 1M	-0.4 to 0.4 (SCE)	95% (5000)	[217]
Co_3O_4	Film	Ammonia precipitation and layered deposition	-	*165*	10 $mV \cdot s^{-1}$	KOH 1M	-0.4 to 0.4 (SCE)	98% (1000)	[218]
Mesoporous Co_3O_4	Brush-like Nanowires	Hydrothermal	250	*1525*	1 $A \cdot g^{-1}$	KOH 30%	0 to 0.8 (Ag/AgCl)	91% (5000)	[219]
Mesoporous Co_3O_4	Flower-like nanowires	Hydrothermal	250	*1199*	1 $A \cdot g^{-1}$	KOH 30%	0 to 0.8 (Ag/AgCl)	91% (5000)	[219]
Co_3O_4	Nanocubes	Hydrothermal	500	*430*	10 $mV \cdot s^{-1}$	KOH 6M	-0.4 to 1 (Ag/AgCl)[2]	85% (1000)	[220]
Co_3O_4	Micro-dumbbells	Surfactant guided assembly	300	*407*	1 $A \cdot g^{-1}$	KOH 6M	-0.1 to 0.5 (Ag/AgCl)	97% (2000)	[221]
Porous Co_3O_4 Co	Nanoparticles	Metal organic framework followed by thermolysis	550	*150*	1 $A \cdot g^{-1}$	KOH 2M	0.0 to 0.5 (Ag/AgCl)	100% (3400)	[222]

Spinel Co_3O_4 and CoO_x as electrode material in lithium-ion batteries

Nonetheless, cobalt oxides (CoO_x) materials are traditionally studied for lithium ion batteries since Tarascon's discovery of the reversible mechanism of lithium storage [223,224]. In particular, it can accommodate up to 8 lithium ions per unit. Its lithium insertion material is very different to that of graphite, exemplified in equations 1.21 to 1.23:

$$M_xO_y + 2yLi^+ \leftrightarrow yLi_2O + xM \quad \text{(eq. 1.21)}$$

$$CoO + 2Li^+ \leftrightarrow Li_2O + Co \quad \text{(eq. 1.22)}$$

$$Co_3O_4 + 8Li^+ \leftrightarrow 4\ Li_2O + 3Co \quad \text{(eq. 1.23)}$$

The main challenge with cobalt oxides for lithium ion batteries is their large initial capacity loss and poor cycling stability. This is caused by large volume changes during the charge-discharge reaction that create local stress and pulverize the electrode [225]. As in the case for electrode material in alkali media, many different synthesis routes have been studied to improve performance by means of nanostructuring [226]. Lee et al. [227] have summarized cobalt oxide synthesis methods and performances for energy storage applications. In their work, they consider hydrothermal and solvothermal synthesis, solution combustion synthesis (cobalt nitrate is mixed with combustion fuels and is transferred to a furnace where reaction takes place), aerosol flame synthesis (nebulizing atomic droplets of cobalt nitrate in methanol and delivering them to a flame for hydrolysis), molten salt synthesis, microemulsion synthesis (water microemulsion by means of surfactants that function as micro-reactors), spray conversion synthesis (cobalt nitrate dissolved in H_2O before being fed through a nozzle and spray-dried at 250^{o}C and then calcinated), chemical vapour deposition, electrodeposition and ultrasonic dispersion with thermal oxidation. As a summary, they state that hydrothermal synthesis enables good control over materials morphology; solution combustion techniques generate lower capacity values; aerosol offers scaling-up advantages in terms of reactivity but is extremely costly; microemulsion is a tedious synthesis although great control over morphology is achieved and, finally, deposition techniques yield impressive capacity values while keeping small particle size and ease of scale-up [227]. A summary of the main reported results for cobalt oxide materials as electrode material in lithium ion batteries is included in Table 1.4.

Electrodeposition serves as a method to produce nanostructured thin-films. Cobalt oxide is generally produced from electrodeposition of its parent form, cobalt hydroxide, and calcination. Do and Dai [228] reported that the composition is temperature dependent. When lower temperatures are used (300^{o}C) pure Co_3O_4 is obtained, while higher temperatures (500^{o}C) decomposes this phase yielding CoO. These materials were deposited by applying 0.5 mA·cm^{-2} to a gold substrate and an electrolyte consisting of 0.175M $Co(NO_3)_2$/0.075 $NaNO_3$ dissolved in a 50:50 mixture of aqueous:ethanol followed by thermal treatment. CoO displayed 715 mA·h·g^{-1} during the first cycle, which decomposed CoO to Co and a decay in discharge potential plateau from 0.72V to 0.02V, which led to a capacity of 433.1 mA·h·g^{-1}. When cobalt hydroxide was used, however, capacity was 1089.2 mA·h·g^{-1} that increased to a value of 1589.4 mA·h·g^{-1} after 25 cycles. Xiao et al. [229] reported that, by using Brij 56 as structure-directing agent, a CoO film is produced by applying 1.0 mA·cm^{-2} cathodic current for 600s and thermal treatment at 350^{o}C for 2h. The material, with nanoflake structure, displayed 710 and 509 mA·h·g^{-1} in 1M $LiPF_6$: ethylene carbonate 50:50 electrolyte at 1C after 0 and 50 cycles respectively. Note that similar benefits (improved cycle stability, volume changes inhibition and enhanced conductivity) can be obtained when combined with other

materials, especially carbon-based materials. For example, Kim et al. [230] synthesized a reduced graphene oxide/cobalt oxide thin-film by co-electrodeposition (Fig. 1.17) . Thus, cobalt nitrate was added to a graphene oxide suspension containing sodium nitrate. Electrodeposition was performed at -1.0V (vs. Ag/AgCl) for 5 minutes on top of stainless steel. Then, calcination at 350ºC for 2h was performed. Furthermore, they reported that by chemically modifying the graphene oxide suspension with poly(ethyleneimine)(PEI), adsorption of Co^{2+} is facilitated while graphene oxide aggregation is avoided. The composite material displayed 1523 $mA \cdot h \cdot g^{-1}$ after 60 cycles.

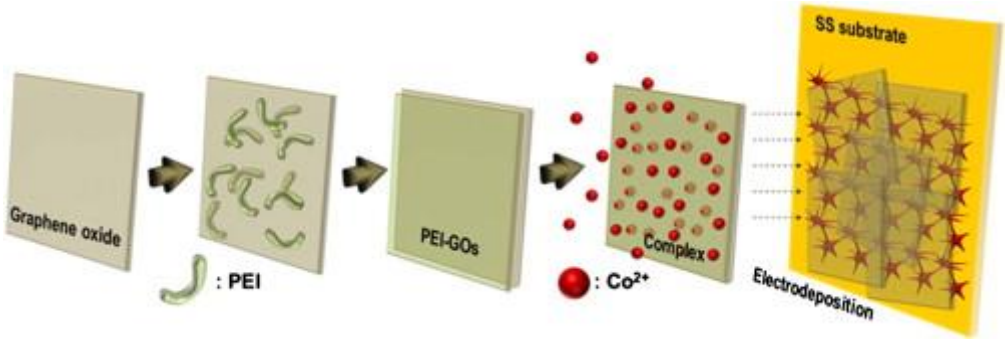

Fig. 1.17. Schematic representation of the co-electrodeposition of cobalt oxide/graphene composite material. Reprinted with copyright permission of [230].

Table 1.4.

Electrochemical performance of cobalt oxide materials used as electrodes for lithium ion batteries. Reprinted with copyright permission from [227].

Material	Morphology (particle size)	Synthesis	Potential range vs. Li/Li^+ (V)	Current density	Initial discharge capacity (mA h g^{-1})	Initial Coulombic efficiency (%)	Capacity retention (number of cycles)	Ref.
C@Co_3O_4	Nanospheres (400–500 nm)	Hydrothermal	3.0–0.5	0.5 C	818	98.3	567 mA·h·g^{-1} (107)	[211]
CoO@CNT core–shell	Nanorod	Multi-step hydrothermal	3.0–0.005	0.1 C	1082	69	1080 mA·h·g^{-1} (100)	[231]
Co_3O_4–C core–shell	Nanowire array	Hydrothermal	3.2–0	0.5 C	1330.8	88.1	989.0 mA·h·g^{-1} (50)	[232]
Co_3O_4	Nanorod array	Fluorine-mediated hydrothermal	3.0–0.005	1 C	1192	80.7	1000 mA·h·g^{-1} (20)	[233]
Porous Co_3O_4	Nanowire array	Microwave-assisted hydrothermal	-	400 mA g^{1}	~1100	~80	600 mA·h·g^{-1} (100)	[225]
Co_3O_4	Hollow spheres (2.5 mm)	Hydrothermal with aging	3.0–0.01	100 mA g^{1}	1334	73	407 mA·h·g^{-1} (100)	[234]
Macroporous CoO_x	Nanoparticles	Solution combustion	3.0–0.01	50 mA g^{1}	1191	76.2	400 mA·h·g^{-1} (100)	[226]
CoO	Nanoparticles (20–30 nm)	Urea-assisted auto-combustion	3.0–0.005	0.1 mA cm^{2}	1159.03	-	565.2 mA·h·g^{-1} (30)	[235]
Co_3O_4	Nanocrystalline (50–85 nm)	Aerosol flame synthesis	3.0–0.01	1 C	1130	66	571 mA·h·g^{-1} (30)	[236]
Co_3O_4	Powder (200 nm)	Molten salt synthesis	3.0–0.005	600 mA g^{1}	-	-	710 mA·h·g^{-1} (50)	[237]
Hierarchical Co_3O_4	Nanosheets	Composite-hydroxide-mediated	3.0–0	140 mA g^{1}	1336	65.1	680 mA·h·g^{-1} (50)	[238]
Porous Co_3O_4	Nanorods (80–150 nm)	Microemulsion	3.0–0.01	50 mA g^{1}	1171	-	850 mA·h·g^{-1} (10)	[239]
Nanosized Co_3O_4	Powder (<60 nm)	Spray conversion synthesis	2.5–0.001	0.2 mA cm^{2}	1100	-	400 mA·h·g^{-1} (50)	[240]

Table 1.4 cont.

Cobalt oxide	Nanomaterials (CoO: 15 nm)	Chemical vapour deposition	3.0–0	0.05 C	~900	-	800 $mA \cdot h \cdot g^{-1}$ (30)	[241]
$NiSi_x$/CoO core–shell	Nanowire arrays	Chemical vapour deposition + radio frequency sputtering	2.5–0.01	0.5 C	1533	60.1	900 $mA \cdot h \cdot g^{-1}$ (200)	[242]
Dendrite-like Co_3O_4/C	Microparticles	Low-temperature hydrothermal + CVD	3.0–0.005	0.1 C	1666	53	500 $mA \cdot h \cdot g^{-1}$ (40)	[243]
Mesoporous cobalt oxide	Film (10–20 nm)	Electrodeposition	3.0–0.02	1 C	1002	71	509 $mA \cdot h \cdot g^{-1}$ (50)	[229]
Graphene/Co_3O_4	Thin-film	Co-electrodeposition	3.0–0.01	700 mA g^{1}	1342	-	1523 $mA \cdot h \cdot g^{-1}$ (60)	[230]
Nanoporous CoO/Co	Thin-film	Electrostatic spray	3.0–0.01	0.4 C	1057	-	1182 $mA \cdot h \cdot g^{-1}$ (70)	[244]
CoO on graphene nanosheets	Quantum dots (3–8 nm)	Ultrasonic dispersion	3.0–0.01	50 mA g^{1}	1756	56	1592 $mA \cdot h \cdot g^{-1}$ (50)	[245]
CoO/RGO nanocomposite	-	Ultrasonic dispersion	3.0–0.01	100 mA g^{1}	1052.1	70	701.7 $mA \cdot h \cdot g^{-1}$ (50)	[246]

Spinel $NiCo_2O_4$ and Ni-Co oxides

Spinel nickel-cobalt oxide combines good electronic conductivity in its discharged state (~62 $S \cdot cm^{-1}$) with high electrochemical activity of its redox reaction (with contribution from both nickel and cobalt ions). For that reason, it exhibits high capacitance values even at short charge-discharge times [63]. Compared to single oxides, spinel nickel cobaltite presents richer redox electrochemistry due to the combination of nickel and cobalt oxide and much better electrical conductivity [247]. The oxidation-reduction reaction of spinel in alkali media is usually depicted as a transformation into cobalt and nickel oxyhydroxides (eq. 1.24):

$$NiCo_2O_4 + OH^- + H_2O \leftrightarrow NiOOH + 2CoOOH + 2e^- \quad \text{(eq. 1.24)}$$

At the same time, oxyhydroxides exhibit a second reaction as in the case of spinel cobalt oxide (eq. 1.25):

$$MOOH + OH^- \leftrightarrow MO_2 + H_2O + e^- \quad \text{(eq. 1.25)}$$

M denotes either Co or Ni. While nickel can only vary between Ni(II) and Ni(III), cobalt can be further oxidized to Co(IV) on the surface of the electrode material. The theoretical capacity for this overall process, including battery-like and pseudocapacitive contributions, is *2005 $F \cdot g^{-1}$* in a 0.6V potential window in alkaline electrolyte. However, further analysis on kinetics of the material are required to separate and understand the capacitive and diffusion contributions to the total charged stored in the material [63].

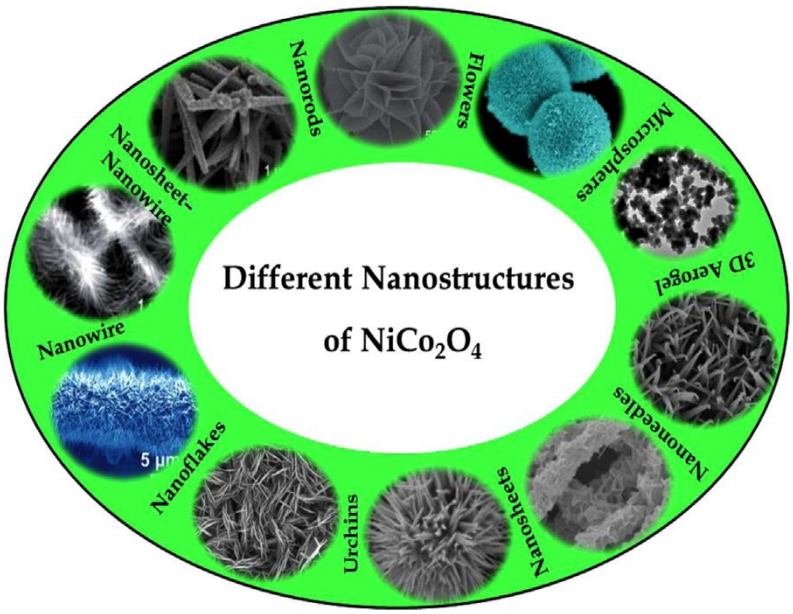

Fig. 1.18. Illustration of the different morphologies that have been reported for nickel cobaltite. Reprinted with copyright permission of [247].

Similar to NiO and Co_3O_4, there are many different synthesis strategies for $NiCo_2O_4$ that result in different morphologies (Fig. 1.18) and electrochemical properties. Dubal et al. [247] have extensively studied current literature on the topic of synthesis and electrochemical properties of nickel cobaltite. Considering nanostructured $NiCo_2O_4$, the main synthesis strategies are: sol-gel method, hydrothermal and solvothermal, chemical precipitation, chemical bath deposition and electrodeposition. A summary of the main reported results is included in Table 1.5.

Table 1.5
Summary of some reported work on the synthesis of $NiCo_2O_4$ and their electrochemical performance as electrode material in alkali media. Adapted with copyright permission from [247].

Material	Morphology	Synthesis	Calcination Temperature (ºC)	*Capacitance ($F \cdot g^{-1}$)*	Current density /Scan rate	Electrolyte	Potential window (V)	Capacity retention (number cycles)	Ref.
$NiCo_2O_4$	3D network of nanoparticles	Aerogel epoxide-drive Sol-gel	200	*719-1400*	25 $mV \cdot s^{-1}$	NaOH 1M	-0.2 to 0.55 (vs. Ag/AgCl)	91% (2000)	[248]
$NiCo_2O_4$	Hexagonal nanoplates	Hydrothermal	300	*294*	1A·g^{-1}	KOH 1M	0.0 to 0.5 (vs. SCE)	89% (3000)	[249]
$NiCo_2O_4$	Urchin-like nanostructures	Hydrothermal	300	*1650*	1A·g^{-1}	KOH 3M	0.0 to 0.4 (vs. SCE)	90.8% (2000)	[250]
$NiCo_2O_4$	3D microspheres with radial nanowires	Hydrothermal and thermal decomposition	300	*1284*	2 A·g^{-1}	KOH 6M	0.0 to 0.45 (vs. Ag/AgCl)	97.5% (3000)	[251]
$NiCo_2O_4$	Flower-like	Hydrothermal	170 (300)	*739(236)*	2.86 A·g^{-1}	KOH 1M	0.0 to 0.45 (vs. Ag/AgCl)	~95% (2500)	[252]
Ni-Co oxides (1:1, 1:2)	Tremella composed of nanoflakes	Solvothermal	250	*971-1550*	4 A·g^{-1}	KOH 2M	0.0 to 0.55 (vs. HgO/Hg)	93.5% (1000)	[253]
$NiCo_2O_4$	Flower-like	Solvothermal	300	*1191*	1A·g^{-1}	KOH 2M	0.0 to 0.55 (vs. HgO/Hg)	78% (1200)	[254]
$NiCo_2O_4$	Nanoflakes	Chemical precipitation	280	*1270*	1A·g^{-1}	KOH 6M	0.0 to 0.6 (vs. Ag/AgCl)	95.2% (5000)	[255]
$NiCo_2O_4$	Flower-like microspheres	Microwave assisted reflux	300	*1006*	1A·g^{-1}	KOH 6M	0.0 to 0.5 (vs. HgO/Hg)	93.2% (1000)	[256]
$NiCo_2O_4$	Nanosheets and nanorods	Chemical bath deposition	300	*330-490*	20 $mV \cdot s^{-1}$	KOH 2M	0.0 to 0.4 (vs. Ag/AgCl)	92% (1000)	[257]
$Co_{0.67}Ni_{0.33}$ DHs /$NiCo_2O_4$/CFP	Nanowires supported nanosheets	Hydrothermal + Electrodeposition	300	*1500*	2 $mA \cdot cm^{-2}$	KOH 1M	-0.1 to 0.45 (vs. SCE)	81.3-68% (2000)	[258]
$NiCo_2O_4$	Microparticles	Electrodeposition	300	*312*	1A·g^{-1}	KOH 1M	0.0 to 0.6 (vs. HgO/Hg)	75% (3000)	[259]
Ni-Co oxyhydroxide	Nanoparticles	Sol-gel + Microwave assisted	100-200 (MW)	*70-215*	5 $mA \cdot cm^{-2}$	NaOH 1M	1.0 to 1.6 (vs. RHE)	-	[260]

Excellent results, close to the theoretical value, have been achieved by $NiCo_2O_4$ nanosheets obtained by means of electrodeposition on top of carbon nanofibers [261]. This is due to the simultaneous and uniform distribution of nickel and cobalt electrodeposition. Lou et al. [262] co-electrodeposited Ni-Co hydroxide on top of Ni foam by applying -1.0V vs. SCE to a solution containing nickel and cobalt nitrates for 5 minutes. After annealing at 300ºC for 2 h, nickel cobaltite was prepared. The material displayed *2010 $F \cdot g^{-1}$* at $2A \cdot g^{-1}$ in KOH 3M in the -0.1Vto 0.3V vs. SCE potential range. Moreover, high rate capabilities, with a *capacitance* of *1450 $F \cdot g^{-1}$* at 20 $A \cdot g^{-1}$ and excellent cycling stability, with an activation to *2278 $F \cdot g^{-1}$* after 400 cycles and a 94% capacity retention after 2400 cycles.

To maximize active surface area and improve overall conductivity, carbon-based composites have been synthesized. For example, $NiCo_2O_4$ has been electrodeposited on top of carbon nanofibers [261]. A potential of -1.0V vs. SCE was applied to an electrolyte containing a Ni/Co ratio 1:2 to electrodeposit spinel nickel cobalt oxide on top of a previously activated carbon foam. After electrodeposition, the material was thermally treated for 2h at 300ºC. The material displayed *2658 $F \cdot g^{-1}$* at $2A \cdot g^{-1}$ in the -0.1V to 0.5V vs. SCE potential range with excellent rate capabilities. Moreover, it presented 80% capacitance retention after 3000 cycles.

Nickel cobaltite has also been combined with reduced graphene oxide by different routes. It has been obtained by microwave-assisted synthesis [263], surface modification of nickel-cobalt hydroxides and self-assembly of appositively charged nanosheets [264,265] and hydrothermal synthesis [266]. When prepared by hydrothermal method, without surfactants, $NiCo_2O_4$@rGO displays *737 $F \cdot g^{-1}$* at $1A \cdot g^{-1}$ in KOH 2M in a 0.7V potential window and 94% retention after 3000 charge-discharge cycles. Similar results were obtained for the microwave assisted synthesis. Interestingly, a capacity of *735 $F \cdot g^{-1}$* (83% retention) for an applied current as high as 33 $A \cdot g^{-1}$ was reported. Due to the enhanced electronic conductivity of rGO, faster charge-discharge redox reactions can be obtained. For that reason, it seems interesting to further explore this composite material and the effect that different synthesis methods may have.

$Ni(OH)_2$

Nickel hydroxide had its major impact on electrochemical energy storage when used as cathode material in nickel-based batteries, which have been relevant since 1901, when Edison developed the first nickel-iron battery. In general, nickel-based batteries consist of a positive electrode of nickel hydroxide, whose reaction is exemplified in eq. 1.26, a porous separator (such as polyvinyl chloride or polypropylene, in many cases soaked in alkali 30%KOH) and a negative electrode.

Cathode reaction: $Ni(OH)_2 + OH^- \leftrightarrow NiO(OH) + H_2O + e^-$ (eq. 1.26)

The negative electrode has been replaced several times with the subsequent change in battery type. The anode reaction of the Ni-Cd battery is eq. 1.27:

$$Cd(OH)_2 + 2e^- \leftrightarrow Cd + 2OH^- \quad \text{(eq. 1.27)}$$

Later, Cd has been substituted by other materials such as zinc oxide in nickel-zinc batteries, metal alloys in metal hydride batteries ($LaNi_5$, $CeNi_5$-based alloys, $TiNi_x$-based alloys, ZrV_2 or $ZrMn_2$ amongst many others) or a platinum catalyst in nickel-hydrogen batteries. A summary of the most relevant parameters of these batteries is included in Table 1.6.

There are many factors that affect the performance of nickel-based batteries. However, it is worth mentioning that, among them, the performance of the nickel-based electrode material is a key parameter in the electrochemical performance of nickel-based secondary batteries. Thus, studying different micro- and nanostructures, physico-chemical properties when combined with other materials, different synthesis procedures and the resulting electrochemical performances is critical in the development of future nickel-based energy storage devices. The main challenges for nickel hydroxide material as electrode material for battery applications, pointed out by Tsai and Chan [267] in their review, are the development of a low-cost simple method with high yield to produce nanostructured nickel hydroxide, the control of phases, compositions, crystallinity, dimensions and morphology of the nanostructure as a method to control the electrochemical performance and to find suitable additives that enhance its performance while not interfering in the synthesis procedure.

It is also important to highlight that, from a structural viewpoint, nickel hydroxide has two very well-known polymorphs, α and β. These polymorphs were first identified by Bode et al. [268] and are shown in Fig. 1.19. This diagram describes that $Ni(OH)_2$ is oxidized to its NiOOH form during charge and that the polymorphs are differentiated by the average oxidation state of nickel ions and the intercalated species/interslab distance in the interspace between nickel hydroxide layers. While α-$Ni(OH)_2$ consists of a disorganized arrangement of nickel-hydroxide layers with an interslab distance of approximately 8Å, due to intercalated water and anions such as carbonates or nitrates, β-$Ni(OH)_2$ is an ordered structured of nickel hydroxide layers without intercalated species between the slabs, resulting in an inter-slab distance (ISD) of only 4.6Å. During oxidation, α-$Ni(OH)_2$ transforms into γ-NiOOH (ISD: 7Å) while β-$Ni(OH)_2$ oxidizes to β-NiOOH (ISD: 4.8Å). Moreover, while α phase transforms into β with ageing, β converts to γ during overcharging. Finally, the theoretical capacity of the α phase is 390 $mA \cdot h \cdot g^{-1}$ in a 0.5V potential range with a theoretically calculated electron exchange of 1.7 in an α-$Ni(OH)_2$/γ-NiOOH phase transformation while β-$Ni(OH)_2$ is limited to 1 electron exchanged in the β/β phase transformation electrochemical reaction and, consequently, has a lower theoretical capacity value of 290 $mA \cdot h \cdot g^{-1}$ [269].

It is worth mentioning that, in bulk material, nickel hydroxide has a purely battery-like response. However, when nanostructured, the capacitance contribution from the active surface area becomes relevant and influences the final electrochemical response to a certain extent. The theoretical chemical reactions occurring during charge-discharge for both phases of nickel hydroxide material are [270–272]:

$$\alpha\text{-}Ni^{II}xNi^{III}_{1-x}(OH)_2(2NO_3^-, CO_3^{2-})_{(1-x)/2}(H_2O)_{0.5} + (0.5-y)(Na^+, K^+) \longleftrightarrow \gamma\text{-}Ni^{II}_xNi^{III}_{1-x}OO(H^+)_y(Na^+, K^+)_{(0.5-y)}(H_2O)_{0.5} + (2-y)H^+ + (1-x)/2\ (2NO_3^-, CO_3^{2-}) + (0.5+x)e^- \quad \text{(eq. 1.28)}$$

$$\beta\text{-}Ni^{II}(OH)_2 \longleftrightarrow \beta\text{-}Ni^{III}OOH + H^+ + e^- \quad \text{(eq. 1.29)}$$

There has been certain controversy regarding the exact mechanism for the charge-discharge of nickel hydroxide. An exhaustive study by means of localized micro-potentiometry is done and presented later in the presented manuscript.

Table 1.6

Brief summary of the displayed properties for the main commercial nickel-based batteries. HER: Hydrogen evolution reaction; OER: Oxygen evolution reaction.

Battery type	Anode material	Electrolyte	Voltage (V)	Specific Energy ($W \cdot h \cdot kg^{-1}$)	Specific Power ($W \cdot kg^{-1}$)	Cycle-life	Tolerance to overcharge/ overdischarge	Self-discharge[1]	Memory-effect[2]	Limitations	Ref.
Ni-Fe	$Fe(OH)_2$	30% KOH	1.23	20-60	100	1000 - 2000	Yes	10%/day	No	Corrosion, HER, OER	[267,273][267,274] [275]
Ni-Cd	$Cd(OH)_2$	30% KOH	1.2	40-60	150	800 - 1000	Yes[1]	10% month	Yes	Passivation of cadmium and HER, price and toxicity	[276] [277] [274] [278]
Ni-H_2	Pt catalyst/ $LaNi_5H_6$	31% KOH	1.25	55-75	220	Up to 19000	No	5%/day	Yes	OER, irreversible oxidation	[279,280]
Ni-Zn	ZnO	30% KOH	1.65-1.75	55-100	>3000	200	No	0.8%/day	No	Dendrite-formation, HER and poor cycling stability	[267,281,282]
Ni-MH	Metal alloys[2]	6M KOH	1.2	60-120	250-2000	200 - 2000	Protection systems developed	1%/day	No	Self-discharge and poor charge-efficiency	[283][284] [285] [286] [287]

1 Self-discharge percentage of nominal capacity

2 Memory effect is the apparent reduction in cell capacity at a fixed cut-off voltage and the inability of the device to become fully charged unless a full discharge is performed [277].

3 By controlling charge balance between the two electrodes

4 The most popular alloys are $LaNi_5$ or $CeNi_5$-based alloys, $TiNi_x$-based alloys, ZrV_2 or $ZrMn_2$ amongst many others.

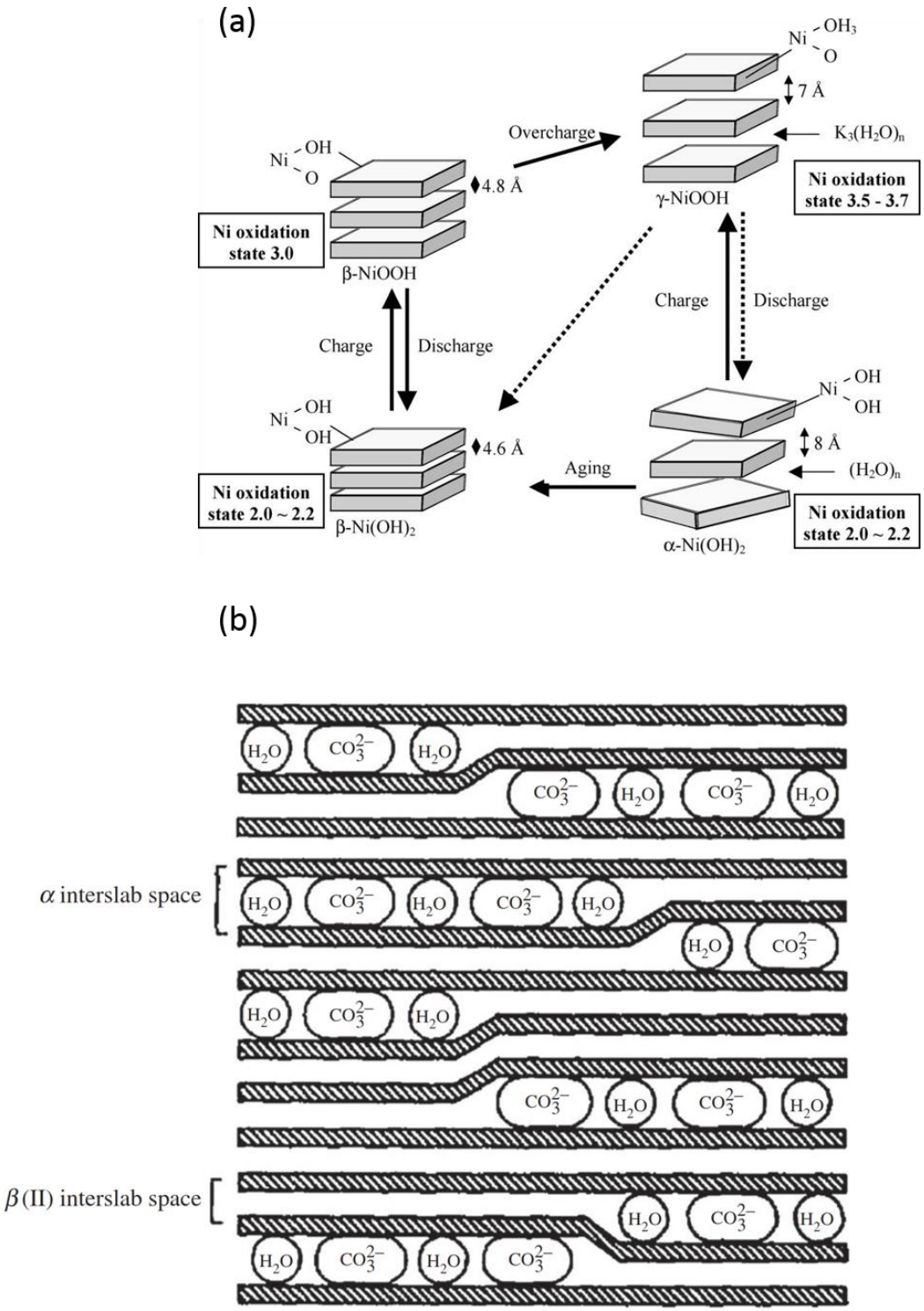

Fig. 1.19. Schematic representation of (a) Bode diagram with the phase transformations during charge, discharge, overcharge and aging of $Ni(OH)_2$ and (b) interslab distance and intercalated species of α and β phases. Reprinted with copyright permission from [268] and [288].

Many different syntheses have been used in the preparation of nickel hydroxide materials. In fact, selecting a method for preparing nickel hydroxide with the right phase, crystallinity, morphology and general form can be a daunting task. Hall et al. [289], in their review on nickel hydroxide, summarize the main synthesis techniques and group

them in: chemical precipitation, electrochemical precipitation and electrodeposition, sol-gel processing, chemical ageing, hydrothermal synthesis and nickel metal oxidation (Fig. 1.20). Nonetheless, some other synthesis routes may be microwave-assisted routes, electrodialysis, sonochemistry, solid-state synthesis and re-crystallization.

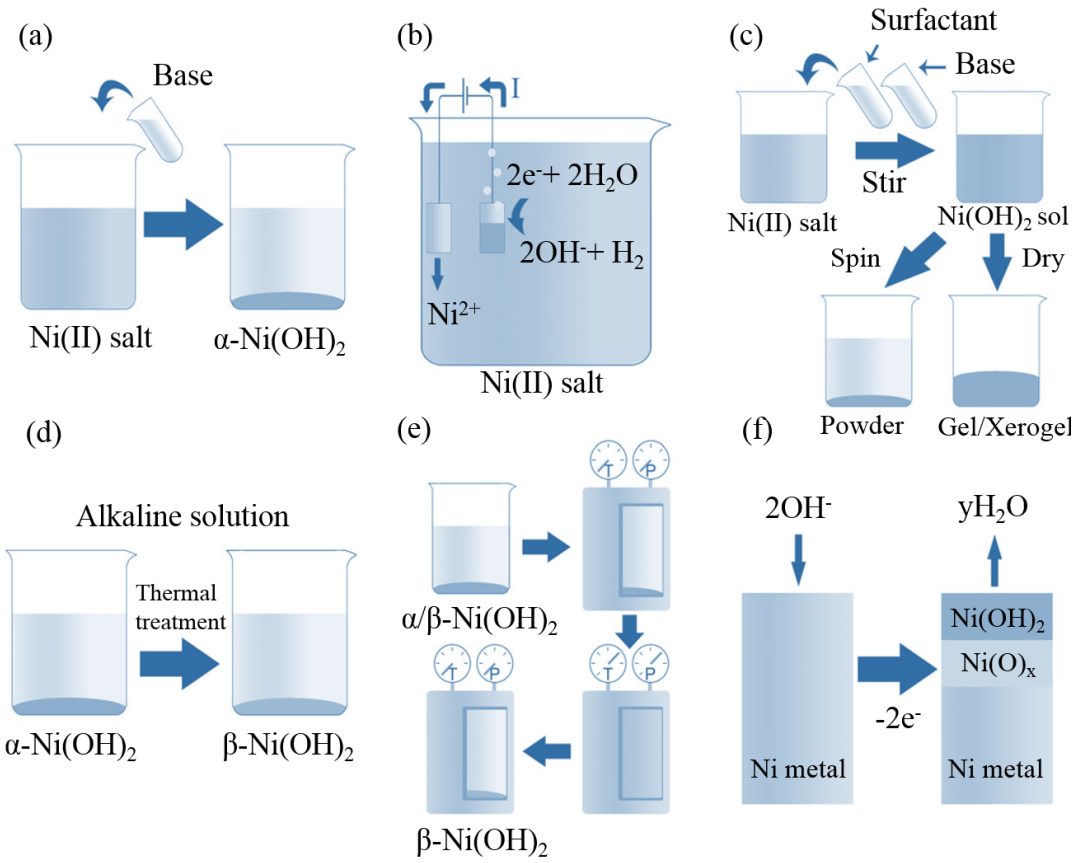

Fig. 1.20. Representation of six synthesis procedures to produce nickel hydroxide. (a) Chemical precipitation by basis addition. (b) Electrochemical precipitation. (c) Sol-gel process. (d) Chemical ageing for phase conversion. (e) Hydrothermal synthesis and treatment. (f) Nickel metal oxidation. Reprinted with copyright permission from [289].

For example, Wu et al. [290] prepared nickel hydroxide by precipitation with NH_4OH and reported a *capacitance* of *~2000 F·g*$^{-1}$ at 5mA in the 0.0V to 0.4V vs. SCE voltage range. However, during the first 5000 cycles, the material exhibited terrible capacity retention, with only a 75% initial capacity after 100 cycles and 45% after 400 cycles. This work, for instance, exemplifies a common issue found in nickel hydroxide literature: the extremely high values of capacitance reported for thin-films. Thin-films are usually extremely low in weight. This may result in an underestimation of active material for the electrode preparation, which leads to extremely high *capacitance* values. In several cases, a value of approximate mass is not even reported which confers added difficulty for result interpretation. Because of it, establishing an adequate benchmark on the expected capacity/capacitance values for certain materials whose energy storage mechanism has been misunderstood has been proven challenging. For an overview of nickel hydroxide as electrode material in alkaline media, a summary of some of the results presented in literature is included in Table 1.7.

Electrodeposition is a recurrent synthesis technique for nickel hydroxide as electrode material. For example, $Ni(OH)_2$ films prepared by electrodeposition using the surfactant Brij56 in a 50% ratio as supporting electrolyte displayed a *specific capacitance* of *578*

F·g^{-1} in the 0.0V to 0.55V vs. Ag/AgCl that, after 400 cycles was reduced by a 4.5% [291]. Yang et al. [292] also electrodeposited a thin-film of nickel hydroxide on top of a nickel foam, creating a 3D porous nanostructure in which the electrode-electrolyte interaction was enhanced. They reported a maximum value of *3152 F·g*$^{-1}$ in the -0.05V to 0.45V (vs. SCE) potential range at 4 A·g^{-1} in 3% KOH and a capacity retention of only a 52% after 300 cycles. However, this specific capacitance is extremely high, and no value of approximate mass was reported. Later, they reported a value of *2188 F·g*$^{-1}$at 1mV·s^{-1} for electrodeposited amorphous nickel hydroxide nanospheres in 1M KOH in the 0.0V to 0.5V (vs. SCE) range (with most of their capacity in the 0.2V to 0.3V potential range) with a mass of 0.12 mg·cm^{-2} and a 76% capacity retention after 10000 cycles.

Concerning the application of exfoliated nanosheets of nickel hydroxide for energy storage applications, Wang et al. [293] exfoliated β-$Ni(OH)_2$ in glycidol by a sol-gel route and re-stacked it by centrifugation. The material exhibited *1729 F·g*$^{-1}$ in the 0.0V to 0.6V (vs. Ag/AgCl) potential range at 5mV·s^{-1} in KOH 6M, although charge-discharge was performed in the 0.0 to 0.45V potential range. Moreover, the material retained 82% of the initial capacity after 2000 cycles. Schneiderová et al. [294] exfoliated nickel hydroxide by lactate intercalation and delamination in water and evaluated the cyclic voltammetry at 100 mV·s^{-1} response of the material in KOH 1M for the -0.1V to 0.5V (vs. SCE) potential range. However, no in-depth evaluation of the material for electrochemical energy storage applications was done.

As in the case of nickel oxide, there are two main limitations, the narrow potential window in which nickel hydroxide acts as active material and the poor capacity retention of the material [295]. For that reason, it is common to combine nickel hydroxide with other materials. Its combination with cobalt in a mixed or double metal hydroxide has been widely studied. For example, $Ni(OH)_2$-$Co(OH)_2$ deposited on top of Y-zeolite was studied by Li et al. [296]. The composite displayed a *specific capacitance* of *479 F·g*$^{-1}$ in 1M KOH at 2 mA·cm^{-2} in the -0.1V to 0.45V vs. SCE potential range. Values up to *1809 F·g*$^{-1}$ at 1A·g^{-1} have been obtained for co-precipitated layered double hydroxides in the same potential range and in 6M KOH [297].

Table 1.7

Summary of some of the results obtained for nickel hydroxide with different morphologies prepared by different synthesis strategies.

Material	Morphology	Synthesis	*Capacitance* ($F \cdot g^{-1}$)	Current density /Scan rate	Electrolyte	Potential window (V)	Capacity retention (number cycles)	Ref.
$Ni(OH)_2$	Hollow nanotubes	Hydrolysis + Cathodic electrodeposition	*1581*	1 $A \cdot g^{-1}$	KOH 1M	0.0 to 0.45 (vs. Ag/AgCl)	~65% (3000)	[298]
$Ni(OH)_2$	Thin film	Cathodic electrodeposition	*569*	1 $A \cdot g^{-1}$	KOH 1M	0.0 to 0.45 (vs. Ag/AgCl)	~65% (3000)	[298]
$Ni(OH)_2$	Bulk – coated ink	Chemical precipitation	220 $mA \cdot h \cdot g^{-1}$	0.2C	KOH 6.5M	0.2-~0.45 (vs. Hg/HgO)	-	[299]
β-$Ni(OH)_2$	Coin-like nanoplates	Chemical precipitation	*847*	4 $A \cdot g^{-1}$	KOH 6M with 10$g \cdot L^{-1}$ LiOH	0.15 to 0.55 (vs. Hg/HgO)	81% (300)	[300]
β-$Ni(OH)_2$	Flower-like structure	Hydrothermal synthesis	*2653*	2 $A \cdot g^{-1}$	KOH 6M	0.15 to 0.55 (vs. Hg/HgO)	80% (600)	[301]
β-$Ni(OH)_2$	Spheres	Continuous flow reactor	245	1C	KOH 6M with 15$g \cdot L^{-1}$ LiOH	0.1 to 0.53 (vs. Hg/HgO)	114% (30)	[302]
β-$Ni(OH)_2$	Honeycomb structure	Chemical bath deposition	*468*	5 $mV \cdot s^{-1}$	KOH 2M	0.0 to 0.5 (vs. SCE)	89% (1000)	[303]
β-$Ni(OH)_2$	Nanorods	Chemical precipitation	*910*	5 $mV \cdot s^{-1}$	KOH, NaOH and LiOH 1M	0.0 to 0.6 (vs. SCE)	99% (5000)	[304]
Co-doped β-$Ni(OH)_2$	Bulk platelet or flower-like aggregates	-	~200 $mA \cdot h \cdot g^{-1}$	7 $mA \cdot cm^{-2}$	KOH 30%	0.1 to 0.5 (vs. Hg/HgO)	-	[305]
α-$Ni(OH)_2$	Flower-like structure	Hydrothermal synthesis	*1715*	5 $mV \cdot s^{-1}$	KOH 1M	-0.05 to 0.55 (vs. Ag/AgCl)	75% (2000)	[306]
α-$Ni(OH)_2$	Nanowires	Reverse micelle/microemulsion synthesis	268.5 $mA \cdot h \cdot g^{-1}$	50 $mA \cdot g^{-1}$	KOH 6M	0.2 to 0.5 (vs. Hg/HgO)	95% (200)	[307]
β-$Ni(OH)_2$	Flower-like structure	Reverse micelle/microemulsion synthesis	251.3 $mA \cdot h \cdot g^{-1}$	50 $mA \cdot g^{-1}$	KOH 6M	0.2 to 0.5 (vs. Hg/HgO)	~87% (200)	[307]
α-$Ni(OH)_2$	Amorphous structure	Chemical precipitation	78 $mA \cdot h \cdot g^{-1}$	0.3C	KOH 6M	1.0 to 1.5 (vs. Hg/HgO)	-	[308]
β-$Ni(OH)_2$	Nanoribbons	Chemical precipitation + hydrothermal treatment	260	0.3C	KOH 6M	1.0 to 1.5 (vs. Hg/HgO)	-	[308]
β-$Ni(OH)_2$	Nanoplatelets	Sonochemical synthesis	*1256*	0.2 $A \cdot g^{-1}$	KOH 1M	0.0 to 0.35 (vs. Ag/AgCl)	85% (2000)	[309]

In regard of the electrodeposition of nickel-cobalt hydroxide, Silva et al. [310] reported the electrodeposition of Ni:Co 30:70 dendritic alloy and evaluated its electrochemical response in 1M KOH, obtaining an electrochemical response from nickel-cobalt hydroxide. The material exhibited 121 $mA \cdot h \cdot g^{-1}$ at 1 $mA \cdot cm^{-2}$ and 70% capacity retention after 8000 cycles. Nguyen et al. [311] prepared $Ni_xCo_{1-x}(OH)_2$ nanosheets on carbon nanofoam with different nickel-cobalt ratios. The material presented a relevant contribution of capacitance from the carbon nanofoam and gravimetric capacities in 1M KOH in the 112-142 $C \cdot g^{-1}$ range, with a maximum response for the 2:1 Co:Ni ratio at 2.1 $mA \cdot cm^{-2}$ in the -0.4V to 0.4V potential range. Moreover, the group also reported layered $Ni(OH)_2$-$Co(OH)_2$ films with a maximum of 762 $C \cdot g^{-1}$ at $1A \cdot g^{-1}$ in the same electrolyte, and compared this result to the 586 $C \cdot g^{-1}$ capacity obtained for $Ni_{1/2}Co_{1/2}(OH)_2$ [312].

Nickel-cobalt hydroxide charge storage mechanism is based on a hydroxide to oxyhydroxide phase transformation that is enhanced in alkali media. Thus, better response is obtained for more concentrated electrolytes. However, this presents two main issues, very alkali solutions are corrosive and more difficult to handle (and to neutralize, creating a major environmental impact) and, therefore, they also produce a much faster degradation of the electrode material.

To the best of the author's knowledge, only two reports have been done regarding the evaluation of exfoliated nickel-cobalt hydroxide nanosheets for energy storage applications. As in the case of nickel hydroxide, Schneiderová et al. [313] exfoliated nickel-cobalt hydroxide nanosheets in aqueous solution and prepared an electrode whose electrochemical performance was studied in KOH 1M. Nevertheless, only cyclic voltammetry was presented at 100 $mV \cdot s^{-1}$ (Fig. 1.21) and further electrochemical characterization of the material is required.

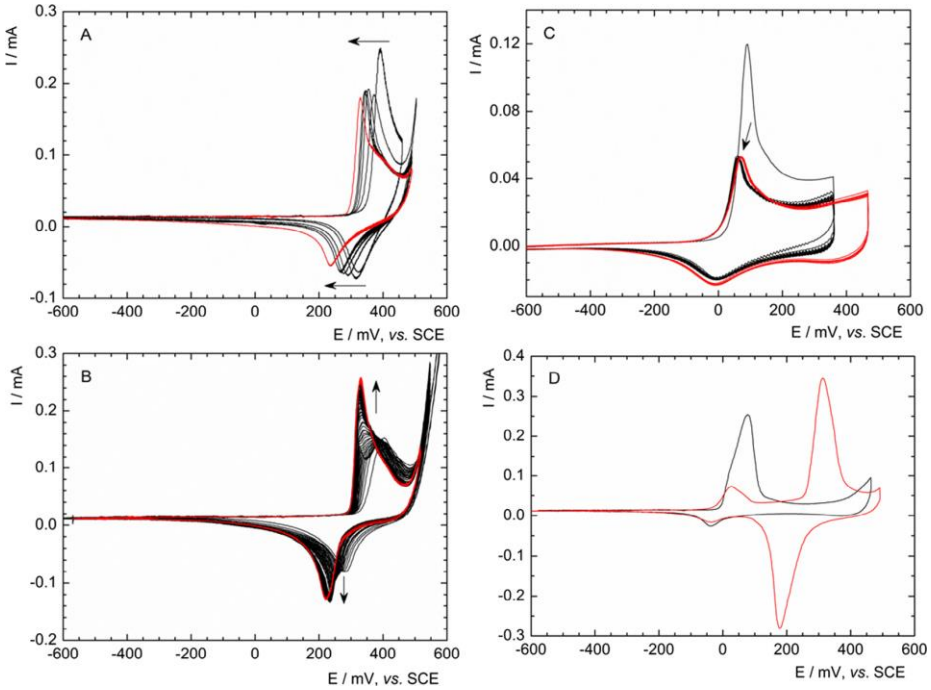

Fig. 1.21. Electrochemical response evaluation by means of cyclic voltammetry at 100$mV \cdot s^{-1}$ in KOH 1M of exfoliated nanosheets by lactate route of (a) nickel-cobalt hydroxide, (b) nickel hydroxide, (c) cobalt hydroxide and (d) mixture 1:1 of nickel and cobalt nanosheets. The arrows indicate the evolution of the peaks with continuous cycling until stable response (red) after 40-50 cycles. Reprinted with copyright permission of [313].

Sebastian et al. [314] exfoliated nickel and cobalt hydroxide in aqueous media by means of p-aminobenzoate intercalation and re-stacked them in a randomly manner by co-precipitation in sodium nitrate. Different Ni:Co ratios were used, namely, 0.25, 1, 4 and 9. Then, they studied the electrochemical performance of the composite material in 2M KOH and concluded that a maximum *capacitance* of *990* $F \cdot g^{-1}$ could be obtained at 1 $A \cdot g^{-1}$ when the nickel hydroxide content represented an 80% of the total composite (Ni:Co ratio of 4). Moreover, they observed a decrease in *capacitance* after 600 cycles of only a 4%.

Another common strategy is to combine nickel hydroxide with carbon-based materials. Of special interest is its combination with reduced graphene oxide. For instance, Liu et al. [315] reported the synthesis of $Ni(OH)_2$/reduced graphene oxide/carbon nanotubes by a two-step solvothermal synthesis in ethanol. The material exhibited *1170* $F \cdot g^{-1}$ at 0.2 $A \cdot g^{-1}$ in 6M KOH, which was higher than $Ni(OH)_2$ (*953* $F \cdot g^{-1}$) and reduced graphene oxide (*178* $F \cdot g^{-1}$) in the 0.0V to 0.55V potential range vs. Hg/HgO. The introduction of rGO and CNTs also induced an improvement of the cycling stability in a 43%. Similar results (*1568* $F \cdot g^{-1}$ at $4A \cdot g^{-1}$) were obtained for $Ni(OH)_2$ rGO obtained by a solid-state reaction [316] and for flower-like $Ni(OH)_2$/rGO obtained by microwave-assisted synthesis (*1735* $F \cdot g^{-1}$ at $1mV \cdot s^{-1}$ in KOH 6M).

Electrodeposition and exfoliation had also been used to form nickel hydroxide – *graphene* composites. On the one hand, Wang et al. [317] synthesized layered α-$Ni(OH)_2$/rGO composites by means of exfoliation of both precursors (nickel hydroxide exfoliation was performed in formamide after SDS intercalation) and electrostatic self-assembly re-stacking. The resultant composite displayed *1568* $F \cdot g^{-1}$ at $1A \cdot g^{-1}$ in the 0.0V to 0.5V (vs. SCE) potential range, as compared to *945* $F \cdot g^{-1}$ for $Ni(OH)_2$, increase rate capability and cycling stability (96% after 400 cycles).

On the other hand, nickel hydroxide has also been electrodeposited on top of reduced graphene oxide. Yang et al. [318] used rGO paper and obtained *1700* $F \cdot g^{-1}$ at 5 $A \cdot g^{-1}$ and *967* $F \cdot g^{-1}$ at 20 $A \cdot g^{-1}$, although their reported stability was not very good (~60% after 500 cycles) while Ruiz-Gómez et al. [319] used a graphene foam, which enhanced the mechanical and electrical properties of nickel hydroxide (*900* $F \cdot g^{-1}$ in 3M KOH at $1A \cdot g^{-1}$ and 98% capacity retention after 3000 cycles). Zhang et al. [320] performed a one-step co-electrophoretic deposition of reduced graphene oxide and $Ni(OH)_2$, resulting in nickel hydroxide decorated on top of reduced graphene oxide that displayed *935* $F \cdot g^{-1}$ at 2.8 $A \cdot g^{-1}$ and 90% capacity retention after 1000 cycles.

Nickel-cobalt hydroxide has also been combined with reduced graphene oxide. For example, Ma et al. prepared Ni-Co hydroxide on top of reduced graphene oxide by means of hydrothermal synthesis [321]. The material exhibited remarkable cycling stability (80% after 17000 cycles) and *1691* $F \cdot g^{-1}$ at 0.5 $A \cdot g^{-1}$ with excellent rate capability (*1327* $F \cdot g^{-1}$ at 40 $A \cdot g^{-1}$). Other strategies have been: using graphene foam as substrate [322] that serves as conductive porous structure leading to *1847* $F \cdot g^{-1}$ at $5A \cdot g^{-1}$ in 1M KOH in the 0.0V to 0.5V (vs. Ag/AgCl) potential range; depositing rGO on top of Ni foam by dip-coating of Ni foam on GO followed by electrochemical reduction and a subsequent potentiodynamic electrodeposition of nickel-cobalt hydroxide [323] resulting in *2133* $F \cdot g^{-1}$ at $4A \cdot g^{-1}$ in NaOH 3M in the 0.0V to 0.45V potential range (vs. Ag/AgCl) or, CVD deposition of graphene followed by electrochemical deposition of Ni-Co LDH material [324]. In this last case, the material displayed *1410* $F \cdot g^{-1}$ at 2 $A \cdot g^{-1}$ in 2M KOH, excellent rate capabilities and cycling stability. To the best of the author knowledge, no direct co-electrodeposition of nickel-cobalt hydroxides with reduced graphene oxide was done prior to this work.

$Co(OH)_2$

As in the case of nickel hydroxide, cobalt hydroxide is an interesting material due to its layered structure and large interlayer space. This enables fast (de)insertion of ions, which correlates with large active surface area. However, due to more scarcity of cobalt as compared to nickel and poorer capacitance values, this material is not as explored on its own.

The charging reaction is based on the transformation from hydroxide to oxyhydroxide, although a secondary reaction in which cobalt (IV) oxide is formed can also occur as exemplified by equations 1.30 to 1.32 [196]:

$$\alpha\text{-}Co^{II}_{x}Co^{III}_{1-x}(OH)_2(2NO_3^-, CO_3^{2-})_{(1-x)/2}(H_2O)_{0.5} + (0.5\text{-}y)(Na^+, K^+) \leftrightarrow \gamma\text{-}Co^{II}_{x}Co^{III}_{1-x}OO(H^+)_y(Na^+, K^+)_{(0.5-y)}(H_2O)_{0.5} + (2\text{-}y)H^+ + (1\text{-}x)/2\ (2NO_3^-, CO_3^{2-}) + (0.5+x)e^- \quad \text{(eq. 1.30)}$$

$$\beta\text{-}Co^{II}(OH)_2 \leftrightarrow \beta\text{-}Co^{III}OOH + H^+ + e^- \quad \text{(eq. 1.31)}$$

$$CoOOH + OH^- \leftrightarrow CoO_2 + H_2O + e^- \quad \text{(eq. 1.32)}$$

Again, many synthesis routes have been explored to obtain cobalt hydroxide, such as chemical precipitation, electrodeposition, microwave-assisted synthesis or hydrothermal synthesis. For instance, Lin et al. [325] synthesized β phases of cobalt hydroxide carbonate by means of hydrothermal synthesis on top of nickel foam. Moreover, they prepared different morphologies by controlling reaction time and studied their effect on the electrochemical performance on 6M KOH. Best results were obtained after 10h hydrothermal treatment, with a reported value of *1548 $F \cdot g^{-1}$* at $2A \cdot g^{-1}$ and *583 $F \cdot g^{-1}$* at $40A \cdot g^{-1}$ in the 0.0V to 0.5V vs. SCE potential range. Another example is that of Chen et al. [326], that synthesized cobalt oxyhydroxide and doped it with nickel, manganese and iron by chemical precipitation with NaOH. Their material exhibited *211 $F \cdot g^{-1}$* at $1\ A \cdot g^{-1}$ in the 0.0V to 0.5V vs. SCE potential range. A summary of some of the representative work done for cobalt hydroxide for energy storage application is included in table 1.8.

Table 1.8
Summary of some representative work obtained for cobalt hydroxide prepared by different synthesis strategies with different morphologies.

Material	Morphology	Synthesis	*Capacitance* ($F \cdot g^{-1}$)	Current density /Scan rate	Electrolyte	Potential window (V)	Capacity retention (number cycles)	Ref.
β-$Co(OH)_2$	Nano-spikes	Hydrothermal	*1548*	2 $A \cdot g^{-1}$	KOH 6M	0.0 to 0.5 (vs. SCE)	92.5% (5000)	[325]
CoOOH	Nano-rings	Chemical precipitation	*211*	1 $A \cdot g^{-1}$	KOH 5M	0.0 to 0.5 (vs. SCE)	-	[326]
β-$Co(OH)_2$	Nano-flakes	Chemical precipitation	*735*	5 $mA \cdot cm^{-2}$	KOH 2M	-0.2 to 0.4 (vs. SCE)	-	[327]
α-$Co(OH)_2$	Nano-platelets	Microwave-assisted	711	1 $A \cdot g^{-1}$	KOH 2M	0.0 to 0.55 (vs. Hg/HgO)	90% (1500)	[328]
β-$Co(OH)_2$	Nano-cones	Hydrothermal	*562*	2 $A \cdot g^{-1}$	KOH 2M	0.0 to 0.55 (vs. Hg/HgO)	88% (3000)	[329]
β-$Co(OH)_2$	Thin-film	Potentiodynamic electrodeposition	890	5 $mV \cdot s^{-1}$	KOH 1M	-0.2 to 0.45 (vs. SCE)	84% (10000)	[330]
α-$Co(OH)_2$	Thin-film	Potentiostatic electrodeposition	*881*	1 $A \cdot g^{-1}$	KOH 1M	-0.1 to 0.45 (vs. Ag/AgCl)	94% (1000)	[331]
β-$Co(OH)_2$	Thin-film	Cathodic electrodeposition	*1125*	1 $A \cdot g^{-1}$	KOH 1M	-0.2 to 0.6 (vs. Ag/AgCl)	93% (2000)	[332]
β-$Co(OH)_2$	Bulk	Chemical precipitation	455 $mA \cdot h \cdot g^{-1}$	1C	KOH 6M	0.6 to 0.82 (vs. Hg/HgO)	96% (50)	[333]
β-$Co(OH)_2$ @ Ni foam	Nano-rods	Chemical bath deposition	*1116*	2 $A \cdot g^{-1}$	KOH 1M	-0.2 to 0.5 (vs. SCE)	-	[334]
Co_3O_4/$Co(OH)_2$	Nano-sheets	Hydrothermal synthesis	1221 $mA \cdot h \cdot g^{-1}$	1C	$LiPF_6$ /EC-DMC	0.02 to 3.0 (vs. Li/Li^+)	85% (50)	[335]

As it can be observed, the capacity values for cobalt hydroxide are much higher than the spinel form, however, it is worth mentioning that cobalt oxide is a more common form for applications in energy storage, because of its well-known crystal structure and electrochemical properties.

Electrodeposition of cobalt hydroxide seems to be one of the preferred methods for energy storage applications. For example, Jagdale et al. [330,336] electrodeposited by potentiodynamic cyclic voltammetry from 0.0V to -1.2V vs. SCE in 0.1M $Co(NO_3)_2$. The material presented a nanosheet-like structure that delivered a maximum of *890 $F \cdot g^{-1}$* in 1M KOH at $5mV \cdot s^{-1}$ and $44F \cdot g^{-1}$ at $5mV \cdot s^{-1}$ in a symmetric assembly. The capacity retention was 84% and 81% after 10000 and 5000 charge-discharge cycles respectively [330,336]. Potentiostatic deposition was used to deposit α-$Co(OH)_2$ on top of a stainless-steel mesh by applying -1.0V vs. Ag/AgCl to a solution containing cobalt nitrates. This resulted in a reported value of *860 $F \cdot g^{-1}$* in 1M KOH for the -0.1V to 0.45V vs. Ag/AgCl potential range [331].

Zhou et al. [337] electrodeposited a mesoporous cobalt hydroxide film on top of a nickel film by using a surfactant, Brij 56, to form a lyotropic liquid crystalline phase, in their electrodeposition process at -0.75V vs. SCE to a 0.9M cobalt nitrate/0.075M $NaNO_3$ electrolyte. They estimated a capacitance of *2646 $F \cdot g^{-1}$* when deposited on top of a nickel mesh at 8 $A \cdot g^{-1}$ in the -0.1V to 0.45V vs. SCE and a 4% capacity loss after 300 cycles. It is worth mentioning that they presented a plateau at the discharge curve and that they probably overestimated mass of their electrodeposited film. Aghazadeh et al. [332] obtained beta phase of cobalt hydroxide by means of saccharide-assisted cathodic electrodeposition in a nanoflaked-structured thin-film form. Their material displayed *1125 $F \cdot g^{-1}$* although no explanation was provided for the apparent increase in capacity.

Cobalt hydroxide has also been exfoliated and applied for energy storage applications. Rovetta et al. [338] exfoliated cobalt hydroxide nanosheets by a cascade liquid exfoliation and sonication in sodium chlorate/isopropanol and evaluated the electrochemical response for energy storage. In their study, exfoliated β-$Co(OH)_2$ sprayed on top of nickel foam displayed *1480 $F \cdot g^{-1}$*, however, their study for energy storage applications could be more detailed. The electrochemical performance of exfoliated cobalt hydroxide nanosheets in aqueous media was introduced by Schneiderová et al. [339] as in the case of nickel and nickel-cobalt hydroxides. Again, further electrochemical studies for energy storage applications are required. A recent report studies the exfoliation of α and β-$Co(OH)_2$ by SDS intercalation and exfoliation in formamide together with its usage as catalyst in lithium-oxygen batteries [340], where they were used to enhance specific capacity, improve cycling capability and reduce over-potential. After obtaining a film, it was mixed with Ketjen Black and PVDF and pasted on carbon paper. Then, they were assembled in a coin cell with holes for oxygen flow (Li as anode, glass fibre as separator, 1 M LiTFSI-EGDME electrolyte and air electrode containing the exfoliated material as collector). The material exhibited 11841 $mA \cdot h \cdot g^{-1}$ after exfoliation at 100 $mA \cdot h \cdot g^{-1}$ and enhanced cycling stability (over 70 cycles), which was higher than the results obtained for the same material without undergoing exfoliation.

Although cobalt hydroxide can provide high capacity values, their potential window range is limited [341]. In an attempt to increase the active potential range, Nayak et al. [341] studied the electrochemical response of cathodically electrodeposited cobalt hydroxide in different electrolytes; NaOH at different concentrations from 1.0M to 0.05M and in Na_2SO_4 1.0 and 0.1M. Results showed that cobalt hydroxide in 1.0M alkali media is limited by a 0.0 to 0.6V potential range vs. Hg/HgO. However, when aqueous media was used, this potential range expanded from 0.0V to 1.5V before OER. The more diluted

the electrolyte, the more expanded the potential range and a more rectangular shape in the voltammogram is obtained and a more linear response in the galvanostatic charge-discharge curve. This entails a more superficial reaction and, therefore, capacitance contribution to the total charge mechanism. Furthermore, when the alkali concentration was more diluted, a lower capacitance value was reported. Again, a trade-off between the power capabilities and energy density is observed. However, it is interesting to see the effect of the electrolyte. Indeed, this parameter shall be optimized to result in a maximum capacity while taking benefit of an expanded potential range and high-rate capabilities of the material.

To further improve the electrochemical behaviour of cobalt hydroxide, several composites have been prepared. For example, Al-substituted α-$Co(OH)_2$ was prepared by potentiostatic deposition. Besides reducing the nanosized domains of cobalt hydroxide nanoflakes, incorporating aluminium produced a transition in which the electrochemical reaction is expanded to a wider potential range instead of having two well-defined redox peaks at defined potentials. The capacitance variance that the authors reported was, however, not significant, resulting in 840 $F \cdot g^{-1}$ for $Co(OH)_2$ and 843 $F \cdot g^{-1}$ for 8wt% Al-substituted cobalt hydroxide at 1A·g in the 0-0.4V potential range [342]. Once the aluminium content is increased, a capacitance drop was observed (520 $F \cdot g^{-1}$for a 59wt% substitution). This exemplifies how certain strategies to increase surface area and therefore capacitance contribution to the total energy stored result in a trade-off of power-capabilities and energy density.

A synergistic effect can also be observed when mixing cobalt hydroxide with carbon-based materials. Graphene derivatives have recently been used in combination with cobalt hydroxide for energy storage applications. For example, Nethravathi et al. [343] synthesized β-$Co(OH)_2$ hexagonal platelets by means of flocculation and chemical precipitation of a suspension of graphene oxide and a cobalt hydroxide colloidal suspension. Then, they thermally treated the material to obtain reduced graphene oxide while partially transforming cobalt hydroxide into its oxide form. In their report, obvious pseudocapacitance contribution, probably from graphene oxide, is observed. This hybrid material exhibits 1337 $F \cdot g^{-1}$ at 1$A \cdot g^{-1}$, with excellent rate capability performance (77.8% at 12$A \cdot g^{-1}$) and capacity retention, 93% after 5000 cycles. Patil et al. [344] anchored cobalt hydroxide nanorods on top of a graphene foam (CVD deposited on top of Ni foam, Fig. 1.22) by means of a chemical bath and studied its electrochemical response in both a 3-electrode system and symmetric configuration. The electrode material displayed, in 1M KOH, a maximum capacity of *1139* $F \cdot g^{-1}$ at 10 $A \cdot g^{-1}$ in the 0.0V to 0.4V potential range (vs. Ag/AgCl), while only *616* $F \cdot g^{-1}$ were obtained for $Co(OH)_2$ obtained by the same technique and coated on top of stainless steel. The symmetric device with the composite material delivered, however, only *69* $F \cdot g^{-1}$ and a capacity retention of 74% after 1000 cycles in a 1.2V potential range, using polypropylene separator soaked in 1M KOH as electrolyte.

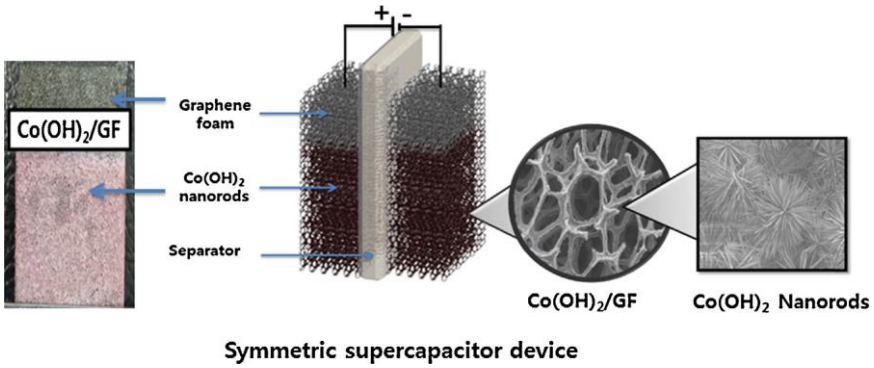

Fig. 1.22. Schematic representation of the $Co(OH)_2$/Graphene@Ni Foam symmetric device used in [344], image of one of the electrodes (left) and SEM image of the coated foam at two different magnifications.

Zhao et al. [345] produced vertically aligned graphene nanosheets by radio-frequency plasma-enhanced chemical vapour deposition, on top of nickel foam, and used the resulting material as substrate for cathodic electrodeposition of cobalt hydroxide nanosheets. Their material displayed *693.8* $F \cdot g^{-1}$ at $2A \cdot g^{-1}$ in the -0.2V to 0.5V vs. SCE potential range in 1M KOH. Moreover, a capacity retention of a 91.9% was obtained after 3000 charge-discharge cycles. However, the scalability of is technique is limited, as compared to direct co-electrodeposition, due to its complexity. Later, Lee et al. [346] electrodeposited reduced graphene oxide and cobalt oxide on top of a previously photolithography-patterned Au/Ti@polyimide substrate by applying a constant potential of -1.2V and -0.94V vs. SCE for 140s and 120s respectively to a suspension containing graphene oxide with sodium sulphate or cobalt nitrate (Fig. 1.23).

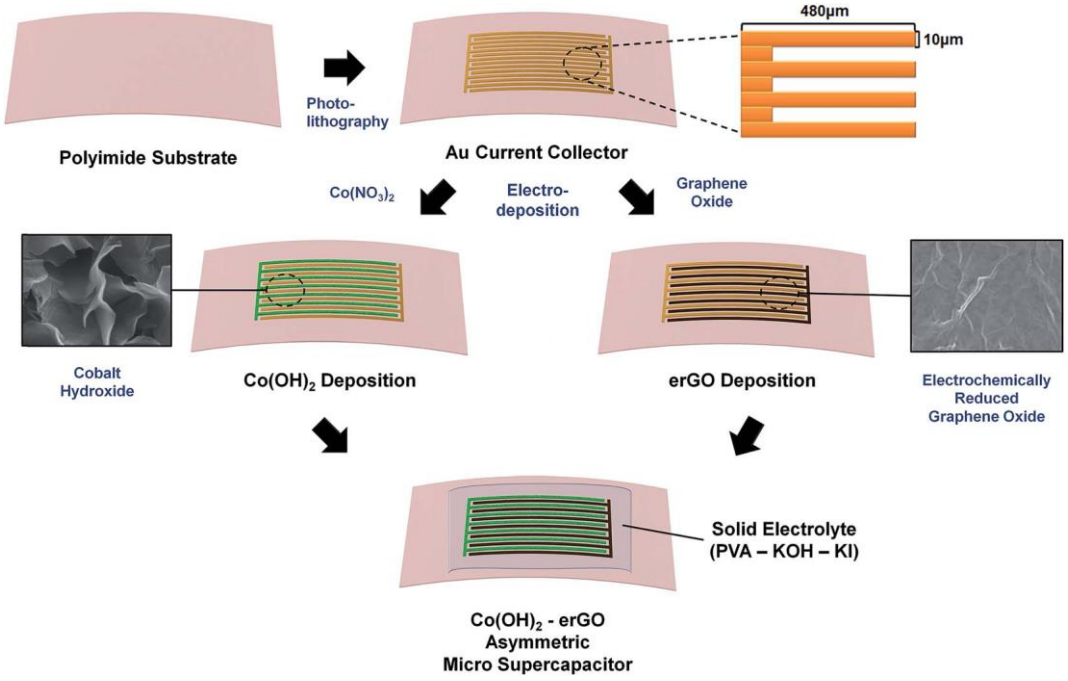

Fig. 1.23. Schematic illustration of the synthesis procedure undertaken by Lee et al in [346]. Reprinted with copyright permission from said reference.

Then, they tested them in 1M KOH, which resulted in *112.5 mF·cm^{-2}* at 1.6 mA·cm^{-2} in the -0.2V to 0.5V vs. Ag/AgCl for $Co(OH)_2$ and 2.0 mF·cm^{-2} at 0.64 mA·cm^{-2} for Er-GO in the -1.0V to 0.0V vs. Ag/AgCl potential range. Finally, they assembled these two both electrodes in an asymmetric device using either 1M KOH as aqueous electrolyte PVA-KOH-KI as solid electrolyte. This configuration delivered 14.2 mF·cm^{-2} at 1.64 mA·cm^{-2} in a 1.4V potential range [346]. The author is not aware of any reports on the direct co-electrodeposition of cobalt hydroxide with reduced graphene oxide.

α-$Co(OH)_2$ was exfoliated by acetate intercalation and delamination in water and combined with exfoliated graphene oxide nanosheets by flocculation [347]. Then, the resulting product was filtrated obtaining a film that would use as electrode material (after mixing with PVDF and acetylene black and coated on Ni foam). The electrochemical performance of the material was evaluated in 2M KOH in the -0.15V to 0.55V vs. Ag/AgCl potential range. However, results were not as high as expected (approximately *25 F·g^{-1}*). Thus, the material was used as negative electrode in Li-ion battery, where displayed 120 mA·h·g^{-1} at 133 mA·g^{-1} during 210 cycles, although the initial capacity was around 500 mA·h·g^{-1}.

1.6 Graphene for energy storage applications

Graphene, since its first isolation in 2004 by Geim and Novoselov [348], has been pinpointed as a very attractive material, with hundreds of publications evidencing its appealing properties. Graphene is described as a 2D carbon monolayer with a honeycomb lattice and was initially thought to be an "academic material" which could not be obtained in a free state [349]. Nonetheless, the first demonstration of graphene isolation was achieved by exfoliating graphite by means of the well-known **"**Scotch tape method" [349]. Since then, many different procedures have been developed to synthesize either graphene or one of its derivatives, such solvothermal synthesis, chemical vapor deposition, liquid-phase exfoliation by means of modified Hummer's method, growth on SiC surfaces, thermal decomposition, molecular beam epitaxy, chemical vapor deposition (CVD), plasma-enhanced CVD (PE-CVD) or roll-to-roll production among others. In fact, new methods are being constantly developed [350–358].

Synthesis methods are of extreme importance when considering the nature of the graphene being used for electrochemical energy storage applications, since it will determine the properties and performance of the carbon-based material [359]. For example, if pristine graphene was to be considered, many interesting properties could be of use. This material exhibits very large theoretical surface area, 2630 $m^2 \cdot g^{-1}$, a very high thermal conductivity with a value greater than 3000 $W \cdot mK^{-1}$, gas impermeability and an extremely high Young's Modulus of 1 TPa [360,361]. Moreover, if the electrical conductivity of graphene is considered, which is a key parameter when evaluating a material for energy storage applications, a value of 4.84–5.30 10^3 $W \cdot mK^{-1}$ is obtained while its charge mobility is around 200.000 $cm^2 \cdot V \cdot s^{-1}$. Theoretically, graphene is conferred with ballistic transport, this is, negligible electrical resistivity. It is ambipolar ("charge carriers can be alternated between holes and electrons depending upon the nature of the gate voltage") and has anomalous quantum hall effect [362,363].

Nonetheless, the chemical reactivity of this material shall be taken into account if composite materials are to be prepared. Pristine graphene is, in general, chemically inert and its reactivity, although not fully understood yet, requires the breaking of sp^2 bonds [363]. For that reason, reduced graphene oxide (rGO) and graphene oxide (GO), which have functional groups that act as reactive regions, are more popular in practical use during the production of the next-generation energy storage electrode materials.

Graphene oxide is one of the easy-to-obtain derivatives of graphene and, at the same time, one of the most important graphene-based materials. It is produced from graphite oxide and contains four types of functional oxygen groups, namely, hydroxyl, epoxy, carbonyl and carboxyl. These oxygen groups break the aromaticity, create localized sp^3 carbons with the consequent variation of the properties of pristine graphene [363,364]. They are the starting point towards functionalization of graphene and, therefore, to the chemical modification of graphene. Thus, although there is plenty of reactivity yet to be explored regarding this material, it is known that they provide graphene with hydrophilic character and chemical reactivity [364]. However, the fact that the C-O bonds break the aromatic structure provokes that GO becomes insulating. The values obtained for its lateral resistivity are around 10^5 $\Omega \cdot cm^{-1}$ [365]. However, if a controlled process of de-oxidation is used, it is possible to obtain an electrically active material with a restored aromatic carbon matrix that is chemically active [366]. When graphene oxide is de-oxygenated, this graphene derivative is known as reduced graphene oxide (rGO). For example, if the electrical conductivity of aqueous solution of graphene oxide is compared to that of reduced graphene oxide, an increase from 17 $S \cdot m^{-1}$ to 1250 $S \cdot m^{-1}$ can be observed [367].

Unfortunately, reduced graphene oxide has yet to achieve the ideal properties of pristine graphene, since it has intermediate properties between graphene oxide and theoretical pristine graphene. The ultimate properties depend on several factors, such as the grade of de-oxidation of GO, the inclusion of defects in the exfoliation process or the presence of impurities.

Given the aforementioned properties, electrochemical studies are usually conducted with reduced graphene oxide, which is usually obtained by means of liquid exfoliation and reduction or functionalized graphene oxide with other materials that is reduced at posteriori [368,369]. Finally, graphene-based materials are classified by Scrosati et al. [370], depending on its participation in the energy storage process, in two main groups, *graphene* as active material and *graphene* as inactive materials.

1.6.1 Graphene as active material for energy storage applications.

When graphene acts as active material, it takes part in the energy storage mechanism. This affects different energy storage systems such as lithium and sodium ion batteries, electrochemical double layer capacitors and metal-air batteries.

Graphene for Lithium-ion batteries

Great interest has been risen on graphene as a lithium ion host or as part of a composite anode material for lithium ion battery applications [370]. Regarding the former, lithium is hosted by adsorption in the exposed surface area of graphene and in the nanopores between layers instead of intercalation. Theoretically, a capacity of 744 $mAh \cdot g^{-1}$ can be achieved, twice the theoretical capacity of graphite ($372 mA \cdot h \cdot g^{-1}$ based on the formation of LiC_6) [371,372]. The first group reporting restacked graphene nanosheets as a potential candidate in lithium-ion anodes was Yoo et al. [373], who reported the exfoliation and re-stacking of graphene layers and prepared a material that displayed 540 $mA \cdot h \cdot g^{-1}$ and was further optimized to 784 $mA \cdot h \cdot g^{-1}$ by the inclusion of fullerenes. It was reported that an expanded matrix eased lithium ion penetration. Different graphene morphologies have been reported since, from reduced graphene oxide paper to graphene monolayers [374,375]. Experimentally, however, most studies are done with rGO, which exhibited a capacity of 100-2000 $mAh \cdot g^{-1}$, much higher than the one calculated for pristine graphene during the first cycle. However, lithium ion insertion is, in this case, not fully reversible due to a surface side-reactions that form passivation layer of the electrolyte, known as solid electrolyte interface, always present in lithium-ion batteries. This is related to the great number of defects and oxygen atoms and expanded active surface area, among many other issues. Graphene derivatives provide geometrically and electronically non-equivalent sites in which oxygen atoms may be chemically bonded to the carbon matrix. Oxygen atoms will be released during the first discharge, partially oxidizing the electrolyte and induce chemical instability[376]. This results in poor energy and Coulombic efficiency, hence, making unfeasible its practical use [377]. This entails that lithium storage greatly depends upon production method, especially the reduction step [378,379]. The final properties are extremely dependent upon the quality and structure of graphene nanosheets and it is said to be different from batch to batch causing inconsistencies in the results reported [380]. For a graphene derivative to reach commercial standards, strategies to prevent the initial lithium ion consumption and avoid re-stacking shall be developed by means of strategies such as pre-lithiation, controlled surface functionalization or the use of composites [370,376,381–383].

Concerning graphene usage in anode composite materials, graphene's energy storage limitation and poor cycling stability have been tried to be overcome by the addition of

electroactive materials, such as metal and metal oxide nanoparticles. Metal oxides have been considered as Li-ion anode materials due to their high capacity (>600 $mA \cdot h \cdot g^{-1}$). However, they suffer from low electrical conductivity and capacity retention [384,385]. Thus, graphene-derivative/metal-oxide composites may create a synergistic effect enhancing the electrochemical performance of the anode. For example, introducing cobalt oxide or iron oxide enables reactivity with lithium resulting in higher capacity values while re-stacking is inhibited [381,386]. Moreover, graphene derivatives act as a conductive matrix, improving electronic conductivity and hindering possible volume changes of the metal oxides during charge-discharge [387]. Some of the results achieved so far display capacities up to 1500 $mA \cdot h \cdot g^{-1}$ for reduced graphene oxide/cobalt oxide nanoparticles, or 1150 $mA \cdot h \cdot g^{-1}$ for RGO/silicon nanoparticles[227]. Nonetheless, reversibility of 20-30% is also observed during the first cycle [56,381]. Grafting redox active organic molecules or conductive polymers on top of graphene nanosheets has also been shown, improving their cycling stability [376]. A more detailed state-of-the art can be found in reviews done by Kleperis et al [388], Scrosati et al. [370] or Kaner et al. [163].

Graphene derivatives have also been applied as cathode composites for Li-ion batteries. The limited capacity and power density of cathode materials such as $LiFeO_4$ has been the main limiting factor up to date. This is consequence of poor electrical and ionic conductivity of the materials forming the electrode and aggregation [376]. By means of reduced graphene oxide certain enhancements can be achieved. For example Cui et al. reported $LiM_{1-x}Fe_xO_4$/rGO with a specific capacitance of 107 $mA \cdot h \cdot g^{-1}$ at 50C and good cycling stability [389]. Finally, graphene layers can avoid dissolution of cathode materials serving as a protective barrier.

Graphene for Sodium-ion batteries

One of the main advantages of graphene in comparison to graphite is that the latter does not allow sodium intercalation [390]. Given the nature of graphene, it can potentially be used as sodium ion host. As a consequence of reduced graphene oxide defects, mainly in the form of oxygen groups, it displayed good electrochemical, cycle life and rate capability behaviour [391]. However, these defects also induce worse reversibility of the charge-discharge reaction. As in the case of lithium-ion batteries, different synthetical methods lead to different performances. To date, one of the best graphene-based materials reported for sodium-ion applications is reduced graphene oxide with a capacity of 300 $mA \cdot h \cdot g^{-1}$ and an acceptable 200-cycle stability [370,392].

Graphene for Supercapacitors

In the recent years, graphene derivatives have been pin-pointed as a competitive electrode material for supercapacitor applications. The potential usage of Er-GO as electrode material for supercapacitors has been extensively proven [393]. This is consequence of its superb chemical stability, its high electrical conductivity and high active surface area, which is crucial in defining double-layer charge. In fact, the theoretical capacitance of pristine graphene is 550 $F \cdot g^{-1}$ or 21 $mF \cdot cm^{-2}$ [394]. Nonetheless, experimental values are well below expected values. Rao et al. [395] developed a graphene-based ultracapacitor in aqueous H_2SO_4 that reached a capacitance value of 117 $F \cdot g^{-1}$ and a maximum of 31.9 $W \cdot h \cdot kg^{-1}$ energy density. This report demonstrated a better performance of graphene and reduced graphene oxide (produced by different methods) in terms of surface area and conductivity compared to carbon nanotubes. Besides, the value achieved for energy density value is one of the highest values achieved to date. Ruoff et al. [396] then reported a chemically modified graphene as an electrode material. The specific capacitances that

they achieved were 135 and 99 $F \cdot g^{-1}$ in aqueous and organic electrolytes respectively. One of the best performances for reduced graphene oxide for supercapacitor applications was achieved by Lei et al. [397], who reduced graphene oxide by using urea. Urea was useful in restoring the conjugated structure, improving conductivity. This led to 255 $F \cdot g^{-1}$ at 0.5 $A \cdot g^{-1}$ and a capacity retention of a 93% after 1200 cycles. The electrochemical performance of urea-reduced graphene oxide was much better than when performed with hydrazine, microwave radiation or hydrothermal treatment [386]. In general, RGO displays a gravimetric capacitance of 100-300 $F \cdot g^{-1}$ for both aqueous and organic electrolytes [56,394]. This is caused by the inaccessibility of the electrolyte to the inner interlayer space between graphene nanosheets and spontaneous re-stacking, driven by strong π- π interactions [354]. Furthermore, the excellent electronic conductivity is compromised by the extent of reduction, the number of defects and intersheet contact. Many strategies have been developed to avoid re-stacking of single-later sheets and increase active surface area, such as specie intercalation (polymers, carbon nanotubes, etc.), compromising the power-density of pristine graphene [398,399]; using solvents as effective "spacer" [400] or curving graphene sheets [398]. Using water as spacer yielded 156 $F \cdot g^{-1}$ at the impressive applied current density of 1080 $A \cdot g^{-1}$ while curving the nanosheets exhibited remarkable energy density (85.6 $W \cdot h \cdot g^{-1}$).

Vertically aligned graphene nanosheets were produced conferring better electrolyte accessibility. With that strategy, values of 145 $F \cdot g^{-1}$ in aqueous electrolyte were obtained [401]. By using a reduction method of graphene oxide with hydrazine, lower agglomeration is produced within the layers of graphene, which leads to an acceptable capacitance value of 205 $F \cdot g^{-1}$ with energy density of 28.5 $W \cdot h \cdot kg^{-1}$ [402]. Not only that, high capacitance retention values of 90% after 1200 cycles were achieved. Another relevant work is that performed by Li et al. [403], who assembled graphene sheets in a densely packed porous structure forming films in presence of non-volatile liquid electrolyte. In that manner, electrolyte was trapped within the graphene sheets with a continuous ion transport network. The fabricated device displayed 60 $W \cdot h \cdot L^{-1}$.

In general, achieving a large active surface area is the main strategy to optimize *graphene*'s electrochemical performance. For example, by chemical exfoliation a BET surface area of 3000 $m^2 \cdot g^{-1}$ with 0.6 to 5nm pores as achieved displaying 70 $W \cdot h \cdot kg^{-1}$ at 5.7 $A \cdot g^{-1}$ in a 3.5V voltage window in organic electrolyte [404,405]. Reduced graphene oxide films (rGO) can also have very large surface areas after activation (2400 $m^2 \cdot g^{-1}$). This is reflected in the capacitance displayed by the electrode material. For example, specific capacitance of 120 $F \cdot g^{-1}$ for a free-standing porous activated graphene film has been reported [386].

Similar results (215 $F \cdot g^{-1}$) with less capacity fading during charge-discharge cycling have been achieved by controlling the stacking and using water to solvate graphene and avoid the loss produced by the aggregation of several layers of graphene [400]. However, there is still a lot of work to do; for example in developing a cost-effective chemical production of graphene, studying pseudo-capacitance to increase the higher density without compromising the ion mobility, reducing the irreversibility of capacity and in understanding how chemical modifications would improve the electrochemical response [361]. To date, the maximum value of capacitance in rGO obtained is 205 $F \cdot g^{-1}$ with a power density of 10 kW/kg in an aqueous electrolyte with an energy density of 28.5 $Wh \cdot kg^{-1}$. Usually, the effective surface area in large surface area materials is directly proportional to the number and characteristics of the pores in the solid-state compound. However, this is not the case for reduced graphene oxide. It depends on the number of

layers. The fewer number of layers entails reduced agglomeration and, therefore better capacitance results [402].

Finally, *graphene*/carbon-based material composites have also been developed to improve the electric double layer. By using, for example, nanosized carbon (carbon black), an opening of the channels for the electrolyte to penetrate is achieved, increasing active surface area [406]. This resulted in a specific capacitance of 138 $F \cdot g^{-1}$ at 10 $mV \cdot s^{-1}$ in 6M KOH and a capacity retention of approximately 97% after 2000 cycles. Another strategy has been to intercalate mesoporous carbon spheres (MCS) by flocculation. Negatively charged GO suspended flocculates with surface positively charged mesoporous silica spheres. The treatment to remove silica spheres produces 3D porous carbon and reduces GO simultaneously. With this method, however, Zhao et al. [407] reported a maximum value of 218 $F \cdot g^{-1}$ at 10 $mV \cdot s^{-1}$ in 6M KOH. Nonetheless, carbon nanotubes (CNTs) have been the most common material for graphene-layer spacing [408,409]. This strategy has led to promising results, such as a specific capacitance of 385 $F \cdot g^{-1}$ at 10 $mV \cdot s^{-1}$ and a capacity increase of a 20% after 2000 cycles [409].

Electrochemically reduced graphene oxide as active electrode material

Tong-Lau et al. [410] developed a supercapacitor based on the electrochemical reduction of GO. For that, they applied a constant potential of -1.7V vs Ag/AgCl for 4.5h to a GO suspension (-1.1V for solid GO as a previously dropcasted film) on a gold substrate. Then, they fabricated a symmetric supercapacitor consisting of two identical Er-GO based electrode films separated by a PVDF filter paper soaked on 1M $NaNO_3$.

Their results on electrodeposition showed that, by generating a pre-film that was then reduced electrochemically, the reduction process was more effective. This is due to the limitations induced by the diffusion effects that mass transport processes entail. Besides, premature precipitation may occur in this case.

The electrochemical investigation for energy applications showed that the Er-GO based asymmetric supercapacitor obtained with this methodology presents a capacitance of 128 $F \cdot g^{-1}$, an energy density of 17.8 $W \cdot h \cdot kg^{-1}$ and a power density of 106.08 $kW \cdot kg^{-1}$ in a 1.0V potential range and with a capacity retention of 84% after 3500 charge/discharge cycles [410]. The fade in capacity with cycling is due to the loss of unstable oxygen groups that had not undergone reduction in the deposition/reduction process.

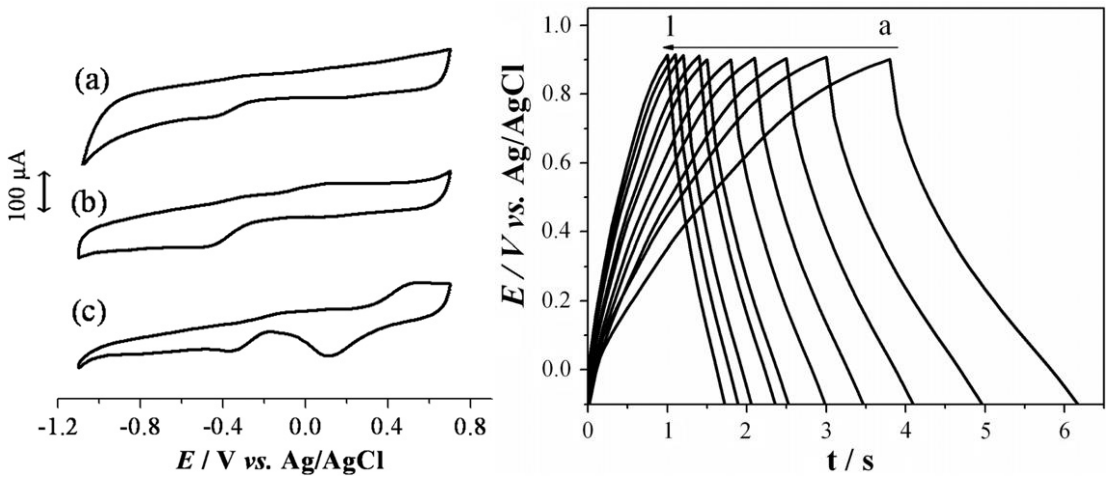

Fig. 1.24. On the left there is the cyclic voltammetry of a) CRGO, b) Er-GO and c) GO films on top of Au-PET substrates using 0.1M KCl as electrolyte and a scan rate of 50 mV s^{-1}. On the right, the galvanostatic charge discharge curves of the Er-GO film in $NaNO_3$ at the potential range of -0.1- 0.9V at a current density ranging from 84.86 to 212.16 A/g. Reprinted with copyright permission of [410].

Gunasekaran et al. [411] performed a similar study in which Er-GO was produced by a repetitive cathodic potential cycling in a potential range going from 0.0 to -1.5V vs. Ag/AgCl in 0.05M PBS for 100 cycles. Their investigation on the electrochemical properties of the electrode material concluded that it had a specific capacitance of 223.6 $F \cdot g^{-1}$ at 5mV s^{-1}; a much higher value than the previously reported. A value of 180.8 $F \cdot g^{-1}$ at 0.2 mA cm^{-2} is presented with a 100% retention after 1000 cycles.

By applying the high value of -1.5V, they removed all instable groups, with the consequent stabilization of the material. Besides, they associated the deposition process to the variation of zeta potential and, therefore, of surface charge of the layers. When GO is suspended in water, the zeta potential is around -30mV. However, when reduced, it tends to zero. It is considered, from the colloidal science perspective, that a suspension with zeta potential around -30mV is stable. Then, when it is reduced, there is an adsorption on the surface of the material of positively charge ions, such as H^+ or Na^+ because of oxygen removal. That induces precipitation on top of the substrate[411].

Yang et al. [412] deposited Er-GO potentiostatically at voltages ranging from -1.0 to -1.3V and different deposition times (400- 800s) on top of nickel foam. For that, they included a 0.15M $LiClO_4$/7.5 $g \cdot L^{-1}$ GO electrolyte and a posterior further reduction by means of a cyclic voltammetry in the 0 to -1.5V range at 50 $mV \cdot s^{-1}$ in 6M KOH. They observed a capacitance of 183.2 $mF \cdot cm^{-1}$ at $1 \cdot mA\ cm^{-1}$ and excellent capacitance retention for both high current and scan rates and continuous cyclability.

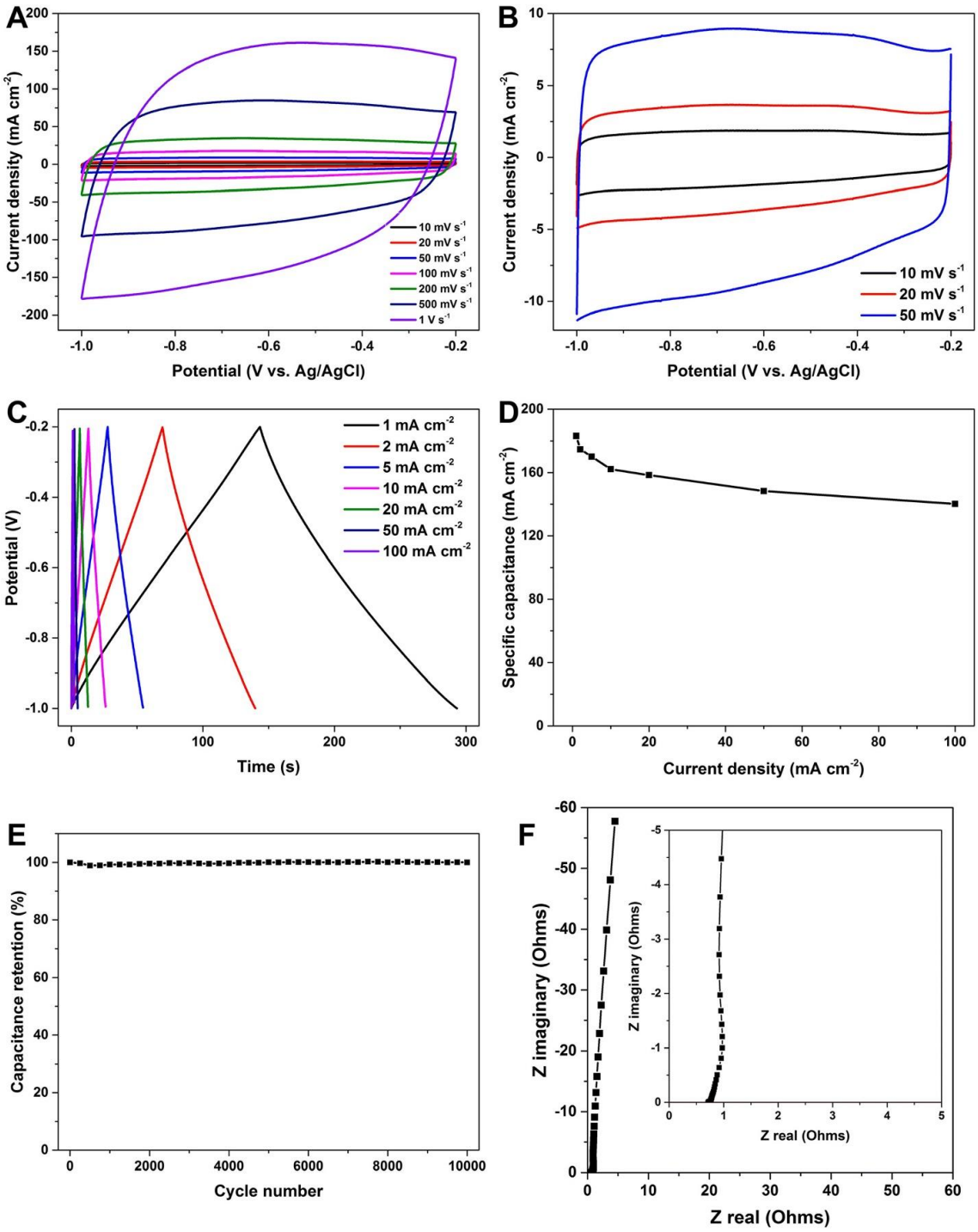

Fig. 1.25. Electrochemical characterization of Er-GO electrodeposited at -1.2V for 500s. a) and b) Cyclic voltammetry at different scan rates. c) Galvanostatic charge discharge curves at different current densities. d) Specific capacity retention at different current densities. e) Capacity retention with continuous scan rate at 500 mV s^{-1} f) Nyquist plot of electrochemical impedance spectroscopy. Re-printed with copyright permission of [412].

Another relevant work was performed by Shi et al. [413]. They developed an ultrahigh-rate supercapacitor by using an aqueous suspension of GO with $LiClO_4$ at -1.2V vs. SCE for 5-60 seconds and a second step of reduction by means of $LiClO_4$ for another 30 seconds on top of a gold substrate coated with tape. They then assembled a symmetrical capacitor with two identical Er-GO electrodes and a 25% KOH electrolyte. With that,

they could achieve scan rates as high as 400 $mV \cdot s^{-1}$ without loss in the quasi rectangular shape of the cyclic voltammetry. Besides, capacities were 487 $\mu F \cdot cm^{-2}$ for 40 $\mu A \cdot cm^{-2}$ and only a 7% loss at 700 $\mu A \cdot cm^{-2}$ and 100% retention after 10.000 cycles.

Shun et al. [414] also produced an electrochemical capacitor based on reduced graphene oxide, in this case with a different morphology: fibre-shaped. As pointed out, the performance of the Er-GO based supercapacitors greatly depend on the composition, the structure and the intrinsic properties of the Er-GO deposited. For that reason, the authors developed a solid and flexible supercapacitor by using Er-GO on top of a gold wire by combining two Er-GO based electrodes separated by a thin solid-electrolyte based on H_3PO_4/PVA/H_2O. The experimental conditions were optimized for electrodeposition of Er-GO on top of Au by using a 3 $mg \cdot mL^{-1}$ GO suspension with 0.1M $LiClO_4$ at an applied potential of -1.2V vs. SCE for 10 seconds. In the two-electrode evaluation they obtained a capacitance vale of 11.4$\mu F \cdot cm^{-1}$/0.726 $mF \cdot cm^{-2}$ with an almost ideal supercapacitor behaviour. Also, the device presented very low internal resistance (0.92 $\Omega \cdot cm^{-2}$) and high capacitance retention with cycling (94% after 2000 GCD cycles).

Dickerson et al. [415] applied the same technique to reduce graphene-based hydrogels for supercapacitor applications. In the preparation of hydrogels, freeze-drying is commonly used to remove entrapped water. However, this water acts as a spacer preventing re-stacking and producing a porous electrolyte-accessible structure. However, if not freeze-dried, the structure collapses and degrades with ease during electrochemical testing. By producing an Er-GO hydrogel by means of electrodeposition this can be avoided. For that reason, they prepare and Er-GO hydrogel on top of a SS mesh by applying a constant potential of 5V to a 2 $g \cdot L^{-1}$ GO suspension with a pH of 1.35 and evaluated its performance as supercapacitor electrode. The material presented a capacitance of 147 $F \cdot g^{-1}$ at 10 $A \cdot g^{-1}$ and a retention of the 93.1% after 10000 cycles.

On the same line of work, Er-GO hydrogel was deposited on top of nickel foam by means of electrophoretic deposition of 6 $g \cdot L^{-1}$ GO at 5V and a posterior reduction voltage of -2.5V for 600s. Said material exhibited a volumetric specific capacitance of 176.5 $F \cdot cm^{-1}$ at 1 $A \cdot g^{-1}$ with a retention of 79-90% after 10000 cycles [416].

These results can be compared to other studies in which 3D porous graphene materials are produced, such as the work undertaken by Li et al. [417]. They prepared the 3D material by first reducing GO in aqueous dispersion and then electrodeposited on top of a copper working electrode. With that, they combined the 3D architecture with conducting polymers, noble metals and a metal oxide. For the Er-GO/PAni composite, capacitance up to 716 $F \cdot g^{-1}$ at 0.47 $A \cdot g^{-1}$ were achieved. In the absence of additives, Er-GO behaves as a pseudocapacitive material, with a rectangular cyclic voltammetry and a capacitance of 102 $F \cdot g^{-1}$. Nonetheless, when PANI is introduced, redox peaks appear, enhancing the capacity response of the material. This exemplifies the advantages of incorporating electrochemically produced graphene derivatives with other materials to produce energy storage materials, namely:

- High surface area that enables the anchoring of other species.
- High conductive matrix in the form of Er-GO.
- Low mass transport resistance.
- In general, no binder is required.
- Facile and tuneable synthesis.

Graphene for Pseudocapacitors

Hybrid structures can surpass supercapacitive values by combining a graphene derivative with a pseudocapacitive metal oxide or a conductive polymer, amongst others. By tailoring graphene, it is possible to fully exploit its properties in synergy with other composites to improve the performance of super- and pseudo-capacitors. It shall be noted, however, that the power performance can be diminished due to the dependence on redox reactions [418]. A summary of the different benefits and disadvantages of combining *graphene* and metal oxides is displayed in Table 1.9. Graphene derivatives and metal oxides can interact by means of oxygen functional groups. Graphene serves as conductive platform enhancing the electrical conductivity of the composite compared to the metal oxides. By an optimized interaction, volume changes and aggregation, agglomeration and re-stacking can be minimized. Furthermore, by stabilizing volume changes the chemical stability of metal oxides is improved. Finally, large capacities may be obtained when including metal oxides, while better power performance is also possible.

Table 1.9

Summary exemplifying the complementary properties that graphene derivatives and metal oxides have and how, by creating a composite material, synergistic effects coming from the interaction can be achieved. Modified from table presented in [381].

Graphene PROs	Metal Oxides PROs
Good electrical conductor	Large capacity/capacitance
Anchoring of functional groups in GO	High packing density
Chemical stability in time	High energy density
High surface area	Rich resources
High surface to volume ratio	
Light and thin	
Flexible	
Broad electrochemical window	
Grade of transparency	
Graphene CONs	**Metal Oxides CONs**
Agglomeration	Poor electrical conductivity
Re-stacking	Large volume change
Large irreversible capacity from oxygen groups	Large irreversible capacity
Low initial coulombic efficiency	Low initial coulombic efficiency
Fast capacity fading	Aggregation/agglomeration
No clear Li^+ storage mechanism	Poor rate capability
Large voltage hysteresis	Low cycling stability
Low capacity/capacitance values (only ECDL)	

For example, composites of graphene layers with manganese oxide can benefit from the higher capacitance of the metal oxide while enhancing its electrical conductivity [419]. For instance, MnO_2/electrochemically reduced GO (Er-GO) was produced by electrodeposition with MnO_2 nanoparticles decorated on top of Er-GO. The material displayed a promising 315 $F \cdot g^{-1}$ capacitance at $2mV \cdot s^{-1}$ which was 4-5 higher than pure MnO_2. However, the most common method to prepare rGO-MnO_2 composites is by direct precipitation in which carbon acts as a reductant and converts aqueous permanganate into insoluble manganese oxide on top of the graphene matrix [420,421].

Other metal oxides such as ruthenium oxide [422], molybdenum oxide [423] or vanadium oxide [424] among many others [387] have been prepared for this purpose, always leading to similar aforementioned conclusions. For instance, RuO_2/chemically exfoliated graphene prepared by a sol-gel method displayed 570 $F \cdot g^{-1}$, enhanced rate capability and a 97.9% retention after 1000 cycles [425].

Fe_3O_4/rGO nanocomposites were prepared by means of benzyl alcohol [426] resulting in a capacitance of 126 $F \cdot g^{-1}$ in 1M Na_2SO_4 in the -0.8V to 0.0V (vs. Ag/AgCl) potential range at 5$mV \cdot s^{-1}$. Authors reported that the ratio iron/rGO has a great impact. When higher concentrations of iron precursor were used ($Fe(acac)_2$/GO ratio used in synthesis of 18.3 in comparison to 3.5), full coverage of the rGO sheets was observed, limiting the graphene layers re-stacking, resulting in higher capacitance than pure iron oxide with the same power capability of rGO. Studies on vanadium oxide with reduced graphene oxide displayed capacitances up to 550 $F \cdot g^{-1}$ while maintaining high power (500 $W \cdot kg^{-1}$) [109]. Cheng et al. [381] reported a detailed review on graphene-based composites with graphene derivatives for energy storage, with an overview of the performances achieved for graphene derivatives with SnO_2 for lithium-ion batteries (LIBs) (~550-2000 $mA \cdot h \cdot g^{-1}$), Co_3O_4 for LIBs and pseudocapacitors (~700-1000 $mA \cdot h \cdot g^{-1}$ and ~150-500 $F \cdot g^{-1}$), Fe_2O_3 (~1300-1700 $mA \cdot h \cdot g^{-1}$), RuO_2 (~200-600 $F \cdot g^{-1}$), MnO_x (~200-650 $F \cdot g^{-1}$) and many others.

An example of graphene-based composite material with conductive polymers is the composite developed by Wang and his group[427]; fibrillar polyaniline (PANI) doped with graphene oxide. This composite reached the capacitance value of 531 $F \cdot g^{-1}$ compared to individual (PANI) whose capacitance was 216 $F \cdot g^{-1}$. Similar cases for PANI/graphene-derivative can be found in literature, with capacitances comprised in the 400 to 600 $F \cdot g^{-1}$ range [428,429]. In situ electrodeposition of PANI on top of Er-GO had a capacitance of 970 $F \cdot g^{-1}$ at 2.5 $A \cdot g^{-1}$ [430]. PPy was also decorated on top of graphene nanolayers. It resulted in an increased surface area for 20-50 nm thickness PPy sheets on top of the carbon matrix [428].

Other energy storage systems with graphene

Other energy storage fields in which graphene is used as active material are lithium-sulphur batteries, lithium-air and sodium-air batteries. Lithium-air batteries consist of metallic lithium and oxygen as cathode and anode respectively and have a theoretical energy density of 3500 to 5.200 $W \cdot h \cdot kg^{-1}$ [370,431]. They are based on the oxidation of lithium, that is reversed during charge by the oxygen evolution reaction. The system, however, suffers from low rate capability and lifetime [432–434]. One of the main factors affecting this performance is the cathode material: the active surface area and porosity of the cathode affect OER. Reduced graphene oxide, because of its extensive active surface area, can, in principle, display high capacity [433]. In a similar way, sodium-air batteries are being explored. RGO has been used as catalyser for the oxygen-reduction and oxygen-evolution reactions [435]. Results are promising but inconclusive so far, thus, further investigation in this field is required.

Lithium-sulphur batteries have a high theoretical capacity of 1672 $mA \cdot h \cdot g^{-1}$ and a specific energy of 2600 $W \cdot h \cdot kg^{-1}$by the complete redox reaction of sulphur with lithium. Moreover, sulphur is naturally abundant and has a low cost and toxicity [376,436,437]. Research on this area is focused on improving the electronic conductivity of sulphur, inhibit volume changes and solubility of polysulfide intermediate states [438,439]. Graphene derivatives are a promising solution, especially considering the potential

immobilization of S/Li_xS during cycling. For that, several approaches have been undertaken, such as wrapping sulphur nanoparticles with rGO (however, this led to insulating domains and incomplete oxidation) or chemical surface modification. Values of approximately 600-1000 $mA \cdot h \cdot g^{-1}$ for 50-100 cycles have been reported [440,441]. More information can be found on Zhang's et al. review on graphene-based energy storage applications [376].

1.6.2. Graphene as inactive material for energy storage applications.

Graphene as inactive material, this is acting as conductive agent, substrate or matrix, is not such an exploited field, nonetheless, it is worth considering. It mainly concerns lithium-ion batteries, sodium-ion batteries and lithium-sulphur batteries applications [370]. Lithium metal oxide electrodes and sodium-ion battery cathode materials tend to have poor electrical conductivity. To overcome this limitation, conductive additives such as carbon black are usually added. Graphene, because of its excellent electronic conductivity, shall be considered for this application.

In fact, the role of graphene derivatives in many composite materials is to act as conductive network. Moreover, graphene oxide is generally reduced at the same time as the lithium metal oxide materials are deposited. This promotes the formation of nanostructures that affect the final lithium intercalation process [388]. Although some reports suggest that simple mixing of rGO worsens the electrochemical response, it is generally reported that it enhances the final properties of the composite material in up to a 160%.

1.6.3. Final note on graphene for energy storage applications

It is worth noting that, to understand the limits of graphene in supercapacitor applications, it is important to not evaluate only single electrode materials, but a full packaged cell. As Kaner et al. [163] reported, if an acetonitrile-based electrolyte is used together with an standard current collector and separator, the two parameters that define the ultimate performance of the device are the density of the graphene-based electrode and the voltage of the cell. If 200-µm thick graphene-based electrodes with a density of 1.5 $g \cdot cm^{-3}$ at an operating voltage of 4V are used, the maximum theoretical energy of the device would be approximately 170 $W \cdot h \cdot kg^{-1}$, which is close to nickel metal hydride and lithium-ion batteries with much higher power density and longer cycle life. However, experimentally, values of only 15-35 $W \cdot h \cdot kg^{-1}$ have been achieved. These results are two-folded. On one hand they are encouraging, graphene-based devices have great potential and shall be further investigated. On the other hand, much work is yet to be done to fully exploit graphene potential capabilities and achieve its scaling up. Despite the intensive research already performed on graphene derivatives, much work remains to be done. Just for energy storage purposes, several new applications have been developed, such as AC-line filtering supercapacitors, flexible and stretchable devices or self-healing batteries amongst others. Not only that, other 2D materials are being obtained, as explained in the exfoliation section of this manuscript. These new two-dimensional materials may overcome graphene limitations for certain applications. Therefore, 2D-materials and composites is a new and exciting field of work with great potential in the production of next-generation energy storage devices.

1.7 Concluding remarks

Considering the current developments in energy storage devices, one of the main goals is to develop materials that exhibit high power capabilities without compromising energy density or vice versa. In the quest for next-generation devices, hybrid composites consisting of a supercapacitive material in combination with a faradaic battery-like material seem one of the most promising alternatives to achieve better performances. Among all materials nickel-cobalt hydroxides and oxides are being considered due to their high energy density capabilities and promising power capabilities, already exhibited to a certain extent in metal hydride batteries. When nano-structuring them, their electrochemical reaction may be confined to superficial reactions and diffusion-transport phenomena may lose relevance during the charge-discharge phase transformation. Kinetically favoured phase-transformation reactions undergone in materials with high theoretical capacity may aid in solving, to a certain extent, the challenges traditionally related to faradaic-related materials. Nonetheless, it is the combination of these nanostructures with carbon-based materials, with supercapacitive nature, that may crucially affect the future of electrochemical energy storage devices. With that combination, fast response times in an extended voltage range supported by the carbonaceous material until reaching the potential in which the faradaic-like material activity is confined may be achieved. It is only recently that this sort of materials are being exploited. In that context, graphene derivatives with very large active surface area, a key parameter in the capacitance performance of a material, have been pin-pointed as candidates for hybrid composites.

The current thesis is developed in the context of the current state-of-the-art of graphene-based composites and metal hydroxides and oxides for hybrid composites. Therefore, two strategies, presented in the next chapter, are undertaken, exfoliation and electrodeposition. The former, performed at the University of Bordeaux, serves as a mean to nanostructure nickel and cobalt hydroxides and oxides, and potentially combine it in its delaminated form with suspended reduced graphene oxide, with the consequent intimate interaction that it may entail. The latter, performed at Instituto Superior Técnico, enables the direct synthesis of nickel and cobalt nano-structures in a single-step process and its combination with reduced graphene oxide. Thus, nickel-cobalt and graphene-based hybrid composites are prepared by these two routes and an exhaustive study of their electrochemical response is performed, mainly at Instituto Superior Técnico, to evaluate their potential use in the next-generation of energy storage devices alongside in-depth solid-state physico-chemical characterization, mostly performed at the Universtiy of Bordeaux. Thus, it is worth highlighting the complementary nature, in regard to facilities and expertise, provided by each university in the course of the work here presented.

Chapter 1 References

[1] J.-F. Morin, Trade and Environment Database Codebook, Quebec City, Canada, 2017. http://www.american.edu/TED/ted.htm.

[2] W. Li, J. Liu, D. Zhao, Mesoporous materials for energy conversion and storage devices, Nat. Rev. Mater. 1 (2016) 16023. doi:10.1038/natrevmats.2016.23.

[3] Monthly Energy Review Report - October 2017, U S Energy InformationAdministration, 2017.

[4] A. Manthiram, Y. Fu, Y.S. Su, In Charge of the World: Electrochemical Energy Storage, J. Phys. Chem. Lett. 4 (2013) 1295–1297.

[5] M. Miroshnikov, K.P. Divya, G. Babu, A. Meiyazhagan, L. Mohana, R. Arava, P.M. Ajayan, G. John, Power from nature: designing green battery materials from electroactive quinone derivatives and organic polymers, J. Mater. Chem. A Mater. Energy Sustain. 4 (2016) 12370–12386. doi:10.1039/c6ta03166h.

[6] Energy storage – the role of electricity, 2017. https://ec.europa.eu/energy/sites/ener/files/documents/swd2017_61_document_travail_service_part1_v6.pdf.

[7] M.S. Saleh, A. Althaibani, Y. Esa, Y. Mhandi, A.A. Mohamed, Impact of clustering microgrids on their stability and resilience during blackouts, 2015 Int. Conf. Smart Grid Clean Energy Technol. ICSGCE 2015. (2016) 195–200. doi:10.1109/ICSGCE.2015.7454295.

[8] F.E.R. Comission, Assessment of Demand Response and Advanced metering Report, 2008.

[9] D. Larcher, J.-M. Tarascon, Towards greener and more sustainable batteries for electrical energy storage, Nat. Chem. 7 (2014) 19–29. doi:10.1038/nchem.2085.

[10] World Energy Council, World Energy Resources: E-Storage, 2016. doi:http://www.worldenergy.org/wp-content/uploads/2013/09/Complete_WER_2013_Survey.pdf.

[11] X. Luo, J. Wang, M. Dooner, J. Clarke, Overview of current development in electrical energy storage technologies and the application potential in power system operation, Appl. Energy. 137 (2015) 511–536. doi:10.1016/j.apenergy.2014.09.081.

[12] U. Eberle, M. Felderhoff, F. Schüth, Chemical and physical solutions for hydrogen storage, Angew. Chemie - Int. Ed. 48 (2009) 6608–6630. doi:10.1002/anie.200806293.

[13] R.E. Association, Energy Storage in the UK: An Overview, 2016. http://www.r-e-a.net/upload/rea_uk_energy_storage_report_november_2015_-_final.pdf.

[14] Christophe Pillot, The Rechargeable Battery Market and Main Trends 2014-2025, 2015.

[15] G. Pistoia, Lithium-Ion Batteries: Advances and Applications, 2014. doi:doi:10.1016/B978-0-444-59513-3.00010-8.

[16] M. Aneke, M. Wang, Energy storage technologies and real life applications – A state of the art review, Appl. Energy. 179 (2016) 350–377. doi:10.1016/j.apenergy.2016.06.097.

[17] A. Borenstein, O. Hanna, R. Attias, S. Luski, T. Brousse, D. Aurbach, Carbon-based composite materials for supercapacitor electrodes: a review, J. Mater. Chem. A. 5 (2017) 12653–12672. doi:10.1039/C7TA00863E.

[18] F. Wang, X. Wu, X. Yuan, Z. Liu, Y. Zhang, L. Fu, Y. Zhu, Q. Zhou, Y. Wu, W. Huang, Latest advances in supercapacitors: from new electrode materials to novel device designs, Chem. Soc. Rev. 46 (2017) 6816–6854. doi:10.1039/C7CS00205J.

[19] B.E. Conway, Electrochemical Supercapacitors Scientific Fundamentals and Technological Applications, Kluwer Academic/Plenum Publishers, 1999.

[20] P. Sharma, T.S. Bhatti, A review on electrochemical double-layer capacitors, Energy Convers. Manag. 51 (2010) 2901–2912. doi:10.1016/j.enconman.2010.06.031.

[21] M. Jayalakshmi, K. Balasubramanian, Simple Capacitors to Supercapacitors - An Overview, 3 (2008) 1196–1217.

[22] G. Wang, L. Zhang, J. Zhang, A review of electrode materials for electrochemical supercapacitors., Chem. Soc. Rev. 41 (2012) 797–828. doi:10.1039/c1cs15060j.

[23] A.G. Pandolfo, A.F. Hollenkamp, Carbon properties and their role in supercapacitors, J. Power Sources. 157 (2006) 11–27. doi:10.1016/j.jpowsour.2006.02.065.

[24] T. Osaka, M. Datta, Energy Storage Systems in Electronics: New Trends Electrochemical Technology, First Edit, Gordon and Breach Science Publishers, 2000.

[25] A. González, E. Goikolea, J.A. Barrena, R. Mysyk, Review on supercapacitors: Technologies and materials, Renew. Sustain. Energy Rev. 58 (2016) 1189–1206. doi:10.1016/j.rser.2015.12.249.

[26] O. Haasc, E.J. Cairnsd, Electrochemical Energy Storage, Annu. Rep. Prog. Chem., Sect. C. 95 (1999) 163—197. doi:10.1039/C4NR02400A.

[27] B.E. Conway, W.G. Pell, Double-layer and pseudocapacitance types of electrochemical capacitors and their applications to the development of hybrid devices, J. Solid State Electrochem. 7 (2003) 637–644. doi:10.1007/s10008-003-0395-7.

[28] P. Simon, Y. Gogotsi, Materials for electrochemical capacitors, (n.d.) 845–854.

[29] T.D. Burchell, Carbon Materials for Advanced Technologies, 1999. doi:10.1016/B978-008042683-9/50012-1.

[30] J.P. Zheng, Ruthenium oxide-carbon composite electrodes for electrochemical capacitors, Electrochem. Solid State Lett. 2 (1999) 359–361.

[31] M.J.W. J.B. Donnet, R.C. Bansal, Carbon Black Science and Technology, Second, 1993.

[32] J.P. Zheng, T.R. Jow, High energy and high power density electrochemical capacitors, J. Power Sources. 62 (1996) 155–159. doi:10.1016/S0378-7753(96)02424-X.

[33] R. Richner, S. Müller, A. Wokaun, Grafted and crosslinked carbon black as an electrode material for double layer capacitors, Carbon N. Y. 40 (2002) 307–314. doi:10.1016/S0008-6223(01)00100-2.

[34] F. Beck, M. Dolata, Electrochemical supercapacitors based on industrial carbon blacks in aqueous H2SO4, J. Appl. Electrochem. 31 (2001) 845–853. doi:10.1023/A:1017529920916.

[35] H. Pröbstle, M. Wiener, J. Fricke, Carbon Aerogels for Electrochemical Double Layer Capacitors, J. Porous Mater. 10 (2003) 213–222. doi:10.1023/B:JOPO.0000011381.74052.77.

[36] W. Li, G. Reichenauer, J. Fricke, Carbon aerogels derived from cresol – resorcinol – formaldehyde for supercapacitors, Carbon N. Y. 40 (2002) 2955–2959.

[37] R.W. Pekala, Organic aerogels from the polycondensation of resorcinol with formaldehyde, J. Mater. Sci. 24 (1989) 3221–3227. doi:10.1007/BF01139044.

[38] K. Otsuka, C.L. Segal, Advanced Capacitor World Summit: Building the Technology Applications and New Business Opportunities for High Performance Electrochemical Capacitors (ECs), 2003.

[39] H. Marsh, F. Rodríguez-Reinoso, Sciences of Carbon Materials, Publicaciones Universidad de Alicante, 2000.

[40] J.P. Randin, E. Yeager, Differential capacitance study on the edge orientation of pyrolytic graphite and glassy carbon electrodes, J. Electroanal. Chem. 58 (1975) 313–322. doi:10.1016/S0022-0728(75)80089-1.

[41] A. Braun, M. Bärtsch, B. Schnyder, R. Kötz, O. Haas, H.-G. Haubold, G. Goerigk, X-ray scattering and adsorption studies of thermally oxidized glassy carbon, J. Non. Cryst. Solids. 260 (1999) 1–14. doi:10.1016/S0022-3093(99)00571-2.

[42] A. Braun, M. Bärtsch, O. Merlo, B. Schnyder, B. Schaffner, R. Kötz, O. Haas, A. Wokaun, Exponential growth of electrochemical double layer capacitance in glassy carbon during thermal oxidation, Carbon N. Y. 41 (2003) 759–765. doi:10.1016/S0008-6223(02)00390-1.

[43] L. Lv, Y. Fan, Q. Chen, Y. Zhao, Y. Hu, Z. Zhang, N. Chen, L. Qu, Three-dimensional multichannel aerogel of carbon quantum dots for high-performance supercapacitors., Nanotechnology. 25 (2014) 235401/1-235401/9, 9. doi:10.1088/0957-4484/25/23/235401.

[44] V.B. Kumar, A. Borenstein, B. Markovsky, D. Aurbach, A. Gedanken, M. Talianker, Z. Porat, Activated Carbon Modified with Carbon Nanodots as Novel Electrode Material for Supercapacitors, J. Phys. Chem. C. 120 (2016) 13406–13413. doi:10.1021/acs.jpcc.6b04045.

[45] W.-W. Liu, Y.-Q. Feng, X.-B. Yan, J.-T. Chen, Q.-J. Xue, Superior Micro-Supercapacitors Based on Graphene Quantum Dots, Adv. Funct. Mater. 23 (2013) 4111–4122. doi:10.1002/adfm.201203771.

[46] N.M. Rodriguez, A review of catalytically grown carbon nanofibers, J. Mater. Res. 8 (1993) 3233–3250. doi:10.1557/JMR.1993.3233.

[47] E. Frackowiak, K. Jurewicz, K. Szostak, S. Delpeux, F. Béguin, Nanotubular materials as electrodes for supercapacitors, Fuel Process. Technol. 77–78 (2002) 213–219. doi:10.1016/S0378-3820(02)00078-4.

[48] C. Niu, E.K. Sichel, R. Hoch, D. Moy, H. Tennent, High power electrochemical capacitors based on carbon nanotube electrodes, Appl. Phys. Lett. 70 (1997) 1480–1482. doi:10.1063/1.118568.

[49] Y.H. Lee, K.H. An, S.C. Lim, W.S. Kim, H.J. Jeong, C.-H. Doh, S.-I. Moon, Applications of carbon nanotubes to energy storage devices., New Diam. Front. Carbon Technol. 12 (2002) 209–228.

[50] M. Noked, S. Okashy, T. Zimrin, D. Aurbach, Composite carbon nanotube/carbon electrodes for electrical double-layer super capacitors, Angew. Chemie - Int. Ed. 51 (2012) 1568–1571. doi:10.1002/anie.201104334.

[51] Y. Qiu, G. Li, Y. Hou, Z. Pan, H. Li, W. Li, M. Liu, F. Ye, X. Yang, Y. Zhang, Vertically aligned carbon nanotubes on carbon nanofibers: A hierarchical three-dimensional carbon nanostructure for high-energy flexible supercapacitors, Chem. Mater. 27 (2015) 1194–1200. doi:10.1021/cm503784x.

[52] G.-P. Hao, W.-C. Li, D. Qian, G.-H. Wang, W.-P. Zhang, T. Zhang, A.-Q. Wang, F. Schüth, H.-J. Bongard, A.-H. Lu, Structurally designed synthesis of mechanically stable poly (benzoxazine-co-resol)-based porous carbon monoliths and their application as high-performance CO2 capture sorbents, J. Am. Chem. Soc. 133 (2011) 11378–11388. doi:10.1021/ja203857g.

[53] Z. Wu, P.A. Webley, D. Zhao, Post-enrichment of nitrogen in soft-templated ordered mesoporous carbon materials for highly efficient phenol removal and CO2 capture, J. Mater. Chem. 22 (2012) 11379. doi:10.1039/c2jm16183d.

[54] X. Wang, C.-G. Liu, D. Neff, P.F. Fulvio, R.T. Mayes, A. Zhamu, Q. Fang, G. Chen, H.M. Meyer, B.Z. Jang, and S. Dai, Nitrogen-enriched ordered mesoporous carbons through direct pyrolysis in ammonia with enhanced capacitive performance, J. Mater. Chem. A. 1 (2013) 7920.

[55] N.P. Wickramaratne, J. Xu, M. Wang, L. Zhu, L. Dai, M. Jaroniec, Nitrogen enriched porous carbon spheres: Attractive materials for supercapacitor electrodes and CO2 adsorption, Chem. Mater. 26 (2014) 2820–2828. doi:10.1021/cm5001895.

[56] Y. Sun, Q. Wu, G. Shi, Graphene based new energy materials, Energy Environ. Sci. 4 (2011) 1113. doi:10.1039/c0ee00683a.

[57] J. Chmiola, C. Largeot, P.L. Taberna, P. Simon, Y. Gogotsi, Desolvation of ions in subnanometer pores and its effect on capacitance and double-layer theory, Angew. Chemie - Int. Ed. 47 (2008) 3392–3395. doi:10.1002/anie.200704894.

[58] P.S. Celine Largeot, Cristelle Portet, John Chmiola, Pierre-Louis Taberna, Yury Gogotsi, Relation between the Ion Size and Pore Size for an Electric Double-Layer Capacitor, J. Am. Chem. Soc. 130 (2008) 2730–2731. doi:10.1016/j.carbon.2007.10.023.(15).

[59] A.J. Chmiola, G. Yushin, Y. Gogotsi, C. Portet, P. Simon, P.L. Taberna, Anomalous Increase in Carbon Capacitance at Pore Sizes Less Than 1 Nanometer, Science (80-.). 313 (2006) 1760–1763.

[60] H.J. Liu, J. Wang, C.X. Wang, Y.Y. Xia, Ordered hierarchical mesoporous/microporous carbon derived from mesoporous titanium-carbide/carbon composites and its electrochemical performance in supercapacitor, Adv. Energy Mater. 1 (2011) 1101–1108. doi:10.1002/aenm.201100255.

[61] M. Li, C. Liu, H. Cao, H. Zhao, Y. Zhang, Z. Fan, KOH self-templating synthesis of three-dimensional hierarchical porous carbon materials for high performance supercapacitors, J. Mater. Chem. A. 2 (2014) 14844. doi:10.1039/C4TA02167C.

[62] K. Jost, G. Dion, Y. Gogotsi, Textile energy storage in perspective, J. Mater. Chem. A. 2 (2014) 10776. doi:10.1039/c4ta00203b.

[63] V. Augustyn, P. Simon, B. Dunn, Pseudocapacitive oxide materials for high-rate electrochemical energy storage, Energy Environ. Sci. 7 (2014) 1597. doi:10.1039/c3ee44164d.

[64] M. Okubo, E. Hosono, J. Kim, M. Enomoto, N. Kojima, T. Kudo, H. Zhou, I. Honma, Nanosize effect on high-rate Li-ion intercalation in LiCoO2 electrode, J. Am. Chem. Soc. 129 (2007) 7444–7452. doi:10.1021/ja0681927.

[65] V. Augustyn, J. Come, M.A. Lowe, J.W. Kim, P.-L. Taberna, S.H. Tolbert, H.D. Abruña, P. Simon, B. Dunn, High-rate electrochemical energy storage through Li+ intercalation pseudocapacitance., Nat. Mater. 12 (2013) 518–22. doi:10.1038/nmat3601.

[66] V. Augustyn, J. Come, M.A. Lowe, J.W. Kim, P.L. Taberna, S.H. Tolbert, H.D. Abruña, P. Simon, B. Dunn, High-rate electrochemical energy storage through Li + intercalation pseudocapacitance, Nat. Mater. 12 (2013) 518–522. doi:10.1038/nmat3601.

[67] M. Salanne, B. Rotenberg, K. Naoi, K. Kaneko, P.L. Taberna, C.P. Grey, B. Dunn, P. Simon, Efficient storage mechanisms for building better supercapacitors, Nat. Energy. 1 (2016). doi:10.1038/nenergy.2016.70.

[68] Y. Wang, Y. Song, Y. Xia, Electrochemical capacitors: mechanism, materials, systems, characterization and applications, Chem. Soc. Rev. 45 (2016) 5925–5950. doi:10.1039/C5CS00580A.

[69] B. Conway, Transition from "Supercapacitor" to "Battery" Behavior in Electrochemical Energy Storage, J. Electrochem. Soc. 138 (1991) 1539–1548. doi:10.1149/1.2085829.

[70] J.P. Zheng, A New Charge Storage Mechanism for Electrochemical Capacitors, J. Electrochem. Soc. 142 (1995) L6. doi:10.1149/1.2043984.

[71] J.P. Zheng, P.J.J. Cygan, T.R.R. Jow, Hydrous ruthenium oxide as an electrode material for electrochemical capacitors, J. Electrochem. Soc. 142 (1995) 2699–2703. doi:10.1149/1.2050077.

[72] L.M. Doubova, A. De Battisti, S. Daolio, C. Pagura, S. Barison, R. Gerbasi, G. Battiston, P. Guerriero, S. Trasatti, Effect of Surface Structure on Behavior of RuO2 Electrodes in Sulfuric Acid Aqueous Solution, Russ. J. Electrochem. (Translation Elektrokhimiya). 40 (2004) 1115–1122. file:///C:/Program Files/EndNote/RuO2/doubova-structureeffect-russJelctro-2004.pdf.

[73] T. Liu, W.G. Pell, B.E. Conway, Self-discharge and potential recovery phenomena at thermally and electrochemically prepared RuO2 supercapacitor electrodes, Electrochim. Acta. 42 (1997) 3541–3552. doi:10.1016/S0013-4686(97)81190-5.

[74] K.E. Swider, C.I. Merzbacher, P.L. Hagans, D.R. Rolison, Synthesis of Ruthenium Dioxide-Titanium Dioxide Aerogels: Redistribution of Electrical Properties on the Nanoscale, Chem. Mater. 9 (1997) 1248–1255. doi:10.1021/cm960622c.

[75] C.K.H. J. P. Zheng, I.D. Raistrick, T.E. Society, C. Hunter, T. Journal, I.D. Raistrick, T. Journal, L.A. Murphy, T. Journal, E. Passalacqua, V. Recupero, M. Vivaldi, E. Passalacqua, V. Alderucci, P. Staiti, L. Pino, H. Mirzaian, E.J. Taylor, G. Wilemski, P. Stonehart, T. Journal, Electrochemical Behavior of Amorphous

and Crystalline Ruthenium Oxide Electrodes, J. New Mater. Mater. Electrochem. Syst. 5 (2002) 41–46.

[76] C.-C. Hu, W.-C. Chen, K.-H. Chang, How to Achieve Maximum Utilization of Hydrous Ruthenium Oxide for Supercapacitors, J. Electrochem. Soc. 151 (2004) A281. doi:10.1149/1.1639020.

[77] W. Sugimoto, K. Yokoshima, Y. Murakami, and Y. Takasu, Charge Storage Mechanism of Nanostructured Anhydrous and Hydrous Ruthenium-Based Oxides, Electrochim. Acta. 52 (2006) 1742–1748.

[78] F. Pico, E. Morales, J.A. Fernandez, T.A. Centeno, J. Ibañez, R.M. Rojas, J.M. Amarilla, J.M. Rojo, Ruthenium oxide/carbon composites with microporous or mesoporous carbon as support and prepared by two procedures. A comparative study as supercapacitor electrodes, Electrochim. Acta. 54 (2009) 2239–2245. doi:10.1016/j.electacta.2008.10.028.

[79] H.Y. Lee, J.B. Goodenough, Supercapacitor Behavior with KCl Electrolyte, J. Solid State Chem. 144 (1999) 220–223. doi:10.1006/jssc.1998.8128.

[80] W. Yan, J.Y. Kim, W. Xing, K.C. Donavan, T. Ayvazian, R.M. Penner, Lithographically Patterned Gold/Manganese Dioxide Core/Shell Nanowires for High Capacity, High Rate, and High Cyclability Hybrid Electrical Energy Storage, 2390 (2012).

[81] M. Toupin, T. Brousse, D. Bélanger, Charge storage mechanism of MnO2 electrode used in aqueous electrochemical capacitor, Chem. Mater. 16 (2004) 3184–3190. doi:10.1021/cm049649j.

[82] W. Wei, X. Cui, W. Chen, D.G. Ivey, Manganese oxide-based materials as electrochemical supercapacitor electrodes, Chem. Soc. Rev. 40 (2011) 1697–1721. doi:10.1039/C0CS00127A.

[83] O. Ghodbane, J.L. Pascal, F. Favier, Microstructural effects on charge-storage properties in MnO 2-based electrochemical supercapacitors, ACS Appl. Mater. Interfaces. 1 (2009) 1130–1139. doi:10.1021/am900094e.

[84] S. Devaraj, N. Munichandraiah, Effect of crystallographic structure of MnO2 on its electrochemical capacitance properties, J. Phys. Chem. C. 112 (2008) 4406–4417. doi:10.1021/jp7108785.

[85] P. Ragupathy, H.N. Vasan, N. Munichandraiah, Synthesis and Characterization of Nano-MnO[sub 2] for Electrochemical Supercapacitor Studies, J. Electrochem. Soc. 155 (2008) A34. doi:10.1149/1.2800163.

[86] G. An, P. Yu, M. Xiao, Z. Liu, Z. Miao, K. Ding, L. Mao, Low-temperature synthesis of Mn3O4 nanoparticles loaded on multi-walled carbon nanotubes and their application in electrochemical capacitors, Nanotechnology. 19 (2008). doi:10.1088/0957-4484/19/27/275709.

[87] Y. Luo, T. Yang, Z. Li, B. Xiao, M. Zhang, High performance of Mn3O4cubes for supercapacitor applications, Mater. Lett. 178 (2016) 171–174. doi:10.1016/j.matlet.2016.04.142.

[88] R. Dong, Q. Ye, L. Kuang, X. Lu, Y. Zhang, X. Zhang, G. Tan, Y. Wen, F. Wang, Enhanced Supercapacitor Performance of Mn3O4 Nanocrystals by Doping Transition-Metal Ions., ACS Appl. Mater. Interfaces. 5 (2013) 9508–9516. doi:10.1021/am402257y.

[89] X. Xia, Y. Zhang, D. Chao, C. Guan, Y. Zhang, L. Li, X. Ge, I.M. Bacho, J. Tu, H.J. Fan, Solution synthesis of metal oxides for electrochemical energy storage applications, Nanoscale. 6 (2014) 5008–5048. doi:10.1039/C4NR00024B.

[90] R.S. Kate, S.A. Khalate, R.J. Deokate, Overview of nanostructured metal oxides and pure nickel oxide (NiO) electrodes for supercapacitors: A review, J. Alloys Compd. 734 (2018) 89–111. doi:10.1016/j.jallcom.2017.10.262.

[91] S.-Y. Wang, K.-C. Ho, S.-L. Kuo, N.-L. Wu, Investigation on Capacitance Mechanisms of Fe[sub 3]O[sub 4] Electrochemical Capacitors, J. Electrochem. Soc. 153 (2006) A75. doi:10.1149/1.2131820.

[92] J. Chen, K. Huang, S. Liu, Hydrothermal preparation of octadecahedron Fe3O4 thin film for use in an electrochemical supercapacitor, Electrochim. Acta. 55 (2009) 1–5. doi:10.1016/j.electacta.2009.04.017.

[93] C. Ban, Z. Wu, D.T. Gillaspie, L. Chen, F. Yan, J.L. Blackburn, A.C. Dillon, Nanostructured Fe3O4/SWNT electrode: Binder-free and high-rate Li-ion anode, Adv. Mater. 22 (2010) 145–149. doi:10.1002/adma.200904285.

[94] Y. Zhao, J. Li, Y. Ding, L. Guan, Single-walled carbon nanohorns coated with Fe2O3 as a superior anode material for lithium ion batteries, Chem. Commun. 47 (2011) 7416. doi:10.1039/c1cc12171e.

[95] S. Jin, H. Deng, D. Long, X. Liu, L. Zhan, X. Liang, W. Qiao, L. Ling, Facile synthesis of hierarchically structured Fe3O4/carbon micro-flowers and their application to lithium-ion battery anodes, J. Power Sources. 196 (2011) 3887–3893. doi:10.1016/j.jpowsour.2010.12.078.

[96] M.-S. Wu, R.-H. Lee, Electrochemical Growth of Iron Oxide Thin Films with Nanorods and Nanosheets for Capacitors, J. Electrochem. Soc. 156 (2009) A737. doi:10.1149/1.3160547.

[97] D. Sarkar, G.G. Khan, A.K. Singh, K. Mandal, High-performance pseudocapacitor electrodes based on α-Fe2O3/MnO2core-shell nanowire heterostructure arrays, J. Phys. Chem. C. 117 (2013) 15523–15531. doi:10.1021/jp4039573.

[98] Q. Xiong, J. Tu, Y. Lu, J. Chen, Y. Yu, X. Wang, C. Gu, Three-dimensional porous nano-Ni/Fe3O4 composite film: enhanced electrochemical performance for lithium-ion batteries, J. Mater. Chem. 22 (2012) 18639. doi:10.1039/c2jm33770c.

[99] M.B. Sassin, A.N. Mansour, K.A. Pettigrew, D.R. Rolison, J.W. Long, Electroless Deposition of Conformal Nanoscale Iron Oxide on Carbon Charge Storage, ACS Nano. 4 (2010) 4505–4514. doi:10.1021/nn100572a.

[100] J. Luo, X. Xia, Y. Luo, C. Guan, J. Liu, X. Qi, C.F. Ng, T. Yu, H. Zhang, H.J. Fan, Rationally designed hierarchical TiO2@Fe2O 3 hollow nanostructures for improved lithium ion storage, Adv. Energy Mater. 3 (2013) 737–743. doi:10.1002/aenm.201200953.

[101] D. Guan, Z. Gao, W. Yang, J. Wang, Y. Yuan, B. Wang, M. Zhang, L. Liu, Hydrothermal synthesis of carbon nanotube/cubic Fe3O4nanocomposite for enhanced performance supercapacitor electrode material, Mater. Sci. Eng. B Solid-State Mater. Adv. Technol. 178 (2013) 736–743. doi:10.1016/j.mseb.2013.03.010.

[102] X. Zhao, C. Johnston, P.S. Grant, A novel hybrid supercapacitor with a carbon nanotube cathode and an iron oxide/carbon nanotube composite anode., J. Mater. Chem. 19 (2009) 8755–8760. doi:10.1039/b909779a.

[103] N. Sinan, E. Unur, Fe3O4/carbon nanocomposite: Investigation of capacitive & magnetic properties for supercapacitor applications, Mater. Chem. Phys. 183 (2016) 571–579. doi:10.1016/j.matchemphys.2016.09.016.

[104] Q. Wang, L. Jiao, H. Du, Y. Wang, H. Yuan, Fe3O4 nanoparticles grown on graphene as advanced electrode materials for supercapacitors, J. Power Sources. 245 (2014) 101–106. doi:10.1016/j.jpowsour.2013.06.035.

[105] J.W. Lee, S.Y. Lim, H.M. Jeong, T.H. Hwang, J.K. Kang, J.W. Choi, Extremely stable cycling of ultra-thin V2O5 nanowire–graphene electrodes for lithium rechargeable battery cathodes, Energy Environ. Sci. 5 (2012) 9889. doi:10.1039/c2ee22004k.

[106] A.Q. Pan, H. Bin Wu, L. Zhang, X.W. (David) Lou, Uniform V2O5 nanosheet-assembled hollow microflowers with excellent lithium storage properties, Energy Environ. Sci. 6 (2013) 1476. doi:10.1039/c3ee40260f.

[107] J. Xie, C. Wu, S. Hu, J. Dai, N. Zhang, J. Feng, J. Yang, Y. Xie, Ambient rutile VO2(R) hollow hierarchitectures with rich grain boundaries from new-state nsutite-type VO2, displaying enhanced hydrogen adsorption behavior, Phys. Chem. Chem. Phys. 14 (2012) 4810. doi:10.1039/c2cp40409e.

[108] A. Pan, H. Bin Wu, L. Yu, X.W.D. Lou, Template-Free Synthesis of VO_2 Hollow Microspheres with Various Interiors and Their Conversion into V_2O_5 for Lithium-Ion Batteries, Angew. Chemie. 125 (2013) 2282–2286. doi:10.1002/ange.201209535.

[109] B. Saravanakumar, K.K. Purushothaman, G. Muralidharan, Interconnected V_2O_5 Nanoporous Network for High-Performance Supercapacitors, ACS Appl. Mater. Interfaces. 4 (2012) 4484–4490. doi:10.1021/am301162p.

[110] G. Wang, X. Lu, Y. Ling, T. Zhai, H. Wang, Supporting Information LiCl / PVA Gel Electrolyte Stabilizes Vanadium Oxide Nanowire Electrodes for Pseudocapacitors, 510275 (2012) 1–5. doi:10.1021/nn304178b.

[111] H. Yamada, K. Tagawa, M. Komatsu, I. Moriguchi, T. Kudo, High Power Battery Electrodes Using Nanoporous V2O5/Carbon Composites, J. Phys. Chem. C. 111 (2007) 8397–8402. doi:10.1021/jp071806p.

[112] W. Zhang, Y. Zeng, N. Xiao, H.H. Hng, Q. Yan, One-step electrochemical preparation of graphene-based heterostructures for Li storage, J. Mater. Chem. 22 (2012) 8455. doi:10.1039/c2jm16315b.

[113] H.Y. Lee, J.B. Goodenough, Ideal supercapacitor behavior of amorphous V2O5 center dot nH(2)O in potassium chloride (KCl) aqueous solution, J. Solid State Chem. 148 (1999) 81–84.

[114] G. Wee, H.Z. Soh, Y.L. Cheah, S.G. Mhaisalkar, M. Srinivasan, Synthesis and electrochemical properties of electrospun V2O5 nanofibers as supercapacitor electrodes., J. Mater. Chem. 20 (2010) 6720–6725. doi:10.1039/c0jm00059k.

[115] W. Dong, Electrochemical Properties of High Surface Area Vanadium Oxide Aerogels, Electrochem. Solid-State Lett. 3 (1999) 457. doi:10.1149/1.1391178.

[116] I.-H. Kim, J.-H. Kim, B.-W. Cho, Y.-H. Lee, K.-B. Kim, Synthesis and Electrochemical Characterization of Vanadium Oxide on Carbon Nanotube Film Substrate for Pseudocapacitor Applications, J. Electrochem. Soc. 153 (2006) A989. doi:10.1149/1.2188307.

[117] M. Jayalakshmi, M.M. Rao, N. Venugopal, K.B. Kim, Hydrothermal synthesis of SnO2-V2O5mixed oxide and electrochemical screening of carbon nano-tubes (CNT), V2O5, V2O5-CNT, and SnO2-V2O5-CNT electrodes for supercapacitor applications, J. Power Sources. 166 (2007) 578–583. doi:10.1016/j.jpowsour.2006.11.025.

[118] M. Li, G. Sun, P. Yin, C. Ruan, K. Ai, Controlling the Formation of Rodlike V 2 O 5 Nanocrystals on Reduced Graphene Oxide for High-Performance Supercapacitors, ACS Appl. Mater. Interfaces. 5 (2013) 11462–11470. doi:10.1021/am403739g.

[119] S.W. Hwang, S.H. Hyun, Synthesis and characterization of tin oxide/carbon aerogel composite electrodes for electrochemical supercapacitors, J. Power Sources. 172 (2007) 451–459. doi:10.1016/j.jpowsour.2007.07.061.

[120] J.H. Shin, H.M. Park, J.Y. Song, Phase transformation of hierarchical nanobranch structure from SnO to SnO2 and its electrochemical capacitance, J. Alloys Compd. 551 (2013) 451–455. doi:10.1016/j.jallcom.2012.11.039.

[121] V. Bonu, B. Gupta, S. Chandra, A. Das, S. Dhara, A.K. Tyagi, Electrochemical supercapacitor performance of SnO2quantum dots, Electrochim. Acta. 203 (2016) 230–237. doi:10.1016/j.electacta.2016.03.153.

[122] S.-L. Kuo, N.-L. Wu, Composite Supercapacitor Containing Tin Oxide and Electroplated Ruthenium Oxide, Electrochem. Solid-State Lett. 6 (2003) A85. doi:10.1149/1.1563872.

[123] K. Rajendra Prasad, N. Miura, Electrochemical synthesis and characterization of nanostructured tin oxide for electrochemical redox supercapacitors, Electrochem. Commun. 6 (2004) 849–852. doi:10.1016/j.elecom.2004.06.009.

[124] S.P. Lim, N.M. Huang, H.N. Lim, Solvothermal synthesis of SnO2/graphene nanocomposites for supercapacitor application, Ceram. Int. 39 (2013) 6647–6655. doi:10.1016/j.ceramint.2013.01.102.

[125] S. Wang, S.P. Jiang, X. Wang, Microwave-assisted one-pot synthesis of metal/metal oxide nanoparticles on graphene and their electrochemical applications, Electrochim. Acta. 56 (2011) 3338–3344. doi:10.1016/j.electacta.2011.01.016.

[126] F. Li, J. Song, H. Yang, S. Gan, Q. Zhang, D. Han, A. Ivaska, L. Niu, One-step synthesis of graphene/SnO2 nanocomposites and its application in electrochemical supercapacitors, Nanotechnology. 20 (2009) 455602.

[127] S.-L. Kuo, J.-F. Lee, N.-L. Wu, Study on Pseudocapacitance Mechanism of Aqueous MnFe[sub 2]O[sub 4] Supercapacitor, J. Electrochem. Soc. 154 (2007) A34. doi:10.1149/1.2388743.

[128] S.L. Kuo, N.L. Wu, Electrochemical characterization on MnFe2O4/carbon black composite aqueous supercapacitors, J. Power Sources. 162 (2006) 1437–1443. doi:10.1016/j.jpowsour.2006.07.056.

[129] A. Goljanian Tabrizi, N. Arsalani, A. Mohammadi, H. Namazi, L. Saleh Ghadimi, I. Ahadzadeh, Facile synthesis of a $MnFe_2O_4$/rGO nanocomposite for an ultra-stable symmetric supercapacitor, New J. Chem. 41 (2017) 4974–4984. doi:10.1039/C6NJ04093D.

[130] P. Xiong, C. Hu, Y. Fan, W. Zhang, J. Zhu, X. Wang, Ternary manganese

ferrite/graphene/polyaniline nanostructure with enhanced electrochemical capacitance performance, J. Power Sources. 266 (2014) 384–392. doi:10.1016/j.jpowsour.2014.05.048.

[131] J. Come, V. Augustyn, J.W. Kim, P. Rozier, P.-L. Taberna, P. Gogotsi, J.W. Long, B. Dunn, P. Simon, Electrochemical Kinetics of Nanostructured Nb2O5 Electrodes, J. Electrochem. Soc. 161 (2014) A718–A725. doi:10.1149/2.040405jes.

[132] K. Brezesinski, J. Wang, J. Haetge, C. Reitz, S.O. Steinmueller, S.H. Tolbert, B.M. Smarsly, B. Dunn, T. Brezesinski, Pseudocapacitive contributions to charge storage in highly ordered mesoporous group v transition metal oxides with iso-oriented layered nanocrystalline domains, J. Am. Chem. Soc. 132 (2010) 6982–6990. doi:10.1021/ja9106385.

[133] J.W. Kim, V. Augustyn, B. Dunn, The effect of crystallinity on the rapid pseudocapacitive response of Nb2O5, Adv. Energy Mater. 2 (2012) 141–148. doi:10.1002/aenm.201100494.

[134] T. Ohzuku, K. Sawai, T. Hirai, Electrochemistry of L-niobium pentoxide a lithium/non-aqueous cell, J. Power Sources. 19 (1987) 287–299. doi:10.1016/0378-7753(87)87005-2.

[135] A.A. Lubimtsev, P.R.C. Kent, B.G. Sumpter, P. Ganesh, Understanding the origin of high-rate intercalation pseudocapacitance in Nb2O5 crystals, J. Mater. Chem. A. 1 (2013) 14951. doi:10.1039/c3ta13316h.

[136] M. Zukalová, M. Kalbáč, L. Kavan, I. Exnar, M. Graetzel, Pseudocapacitive lithium storage in TiO2(B), Chem. Mater. 17 (2005) 1248–1255. doi:10.1021/cm048249t.

[137] J. Li, Z. Tang, Z. Zhang, Pseudocapacitive characteristic of lithium ion storage in hydrogen titanate nanotubes, Chem. Phys. Lett. 418 (2006) 506–510. doi:10.1016/j.cplett.2005.11.024.

[138] J. Li, Z. Tang, Z. Zhang, Layered hydrogen titanate nanowires with novel lithium intercalation properties, Chem. Mater. 17 (2005) 5848–5855. doi:10.1021/cm0516199.

[139] Y. Wang, Z. Hong, M. Wei, Y. Xia, Layered H2Ti6O13-nanowires: A new promising pseudocapacitive material in non-aqueous electrolyte, Adv. Funct. Mater. 22 (2012) 5185–5193. doi:10.1002/adfm.201200766.

[140] J. Rajeswari, P.S. Kishore, B. Viswanathan, T.K. Varadarajan, One-dimensional MoO2 nanorods for supercapacitor applications, Electrochem. Commun. 11 (2009) 572–575. doi:10.1016/j.elecom.2008.12.050.

[141] H.-S. Kim, J.B. Cook, S.H. Tolbert, B. Dunn, The Development of Pseudocapacitive Properties in Nanosized-MoO2, J. Electrochem. Soc. 162 (2015) A5083–A5090. doi:10.1149/2.0141505jes.

[142] M. Qiu, P. Sun, L. Shen, K. Wang, S. Song, X. Yu, S. Tan, C. Zhao, W. Mai, WO 3 nanoflowers with excellent pseudo-capacitive performance and the capacitance contribution analysis, J. Mater. Chem. A. 4 (2016) 7266–7273. doi:10.1039/C6TA00237D.

[143] S.K.J. D.Q. Liu, S.H. Yu, S.W. Son, Electrochemical Performance of Iridium Oxide Thin Film for Supercapacitor Prepared by Radio Frequency Magnetron

Sputtering Method, ECS Trans. 16 (2008) 103–109.

[144] S. Suematsu, Y. Oura, H. Tsujimoto, H. Kanno, K. Naoi, Conducting polymer films of cross-linked structure and their QCM analysis, Electrochim. Acta. 45 (2000) 3813–3821. doi:10.1016/S0013-4686(00)00466-7.

[145] G.A. Snook, P. Kao, A.S. Best, Conducting-polymer-based supercapacitor devices and electrodes, J. Power Sources. 196 (2011) 1–12. doi:10.1016/j.jpowsour.2010.06.084.

[146] H. Talbi, P.E. Just, L.H. Dao, Electropolymerization of aniline on carbonized polyacrylonitrile aerogel electrodes: Applications for supercapacitors, J. Appl. Electrochem. 33 (2003) 465–473. doi:10.1023/A:1024439023251.

[147] H. Guo, W. He, Y. Lu, X. Zhang, Self-crosslinked polyaniline hydrogel electrodes for electrochemical energy storage, Carbon N. Y. 92 (2015) 133–141. doi:10.1016/j.carbon.2015.03.062.

[148] Y. Huang, J. Tao, W. Meng, M. Zhu, Y. Huang, Y. Fu, Y. Gao, C. Zhi, Super-high rate stretchable polypyrrole-based supercapacitors with excellent cycling stability, Nano Energy. 11 (2015) 518–525. doi:10.1016/j.nanoen.2014.10.031.

[149] L.M. Huang, T.C. Wen, A. Gopalan, Electrochemical and spectroelectrochemical monitoring of supercapacitance and electrochromic properties of hydrous ruthenium oxide embedded poly(3,4-ethylenedioxythiophene)-poly(styrene sulfonic acid) composite, Electrochim. Acta. 51 (2006) 3469–3476. doi:10.1016/j.electacta.2005.09.049.

[150] M. Mallouki, F. Tran-Van, C. Sarrazin, P. Simon, B. Daffos, A. De, C. Chevrot, J.F. Fauvarque, Polypyrrole-Fe2O3 nanohybrid materials for electrochemical storage, J. Solid State Electrochem. 11 (2007) 398–406. doi:10.1007/s10008-006-0161-8.

[151] P. Gómez-Romero, M. Chojak, K. Cuentas-Gallegos, J.A. Asensio, P.J. Kulesza, N. Casañ-Pastor, M. Lira-Cantú, Hybrid organic-inorganic nanocomposite materials for application in solid state electrochemical supercapacitors, Electrochem. Commun. 5 (2003) 149–153. doi:10.1016/S1388-2481(03)00010-9.

[152] P. Gómez-Romero, K. Cuentas-Gallegos, M. Lira-Cantú, N. Casañ-Pastor, Hybrid nanocomposite materials for energy storage and conversion applications, J. Mater. Sci. 40 (2005) 1423–1428. doi:10.1007/s10853-005-0578-y.

[153] P.J. Kulesza, M. Skunik, B. Baranowska, K. Miecznikowski, M. Chojak, K. Karnicka, E. Frackowiak, F. Béguin, A. Kuhn, M.H. Delville, B. Starobrzynska, A. Ernst, Fabrication of network films of conducting polymer-linked polyoxometallate-stabilized carbon nanostructures, Electrochim. Acta. 51 (2006) 2373–2379. doi:10.1016/j.electacta.2005.06.041.

[154] K. Lota, V. Khomenko, E. Frackowiak, Capacitance properties of poly(3,4-ethylenedioxythiophene)/carbon nanotubes composites, J. Phys. Chem. Solids. 65 (2004) 295–301. doi:10.1016/j.jpcs.2003.10.051.

[155] M. Wu, G.A. Snook, V. Gupta, M. Shaffer, D.J. Fray, G.Z. Chen, Electrochemical fabrication and capacitance of composite films of carbon nanotubes and polyaniline, J. Mater. Chem. 15 (2005) 2297. doi:10.1039/b418835g.

[156] K.S. Ryu, K.M. Kim, Y.J. Park, N.G. Park, M.G. Kang, S.H. Chang, Redox supercapacitor using polyaniline doped with Li salt as electrode, Solid State Ionics.

152–153 (2002) 861–866. doi:10.1016/S0167-2738(02)00386-7.

[157] G.A. Snook, C. Peng, D.J. Fray, G.Z. Chen, Achieving high electrode specific capacitance with materials of low mass specific capacitance: Potentiostatically grown thick micro-nanoporous PEDOT films, Electrochem. Commun. 9 (2007) 83–88. doi:10.1016/j.elecom.2006.08.037.

[158] C. Arbizzani, M. Mastragostino, L. Meneghello, Characterization by impedance spectroscopy of a polymer-based supercapacitor., Electrochim. Acta. 40 (1995) 2223–2228. doi:10.1016/0013-4686(95)00167-D.

[159] D. Villers, D. Jobin, C. Soucy, D. Cossement, R. Chahine, L. Breau, D. Bélanger, The Influence of the Range of Electroactivity and Capacitance of Conducting Polymers on the Performance of Carbon Conducting Polymer Hybrid Supercapacitor, J. Electrochem. Soc. 150 (2003) A747. doi:10.1149/1.1571530.

[160] J.-I. Hong, I.-H. Yeo, W.-K. Paik, Conducting polymer with metal oxide for electrochemical capacitor poly(3,4-ethylenedioxythiophene) RuOx electrode., J. Electrochem. Soc. 148 (2001) A156–A163. doi:10.1149/1.1342166.

[161] J.D. Stenger-Smith, C.K. Webber, N. Anderson, A.P. Chafin, K. Zong, J.R. Reynolds, Poly(3,4-alkylenedioxythiophene)-Based Supercapacitors Using Ionic Liquids as Supporting Electrolytes, J. Electrochem. Soc. 149 (2002) A973. doi:10.1149/1.1485773.

[162] G.A. Snook, G.Z. Chen, The measurement of specific capacitances of conducting polymers using the quartz crystal microbalance, J. Electroanal. Chem. 612 (2008) 140–146. doi:10.1016/j.jelechem.2007.08.024.

[163] M.F. El-kady, Y. Shao, R.B. Kaner, Graphene for batteries, supercapacitors and beyond, Nat. Rev. Mater. 1 (2016) 16033. doi:10.1038/natrevmats.2016.33.

[164] P. Simon, Y. Gogotsi, B. Dunn, Where do batteries end and supercapacitors begin?, Science (80-.). 343 (2014) 1210–1211. doi:10.1126/science.1249625.

[165] T. Brousse, D. Belanger, J.W. Long, To Be or Not To Be Pseudocapacitive?, J. Electrochem. Soc. 162 (2015) A5185–A5189. doi:10.1149/2.0201505jes.

[166] Y. Gogotsi, R.M. Penner, Energy Storage in Nanomaterials - Capacitive, Pseudocapacitive, or Battery-like?, ACS Nano. 12 (2018) 2081–2083. doi:10.1021/acsnano.8b01914.

[167] T. Brezesinski, J. Wang, S.H. Tolbert, B. Dunn, Ordered mesoporous α-MoO3with iso-oriented nanocrystalline walls for thin-film pseudocapacitors, Nat. Mater. 9 (2010) 146–151. doi:10.1038/nmat2612.

[168] H. Lindström, S. Södergren, A. Solbrand, H. Rensmo, J. Hjelm, A. Hagfeldt, S.-E. Lindquist, Li $^{+}$ Ion Insertion in TiO $_{2}$ (Anatase). 2. Voltammetry on Nanoporous Films, J. Phys. Chem. B. 101 (1997) 7717–7722. doi:10.1021/jp970490q.

[169] A.J. Bard, L.R. Faulkner, Electrochemical methods : fundamentals and applications, Second, JOHN WILEY & SONS, INC, New York, 2001. doi:10.1016/j.aca.2010.06.020.

[170] D. Baronetto, N. Krstajic, S. Trasatti, Reply to Note on a method to interrelate inner and outer electrode areas by H. Vogt, Electrochim. Acta. 39 (1994) 1981–1983. doi:10.1016/0013-4686(94)85077-1.

[171] T. Nguyen, M.F. Montemor, Redox active materials for metal compound based

hybrid electrochemical energy storage : a perspective view, Appl. Surf. Sci. 422 (2017) 492–497. doi:10.1016/j.apsusc.2017.06.008.

[172] D.P. Dubal, O. Ayyad, V. Ruiz, P. Gómez-Romero, Hybrid energy storage: the merging of battery and supercapacitor chemistries, Chem. Soc. Rev. 44 (2015) 1777–1790. doi:10.1039/C4CS00266K.

[173] E. Castro, Electrochemical characterization of porous nickel–cobalt oxide electrodes, Int. J. Hydrogen Energy. 29 (2004) 255–261. doi:10.1016/S0360-3199(03)00133-2.

[174] M.S. Wu, Y.A. Huang, J.J. Jow, W.D. Yang, C.Y. Hsieh, H.M. Tsai, Anodically potentiostatic deposition of flaky nickel oxide nanostructures and their electrochemical performances, Int. J. Hydrogen Energy. 33 (2008) 2921–2926. doi:10.1016/j.ijhydene.2008.04.012.

[175] V. Gupta, T. Kawaguchi, N. Miura, Synthesis and electrochemical behavior of nanostructured cauliflower-shape Co-Ni/Co-Ni oxides composites, Mater. Res. Bull. 44 (2009) 202–206. doi:10.1016/j.materresbull.2008.04.020.

[176] Y.Q. Zhang, X.H. Xia, J.P. Tu, Y.J. Mai, S.J. Shi, X.L. Wang, C.D. Gu., Self-assembled synthesis of hierarchically porous NiO film and its application for electrochemical capacitors, J. Power Sources. 199 (2012) 413–417. doi:10.1016/j.jpowsour.2011.10.065.

[177] X. Xia, J. Tu, Y. Mai, R. Chen, X. Wang, C. Gu, X. Zhao, Graphene sheet/porous NiO hybrid film for supercapacitor applications., Chemistry. 17 (2011) 10898–905. doi:10.1002/chem.201100727.

[178] X. Xia, J. Tu, X. Wang, C. Gu, X. Zhao, Hierarchically porous NiO film grown by chemical bath depositionvia a colloidal crystal template as an electrochemical pseudocapacitor material, J. Mater. Chem. 21 (2011) 671–679. doi:10.1039/C0JM02784G.

[179] V. Srinivasan, J.W. Weidner, J.E. Soc, P. L-l, V. Srinivasan, J.W. Weidner, An Electrochemical Route for Making Porous Nickel Oxide Electrochemical Capacitors An Electrochemical Route for Making Porous Nickel Oxide Electrochemical Capacitors, J. Electrochem. Soc. 144 (1997). doi:10.1149/1.1837859.

[180] V. Srinivasan, J.W. Weidner, Studies on the capacitance of nickel oxide films: effect of heating temperature and electrolyte concentration, J. Electrochem. Soc. 147 (2000) 880–885. doi:10.1149/1.1393286.

[181] U.M. Patil, R.R. Salunkhe, K. V Gurav, C.D. Lokhande, Chemically deposited nanocrystalline NiO thin films for supercapacitor application, Appl. Surf. Sci. 255 (2008) 2603–2607. doi:10.1016/j.apsusc.2008.07.192.

[182] D.-W. Wang, F. Li, H.-M. Cheng, Hierarchical porous nickel oxide and carbon as electrode materials for asymmetric supercapacitor., J. Power Sources. 185 (2008) 1563–1568. doi:10.1016/j.jpowsour.2008.08.032.

[183] X. Zhang, W. Shi, J. Zhu, W. Zhao, J. Ma, S. Mhaisalkar, T.L. Maria, Synthesis of Porous NiO Nanocrystals with Controllable Surface Area and Their Application as Supercapacitor Electrodes, Nano Res. 3 (2010) 643–652. doi:10.1007/s12274-010-0024-6.

[184] J. Lang, L. Kong, W. Wu, Y. Luo, L. Kang, Facile approach to prepare loose-

packed NiO nano-flakes materials for supercapacitors, Chem. Commun. (2008) 4213–4215. doi:10.1039/b800264a.

[185] Z. Zhang, Q. Gao, H. Gao, Z. Shi, J. Wu, M. Zhi, Z. Hong, Nickel oxide aerogel for high performance supercapacitor electrodes, RSC Adv. 6 (2016) 112620–112624. doi:10.1039/C6RA24436J.

[186] J.-W. Lang, L.-B. Kong, W.-J. Wu, Y.-C. Luo, L. Kang, Facile approach to prepare loose-packed NiO nano-flakes materials for supercapacitors., Chem. Commun. (2008) 4213–4215. doi:10.1039/b800264a.

[187] Y. Ren, L. Gao, From three-dimensional flower-like α-Ni(OH)2nanostructures to hierarchical porous NiO nanoflowers: Microwave-assisted fabrication and supercapacitor properties, J. Am. Ceram. Soc. 93 (2010) 3560–3564. doi:10.1111/j.1551-2916.2010.04090.x.

[188] C. Yuan, X. Zhang, L. Su, B. Gao, L. Shen, Facile synthesis and self-assembly of hierarchical porous NiO nano/micro spherical superstructures for high performance supercapacitors, J. Mater. Chem. 19 (2009) 5772. doi:10.1039/b902221j.

[189] J. Zhu, J. Jiang, J. Liu, R. Ding, H. Ding, Y. Feng, G. Wei, X. Huang, Direct synthesis of porous NiO nanowall arrays on conductive substrates for supercapacitor application, J. Solid State Chem. 184 (2011) 578–583. doi:10.1016/j.jssc.2011.01.019.

[190] A.D. Jagadale, V.S. Kumbhar, D.S. Dhawale, C.D. Lokhande, Potentiodynamically deposited nickel oxide (NiO) nanoflakes for pseudocapacitors., J. Electroanal. Chem. 704 (2013) 90–95. doi:10.1016/j.jelechem.2013.06.020.

[191] K.-W. Nam, K.-B. Kim, A Study of the Preparation of NiO[sub x] Electrode via Electrochemical Route for Supercapacitor Applications and Their Charge Storage Mechanism, J. Electrochem. Soc. 149 (2002) A346. doi:10.1149/1.1449951.

[192] F.I. Dar, K.R. Moonoosawmy, M. Es-Souni, Morphology and property control of NiO nanostructures for supercapacitor applications., Nanoscale Res. Lett. 8 (2013) 363. doi:10.1186/1556-276X-8-363.

[193] H.Y. Wu, H.W. Wang, Electrochemical synthesis of nickel oxide nanoparticulate films on nickel foils for high-performance electrode materials of supercapacitors, Int. J. Electrochem. Sci. 7 (2012) 4405–4417.

[194] M. Wu, Y. Huang, C. Yang, J. Jow, Electrodeposition of nanoporous nickel oxide film for electrochemical capacitors, Int. J. Hydrogen Energy. 32 (2007) 4153–4159. doi:10.1016/j.ijhydene.2007.06.001.

[195] M. Ates, M.A. Serin, I. Ekmen, Y.N. Ertas, M. Hassan, K.R. Reddy, E. Haque, S.N. Faisal, S. Ghasemi, A. I. Minett, V.G. Gomes, K. Krishnamoorthy, G.K. Veerasubramani, S.J. Kim, S. Radhakrishnan, S.J. Kim, A.N. Rao, S.J. Kim, C. Masarapu, H.F. Zeng, K.H. Hung, B. Wei, A. Orphanou, T. Yamada, C.Y. Yang, P.L. Taberna, P. Simon, J.F. Fauvarque, G.K. Veerasubramani, K. Krishnamoorthy, S. Radhakrishnan, N.-J. Kim, S.J. Kim, J. Wu, X.-Y. Wu, X. Wei, K.-X. Wang, J.-S.J. Chen, J. Liu, Y. Ma, M. Yu, J. An, S. Li, K. Pandey, P. Yadav, I. Mukhopadhyay, D. Saha, Y. Li, Z. Bi, J.-S.J. Chen, J.K. Keum, D.K. Hensley, H.A. Grappe, H.M. 3rd Meyer, S. Dai, M.P. Paranthaman, A.K. Naskar, R.

Tholkappiyan, A.N. Naveen, K. Vishista, Studies on supercapacitor electrode material from activated lignin-derived mesoporous carbon, IEEE Nanotechnol. Mater. Devices Conf. 30 (2014) 900–910. doi:10.3969/j.issn.0251-0790.2012.07.032.

[196] G. Wang, L. Zhang, J. Zhang, A review of electrode materials for electrochemical supercapacitors, Chem. Soc. Rev. 41 (2012) 797–828. doi:10.1039/C1CS15060J.

[197] Z. Fan, J. Chen, K. Cui, F. Sun, Y. Xu, Y. Kuang, Preparation and capacitive properties of cobalt – nickel oxides / carbon nanotube composites, Electrochim. Acta. 52 (2007) 2959–2965. doi:10.1016/j.electacta.2006.09.029.

[198] K.-W. Nam, E.-S. Lee, J.-H. Kim, Y.-H. Lee, K.-B. Kim, Synthesis and Electrochemical Investigations of Ni[sub 1−x]O Thin Films and Ni[sub 1−x]O on Three-Dimensional Carbon Substrates for Electrochemical Capacitors, J. Electrochem. Soc. 152 (2005) A2123. doi:10.1149/1.2039647.

[199] N.B. Trung, T. Van Tam, D.K. Dang, K.F. Babu, E.J. Kim, J. Kim, W.M. Choi, Facile synthesis of three-dimensional graphene/nickel oxide nanoparticles composites for high performance supercapacitor electrodes, Chem. Eng. J. 264 (2015) 603–609. doi:10.1016/j.cej.2014.11.140.

[200] L. Wang, X. Liu, X. Wang, X. Yang, L. Lu, Preparation and electrochemical properties of mesoporous Co3O4 crater-like microspheres as supercapacitor electrode materials, Curr. Appl. Phys. 10 (2010) 1422–1426. doi:10.1016/j.cap.2010.05.007.

[201] S.G. Kandalkar, D.S. Dhawale, C.K. Kim, C.D. Lokhande, Chemical synthesis of cobalt oxide thin film electrode for supercapacitor application, Synth. Met. 160 (2010) 1299–1302. doi:10.1016/j.synthmet.2010.04.003.

[202] V.R. Shinde, S.B. Mahadik, T.P. Gujar, C.D. Lokhande, Supercapacitive cobalt oxide (Co3O4) thin films by spray pyrolysis, Appl. Surf. Sci. 252 (2006) 7487–7492. doi:10.1016/j.apsusc.2005.09.004.

[203] C. Lin, J.A. Ritter, B.N. Popov, Characterization of Sol − Gel − Derived Cobalt Oxide Xerogels as Electrochemical Capacitors, J. Electrochem. Soc. 145 (1998) 4097–4103. doi:10.1149/1.1838920.

[204] T.Y. Wei, C.H. Chen, K.H. Chang, S.Y. Lu, C.C. Hu, Cobalt oxide aerogels of ideal supercapacitive properties prepared with an epoxide synthetic route, Chem. Mater. 21 (2009) 3228–3233. doi:10.1021/cm9007365.

[205] Y. Gao, S. Chen, D. Cao, G. Wang, J. Yin, Electrochemical capacitance of Co3O4 nanowire arrays supported on nickel foam, J. Power Sources. 195 (2010) 1757–1760. doi:10.1016/j.jpowsour.2009.09.048.

[206] G. Wang, X. Shen, J. Horvat, B. Wang, H. Liu, A. Guoxiu Wang, D. Wexler, J. Yao, Hydrothermal synthesis and optical, magnetic and supercapacitance properties of nanoporous cobalt oxide nanorodes Hydrothermal Synthesis and Optical, Magnetic, and Supercapacitance Properties of Nanoporous Cobalt Oxide Nanorods, J. Phys. Chem. Part C Nanomater. Interfaces. 113 (2009) 4357–4361. doi:10.1021/jp8106149.

[207] H. Luo, F. Zhang, X. Zhao, D. Zhang, Y. Sun, P. Yang, Preparation and properties of coke powder activated carbon/α-Co(OH)2 composite electrode materials, J. Mater. Sci. Mater. Electron. 24 (2013) 2473–2478. doi:10.1007/s10854-013-1120-

7.

[208] Y. Xu, Z. Liu, D. Chen, Y. Song, R. Wang, Synthesis and Electrochemical Properties of Porous α-Co(OH)2 and Co3O4 Microspheres, Prog. Nat. Sci. Mater. Int. 27 (2017) 197–202. doi:10.1016/j.pnsc.2017.03.001.

[209] S.G. Kandalkar, H.-M. Lee, H. Chae, C.-K. Kim, Structural, morphological, and electrical characteristics of the electrodeposited cobalt oxide electrode for supercapacitor applications., Mater. Res. Bull. 46 (2011) 48–51. doi:10.1016/j.materresbull.2010.09.041.

[210] C. Yuan, L. Yang, L. Hou, L. Shen, X. Zhang, X.W. (David) Lou, Growth of ultrathin mesoporous Co3O4 nanosheet arrays on Ni foam for high-performance electrochemical capacitors, Energy Environ. Sci. 5 (2012) 7883. doi:10.1039/c2ee21745g.

[211] N. Jayaprakash, W.D. Jones, S.S. Moganty, L.A. Archer, Composite lithium battery anodes based on carbon@Co3O4nanostructures: Synthesis and characterization, J. Power Sources. 200 (2012) 53–58. doi:10.1016/j.jpowsour.2011.10.018.

[212] X. Dong, H. Xu, X. Wang, Y. Huang, M.B. Chan-park, H. Zhang, 3D Graphene À Cobalt Oxide Electrode for High-Performance Supercapacitor and Enzymeless Glucose Detection, (2012) 3206–3213.

[213] G. He, J. Li, H. Chen, J. Shi, X. Sun, S. Chen, X. Wang, Hydrothermal preparation of Co3O4@graphene nanocomposite for supercapacitor with enhanced capacitive performance, Mater. Lett. 82 (2012) 61–63. doi:10.1016/j.matlet.2012.05.048.

[214] G. Wang, L. Zhang, J. Zhang, A review of electrode materials for electrochemical supercapacitors, Chem. Soc. Rev. 41 (2012) 797–828. doi:Doi 10.1039/C1cs15060j.

[215] Y. Shan, L. Gao, Formation and characterization of multi-walled carbon nanotubes/Co3O4nanocomposites for supercapacitors, Mater. Chem. Phys. 103 (2007) 206–210. doi:10.1016/j.matchemphys.2007.02.038.

[216] A. García-Gómez, R.G. Duarte, S. Eugénio, T.M. Silva, M.J. Carmezim, M.F. Montemor, Fabrication of electrochemically reduced graphene oxide/cobalt oxide composite for charge storage electrodes, J. Electroanal. Chem. 755 (2015) 151–157. doi:10.1016/j.jelechem.2015.07.053.

[217] H. Cheng, Z.G. Lu, J.Q. Deng, C.Y. Chung, K. Zhang, Y.Y. Li, A Facile Method to Improve the High Rate Capability of Co3O4 Nanowire Array Electrodes, 3 (2010) 895–901. doi:10.1007/s12274-010-0063-z.

[218] S.G. Kandalkar, J.L. Gunjakar, C.D. Lokhande, Preparation of cobalt oxide thin films and its use in supercapacitor application, Appl. Surf. Sci. 254 (2008) 5540–5544. doi:10.1016/j.apsusc.2008.02.163.

[219] R.B. Rakhi, W. Chen, D. Cha, H.N. Alshareef, Substrate Dependent Self-Organization of Mesoporous Cobalt Oxide Nanowires with Remarkable Pseudocapacitance, (2012). doi:10.1021/nl300779a.

[220] G. Jang, S. Ameen, M.S. Akhtar, H. Shin, Cobalt oxide nanocubes as electrode material for the performance evaluation of electrochemical supercapacitor, Ceram. Int. 44 (2017) 1. doi:10.1016/j.ceramint.2017.09.217.

[221] D.T. Dam, J. Lee, Three-Dimensional Cobalt Oxide Microstructures with Brush-like Morphology via Surfactant-Dependent Assembly, (2014).

[222] F. Meng, Z. Fang, Z. Li, W. Xu, M. Wang, Y. Liu, J. Zhang, W. Wang, D. Zhaob, X. Guo, Porous Co3O4 materials prepared by solid-state thermolysis of a novel Co-MOF crystal and their superior energy storage performances for supercapacitors, J. Mater. Chem. A. 1 (2013) 7235–7241. doi:10.1039/c3ta11054k.

[223] J. Tarascon, P. Poizot, S. Laruelle, S. Grugeon, L. Dupont, Nano-sized transition-metal oxides as negative-electrode materials for lithium-ion batteries, Nature. 407 (2000) 496–499. doi:10.1038/35035045.

[224] J. Jiang, Y. Li, X. Huang, Nanoscale Building one-dimensional oxide nanostructure arrays on conductive metal substrates for lithium-ion battery anodes, (2011) 45–58. doi:10.1039/c0nr00472c.

[225] J. Wang, B. Niu, G. Du, R. Zeng, Z. Chen, Z. Guo, S. Dou, Microwave homogeneous synthesis of porous nanowire Co3O4arrays with high capacity and rate capability for lithium ion batteries, Mater. Chem. Phys. 126 (2011) 747–754. doi:10.1016/j.matchemphys.2010.12.049.

[226] W. Wen, J.M. Wu, J.P. Tu, A novel solution combustion synthesis of cobalt oxide nanoparticles as negative-electrode materials for lithium ion batteries, J. Alloys Compd. 513 (2012) 592–596. doi:10.1016/j.jallcom.2011.11.019.

[227] W.W. Lee, J.-M. Lee, Novel synthesis of high performance anode materials for lithium-ion batteries (LIBs), J. Mater. Chem. A. 2 (2014) 1589–1626. doi:10.1039/C3TA12830J.

[228] J.S. Do, R.F. Dai, Cobalt oxide thin film prepared by an electrochemical route for Li-ion battery, J. Power Sources. 189 (2009) 204–210. doi:10.1016/j.jpowsour.2008.09.093.

[229] A. Xiao, J. Yang, W. Zhang, Mesoporous cobalt oxide film prepared by electrodeposition as anode material for Li ion batteries, J. Porous Mater. 17 (2010) 583–588. doi:10.1007/s10934-009-9327-y.

[230] G.P. Kim, I. Nam, N.D. Kim, J. Park, S. Park, J. Yi, A synthesis of graphene/Co3O4 thin films for lithium ion battery anodes by coelectrodeposition, Electrochem. Commun. 22 (2012) 93–96. doi:10.1016/j.elecom.2012.05.032.

[231] F.D. Wu, Y. Wang, Self-assembled echinus-like nanostructures of mesoporous CoO nanorod@CNT for lithium-ion batteries, J. Mater. Chem. 21 (2011) 6636. doi:10.1039/c0jm04346j.

[232] J. Chen, X. Xia, J. Tu, Q. Xiong, Y.-X. Yu, X. Wang, C. Gu, Co3O4–C core–shell nanowire array as an advanced anode material for lithium ion batteries, J. Mater. Chem. 22 (2012) 15056. doi:10.1039/c2jm31629c.

[233] W. Mei, J. Huang, L. Zhu, Z. Ye, Y. Mai, J. Tu, Synthesis of porous rhombus-shaped Co3O4 nanorod arrays grown directly on a nickel substrate with high electrochemical performance, J. Mater. Chem. 22 (2012) 9315. doi:10.1039/c2jm00123c.

[234] M.M. Rahman, J.Z. Wang, X.L. Deng, Y. Li, H.K. Liu, Hydrothermal synthesis of nanostructured Co3O4 materials under pulsed magnetic field and with an aging technique, and their electrochemical performance as anode for lithium-ion battery,

Electrochim. Acta. 55 (2009) 504–510. doi:10.1016/j.electacta.2009.08.068.

[235] A.K. Rai, L.T. Anh, J. Gim, J. Kim, One-step synthesis of CoO anode material for rechargeable lithium-ion batteries, Ceram. Int. 39 (2013) 9325–9330. doi:10.1016/j.ceramint.2013.05.049.

[236] Y. Kim, Y. Yoon, D. Shin, Charge – discharge characteristics of nanocrystalline Co3O4 powders via aerosol flame synthesis, Solid State Ionics. 192 (2011) 308 – 312.

[237] M. V. Reddy, Z. Beichen, L.J. Nicholette, Z. Kaimeng, B.V.R. Chowdari, Molten Salt Synthesis and Its Electrochemical Characterization of Co3O4 for Lithium Batteries, Electrochem. Solid-State Lett. 14 (2011) A79. doi:10.1149/1.3556984.

[238] M. Xu, F. Wang, M. Zhao, S. Yang, X. Song, Molten hydroxides synthesis of hierarchical cobalt oxide nanostructure and its application as anode material for lithium ion batteries, Electrochim. Acta. 56 (2011) 4876–4881. doi:10.1016/j.electacta.2011.03.027.

[239] R. Xu, J. Wang, Q. Li, G. Sun, E. Wang, S. Li, J. Gu, M. Ju, Porous cobalt oxide (Co3O4) nanorods: Facile syntheses, optical property and application in lithium-ion batteries, J. Solid State Chem. 182 (2009) 3177–3182. doi:10.1016/j.jssc.2009.08.033.

[240] S.-H. Hong, J.-S. Bae, H.-J. Ahn, Synthesis of Nano-Sized Co3O4 Powder by Spray Conversion Method for Anode Material of Lithium Battery, Met. Mater. Int. 14 (2008) 229–232. doi:10.3365/met.mat.2008.04.229.

[241] D. Barreca, M. Cruz-Yusta, A. Gasparotto, C. MacCato, J. Morales, A. Pozza, C. Sada, L. Sánchez, E. Tondello, Cobalt oxide nanomaterials by vapor-phase synthesis for fast and reversible lithium storage, J. Phys. Chem. C. 114 (2010) 10054–10060. doi:10.1021/jp102380e.

[242] Y. Qi, N. Du, H. Zhang, X. Fan, Y. Yang, D. Yang, CoO/NiSix core–shell nanowire arrays as lithium-ion anodes with high rate capabilities, Nanoscale. 4 (2012) 991–996. doi:10.1039/C2NR11545J.

[243] S. Zhou, G. Wang, Y. Xie, H. Wang, J. Bai, Synthesis of carbon-coated Co3O4 composite with dendrite-like morphology and its electrochemical performance for lithium-ion batteries, J. Nanoparticle Res. 15 (2013) 1740. doi:10.1007/s11051-013-1740-0.

[244] Y. Jiang, T. Yuan, M. Yan, W. Sun, Electrostatic spray deposition of porous SnO2/graphene anode films and their enhanced lithium storage properties., ACS Appl. Mater. Interfaces. c (2012) 2–6. doi:10.1021/am301788m.

[245] C. Peng, B. Chen, Y. Qin, S. Yang, C. Li, Y. Zuo, S. Liu, J. Yang, Facile ultrasonic synthesis of coo quantum dot/graphene nanosheet composites with high lithium storage capacity, ACS Nano. 6 (2012) 1074–1081. doi:10.1021/nn202888d.

[246] M. Zhang, M. Jia, Y. Jin, X. Shi, Synthesis and electrochemical performance of CoO/graphene nanocomposite as anode for lithium ion batteries, Appl. Surf. Sci. 263 (2012) 573–578. doi:10.1016/j.apsusc.2012.09.111.

[247] D.P. Dubal, P. Gomez-Romero, B.R. Sankapal, R. Holze, Nickel cobaltite as an emerging material for supercapacitors: An overview, Nano Energy. 11 (2015) 377–399. doi:10.1016/j.nanoen.2014.11.013.

[248] T.-Y. Wei, C.-H. Chen, H.-C. Chien, S.-Y. Lu, C.-C. Hu, A cost-effective supercapacitor material of ultrahigh specific capacitances: spinel nickel cobaltite aerogels from an epoxide-driven sol-gel process., Adv. Mater. 22 (2010) 347–51. doi:10.1002/adma.200902175.

[249] J. Pu, J. Wang, X. Jin, F. Cui, E. Sheng, Z. Wang, Acta Porous hexagonal NiCo2O4 nanoplates as electrode materials for supercapacitors, Electrochim. Acta. 106 (2013) 226–234. doi:10.1016/j.electacta.2013.05.092.

[250] J.M. Chem, Q. Wang, B. Liu, X. Wang, S. Ran, L. Wang, D. Chen, G. Shen, Morphology evolution of urchin-like NiCo2O4 nanostructures and their applications as psuedocapacitors and photoelectrochemical cells, J. Mater. Chem. 22 (2012) 21647–21653. doi:10.1039/c2jm34705a.

[251] R. Zou, K. Xu, T. Wang, G. He, Q. Liu, X. Liu, Z. Zhang, and J. Hu, Chain-like NiCo2O4 nanowires with different exposed reactive planes for high-performance supercapacitors, J. Mater. Chem. A. (2013) 8560–8566. doi:10.1039/c3ta11361b.

[252] Q. Lu, Y. Chen, W. Li, J.G. Chen, J.Q. Xiao, F. Jiao, Ordered mesoporous nickel cobaltite spinel with ultra-high supercapacitance, J. Mater. Chem. A. 1 (2013) 2331–2336. doi:10.1039/c2ta00921h.

[253] J. Chang, J. Sun, C. Xu, H. Xu, and L. Gao, Template-free approach to synthesize hierarchical porous nickel cobalt oxides for supercapacitors, Nanoscale. 4 (2012) 6786–6791. doi:10.1039/c2nr31725g.

[254] C. An, Y. Wang, Y. Huang, Y. Xu, C. Xu, L. Jiao, H. Yuan, Novel three-dimensional NiCo2O4 hierarchitectures: solvothermal synthesis and electrochemical properties, CrystEngComm. 16 (2014) 385–392. doi:10.1039/c3ce41768a.

[255] I. Shakir, M. Sarfraz, A. Rana, Synthesis of hierarchical porous spinel nickel cobaltite nano fl akes for high performance electrochemical energy storage supercapacitors, RSC Adv. 3 (2013) 21386–21389. doi:10.1039/c3ra43973a.

[256] Y. Lei, J. Li, Y. Wang, L. Gu, Y. Chang, H. Yuan, D. Xiao, Rapid Microwave-Assisted Green Synthesis of 3D Hierarchical Flower-Shaped NiCo2O4 Microsphere for High-Performance Supercapacitor, ACS Appl. Mater. Interfaces. 6 (2014) 1773–1780.

[257] R.R. Salunkhe, K. Jang, H. Yu, S. Yu, T. Ganesh, S. Han, H. Ahn, Chemical synthesis and electrochemical analysis of nickel cobaltite nanostructures for supercapacitor applications, J. Alloys Compd. 509 (2011) 6677–6682. doi:10.1016/j.jallcom.2011.03.136.

[258] L. Huang, D. Chen, Y. Ding, S. Feng, Z.L. Wang, M. Liu, Nickel-cobalt hydroxide nanosheets coated on NiCo2O4 nanowires grown on carbon fiber paper for high-performance pseudocapacitors, Nano Lett. 13 (2013) 3135–3139. doi:10.1021/nl401086t.

[259] R. Ding, L. Qi, H. Wang, Scalable Electrodeposition of Cost-Effective Microsized NiCo2O4 Electrode Materials for Practical Applications in Electrochemical, ECS Electrochem. Lett. 1 (2012) 2012–2015. doi:10.1149/2.001203eel.

[260] C. Hu, C. Hsu, K. Chang, H. Hsu, Microwave-assisted hydrothermal annealing of binary Ni e Co oxy-hydroxides for asymmetric supercapacitors, J. Power Sources. 238 (2013) 180–189. doi:10.1016/j.jpowsour.2013.03.019.

[261] J. Du, G. Zhou, H. Zhang, C. Cheng, J. Ma, W. Wei, L. Chen, T. Wang, Ultrathin Porous NiCo2O4 Nanosheet Arrays on Flexible Carbon Fabric for High-Performance Supercapacitors, (2013) 7405–7409.

[262] C. Yuan, J. Li, L. Hou, X. Zhang, L. Shen, X.W. Lou, Ultrathin mesoporous NiCo 2O 4 nanosheets supported on Ni foam as advanced electrodes for supercapacitors, Adv. Funct. Mater. 22 (2012) 4592–4597. doi:10.1002/adfm.201200994.

[263] D. Carriazo, J. Patiño, M.C. Gutiérrez, M.L. Ferrer, F. del Monte, Microwave-assisted synthesis of NiCo2O4–graphene oxide nanocomposites suitable as electrodes for supercapacitors, RSC Adv. 3 (2013) 13690. doi:10.1039/c3ra42610f.

[264] H.-W. Wang, Z.-A. Hu, Y.-Q. Chang, Y.-L. Chen, H.-Y. Wu, Z.-Y. Zhang, Y.-Y. Yang, Design and synthesis of NiCo2O4–reduced graphene oxide composites for high performance supercapacitors, J. Mater. Chem. 21 (2011) 10504. doi:10.1039/c1jm10758e.

[265] X. Wang, W.S. Liu, X. Lu, P.S. Lee, Dodecyl sulfate-induced fast faradic process in nickel cobalt oxide–reduced graphite oxide composite material and its application for asymmetric supercapacitor device, J. Mater. 22 (2012) 23114–23119. doi:10.1039/c2jm35307e.

[266] G. He, L. Wang, H. Chen, X. Sun, X. Wang, Preparation and performance of NiCo2O4 nanowires-loaded graphene as supercapacitor material, Mater. Lett. 98 (2013) 164–167. doi:10.1016/j.matlet.2013.02.035.

[267] P.J. Tsai, S.L.I. Chan, Nickel-based batteries: materials and chemistry, Woodhead Publishing Limited, 2013. doi:10.1533/9780857097378.3.309.

[268] H. Bode, K. Dehmelt, J. Witte, Zur Kenntnis der Nickelhydroxidelektrode - I. Über das Nickel(II)-Hydroxidhydrat, Electrochim. Acta. 11 (1966) 1079–1087. doi:10.1016/0013-4686(66)80045-2.

[269] R.S. Jayashree, P. Vishnu Kamath, Suppression of the α → β-nickel hydroxide transformation in concentrated alkali: Role of dissolved cations, J. Appl. Electrochem. 31 (2001) 1315–1320. doi:10.1023/A:1013876006707.

[270] Y. Mo, E. Hwang, D.A. Scherson, In Situ Quarlz Crystal Microbalance Studies of Nickel Hydrous Oxide Films in Alkaline Electrolytes, J. Electrochem. Soc. 143 (1996) 5–11.

[271] G. Feuillade, R. Jacoud, Transferts ioniques durant l'oxydation anodique d'un hydroxyde de nickel, Electrochim. Acta. 14 (1969) 1297–1311. doi:10.1016/0013-4686(69)87023-4.

[272] S.I. Cordoba-Torresi, A. A. Hugot-Le Gaff, S. Joiret, Electrochromic Behavior of Nickel Oxide Electrodes II . Identification of the Bleached State by Raman Spectroscopy and Nuclear Reactions, J. Electrochem. Soc. 138 (1991) 1554–1559.

[273] T. Nguyen, M. Fátima Montemor, γ-FeOOH and amorphous Ni-Mn hydroxide on carbon nanofoam paper electrodes for hybrid supercapacitors, J. Mater. Chem. A. 6 (2018) 2612–2624. doi:10.1039/c7ta05582j.

[274] A.K. Shukla, S. Venugopalan, B. Hariprakash, Nickel-based rechargeable batteries, J. Power Sources. 100 (2001) 125–148. doi:10.1016/S0378-7753(01)00890-4.

[275] Y. Borthomieu, P. Bernard, SECONDARY BATTERIES – NICKEL SYSTEMS | Nickel–Hydrogen, Encycl. Electrochem. Power Sources. (2009) 482–493. doi:10.1016/B978-044452745-5.00157-X.

[276] H. Chen, T.N. Cong, W. Yang, C. Tan, Y. Li, Y. Ding, Progress in electrical energy storage system: A critical review, Prog. Nat. Sci. 19 (2009) 291–312. doi:10.1016/j.pnsc.2008.07.014.

[277] C. Daniel, J.O. Besenhard, Handbook of Battery Materials: Second Edition, 2011. doi:10.1002/9783527637188.

[278] E. Cattaneo, B. Riegel, Chemistry, electrochemistry, and electrochemical applications | nickel, in: Encycl. Electrochem. Power Sources, Amsterdam: Elsevier, 2009.

[279] M.A. Manzo, Nickel-hydrogen capacity loss on storage, J. Power Sources. 29 (1990) 541–554.

[280] T.P.J. Crompton, Battery reference book, Newnes, 2000.

[281] E.J. Cairns, Secondary batteries – nickel systems | nickel-zinc, in: Encycl. Electrochem. Power Sources, Elsevier, 2009: pp. 528–533.

[282] J.T. Nichols, F.R. McLarnon, E.J. Carins, ZINC ELECTRODE CYCLE-LIFE PERFORMANCE IN ALKALINE ELECTROLYTES HAVING REDUCED ZINC SPECIES SOLUBILITY, Chem. Eng. Commun. 37 (1984) 355–379. doi:10.1080/00986448508911290.

[283] M.A. Fetcenko, S.R. Ovshinsky, B. Reichman, K. Young, C. Fierro, J. Koch, A. Zallen, W. Mays, T. Ouchi, Recent advances in NiMH battery technology, 165 (2007) 544–551. doi:10.1016/j.jpowsour.2006.10.036.

[284] S. Bliznakov, E. Lefterova, N. Dimitrov, K. Petrov, A. Popov, A study of the Al content impact on the properties of MmNi4.4−xCo0.6Alx alloys as precursors for negative electrodes in NiMH batteries, J. Power Sources. 176 (2008) 381–386. doi:10.1016/j.jpowsour.2007.10.028.

[285] P.H.L. Notten, M. Latroche, SECONDARY BATTERIES – NICKEL SYSTEMS | Nickel – Metal Hydride :Overview, in: J. Garche (Ed.), Encycl. Electrochem. Power Sources, Elsevier, 2009. doi:10.1016/B978-044452745-5.00164-7.

[286] G. Pistoia, Battery Operated Devices and Systems: From Portable Electronics to Industrial Products, Elsevier, 2009.

[287] M. Anik, H. Gasan, S. Topcu, Electrochemical hydrogen storage characteristics of Mg1.5Al0.5-xZrxNi (x= 0,0.1,0.2,0.3,0.4,0.5) alloys synthesized by mechanical alloying, Int. J. Hydrog. Energyy. 34 (2009) 2692–2700. doi:10.1016/j.ijhydene.2009.01.062.

[288] L. Guerlou-Demourgues, C. Delmas, New manganese-substituted nickel hydroxides, J. Power Sources. 52 (1994) 275–281. doi:10.1016/0378-7753(94)02024-8.

[289] D.S. Hall, D.J. Lockwood, C. Bock, B.R. MacDougall, Nickel hydroxides and related materials: a review of their structures, synthesis and properties., Proc. Math. Phys. Eng. Sci. 471 (2015) 20140792. doi:10.1098/rspa.2014.0792.

[290] J. Lang, L. Kong, W. Wu, A facile approach to the preparation of loose-packed Ni(OH)2 nanoflake materials for electrochemical capacitors, J Solid State

Electrochem. 13 (2009) 333–340. doi:10.1007/s10008-008-0560-0.

[291] D.D. Zhao, S.J. Bao, W.J. Zhou, H.L. Li, Preparation of hexagonal nanoporous nickel hydroxide film and its application for electrochemical capacitor, Electrochem. Commun. 9 (2007) 869–874. doi:10.1016/j.elecom.2006.11.030.

[292] G.-W. Yang, C.-L. Xu, H.-L. Li, Electrodeposited nickel hydroxide on nickel foam with ultrahigh capacitance, Chem. Commun. (2008) 6537. doi:10.1039/b815647f.

[293] H. Cui, J. Xue, W. Ren, M. Wang, Ultra-high specific capacitance of β-Ni(OH)2monolayer nanosheets synthesized by an exfoliation-free sol-gel route, J. Nanoparticle Res. 16 (2014). doi:10.1007/s11051-014-2601-1.

[294] B. Schneiderová, J. Demel, J. Pleštil, P. Janda, J. Bohuslav, D. Ihiawakrim, O. Ersen, G. Rogez, K. Lang, Nickel hydroxide ultrathin nanosheets as building blocks for electrochemically active layers, J. Mater. Chem. A. 1 (2013) 11429. doi:10.1039/c3ta12129a.

[295] Y. Hu, Y. V Tolmachev, D.A. Scherson, Rotating ring-disk studies of oxidized nickel hydrous oxide: oxygen evolution and pseudocapacitance., J. Electroanal. Chem. 468 (1999) 64–69. doi:10.1016/S0022-0728(99)00029-7.

[296] Y.Y. Liang, S.J. Bao, H.L. Li, Nanocrystalline nickel cobalt hydroxides/ultrastable y zeolite composite for electrochemical capacitors, J. Solid State Electrochem. 11 (2007) 571–576. doi:10.1007/s10008-006-0197-9.

[297] Z. Hu, Y. Xie, Y. Wang, H. Wu, Y. Yang, Z. Zhang, Synthesis and electrochemical characterization of mesoporous CoxNi1−x layered double hydroxides as electrode materials for supercapacitors, Electrochim. Acta. 54 (2009) 2737–2741. doi:10.1016/j.electacta.2008.11.035.

[298] M.-S. Wu, J.-F. Wu, Nickel hydroxide electrode with porous nanotube arrays prepared by hydrolysis and cathodic deposition for high-performance supercapacitors, J. Power Sources. 240 (2013) 397–403. doi:10.1016/j.jpowsour.2013.04.035.

[299] N.W. Duffy, W. Baldsing, A.G. Pandolfo, The nickel-carbon asymmetric supercapacitor-Performance, energy density and electrode mass ratios, Electrochim. Acta. 54 (2008) 535–539. doi:10.1016/j.electacta.2008.07.047.

[300] H. Li, S. Liu, C. Huang, Z. Zhou, Y. Li, D. Fang, Characterization and supercapacitor application of coin-like β-nickel hydroxide nanoplates., Electrochim. Acta. 58 (2011) 89–94. doi:10.1016/j.electacta.2011.08.120.

[301] Y. Tang, Y. Liu, S. Yu, Y. Zhao, S. Mu, F. Gao, Hydrothermal synthesis of a flower-like nano-nickel hydroxide for high performance supercapacitors., Electrochim. Acta. 123 (2014) 158–166. doi:10.1016/j.electacta.2013.12.187.

[302] W. Zhang, W. Jiang, L. Yu, Z. Fu, W. Xia, M. Yang, Effect of nickel hydroxide composition on the electrochemical performance of spherical Ni(OH)2 positive materials for Ni-MH batteries, Int. J. Hydrogen Energy. 34 (2009) 473–480. doi:10.1016/j.ijhydene.2008.07.129.

[303] D.P. Dubal, V.J. Fulari, C.D. Lokhande, Effect of morphology on supercapacitive properties of chemically grown β-Ni(OH) 2 thin films, Microporous Mesoporous Mater. 151 (2012) 511–516. doi:10.1016/j.micromeso.2011.08.034.

[304] V. Lakshmi, R. Ranjusha, S. Vineeth, S. V. Nair, A. Balakrishnan, Supercapacitors

based on microporous β-Ni(OH)2nanorods, Colloids Surfaces A Physicochem. Eng. Asp. 457 (2014) 462–468. doi:10.1016/j.colsurfa.2014.06.016.

[305] K. Watanabe, T. Kikuoka, N. Kumagai, Physical and electrochemical characteristics of nickel hydroxide as a positive material for rechargeable alkaline batteries, J. Appl. Electrochem. 25 (1995) 219–226. doi:10.1007/BF00262959.

[306] H. Jiang, T. Zhao, C. Li, J. Ma, Hierarchical self-assembly of ultrathin nickel hydroxide nanoflakes for high-performance supercapacitors, J. Mater. Chem. 21 (2011) 3818. doi:10.1039/c0jm03830j.

[307] M. Cao, X. He, J. Chen, C. Hu, Self-assembled nickel hydroxide three-dimensional nanostructures: A nanomaterial for alkaline rechargeable batteries, Cryst. Growth Des. 7 (2007) 170–174. doi:10.1021/cg060524w.

[308] D. Yang, R. Wang, M. He, J. Zhang, Z. Liu, Ribbon- and boardlike nanostructures of nickel hydroxide: Synthesis, characterization, and electrochemical properties, J. Phys. Chem. B. 109 (2005) 7654–7658. doi:10.1021/jp050083b.

[309] A. Numan, N. Duraisamy, F. Saiha Omar, D. Gopi, K. Ramesh, S. Ramesh, Sonochemical synthesis of nanostructured nickel hydroxide as an electrode material for improved electrochemical energy storage application, Prog. Nat. Sci. Mater. Int. 27 (2017) 416–423. doi:10.1016/j.pnsc.2017.06.003.

[310] R.P. Silva, S. Eugénio, R. Duarte, T.M. Silva, M.J. Carmezim, M.F. Montemor, Electrochemical response of 70Co-30Ni highly branched 3D-dendritic structures for charge storage electrodes, Electrochim. Acta. 167 (2015) 13–19. doi:10.1016/j.electacta.2015.03.083.

[311] T. Nguyen, M. Boudard, M. João Carmezim, M. Fátima Montemor, NixCo1-x(OH)2 nanosheets on carbon nanofoam paper as high areal capacity electrodes for hybrid supercapacitors, Energy. 126 (2017) 208–216. doi:10.1016/j.energy.2017.03.024.

[312] T. Nguyen, M. Boudard, M.J. Carmezim, M.F. Montemor, Layered Ni(OH)2-Co(OH)2 films prepared by electrodeposition as charge storage electrodes for hybrid supercapacitors, Sci. Rep. (2017) 1–10. doi:10.1038/srep39980.

[313] B. Schneiderová, J. Demel, A. Zhigunov, J. Bohuslav, H. Tarábková, P. Janda, K. Lang, Nickel-cobalt hydroxide nanosheets : Synthesis , morphology and electrochemical properties, J. Colloid Interface Sci. 499 (2017) 138–144. doi:10.1016/j.jcis.2017.03.096.

[314] M. Sebastian, C. Nethravathi, M. Rajamathi, Interstratified hybrids of a -hydroxides of nickel and cobalt as supercapacitor electrode materials, Mater. Res. Bull. 48 (2013) 2715–2719. doi:10.1016/j.materresbull.2013.03.029.

[315] Y.F. Liu, G.H. Yuan, Z.H. Jiang, Z.P. Yao, M. Yue, Preparation of Ni(OH)2-graphene sheet-carbon nanotube composite as electrode material for supercapacitors, J. Alloys Compd. 618 (2014) 37–43. doi:10.1016/j.jallcom.2014.08.167.

[316] Z. Sun, X. Lu, A Solid-State Reaction Route to Anchoring Ni (OH) 2 Nanoparticles on Reduced Graphene Oxide Sheets for Supercapacitors, (2012).

[317] J. Bai, H. Yan, Q. Liu, J. Liu, Z. Li, X. Bai, R. Li, J. Wang, Synthesis of layered α-Ni(OH)2/RGO composites by exfoliation of α-Ni(OH)2for high-performance asymmetric supercapacitors, Mater. Chem. Phys. 204 (2018) 18–26.

doi:10.1016/j.matchemphys.2017.10.028.

[318] Z. Yang, C. Fang, Y. Fang, Y. Zhou, F. Zhu, Electrodeposited Nickel Hydroxide on the Reduced Graphene Oxide with High Capacitance, 10 (2015) 1574–1581.

[319] S. Ruiz-Gómez, A. Boscá, L. Pérez, J. Pedrós, J. Martínez, A. Páez, F. Calle, Graphene foam functionalized with electrodeposited nickel hydroxide for energy applications, Diam. Relat. Mater. 57 (2015) 63–67. doi:10.1016/j.diamond.2015.03.003.

[320] H. Zhang, X. Zhang, D. Zhang, X. Sun, H. Lin, C. Wang, One-Step Electrophoretic Deposition of Reduced Graphene Oxide and Ni(OH)2 Composite Films for Controlled Syntheses Supercapacitor Electrodes, J. Phys. Chem. B. 117 (2012) 1616–1627. doi:10.1021/jp305198j.

[321] H. Ma, J. He, D.B. Xiong, J. Wu, Q. Li, V. Dravid, Y. Zhao, Nickel Cobalt Hydroxide @Reduced Graphene Oxide Hybrid Nanolayers for High Performance Asymmetric Supercapacitors with Remarkable Cycling Stability, ACS Appl. Mater. Interfaces. 8 (2016) 1992–2000. doi:10.1021/acsami.5b10280.

[322] U.M. Patil, J.S. Sohn, S.B. Kulkarni, S.C. Lee, H.G. Park, K. V. Gurav, J.H. Kim, S.C. Jun, Enhanced supercapacitive performance of chemically grown cobalt-nickel hydroxides on three-dimensional graphene foam electrodes, ACS Appl. Mater. Interfaces. 6 (2014) 2450–2458. doi:10.1021/am404863z.

[323] S. Shahrokhian, S. Rahimi, R. Mohammadi, Nickel-cobalt layered double hydroxide ultrathin nanosheets coated on reduced graphene oxide nonosheets/nickel foam for high performance asymmetric supercapacitors, Int. J. Hydrogen Energy. 43 (2017) 2256–2267. doi:10.1016/j.ijhydene.2017.12.019.

[324] Y. Bai, W. Wang, R. Wang, J. Sun, L. Gao, Controllable synthesis of 3D binary nickel–cobalt hydroxide/graphene/nickel foam as a binder-free electrode for high-performance supercapacitors, J. Mater. Chem. A. 3 (2015) 12530–12538. doi:10.1039/C5TA01804H.

[325] X. Lin, H. Li, F. Musharavati, E. Zalnezhad, S. Bae, B.-Y. Cho, O.K.S. Hui, Synthesis and characterization of cobalt hydroxide carbonate nanostructures, RSC Adv. 7 (2017) 46925–46931. doi:10.1039/C7RA09050A.

[326] Y. Chen, J. Zhou, P. Maguire, R. O'Connell, W. Schmitt, Y. Li, Z. Yan, Y. Zhang, H. Zhang, Enhancing capacitance behaviour of CoOOH nanostructures using transition metal dopants by ambient oxidation, Sci. Rep. 6 (2016) 1–8. doi:10.1038/srep20704.

[327] L. Kong, J. Lang, M. Liu, Y. Luo, L. Kang, Facile approach to prepare loose-packed cobalt hydroxide nano-flakes materials for electrochemical capacitors, 194 (2009) 1194–1201. doi:10.1016/j.jpowsour.2009.06.016.

[328] W. Yang, Y. Feng, N. Wang, H. Yuan, D. Xiao, Facile microwave-assisted synthesis of sheet-like cobalt hydroxide for energy-storage application: Effect of the cobalt precursors, J. Alloys Compd. 644 (2015) 836–845. doi:10.1016/j.jallcom.2015.05.055.

[329] F. Cao, G.X. Pan, P.S. Tang, H.F. Chen, Hydrothermal-synthesized Co(OH)2nanocone arrays for supercapacitor application, J. Power Sources. 216 (2012) 395–399. doi:10.1016/j.jpowsour.2012.05.073.

[330] A.D. Jagadale, V.S. Jamadade, S.N. Pusawale, C.D. Lokhande, Effect of scan rate

on the morphology of potentiodynamically deposited alpha-Co(OH)2 and corresponding supercapacitive performance, Electrochim. Acta. 78 (2012) 92–97. doi:10.1016/j.electacta.2012.05.137.

[331] V. Gupta, T. Kusahara, H. Toyama, S. Gupta, N. Miura, Potentiostatically deposited nanostructured α-Co(OH)2: A high performance electrode material for redox-capacitors, Electrochem. Commun. 9 (2007) 2315–2319. doi:10.1016/j.elecom.2007.06.041.

[332] M. Aghazadeh, M.R. Ganjali, M.G. Maragheh, Cobalt hydroxide nanoflakes prepared by saccharide-assisted cathodic electrochemical deposition as high performance supercapacitor electrode material, Int. J. Electrochem. Sci. 12 (2017) 5792–5803. doi:10.20964/2017.06.48.

[333] X.-P. Gao, S.-M. Yao, T.-Y. Yan, Z. Zhou, Alkaline rechargeable Ni/Co batteries: Cobalt hydroxides as negative electrode materials, Energy Environ. Sci. 2 (2009) 502. doi:10.1039/b901934k.

[334] R.R. Salunkhe, B.P. Bastakoti, C.T. Hsu, N. Suzuki, J.H. Kim, S.X. Dou, C.C. Hu, Y. Yamauchi, Direct growth of cobalt hydroxide rods on nickel foam and its application for energy storage, Chem. - A Eur. J. 20 (2014) 3084–3088. doi:10.1002/chem.201303652.

[335] X. Xia, J. Tu, Y. Zhang, J. Chen, X. Wang, C. Gu, C. Guan, J. Luo, H.J. Fan, Porous hydroxide nanosheets on preformed nanowires by electrodeposition: Branched nanoarrays for electrochemical energy storage, Chem. Mater. 24 (2012) 3793–3799. doi:10.1021/cm302416d.

[336] A.D. Jagadale, V.S. Kumbhar, D.S. Dhawale, C.D. Lokhande, Performance evaluation of symmetric supercapacitor based on cobalt hydroxide [Co(OH)2] thin film electrodes, Electrochim. Acta. 98 (2013) 32–38. doi:10.1016/j.electacta.2013.02.094.

[337] W. Zhou, M. Xu, D. Zhao, C. Xu, H. Li, Electrodeposition and characterization of ordered mesoporous cobalt hydroxide films on different substrates for supercapacitors, Microporous Mesoporous Mater. 117 (2009) 55–60. doi:10.1016/j.micromeso.2008.06.004.

[338] A.A.S. Rovetta, M.P. Browne, A. Harvey, I.J. Godwin, J.N. Coleman, And, M.E.G. Lyons, Cobalt Hydroxide Nanoflakes and their Application as Supercapacitors and Oxygen Evolution Catalysts, Nanotechnology. 28 (2017) 375401.

[339] B. Schneiderov, J. Demel, J. Ple, H. Tar, J. Bohuslav, K. Lang, Electrochemical performance of cobalt hydroxide nanosheets formed by the delamination of layered cobalt hydroxide in water †, (2014) 10484–10491. doi:10.1039/c4dt00141a.

[340] Z. Sun, L. Lin, M. Yuan, H. Li, G. Sun, C. Nan, S. Ma, X. Yang, Two-dimensional β-cobalt hydroxide phase transition exfoliated to atom layers as efficient catalyst for lithium-oxygen batteries, Electrochim. Acta. (2018). doi:10.1016/j.electacta.2018.05.201.

[341] P.K. Nayak, N. Munichandraiah, Cobalt Hydroxide as a Capacitor Material: Tuning Its Potential Window, J. Electrochem. Soc. 155 (2008) A855. doi:10.1149/1.2977976.

[342] V. Gupta, S. Gupta, N. Miura, Al-substituted α-cobalt hydroxide synthesized by

potentiostatic deposition method as an electrode material for redox-supercapacitors, J. Power Sources. 177 (2008) 685–689. doi:10.1016/j.jpowsour.2007.10.091.

[343] C. Nethravathi, C.R. Rajamathi, M. Rajamathi, X. Wang, U.K. Gautam, D. Golberg, Y. Bando, Cobalt hydroxide/oxide hexagonal ring-graphene hybrids through chemical etching of metal hydroxide platelets by graphene oxide: Energy storage applications, ACS Nano. 8 (2014) 2755–2765. doi:10.1021/nn406480g.

[344] U.M. Patil, S.C. Lee, J.S. Sohn, S.B. Kulkarni, K. V Gurav, J.H. Kim, J.H. Kim, S. Lee, S.C. Jun, Enhanced Symmetric Supercapacitive Performance of Co(OH)2 Nanorods Decorated Conducting Porous Graphene Foam Electrodes, Electrochim. Acta. 129 (2014) 334–342. doi:10.1016/j.electacta.2014.02.063.

[345] C. Zhao, X. Wang, S. Wang, Y. Wang, Y. Zhao, W. Zheng, Synthesis of Co(OH)2/graphene/Ni foam nano-electrodes with excellent pseudocapacitive behavior and high cycling stability for supercapacitors, Int. J. Hydrogen Energy. 37 (2012) 11846–11852. doi:10.1016/j.ijhydene.2012.05.138.

[346] S.C. Lee, U.M. Patil, S.J. Kim, S. Ahn, S.-W. Kang, S.C. Jun, All-solid-state flexible asymmetric micro supercapacitors based on cobalt hydroxide and reduced graphene oxide electrodes, RSC Adv. 6 (2016) 43844–43854. doi:10.1039/C6RA06034J.

[347] K.Y. Ma, W.J. Zhao, J.P. Cheng, F. Liu, X. Bin Zhang, Free-standing alpha-Co(OH)2/graphene oxide thin films fabricated through delamination and reassembling of acetate anions intercalated alpha-Co(OH)2 and graphene oxide in water, J. Colloid Interface Sci. 468 (2016) 238–246. doi:10.1016/j.jcis.2016.01.058.

[348] a K. Geim, K.S. Novoselov, The rise of graphene., Nat. Mater. 6 (2007) 183–91. doi:10.1038/nmat1849.

[349] K.S. Novoselov, A.K. Geim, S. V Morozov, D. Jiang, Y. Zhang, S. V Dubonos, I. V Grigorieva, a a Firsov, Electric field effect in atomically thin carbon films., Science. 306 (2004) 666–9. doi:10.1126/science.1102896.

[350] I.W. Frank, D.M. Tanenbaum, a. M. van der Zande, P.L. McEuen, Mechanical properties of suspended graphene sheets, J. Vac. Sci. Technol. B Microelectron. Nanom. Struct. 25 (2007) 2558. doi:10.1116/1.2789446.

[351] P. Avouris, C. Dimitrakopoulos, Graphene: synthesis and applications, Mater. Today. 15 (2012) 86–97. doi:10.1016/S1369-7021(12)70044-5.

[352] M. Hirata, T. Gotou, S. Horiuchi, M. Fujiwara, M. Ohba, Thin-film particles of graphite oxide 1: High-yield synthesis and fleibility of the particles, Carbon N. Y. 42 (2004) 2929–2937. doi:10.1016/j.carbon.2004.07.003.

[353] W.S. Hummers, R.E. Offeman, Preparation of Graphitic Oxide, J. Am. Chem. Soc. 80 (1958) 1939–1939.

[354] S. Stankovich, D. a. Dikin, R.D. Piner, K. a. Kohlhaas, A. Kleinhammes, Y. Jia, Y. Wu, S.T. Nguyen, R.S. Ruoff, Synthesis of graphene-based nanosheets via chemical reduction of exfoliated graphite oxide, Carbon N. Y. 45 (2007) 1558–1565. doi:10.1016/j.carbon.2007.02.034.

[355] E. Moreau, F.J. Ferrer, D. Vignaud, S. Godey, X. Wallart, Graphene growth by molecular beam epitaxy using a solid carbon source, Phys. Status Solidi. 207

(2010) 300–303. doi:10.1002/pssa.200982412.

[356] P.N. First, W.A. De Heer, T. Seyller, C. Berger, A. Joseph, J. Moon, Epitaxial Graphenes on Silicon Carbide, MRS Bull. 35 (2010) 1–35.

[357] M. Taghioskoui, Trends in graphene research, Mater. Today. 12 (2009) 34–37. doi:10.1016/S1369-7021(09)70274-3.

[358] M. Chhowalla, K.B.K. Teo, C. Ducati, N.L. Rupesinghe, G. a. J. Amaratunga, a. C. Ferrari, D. Roy, J. Robertson, W.I. Milne, Growth process conditions of vertically aligned carbon nanotubes using plasma enhanced chemical vapor deposition, J. Appl. Phys. 90 (2001) 5308. doi:10.1063/1.1410322.

[359] A. Adán-Más, D. Wei, Photoelectrochemical Properties of Graphene and Its Derivatives, Nanomaterials. 3 (2013) 325–356. doi:10.3390/nano3030325.

[360] L.-L. Tan, S.-P. Chai, A.R. Mohamed, Synthesis and applications of graphene-based TiO(2) photocatalysts., ChemSusChem. 5 (2012) 1868–82. doi:10.1002/cssc.201200480.

[361] K.S. Novoselov, V.I. Fal'ko, L. Colombo, P.R. Gellert, M.G. Schwab, K. Kim, A roadmap for graphene., Nature. 490 (2012) 192–200. doi:10.1038/nature11458.

[362] W. Choi, I. Lahiri, R. Seelaboyina, Y.S. Kang, Synthesis of Graphene and Its Applications: A Review, Crit. Rev. Solid State Mater. Sci. 35 (2010) 52–71. doi:10.1080/10408430903505036.

[363] K.P. Loh, Q. Bao, P.K. Ang, J. Yang, The chemistry of graphene, J. Mater. Chem. 20 (2010) 2277. doi:10.1039/b920539j.

[364] V. Georgakilas, M. Otyepka, A.B. Bourlinos, V. Chandra, N. Kim, K.C. Kemp, P. Hobza, R. Zboril, K.S. Kim, Functionalization of graphene: covalent and non-covalent approaches, derivatives and applications., Chem. Rev. 112 (2012) 6156–214. doi:10.1021/cr3000412.

[365] S.-S. Li, K.-H. Tu, C.-C. Lin, C.-W. Chen, M. Chhowalla, Solution-processable graphene oxide as an efficient hole transport layer in polymer solar cells., ACS Nano. 4 (2010) 3169–74. doi:10.1021/nn100551j.

[366] K.P. Loh, Q. Bao, G. Eda, M. Chhowalla, Graphene oxide as a chemically tunable platform for optical applications., Nat. Chem. 2 (2010) 1015–24. doi:10.1038/nchem.907.

[367] Y. Si, E.T. Samulski, C. Hill, N. Carolina, Synthesis of Water Soluble Graphene 2008, (2008).

[368] Z. Chen, J. Li, Y. Chen, Y. Zhang, G. Xu, J. Yang, Y. Feng, Microwave-hydrothermal preparation of a graphene/hierarchy structure MnO2 composite for a supercapacitor., Particuology. 15 (2014) 27–33. doi:10.1016/j.partic.2012.12.008.

[369] S. Stankovich, D.A. Dikin, G.H.B. Dommett, K.M. Kohlhaas, E.J. Zimney, E.A. Stach, R.D. Piner, S.B.T. Nguyen, R.S. Ruoff, Graphene-based composite materials, Nature. 442 (2006) 282–286. doi:10.1038/nature04969.

[370] R. Raccichini, A. Varzi, S. Passerini, B. Scrosati, The role of graphene for electrochemical energy storage, Nat. Mater. 14 (2015) 271–279. doi:10.1038/NMAT4170.

[371] J.M. Tarascon, M. Armand, Issues and challenges facing rechargeable lithium

batteries., Nature. 414 (2001) 359–367. http://www.ncbi.nlm.nih.gov/pubmed/11713543.

[372] J.R. Dahn, T. Zheng, Y. Liu, J.S. Xue, Mechanisms for Lithium Insertion in Carbonaceous Materials, Science (80-.). 270 (1995) 590–593. doi:10.1126/science.270.5236.590.

[373] E.J. Yoo, J. Kim, E. Hosono, H.S. Zhou, T. Kudo, I. Honma, Large reversible Li storage of graphene nanosheet families for use in rechargeable lithium ion batteries, Nano Lett. 8 (2008) 2277–2282. doi:10.1021/nl800957b.

[374] C. Wang, D. Li, C.O. Too, G.G. Wallace, Electrochemical Properties of Graphene Paper Electrodes Used in Lithium Batteries, Chem. Mater. 21 (2009) 2604–2606. doi:10.1021/cm900764n.

[375] F. Yao, F. Güneş, H.Q. Ta, S.M. Lee, S.J. Chae, K.Y. Sheem, C.S. Cojocaru, S.S. Xie, Y.H. Lee, Diffusion mechanism of lithium ion through basal plane of layered graphene, J. Am. Chem. Soc. 134 (2012) 8646–8654. doi:10.1021/ja301586m.

[376] J. Zhu, D. Yang, Z. Yin, Q. Yan, H. Zhang, Graphene and graphene-based materials for energy storage applications, Small. 10 (2014) 3480–3498. doi:10.1002/smll.201303202.

[377] O.A. Vargas C., Á. Caballero, J. Morales, Can the performance of graphene nanosheets for lithium storage in Li-ion batteries be predicted?, Nanoscale. 4 (2012) 2083. doi:10.1039/c2nr11936f.

[378] P. Lian, X. Zhu, S. Liang, Z. Li, W. Yang, H. Wang, Large reversible capacity of high quality graphene sheets as an anode material for lithium-ion batteries, Electrochim. Acta. 55 (2010) 3909–3914. doi:10.1016/j.electacta.2010.02.025.

[379] M. Winter, J.O. Besenhard, M.E. Spahr, P. Novák, Insertion electrode materials for rechargeable lithium batteries, Adv. Mater. 10 (1998) 725–763. doi:10.1002/(SICI)1521-4095(199807)10:10<725::AID-ADMA725>3.0.CO;2-Z.

[380] P. Camphebell, The long game, Nature. 473 (2011) 419.

[381] Z.-S. Wu, G. Zhou, L.-C. Yin, W. Ren, F. Li, H.-M. Cheng, Graphene/metal oxide composite electrode materials for energy storage, Nano Energy. 1 (2012) 107–131. doi:10.1016/j.nanoen.2011.11.001.

[382] O. Vargas, Á. Caballero, J. Morales, Enhanced Electrochemical Performance of Maghemite/Graphene Nanosheets Composite as Electrode in Half and Full Li-Ion Cells, Electrochim. Acta. 130 (2014) 551–558. doi:10.1016/j.electacta.2014.03.037.

[383] J. Hassoun, F. Bonaccorso, M. Agostini, M. Angelucci, M.G. Betti, R. Cingolani, M. Gemmi, C. Mariani, S. Panero, V. Pellegrini, B. Scrosati, An advanced lithium-ion battery based on a graphene anode and a lithium iron phosphate cathode, Nano Lett. 14 (2014) 4901–4906. doi:10.1021/nl502429m.

[384] M.Y. Cheng, B.J. Hwang, Mesoporous carbon-encapsulated NiO nanocomposite negative electrode materials for high-rate Li-ion battery, J. Power Sources. 195 (2010) 4977–4983. doi:10.1016/j.jpowsour.2010.02.059.

[385] X. Wang, L. Yu, X.-L. Wu, F. Yuan, Y.-G. Guo, Y. Ma, J. Yao, Synthesis of Single-Crystalline Co 3 O 4 Octahedral Cages with Tunable Surface Aperture and Their Lithium Storage Properties, J. Phys. Chem. C. 113 (2009) 15553–15558.

doi:10.1021/jp904652m.

[386] C. Xu, B. Xu, Y. Gu, Z. Xiong, J. Sun, X.S. Zhao, Graphene-based electrodes for electrochemical energy storage, Energy Environ. Sci. 6 (2013) 1388. doi:10.1039/c3ee23870a.

[387] X. Huang, Z. Zeng, Z. Fan, J. Liu, H. Zhang, Graphene-based electrodes, Adv. Mater. 24 (2012) 5979–6004. doi:10.1002/adma.201201587.

[388] G. Kucinskis, G. Bajars, J. Kleperis, Graphene in lithium ion battery cathode materials: A review, J. Power Sources. 240 (2013) 66–79. doi:10.1016/j.jpowsour.2013.03.160.

[389] H. Wang, Y. Yang, Y. Liang, L.F. Cui, H. Sanchez Casalongue, Y. Li, G. Hong, Y. Cui, H. Dai, LiMn1-xFexPO4 nanorods grown on graphene sheets for ultrahigh-rate-performance lithium ion batteries, Angew. Chemie - Int. Ed. 50 (2011) 7364–7368. doi:10.1002/anie.201103163.

[390] Y. Cao, L. Xiao, M.L. Sushko, W. Wang, B. Schwenzer, J. Xiao, Z. Nie, L. V. Saraf, Z. Yang, J. Liu, Sodium ion insertion in hollow carbon nanowires for battery applications, Nano Lett. 12 (2012) 3783–3787. doi:10.1021/nl3016957.

[391] Y.X. Wang, S.L. Chou, H.K. Liu, S.X. Dou, Reduced graphene oxide with superior cycling stability and rate capability for sodium storage, Carbon N. Y. 57 (2013) 202–208. doi:10.1016/j.carbon.2013.01.064.

[392] J. Ding, H. Wang, Z. Li, A. Kohandehghan, K. Cui, Z. Xu, B. Zahiri, X. Tan, E.M. Lotfabad, B.C. Olsen, D. Mitlin, Carbon nanosheet frameworks derived from peat moss as high performance sodium ion battery anodes, ACS Nano. 7 (2013) 11004–11015. doi:10.1021/nn404640c.

[393] M.F. El-Kady, V. Strong, S. Dubin, R.B. Kaner, Laser Scribing of High-Performance and Flexible Graphene-Based Electrochemical Capacitors, Science (80-.). 335 (2012) 1326–1330. doi:10.1126/science.1216744.

[394] J. Chen, C. Li, G. Shi, Graphene Materials for Electrochemical Capacitors, (2013).

[395] S.R.C. Vivekchand, C.S. Rout, K.S. Subrahmanyam, a. Govindaraj, C.N.R. Rao, Graphene-based electrochemical supercapacitors, J. Chem. Sci. 120 (2008) 9–13. doi:10.1007/s12039-008-0002-7.

[396] M.D. Stoller, S. Park, Y. Zhu, J. An, R.S. Ruoff, Graphene-based ultracapacitors, Nano Lett. 8 (2008) 3498–502. doi:10.1021/nl802558y.

[397] Z. Lei, L. Lu, X.S. Zhao, The electrocapacitive properties of graphene oxide reduced by urea, Energy Environ. Sci. 5 (2012) 6391–6399. doi:10.1039/C1EE02478G.

[398] C. Liu, Z. Yu, D. Neff, A. Zhamu, B.Z. Jang, Graphene-based supercapacitor with an ultrahigh energy density., Nano Lett. 10 (2010) 4863–8. doi:10.1021/nl102661q.

[399] Z. Weng, Y. Su, D.-W. Wang, F. Li, J. Du, H.-M. Cheng, Graphene-cellulose paper flexible supercapacitors., Adv. Energy Mater. 1 (2011) 917–922. doi:10.1002/aenm.201100312.

[400] X. Yang, J. Zhu, L. Qiu, D. Li, Bioinspired effective prevention of restacking in multilayered graphene films: towards the next generation of high-performance supercapacitors., Adv. Mater. 23 (2011) 2833–8. doi:10.1002/adma.201100261.

[401] Y. Yoon, K. Lee, S. Kwon, S. Seo, H. Yoo, S. Kim, Y. Shin, Y. Park, D. Kim, J.Y. Choi, H. Lee, Vertical alignments of graphene sheets spatially and densely piled for fast ion diffusion in compact supercapacitors, ACS Nano. 8 (2014) 4580–4590. doi:10.1021/nn500150j.

[402] Y. Wang, Z. Shi, Y. Huang, Y. Ma, C. Wang, M. Chen, Y. Chen, Supercapacitor Devices Based on Graphene Materials, J. Phys. Chem. C. 113 (2009) 13103–13107. doi:10.1021/jp902214f.

[403] X. Yang, C. Cheng, Y. Wang, L. Qiu, D. Li, Liquid-mediated dense integration of graphene materials for compact capacitive energy storage, Science (80-.). 341 (2013) 534–537. doi:10.1126/science.1239089.

[404] Y. Zhu, S. Murali, M.D. Stoller, K.J. Ganesh, W. Cai, P.J. Ferreira, A. Pirkle, R.M. Wallace, K.A. Cychosz, M. Thommes, D. Su, E.A. Stach, R.S. Ruoff, Carbon-Based Supercapacitors Produced by Activation of Graphene, 332 (2011) 1537–1542. doi:10.1126./science.1200770.

[405] L.L. Zhang, X. Zhao, M.D. Stoller, Y. Zhu, H. Ji, S. Murali, Y. Wu, S. Perales, B. Clevenger, R.S. Ruoff, Highly conductive and porous activated reduced graphene oxide films for high-power supercapacitors, Nano Lett. 12 (2012) 1806–1812. doi:10.1021/nl203903z.

[406] G. Wang, X. Sun, F. Lu, H. Sun, M. Yu, W. Jiang, C. Liu, J. Lian, Flexible pillared graphene-paper electrodes for high-performance electrochemical supercapacitors, Small. 8 (2012) 452–459. doi:10.1002/smll.201101719.

[407] Z. Lei, N. Christov, X.S. Zhao, Intercalation of mesoporous carbon spheres between reduced graphene oxide sheets for preparing high-rate supercapacitor electrodes., Energy Environ. Sci. 4 (2011) 1866–1873. doi:10.1039/c1ee01094h.

[408] U. Khan, I. O'Connor, Y.K. Gun'Ko, J.N. Coleman, The preparation of hybrid films of carbon nanotubes and nano-graphite/graphene with excellent mechanical and electrical properties, Carbon N. Y. 48 (2010) 2825–2830. doi:10.1016/j.carbon.2010.04.014.

[409] Z. Fan, J. Yan, L. Zhi, Q. Zhang, T. Wei, J. Feng, M. Zhang, W. Qian, F. Wei, A three-dimensional carbon nanotube/graphene sandwich and its application as electrode in supercapacitors., Adv. Mater. 22 (2010) 3723–8. doi:10.1002/adma.201001029.

[410] X. Peng, D. Diamond, K.T. Lau, Synthesis of electrochemically-reduced graphene oxide film with controllable size and thickness and its use in supercapacitor, Carbon N. Y. 49 (2011) 3488–3496. doi:10.1016/j.carbon.2011.04.047.

[411] J. Yang, S. Gunasekaran, Electrochemically reduced graphene oxide sheets for use in high performance supercapacitors, Carbon N. Y. 51 (2012) 36–44. doi:10.1016/j.carbon.2012.08.003.

[412] S. Yang, B. Deng, R. Ge, L. Zhang, H. Wang, Z. Zhang, W. Zhu, G. Wang, Electrodeposition of porous graphene networks on nickel foams as supercapacitor electrodes with high capacitance and remarkable cyclic stability, Nanoscale Res. Lett. 9 (2014) 672. doi:10.1186/1556-276X-9-672.

[413] K. Sheng, Y. Sun, C. Li, W. Yuan, G. Shi, Ultrahigh-rate supercapacitors based on eletrochemically reduced graphene oxide for ac line-filtering., Sci. Rep. 2 (2012) srep00247, 5 pp. doi:10.1038/srep00247.

[414] Y. Li, K. Sheng, W. Yuan, G. Shi, A high-performance flexible fibre-shaped electrochemical capacitor based on electrochemically reduced graphene oxide, Chem. Commun. 49 (2013) 291–293. doi:10.1039/C2CC37396C.

[415] V.H. Pham, T. Gebre, J.H. Dickerson, Facile electrodeposition of reduced graphene oxide hydrogels for high-performance supercapacitors., Nanoscale. 7 (2015) 5947–5950. doi:10.1039/C4NR07508K.

[416] V.H. Pham, J.H. Dickerson, Reduced Graphene Oxide Hydrogels Deposited in Nickel Foam for Supercapacitor Applications: Toward High Volumetric Capacitance, J. Phys. Chem. C. 120 (2016) 5353–5360. doi:10.1021/acs.jpcc.6b00326.

[417] J.M. Chem, K. Chen, L. Chen, Y. Chen, H. Bai, L. Li, Three-dimensional porous graphene-based composite materials: electrochemical synthesis and application†, J. Mate. 22 (2012) 20968–20976. doi:10.1039/c2jm34816k.

[418] Y. Huang, J. Liang, Y. Chen, An overview of the applications of graphene-based materials in supercapacitors, Small. 8 (2012) 1805–1834. doi:10.1002/smll.201102635.

[419] G. Yu, L. Hu, M. Vosgueritchian, H. Wang, X. Xie, J.R. McDonough, X. Cui, Y. Cui, Z. Bao, Solution-processed graphene/MnO2nanostructured textiles for high-performance electrochemical capacitors, Nano Lett. 11 (2011) 2905–2911. doi:10.1021/nl2013828.

[420] Z. Fan, J. Yan, T. Wei, L. Zhi, G. Ning, T. Li, Asymmetric Supercapacitors Based on Graphene / MnO 2 and Activated Carbon Nanofi ber Electrodes with High Power and Energy Density, (2011) 2366–2375. doi:10.1002/adfm.201100058.

[421] J. Yan, Z. Fan, T. Wei, W. Qian, M. Zhang, F. Wei, Fast and reversible surface redox reaction of graphene – MnO 2 composites as supercapacitor electrodes, 8 (2010). doi:10.1016/j.carbon.2010.06.047.

[422] A.A. Ensafi, M. Jafari-Asl, A. Nabiyan, B. Rezaei, Preparation of Three-Dimensional Ruthenium Oxide @ Graphene Oxide Based on Etching of Ni-Al/Layered Double Hydroxides: Application for Electrochemical Hydrogen Generation, J. Electrochem. Soc. 163 (2016) H610–H617. doi:10.1149/2.0011608jes.

[423] R. Giardi, S. Porro, T. Topuria, L. Thompson, C.F. Pirri, H.C. Kim, One-pot synthesis of graphene-molybdenum oxide hybrids and their application to supercapacitor electrodes, Appl. Mater. Today. 1 (2015) 27–32. doi:10.1016/j.apmt.2015.08.001.

[424] X. Hu, Z. Yan, Q. Li, Q. Yang, L. Kang, Z. Lei, Z.H. Liu, Graphene/vanadium oxide hybrid electrodes for electrochemical capacitor, Colloids Surfaces A Physicochem. Eng. Asp. 461 (2014) 105–112. doi:10.1016/j.colsurfa.2014.07.032.

[425] B.Z. Wu, D. Wang, W. Ren, J. Zhao, G. Zhou, Anchoring Hydrous RuO 2 on Graphene Sheets for High-Performance Electrochemical Capacitors, Adv. Funct. Mater. (2010) 3595–3602. doi:10.1002/adfm.201001054.

[426] P.C. Gao, P.A. Russo, D.E. Conte, S. Baek, F. Moser, N. Pinna, T. Brousse, F. Favier, Morphology Effects on the Supercapacitive Electrochemical Performances of Iron Oxide/Reduced Graphene Oxide Nanocomposites, ChemElectroChem. 1 (2014) 747–754. doi:10.1002/celc.201300087.

[427] H. Wang, Q. Hao, X. Yang, L. Lu, X. Wang, Graphene oxide doped polyaniline for supercapacitors, Electrochem. Commun. 11 (2009) 1158–1161. doi:10.1016/j.elecom.2009.03.036.

[428] C. Xu, J. Sun, L. Gao, Synthesis of novel hierarchical graphene/polypyrrole nanosheet composites and their superior electrochemical performance, J. Mater. Chem. 21 (2011) 11253. doi:10.1039/c1jm11275a.

[429] J. Xu, K. Wang, S.-Z. Zu, B.-H. Han, Z. Wei, Hierarchical Nanocomposites of Polyaniline Nanowire Arrays on Graphene Oxide Sheets with Synergistic Effect for Energy Storage, ACS Nano. 4 (2010) 5019–5026. doi:10.1021/nn1006539.

[430] M. Xue, F. Li, J. Zhu, H. Song, M. Zhang, T. Cao, Structure-based enhanced capacitance: In situ growth of highly ordered polyaniline nanorods on reduced graphene oxide patterns, Adv. Funct. Mater. 22 (2012) 1284–1290. doi:10.1002/adfm.201101989.

[431] J.S. Lee, S.T. Kim, R. Cao, N.S. Choi, M. Liu, K.T. Lee, J. Cho, Metal-air batteries with high energy density: Li-air versus Zn-air, Adv. Energy Mater. 1 (2011) 34–50. doi:10.1002/aenm.201000010.

[432] T. Ogasawara, A. Débart, M. Holzapfel, P. Novák, P.G. Bruce, Rechargeable Li2O2 Electrode for Lithium Batteries, J. Am. Chem. Soc. 128 (2006) 1390–1393. doi:10.1021/ja056811q.

[433] H. Kim, H.-D. Lim, J. Kim, K. Kang, Graphene for advanced Li/S and Li/air batteries, J. Mater. Chem. A. 2 (2014) 33–47. doi:10.1039/C3TA12522J.

[434] G. Girishkumar, B. McCloskey, A.C. Luntz, S. Swanson, W. Wilcke, Lithium-air battery: Promise and challenges, J. Phys. Chem. Lett. 1 (2010) 2193–2203. doi:10.1021/jz1005384.

[435] W. Liu, Q. Sun, Y. Yang, J.-Y. Xie, Z.-W. Fu, An enhanced electrochemical performance of a sodium–air battery with graphene nanosheets as air electrode catalysts, Chem. Commun. 49 (2013) 1951. doi:10.1039/c3cc00085k.

[436] X. Ji, K.T. Lee, L.F. Nazar, A highly ordered nanostructured carbon-sulphur cathode for lithium-sulphur batteries, Nat. Mater. 8 (2009) 500–506. doi:10.1038/nmat2460.

[437] J. Guo, Y. Xu, C. Wang, Sulfur-impregnated disordered carbon nanotubes cathode for lithium-sulfur batteries, Nano Lett. 11 (2011) 4288–4294. doi:10.1021/nl202297p.

[438] Y. Yang, G. Yu, J.J. Cha, H. Wu, M. Vosgueritchian, Y. Yao, Z. Bao, Y. Cui, Improving the performance of lithium-sulfur batteries by conductive polymer coating, ACS Nano. 5 (2011) 9187–9193. doi:10.1021/nn203436j.

[439] A. Manthiram, Y. Fu, Y.S. Su, Challenges and prospects of lithium-sulfur batteries, Acc. Chem. Res. 46 (2013) 1125–1134. doi:10.1021/ar300179v.

[440] F. Zhang, X. Zhang, Y. Dong, L. Wang, Facile and effective synthesis of reduced graphene oxide encapsulated sulfur via oil/water system for high performance lithium sulfur cells, J. Mater. Chem. 22 (2012) 11452. doi:10.1039/c2jm16543k.

[441] H. Wang, Y. Yang, Y. Liang, J.T. Robinson, Y. Li, A. Jackson, Y. Cui, H. Dai, Graphene-wrapped sulfur particles as a rechargeable lithium-sulfur battery cathode material with high capacity and cycling stability, Nano Lett. 11 (2011) 2644–2647.

doi:10.1021/nl200658a.

2. Synthesis strategies

2.1 Electrodeposition

Electrodeposition is a technique with a very long history. It has been reported that it was first used by pre-Columbian Andean metalworkers as a surface colouring method. They used a very primitive form of electrochemical plating to create a very thin and uniform layer of gold on top of copper. Unknowingly, they produced a self-contained system that generates electric current to balance the charges produced[1]. Despite its antiquity, it is a very relevant and commonly used technique in both research and industry.

For example, IBM used it as a cost-effective technique to deposit copper on chips for integrated circuits. By means of electrodeposition they could achieve a superfilling structure that could not be obtained by any other procedure. Not only that, they improved the throughput and costs associated to this process[2].

Nowadays, electrodeposition plays a key role in nanofabrication processes and the development of novel materials. The process is based on the growth of a film on top of a conductive substrate. By means of an applied current, several redox reactions occur at the interface between an electrolyte, containing the ions to be electrodeposited, and the substrate (colloids may also be deposited, in this case the term electrophoretic deposition shall be used). The electrolyte acts as an ionic conductor in which diffusion of ions occurs and, after the redox reaction, the desired film is formed. The exact mechanism depends upon the material to deposit[3].

Electrodeposition presents several advantages when compared to other nanofabrication techniques, namely[4]:

- Low cost.
- Rapidity and simplicity.
- Controlled porosity.
- Controlled nanostructures and morphology.
- High Purity.
- Industrially applicable.
- High deposition rates.
- Ability to produce coatings on different substrates.
- Ability to produce metastable materials.
- Possibility of multilayer deposition.
- No post-treatments required.

For these reasons electrodeposition has been considered as an extremely promising technique in the development of nanostructured materials for energy storage.

2.1.1 Electrodeposition setup.

Probably due to the simplicity of its setup, this technique has become extremely convenient in several industrialized processes. Electrodeposition in laboratory scale synthesis requires the following constituents[5]:

- **Reference electrode**: Electrode with a stable and well-known electrode potential because of the high stability of the redox reaction contained within, and the fact that the concentration of the elements present is known. The potential in comparison to the standard hydrogen electrode (assigned to a 0.000V potential) is known. An ideal characteristic is that it has non-polarizability when current is applied. When the passing current generates a relevant resistance, an auxiliary electrode may be used.
- **Counter electrode**. Electrode whose electrochemical behavior does not affect the system of interest and serves to create a potential difference with the working electrode.
- **Working Electrode**: Electrode system of interest.
- **Electrochemical Cell**: Container of the electrochemical system.
- **Potentiostat**: Hardware used to control the three-electrode cell and apply the electrical conditions for the electrochemical experiments. Has control over the voltage across the working electrode and the counter electrode pair and can adjust the voltage to control the potential difference accordingly.

It is worth noticing that some of these components may not be necessary or may be substituted in optimized or industrialized conditions.

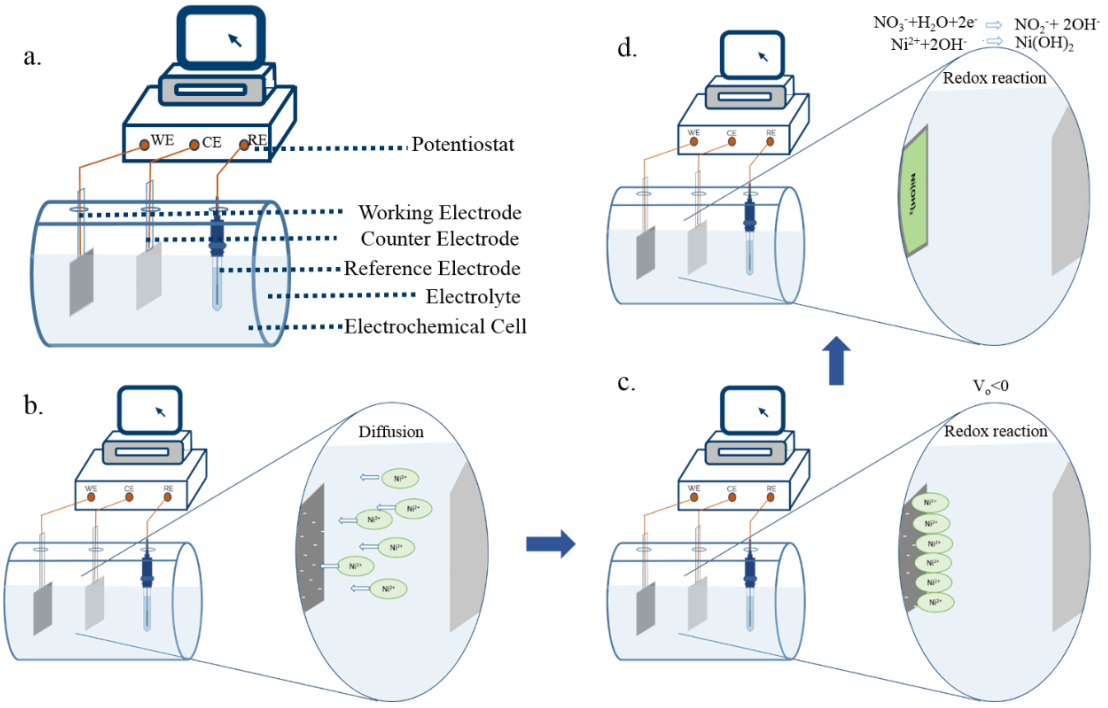

Fig. 2.1. Simplified representation of (a) the electrodeposition arrangement and (b-d) the electrodeposition process for a nickel hydroxide film.

2.1.2 Physico-Chemical process.

This section aims to introduce the fundamental theory behind the electrodeposition process. It is mainly based on the Book "*Fundamentals of electrochemical deposition"* by Milan Paunovic and Mordechay Schlesinger [6], whose lecture is recommended for further study. In the electrodeposition process, a *z* number of electrons is provided by an external current supplier. Those electrons interact with the ions present in the electrolyte at the interface between a conductive substrate and the liquid to form a film. There are four main parameters involved in this process, namely; the substrate-solution interface, the kinetics and mechanisms of the process, the nucleation and growth of the layer and the structure and properties of this newly-formed lattice [6].

1. **Substrate-solution interface**: The substrate must be conductive, and may be metals, alloys or conductive materials such as carbon derivatives. It is important to point out that the structure and electronic properties of the materials (both solvent and substrate) greatly affect the electrodeposition outcome.
2. **Kinetics and mechanism of the electrodeposition**: Mass transport processes associated to the mobilization of the ions from solution to the interface and the rate of deposition (number of moles of layer deposited per second per unit area). The latter is influenced by the activation energy, which is a function of the electrode potential. Mass transport can either be diffusion (chemical potential/concentration gradient), migration (movement of electric charges/charged species due to an effect of an electric field) and convection (hydrodynamic flow, either natural or forced)[5]).
3. **Nucleation and growth of the film**: Formation of monolayers and multilayers. Current density is assumed to be uniform across the area of electrodeposition. Nonetheless, it must be highlighted that any surface contains heterogeneities that produce prevalent places with higher energy. Here, the electrodeposition process will start. These active sites are known as active centers or nucleation points.
4. **Structure and properties of the deposit**: Physico-chemical properties of interest of the layer deposited. In particular, charge storage properties of the materials and structural characterization are relevant in this work.

2.1.2.1 Substrate-Solution Interface

There are several models to explain the substrate – solution interface. However, only three, due to their relevance, are included in this work.

The **Helmholtz compact double-layer model** assumes that all the excess charge produced in the interphase, more particularly on the solution side, is lined up at the same plane with a constant distance from the electrode. This distance comprises the ionic radius in addition to the solvation sphere of the ion. At the same time, the substrate consists of an equal and oppositely charged layer, forming a double layer. This is equivalent to that of a double-layer present in a capacitor. However, this is an oversimplified model since the interphase has been proven, experimentally, to not behave in such manner. Thus, more accurate models have been developed, such as the **Stern model**.

The Stern model considers the contribution of a diffusion layer model, previously developed by Gouy and Chapman, in addition to the double layer considered by Helmholtz. In this model, some ions are at a fixed distance, confined in a single plane, while others are distributed in the solution. Finally, Grahame modified Sterns' model and resulting in the **Grahame model**, that considers the same principles but introduces an inner plane of approach (inner Helmholtz plane) with partially not solvated adsorbed ions

and an outer Helmholtz plane with fully solvated ions [6]. This model varies by including two planes of closest approach, one for fully hydrated ions and another for partially hydrated or fully dehydrated specifically adsorbed ions.

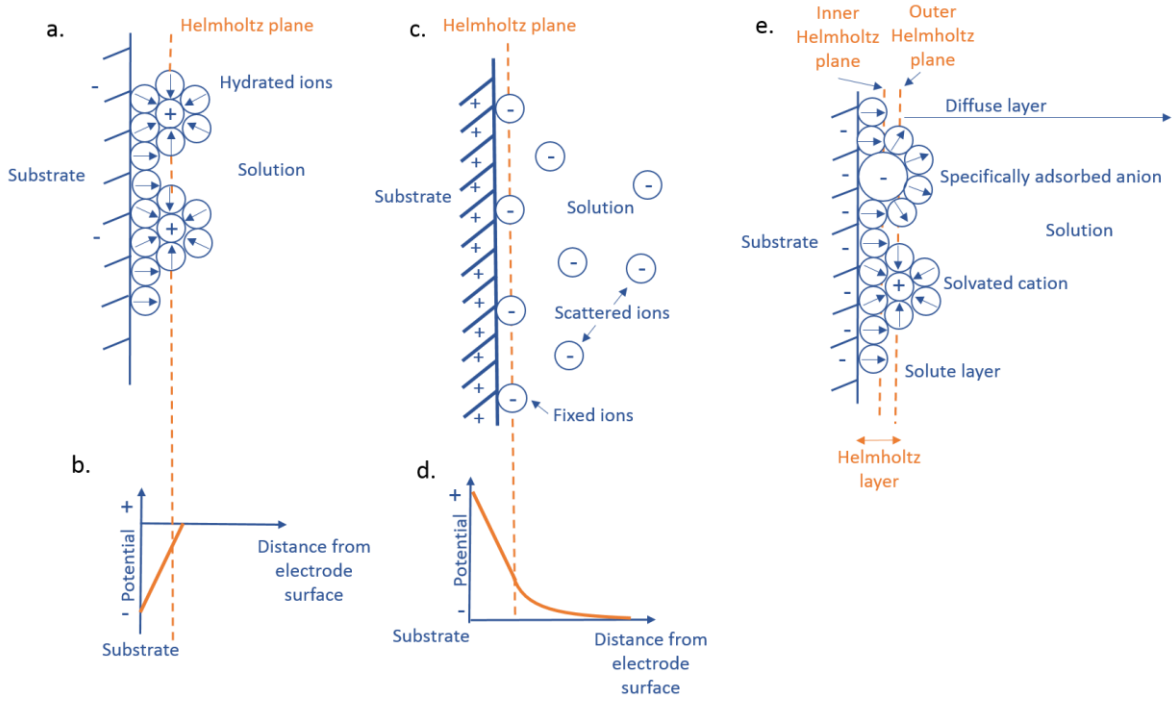

Fig. 2.2. a) Helmholtz double layer model of a double layer. b) Linear variation of potential in the double layer with distance from the electrode. c) Stern model with d) its variation of potential based on the distance from the electrode. e) Triple-layer Grahame model. Reprinted with copyright permission of [6].

When no external potential/current is applied in the system, there is a potential difference at the interphase. This potential difference cannot be directly measured unless another interphase is placed by means of a counter electrode. This results in an electrochemical cell in which the potential can be measured. An electrode's equilibrium potential is described by Nernst equation for redox electrode potentials, resulting in an exchange of electrons between the metal and the electrolyte:

$$\Delta\emptyset_{eq} = \Delta\emptyset^0 + \frac{RT}{zF} ln\left(\frac{[Ox]}{[Red]}\right) \qquad (eq.\,2.1)$$

In equilibrium, a redox reaction interphase has an equal number of electrons crossing in both directions across the substrate/electrolyte interphase. When an external current is applied, the potential will vary resulting in a current flow that will create an overpotential in the interphase. This will lead to four types of rate control in an electrodeposition process, explained in the following sections.

2.1.2.2 Kinetics and mechanism of electrodeposition

There are four possible phenomena occurring during electrodeposition, namely: charge transfer, diffusion, chemical reaction and crystallization. Charge transfer is related to the transfer of charge across the double layer, determined by the electrode potential. Moreover, during the whole electrodeposition process, mass transport is present, in which the substances involved in the reactor shall be transported from the bulk electrolyte to the electrode surface, the interface and vice versa. This process is governed by diffusion.

Chemical reactions are then involved. Although they may be homogeneous in the solution, they can be heterogeneously distributed on top of the electrode's surface. The rate at which chemical reactions occur is not dependent on the applied potential but it is affected by a diminution of the current flow. At the same time, this is affected by the species and processes of the interface. Finally, when metal/metal-ion interfaces are present, there is a crystallization of partial reactions. This is the incorporation/de-incorporation of atoms into the crystal lattice.

All the processes mentioned before can become the kinetically limiting process and, therefore, the rate determining process. According to it, different models have been developed to explain the kinetics of the reaction, which are out of the scope of the present work.

Summarizing, the reaction rate of a general electrochemical redox reaction, in terms of current density, is given by:

$$\text{Reduction rate: } \vec{v} = \vec{k}[Ox] \qquad (eq.\,2.2)$$

$$\text{Reduction current density: } \vec{\imath} = zF\vec{k}[Ox] \qquad (eq.\,2.3)$$

$$\text{Oxidation rate: } \overleftarrow{v} = \overleftarrow{k}[Red] \qquad (eq.\,2.4)$$

$$\text{Oxidation current density: } \overleftarrow{\imath} = zF\overleftarrow{k}[Red] \qquad (eq.\,2.5)$$

where $\vec{k}$ is the rate constant of the reduction reaction. When the charge-transfer processes are the limiting process of the electrodeposition, the relationship between the current density i and the transfer overpotential η is described in terms of two parameters, the exchange current density i_o and the transfer coefficient α by the **Butler-Volmer equation**. This relationship is given by k, which can be derived to be:

$$i = i_o\left[exp\left(\frac{(1-\alpha)zF\eta}{RT}\right) - exp\left(-\frac{\alpha zF\eta}{RT}\right)\right] \qquad (eq.\,2.6)$$

where F is the Faraday's constant, z is the number of electrons transferred across the electrode-electrolyte interphase and R is the gas constant. Finally, the transfer coefficient α is a constant that can take values from 0 to 1 and is, usually, 0.5 (depending on the symmetry of the energy barrier).

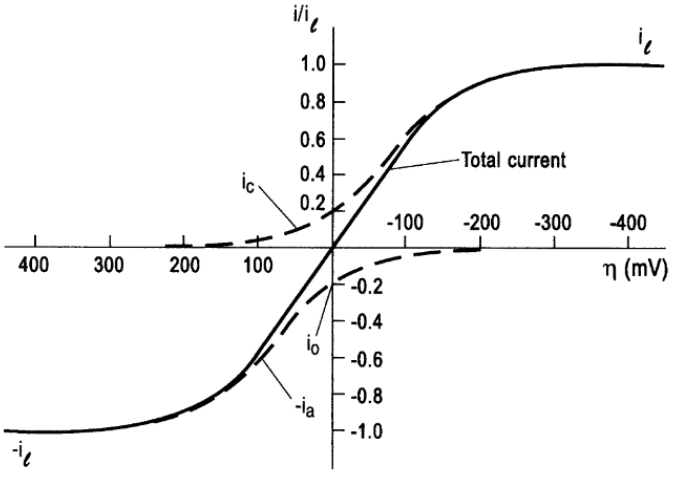

Fig. 2.3. Variation of partial current densities (dashed line) and net current density (solid line) with overpotential η. Reprinted with copyright permission of [6].

When mass transport is the determining process, there are several models. The **diffusion-layer model** can be applied. In equilibrium, the concentration of the electrolyte is homogeneous in the whole system apart from the region from the outer Helmholtz layer to the electrode's surface. When the electrodeposition is occurring, there is a consumption of the species at the interphase. This depletion extends further as the reaction progresses. Then the rate of the reaction depends on the diffusion of the species according to:

$$i = zFD_{ox}\left(\frac{\partial C_{ox}}{\partial x}\right)_{x=0} \qquad (eq.2.7)$$

However, an evaluation of the presented model is complicated and different models can be applied such as the **Nerst Diffusion-Layer model.** This model assumes that the concentration of oxidant has a constant bulk concentration that drops linearly at the electrode at a single electrochemical reaction. However, when multiple reaction steps are considered, more complex models are required and have been developed.

2.1.2.3 Nucleation and growth of the film

In the formation and growth of clusters there are two main processes to be considered: the arrival and adsorption of ions at the surface and their motion on the surface. If a crystal was perfect, the deposition of an ion would only be temporary because the binding energy to the surface would be very small. However, it can increase its stability by forming clusters. The energy associated to this process is based on the transfer of ions from solution onto the surface and the decrease in surface energy due to the creation of the surface of a cluster. When the charge transfer process is fast, the growth rate is determined by either lattice incorporation step or the diffusion of electrodepositing ions into the nucleus.

The first order kinetic model of nucleation is given by the equation:

$$N = N_0(1 - \exp(-At) \qquad (eq.2.8)$$

Where N_0 is the total number of sites and A the nucleation rate constant. The rate of a 2D nucleation is given by:

$$J = k_1 \exp\left(-\frac{bs\varepsilon^2}{zekT\eta}\right) \qquad (eq.2.9)$$

Where k_1 is a rate constant, b is a geometric factor, s is the area occupied by one atom, ε is the specific edge energy, k is the Boltzmann constant, z is, e is the electron charge, T is the temperature and η is the overpotential.

At the initial stage of deposition, the nucleation constant is very big and, therefore $N \cong N_0$. This means that all electrodeposited sites convert into nuclei instantly, this is known as **instantaneous nucleation**. When A is small, $N \cong AN_0t$. This is known as **progressive** nucleation.

Regarding the lattice incorporation step, there are four models describing the process. At the initial stages, it can be assumed that the nuclei are independent one from each other. Then, the rate of growth is given by the 2D cylindrical nucleus model, described as:

$$i = \frac{nFk^2 \cdot 2\pi hM}{\rho}t \quad (eq.2.10)$$

Where k is the rate constant of 2D nucleus growth ($mol \cdot cm^{-2}s^{-1}$), h is the height of a cylindrical nucleus (height of a monolayer), M is the molecular weight, t is time of deposition, n is the number of electrons involved in the reaction, F is Faraday's constant

and ρ is the density of deposit. Then, the 2D nucleus may only grow laterally or may grow into a 3D structure. This is when the other three models apply, they being a hemisphere, a right-circular cone and a truncated four-sided pyramid.

When analysing the diffusion of electrodepositing ions into the nucleus, the process by which nuclei interact is evaluated. At a certain time, nuclei will no longer be independent one from the other and there will be an overlap of the diffusion films. This overlap is translated into local concentration regions and different overpotential/current distribution in the surroundings of the clusters. Thus, they will have reduced nucleation rate. At the point of the contact, growth will be stopped.

When a monolayer applies, the nucleation process is based on either the instant nucleation or the progressive nucleation mechanism. However, when multilayers are formed, there are also two different possible mechanisms.

Monolayer layer-by-layer growth occurs at low potentials when the applied potential is barely above the critical deposition overpotential. In this case, growth is faster than nucleation and each nucleus spreads over the entire surface and each layer is based on a single nucleus (see Fig. 2.4). **Multinuclear multilayer growth** happens when the nucleation rate is faster than the growth rate. This occurs at potentials over the propagation rate and the electrodeposition is based on multiple clusters.

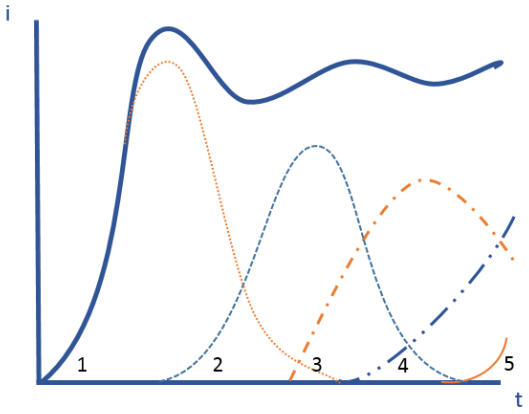

Fig. 2.4. Potentitostatic current-time transient for the deposition of up to 5 individual layers. This exemplifies 2D progressive nucleation with overlap. Reprinted with copyright permission of [6].

During potentiostatic current-time transients (see Fig. 2.5) the process can be divided into three-time intervals. First, the current decays during nucleation and growth, then it increases due to the growth of independent nuclei and simultaneous increase of the number of nuclei (linear increase for instantaneous nucleation and squared dependence for progressive nucleation). Finally, there are two opposing effects, the growth of independent nuclei and the overlap of clusters. This produces a maximum that will decrease over time. When two clusters collapse, the growth stops and the current decreases due to the reduction of effective electrode surface area.

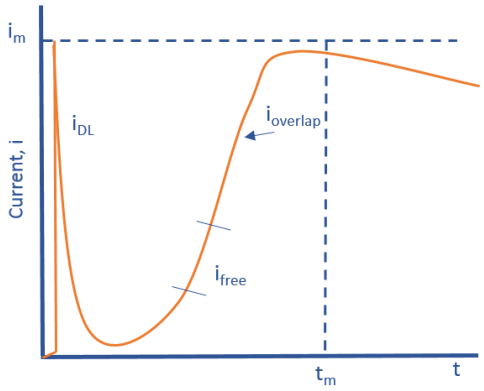

Fig. 2.5. Theoretical potentiostatic current-time transient, including the effect of overlap. Reprinted with copyright permission of [6].

However, real electrodepositions are not based on a monolayer nor a few monoatomic layers deposition. They are usually based on coherent domains that joined together and coalescence. There are two mechanisms for coherent deposits. First one is **layer growth mechanism**. This is related to the formation of steps (microsteps and macrosteps) or grown layers such as columnar crystals, whiskers, etc. Second one is the nucleation-growth mechanism. This process is subdivided in four sequences: a) formation of isolated nuclei and their growth into three-dimensional structures. b) coalescence of these structures. c) formation of a linked network and, finally d) formation of a continuous deposit.

Finally, it is worth mentioning that during electrodeposition many orientations may occur. Single-crystals are deposited when a single orientation is achieved. However, deposits tend to have different textures such as polycrystalline or amorphous that have different crystal orientations or no epitaxial influence respectively. Also, the texture obtained in the perpendicular plane to the substrate shall be considered, the most important being columnar microstructures (grains that become larger the further they go from the substrate).

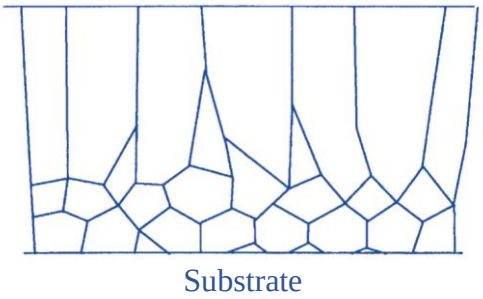

Fig. 2.6. Schematic cross section of the columnar deposit. Reprinted with copyright permission of [6].

2.1.2.4 Structure and properties of the deposit

Properties of the electrodeposited material will be defined by the materials deposited themselves. However, all deposited structures can be classified within one of the seven main groups, namely; single crystal, polycrystalline columnar, polycrystalline equiaxed, polycrystalline fibrous, polycrystalline dendritic, polycrystalline nodular and amorphous (Fig. 2.7).

Single crystals appear when the periodicity of an atomic pattern extends to the whole crystal. When that periodicity is interrupted, and several orientations of the patterns

appear, forming grains, they become polycrystalline. Finally, when the size of the pattern unit is comparable to that of the size of the grains they are known as amorphous materials.

Regarding the different types of polycrystalline structures, **columnar** refers to those that have a preferential growth direction. **Fibrous** materials are those that only cover partially the substrate, resulting in oriented growth of grains. **Nodular** structures have a cauliflower-like structure whose nature has yet to be explained. **Dendritic** structures may result as mass-transport controlled growth. Finally, **Equiaxed** are those similar to columnar that grow to larger sizes.

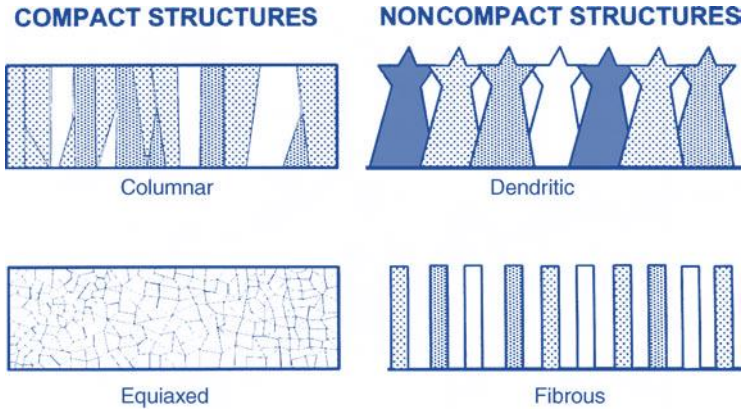

Fig. 2.7. Representation of the different structures of electrodeposited thin films. Reprinted with copyright permission of [6].

There are many parameters that influence the structure of the deposit. For example, metal-ion concentration, additives, current density, temperature, agitation or polarization. Although an in-depth discussion of the different parameters is out of the scope of the present manuscript, some of the factors that have greater relevance in the final structure of a deposit are:

Crystallographic planes, this is the periodic arrangement of atoms, is vital in understanding the solid-state chemistry of the material. Depending on the electrodeposition conditions, they may have one out of the 230 possible distinct space groups.

Homogeneity of the deposit and **phase changes** must be considered as well. This can be correlated to the degree of crystallinity, this is, the extent to which a crystallographic orientation is maintained throughout the deposit.

Impurities such as oxidized materials due to ambient atmosphere, added chemicals, production of bubbles or subproducts may play an important role in the ultimate performance of the deposited material.

The **substrate** is also a key parameter in defining the final structure and properties of the electrodeposited material. In this regard, there are two main phenomena to consider: epitaxy and pseudomorphism. The former refers to the goodness of the adaptation of the deposit to the structure of the substrate. The latter refers to the continuation of grain boundaries and geometric features of the substrate.

Finally, it should be mentioned that every deposited material will have different intrinsic properties such as thermal and electrical conductivity, magnetoresistance, mechanical properties, etc.

2.1.2.5 Other parameters affecting the electrodeposition.

Additives affect the electrodeposition process by acting as adsorbates at the surface of the electrode. Depending on the nature of this interaction there is chemisorption (based on chemical covalent bonding of the additive to the surface) and physisorption (based on weak interactions without electron transfer from the additive the substrate). Additives affect nucleation and growth processes and the kinetics of the electrodeposition. The concentration of adions (superficial ions), the diffusion coefficient and the activation energy are affected among others.

When electrodeposition occurs, ions become attached to favoured places. That creates discontinuities in the form of pores and cracks. Thus, **current density distribution** plays a fundamental role in this process. It is defined as the total current divided by the unit area. Current density varies over the substrate surface tending to be lower in cavities and greater at points closer to the opposite electrode.

Temperature, agitation, polarization, metal-ion concentration, deposit stress while forming, roughness of the surface and surface morphology, electrolyte density or impurities are other parameters that may affect the electrodeposition process and that shall be considered in the experimental setup since they will affect the resulting material in parameters as important as, for example, grain size.

2.1.3 Modes of electrodeposition.

There are several techniques that can be applied in the electrodeposition process for energy storage applications (and other applications). In this section they are briefly described.

In the **Galvanostatic Transient technique** the current applied between the working electrode and the counter electrode is constant and the potential between the working electrode and the reference electrode is time-variant. The response, E=f(t), requires a certain time to reach a potential at which the electrode reaction happens at a measurable rate. The charge is used to charge the double-layer capacitance up to the potential at which the reaction occurs at a measurable velocity and charge transfer (Fig. 2.8). The total Galvanostatic current density is therefore given by the addition of the double layer contribution together with the charge transfer current: $i_g=i_{dl}+i_{ct}$.

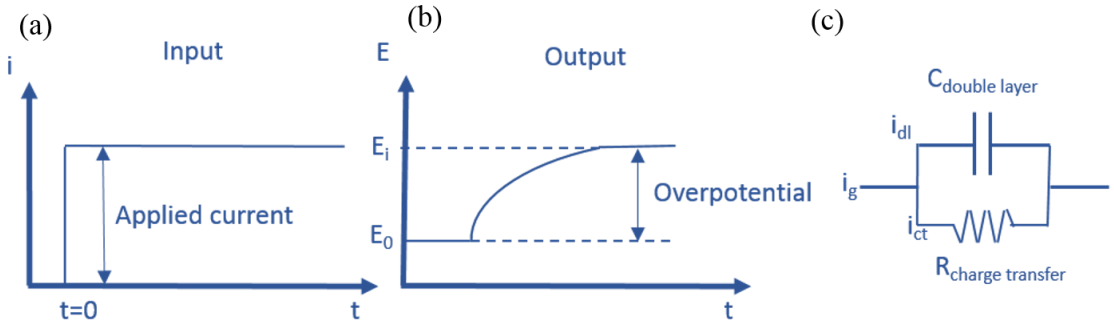

Fig. 2.8. (a) Scheme of galvanostatic current (constant current) applied in a given time. (b) Variation of potential of the electrode with time when a constant current is applied. (c) Equivalent circuit for a single-electrode reaction taking into consideration the double-layer capacitance and the charge transfer resistance. Reprinted with copyright permission of [6]

When a negative current is applied at the working electrode (WE), positive ions are attracted to it. Then, the working electrode is considered as the cathode and the technique

is known as **cathodic galvanostatic electrodeposition** since the WE undergoes a cathodic polarization (Fig. 2.9). When the current is applied to make the electrons flow to the working electrode, the process is known as **anodic galvanostatic electrodeposition** since the working electrode gets positively polarized, becoming the anode and attracting negatively charged species (Fig. 2.9).

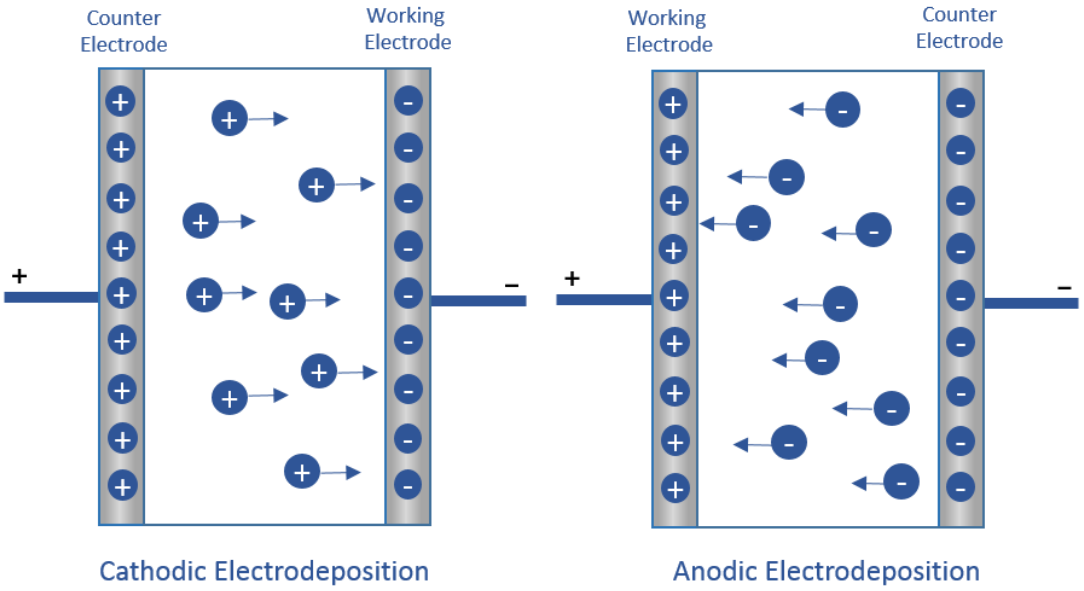

Fig. 2.9. Scheme comparing cathodic electrodeposition versus anodic electrodeposition.

An analogous technique, known as **Potentiostatic Transient technique**, consists in maintaining a constant potential while having the current density as a time-dependent function. I= f(t). In the same manner, cathodic for a negative applied potential and anodic for a positive applied potential can be used (Fig. 2.10).

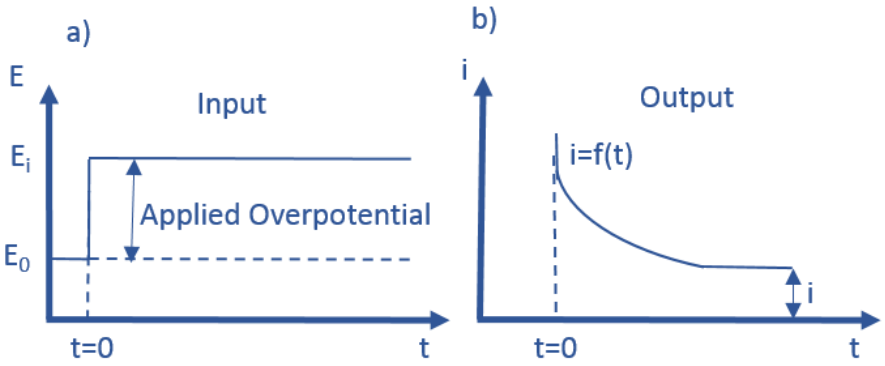

Fig.2.10. Variation of current with time for potentiostatic electrodeposition. Reprinted with copyright permission of [6].

Pulsed electrodeposition is a technique in which either the current or the potential (depending if it is a galvanostatic or potentiostatic technique) is either alternated between positive and negative values, or between two different positive/negative/zero potentials/currents. This is done to generate pulses of equal amplitude, duration and polarity. By modifying the amplitude or width (time) of the pulse, different materials can be preferentially deposited to different values, allowing the formation of different compositions, morphologies or thicknesses.

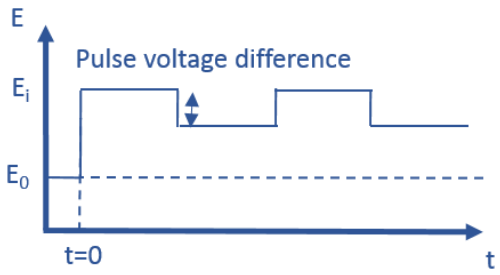

Fig.2.11. Variation of potential with time in a pulsed electrodeposition. Reprinted with copyright permission of [6].

Finally, another method is the **Potential Sweep technique** (Fig. 2.12). In this case, the potential is varied with time. When this variation is linear, the technique is known as **Linear Sweep Voltammetry**. The sweep rate ν ($mV \cdot s^{-1}$) must be considered in this case. The potential at a given time and with an initial potential E_0 will be:

$$E_t = E_0 - \nu t \ (eq. 2.11)$$

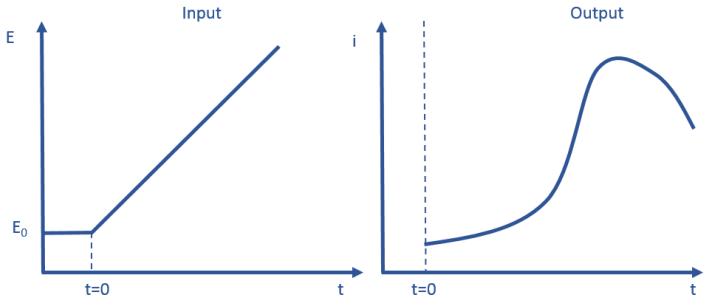

Fig. 2.12. Linear potential sweep voltammetry comparison for the input and output responses. Reprinted with copyright permission of [6].

Finally, it is worth mentioning **electrophoretic deposition** (EPD) making distinction with electrodeposition (electrolytic deposition) because EDP refers to the deposition of colloidal suspensions of particles instead of dissolved ions. In this case, the colloids migrate under the effect of an electric field and are deposited on top of an electrode [7].

During the extent of this work, electrodeposited materials of graphene and nickel and cobalt hydroxides. Therefore, an in-depth state-of-the-art in the work reported in literature so far is here presented.

2.1.4 Electrodeposited graphene.

Efficiently reducing graphene oxide is still a challenging and an ongoing study. Different methods such as chemical or thermal reduction have been reported [8,9]. In fact, more than 50 reducing agents have been reported leading to different types of chemically reduced graphene with different properties. This highlights the importance of the reduction of graphene oxide to mass-produce reduced graphene oxide, with tailored properties depending upon the final application.

Electrodeposition has been pin-pointed as a potentially prosperous technique to produce reduced graphene oxide due to the advantages aforementioned. Not only that, chemical reduction usually entails the usage of dangerous chemicals that, by means of electrodeposition, are avoided. Moreover, chemical processing usually requires high temperature, high processing times or results in a very small layout. By means of electrochemical reduction of graphene oxide, milligrams, or even grams or Er-GO can be obtained [10].

The electrochemical approach, in comparison to the chemical methods, has the advantages of being single-step, easy to operate, environmentally friendly and possible to be produced at ambient conditions [11]. Not only that, other existing methods to produce reduced graphene oxide are based on a pre-step of graphene oxide deposition by means of diverse techniques such as membrane filtration, dip coating, layer by layer deposition, spray coating or spin coating [12–19]. Consequently, all of them present the disadvantage of uncontrolled thickness and uniformity. However, electrodeposition techniques can enable accurately control over them[15]. There are several procedures to produce reduced graphene oxide electrochemically that will be considered in this work. To prepare Er-GO, either the application of a cathodic or anodic potential is required. Also, the electrolyte in which the reduction is produced is a determining parameter. The monolayers can be either suspended in a chemically exfoliated graphene oxide solution or coming from a working electrode of graphite. If based on a graphite working electrode, first intercalation for the expansion of the monolayers is required by means of cations or anions present in the electrolyte. After that, a different potential/current is applied to reduce the suspended graphene oxide layers. In general, a constant potential/current or a potentiodynamic cyclic voltammetry between two prefixed potential is applied [20].

2.1.4.1 Production of Graphene Oxide by Anodic oxidation.

The production of graphene oxide based on the anodic oxidation requires the application of a positive potential to a graphite working electrode to oxidize it. This produces the intercalation of anions within the interslab structure of graphite and results in the ultimate exfoliation of the monolayer [21]. The process is based on the hydrolysis of the highly oriented pyrolitic graphite (HOPG) to produce alcohol radicals on the surface. Negative ions then get intercalated by means of oxygen production. This entails an expansion of the graphene interslab distances that produce graphene oxidized layers [20]. Several acidic media have been tested, resulting in different quantities of defects produced, hence, different qualities of graphene oxide. This process is exemplified in Fig. 2.13 and a summary of the different experimental procedures is included in table 2.1.

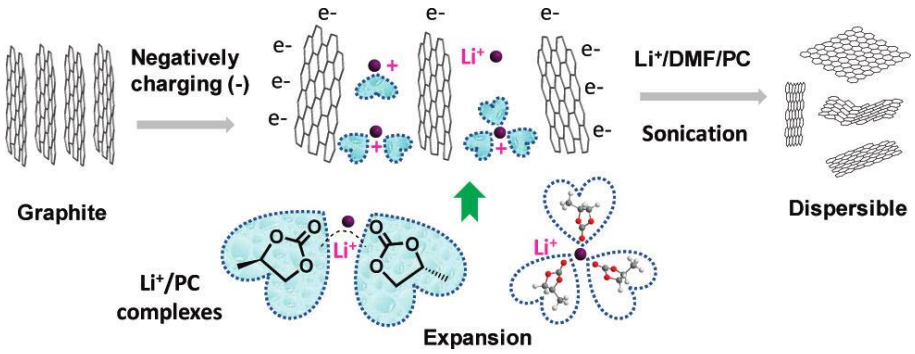

Fig 2.13. Exemplification scheme of the exfoliation of graphene into Er-GO via intercalation of Li^+ ions as presented in [10]. Re-printed with copyright permission of [10].

Table 2.1. Summary of experimental conditions used in the production of electrochemically exfoliated graphene oxide nanosheets. Modified and reprinted with permission of [20]. WE: working electrode. CE: Counter Electrode. RE: Reference Electrode. T: Temperature. HOPG: Highly oriented pyrolityc graphite. GE: Graphite electrode column. Grafoil®: Flexible graphite foil. Pt: Platinum. SCE: Saturated calomel. NHE: Normal hydrogen electrode. SSCE: sodium saturated calomel electrode. SCE: saturated calomel electrode. MSE: Mercury-mercurous sulfate electrode. NM: Not measured. CV: Cyclic voltammetry. DI: Deionized water. IL^1: triethyl sulfonium bis (trifluoromethylsulfoniyl)imide ionic liquid. BMIM: 1-butyl-3-methylimidazolium. IL^2: 1-octyl-3-methylimidazolium hexafluorophosphate. IL^3: 1-methyl-3-butyilimidazolium tetrafluroboate. PSS: polystyrene sulfonic acid.

WE	CE	RE	Electrolyte	T(°C)	Potential/ Current	Comments	Ref.
Flexible graphite	Pt rod	Ag/AgCl	([BMIM][BF_4]) %DI water + $LiClO_4$	NM	from -2V to 3V scan	CV for 50 cycles	[22]
Pencil (9B)+Graphite flakes or HOPG	Pt spiral	Pt	10 mL IL^1	NM	0V, +8V and -8V	0V for 120 s, the rest 600s	[23]
Graphite flakes or HOPG	Pt wire	-	4.8 g 98% H_2SO_4 + 100 mL DI + 11 mL 30%KOH	25±3	from -10 to 10V	Static potential 2.5V 1min first	[24]
Graphite foil	Carbon sheet	NHE	1M $HClO_4$	25±3	from -1.5 to +1.7V	Double potential step 1200s	[25]
Graphite rod	Pt foil	Platinum wire	0.1M SDS	NM	1.4-2V then -1V	12h intercal. 2h exfol	[26]
Graphite	Lithium metal	-	30 mg mL^{-1} $LiClO_4$/PC or LiCl/DMF/PC	NM	Potential of -15±5V	$LiClO_4$ for intercal. LiCl for exfol.	[10]
HOPG	-	SSCE	1M KNO_3/$LiClO_4$/ $(NH_4)_2SO_4$/H_2SO_4/ KOH/K_2HPO_4	NM	0.135V, 1.5V and 1.95V	Potential scans	[27]
HOPG	-	MSE	5M H_2SO_4 + HCOOH	NM	1.3V	8000C g^{-1} for exfoliation	[28]
Graphite rod	Graphite rod	-	10 mL IL^2 and 10 mL water	NM	15V	anodic corrosion for 6h	[29]
Graphite rod/HOPH	Pt wire	-	IL^3	NM	1.5-15V	10%, 60%, 90% wt. H_2O used	[30]
GE	-	Ag/AgCl	0.1M Na_2SO_4 (aq.)	NM	from -1.0V to 3.0V	Scan rate 5000 mV s^{-1}	[31]
Grafoil ®	Copper foil	-	0.001M PSS (aq.)	NM	300 mA (1min to 2h)	2 cm interlectrode gap	[32]
Graphite plate	Pt foil	SCE	96% H_2SO_4	0	10V	Anodic electrolysis	[33]
HOPG	Pt wire	-	$FeSO_4$/$CoSO_4$ + Na_2SO_4 (aq.)	NM	0, 0.7, 10V	Alternate step voltages 5min	[34]
Graphite rod	Graphite rod	-	0.001M PSS (aq.)	NM	5V; 4h	15% yield	[21]

2.1.4.2 Production of Graphene Oxide by Cathodic oxidation.

Although electrochemical methods can be used to generate exfoliated graphene oxide, to produce electrochemically reduced graphene oxide, a cathodic potential shall be applied. Fortunately, if a cathodic potential is directly applied, no strong oxidizing media must be employed, leading to a reduced number of defects present in the nanolayers. The process is similar to that of the anodic potential but with the intercalation of cations instead and the expansion by means of hydrogen release instead of oxygen. However, this direct procedure entails very small yields and has not been investigated thoroughly [10,20]. In this case, lithium ions or surfactants were required to be present in the electrolyte for the exfoliation to occur.

2.1.4.3 Production of Er-GO by Electrophoretic Deposition.

Electrophoretic deposition (EPD) is a promising technique for large area Er-GO production. The colloidal particles, suspended in an aqueous electrolyte, migrate under the effect of an electric field and deposit onto the electrode. There have been several strategies in the EPD of GO, including the deposition of GO with posterior conversion [35], direct deposition-reduction of Er-GO [15,36], pre-reduction of GO and deposition [37,38] and modified GO with metal oxides EPD [39]. Due to the large number of reports presented regarding the EPD of Er-GO, only those strategies related to electrode materials for charge storage are included in this report.

The first GO deposition and subsequent reduction by electrochemical methods was done by Liu et al. They measured the zeta potential of GO suspensions, obtaining a value of -64.7 mV, which can be related to a big negative surface charge. Then, they deposited it on top of ITO by applying 150V for 45s and then reduced the film by applying a constant potential or scanning potential ranging from 0.0 to -1.0V at a scan rate of 10 mV s^{-1} in 0.1M KCl [35]. Finally, they measured its characteristics as electrode material for energy storage applications. They investigated the material in 0.1M Na_2SO_4 in the potential range from -0.2V to 0.8V vs Ag/AgCl. For that they calculated a specific capacitance of 156 F g^{-1} at 150 mA g^{-1} and obtained a good capacitance retention (93 F g^{-1} after 400 cycles) with a pseudocapacitive response from the material.

The direct deposition and reduction of Er-GO was achieved when Ruoff et al. [40] wanted to study the improvement in electronic conductivity when graphene oxide is reduced. For that, they deposited a film of GO and reduced it by Electrophoretic deposition. They observed an improved electrical conductivity, from $0.53 \cdot 10^{-3}$ S m^{-1} to $1.43 \cdot 10^{4}$ S m^{-1}. To achieve the reduction and deposition on top of a stainless-steel mesh, copper nickel or aluminum; they suspended GO in water with a 1.5 g L^{-1} concentration and applied a DC current for 1 to 10 minutes at 10V. The suggested reduction reactions are:

$$RCOO^- \rightarrow RCOO\cdot + e^- \text{ (oxidation of carboxylate)} \qquad \text{(eq. 2.12)}$$

$$RCOO\cdot \rightarrow R\cdot + \cdot CO_2 \text{ (oxidative decarboxylation)} \qquad \text{(eq. 2.13)}$$

$$2R\cdot \rightarrow R\text{-}R \text{ (dimerization of radicals)} \qquad \text{(eq. 2.14)}$$

GO flakes, which are negatively charged, are electrophoretically drawn to the positive electrode. Then, once contact is done in the anode, electrons can flow away from the flakes oxidizing the samples. Then, there is a loss of carbon dioxide. However, reported results were counter-intuitive because oxidation usually occurs at the anode of an electrochemical cell and they exposed de-oxidation in this case. Furthermore, the oxidation of epoxides was not explained [15].

Sandhu et al. [36] reported another direct electrophoretic deposition GO, in this case with partial reduction of the GO film during the process. They deposited the film on SiO_2/Si and glass. For that, they used conductive Cu tape on the back of the glass substrate and treated the substrates with O_2 plasma. Then, they applied a constant potential ranging between 1 and 30V for 5 minutes and found out that the C-C% of bonds increased from 49% to 81%, with the consequent reduction of C-O bonds, in comparison to the GO precursor [36].

Regarding the last strategy, the pre-reduction of GO by means of chemical ways and then electrodeposited the reduced layers. Chen et al. pre-reduced a GO suspension by means of *p*-phenylene diamine in ethanol and then electrodeposited them on a 3D nickel foam at 50V. A final step of annealing was performed at 400ºC for 3h [37]. Lee and coworkers used a similar two-step method in two different ways. First, they EPD an aqueous suspension of GO and then reduced it by immersing it into hydrazine. Second, GO was pre-reduced in an alkali solution and then EPD [41].

In the first case, similar values to those obtained by Liu et al. are achieved. A high capacitance of 164 F g^{-1} at 10 mV s^{-1} and 139/100 F g^{-1} at 3 and 6 A g^{-1} respectively. However, the retention of the capacitance faded to approximately a 60% after 700 cycles [37].

By means of this technique, graphene has been deposited with other nanostructures. For example, Kim et al. did an electrophoretic deposition of RGO with multiwall carbon nanotubes assisted by nickel ions. For that, they used an aqueous solution of MWCNT and RGO, an aluminum foil as counter electrode and aluminum foil as working electrode. RGO was prepared electrochemically by applying 300mA for 1h to a Grafoil® electrode in a PSS solution. The electrophoretic deposition was carried at 100V for 10 minutes. The material showed promising results and, overall electrophoretic deposition may be a potential route for industrial production of Er-GO. However, further development is required [42]. The capacity values obtained were of 1700 mAh·g^{-1} at 0.2C on the first cycle and 600 mAh·g^{-1} for the second cycle and 282 mAh·g^{-1} after the 10^{th} cycle.

Nam et al. reported the electrophoretic deposition of chemically reduced GO and its detachment from the substrate as a self-sustained film. For that, they used hydrazine as a reducing agent and then applied a 3V direct current to stainless steel for 15 minutes. Then, they electrochemically edged the film by applying a 5V current to the RGO/SS cathode in an H_2SO_4 solution. The detachment was possible thanks to the hydrogen bubbling on the electrode. Then, they further reduced the film by applying thermal annealing. The best C/O ratio achieved was 16.66 after annealing at 100ºC [41]. The inconvenient of this technique is, evidently, the high number of steps that must be performed in many cases in other to obtain the reduced film and the usage of chemicals in the reduction process of the GO suspension.

2.1.4.4 Production of Er-GO from Graphene Oxide Suspensions.

The first strategy employed for the electrochemical reduction of graphene oxide was to pre-apply GO onto an electrode and then reduce it in an appropriate electrolyte [11] in a two-step electrochemical reduction approach. By pre-applying GO, a controlled synthesis in terms of shape, size and thickness can be achieved [43]. It greatly depends upon the technique used for the deposition, for instance, dip-coating, drop-casting, layer-by-layer or spray coating [44,45].

Dong et al. first reported the reduction of graphene oxide by applying a sweep voltammetry after GO was spray-coated with different forms on top of various substrates

by means of a patterned template at -0.90V during 5000s. The obtained O/C ratio was of a 4.2% [44]. Xia et al. dropcasted GO on top of glassy carbon or graphite and reduced it potentiostatically at -1.5V or -1.3V vs SCE in 10 mmol/L pH 5.0 PBS [46]. Finally, also Engelhard et al. deposited GO on top of glass by dropcasting and reduced it by means of a CV between -1.0 and 1.0V vs. RHE at 50 mV s^{-1} in Na_2SO_4s. Engelhard et al. explained that the reduction of GO is an accumulative process in which, at the beginning, GO is insulating. Thus, only the GO in direct contact with the substrate can be reduced. Then, as it turns more and more into conductive graphene, more GO becomes accessible and the reduction peak at -0.75V increases. After a certain number of cycles, the amount of GO left is substantially reduced and this reduction peak decreases until vanishing. Once this happens, the CV response remains constant, see Fig. 2.14. Therefore, the reduction can be monitored by the variability in the -0.75 V redox peak [47].

It is worth noticing that there are two peaks around 0.5V vs. RHE that are maintained after the reduction of GO. Electrochemical reduction has been reported to only partially remove the oxygen groups leaving some functional groups in the basal plane due to a fast electron transfer around the edges of GO [48]. This denotes the presence of oxygen groups that maintain its functionality and are stabilized, resulting in a faradaic electrochemical response. When the electrochemical capacitance was investigated by CV and galvanostatic charge/discharge, values of 164.8 F/g at 20 mV s^{-1} in a 0.9V potential window and 150.4F/g at 150.4 A g^{-1} in 0.1M Na_2SO_4 were achieved. Moreover, only a degradation of a 10% was observed after 1200 charge/discharge cycles.

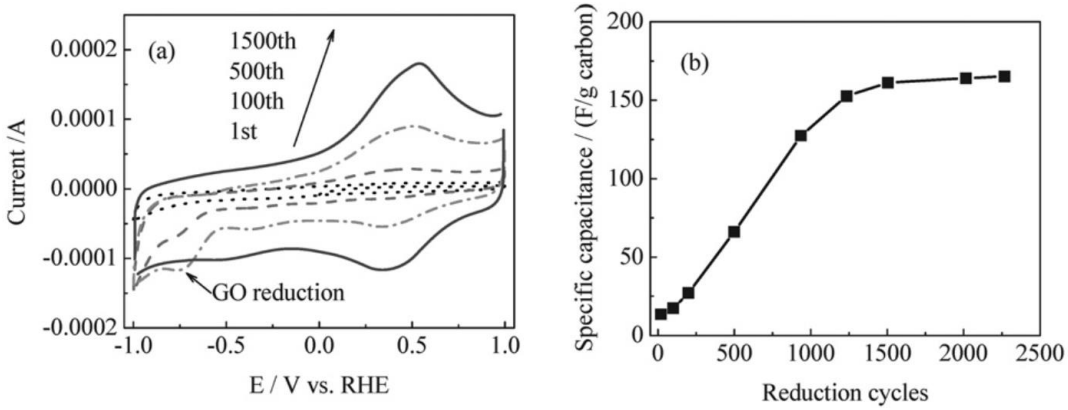

Fig. 2.14. a) Cyclic voltammogram showing the evolution of graphene oxide in 0.1M Na_2SO_4 at 50 mV s^{-1}in the reduction process. b) Specific capacitance measured with the evolution of the reduction cycles, measured in the range 0-0.9V vs RHE at 20 mV s^{-1}. Reprinted with copyright permission of [47].

A second strategy was to functionalize the electrode in order to add templating properties to GO [11]. For instance, Zhang et al. reported the electrochemical reduction of graphene oxide suspensions and then used it for biosensing. To reduce the GO flakes, they adsorbed GO on the surface of 3-aminopropyltriethoxysilane functionalized glassy carbon. Then, they performed a cyclic voltammogram from 0.7 to -1.1V in NaCl saturated with N_2 at a scan rate of 50 mV s^{-1} and observed that reduction occurred during the first cycle of scanning [49]. Another example of this approach was undertaken by Ramesha et al. [50]. They first assembled GO on top of a gold substrate by means of a cystamine monolayer and was then reduced by scanning between the potentials 0 to -1V vs. SCE. They observed the increase in conductivity because of the reduction process and analyzed it by Raman spectroscopy.

Kvarnström et al. modified Au surfaces with mercaptoethylamine. Then, they modified the GO aqueous solution to obtain a positively charged on the surface of the layers. Finally, they adsorbed GO by means of an integrated surface plasmon resonance affinity sensor. Then, they cycled the thin films in 0.1M NaF aqueous solutions at 10 mV s^{-1} vs. SCE in a potential range from -1.0V to 0.0V [51].

A third route was to functionalize GO and then deposit it by means of organic solvents [11]. Xue et al. reported the simultaneous electrodeposition of electrochemically graphene oxide and amorphous carbon nanoparticles in a methanol suspension. For that, they used a (PDDA)-modified chemically reduced graphene oxide suspended in methanol and applied a DC voltage of 1600V at 50ºC during 8h [52].

As observed, typically, after the deposition of the GO layer, the reduction takes place in either acidic or neutral pH since there is a greater concentration of protons, which are believed to participate in the process [53]. It can also be observed that there is a difference of the cathodic peak reported in the cyclic voltammetry for the reduction process, depending on the media and the different reference electrode. However, the cathodic peak decreases in most cases until its disappearance, as observed in figure 2.14.

The reduction process greatly depends upon the used potential range and the cycling time in a CV reduction and upon the reduction potential and time in the potentiostatic method. Zhou et al. showed the great dependence of the reduction with pH, shifting towards lower values with the increase of pH [44]. However, if too low potentials are used, hydrogen bubbling can lead to layer peeling and the formation of defects. For that reason, the range from -1.0V to -1.5V vs Ag/AgCl has shown the best results [46,54]

Table 2.2

Summary of experimental conditions for the electrochemical reduction of pre-deposited GO layers. PS, potentiostatic; CV, cyclic voltammetry; GC, glassy carbon; SCE, saturated calomel electrode; RHE, reversible hydrogen electrode; Pt, platinum; Au, gold; APTES, 3-aminopropyltriethoxysilane; Cyst, cystamine; HAD, 1,6-hexadiamine; PET, polyethylene terephthalate; PBS, phosphate buffered saline. Re-printed with copyright permission of [54].

Technique	RE	CE	WE	GO pre-step	Electrolyte	pH	Applied potential (V)	Scan Rate (mV/s)	Time/ number of cycles	C/O ratio	Ref
PS	SCE	Pt wire	GC/GO	Drop-casting	PBS(KH_2PO_4/ K_2HPO_4)	5.1-5.5	-0.8, -0.10, -0.12-0.14,-0.16	-	3 min	3.57, 3.85, 4.35, 5.00, 5.56	[55]
PS	Ag/ AgCl	Pt disc	Au/PET/ GO	Drop-casting	0.5M $NaNO_3$	-	-1.1	-	4.5h	-	[56]
PS	SCE	Pt wire	GC/GO	Drop-casting	0.05M PBS (KH_2PO_4/ K_2HPO_4)	6.5	-1.2, -1.7	-	600 s	-	[57]
PS	Ag/ AgCl	Pt foil	GC/GO	Drop-casting	0.1M KCl	-	-1.1	-	5 min	-	[58]
PS	Ag/ AgCl	Pt wire	GC/GO	Spray-coating	1M PBS (NaH_2PO_4/ Na_2HPO_4)	4.12	-0.90	-	5000s	24.3	[44]
CV	Ag/ AgCl	Pt wire	GC/HDA /GO	Dip-coating	0.2M PBS (NaH_2PO_4/ Na_2HPO_4)	7	0 to -1.4	50	15 cycles	-	[59]
CV	SCE	Pt wire	GC/GO	Drop-casting	0.05M PBS (NaH_2PO_4/ Na_2HPO_4)	5	0 to -1.5	100	100 cycles	-	[60]
CV	SCE	Pt foil	Au/Cyst/ GO	Layer-by-layer	0.1M KNO_3	-	0 to -1.0	10	2 cycles	-	[61]
CV	RHE	Pt foil	GC/GO	Drop-casting	0.1M Na_2SO_4	-	-1.0 to 1.0	50	1500 cycles	-	[62]
CV	SCE	Pt	GC/GO	Drop-casting	0.01M PBS (KH_2PO_4/ K_2HPO_4)	5	0 to -1.5	50	-	-	[63]
CV	Ag/ AgCl	Pt wire	Au/GO	Dip-coating	0.1M KNO_3	2	0.1 to -1.1	100	2 cycles	-	[64]
CV	Ag/ AgCl	Pt	GC/APT ES/GO	Dip-coating	0.5M NaCl	-	0.7 to -1.1	50	3cycles	-	[49]

Finally, McFarlane et al. reduced graphene oxide from aqueous suspensions for the first time by applying a potentiostatic reduction voltage varying from -1.0V to -1.4V (-1.2V showed the best results). They reported the direct electro-chemical reduction of graphene oxide from an aqueous suspension. They performed an in-depth investigation of the reduction conditions and concluded that the reduction process greatly depends upon the conductivity of the electrolyte (which must vary from 4 to 25 $mS \cdot cm^{-1}$ for successful reduction) and that it can be deposited over the wide range of pH of 1.5-12.5. They reported a conductivity of the later of approximately 20 $mS \cdot cm^{-1}$[11].

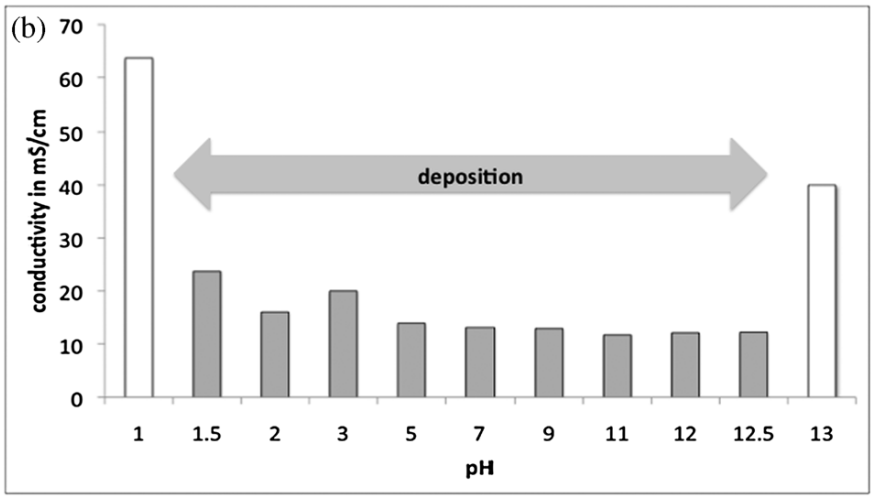

Fig. 2.15 Deposition behaviour of graphene oxide suspension (0.5 g L^{-1}) with NaCl 0.25M for optimum conductivity at different pH values. Deposited were obtained by Li et al. in a pH range from 1.5 to 12.5 at a potentiostatic deposition performed at -1.2V vs. SCE [11] . Reprinted with copyright permission of [11].

YanWei et al. also reported the reduction of graphene oxide by means of -0.9 to 0 V (vs. Hg/HgO) cycling voltammetry at a 6M KOH electrolyte resulting in a Er-GO film with a O/C ratio of 1.29% (and a specific capacitance of 152 F/g at 5 A/g, 99% retention after 3000 cycles) [65].

A one-step approach was developed afterwards for the reduction of graphene oxide. The GO sheets were directly reduced from an aqueous suspension while being deposited on top of the substrate. The reduction can be either done by cyclic voltammetry [66,67]; linear sweep voltammetry [68], or at a constant potential mode [54,68,69].

The process is believed to be as follows. The GO sheets close to the substrate accept electrons, hence producing Er-GO. The carbon-based reduced material is insoluble in nature and precipitates on top of the working electrode. Therefore, according to Liu et al., this deposition is based on the different solubility of Er-GO as compared to GO aqueous suspension [54,66].

This process comprises a redox reaction that requires a buffer solution in the electrolyte for the reduction process. For that PBS [70,71], NaCl [11] or Na_2SO_4 [47] have been, for instance, used. They affect the conductivity of the medium, which is a critical parameter in the formation of the Er-GO films [11]. The optimal conditions for the electrodeposition of Er-GO directly from an aqueous suspension of GO have been found to be a constant potential of -1.2V vs. SCE at a neutral pH media with a conductivity ranging from 4 to 25 $mS \cdot cm^{-1}$.

By potentiostatic deposition, a cathodic current must be applied to fully reduce GO. The more GO is consumed, the more the current decreases. When the conversion is complete, the current shall be zero. As exposed, the potential of reduction is a critical parameter that affects the reduction rate along with the time of the process. Guo et al. did a complete study in which they observed that ketone groups get reduced at -1.3V vs SCE, while hydroxyl and ether groups only get reduced at potentials lower than -1.5V vs SCE. Nonetheless, the usage of this low voltages lead to hydrogen evolution reactions that limit the diffusion of the nanosheets to the working electrode's surface, thus limiting the electrodeposition process [46].

On the other hand, cyclic voltammetry can be used as a deposition-reduction technique. By sweeping the potential in a determined range, usually from 0V to -1.5V at 20-100 mVs^{-1}, in both directions; Er-GO is produced. The advantage of this technique is that it gives information about the reversibility of the process and provides information about the redox behaviour of the sample.

According to literature, the redox reactions associated to the electrochemical reduction of graphene oxide may be the following [65]:

$$>C=O + H^+ + e^- \leftrightharpoons >C\text{-}OH \qquad \text{(eq. 2.15)}$$

$$>C=O + e^- \leftrightharpoons C\text{-}O^- \qquad \text{(eq. 2.16)}$$

$$-COO + H^+ + e^- \leftrightharpoons -COOH \qquad \text{(eq. 2.17)}$$

In the negative potential region vs. Ag/AgCl there are two visible peaks, associated to two different reactions. First, there is a reversible reaction in the range of -0.4V to -0.6V and, second, a reaction in the -0.6V to -1.0V potential range vs Ag/AgCl. While the second reaction is associated to the reduction process and disappears as the reaction evolves, the former is associated to oxygen groups in the basal plane that are too stable to be eliminated [54,64,66,72].

Finally, the resulting CV resembles to that of a pseudocapacitive material, with a nearly squared response with a peak at around -0.6V, see Fig. 2.16. It is worth mentioning that, in this case, the response was studied in negative potentials while, in the case of Engelhard et al. [47], they studied the -1.0 to 1V range.

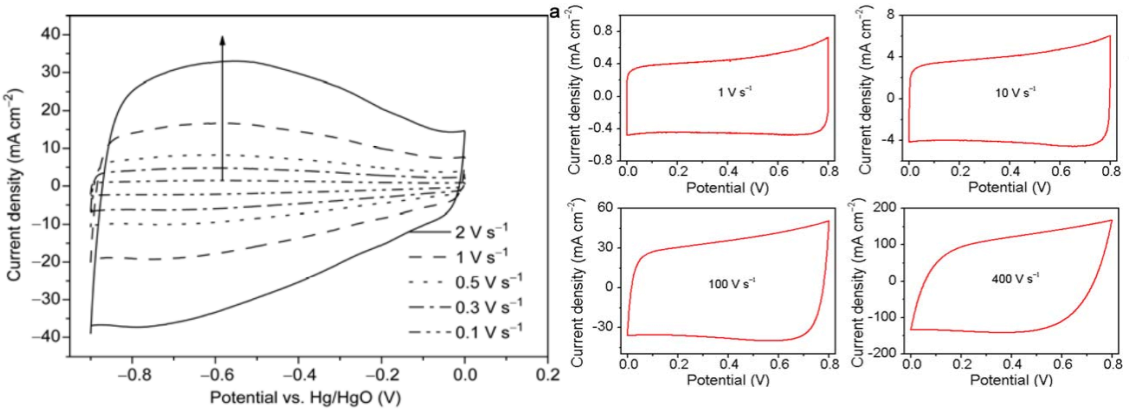

Fig. 2.16. Cyclic voltammetry curves for the electrochemical investigation of Er-GO deposited by the process presented in [65] and variations with scan rate for the Er-GO electrochemistry presented in reference [73]. Reprinted with copyright permission of [65] and [73].

The ease by which GO can be effectively reduced by electrochemical routes using aqueous electrolytes as solvent gave rise to numerous experiences in which Er-GO was applied. From Lipase enzyme biosensors based on Er-GO electrodeposited on ITO by a 60s chronoamperometry at -1.2V [74] to fundamental studies of the different properties of graphene derivatives [75]. Nonetheless, the field of supercapacitors and energy storage is probably one of the most affected by this achievement, which has been reviewed in the previous chapter.

2.1.5 Electrodeposition of nickel and cobalt oxides and hydroxides.

Nickel hydroxide

The electrochemical deposition of nickel hydroxide from nitrate solutions has been well studied. When considering the synthesis of nickel hydroxide, two main difficulties arise. Nickel hydroxide can crystalize in two different polymorphs, α and β, and it is a semiconductor that must be bonded to a conducting support. Electrodeposition enables the selective deposition of α or β by controlling the electrodeposition parameters and direct bonding to porous conductive substrates without binders or external agents [76]. Besides, one of the added benefits that electrodeposition imposes is that it can be applied to different substrates by adjusting the electrodeposition potential.

The electrodeposition of nickel hydroxide is carried out by the electrochemical reduction of salt solutions, which is a simple and yet effective technique whose reactions have been in-depth studied. In general, deposition currents of a few $mA \cdot cm^{-2}$ generate an α phase while larger currents tend to produce an α/β mixture. Nonetheless, it is difficult to predict the exact product phase, given the influential effect of salt concentration, deposition current, temperature, counterions, nature of the substrate, etc. [77]. Moreover, this process can be performed either anodically or cathodically [78].

Wu et al. introduced the **anodic electrodeposition** of $Ni(OH)_2$ nanoflake arrays by means of a mixed solution of $NiSO_4$, Na_2SO_4 and CH_3COONa [79]. Nonetheless, the most common route to produce nickel hydroxide is **cathodic** electrodeposition. Although many counter ions have been used, Cl^-, SO_4^{2-}, etc., NO_3^- is the most utilized anion. By placing a conductive substrate in a solution containing nickel (II) nitrate, in the electrolyte, and by applying a negative potential, the nitrate anions will reduce. This will lead to the production of hydroxyl ions that will react with Ni^{2+}, forming $Ni(OH)_2$, which has very low solubility and will immediately precipitate at the surface of the substrate [77]. It is worth mentioning that, during this process, the oxidation state of nickel does not change. While the nickel-hydroxyl reaction is well-established (eq. 2.18), the pre-required nitrate reduction is not, and it greatly affects the deposition efficiency.

$$Ni^{2+} + 2OH^- \leftrightarrow Ni(OH)_2 \qquad \text{(eq. 2.18)}$$

The reaction for the nitrate reduction is highly dependent on cathode material and pH of the bath. Four possible mechanisms for the reduction of nitrates were initially postulated by MacArthur [80]:

- Mechanism 1: Direct nitrate reduction to nitrous acid (eq. 2.19).

$$2NO_3^- + 4H^+ + 4e^- \rightarrow 2HNO_2 + 2(OH)^- \qquad \text{(eq. 2.19)}$$

$$Ni^{2+} + 2NO_3^- + 4H^+ + 4e^- \rightarrow 2HNO_2 + Ni(OH)_2 \qquad \text{(eq. 2.20)}$$

- Mechanism 2: Direct reduction to hydroxylamine (eq. 2.21).

$$NO_3^- + 5H^+ + 6e^- \rightarrow NH_2OH + 2(OH)^- \qquad \text{(eq. 2.21)}$$

$$Ni^{2+} + NO_3^- + 5H^+ + 6e^- \rightarrow 2HNO_2 + Ni(OH)_2 \qquad \text{(eq. 2.22)}$$

- Mechanism 3: Indirect reduction to nitrite (eq. 2.23 and 2.24).

$$2\ H_2O + 2e^- \rightarrow 2H^* + 2(OH)^- \qquad \text{(eq. 2.23)}$$

$$2H^* + NO_3^- \rightarrow H_2O + NO_2^- \qquad \text{(eq. 2.24)}$$

$$Ni^{2+} + NO_3^- + H_2O + 2e^- \rightarrow NO_2^- + Ni(OH)_2 \qquad \text{(eq. 2.25)}$$

- Mechanism 4: Indirect reduction to hydroxylamine (eq. 2.26 to 2.27).

$$12H_2O + 12e^- \rightarrow 12(OH)^- + 12H^* \text{(eq. 2.26)}$$

$$2\ NO_3^- + 12H^{+-} \rightarrow 2\ NH_2OH + 2\ H_2O + 2OH^- \text{(eq. 2.27)}$$

$$7Ni^{2+} + 2NO_3^- + 10H_2O + 12e^- \rightarrow 7Ni(OH)_2 + 2NH_2OH \text{ (eq. 2.28)}$$

Many more mechanisms have been postulated [76,81,82], however, recent results establish that the reaction mechanism may be caused by [83,84]:

- Nitrate to ammonium reduction (eq. 2.29):

$$NO_3^- + 7H_2O + 8e^- \rightarrow NH_4^+ + 10OH^- \text{ (eq. 2.29)}$$

- Nitrate to nitrite reduction and further reduction to ammonium (eq. 2.30 and 2.31):

$$NO_3^- + H_2O + 2e^- \rightarrow NO_2^- + 2OH^- \text{ (eq. 2.30)}$$

$$NO_2^- + 6H_2O + 6e^- \rightarrow NH_4^+ + 8OH^- \text{ (eq. 2.31)}$$

- Mixed route of eq. 2.29 to 2.31.

In any case, the overall route follows the nitrate to ammonium reduction [84]. Reactivity is important to understand since this step will determine the current efficiency of the reaction. Moreover, besides nitrate reduction, formation of hydrogen must be considered (eq. 2.32):

$$2H_2O + 2e^- \rightarrow H_2\ (g) + 2OH^- \qquad \text{(eq. 2.32)}$$

However, there are still some undergoing studies in that regard [85].

Nickel hydroxide electrodeposition from nickel nitrates involves several parameters that are very important, such as $[OH^-]/[Ni^{2+}]$ ratio [83,86–88], which correlates to the α/β ratio. Furthermore, this $[OH^-]/[Ni^{2+}]$ ratio is controlled by applied current density. When high absolute current densities are applied (<-500 $A \cdot m^{-2}$), the β phase is produced, while a mixture of phases is obtained for lower current densities (50-500 $A \cdot m^{-2}$) [85]. Moreover, when the current density is higher, the current efficiency is also increased [89]. Nickel nitrate concentration also affects this ratio while pH has an influence on potential variation, but it does not affect electrode kinetics and its effect is insignificant.

At low concentrations, the Faradaic efficiency of the deposition is nearly 100%, this is for a concentration below 0.2M and at 0.5mA·cm^{-2}. For every two mols of OH^- produced at the surface, nearly one mol of $Ni(OH)_2$ is obtained, as observed in Fig. 2.17. However, at higher concentrations, this efficiency can decrease to 10-20% [90]. Moreover, the concentration of nickel is the most important aspect in the efficiency of the deposition. When the electrolyte is varied and saturated in nitrates, the efficiency only drops to 75% while acidification changes the deposition rate by less than a 10%. At all currents, the utilization of hydroxyl ions is 100% for dilute concentrations and 10-20% for concentrated electrolyte. Below 0.02M, some mass transportation effects for Ni occur and there is a limit for the total mass deposited) [90].

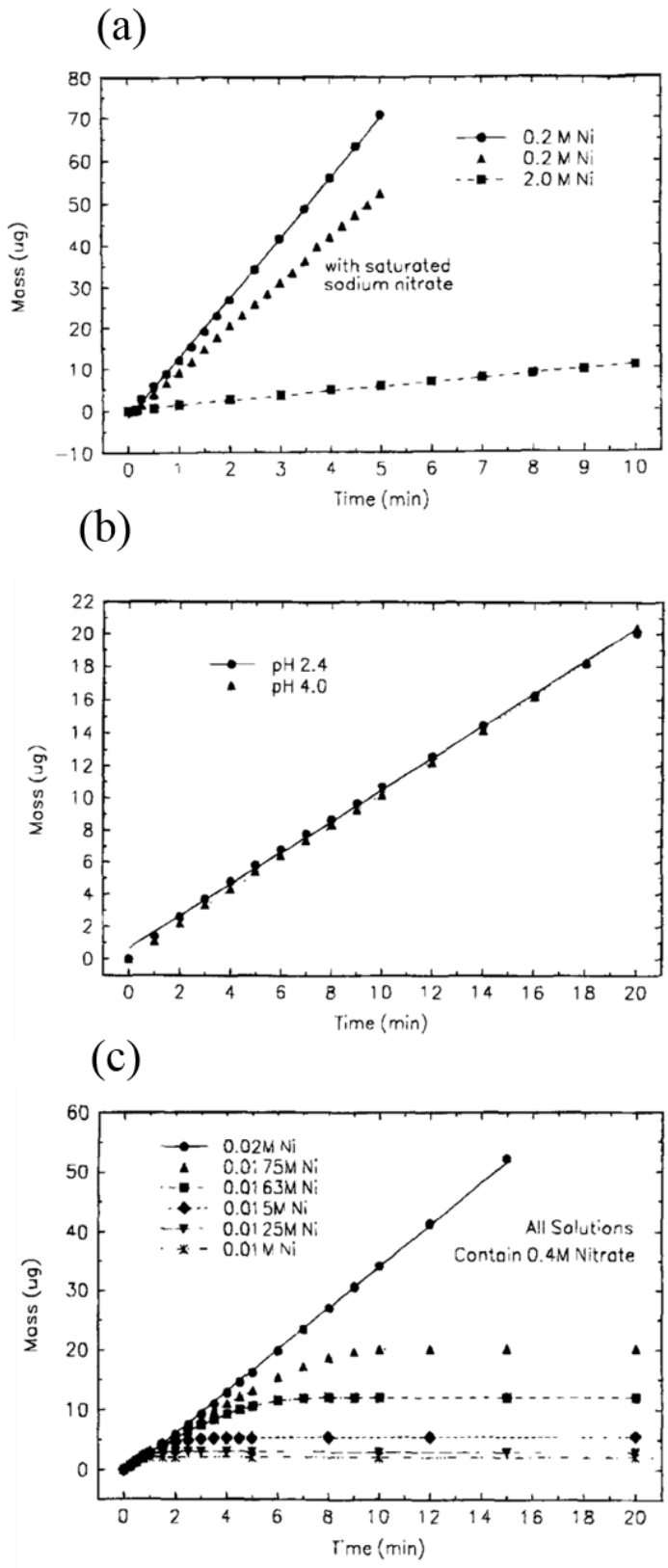

Fig. 2.17. (a) Variation of mass vs. time for 0.2M $Ni(NO_3)_2$, 2.0M $Ni(NO_3)_2$ and 0.2M $Ni(NO_3)_2$ saturated with $NaNO_3$. (b) Mass vs. time for deposition of 2.0M $Ni(NO_3)_2$ in basified conditions. (c) Mass vs. time at 0.1 mA in diluted $Ni(NO_3)_2$ solutions (<0.2M). Reprinted with copyright permission of [90].

An increase in temperature produces a decrease in current efficiency, while density is increased. Nitrate ion concentration has a marginal effect on the electrodeposition process. Finally, increase in current density produces alterations in particle size. At higher current density bigger particles are produced and it has been proven that the smaller the crystalline size, the better the charge-discharge performance of the material [89]. The effect of nitrate concentration, nickel concentration, temperature, particle size and temperature are displayed in figure 2.18. The effect of ethanol was also studied and resulted to be insignificant for current efficiency (this is, the amount of electrodeposited material, apart from when 100% ethanol was used) while increased molecular weight, confirming that solvent was trapped during the deposition [82]. This led to better results for a 50% ethanol content.

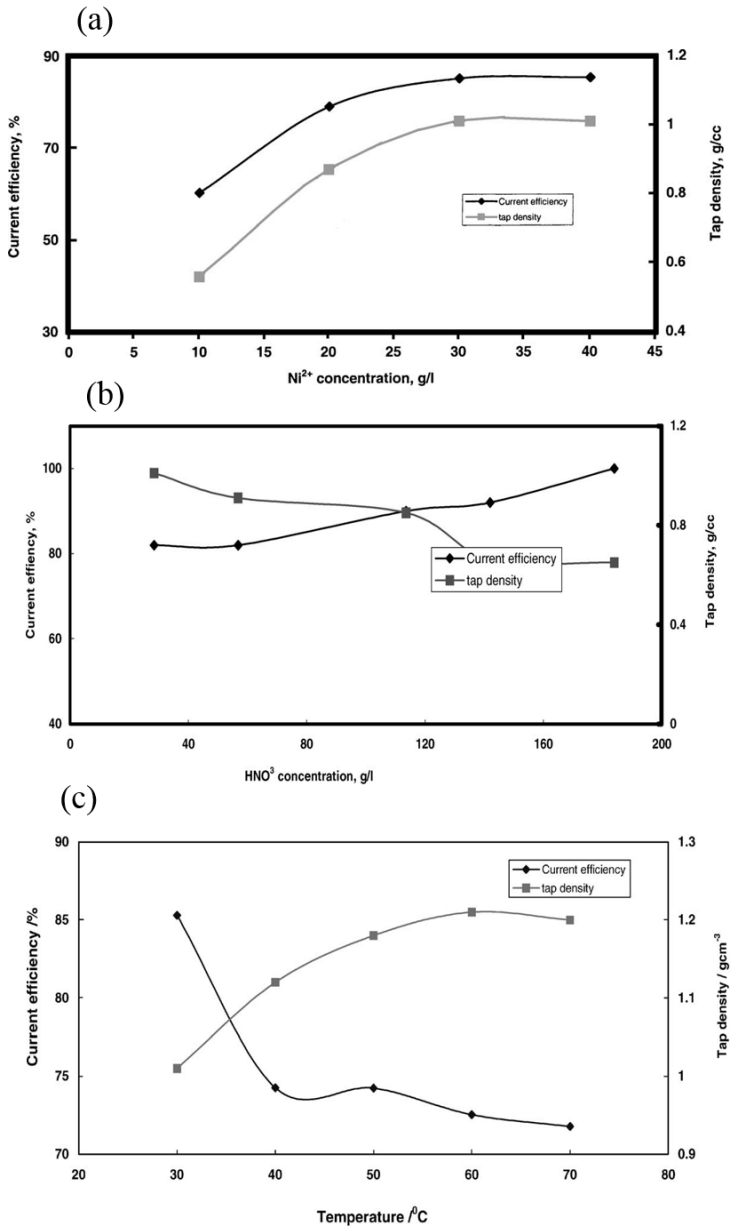

Fig. 2.18. Effect of (a) nickel concentration, (b) nitrate concentration and (c) temperature in the current efficiency and density of nickel hydroxide electrodeposited films. Reprinted with copyright permission of [89].

Finally, nickel hydroxide deposited at current densities below -1.0 $mA \cdot cm^{-2}$ display the highest density and tend to agglomerate, while at higher current densities certain porosity was observed and the material consisted of small particles of approximately 0.1µm of diameter [91].

$NiSO_4$ and $NiCl_2$ have also been used as precursors of $Ni(OH)_2$ electrodeposition [92][93]. Slightly different properties can be achieved since the intercalated ion in α phases has certain influence in the electrochemical properties of the material. However, the exact mechanism of these anions is not as studied as nitrates.

To summarize, nickel hydroxide electrodeposition is usually performed galvanostatically at current densities in the -0.1 to -5 $mA \cdot cm^{-2}$ range, or at -0.8V vs. SCE [94] or by means of cyclic voltammetry from 0.0V to -0.7V at 10 $mV \cdot s^{-1}$ [95,96] for 90 seconds to 6 minutes, from nickel nitrate dissolved in mineralized water that may contain up to 50% ethanol since Weider et al. found that it may lead to better results [82,90,97].

Moreover, nickel oxide can again be obtained by annealing at 300ºC for 2h [78]. Thus, it is generally first electrodeposited and then thermally treated to oxidize it [97]:

$$Ni(OH)_2 \rightarrow NiO + H_2O \qquad \text{(eq. 2.33)}$$

$$NiOOH \cdot H_2O + e^- \rightarrow Ni(OH)_2 + OH^-,\ Ni(OH)_2 \rightarrow NiO + H_2O \qquad \text{(eq. 2.34)}$$

Cobalt hydroxide

Most of the publications concerning the electrodeposition of cobalt hydroxide involve cathodic electrodeposition. As in the case of nickel hydroxide electrodeposition, two polymorphs, α and β, can be obtained and nitrate salts are often used. Using other cobalt sources leads to other products because of the unique reaction mechanism to form cobalt hydroxide [78]. For example, in the presence of chloride anions, hydrogen peroxide is formed and stabilizes Co(III) [98]. Nonetheless, some groups have achieved electrodeposition from acetate precursors [99] or anodic deposition from sulphate precursors [100].

The overall reaction also depends on the nitrate reduction and cobalt precipitation in alkali media, as exemplified in eq. 2.35 [101–103]:

$$Co^{2+} + 2OH^- \rightarrow Co(OH)_2 \qquad \text{(eq. 2.35)}$$

This reaction can be done on top of numerous conductive substrates. Besides, cobalt metal cannot be deposited due to the much more negative potential of the Co(II)/Co(0) reduction potential when compared to the NO_3^-/NO_2^- potential [104]. Electrodeposited cobalt hydroxide exhibits a nanosheet-like structure that forms a percolation network [78].

Cobalt responds in a similar way to nickel to variation in temperature, cobalt concentration and nitrates concentration [89]. Similar morphologies are obtained for increasing current densities from -0.5 $mA \cdot cm^{-2}$ to -1.5 $mA \cdot cm^{-2}$. However, at more positive currents, the material presents increased porosity [104].

Lokhande et al. [105] studied different modes to electrodeposit cobalt hydroxide, namely, galvanostatic deposition at -3 $mA \cdot cm^{-2}$ for 5 minutes, potentiostatic deposition at -0.9V vs. SCE for 5 minutes and cyclic voltammetry at 50 $mV \cdot s^{-1}$ in the 0.0V to -1.2V vs. SCE for 30 cycles. They concluded that different modes induce different porosity, morphology, density and microstructure, as depicted in Fig. 2.19. Consequently, the

materials have different electrode-electrolyte interaction, which is reflected in the final electrochemical properties of the material [105].

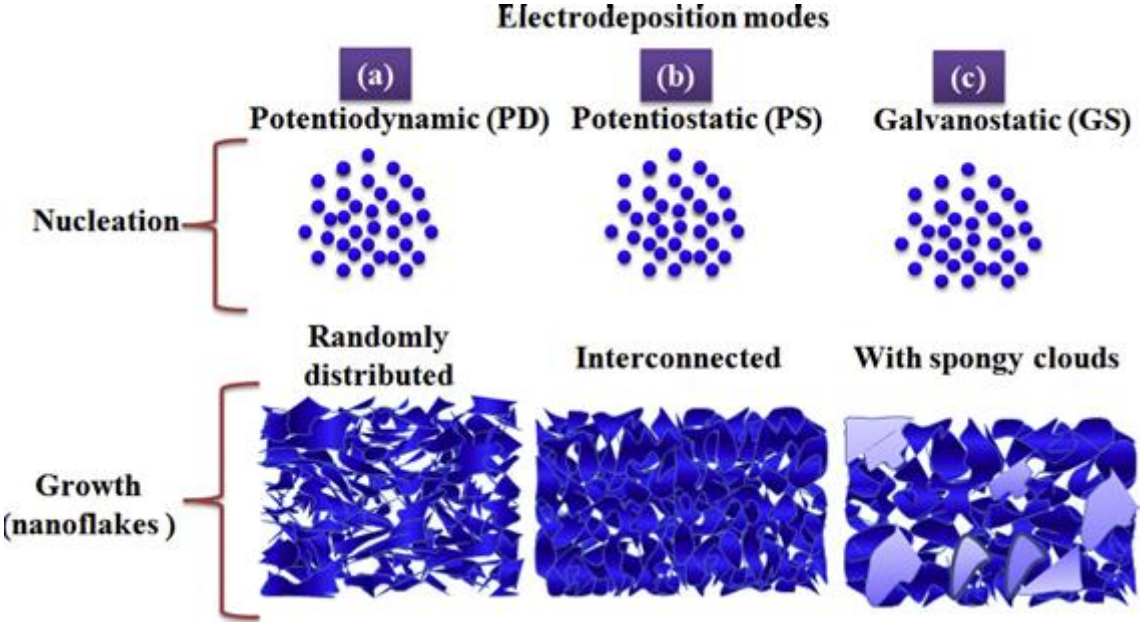

Fig. 2.19. Morphological variations caused by different electrodeposition modes for cobalt hydroxide. Extracted from [105] with copyright permission.

Porosity can be tailored by controlling the deposition parameters, such as cobalt concentration. Nanoflake size is reduced for lower concentrations (0.025M), leading to a more porous material. When higher concentrations are used (0.1M), less porous structures are obtained, leading to worse electrochemical response for energy storage applications. Less negative applied current (-100 $mA \cdot g^{-1}$ as compared to -200 $mA \cdot g^{-1}$ or -400 $mA \cdot g^{-1}$) also lead to thinner films that are more accessible by the electrolyte [101]. Higher temperature or pH seem to increase the amount of deposited material, although tests were done in glycine-containing electrolyte and further studies are required [106].

Kamath et al. [107,108] studied the effect of the applied current density in the resulting phase of cobalt hydroxide. At higher current densities (-0.15 $mA \cdot g^{-1}$), the formation of α phase is favoured due to the simultaneous chemical corrosion of the substrate with electrodeposition. Chemical corrosion leads to the formation of basic salts, isostructural to α-nickel hydroxide, that are related to the formation of α phase, since they promote its nucleation and growth. When these basic salts are formed, the anions in the basic salts are loosely bonded to nickel hydroxide sheets. This loose intercalation causes the disordering of the sheets leading to a turbostratic structure. When intermediate currents are applied (-0.3 $mA \cdot g^{-1}$) a mixed α/β phase is obtained. Higher currents supress chemical corrosion (hydrogen evolution acts as a protective coverture of the electrode, impeding the formation of basic salts), favouring β phase due to the ordered stacking of the hydroxide nanosheets in nitrate media. Hun-Lin et al. [109] also evaluated the effect of potential in potentiostatic electrodeposition and concluded that the best potential was -0.75V vs. SCE, value at which diffusion and kinetic controlled. At more positive potentials, the process was kinetically controlled while it was diffusion-controlled at more negative values of potential. Moreover, they evaluated the morphology of the material and determined that at potentials <-0.85V vs. SCE, the surface is rough and cracked. When potential is increased from -0.85V to -0.65V vs. SCE, the size of the nanosheets increases, as shown in Fig. 2.20. It was concluded that at -0.85V vs. SCE a mass-transport-controlled dense material was formed while at -0.65V vs. SCE surface

smoothness reduced pore size and therefore electrolyte penetration. Finally, they studied the effect of temperature and reported that at lower temperatures (28°C and 40°C) the material is very dense with narrow area of nanosheets. When temperature is increased to 50°C, the surface becomes smoother, however, at higher temperatures it becomes irregular and coarse. It is worth mentioning that electrodeposition in this study was, nonetheless, in presence of Brij 56 surfactant as 50% of solvent on top of titanium working electrode that acts as a hexagonal liquid crystalline template and may affect ultimate results.

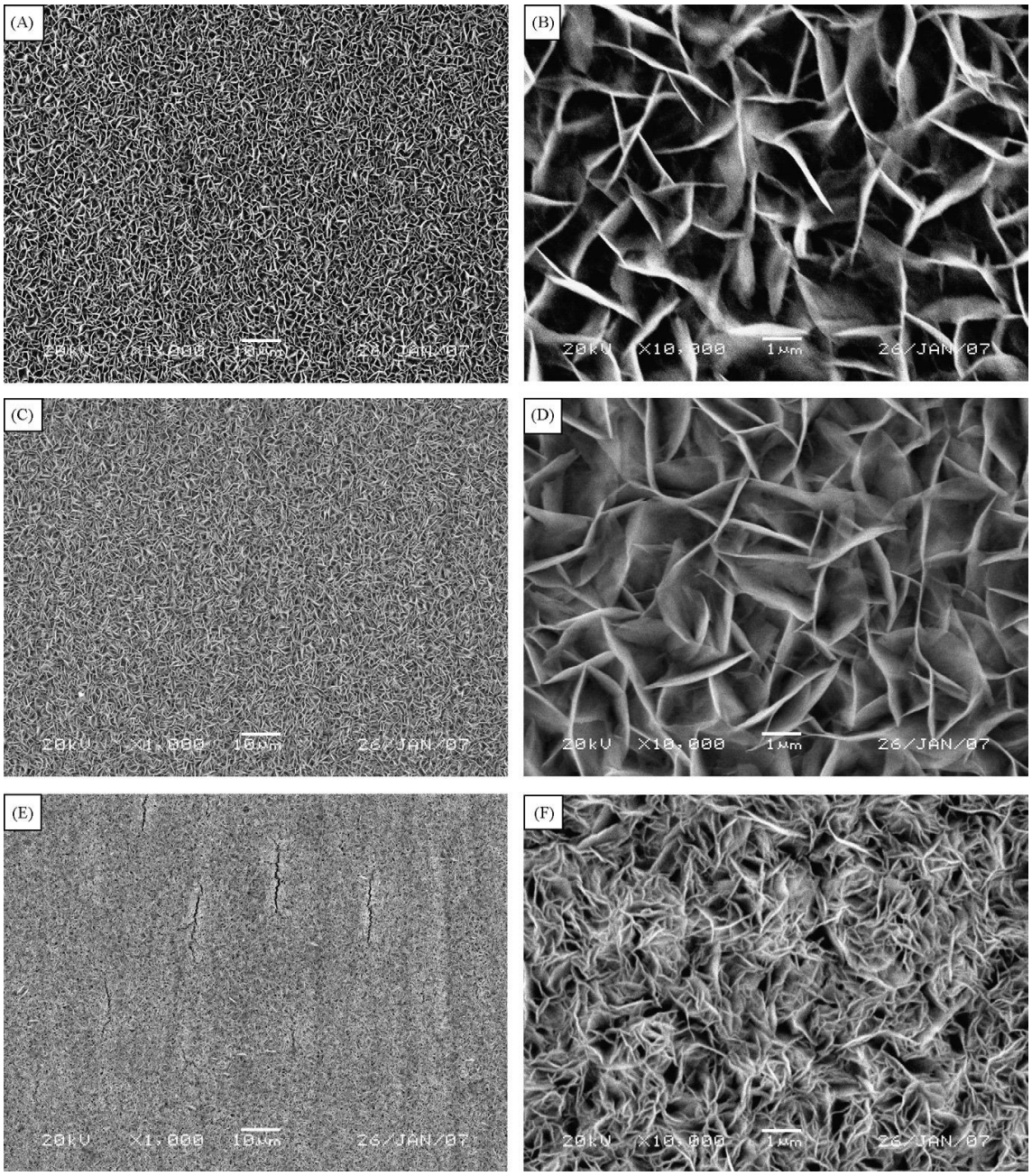

Fig. 2.20. Morphology of cobalt hydroxide electrodeposited at (A), (B) -0.65V, (C),(D) -0.75V and (E), (F) -0.85V at 50°C from cobalt nitrates in aqueous electrolyte containing 50% in weight of surfactant Brij 56. Reprinted with copyright permission of [109].

The effect of different nitrate and nitrite concentration was also considered. By reducing the concentration of these anions (<0.1M), the material is prone to generate

nanostructures, while bulk microstructures are produced at higher concentrations. Moreover, α phases were formed at 60ºC, while β phases were obtained when electrodeposition was carried out at 90ºC [98,110]

Moreover, the nitrate mechanism is expected to be analogous to the one explained for nickel hydroxide [101,110–112]. However, there are few studies investigating the effect of different parameters in this synthetic procedure. Given that the electrodeposition parameters are not as well-defined as in the case of nickel hydroxide, Table 2.3 includes some of the main references regarding cobalt hydroxide electrodeposition.

As a final note, as it is the case for nickel oxide, cobalt oxide is obtained by thermal annealing at 300ºC for 2h of the hydroxide parent [100,104,112,114–116].

Table 2.3.

Summary of some of the main work concerning electrodeposition of cobalt hydroxide.

Cobalt precursor	Concentration ($mol \cdot L^{-1}$)	Applied current /potential	Dep. time (min)	T (ºC)	Substrate	Phase	Ref.
$Co(NO_3)_2$	0.025 to 0.1	1.0 $mA \cdot cm^{-2}$	-	-	Ni sheets	β	[101]
$Co(NO_3)_2$	0.01	-1V vs. Ag/AgCl	-	-	SS 304	β	[102]
GO **PEG** **$Co(NO_3)_2$** **$NaNO_3$**	0.3g 0.1g 0.05M 0.075M	-1.0V vs. Ag/AgCl	5	RT	SS	-	[103]
$Co(NO_3)_2$	0.025	1.0 $mA \cdot cm^{-2}$	3, 10, 20	-	SS	-	[113]
$Co(NO_3)_2$	0.1	1.0 $mA \cdot cm^{-2}$	15	RT	SS304	α	[111]
$Co(NO_3)_2$	0.05	-1.0V vs. SCE	20	RT	Ni Foam	α	[114]
$Co(NO_3)_2$	0.1	-1.0V vs. Ag/AgCl	4	-	Ti foil	α	[112]
$Co(NO_3)_2$ **$NaNO_3$**	0.9 0.075	1.0 $mA \cdot cm^{-2}$	10	-	Ni foam	α	[100]
$CoSO_4$ **Na_2SO_4** **$Na(CH_3COO)$**	0.25 0.25 0.2	Anodic current 0.25 $mA \cdot cm^{-2}$	60	-	Ni foam	γ	[100]
$Co(NO_3)_2$ **$NaNO_3$**	1.0 0.1	0.5 $mA \cdot cm^{-2}$	6.6	20ºC	Ni foil with PS template	-	[115]
$Co(NO_3)_2$ **$NaNO_3$** **$EtOH/H_2O$ solv.**	0.175 0.075	1.0 $mA \cdot cm^{-2}$	8	RT	Au	-	[116]
$Co(CH_3COO)_2$	0.1M	-0.75V vs. SCE	Up to 50$mC \cdot cm^{-2}$ total charge	RT	Ni foil	-	[99]

2.2 Chemical exfoliation

Chemical exfoliation routes are not as well studied and well-established as electrodeposition techniques for nickel and cobalt hydroxides and oxides. In fact, it has only been recently, after the synthesis of graphene in 2004 by Novoselov et al. [117], that the synthesis of 2D materials has been extensively studied.

The unexpected properties of graphene provoked an increasing interest in the production of 2D nanomaterials and the exciting potential properties that they could have. 2D structured materials are nanostructured in nature, and therefore differ from their analogous bulk materials: they present unprecedented properties that are related to their size domains and the electronic confinement and quantum properties thereof [118].

The exfoliation of many different layered materials is being studied and have been classified in eleven major groups, as shown in figure 2.21 [119]: hexagonal-boron nitride (h-BN), transition metal dichalcogenides (TMDs; MoS_2, TiS_2, TaS_2, etc.), grafitic carbon nitride (g-C_3N_4), layered metal oxides, layered metal hydroxides (LDHs), metal-organic frameworks (MOFs), covalent-organic frameworks (COFs), polymers, metals, black phosphorus (BP), and MXenes (including silecenes).

Similar to the case of graphene, two-dimensional structures have been achieved by many different routes, such as mechanical cleavage, liquid exfoliation, ion intercalation, anion exchange, chemical vapour deposition, etc. [119]. These techniques are always subjected to the strength of the interlayer interaction, for that reason, most of the techniques rely on the weakening of those interactions as a prior step to a successful exfoliation [118].

Besides electronic confinement, their atomic thickness offers, in general, excellent mechanical properties and optical transparency. Their properties are tuneable by means of external stimulus, such as chemical bonding or mechanical deformations and they have high active surface areas, related to the exposed surface of the atoms in these nanostructures. Given these properties, many different applications, from catalysis to opto-electronics can benefit from the 2-dimensional nature of single-layer materials [119].

Given the wide range of 2D materials that have been studied and the different techniques that can be applied to exfoliate them, only those procedures related to the chemical exfoliation of LDHs and metal oxides, with special focus on nickel and cobalt oxides and hydroxides are considered in the present work.

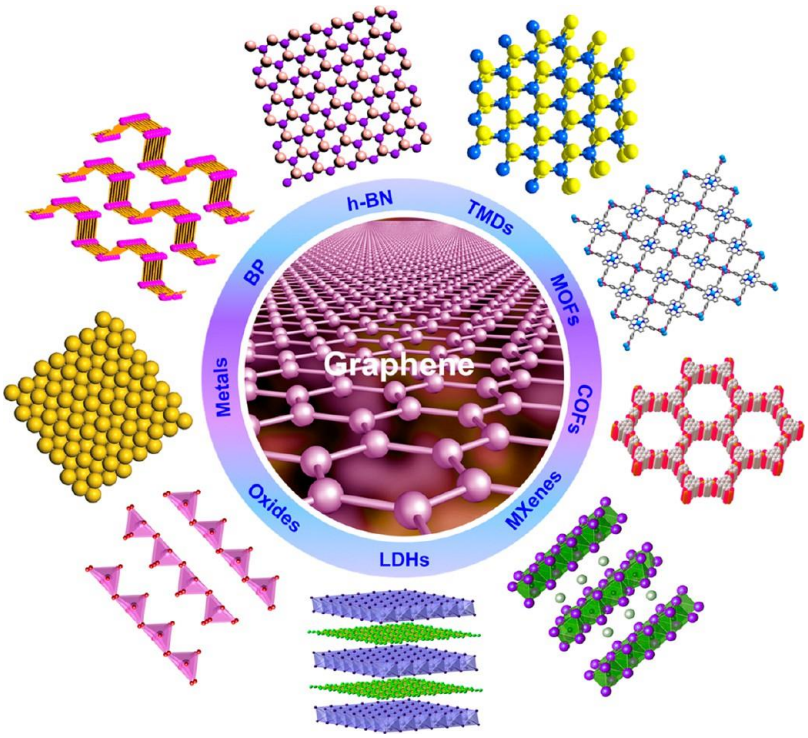

Fig. 2.21. Illustration of the different groups of 2D nanomaterials whose delamination is currently under investigation. Reprinted with permission of [119].

2.2.1 Chemical exfoliation of nickel-cobalt LDHs

Layered double hydroxide nanosheets (LDHs) materials are a class of ionic lamellar compounds made of brucite-like layers with positive charge and an inter-lamellar space containing charge compensating anions and solvating molecules. In these, metal cations occupy the centre of edge-sharing octahedra that have hydroxide ions in the vertex, forming infinite 2D sheets. They have a generic formula $[M^{2+}_{1-x}M^{3+}_{x}(OH)_2][A^{n-}]_{x/n}\cdot zH_2O$ where M^{2+} can as an example either be Mg^{2+}, Zn^{2+} or Ni^{2+} and M^{3+} may be Ga^{3+}, Fe^{3+}, Mn^{3+}, Al^{3+}or Co^{3+}. The high energy density and ion content in the interlayer space result in strong interactions with hydrophilic properties. For that reason, it is quite challenging to achieve exfoliation of two-dimensional layers in water. As a result, many research groups have been focused on the delamination in organic solvents such as formamide [120].

Generally speaking, there are two main approaches in the synthesis of LDHs nanosheets, namely, top-down and bottom-up. While top-down strategies are based on the modification of the inter-lamellar space that enables subsequent delamination in the right solvent; in the bottom-up approach reverse micelles are formed by introducing traditional co-precipitation into an oil phase.

Bottom-up exfoliation

The first time bottom-up exfoliation was used, it was performed by Hu et al., who used a reversed micro-emulsion method. They used co-precipitation of magnesium nitrates with aluminium nitrates at pH>10 and introduced it into an oil phase of isooctane with DDS and 1-butanol as surfactants [121]. In that manner, the aqueous phase, in which the co-precipitation reaction is undertaken, is dispersed in the oil phase in the form of droplets that are surrounded by DDS. The size-limited micro-droplets, formed by Na-DDS and 1-Butanol encapsulating water, control the size of the particulate created. Thus, by choosing the right ratio of solvents, tailored-size particles are achieved to the extent of producing

single layer LDH nanosheets. This system has been recently expanded to other LDH materials such as Ni-Al [122] and Co-Al [121] LDHs, but this field is still much less developed than its top-down counterpart. This route, however, was not yet considered in the exfoliation of Ni-Co LDH materials.

Top-down exfoliation approaches

Generally, LDH materials are intercalated with surfactant molecules, such as dimethyldicholorosilane (DDS), intercalated prior to exfoliation. The aliphatic tail of DDS, which is negatively charged, exhibit high degree of interdigitation. If the solvent molecules can solvate the hydrophobic tails of the intercalated anion, delamination becomes possible. Exfoliation has been achieved in different solvents, namely; butanol, acrylates, chloroform, toluene, formamide, N, N-dimethylformamide and, finally, water. An overview for the exfoliation process and materials affected for each solvent is here introduced.

The first reported delamination was achieved by Adachi-Pagano et al in 1999, when they delaminated Zn-Al-NO_3 using DDS as surfactant and butanol as solvent [120,123], although more solvents were considered. Similar results have been achieved with higher alcohols such as pentanol and hexanol, but the exfoliation in water, hexane, ethanol or propanol was unsuccessful. Methanol was only partially successful.

One key parameter during this exfoliation was the hydration state of the LDH material since delamination was only achieved when pre-drying treatment was undertaken. However, not all LDH materials can be achieved in butanol, such as Li-Al LDHs. Thus, dependence on the surfactant in terms of length and headgroup, the hydration state of the material among other parameters shall be considered [124].

O'Leary et al. studied exfoliation routes in polar acrylate monomers (HEMA, ethyl-methacrylate, methyl methacrylate, ethyl-acrylate and methyl acrylate) for Mg-Al-DDS. After thermal treatment at 70^{o}C and subjecting the mixtures to high shear, delamination was achieved [125].

Mg-Al-DDS was delaminated in CCl_4 by Jobbágy and Regazzoni. CCl_4 and toluene expanded the hydrophobic interlayer space. However, in the presence of CCl_4, the inorganic sheets lose their correlation, being successfully delaminated [126]. However, posterior evidence of exfoliation of Mg-Al, Co-Al, Ni-Al and Zn-Al LDHs materials has been obtained in toluene by means of stirring and sonication in toluene suspended LDHs. Mg-Al-CO_3 LDH was also exfoliated in N,N-dimethylformamide mixed with ethanol by induced de-carbonization [127].

The first delamination in formamide was conducted by Hibino and Jones [128], who used Mg-Al-glycine and the strong hydrogen bonding between intercalated anions and the polar solvent to create a colloidal exfoliated dispersion. Later, they applied an analogous procedure to delaminate Ni-Al, Co-Al and Zn-Al LDHs materials [129]. Some other amino acids were also used with successful results when the amino-acid content did not exceed a 15-20% of the charge occupation rate. Later, Mg-Al-NO_3 was exfoliated in formamide with mechanical shaking by Sasaki et al. [130] and ultrasonic treatment by Wu et al. [131]. Hibino et al. tested different polar solvents and observed that formamide was the only solvent capable of penetrating the interlayer space of the LDH materials and suggested hydrogen bonding as the driving force of this interaction [129].It is assumed that formamide, being highly polar, would have a strong interaction with the hydrogen bonds presents in the hydroxyl layers, expelling the water molecules present in the interslab space. There is a replacement that weakens the interaction between the LDH

layers, due to the weaker bonding nature of the NH_2 bonds at the end of the formamide chain. Again, this procedure has been expanded to Co-Al, that was studied with a different range of intercalated anions [132], Zn-Al, Zn-Co-Al, Ni-Fe and Ni-Al [133,134].

Although not strictly LDH material, due to their structural similitudes, studies on the exfoliation of $Ni(OH)_2$ and $Co(OH)_2$ were also undertaken. The first time the exfoliation of nickel hydroxide was reported, it was done by Matsumoto et al. who first intercalated SDS surfactant ions in the inter-lamellar space that enabled their exfoliation in formamide [135]. Other intercalated molecules, such as urea[136], have also been used for the same purpose. An alternative route was employed by Cui et al, in which β-$Ni(OH)_2$ was synthesized by means of a sol-gel route including nickel chloride in benzyl alcohol, glycidol and carbon tetrachloride [137].

On the other hand, Sasaki et al. produced cobalt hydroxide exfoliated nanosheets and tuned their morphology, forming SDS-intercalated cobalt hydroxide in nano-cone shape by means of a microwave assisted exfoliation[138]. α-$Co(OH)_2$ was also exfoliated by precipitating cobalt aqueous complexes with propylene oxide to produce α-$Co(OH)_2$ that exfoliates in formamide [139].

Sasaki et al. also reported the topochemical synthesis and exfoliation of LDHs materials by means of homogeneous precipitation of an aqueous solution of divalent cobalt and iron through HMT hydrolysis under nitrogen gas atmosphere. Then, iodine in chloroform was used in an oxidative intercalation, followed by ion-exchange and ultrasonication that would exfoliate the material into unilamellar nanosheets [140]. Later, they applied a similar synthesis route for nickel-cobalt hydroxide materials. They co-precipitated nickel-cobalt LDH from chloride solutions in reflux, treated the resulting material in acetonitrile/bromine solution and posterior anion exchange and, finally, exfoliated the material in formamide[141].

This route was considered for nickel-cobalt LDH materials. Co^{2+}-Co^{3+} and Co-Ni LDHs were, therefore, successfully exfoliated in formamide[141,142]. For the first time, Ni-Co LDHs were delaminated into single nanosheets. However, these suffer re-stacking upon washing with water, drying and ageing [130,143].

An alternative method was used by Hu and Song for OER studies. In their study, Co-Co and Ni-Co LDHs were delaminated by means of a topochemical approach with Br^- ions by oxidizing the corresponding hydroxides in a Br_2/acetonitrile solution, followed by anion exchange in ethanol/water sodium nitrate solution and delamination in formamide [144].

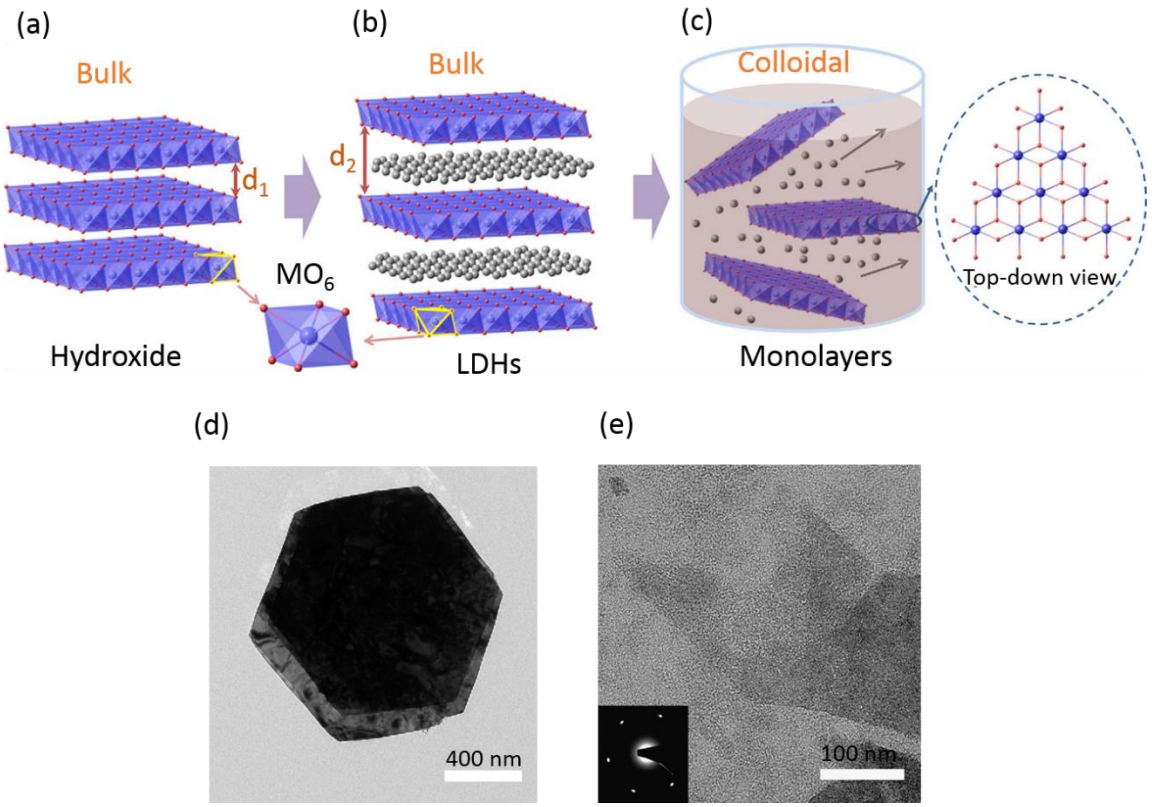

Fig. 2.22. Schematic representation the exfoliation process undergone and the corresponding materials' structures. (a) Representation of a hydroxide material with d_1 as interlayer distance. (b) LDHs structure with inter-slab anions and water molecules. (c) Exfoliated LDH monolayers in colloidal suspension. Each layer corresponds to edge-sharing octahedral MO_6 unities where M denotes a metal element. (d) Transmission electron microscopy image of bulk LDH Ni-Co material. (e) Transmission electron microscopy image of single-layer exfoliated Ni-Co LDH. Reprinted with permission of [144].

To prevent re-stacking, Kang et al. added carboxymethyl cellulose (CMC) to their topochemical approach. The introduction of CMC enables the nanosheet to be attached to it without destroying its colloidal state[143].

Jin et al. further developed topochemical routes by controlling the precursor morphology. For that purpose, they developed a hydrothermal continuous flow reaction in which synthesis conditions could be manipulated to control the morphology and size of the LDH platelets. Then, they proceeded with exfoliation of said materials in formamide while avoiding the oxidation step by introducing oxygen in the precursor formation solution and directly oxidize the material. Their work brought light to the effect of precursor morphology in the exfoliation process and avoided one of the intermediate steps required in the topological standard synthesis [145].

Nonetheless, the use of organic solvents is being substituted by water as solvent due to its lower cost and environmental impact. The first delamination reported in water was achieved by Gardner et al.[146], who hydrolysed Mg-Al-methoxide in water at room temperature. However, to achieve this delamination process, the parent alkoxide-LDHs must be synthesized in non-aqueous media.

To avoid using a non-aqueous solvent in the synthesis process, Hibino et al. used Mg-Al-lactate that, once rinsed or stored and matured in water, delaminate without the need of

thermal treatment. This was considered to be a consequence of the interaction of lactates, which were in a large stoichiometric excess, with water. In a similar fashion, Zn-Al-lactate [147], was exfoliated. Moreover, upon drying, all samples restacked giving a better ordered layer stacking arrangement.

Nethravathi et al were one of the first groups to claim exfoliation of nickel-cobalt hydroxides in water [148]. Although they had previously reported the exfoliation of said material in organic solvents such as butanol [149], in their attempt to exfoliate the material in aqueous solution, they intercalated p-Aminobenzoate ions in the interlamellar space of the LDH material by means of precipitation in ammonia. In the washing process, once the supernatant solution reached a pH of 7, a colloidal suspension of nanosheets was produced [148]. They later exfoliated α phases of nickel and cobalt by means of *p*-aminobenzoate intercalation and subsequent exfoliation in water. Then, they mixed the colloidal dispersions and co-stacked them by adding nitrate ions and studied their electrochemical properties for supercapacitor applications [150].

Ma et al. produced free-standing α-$Co(OH)_2$/GO thin films by means of acetate-intercalated cobalt hydroxide delamination. Although they could ultimately delaminate the nanosheets in water, the process required DMF to allow the exfoliation process. Once exfoliated, it was mixed with a GO suspension. Given the different surface charge in both, a flocculation driven electrostatic process occurred [151].

The chemical delamination of nickel hydroxide, cobalt hydroxide and nickel-cobalt hydroxide in water was thoroughly investigated by Schneiderová [152–154] in a similar process to that of Hibino et al. [155] for Mg-Al LDHs. They exfoliated the three hydroxides following analogous procedures. Thus, they first synthesized dodecyl sulphate (DS^-) intercalated hydroxide materials by hydrothermal precipitation in presence of HMT. Then, they proceeded to the anion exchange of DS^- by lactate molecules in a $H_2O/CHCl_3$ mixture in the presence of CTAB. During the anion exchange reaction, the lactate intercalated hydroxide materials would become exfoliated when interacting with water. Furthermore, they investigated the electrochemical properties of the nanosheets after spin-coating and drop-casting on top of HOPG in KOH 1M. However, these materials were not extensively studied for energy storage purposes [152,153,156].

2.2.2 Chemical exfoliation of nickel-cobalt oxides

The delamination of nickel and cobalt oxides is less studied than the exfoliation of nickel and cobalt LDH materials. Nickel is usually exfoliated by means of alpha-nickel hydroxide and no report has been found regarding its delamination despite its layered structure. As seen in Fig. 2.23, Sasaki et al. reported the formation of a highly swollen nickel oxide phase by means of bromine oxidation and acid treatment. However, exfoliation was not reported[157].

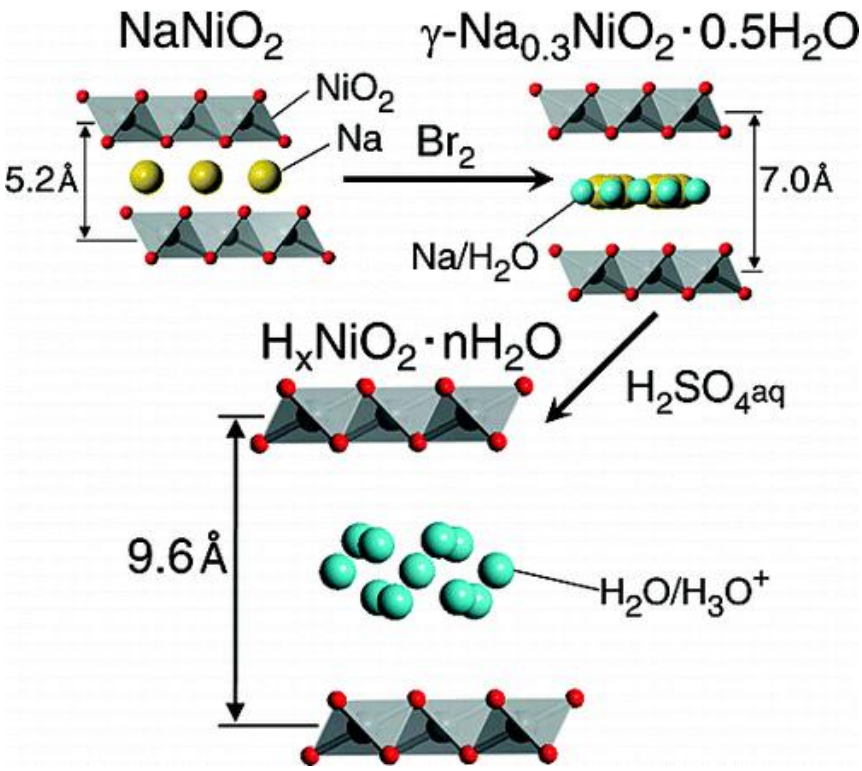

Fig. 2.23. Interlamellar expansion process for nickel oxide. Reprinted with copyright permission of [157].

On the other hand, the delamination of cobalt oxides was first reported by Kim et al. An initial attempt undergone by Masuda et al. to exfoliate $Na_{0.7}Co^{3.3+}O_2$ through the intercalation of ethylamine only resulted in the formation of rocksalt-structured $Co^{2+}O$ nanocrystallites due to the instability of $Co^{4+}O_2$[158,159]. The first successful attempt consisted on the exfoliation of $LiCoO_2$ in tetramethylamine hydroxide (TMA-OH). After $LiCoO_2$ preparation, it was subjected to proton exchange in HCl 1M followed by its reaction with tetramethylammonium hydroxide in a TMA^+/H^+ ratio of 0.15-75 and centrifugation at 6000 rpm for 10 minutes. Then, they proceeded to their stacking by means of layer-by-layer self-assembly or electrophoretic process[158].

An alternative method developed by the same group involved synthesis of $Na_{0.7}CoO_2$ that was subsequently oxidized to cobalt oxide mono- or bi-hydrate ($Na_{0.35}CoO_2{\cdot}0.6H_2O$/ $Na_{0.35}CoO_2{\cdot}1.3H_2O$) by means of $Na_2S_2O_8$. Finally, the material was exfoliated into Na_xCoO_2 nanolayers by reaction with organic amine or ammonium compounds[160,161]. The work reported the enhanced thermoelectric properties of 2D-nanostructured cobalt oxide after exfoliation of $Na_{0.7}CoO_2$ and restacking with $CaCl_2$.

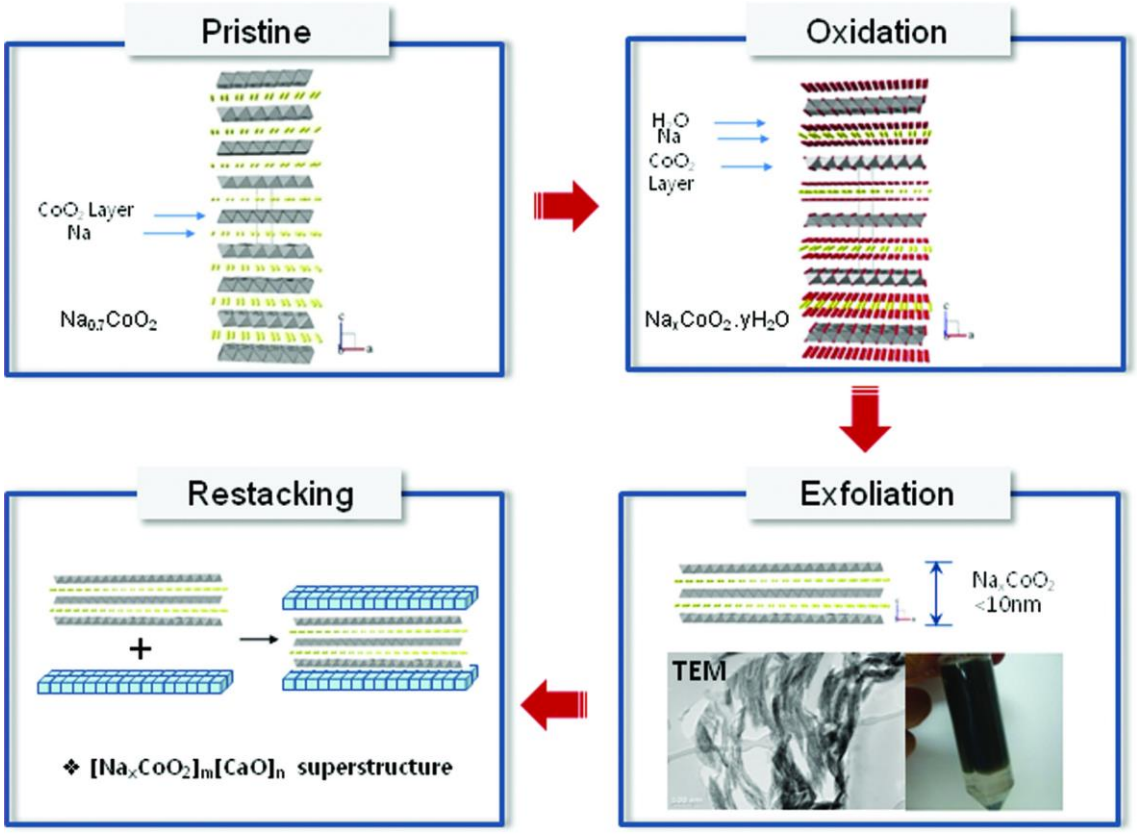

Fig. 2.24. Exfoliation and restacking procedure followed by Kim et al. Reprinted with copyright permission of [160].

Owen et al.[162] synthesized $HCoO_2$ as precursor material in which TBA^+ was intercalated. The intercalation of the sterically large cation in the interslab distance promoted the delamination of $HCoO_2$ when ultrasonicated, producing $[CoO_2]^-$ nanosheets while the excess of H^+ is neutralized with excess of hydroxide material. Different combination of reactants such as $LiCoO_2$/TBA-OH, $LiCoO_2$/LiOH and $HCoO_2$/TBA-Br were unsuccessfully tested. For that reason, the formation of water by means of the $HCoO_2$/TBA-OH reactant pair has been pin-pointed as a critical step in the delamination of this material. Once delaminated, they employed vacuum-assisted self-assembly (VASA method) to re-stack the material and use it as cathode material in reversible lithium ion batteries after cycling activation.

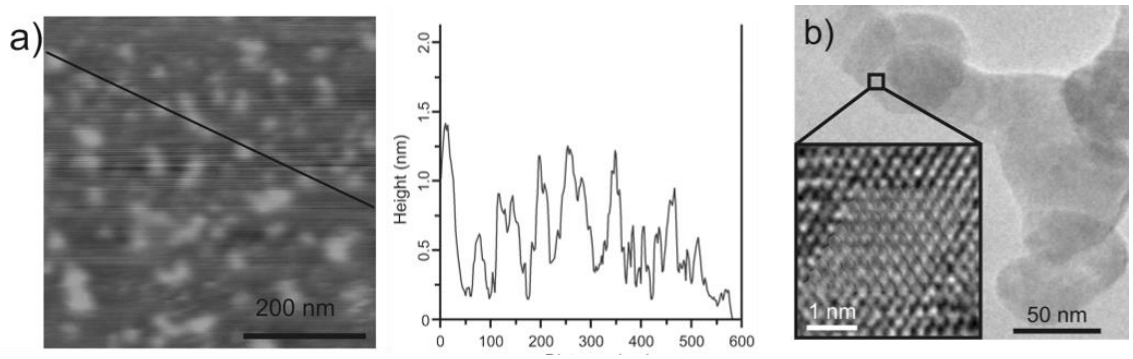

Fig. 2.25. (a) AFM image of $[CoO_2]^-$ nanosheets dropcasted from the exfoliated suspension onto mica substrate with the correspondent height profile revealing the presence of individual sheets with 0.35 nm thickness and (b) a bright-field HRTEM image of the cobalt oxide nanosheets revealing hexagonal closed-packed arrangement of cobalt atoms. Reprinted with permission of [162].

It is worth mentioning that the intermediate proton-exchange step is required, resulting in the formation of $HCoO_2$, since the direct exfoliation of $LiCoO_2$ has been reported to be unsuccessful. However, the irreversible binding of proton ions or the formation of hydrated phases can lead to detrimental effects on the electrochemical properties of the material for lithium storage applications, since less amount of lithium ions can be intercalated and de-intercalated, resulting in lower capacity. To avoid such intermediate step, an alternative method was developed by Chan et al. in which electrochemical oxidation was used to avoid the proton exchange step. After this treatment, it could be successfully delaminated by means of tetraethylammonium intercalation. The nanosheets were purified by dialysis and reassembled by either dialysis or electrophoresis and applied the resulting material for Li-ion battery applications. The restacked material showed an slightly lower capacity than bulk material[163].

Tang et al. [164] recently reported the delamination of few-layer cobalt oxide by co-precipitation, acidification and TBAOH intercalation, resulting in 1-4 nm slabs. Then, they re-stacked the nanosheets with exfoliated manganese oxide. The evaluation of the electrochemical performance of exfoliated cobalt oxide in 0.5M K_2SO_4 was done, which displayed a maximum of approximately 35 $F \cdot g^{-1}$, more than double than the non-exfoliated precursor (~ 15 $F \cdot g^{-1}$) at 0.5 $mV \cdot s^{-1}$. When they co-stacked exfoliated birnessite manganese oxide and cobalt oxide, the material with a 3:1 Mn:Co ratio displayed a maximum capacitance of 97 $F \cdot g^{-1}$ at 0.5$mV \cdot s^{-1}$. Co-stacking after delamination was compared to simply mechanically grinding and mixing the precursor materials. The composite exhibited enhanced active surface area and intimate contact between the integrating materials that greatly improved the electrochemical performance. Moreover, better rate capability performance was observed at higher applied scan rates when compared to pristine manganese oxide as a result of the inclusion of conductive cobalt oxide phases [165].

At the present time, the author is not aware of publications on the exfoliation of nickel-cobalt oxide into individual monolayers, which is the focus of one of the chapters presented in this manuscript.

2.2.3 Beyond exfoliation: re-stacking Ni-Co nanosheets for energy storage applications.

The main objective behind the exfoliation of layered materials is its usage in composites and/or final applications. It is out of the scope of the present work to make an exhaustive description of re-stacked materials and techniques. Once exfoliated, the materials shall be re-stacked. The way in which they recover their 3-dimensional structure can be engineered to further exploit their properties. For that, they can be stacked either as a single material or as part of a composite material. The former intends to increase the active surface which, ultimately, increases the number of active sites. In energy storage, this potentially leads to increased capacity response. The latter, exemplified in Fig. 2.26, benefits from the synergistic effect induced by mixing two materials with different properties.

Many macro-scale assembling techniques have been developed to use nanosheets as 2D functional blocks for composite materials, such as freeze-drying, spin-coating, dip-coating, electrophoretic deposition, drop-coating or dialysis. Nonetheless, the development of more controlled techniques, in which the orientation and composition of the resulting material can be controlled have been developed. These are: flocculation, electrostatic sequential adsorption and Langmuir-Blodgett deposition. An overview of these techniques can be found in the extensive review on oxide and hydroxide nanosheets prepared by Ma and Sasaki [166].

As aforementioned, the unique properties of 2D structured materials result in a vast number of potential applications. Layered materials have been applied in photovoltaic devices, water splitting and CO_2 reduction or piezoelectric energy harvesting. They are of special interest in the field of energy storage, in particular, for supercapacitor and battery applications [167].

The investigation of the electrochemical properties of $Ni(OH)_2$ was promising due to the regular shape and size of the crystals formed. However, they degraded after 250 cycles due to the breakage of the nanoplatelets in smaller domains. However, tuneable porosity in the formation of 3D-materials from 2D precursors has been pin-pointed as a potential route to enhance the properties of this material [135,167]. Cui et al. also studied the energy storage properties of the nickel hydroxide nanosheets that they synthesized by a sol-gel route. However, they reported $933 F \cdot g^{-1}$ at $50 mV \cdot s^{-1}$ despite their battery like behaviour and no evaluation of their discharge response was done [137].

The performance of exfoliated cobalt hydroxide has also been studied. α-$Co(OH)_2$ exfoliated in formamide was re-stacked and electrodes with 80:15:5 of active material:carbon black:PTFE were prepared. Pseudocapacitive performance was observed, with a maximum of $952 F \cdot g^{-1}$ at $5 mA \cdot cm^{-2}$ for 10mg of active material in 6M KOH on top of nickel foam, slightly higher than the un-exfoliated material. Also better rate capability and cycling stability properties were presented [168]. A recent study performed by Rovetta et al. reported the liquid phase exfoliation of layered $Co(OH)_2$ by means of a cascade process. First, the non-exfoliated precursor was washed with sonication and de-ionized water. Then, it was placed in a $9 mg \cdot mL^{-1}$ sodium chlorate/isopropyl alcohol solution and exfoliated by means of 4-hour ultrasonication. The material was centrifuged for 2 hours at 1500 rpm. The sediment underwent the first ultrasonication. The supernatant was centrifuged at higher speed to isolate the nanosheets. After repeating this procedure several times, any non-exfoliated material was discarded. Then, their electrochemical performance was studied by spraying the material on top of

glassy carbon or Ni foam. A maximum capacity of 1480 $F \cdot g^{-1}$ at 40 $mV \cdot s^{-1}$ for a 0.89 mg mass loading of active material in 1M NaOH [169].

Rajamathi et al., as previously explained, exfoliated α phases of nickel and cobalt by means of *p*-aminobenzoate and co-stacked them by adding nitrate ions. They obtained a maximum of 990 $F \cdot g^{-1}$ at $1A \cdot g^{-1}$ for a [Ni]/[Co] ratio of 4 in 2M KOH (no amount of active material used was reported) [150].

Composite materials with interesting properties have already been produced. Exfoliated graphene is usually used for this purpose since it is the most studied 2D material with more standardized procedures to obtain and it presents excellent properties. For instance, in the particular case of exfoliated nickel hydroxide, the synthesis of reduced graphene oxide – nickel oxide composite was conducted by means of metathesis synthesis of graphene oxide intercalated α-$Ni(OH)_2$ and posterior thermal treatment [170]. Further studies in the field of energy storage shall be done for this material.

Wang et al. studied the electrochemical properties of exfoliated nickel hydroxide in combination with r-GO. They delaminated nickel hydroxide by intercalating SDS and delaminating in formamide and then mixed it with a GO suspension with the consequent flocculation. To obtain the reduced form of the composite, it was treated with hydrazine. They used an 85:10:5 mixture to proceed to the electrochemical characterization, which resulted in 1184.6 $F \cdot g^{-1}$ at $2A \cdot g^{-1}$ as compared to the 945.8 $F \cdot g^{-1}$ for the electrode without r-GO (despite the battery-like behaviour observed) and a 96.4% retention after 400 cycles [171].

A similar route was used for cobalt oxide, which was also combined with reduced graphene oxide by means of surface-modification assembly in which isocharged nanosheets of cobalt oxide were used. In their work, Hwang et al. modified reduced graphene oxide layers by means of surfactants and mixed them with anionic cobalt oxide and applied the resulting material as electrode material for lithium-ion batteries were promising results were obtained [172]. Similar studies have been done for energy storage. For instance, the composite material was studied for energy storage applications as electrode material, resulting in a reported value of 567.1 $F \cdot g^{-1}$ at $1A \cdot g^{-1}$ in 1M KOH with increased rate capability and cycling stability. In general, r-GO tends to improve the electrochemical response of cobalt hydroxide by improving the hydroxide conductivity [173].

Zhang et al. reported the delamination of cobalt hydroxide by means of acetate intercalation and delamination in water by sonication, despite using DMF in their experimental procedure. After flocculation, the re-stacked material was used as Li-ion electrode material with a capacity of 120 $mA \cdot g^{-1}$ which was kept after 200 cycles [151].

Liu et al. went a step further and, after delamination of α-$Co(OH)_2$ in formamide and flocculation with GO, the resulting product was calcinated at 300-450 ^oC for 2 hours and thermal annealing at 500-700 ^oC for 90 minutes in Ar atmosphere. This resulted in Co_3O_4/r-GO, whose electrochemical properties were studied. Whereas r-GO showed pseudocapacitive behaviour, once the two materials were combined, two redox peaks were clearly visible. Nevertheless, they reported a maximum specific capacitance of 331 $F \cdot g^{-1}$ at 5 $A \cdot g^{-1}$ while 130 $F \cdot g^{-1}$ and 260 $F \cdot g^{-1}$ were obtained for r-GO and Co_3O_4 respectively. The material also exhibited a 122% capacity after 5000 cycles. This was explained by electrolyte penetration and material activation [174].

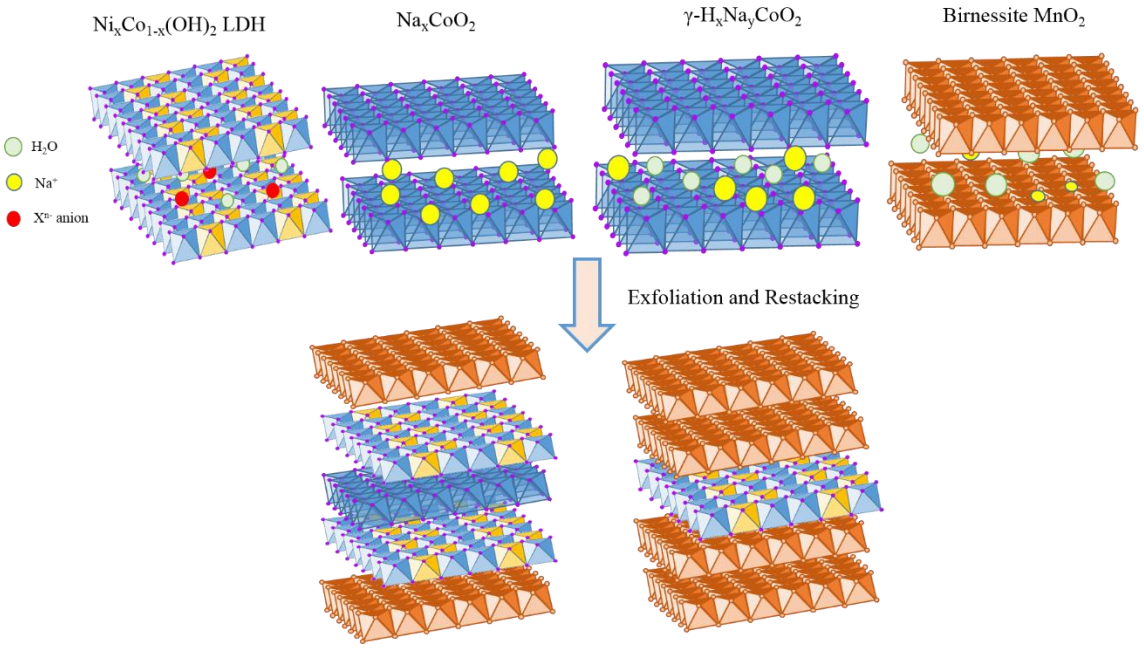

Fig. 2.26. Schematic illustration of the resulting structures after exfoliation, combination and re-stacking.

A similar approach was used by Yang et al. They delaminated Ni-Co hydroxide layer by means of *p*-aminobenzoate ions and graphite oxide into graphene oxide. Then, they mixed both solutions, which assembled oppositely charged nanosheets and formed the heterostructured materials. Finally, they did a thermal treatment at 200 ºC for 6 hours to transform the material into $NiCo_2O_4$/r-GO. They studied the energy storage properties of the resulting composite, with a reported value of 835 $F \cdot g^{-1}$ at 1$A \cdot g^{-1}$ in KOH 1M after the 1st cycle and 908 $F \cdot g^{-1}$ after the 4000th [175].

Anionic r-GO colloids interact favourably with cationic LDH via coulombic interaction. Sasaki et al. conducted direct hetero-stacking studies of Co-Ni and Co-Al LDHs exfoliated in formamide with graphene oxide by z-potential evaluation. Positively charged LDHs nanosheets (+50±4 mV) were combined with negatively charged Er-GO aqueous suspensions (-36.5±8 mV, after reduction with hydrazine). Reduced graphene oxide improved the charge transfer efficiency for energy storage applications of the composite materials. They reported values of 500-800 $F \cdot g^{-1}$ for LDHs and reduced graphene oxide composites at 1-10 $A \cdot g^{-1}$ with 97% retention after 2000 cycles [176].

2.3. Concluding remarks

An overview of electrodeposition and chemical exfoliation has been done as synthesis strategies to obtain nanostructured nickel and cobalt oxides and hydroxides from an energy storage point of view.

One of the main goals in current research is to obtain high-power density, high energy-density materials (HPEM), without compromising one for another. Obviously, the selection of material with adequate properties will greatly depend upon final application. Nonetheless, several strategies have been reported in literature and summarized in these introductory chapters to address certain challenges for the next-generation of energy storage materials; from different morphologies (to increase active surface area) to strategies to expand the voltage range in which a material is active.

If the main goal is to increase energy density and power density, two overall approaches can be undertaken. On the one hand, increasing energy density of capacitive (high-power) materials. For that reason, different composite materials, doping strategies and device configurations have been developed. Another line of work is to increase power capabilities of high energy density materials. This would consist on using traditionally battery-like materials and try to increase their rate capabilities by means of nanostructuring and composite engineering. Among all possible materials to study, nickel and cobalt oxides and hydroxides are of special interest.

Nickel and cobalt-based materials have been extensively used for energy storage applications. In fact, nickel hydroxide has been widely used as positive electrode material in alkaline batteries, among them nickel hydride and nickel cadmium batteries are the best known. This is because of its excellent charge storage properties and theoretical capacity. Consequently, it is interesting to study if these materials and their combination thereof can be tuned to exhibit high rate capabilities.

With that in mind, two different strategies have been undertaken in the present manuscript, based on two contrary approaches. On the one hand, electrodeposition works as a bottom-up approach in which, during electrodeposition, nucleation starts and leads to crystallization from small nanoparticles to thin-films. By controlling certain parameters, such as potential, applied charge and time, different morphologies, film thicknesses, specific capacities and rate capabilities can be obtained.

On the other hand, exfoliation starts from bulk material and, by means of a chemical approach, reduces interslab interactions in layered materials until, ideally, individual nanosheets are obtained. This is, essentially, a bottom-down approach. It is worth mentioning that nickel and cobalt hydroxide exfoliation in aqueous media have been recently reported while no report for nickel-cobalt oxides has been done so far. Regarding the former, no extensive electrochemical evaluation had been done for energy storage materials. Thus, this is an opportunity for further investigation on the exfoliation of these materials and their potential application as energy storage materials. It is worth mentioning that, for scaling-up, environmental and ease-to-manipulate purposes, research is focused on aqueous media since exfoliation in other solvents has been already reported.

Furthermore, nickel and cobalt-based materials present certain disadvantages. To address them, a common strategy is to combine the material with carbon-based materials to improve their conductivity and reduce agglomeration. As reported, many different materials have been tested. Nonetheless, given its layered nanostructure, graphene has intrinsic potential to exhibit synergistic effects with nickel and cobalt oxides and hydroxides. Therefore, when considering synthesis of nickel and cobalt (hydr)oxides,

their possible combination with composite materials must be born in mind to maximize the synergy. In that regard, mixing graphene derivatives with nickel and cobalt (hydr)oxides had already been reported, but synthesis techniques usually require multiple-step and complex procedures. The co-electrodeposition of nickel-cobalt hydroxide and oxide with reduced graphene oxide had not yet been done and has two main advantages, namely, it is a single step process and no binders are required. For that reason, it has been in-depth studied and presented in this manuscript. Unfortunately, the combination of exfoliated nickel-cobalt hydr(oxide) nanoslabs has not been achieved, for timing reasons, in the present work. Nonetheless, once exfoliated, different strategies for the combination of nickel-cobalt (hydr)oxide with exfoliated graphene layers may be applied and, for that reason, the exfoliation here presented serves as an excellent route to produce a reduced graphene oxide/metal (hydr)oxide composite with intimate contact in which a synergistic effect may be possible. Thus, although the work presented in this manuscript addresses some challenges currently present in literature, expanding and complementing the work reported in literature, it also serves as a starting point for future research work.

Chapter 2 references

[1] H. Lechtman, Precolumbian surface metallurgy, Technol. Cult. 25 (1984) 1–36.

[2] P.C. Andricacos, Copper On-Chip Interconnections: A Breakthrough in Electrodeposition to Make Better Chips, Interface. 8 (1999) 32–37.

[3] Y.D. Gamburg, G. Zangari, Theory and Practice of Metal Electrodeposition, Springer Science+Business Media, 2011.

[4] I. Gurrappa, L. Binder, their characterization — A review Electrodeposition of nanostructured coatings and their characterization — a review, 6996 (2017). doi:10.1088/1468-6996/9/4/043001.

[5] A.J. Bard, L.R. Faulkner, Electrochemical methods : fundamentals and applications, Second, JOHN WILEY & SONS, INC, New York, 2001. doi:10.1016/j.aca.2010.06.020.

[6] M. Pauvonic, M. Schlensinger, Fundamentals of Electrochemical Deposition, 2nd Editio, Wiley-Interscience, 2006.

[7] L. Besra, M. Liu, A review on fundamentals and applications of electrophoretic deposition (EPD), Prog. Mater. Sci. 52 (2007) 1–61. doi:10.1016/j.pmatsci.2006.07.001.

[8] M.D. Stoller, S. Park, Y. Zhu, J. An, R.S. Ruoff, Graphene-based ultracapacitors, Nano Lett. 8 (2008) 3498–502. doi:10.1021/nl802558y.

[9] C.K. Chua, M. Pumera, Chemical reduction of graphene oxide: a synthetic chemistry viewpoint., Chem. Soc. Rev. 43 (2014) 291–312. doi:10.1039/c3cs60303b.

[10] J. Wang, K.K. Manga, Q. Bao, K.P. Loh, High-Yield Synthesis of Few-Layer Graphene Flakes through Electrolyte, J. Am. Chem. Soc. 133 (2011) 8888–8891. doi:dx.doi.org/10.1021/ja203725d.

[11] M. Hilder, B. Winther-Jensen, D. Li, M. Forsyth, D.R. MacFarlane, Direct electro-deposition of graphene from aqueous suspensions., Phys. Chem. Chem. Phys. 13 (2011) 9187–9193. doi:10.1039/c1cp20173e.

[12] X. Wang, L. Zhi, K. Müllen, Transparent, conductive graphene electrodes for dye-sensitized solar cells., Nano Lett. 8 (2008) 323–7. doi:10.1021/nl072838r.

[13] V.C. Tung, L.M. Chen, M.J. Allen, J.K. Wassei, K. Nelson, R.B. Kaner, Y. Yang, Low-Temperature Solution Processing of Graphene- Carbon Nanotube Hybrid Materials for High-Performance Transparent Conductors, Nano Lett. 9 (2009) 2513. doi:10.1021/nl9001525.

[14] M.W. S. Gilje, S. Han, A Chemical Route to Graphene for Devie Applications, Nano Lett. 7 (2007) 3394–3398.

[15] S.J. An, Y. Zhu, S.H. Lee, M.D. Stoller, T. Emilsson, S. Park, A. Velamakanni, J. An, R.S. Ruoff, Thin Film Fabrication and Simultaneous Anodic Reduction of Deposited Graphene Oxide Platelets by Electrophoretic Deposition, (2010) 1259–1263. doi:10.1021/jz100080c.

[16] L.J. Cote, F. Kim, J. Huang, Langmuir-blodgett assembly of graphite oxide single

layers, J. Am. Chem. Soc. 131 (2009) 1043–1049. doi:10.1021/ja806262m.

[17] X. Li, G. Zhang, X. Bai, X. Sun, X. Wang, E. Wang, H. Dai, Highly conducting graphene sheets and Langmuir-Blodgett films., Nat. Nanotechnol. 3 (2008) 538–42. doi:10.1038/nnano.2008.210.

[18] S. Park, J. An, R.D. Piner, I. Jung, D. Yang, A. Velamakanni, S.B.T. Nguyen, R.S. Ruoff, Aqueous suspension and characterization of chemically modified graphene sheets, Chem. Mater. 20 (2008) 6592–6594. doi:10.1021/cm801932u.

[19] S. Saha, M. Jana, P. Khanra, P. Samanta, H. Koo, N.C. Murmu, T. Kuila, Band Gap Engineering of Boron Nitride by Graphene and Its Application as Positive Electrode Material in Asymmetric Supercapacitor Device., ACS Appl. Mater. Interfaces. 7 (2015) 14211–14222. doi:10.1021/acsami.5b03562.

[20] C.T.J. Low, F.C. Walsh, M.H. Chakrabarti, M.A. Hashim, M.A. Hussain, Electrochemical approaches to the production of graphene flakes and their potential applications, Carbon N. Y. 54 (2013) 1–11. doi:10.1016/j.carbon.2012.11.030.

[21] G. Wang, B. Wang, J. Park, Y. Wang, B. Sun, J. Yao, Highly efficient and large-scale synthesis of graphene by electrolytic exfoliation, Carbon N. Y. 47 (2009) 3242–3246. doi:10.1016/j.carbon.2009.07.040.

[22] Y. Xu, Y. Huang, W. Yan, L. Zhang, Y. Chen, Environmentally friendly approaches toward the production of processable graphene by exfoliation of graphite using ionic liquid, J Nanosci Nanotechnol. 13 (2013) 1116–1119. doi:10.1166/jnn.2013.5995.

[23] V. V. Singh, G. Gupta, A. Batra, A.K. Nigam, M. Boopathi, P.K. Gutch, B.K. Tripathi, A. Srivastava, M. Samuel, G.S. Agarwal, B. Singh, R. Vijayaraghavan, Greener electrochemical synthesis of high quality graphene nanosheets directly from pencil and its SPR sensing application, Adv. Funct. Mater. 22 (2012) 2352–2362. doi:10.1002/adfm.201102525.

[24] C.Y. Su, A.-Y. Lu, Y. Xu, F.-R. Chen, A.N. Khlobystov, L.-J. Li, High-Quality Thin Graphene Films from Fast Elecrochemical Exfoliation, ACS Nano. 5 (2011) 2332–2339. doi:10.1021/nn200025p.

[25] G.M. Morales, P. Schifani, G. Ellis, C. Ballesteros, G. Martínez, C. Barbero, H.J. Salavagione, High-quality few layer graphene produced by electrochemical intercalation and microwave-assisted expansion of graphite, Carbon N. Y. 49 (2011) 2809–2816. doi:10.1016/j.carbon.2011.03.008.

[26] M. Alanyalioğlu, J.J. Segura, J. Oró-Sol, N. Casañ-Pastor, The synthesis of graphene sheets with controlled thickness and order using surfactant-assisted electrochemical processes, Carbon N. Y. 50 (2012) 142–152. doi:10.1016/j.carbon.2011.07.064.

[27] K.W. Hathcock, J.C. Brumfield, C. a Goss, E. a Irene, R.W. Murray, Incipient Electrochemical Oxidation of Highly Oriented Pyrolytic Graphite: Correlation between Surface Blistering and Electrolyte Anion Intercalation, Anal. Chem. 67 (1995) 2201–2206. doi:10.1021/ac00109a045.

[28] E. Bourelle, B. Claude-montigny, A. Metrot, Electrochemical Exfoliation of

HOPG in Formic - Sulfuric Acid Mixtures, Mol. Cryst. Liq. Cryst. Sci. Technol. Sect. A. Mol. Cryst. Liq. Cryst. 310 (1998) 321–326. doi:10.1080/10587259808045356.

[29] N. Liu, F. Luo, H. Wu, Y. Liu, C. Zhang, J. Chen, One-step ionic-liquid-assisted electrochemical synthesis of ionic-liquid-functionalized graphene sheets directly from graphite, Adv. Funct. Mater. 18 (2008) 1518–1525. doi:10.1002/adfm.200700797.

[30] J. Lu, J. Yang, J. Wang, A. Lim, S. Wang, K.P. Loh, One-Pot Synthesis of Fluorescent Carbon Graphene by the Exfoliation of Graphite in Ionic Liquids, ACS Nano. 3 (2009) 2367–2375. doi:10.1021/nn900546b.

[31] B. Qi, L. He, X. Bo, H. Yang, L. Guo, Electrochemical preparation of free-standing few-layer graphene through oxidation-reduction cycling, Chem. Eng. J. 171 (2011) 340–344. doi:10.1016/j.cej.2011.03.078.

[32] S.H. Lee, S.D. Seo, Y.H. Jin, H.W. Shim, D.W. Kim, A graphite foil electrode covered with electrochemically exfoliated graphene nanosheets, Electrochem. Commun. 12 (2010) 1419–1422. doi:10.1016/j.elecom.2010.07.036.

[33] T. Shen, Y. Shen, X.T. Ma, W.T. Gao, M. Cao, F. Gu, L.J. Wang, Preparation of Graphene Films and their Applications in dye-sensitized solar cells, Prog. Funct. Mater. 538 (2013) 332–336. doi:DOI 10.4028/www.scientific.net/KEM.538.332.

[34] W. Zhang, Y. Zeng, N. Xiao, H.H. Hng, Q. Yan, One-step electrochemical preparation of graphene-based heterostructures for Li storage, J. Mater. Chem. 22 (2012) 8455. doi:10.1039/c2jm16315b.

[35] S. Liu, J. Ou, J. Wang, X. Liu, S. Yang, A simple two-step electrochemical synthesis of graphene sheets film on the ITO electrode as supercapacitors, J. Appl. Electrochem. 41 (2011) 881–884. doi:10.1007/s10800-011-0304-1.

[36] R. Ishikawa, P.J. Ko, Y. Kurokawa, M. Konagai, a Sandhu, Electrophoretic deposition of high quality transparent conductive graphene films on insulating glass substrates, J. Phys. Conf. Ser. 352 (2012) 012003. doi:10.1088/1742-6596/352/1/012003.

[37] Y. Chen, X. Zhang, P. Yu, Y. Ma, Electrophoretic deposition of graphene nanosheets on nickel foams for electrochemical capacitors, J. Power Sources. 195 (2010) 3031–3035. doi:10.1016/j.jpowsour.2009.11.057.

[38] R.P. Gandhiraman, D. Nordlund, C. Javier, J.E. Koehne, B. Chen, M. Meyyappan, X-ray Absorption Study of Graphene Oxide and Transition Metal Oxide Nanocomposites, J. Phys. Chem. C. 118 (2014) 18706–18712. doi:Doi 10.1021/Jp503941t.

[39] a Chavez-Valdez, M.S.P. Shaffer, a R. Boccaccini, Applications of graphene electrophoretic deposition. A review., J. Phys. Chem. B. 117 (2013) 1502–15. doi:10.1021/jp3064917.

[40] S. Stankovich, D. a. Dikin, R.D. Piner, K. a. Kohlhaas, A. Kleinhammes, Y. Jia, Y. Wu, S.T. Nguyen, R.S. Ruoff, Synthesis of graphene-based nanosheets via chemical reduction of exfoliated graphite oxide, Carbon N. Y. 45 (2007) 1558–1565. doi:10.1016/j.carbon.2007.02.034.

[41] T. Hwang, Y. Lee, J. Nam, Large-Area, Conductive and Flexible Reduced Graphene Oxide (RGO) Membrane Fabricated by Electrophoretic Deposition (EPD), ACS Appl. Mater. Interfaces. 6 (2014) 1747–1753.

[42] S.D. Seo, I.S. Hwang, S.H. Lee, H.W. Shim, D.W. Kim, 1D/2D carbon nanotube/graphene nanosheet composite anodes fabricated using electrophoretic assembly, Ceram. Int. 38 (2012) 3017–3021. doi:10.1016/j.ceramint.2011.11.083.

[43] J.I. Paredes, A. Marti, J.M.D. Tasco, A. Martı, Graphene Oxide Dispersions in Organic Solvents Graphene Oxide Dispersions in Organic Solvents, Langmuir. 24 (2008) 10560–10564. doi:10.1021/la801744a.

[44] M. Zhou, Y. Wang, Y. Zhai, J. Zhai, W. Ren, F. Wang, S. Dong, Controlled synthesis of large-area and patterned electrochemically reduced graphene oxide films, Chem. - A Eur. J. 15 (2009) 6116–6120. doi:10.1002/chem.200900596.

[45] G. Eda, M. Chhowalla, Chemically derived graphene oxide: Towards large-area thin-film electronics and optoelectronics, Adv. Mater. 22 (2010) 2392–2415. doi:10.1002/adma.200903689.

[46] H. Guo, X. Wang, Q. Qian, F. Wang, X. Xia, A Green Approach to the Synthesis of Graphene Nanosheets, ACS Nano. 3 (2009) 2653–2659. doi:10.1021/nn900227d.

[47] Y. Shao, J. Wang, M. Engelhard, C. Wang, Y. Lin, Facile and controllable electrochemical reduction of graphene oxide and its applications, J. Mater. Chem. 20 (2010) 743. doi:10.1039/b917975e.

[48] L.C.S. Figueiredo-Filho, D. a C. Brownson, O. Fatibello-Filho, C.E. Banks, Exploring the origins of the apparent "electrocatalytic" oxidation of kojic acid at graphene modified electrodes., Analyst. 138 (2013) 4436–42. doi:10.1039/c3an00856h.

[49] Z. Wang, X. Zhou, J. Zhang, F. Boey, H. Zhang, Direct electrochemical reduction of single-layer graphene oxide and subsequent functionalization with glucose oxidase, J. Phys. Chem. C. 113 (2009) 14071–14075. doi:10.1021/jp906348x.

[50] G.K. Ramesha, S. Sampath, Electrochemical Reduction of Oriented Graphene Oxide Films: An in Situ Raman Spectroelectrochemical Study, J. Phys. Chem. C. 113 (2009) 7985–7989.

[51] A. Viinikanoja, Z. Wang, J. Kauppila, C. Kvarnström, Electrochemical reduction of graphene oxide and its in situ spectroelectrochemical characterization., Phys. Chem. Chem. Phys. 14 (2012) 14003–9. doi:10.1039/c2cp42253k.

[52] J. Yang, J. Chen, S. Yu, X. Yan, Q. Xue, Synthesis of a graphene nanosheet film with attached amorphous carbon nanoparticles by their simultaneous electrodeposition, Carbon N. Y. 48 (2010) 2665–2668. doi:10.1016/j.carbon.2010.03.037.

[53] O.C. Compton, S.T. Nguyen, Graphene oxide, highly reduced graphene oxide, and graphene: versatile building blocks for carbon-based materials., Small. 6 (2010) 711–23. doi:10.1002/smll.200901934.

[54] S.Y. Toh, K.S. Loh, S.K. Kamarudin, W.R.W. Daud, Graphene production via electrochemical reduction of graphene oxide: Synthesis and characterisation,

Chem. Eng. J. 251 (2014) 422–434. doi:10.1016/j.cej.2014.04.004.

[55] W. Li, J. Liu, C. Yan, Reduced graphene oxide with tunable C/O ratio and its activity towards vanadium redox pairs for an all vanadium redox flow battery, Carbon N. Y. 55 (2013) 313–320. doi:10.1016/j.carbon.2012.12.069.

[56] X. Peng, D. Diamond, K.T. Lau, Synthesis of electrochemically-reduced graphene oxide film with controllable size and thickness and its use in supercapacitor, Carbon N. Y. 49 (2011) 3488–3496. doi:10.1016/j.carbon.2011.04.047.

[57] K.Q. Deng, J. hong Zhou, X.F. Li, Direct electrochemical reduction of graphene oxide and its application to determination of l-tryptophan and l-tyrosine, Colloids Surfaces B Biointerfaces. 101 (2013) 183–188. doi:10.1016/j.colsurfb.2012.06.007.

[58] D. Wang, W. Yan, S.H. Vijapur, G.G. Botte, Electrochemically reduced graphene oxide-nickel nanocomposites for urea electrolysis, Electrochim. Acta. 89 (2013) 732–736. doi:10.1016/j.electacta.2012.11.046.

[59] M.A. Raj, S.A. John, Simultaneous determination of uric acid, xanthine, hypoxanthine and caffeine in human blood serum and urine samples using electrochemically reduced graphene oxide modified electrode, Anal. Chim. Acta. 771 (2013) 14–20. doi:10.1016/j.aca.2013.02.017.

[60] J. Yang, S. Deng, J. Lei, H. Ju, S. Gunasekaran, Electrochemical synthesis of reduced graphene sheet-AuPd alloy nanoparticle composites for enzymatic biosensing, Biosens. Bioelectron. 29 (2011) 159–166. doi:10.1016/j.bios.2011.08.011.

[61] G.K. Ramesha, N.S. Sampath, Electrochemical reduction of oriented Graphene oxide films: An in situ Raman spectroelectrochemical study, J. Phys. Chem. C. 113 (2009) 7985–7989. doi:10.1021/jp811377n.

[62] J. Wang, Facile and controllable electrochemical reduction of graphene oxide and its applications and its applications †, (2015). doi:10.1039/b917975e.

[63] H.-L. Guo, X.-F. Wang, Q.-Y. Qian, F.-B. Wang, X.-H. Xia, A green approach to the synthesis of graphene nanosheets., ACS Nano. 3 (2009) 2653–2659. doi:10.1021/nn900227d.

[64] H.Ö. Doğan, D. Ekinci, Ü. Demir, Atomic scale imaging and spectroscopic characterization of electrochemically reduced graphene oxide, Surf. Sci. 611 (2013) 54–59. doi:10.1016/j.susc.2013.01.014.

[65] X. Zhang, D. Zhang, Y. Chen, X. Sun, Y. Ma, Electrochemical reduction of graphene oxide films: Preparation, characterization and their electrochemical properties, Chinese Sci. Bull. 57 (2012) 3045–3050. doi:10.1007/s11434-012-5256-2.

[66] C. Liu, K. Wang, S. Luo, Y. Tang, L. Chen, Direct Electrodeposition of Graphene Enabling the One- Step Synthesis of Graphene – Metal Nanocomposite Films, (2011) 1203–1206. doi:10.1002/smll.201002340.

[67] Y. Jiang, Y. Lu, F. Li, T. Wu, L. Niu, W. Chen, Facile electrochemical codeposition of "clean" graphene-Pd nanocomposite as an anode catalyst for formic acid electrooxidation, Electrochem. Commun. 19 (2012) 21–24.

doi:10.1016/j.elecom.2012.02.035.

[68] J. Ping, Y. Wang, K. Fan, J. Wu, Y. Ying, Direct electrochemical reduction of graphene oxide on ionic liquid doped screen-printed electrode and its electrochemical biosensing application, Biosens. Bioelectron. 28 (2011) 204–209. doi:10.1016/j.bios.2011.07.018.

[69] H.-H. Chang, C.-K. Chang, Y.-C. Tsai, C.-S. Liao, Electrochemically synthesized graphene/polypyrrole composites and their use in supercapacitor., Carbon N. Y. 50 (2012) 2331–2336. doi:10.1016/j.carbon.2012.01.056.

[70] F. Gao, X. Qi, X. Cai, Q. Wang, F. Gao, W. Sun, Electrochemically reduced graphene modified carbon ionic liquid electrode for the sensitive sensing of rutin, Thin Solid Films. 520 (2012) 5064–5069. doi:10.1016/j.tsf.2012.03.002.

[71] L. Chen, Y. Tang, K. Wang, C. Liu, S. Luo, Electrochemistry Communications Direct electrodeposition of reduced graphene oxide on glassy carbon electrode and its electrochemical application, Electrochem. Commun. 13 (2011) 133–137. doi:10.1016/j.elecom.2010.11.033.

[72] L. Chen, Y. Tang, K. Wang, C. Liu, S. Luo, Direct electrodeposition of reduced graphene oxide on glassy carbon electrode and its electrochemical application, Electrochem. Commun. 13 (2015) 133–137. doi:10.1016/j.elecom.2010.11.033.

[73] K. Sheng, Y. Sun, C. Li, W. Yuan, G. Shi, Ultrahigh-rate supercapacitors based on eletrochemically reduced graphene oxide for ac line-filtering., Sci. Rep. 2 (2012) srep00247, 5 pp. doi:10.1038/srep00247.

[74] S.K. Bhardwaj, P. Yadav, S. Ghosh, T. Basu, A.K. Mahapatro, Biosensing Test-Bed Using Electrochemically Deposited Reduced Graphene Oxide, ACS Appl. Mater. Interfaces. 8 (2016) 24350–24360. doi:10.1021/acsami.6b04562.

[75] Z. Zhang, M. Ma, C. Chen, Z. Cai, X. Huang, The morphology, structure and electrocatalytic ability of graphene prepared with different drying methods, RSC Adv. 6 (2016) 28005–28014. doi:10.1039/C5RA23123J.

[76] R.S. Jayashree, P.V. Kamath, Nickel hydroxide electrodeposition from nickel nitrate solutions: Mechanistic studies, J. Power Sources. 93 (2001) 273–278. doi:10.1016/S0378-7753(00)00568-1.

[77] D.S. Hall, D.J. Lockwood, C. Bock, B.R. MacDougall, Nickel hydroxides and related materials: a review of their structures, synthesis and properties., Proc. Math. Phys. Eng. Sci. 471 (2015) 20140792. doi:10.1098/rspa.2014.0792.

[78] X. Xia, Y. Zhang, D. Chao, C. Guan, Y. Zhang, L. Li, X. Ge, I.M. Bacho, J. Tu, H.J. Fan, Solution synthesis of metal oxides for electrochemical energy storage applications, Nanoscale. 6 (2014) 5008–5048. doi:10.1039/C4NR00024B.

[79] M.S. Wu, C.H. Yang, Electrochromic properties of intercrossing nickel oxide nanoflakes synthesized by electrochemically anodic deposition, Appl. Phys. Lett. 91 (2007) 1–4. doi:10.1063/1.2759270.

[80] D.M. MacArthur, The Hydrated Nickel Hydroxide Electrode Potential Sweep Experiments, J. Electrochem. Soc. 117 (1970) 1970.

[81] M. Murthy, A Model for the Galvanostatic Deposition of Nickel Hydroxide, J.

Electrochem. Soc. 143 (1996) 2319. doi:10.1149/1.1837000.

[82] C.C. Streinz, The Effect of Temperature and Ethanol on the Deposition of Nickel Hydroxide Films, J. Electrochem. Soc. 142 (1995) 4051. doi:10.1149/1.2048461.

[83] B. Ash, R.K. Paramguru, B.K. Mishra, A Fundamental Investigation of Electrochemical Preparation of Battery Grade Nickel Hydroxide, Adv. Mater. Res. 117 (2010) 15–20. doi:10.4028/www.scientific.net/AMR.117.15.

[84] B. Ash, R.K. Paramguru, B.K. Mishra, Electrode reactions during electrolytic preparation of nickel hydroxide, Electrochem. Commun. 12 (2010) 48–51. doi:10.1016/j.elecom.2009.10.033.

[85] B. Ash, K.G. Mishra, T. Subbaiah, R.K. Paramguru, B.K. Mishra, Electrochemical studies on electrolytic preparation of battery grade nickel hydroxide - Effect of (OH)-to Ni2+ratio, J. Power Sources. 275 (2015) 55–63. doi:10.1016/j.jpowsour.2014.10.141.

[86] G.T. Zhou, Q.Z. Yao, X. Wang, J.C. Yu, Preparation and characterization of nanoplatelets of nickel hydroxide and nickel oxide, Mater. Chem. Phys. 98 (2006) 267–272. doi:10.1016/j.matchemphys.2005.09.030.

[87] T.N. Ramesh, P.V. Kamath, C. Shivakumara, Correlation of Structural Disorder with the Reversible Discharge Capacity of Nickel Hydroxide Electrode, J. Electrochem. Soc. 152 (2005) A806. doi:10.1149/1.1865852.

[88] L. Dong, Y. Chu, W. Sun, Controllable synthesis of nickel hydroxide and porous nickel oxide nanostructures with different morphologies, Chem. - A Eur. J. 14 (2008) 5064–5072. doi:10.1002/chem.200701627.

[89] T. Subbaiah, S.C. Mallick, K.G. Mishra, K. Sanjay, R.P. Das, Electrochemical precipitation of nickel hydroxide, J. Power Sources. 112 (2002) 562–569. doi:10.1016/S0378-7753(02)00470-6.

[90] C.C. Streinz, The Effect of Current and Nickel Nitrate Concentration on the Deposition of Nickel Hydroxide Films, J. Electrochem. Soc. 142 (1995) 1084. doi:10.1149/1.2044134.

[91] K.-W. Nam, K.-B. Kim, A Study of the Preparation of NiOx Electrode via Electrochemical Route for Supercapacitor Applications and Their Charge Storage Mechanism, J. Electrochem. Soc. 149 (2002) A346. doi:10.1149/1.1449951.

[92] R. Oriňáková, M. Strečková, L. Trnková, R. Rozik, M. Gálová, Comparison of chloride and sulphate electrolytes in nickel electrodeposition on a paraffin impregnated graphite electrode, J. Electroanal. Chem. 594 (2006) 152–159. doi:10.1016/j.jelechem.2006.05.031.

[93] W.A. WESLEY, A.J.W. CAREY, THE ELECTRODEPOSITION OF NICKEL FROM NICKEL CHLORIDE SOLUTIONS, Electrochem. Soc. 75 (1939) 209–236.

[94] R. Etchenique, E.J. Calvo, Electrochemical Quartz Crystal Microbalance Gravimetric and Viscoelastic Studies of Nickel Hydroxide Battery Electrodes, J. Electrochem. Soc. 148 (2001) A361. doi:10.1149/1.1357170.

[95] H.M. French, M.J. Henderson, A.R. Hillman, E. Vieil, Ion and solvent transfer

discrimination at a nickel hydroxide film exposed to LiOH by combined electrochemical quartz crystal microbalance (EQCM) and probe beam deflection (PBD) techniques, J. Electroanal. Chem. 500 (2001) 192–207. doi:10.1016/S0022-0728(00)00373-9.

[96] M. Gonsalves, A. Robert Hillman, Effect of time scale on redox-driven ion and solvent transfers at nickel hydroxide films in aqueous lithium hydroxide solutions, J. Electroanal. Chem. 454 (1998) 183–202. doi:10.1016/S0022-0728(98)00262-9.

[97] E. Kalu, E. Kalu, T. Nwoga, T. Nwoga, V. Srinivasan, V. Srinivasan, W. Weidner, W. Weidner, Cyclic voltammetric studies of the effects of time and temperature on the capacitance of electrochemically deposited nickel hydroxide, Nano. 92 (2001) 163–167. doi:10.1016/S0378-7753(00)00520-6.

[98] J.R.S. Brownson, C. Lévy-Clément, Electrodeposition of α- and β-cobalt hydroxide thin films via dilute nitrate solution reduction, Phys. Status Solidi Basic Res. 245 (2008) 1785–1791. doi:10.1002/pssb.200879534.

[99] J.-K. Chang, C.-M. Wu, I.-W. Sun, Nano-architectured Co(OH)2 electrodes constructed using an easily-manipulated electrochemical protocol for high-performance energy storage applications, J. Mater. Chem. 20 (2010) 3729. doi:10.1039/b925176f.

[100] J.B. Wu, Y. Lin, X.H. Xia, J.Y. Xu, Q.Y. Shi, Pseudocapacitive properties of electrodeposited porous nanowall Co3O4 film., Electrochim. Acta. 56 (2011) 7163–7170. doi:10.1016/j.electacta.2011.05.067.

[101] S.L. Chou, J.Z. Wang, H.K. Liu, S.X. Dou, Electrochemical deposition of porous Co3O4 nanostructured thin film for lithium-ion battery, J. Power Sources. 182 (2008) 359–364. doi:10.1016/j.jpowsour.2008.03.083.

[102] H.C. Liu, S.K. Yen, Characterization of electrolytic Co3O4 thin films as anodes for lithium-ion batteries, J. Power Sources. 166 (2007) 478–484. doi:10.1016/j.jpowsour.2007.01.072.

[103] G.P. Kim, I. Nam, N.D. Kim, J. Park, S. Park, J. Yi, A synthesis of graphene/Co3O4 thin films for lithium ion battery anodes by coelectrodeposition, Electrochem. Commun. 22 (2012) 93–96. doi:10.1016/j.elecom.2012.05.032.

[104] X.H. Xia, J.P. Tu, J.Y. Xiang, X.H. Huang, X.L. Wang, X.B. Zhao, Hierarchical porous cobalt oxide array films prepared by electrodeposition through polystyrene sphere template and their applications for lithium ion batteries, J. Power Sources. 195 (2010) 2014–2022. doi:10.1016/j.jpowsour.2009.11.009.

[105] A.D. Jagadale, V.S. Kumbhar, R.N. Bulakhe, C.D. Lokhande, Influence of electrodeposition modes on the supercapacitive performance of Co3O4 electrodes, Energy. 64 (2014) 234–241. doi:10.1016/j.energy.2013.10.016.

[106] C. Mansour, T. Pauporté, a. Ringuedé, V. Albin, M. Cassir, Protective coating for MCFC cathode: Low temperature potentiostatic deposition of CoOOH on nickel in aqueous media containing glycine, J. Power Sources. 156 (2006) 23–27. doi:10.1016/j.jpowsour.2005.08.020.

[107] R.S. Jayashree, P.V. Kamath, Electrochemical synthesis of alpha-cobalt hydroxide, J. Mater. Chem. 9 (1999) 961–963.

[108] M. Rajamathi, P.V. Kamath, On the relationship between α-nickel hydroxide and the basic salts of nickel, J. Power Sources. 70 (1998) 118–121. doi:10.1016/S0378-7753(97)02656-6.

[109] W.J. Zhou, D.D. Zhao, M.W. Xu, C.L. Xu, H.L. Li, Effects of the electrodeposition potential and temperature on the electrochemical capacitance behavior of ordered mesoporous cobalt hydroxide films, Electrochim. Acta. 53 (2008) 7210–7219. doi:10.1016/j.electacta.2008.05.007.

[110] J.R.S. Brownson, C. Lévy-Clément, Nanostructured α- and β-cobalt hydroxide thin films, Electrochim. Acta. 54 (2009) 6637–6644. doi:10.1016/j.electacta.2009.06.034.

[111] B.E. Prasad, P.V. Kamath, S. Upadhya, Electrochemical synthesis of macroporous oxide coatings on stainless-steel substrates, J. Am. Ceram. Soc. 91 (2008) 3870–3874. doi:10.1111/j.1551-2916.2008.02792.x.

[112] C. Kung, H. Chen, C. Lin, R. Vittal, K. Ho, Synthesis of Co3O4 nanosheets via electrodeposition followed by ozone treatment and their application to high-performance supercapacitors, J. Power Sources. 214 (2012) 91–99. doi:10.1016/j.jpowsour.2012.04.076.

[113] S.-L. Chou, J.-Z. Wang, H.-K. Liu, S.-X. Dou, Electrochemical Deposition of Porous Co(OH)[sub 2] Nanoflake Films on Stainless Steel Mesh for Flexible Supercapacitors, J. Electrochem. Soc. 155 (2008) A926. doi:10.1149/1.2988739.

[114] C. Yuan, L. Yang, L. Hou, L. Shen, X. Zhang, X.W. (David) Lou, Growth of ultrathin mesoporous Co3O4 nanosheet arrays on Ni foam for high-performance electrochemical capacitors, Energy Environ. Sci. 5 (2012) 7883. doi:10.1039/c2ee21745g.

[115] X.-H. Xia, J.-P. Tu, X.-L. Wang, C.-D. Gu, X.-B. Zhao, Mesoporous Co3O4 monolayer hollow-sphere array as electrochemical pseudocapacitor material, Chem. Commun. 47 (2011) 5786. doi:10.1039/c1cc11281c.

[116] V. Srinivasan, J.W. Weidner, Capacitance studies of cobalt oxide films formed via electrochemical precipitation, 108 (2002) 15–20.

[117] a K. Geim, K.S. Novoselov, The rise of graphene., Nat. Mater. 6 (2007) 183–91. doi:10.1038/nmat1849.

[118] H.T. Tan, W. Sun, L. Wang, Q. Yan, 2D Transition Metal Oxides/Hydroxides for Energy-Storage Applications, ChemNanoMat. 2 (2016) 562–577. doi:10.1002/cnma.201500177.

[119] H. Zhang, Ultrathin Two-Dimensional Nanomaterials, ACS Nano. 9 (2015) 9451–9469. doi:10.1021/acsnano.5b05040.

[120] Q. Wang, D.O. Hare, Recent Advances in the Synthesis and Application of Layered Double Hydroxide (LDH) Nanosheets, (2012).

[121] G. Hu, N. Wang, D. O'Hare, J. Davis, One-step synthesis and AFM imaging of hydrophobic LDH monolayers, Chem. Commun. 1 (2006) 287–289. doi:10.1039/B514368C.

[122] M.E. Pérez-Bernal, R.J. Ruano-Casero, F. Benito, V. Rives, Nickel-aluminum

layered double hydroxides prepared via inverse micelles formation, J. Solid State Chem. 182 (2009) 1593–1601. doi:10.1016/j.jssc.2009.03.005.

[123] M. Adachi-pagano, C. Forano, J. Besse, M. Inorganiques, C. Esa, U.B. Pascal, A. Cedex, Delamination of layered double hydroxides by use of surfactants, (2000) 91–92.

[124] M. Singh, M.I. Ogden, G.M. Parkinson, C.E. Buckley, Delamination and re-assembly of surfactant-containing Li / Al layered double hydroxides, Mater. Res. 2 (2004) 10–13. doi:10.1039/b314288d.

[125] S. O'Leary, D. O'Hare, G. Seeley, Delamination of layered double hydroxides in polar monomers: new LDH-acrylate nanocomposites., Chem. Commun. (Camb). (2002) 1506–1507. doi:10.1039/b204213d.

[126] M. Jobbágy, A.E. Regazzoni, Delamination and restacking of hybrid layered double hydroxides assessed by in situ XRD, 275 (2004) 345–348. doi:10.1016/j.jcis.2004.01.082.

[127] C.R. Gordijo, V.R. Leopoldo Constantino, D. de Oliveira Silva, Evidences for decarbonation and exfoliation of layered double hydroxide in N,N-dimethylformamide-ethanol solvent mixture, J. Solid State Chem. 180 (2007) 1967–1976. doi:10.1016/j.jssc.2007.05.003.

[128] T. Hibino, W. Jones, New approach to the delamination of layered double hydroxides, J. Mater. Chem. 11 (2001) 1321–1323. doi:10.1039/b101135i.

[129] T. Hibino, Delamination of layered double hydroxides containing amino acids, Chem. Mater. 16 (2004) 5482–5488. doi:10.1021/cm048842a.

[130] L. Li, R. Ma, Y. Ebina, N. Iyi, T. Sasaki, Positively Charged Nanosheets Derived via Total Delamination of Layered Double Hydroxides, (2005) 4386–4391.

[131] Q. Wu, A. Olafsen, Ø.B. Vistad, J. Roots, P. Norby, Delamination and restacking of a layered double hydroxide with nitrate as counter anion, J. Mater. Chem. 15 (2005) 4695. doi:10.1039/b511184f.

[132] Z. Liu, R. Ma, M. Osada, N. Iyi, Y. Ebina, K. Takada, T. Sasaki, Synthesis , Anion Exchange , and Delamination of Co - Al Layered Double Hydroxide : Assembly of the Exfoliated Nanosheet / Polyanion Composite Films and Magneto-Optical Studies, (2006) 4872–4880.

[133] Z. Liu, R. Ma, Y. Ebina, N. Iyi, K. Takada, T. Sasaki, General synthesis and delamination of highly crystalline transition-metal-bearing layered double hydroxides, Langmuir. 23 (2007) 861–867. doi:10.1021/la062345m.

[134] G. Abellán, E. Coronado, C. Martí-Gastaldo, E. Pinilla-Cienfuegos, A. Ribera, Hexagonal nanosheets from the exfoliation of Ni2+-Fe3+ LDHs: a route towards layered multifunctional materials, J. Mater. Chem. 20 (2010) 7451. doi:10.1039/c0jm01447h.

[135] S. Ida, D. Shiga, M. Koinuma, Y. Matsumoto, Synthesis of hexagonal nickel hydroxide nanosheets by exfoliation of layered nickel hydroxide intercalated with dodecyl sulfate ions, J. Am. Chem. Soc. 130 (2008) 14038–14039. doi:10.1021/ja804397n.

[136] D. Wang, W. Yan, G.G. Botte, Exfoliated nickel hydroxide nanosheets for urea electrolysis, Electrochem. Commun. 13 (2011) 1135–1138. doi:10.1016/j.elecom.2011.07.016.

[137] H. Cui, J. Xue, W. Ren, M. Wang, Ultra-high specific capacitance of β-Ni(OH)2monolayer nanosheets synthesized by an exfoliation-free sol-gel route, J. Nanoparticle Res. 16 (2014). doi:10.1007/s11051-014-2601-1.

[138] S. Modification, X. Liu, R. Ma, Y. Bando, T. Sasaki, Layered Cobalt Hydroxide Nanocones : Microwave-Assisted Synthesis , Zuschriften, (2010) 8429–8432. doi:10.1002/ange.201004033.

[139] H. Cui, W. Ma, L. Wang, J. Xue, Preparation of α-Co(OH)2 monolayer nanosheets by an intercalation agent-free exfoliation process, J. Sol-Gel Sci. Technol. 78 (2016) 293–298. doi:10.1007/s10971-015-3943-6.

[140] R. Ma, Z. Liu, K. Takada, N. Iyi, Y. Bando, T. Sasaki, Synthesis and Exfoliation of Co − Fe Layered Double Hydroxides : An Innovative Topochemical Approach Hydroxides : An Innovative Topochemical Approach, (2007) 5257–5263. doi:10.1021/ja0693035.

[141] J. Liang, R. Ma, N. Iyi, Y. Ebina, K. Takada, T. Sasaki, Topochemical Synthesis , Anion Exchange , and Exfoliation of Co - Ni Layered Double Hydroxides : A Route to Positively Charged Co - Ni Hydroxide Nanosheets with Tunable Composition, (2010) 371–378. doi:10.1021/cm902787u.

[142] K. Takada, K. Fukuda, N. Iyi, Y. Bando, T. Sasaki, Topochemical Synthesis of Monometallic (Co2+ - Co3+) Layered Double Hydroxide and its Exfoliation into Positively Charged Co(OH)2 nanosheets, Angew. Chemie - Int. Ed. 120 (2008) 92–95. doi:10.1002/ange.200703941.

[143] H. Kang, G. Huang, S. Ma, Y. Bai, H. Ma, Y. Li, X. Yang, Coassembly of inorganic macromolecule of exfoliated LDH nanosheets with cellulose, J. Phys. Chem. C. 113 (2009) 9157–9163. doi:10.1021/jp900861k.

[144] F. Song, X. Hu, Exfoliation of layered double hydroxides for enhanced oxygen evolution catalysis, Nat. Commun. 5 (2014) 1–9. doi:10.1038/ncomms5477.

[145] H. Liang, F. Meng, L. Li, A. Forticaux, L. Xiu, Z. Wang, S. Jin, Hydrothermal Continuous Flow Synthesis and Exfoliation of NiCo Layered Double Hydroxide Nanosheets for Enhanced Oxygen Evolution Catalysis, (2015). doi:10.1021/nl504872s.

[146] E. Gardner, K.M. Huntoon, T.J. Pinnavaia, Direct synthesis of alkoxide-intercalated derivatives of hydrotalcite-like layered double hydroxides: Precursors for the formation of colloidal layered double hydroxide suspensions and transparent thin films, Adv. Mater. 13 (2001) 1263–1266. doi:10.1002/1521-4095(200108)13:16<1263::AID-ADMA1263>3.0.CO;2-R.

[147] C. Jaubertie, M.J. Holgado, M.S. San Roman, V. Rives, Structural characterization and delamination of lactate-intercalated Zn,Al- layered double hydroxides, Chem. Mater. 18 (2006) 3114–3121. doi:10.1021/cm060512y.

[148] C. Nethravathi, B. Viswanath, M. Sebastian, M. Rajamathi, Exfoliation of alpha-hydroxides of nickel and cobalt in water, J. Colloid Interface Sci. 345 (2010) 109–

115. doi:10.1016/j.jcis.2010.01.047.

[149] C. Nethravathi, G. Harichandran, C. Shivakumara, N. Ravishankar, M. Rajamathi, Surfactant intercalated α -hydroxides of cobalt and nickel and their delamination-restacking behavior in organic media, J. Colloid Interface Sci. 288 (2005) 629.

[150] M. Sebastian, C. Nethravathi, M. Rajamathi, Interstratified hybrids of a -hydroxides of nickel and cobalt as supercapacitor electrode materials, Mater. Res. Bull. 48 (2013) 2715–2719. doi:10.1016/j.materresbull.2013.03.029.

[151] K.Y. Ma, W.J. Zhao, J.P. Cheng, F. Liu, X. Bin Zhang, Free-standing α-Co(OH)2/graphene oxide thin films fabricated through delamination and reassembling of acetate anions intercalated α-Co(OH)2 and graphene oxide in water, J. Colloid Interface Sci. 468 (2016) 238–246. doi:10.1016/j.jcis.2016.01.058.

[152] B. Schneiderová, J. Demel, A. Zhigunov, J. Bohuslav, H. Tarábková, P. Janda, K. Lang, Nickel-cobalt hydroxide nanosheets : Synthesis , morphology and electrochemical properties, J. Colloid Interface Sci. 499 (2017) 138–144. doi:10.1016/j.jcis.2017.03.096.

[153] B. Schneiderová, J. Demel, J. Pleštil, P. Janda, J. Bohuslav, D. Ihiawakrim, O. Ersen, G. Rogez, K. Lang, Nickel hydroxide ultrathin nanosheets as building blocks for electrochemically active layers, J. Mater. Chem. A. 1 (2013) 11429. doi:10.1039/c3ta12129a.

[154] B. Schneiderová, J. Demel, J. Pleštil, H. Tarábková, J. Bohuslav, K. Lang, Electrochemical performance of cobalt hydroxide nanosheets formed by the delamination of layered cobalt hydroxide in water, Dalt. Trans. 43 (2014) 10484. doi:10.1039/c4dt00141a.

[155] T. Hibino, Delamination of layered double hydroxides containing amino acids, Chem. Mater. 16 (2004) 5482–5488. doi:10.1021/cm048842a.

[156] J. Demel, J. Bohuslav, K. Lang, Electrochemical performance of cobalt hydroxide nanosheets formed by the delamination of layered cobalt hydroxide in water †, (2014) 10484–10491. doi:10.1039/c4dt00141a.

[157] X. Yang, K. Takada, M. Itose, Y. Ebina, R. Ma, K. Fukuda, T. Sasaki, Highly swollen layered nickel oxide with a trilayer hydrate structure, Chem. Mater. 20 (2008) 479–485. doi:10.1021/cm702981a.

[158] T.W. Kim, E. Oh, A. Jee, T. Lim, H. Park, Soft-Chemical Exfoliation Route to Layered Cobalt Oxide Monolayers and Its Application for Film Deposition and Nanoparticle Synthesis, (2009) 10752–10761. doi:10.1002/chem.200901590.

[159] Y. Masuda, Y. Hamada, W.S. Seo, K. Koumoto, Exfoliation of Layers in NaxCoO2, 6 (2006) 1632–1638. doi:10.1166/jnn.2006.224.

[160] J. Kim, J. Kim, S. Choi, Y.S. Lim, W. Seo, H.J. Hwang, J. Kim, J. Kim, S. Choi, Y.S. Lim, W. Seo, Nanostructured thermoelectric cobalt oxide by exfoliation / restacking route Nanostructured thermoelectric cobalt oxide by exfoliation / restacking route, 113705 (2014). doi:10.1063/1.4768258.

[161] J.-Y. Kim, J.-I. Kim, W.-S. Seo, Exfoliation Route to Nanostructured Cobalt Oxide with Enhanced Thermoelectric Performance, Appl. Phys. Express. 4 (2011)

065201-1. doi:10.1143/APEX.4.065201.

[162] O.C. Compton, A. Abouimrane, Z. An, M.J. Palmeri, L.C. Brinson, Exfoliation and Reassembly of Cobalt Oxide Nanosheets into a Reversible Lithium-Ion Battery Cathode, Small. 8 (2012) 1110–1116. doi:10.1002/smll.201101131.

[163] Q. Cheng, T. Yang, Y. Li, M. Li, C.K. Chan, Oxidation–reduction assisted exfoliation of LiCoO 2 into nanosheets and reassembly into functional Li-ion battery cathodes, J. Mater. Chem. A. 4 (2016) 6902–6910. doi:10.1039/C5TA09069E.

[164] C. Tang, D. Giaume, L. Guerlou-demourgues, G. Lefèvre, P. Barboux, Prediction of isoelectric point of manganese and cobalt lamellar oxides : application to controlled synthesis of mixed oxides, Langmuir. 34 (2018) 6670–6677. doi:10.1021/acs.langmuir.8b00190.

[165] C. Tang, Exfoliation and restacking of manganese and cobalt based lamellar oxides for supercapacitor electrodes, Université de Bordeaux, 2017. doi:HAL Id: tel-01696266.

[166] R. Ma, T. Sasaki, Nanosheets of Oxides and Hydroxides: Ultimate 2D Charge-Bearing Functional Crystallites, Adv. Mater. 22 (2010) 5082–5104. doi:10.1002/adma.201001722.

[167] J.E. ten Elshof, H. Yuan, P. Gonzalez Rodriguez, Two-Dimensional Metal Oxide and Metal Hydroxide Nanosheets: Synthesis, Controlled Assembly and Applications in Energy Conversion and Storage, Adv. Energy Mater. 6 (2016). doi:10.1002/aenm.201600355.

[168] Z. Gao, W. Yang, Y. Yan, J. Wang, J. Ma, X. Zhang, B. Xing, L. Liu, Synthesis and exfoliation of layered α-Co(OH)2 nanosheets and their electrochemical performance for supercapacitors, Eur. J. Inorg. Chem. (2013) 4832–4838. doi:10.1002/ejic.201300525.

[169] A.A.S. Rovetta, M.P. Browne, A. Harvey, I.J. Godwin, J.N. Coleman, And, M.E.G. Lyons, Cobalt Hydroxide Nanoflakes and their Application as Supercapacitors and Oxygen Evolution Catalysts, Nanotechnology. 28 (2017) 375401.

[170] C. Nethravathi, M. Rajamathi, Synthesis of graphene oxide-intercalated a -hydroxides by metathesis and their decomposition to graphene / metal oxide composites, Carbon N. Y. 48 (2010) 4343–4350. doi:10.1016/j.carbon.2010.07.047.

[171] J. Bai, H. Yan, Q. Liu, J. Liu, Z. Li, X. Bai, R. Li, J. Wang, Synthesis of layered α-Ni(OH)2/RGO composites by exfoliation of α-Ni(OH)2for high-performance asymmetric supercapacitors, Mater. Chem. Phys. 204 (2018) 18–26. doi:10.1016/j.matchemphys.2017.10.028.

[172] K. Adpakpang, S.M. Oh, X. Jin, S. Hwang, A Direct Hybridization between Isocharged Nanosheets of Layered Metal Oxide and Graphene through a Surface-Modification Assembly Process, (2014) 15459–15466. doi:10.1002/chem.201403871.

[173] J.P. Cheng, L. Liu, K.Y. Ma, X. Wang, Q.Q. Li, J.S. Wu, F. Liu, Hybrid

nanomaterial of alpha-Co(OH)2 nanosheets and few-layer graphene as an enhanced electrode material for supercapacitors, J. Colloid Interface Sci. 486 (2017) 344–350. doi:10.1016/j.jcis.2016.09.064.

[174] Q. Li, X. Hu, Q. Yang, Z. Yan, L. Kang, Z. Lei, Z. Yang, Z. Liu, Electrocapacitive performance of graphene/Co3O4 hybrid material prepared by a nanosheet assembly route., Electrochim. Acta. 119 (2014) 184–191. doi:10.1016/j.electacta.2013.12.066.

[175] H.-W. Wang, Z.-A. Hu, Y.-Q. Chang, Y.-L. Chen, H.-Y. Wu, Z.-Y. Zhang, Y.-Y. Yang, Design and synthesis of NiCo2O4–reduced graphene oxide composites for high performance supercapacitors, J. Mater. Chem. 21 (2011) 10504. doi:10.1039/c1jm10758e.

[176] X. Liu, J. Liang, Y. Bando, T. Sasaki, Molecular-Scale Heteroassembly of Redoxable Hydroxide Nanosheets and Conductive Graphene into Superlattice Composites for High-Performance Supercapacitors, (2014) 4173–4178. doi:10.1002/adma.201400054.

Experimental results

3. Experimental results

3.1 Enhancement of the Ni-Co hydroxide response as Energy Storage Material by Electrochemically Reduced Graphene Oxide.

Alberto Adán-Más[a,b,*] , Raquel G. Duarte[a,c] , Teresa M. Silva[a,d], Liliane Guerlou-Demourgues[b], Maria Fátima G. Montemor[a,*]

[a] Centro de Química Estrutural-CQE, DEQ, Instituto Superior Técnico, Universidade de Lisboa, 1049-001, Lisboa, Portugal

[b] CNRS, University of Bordeaux, Bordeaux INP, ICMCB UPR 9048, 33600 Pessac, France

[c] ESTBarreiro, Instituto Politécnico de Setubal, Setubal, Portugal

[d] ADEM, GI-MOSM, ISEL-Instituto Superior de Engenharia de Lisboa, Instituto Politécnico de Lisboa, Lisboa, Portugal

Keywords: Electrochemically Reduced Graphene Oxide; Nickel-Cobalt Hydroxide; Energy Storage Electrode; Electrochemical Impedance Spectroscopy

Abstract

Nickel-Cobalt double hydroxide materials are combined with Electrochemically Reduced Graphene Oxide (Er-GO) on top of Stainless Steel collectors by means of a one-step pulsed electrodeposition technique. Results show that, when Er-GO is integrated into the Nickel-Cobalt hydroxide matrix, there is an improvement of the electrochemical performance of the material, which shows increased capacity, stability and rate capability. As seen by Scanning Electron Microscopy (SEM), X-Ray Photoelectron Spectroscopy (XPS), Grazing-Incidence X-Ray Diffraction (GIXD) and Raman Spectroscopy, there is an excellent integration between the materials that leads to the enhanced electrochemical response. Capacity values up to 96 mA·h/g and a 62% capacity retention after 5000 cycles were achieved. Moreover, scan rates up to 2000 mV/s without loss in electrochemical response were possible proving its good rate capabilities. A detailed study of the cycling degradation phenomena was also done by means of electrochemical impedance spectroscopy (EIS). Thus, this novel electrodeposited material serves as an excellent material for energy storage applications.

3.1.1. Introduction

Achieving a sustainable development requires society to migrate from fossil fuels and traditional energy usage systems to greener energetic arrangements, from production to usage and storage [1,2]. This ever-growing society relies more and more on off-grid technologies, requiring an optimisation on the cost-effectiveness, eco-friendliness and performance of energy storage devices. However, some challenges are currently being faced in order to keep up with this increasing demand of efficient energy.

On one hand, Lithium-based batteries have been traditionally used and considered best candidates due to their high energy density, light weight and relatively long lifetime. However, they are potentially unsafe, their cost-effectiveness is not optimal and have issues regarding their eco-friendliness. Besides, the redox reactions associated to the lithium intercalation and de-intercalation entail two major problems: the degradation of electrode and electrolyte materials during cycling and hence limited lifetime and large activation barriers that prolong the charging process [3].

On the other hand, Capacitors and Electric Double Layer Capacitors or Supercapacitors can efficiently store and supply energy in a very fast way during millions of cycles. This high-power density is a consequence of the absence of Faradaic reactions. Nonetheless, their energy density, especially compared to batteries, is extremely low, leaving room for research to exploit.

During the last decade researchers have been extensively working to bridge the gap between supercapacitors and batteries. The goal is to achieve high power, high energy density and long lifetime within the same material. That led to the development of three different intermediate systems, namely; Pseudocapacitors, Faradaic-like Capacitors, also called Redox Pseudocapacitors and High-Power High-Lifetime Batteries or Pseudocabatteries. They are differentiated based on their electrochemical responses, and therefore, their constituent materials [4–6]. The first group is based on surface redox reactions that emulate supercapacitor behaviour, i.e. they do not have pronounced redox peaks in their voltammetric response and present linear dependence of the charge stored throughout the whole potential window. The most well-known group of pseudocapacitive materials are MnO_2 and RuO_2. On the other hand, Redox Pseudocapacitors have different redox and charge mechanisms, presenting redox peaks in the voltammogram and pseudo-linearity in their charge-discharge which is a consequence of their nanostructured nature. This is, for example, the case of $LiCoO_2$ [7–9].

The scope of this paper is based on the third group of energy storage devices; high-power, high-rate batteries or, as Chae and Brousse et al. and others have defined, the development of an electrode material that can be used in pseudocabatteries. These devices display redox peaks in their voltammogram and a voltage-dependent response in the charge-discharge curve, leading to higher energy and power densities and improved cycle lifetime.

For the material to be optimal for this purpose, it not only has to have good capacity and a wide operational voltage window, but it must have, among others, good chemical stability, high surface area and good ionic and electronic conductivity. Finally, low cost and environmentally friendliness should also be considered. Bearing all these properties in mind, transition metal hydroxides (TMH) of Cobalt and Nickel in combination with graphene species have been studied as potentially good candidates for energy-storage electrode materials [6,10].

Nickel and cobalt composites have been extensively used for energy storage. On one hand, Nickel compounds are usually selected for its relatively low cost, good capacity and electrochemical activity (theoretical value for the α/β couple of 490 mA·h/g) [11–13]. On the other hand, $Co(OH)_2$-based composites stand out for their high capacity values, reliable redox activity and large surface area, consequence of its layered structure [14,15]. Nonetheless, it is the combination of both hydroxides what has been proven to have the best performance [16] and often synergistic effects have been pin pointed [17].

In the recent past, binary metal oxides and hydroxides have become an interesting field for researchers to exploit due to their low cost, larger electrical conductivity and higher electrochemical activity than the individual components. For example, $NiCo_2O_4$ presents better electrochemical activity and electrical conductivity, which is at least two orders of magnitude higher than the single metal oxides. Several groups, such as Wang and Song or Gupta et al. have already developed Ni-Co hydroxide nanosheets that have high capacity, increased rate capability and better cycling stability than nickel and cobalt hydroxides individually due to a synergistic effect [16,18].

However, Nickel and Cobalt Hydroxides and combinations thereof present some drawbacks that include increased series resistance and decreased chemical stability during cycling. These effects decrease efficiency over time. Formation of aggregates may also occur, reducing the total active surface area and porosity, so limiting the electrolyte penetration and ionic conductivity [19,20]. Contrarily to these metal hydroxides, carbon materials, often used in Supercapacitors, have very good electrical conductivity, chemical stability and large active surface area [21]. Notwithstanding, their capacity values are, comparatively, extremely low. Thus, the incorporation of carbon-based materials with metallic species is becoming a field with great potential.

Recently, there has been extensive research in the field of graphene and its derivatives, since its discovery by Novoselov et al. [22]. Graphene-based materials properties include excellent electrical conductivity associated with fast electron transfer, a high theoretical specific surface area (2630 m^2/g which is lower in the case of graphene oxide derivatives but the oxygen groups can be used as anchoring points for metal hydroxide particles) and chemical stability [22]. Graphene derivatives also tend to aggregate but, due to its monolayer nature, they can be potentially combined with metal hydroxides to achieve a synergistic effect where both the single metal and single graphene derivatives reduce their tendency to agglomerate/aggregate and thus maximizing the electrochemical properties [23–25].

Reduced graphene oxide has already been combined with metal hydroxides and mixed double hydroxides in the past for energy storage purposes. Several methods have been used to produce such composite materials, such as chemical precipitation [26,27], hydrothermal [28], sol-gel [29], microwave assisted [30], electrophoretic deposition [31–33] or potentiostatic and potentiodynamic electrodeposition [34].

Despite the very promising results achieved, there is little understanding concerning the long-term behaviour, ageing and degradation processes of the metal/reduced graphene oxide composites. Thus, the present work focuses not only on the capacity performance of electrodeposited double Cobalt-Nickel hydroxides combined with Electrochemically Reduced Graphene Oxide (Er-GO) but also in its long-term degradation mechanisms by means of SEM and a detailed study of ageing by impedance spectra. Results show that graphene has two main contributions. On one hand, Er-GO stabilizes the metal hydroxide structures, accommodating strain in the charge discharge process. On the other hand, it provides a conductive matrix that reduces the total equivalent series resistance. Besides,

this improved conductivity may be related to the outstanding scan rate capabilities of the composites, whose values are above what is commonly reported in literature.

3.1.2. Experimental

3.1.2.1. Materials

A commercial Graphene Oxide (GO) aqueous solution 4 g L^{-1} obtained from Graphenea Tech. Co. was used to prepare the composite electrode material. $Ni(NO_3)_2 \cdot 6H_2O$, $Co(NO_3)_2 \cdot 6H_2O$ and $NaNO_3$ (pro-analysis grade) were obtained from Sigma-Aldrich and used in the preparation of electrode materials as received. AISI 304 (Goodfellow) 0.914mm thick stainless-steel plates were used as current collector and substrate for the electrodeposition, and previously polished with emery paper to a rough finish and double-rinsed with water and acetone to eliminate abrasive particles and, finally, air-dried. Potassium hydroxide was used as received from Sigma-Aldrich and used to prepare a 1M KOH electrolyte solution.

3.1.2.2. Synthesis of electrodeposited Electrochemically Reduced Graphene Oxide (Er-GO), $Ni_xCo_{1-x}(OH)_2$ and $Ni_xCo_{1-x}(OH)_2$/Er-GO composites on Stainless Steel.

Electrodeposition was carried out in a three-electrode electrochemical cell by means of an Interface IFC1000-07087 Potentiostat (Gamry Instruments) in a limited circular area of $1cm^2$. The as-prepared commercial solution of GO was diluted to a concentration of 1g L^{-1} and mixed with $Ni(NO_3)_2 \cdot 6H_2O$ and $Co(NO_3)_2 \cdot 6H_2O$ with 6mM:3mM and 3mM:6mM Ni:Co molar ratios. Different molarities and Nickel-Cobalt ratios were tested, however, only results for these molarities are presented in this work since they presented the best electrochemical response. To simplify, they will be designated as Ni-$Co(OH)_2$ (2:1) and Ni-$Co(OH)_2$ (1:2) throughout this paper. A mixed solution of the metal nitrates with graphene oxide was obtained. Before electrodeposition, the aqueous solution of GO and its mixture with metal nitrates were ultrasonicated for 30 minutes to create a stabilised dispersion of the aforementioned components.

To evaluate the response of electrochemically reduced graphene oxide deposited individually, a 1g·L^{-1} solution of GO solution was mixed with the appropriate quantity of $NaNO_3$ to obtain the same electrolyte conditions. Nickel and Cobalt hydroxides were also electrodeposited individually under the same conditions.

The electrodeposition process (ED) was performed using a platinum foil of 2.5x2.5 cm^2 as counter electrode and SCE electrode as reference. Pulsed Potentiostatic ED method was carried out with two cathodic potentials in a 10 second pulse for 30 cycles. The potential range studied for the pulsed potentiostatic depositions was from -0.8V to -1.2V. The results presented in this work correspond to a pulsed deposition between the voltages -0.9V and -1.2V since they presented the best electrochemical response for the deposited materials. The electrodes were washed with distilled water and dried for 24-48h before electrochemical measurements.

The mass of the samples was determined by means of a micro-balance Sartorius MC5-0CE with an accuracy of 0.01mg. The deposited mass of the composites was always comprised between 0.1 and 0.2 mg.

3.1.2.3. Electrochemical Study of $Ni_xCo_{1-x}(OH)_2$ and $Ni_xCo_{-1x}(OH)_2$/Er-GO composites.

All electrochemical characterization was performed using the aforementioned equipment and a three-electrode electrochemical cell with KOH 1M as electrolyte. Cyclic Voltammetry was carried out at the different scan rates (20-2000) mV·s^{-1} in a potential

window ranging from -0.2V to 0.5V vs SCE electrode. Galvanostatic Charge/Discharge was also carried out at different current values (1 to 10 $A \cdot g^{-1}$) in the same voltage range.

Lifetime cycling test was performed during 5000 charge-discharge cycles at 10 A/g. Finally, Electrochemical Impedance Spectroscopy (EIS) of the electrode material was measured. Prior to the measurement, a conditioning at the desired measuring voltage for 1000 seconds was done. EIS measurements were carried out at different applied potentials (corresponding to charged and discharged conditions) by applying a sinusoidal perturbation with 10 mV of amplitude (RMS) in the frequency range of 0.01 to 10^5 Hz.

3.1.2.4. Characterization

Surface morphology and chemical composition of the as-prepared and cycled samples were studied by means of a Scanning Electron Microscopy (SEM) direct imagining and Energy-Dispersive X-ray Spectroscopy (FEG-SEM JEOL JSM 7800F Prime coupled with an EDS SDD X-Max 80mm^2 Oxford Instruments AZtecEnergy detector), which is located at the centre of micro-characterization Raimond Castaing, Toulouse. To obtain additional chemical information, Raman spectroscopy, Grazing-incidence X-Ray Diffraction (GIXD) and X-ray Photoelectron Spectroscopy (XPS) were used.

High Resolution Transmission Electron Microscopy (TEM) images and Energy Dispersive X-ray Spectroscopy, located at the Platform of Materials Characterization of Aquitaine (PLACAMAT), were obtained by means of a TEM JEOL 2200FS + EDX JEOL Si-Li working at 200kV with an image resolution of 0.19 nm and an EDS point resolution of 1.5nm. The images were obtained by scratching a portion of the electrodeposited layer and dispersing it in ethanol on top of a carbon grid.

Raman Spectra were acquired using a LabRAM HR Evolution Raman spectrometer (HORIBA, Jobin Yvon, Edison, NJ) with integrated BX41 microscope (Olympus) with an operating laser at 532 nm focused with a 50x objective lens. The spectra were obtained with an acquisition time of 10s and 10 accumulations. A spectrograph with a 600 lines/mm grating was used to provide a spectral resolution of 2 cm^{-1}, and the confocal hole size was set at 100 mm. The Raman spectra of each sample were truncated (100 and 3500 cm^{-1}).

Regarding XPS surface analysis, a ThermoFisher Scientific K-ALPHA spectrometer was used with a monochromatized Al Kα source (hν = 1486.6 eV) and a 200 microns spot size. A pressure of $3 \cdot 10^{-7}$ mbar was reached in the load lock chamber before the insertion of the samples in the analysis chamber and a pressure lower than 10^{-8} mbar inside the analysis chamber was attained for all the measurements. The spectra were acquired from 0 to 1100 eV at a constant pass energy of 200 eV and the high-resolution spectra for the elements (C1s, O1s, N1s, Ni2p, Ni3p, Co2p, Co3p, Fe2p, Fe3p, Cr2p and Si 2p) were obtained at a constant pass energy of 40 eV. Charge neutralization was applied during analysis. High resolution spectra were fitted and quantified using the AVANTAGE® software provided by ThermoFisher Scientific.

Finally, GIXD analysis were carried out by means of a BRUKER D8 Advance with Cu radiation (λ_{Cu} = 1.54056Å) operating at 40kV and 40 mA with a moving detector. The incidence angle was fixed around 1-1.5º according to the sample measured.

3.1.3. Results and Discussion

3.1.3.1. Physico-Chemical Characterization

Results in Fig. 3.1.1 reveal the morphology of the $Ni_xCo_{1-x}(OH)_2$ and $Ni_xCo_{1-x}(OH)_2$/Er-GO composite electrode materials synthesized by pulsed potentiostatic electrodeposition at room temperature. In combination with Energy Dispersive X-Ray Spectroscopy (EDS), whose results are shown in Table 3.1.1, the results evidence that there is no presence of iron and therefore full coverage of the current collector. Results suggest that the electrodeposited material seems to grow thanks to stacking of nickel and cobalt hydroxide platelets in a randomly oriented but densely packed manner, which results in a surface film. As opposed to previously reported Ni-Co hydroxide materials, which usually show a more porous spike-like or flower-like structure that consist of individual platelets [35–38], the electrodeposited $Ni_xCo_{1-x}(OH)_2$ materials seem to be more compact, with platelets mostly oriented on a parallel level to the substrate instead of being aligned perpendicularly to the substrate. Nonetheless, spike-like features can still be observed on the external surface of the material, showing the expected structure previously reported for these materials. This produces some roughness in the surface morphology that is clearly visible by SEM and that would correspond to superficial electrodeposited platelets.

On the other hand, $Ni_xCo_{1-x}(OH)$/Er-GO materials present, as expected, additional features in the film, corresponding to Electrochemically Reduced Graphene Oxide (Er-GO) whose flexible two-dimensional sheets present wrinkles and folded regions. On top of the Er-GO surface, the same spike-like structure appears due to the presence of the electrodeposited transition metal hydroxides. However, a less compact structure is observable compared to the individual double hydroxides. Thus, it can be concluded that Er-GO acts as a platform that embeds the metal hydroxide spike-like nanostructure and avoids its stacking to a certain extent.

It can be seen that there is an excellent interaction and integration in terms of morphology between these two materials. This is in accordance to the previously reported Er-GO/electrodeposited metal materials [34,39–43]. Presence of spike-like structures at different regions and depths of the composite can be observed. From that, it can be assumed that the electrodeposition of the metal hydroxides and Er-GO is simultaneous and that, once an Er-GO layer is electrodeposited, it is immediately covered by the hydroxides. Then, it successively deposits another Er-GO layer continuing the growth process. Thus, by combining these two materials it seems that Er-GO agglomeration is also avoided up to an extent, creating surface hydroxide layers on top of Er-GO that reduce stacking and agglomeration of the two integrating materials. This may contribute to a better electron/ion transfer in the material improving the electrochemical response by a synergistic effect. This is corroborated by an enhanced electrochemical response due to increased exposed active surface area as discussed below.

Analogous results are obtained by means of TEM and are presented in Fig. 3.1.2. Fine structure of the composite materials is presented showing the poor crystallization and turbostratic nature of the materials where only in the thinnest regions it is possible to observe the plane structures. Moreover, when Er-GO is introduced the samples are even less crystalline as in agreement with GIXD, presented later in this section. Energy Dispersive X-Ray Spectroscopy results are presented in Fig. 3.1.3 and 3.1.4. Both chemical composition; showing the good integration between Nickel hydroxide, Cobalt hydroxide and Er-Go; and mass percentage semi-quantification are presented. It is worth

mentioning that the resolution of EDS spot point is smaller than that of the Nickel-Cobalt atoms distance and, therefore, superposing points are obtained.

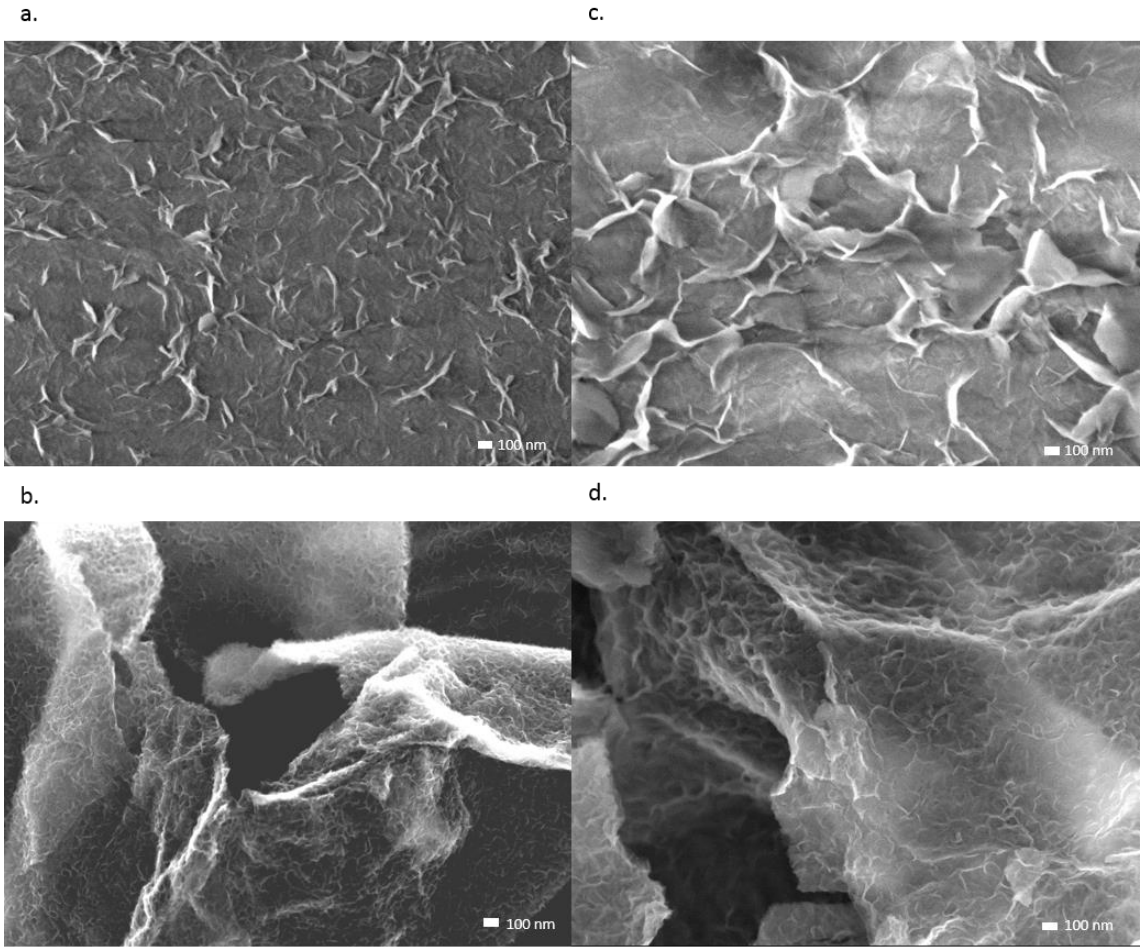

Fig. 3.1.1. SEM images of (a)Ni-Co$(OH)_2$ (2:1) (b) Ni-Co$(OH)_2$ (2:1) /Er-GO (c) Ni-Co$(OH)_2$ (1:2) and (d) Ni-Co$(OH)_2$ (1:2)/Er-GO electrode materials electrodeposited over Stainless Steel.

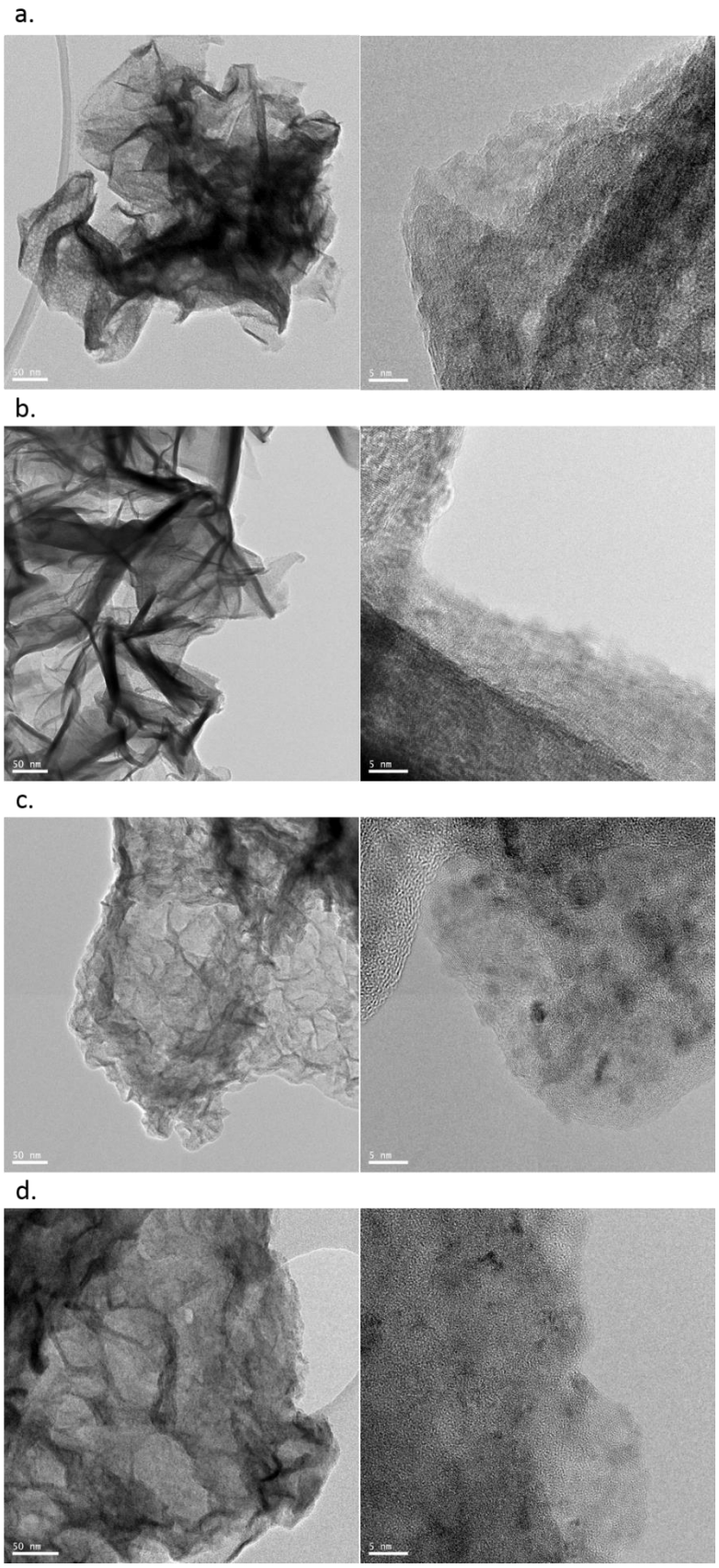

Fig. 3.1.2. High-Resolution and fine structure Transmission Electron Microscopy (HR-TEM) images of (a) Ni-Co$(OH)_2$ (2:1), (b) Ni-Co$(OH)_2$ (1:2), (c) Ni-Co$(OH)_2$/Er-GO (2:1) and (d) Ni-Co$(OH)_2$/Er-GO (1:2).

(a)

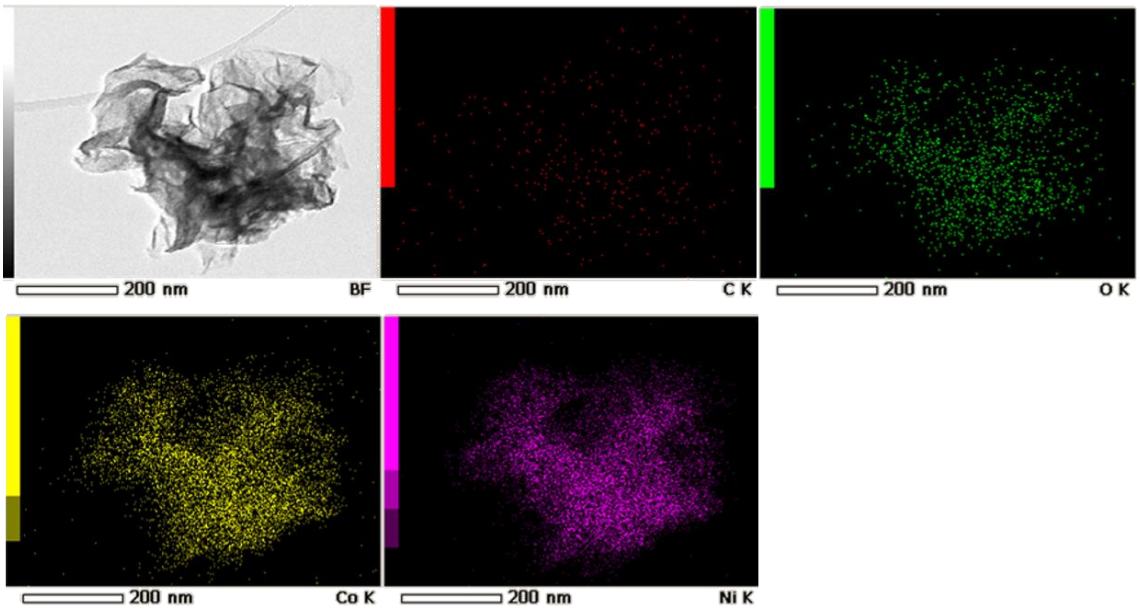

(b)

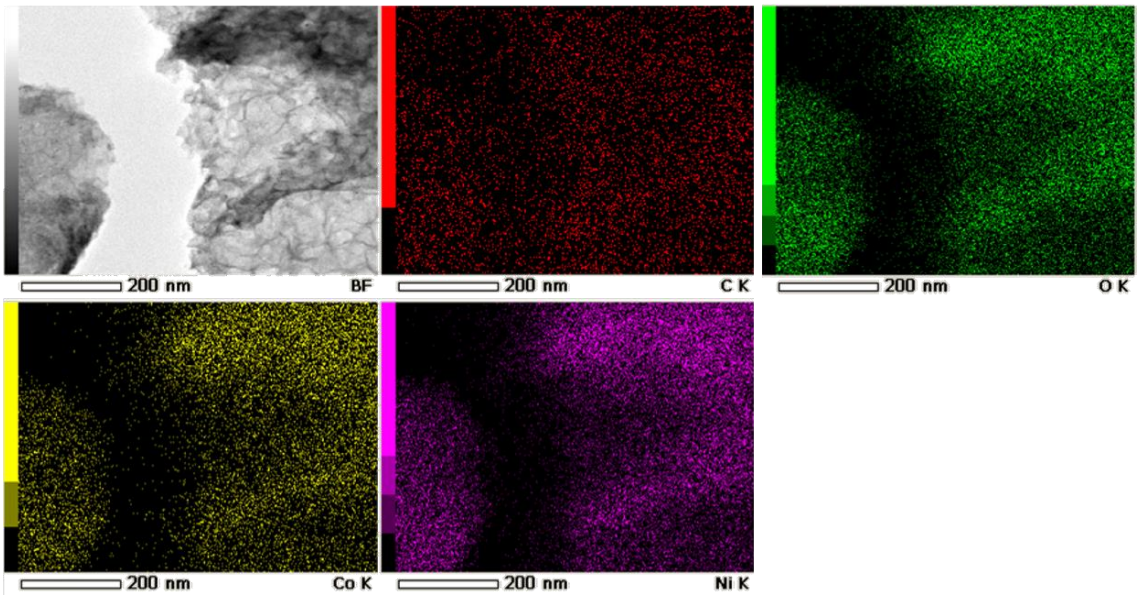

Fig. 3.1.3. Elemental mapping of Carbon, Oxygen, Cobalt and Nickel detected by EDS analysis for (a) Ni-Co(OH)2 (2:1) and (b) Ni-Co(OH)2/Er-GO (2:1).

(a)

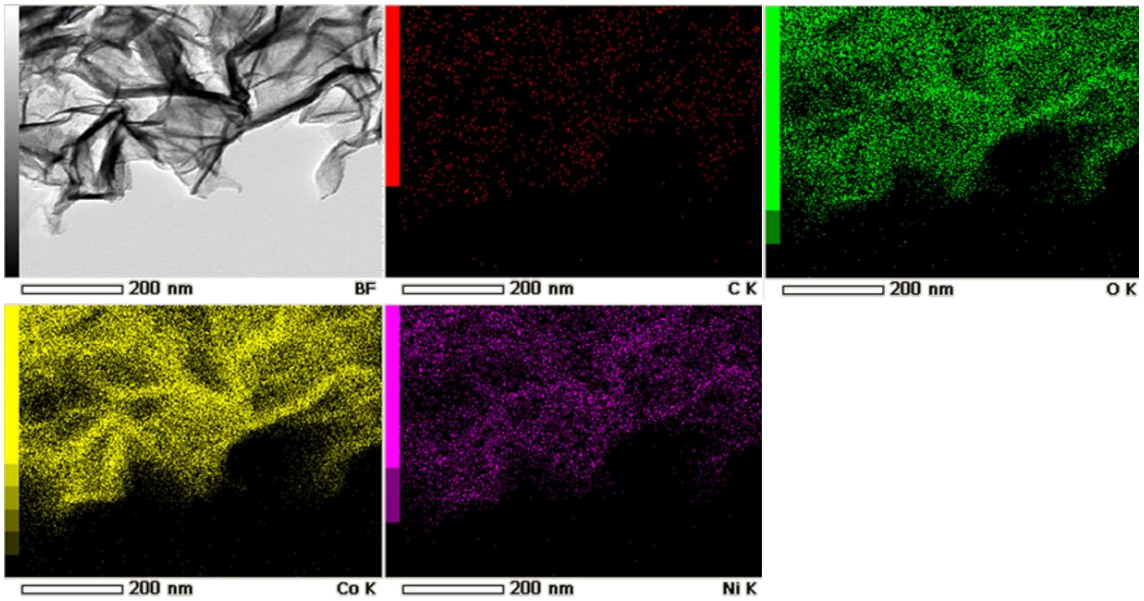

(b)

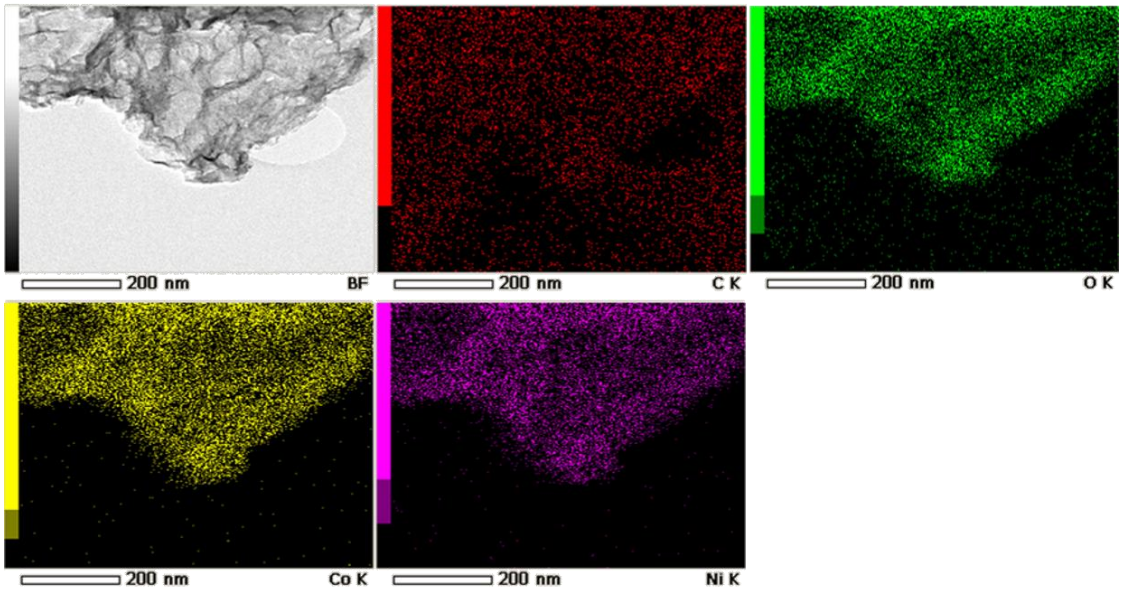

Fig. 3.1.4. Elemental mapping of Carbon, Oxygen, Cobalt and Nickel detected by EDS analysis for (a) Ni-$Co(OH)_2$ (1:2) and (b) Ni-$Co(OH)_2$/Er-GO (1:2).

EDS can serve as a semi-quantitative technique of chemical analysis for the composite materials as shown in table 3.1.1. If the ratios between Nickel and Cobalt are taken into account, the empiric formula calculated for them would approximately be $Ni_{0.33}Co_{0.66}(OH)_2$, $Ni_{0.33}Co_{0.66}(OH)_2$/Er-GO, $Ni_{0.66}Co_{0.33}(OH)_2$, $Ni_{0.66}Co_{0.33}(OH)_2$/Er-GO; which is in accordance to the molar ratios used in the electrodeposition procedure. Similar results can be obtained by studying semi-quantitatively the atomic percentage by means of X-Ray Photoelectron Spectroscopy (XPS).

Table 3.1.1
Semi-quantitative mass percentage results obtained by means of Energy Dispersive X-Ray Spectroscopy (EDS) for the electrodeposited samples.

	Ni-Co(OH)$_2$ (1:2)	Ni-Co(OH)$_2$ (1:2) /Er-GO	Ni-Co(OH)$_2$ (2:1)	Ni-Co(OH)$_2$ (2:1) /Er-GO
Cobalt	46.1±0.7	40.2±2.5	23.7±0.5	21.1±0.9
Nickel	26.2±0.7	25.1±1.4	43.6±0.4	42.3±1.1
Oxygen	25.6±0.6	29.2±1.7	29.5±0.7	29.1±1.8
Carbon	1.1±0.2	5.3±1.2	1.7±0.3	7.2±1.3
Nitrogen	1.0±0.3	0.2±0.2	1.5±0.1	0.3±0.3

XPS confirms the presence of Nickel-Cobalt hydroxides and that Er-GO does not alter the chemical composition of the metal hydroxide by having a similar ionization response. A semi-quantitative XPS analysis of the atomic percentages of the samples was also done. To obtain the presented results, the area beneath each peak was evaluated at five different points of the sample and used to calculate the atomic percentage of each element in each sample. A similar procedure for area calculation is used for all the samples. Since peak shape and position are also identical for the different samples, they are not shown. Average atomic percentage results are shown at table 3.1.2. Shake-up satellite peaks for both Cobalt and Nickel were not considered in this calculation, only the main peak at the Ni2p3/2 and Co2p3/2 were considered as seen in Fig. 3.1.5. On the other hand, the whole area was used to evaluate the quantity of the rest of components, namely, oxygen, nitrogen and carbon. Fe, Cr, N and Si were also investigated to study the possible presence of substrate signal. Fe, Cr and Si material species were not detected, while traces of N could be sometimes observed. This may be result of intercalated ions from the nitrates present in the electrodeposition electrolyte, intercalation commonly observed in Nickel-Cobalt α phases, as explained later in this work.

Table 3.1.2

Semi-quantitative atomic percentages with their corresponding errors obtained by means of X-Ray Photoelectron Spectroscopy for the samples Ni-Co(OH)$_2$(2:1), Ni-Co(OH)$_2$(2:1)/Er-GO, Ni-Co(OH)$_2$(1:2) and Ni-Co(OH)$_2$(1:2)/Er-GO.

	Ni-Co(OH)$_2$ (1:2)	Ni-Co(OH)$_2$ (1:2) /Er-GO	Ni-Co(OH)$_2$ (2:1)	Ni-Co(OH)$_2$ (2:1) /Er-GO
Cobalt	8±1	5.0±0.6	3.1±0.7	3.3±0.8
Nickel	3.2±0.7	2.6±0.1	7.0±0.2	5.8±0.5
Oxygen	50±1	39±2	49.3±0.8	44±4
Carbon	37±2	52±3	38±1	47±5
Nitrogen	1.8±0.6	1.3±0.2	1.6±0.3	0

A significant increase in Carbon atomic percentage is obtained when Er-GO is included as expected. If Nickel/Cobalt ratios are studied, the following values are obtained: 0.32/0.68; 0.37/0.63; 0.67/0.33 and 0.65/0.35. Although these values, as in EDS, are semi-quantitative, they can give an idea of the chemical composition of the composite materials and show their accordance to the molar ratios used during the electrodeposition process.

The ratio is preserved throughout the different Ni-Co(OH)$_2$ layers and is in accordance with EDS. As expected from the molar concentration present in the electrolyte, results give an empiric formula of $Ni_{0.33}Co_{0.66}(OH)_2$ and $Ni_{0.66}Co_{0.33}(OH)_2$ and their respective Er-GO based equivalent composites.

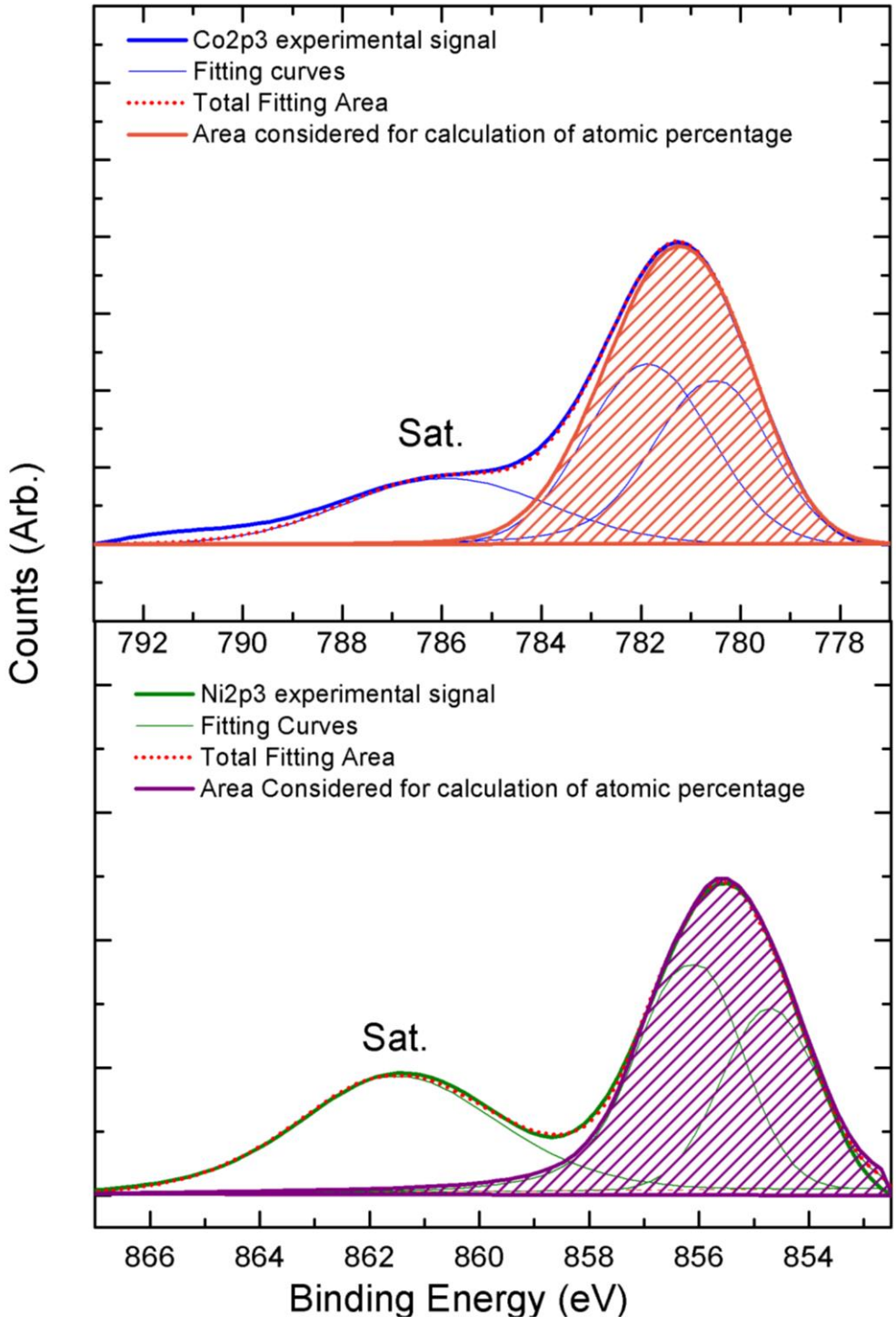

Fig. 3.1.5. Example of the area considered for semi-quantitative analysis calculation by means of XPS for Ni2p3 and Co2p3 for Ni-Co(OH)$_2$(2:1). Analogous fittings and calculations were performed for Ni-Co(OH)$_2$(2:1) /Er-GO, Ni-Co(OH)$_2$(1:2) and Ni-Co(OH)$_2$(1:2) /Er-GO.

Fig. 3.1.6 shows the Grazing-Incidence X-Ray Diffraction (GIXD) patterns for the $Ni_xCo_{1-x}(OH)_2$ compounds. Results show that the GIXD patterns for the composites without introducing electrochemically reduced graphene oxide (Er-GO) have two main peaks. The values correspond to an α phase of Ni-$Co(OH)_2$ with an interlayer distance and diffraction peaks in accordance to previously reported literature [18,44–48].

The values are analogous to those obtained for well-crystalized references of the metal hydroxides, where they are indexed as the {00l} family of plane reflections, in particular {003} and {006} [49,50]. As reported by Delmas [51] and co-workers and Bing et al. [52], one of the most important differences when distinguishing between the two main phases of Nickel and Cobalt hydroxides, α and β, is the stacking of layers along the c-axis. While β phases present an interlamellar distance of 4.8 Å without any intercalated species, α phases show a much larger distance of ranging from 7.5 to 8.5 Å depending on the intercalated anion and a random orientation of the layers with water intercalated between the hydroxyl groups. Since the samples show values close to 8 Å for the first family plane, it can be unequivocally identified as an α phase [44,51–53]. The expanded interlayer space of α phases has been extensively studied and is a consequence of anionic species and water intercalation in the interslab space. Several anionic species have been reported to be intercalated, such as CO_3^{-2}, SO_4^{2-} or NO_3^-[51]. In this case, it is likely that some of the intercalated anions to form the α phase are NO_3^- since they are present in the initial electrodeposition electrolyte and the presence of nitrogen is confirmed by XPS.

Additionally, the composites in which Er-GO is introduced have poorer peak resolution. As observed by SEM, the crystal structure for the electrodeposited metal hydroxides is much smaller when incorporated onto the Er-GO matrix. These thinner crystals create smaller coherence domains that lead to a widening of the spectra lines. That reduction of the coherence domain leads to a response that virtually has the same peaks as their parental hydroxide, with approximately the same peak positions but much broadened and less defined. Thus, broad peaks are associated to smaller particle size.

Deposited samples are nanostructured in nature and present apparent low thickness. As a consequence, this has made impossible to measure the XRD signal of Er-GO and has led to low signal/noise ratio results for the composite materials. A low-ordered and high interlamellar distance material is in accordance with the resolution of the XRD peaks obtained. Therefore, this can be correlated to a higher active surface area and, hence, a better electrochemical response is expected. In conclusion, GIXD results are associated to an α-phase of nickel and cobalt hydroxide and Ni-$Co(OH)_2$ embedded into the surface of Er-GO layers, as observed by SEM.

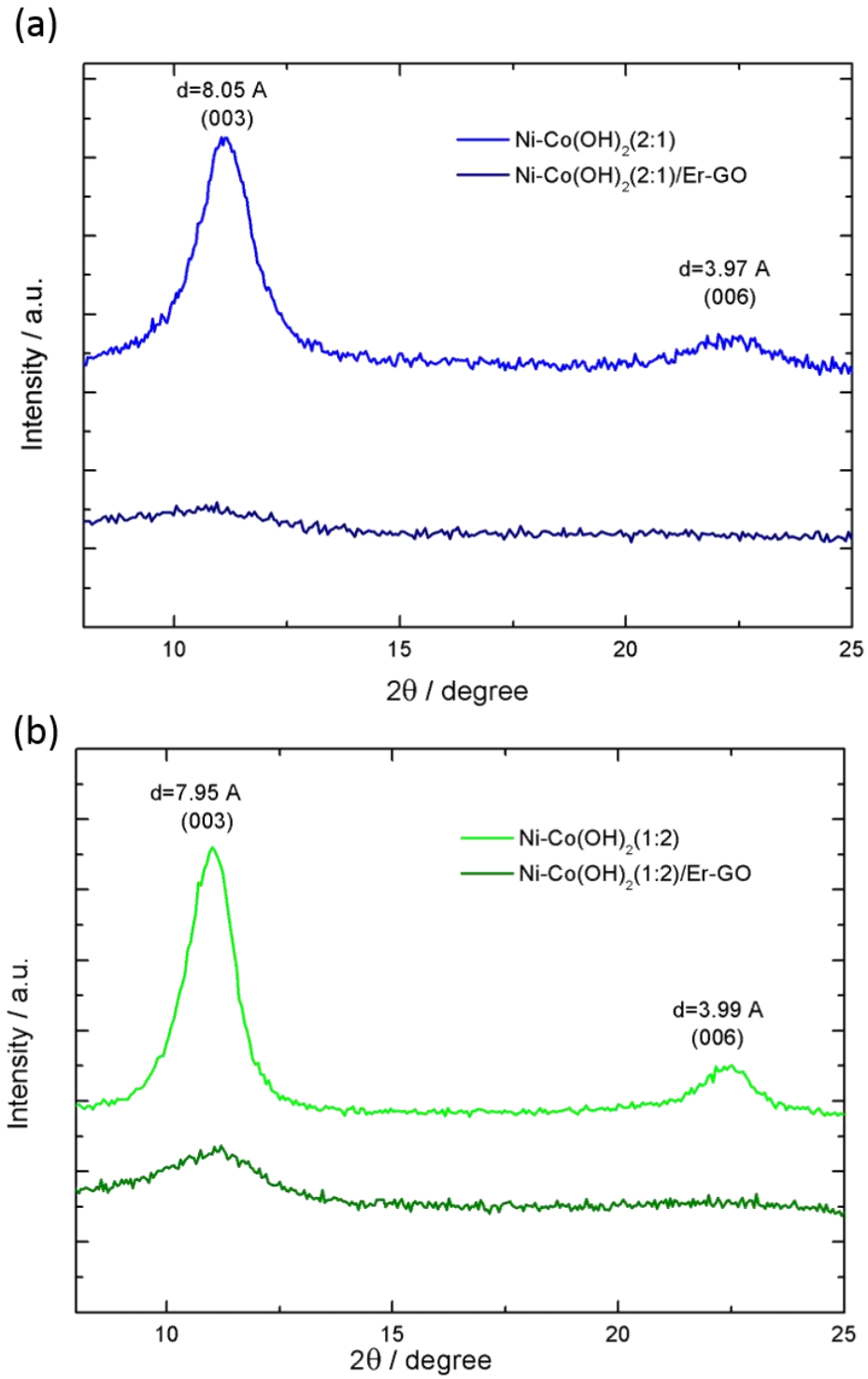

Fig. 3.1.6. Comparative GIXD results for the samples (a) Ni-$Co(OH)_2$(1:2)$_2$ and Ni-$Co(OH)_2$(1:2)/Er-GO (b) Ni-$Co(OH)_2$(2:1) and Ni-$Co(OH)_2$(2:1)/Er-GO.

Raman spectroscopy was used to further characterize the composite. Raman spectroscopy has been proven to be an excellent tool to characterize carbon derivatives and, in particular, graphene derivatives. Fig. 3.1.7 shows the Raman spectra obtained for the different composites (Raman spectra for dropcasted non-reduced graphene oxide in comparison to Er-GO is presented in Fig. 3.1.7). All the peaks shown in the lower region of the spectrum are associated to Nickel and Cobalt hydroxide whereas the peaks from 1000 cm^{-1} upwards are related to graphene derivatives.

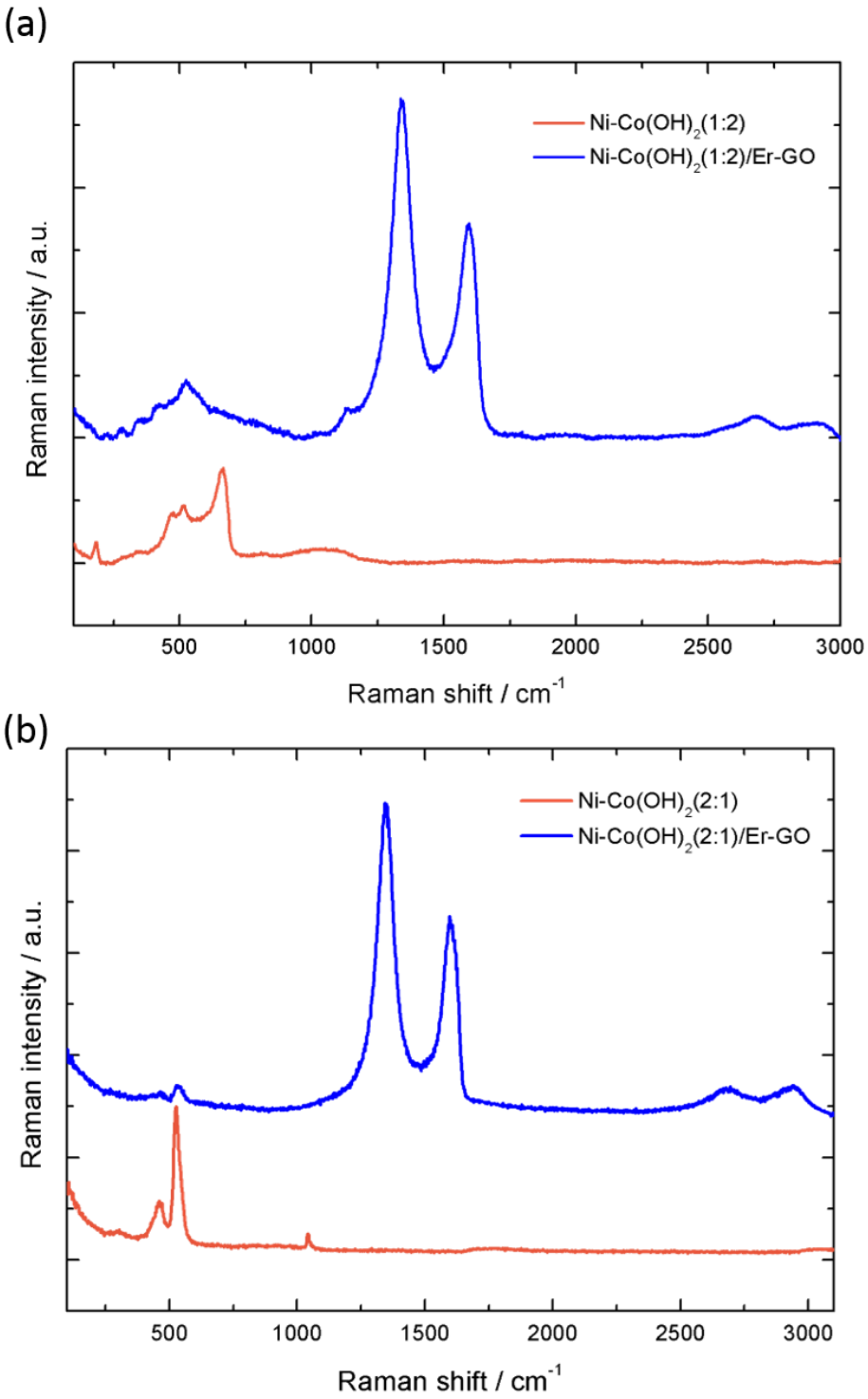

Fig. 3.1.7. Raman Spectra for (a) Ni-Co(OH)$_2$(1:2) and Ni-Co(OH)$_2$(1:2)/Er-GO and (b) Ni-Co(OH)$_2$(2:1) and Ni-Co(OH)$_2$(2:1)/Er-GO Electrodeposited on Stainless Steel.

For all the samples shown, the D band assigned to Er-GO or GO is located at around 1340 cm^{-1} and the G band at approximately 1590 cm^{-1}, which is characteristic of this group of materials. On the one hand, the D band is ascribed to the breathing modes of the sp^2 configuration of the aromatic carbon rings, this is defects and disorder. On the other hand, the G peak at around 1590 cm^{-1} is related to first-order scattering of the E_{2g} phonon of sp^2 carbon atoms, i. e. in-plane-bond-stretching motion of the pairs of Csp^2. Finally, they also

present 2D bands at around 2700 cm^{-1} associated to stacked graphene oxide or reduced graphene oxide layers, indicating a higher number of agglomerated material[54,55].

It is worth noticing that two extra peaks are observed in the case of drop-casted graphene oxide at 1143 cm^{-1} and 1754 cm^{-1} which, according to some authors [56,57], are exclusive from non-reduced forms of graphene derivatives. This is in accordance with our results, since they disappear in the reduction process of electrodeposition. However, the most significant characteristic is the attenuation of the G band for Er-GO in relation to the D band. As previously reported in literature [56], the G band is associated to sp^2 carbons, suggesting a decrease in the size of the hybridized domains, related to the removal of oxygen groups in the restoration of the graphene-like network. Similar results were obtained for the composites with nickel and cobalt hydroxide, indicating a good reduction process for graphene oxide when transition metals are present in the system. Moreover, if the intensity ratios obtained for I_D/I_G are compared, the values obtained are 1, 1.17, 1.38 and 1.36 for dropcasted GO, Er-GO, Ni-$Co(OH)_2$(1:2)/Er-GO and Ni-$Co(OH)_2$(2:1)/Er-GO respectively, which can be correlated to a better reduction process of the carbon monolayers by integrating metal hydroxide particles [34,56,57].

As opposed to XPS, where nickel and cobalt compounds could be easily characterized, due to the nanostructured nature of the metal hydroxides it is extremely difficult to accurately assign a response for such materials, being Raman mainly used to characterize the carbon form than the metal hydroxides. Despite that, some metal hydroxide bands can still be assigned according to literature. For Ni-$Co(OH)_2$(1:2) four main peaks are present, at approximately 185.5 cm^{-1}, 473.6 cm^{-1}, an intense band at 519.2 cm^{-1}, 661.3 cm^{-1}. These values are close to previously reported literature and may be associated to E_g mode, O-M-O bending, M-O A_g vibrations, and A_g modes respectively. Also, a broad band at 1066 cm^{-1} is associated to the presence of residual nitrates or hydroxyl deformation modes. The fact that the two main peaks are located at 473 and 519cm^{-1} would suggest a majority of α phases in the composite, as previously reported in literature for both nickel and cobalt. Nonetheless, although they can be somehow correlated, there is a displacement of the peaks when Er-GO is incorporated. It is well known that the position of $Co(OH)_2$ bands are greatly dependent upon the substrate and the coating process. When incorporating Er-GO, the electrodeposition of the metal hydroxide is switched from the stainless steel surface to the active surface area of Er-GO, which can explain the different response under Raman stimulus [34,58–60].

Ni-$Co(OH)_2$(2:1) has three main peaks at 463cm^{-1}, 524 cm^{-1} and 1039cm^{-1}. This can be assigned to O-M-O bending, M-O A_g vibrations, and either –OH deformation modes or residual nitrates in the structure that would come from the electrodeposition process. In this case, more similar peaks are present in the Er-GO based composite. Once again, this is in accordance with XRD since it is related to an α structure according to literature for both $Ni(OH)_2$ and $Co(OH)_2$ [58,61–63].

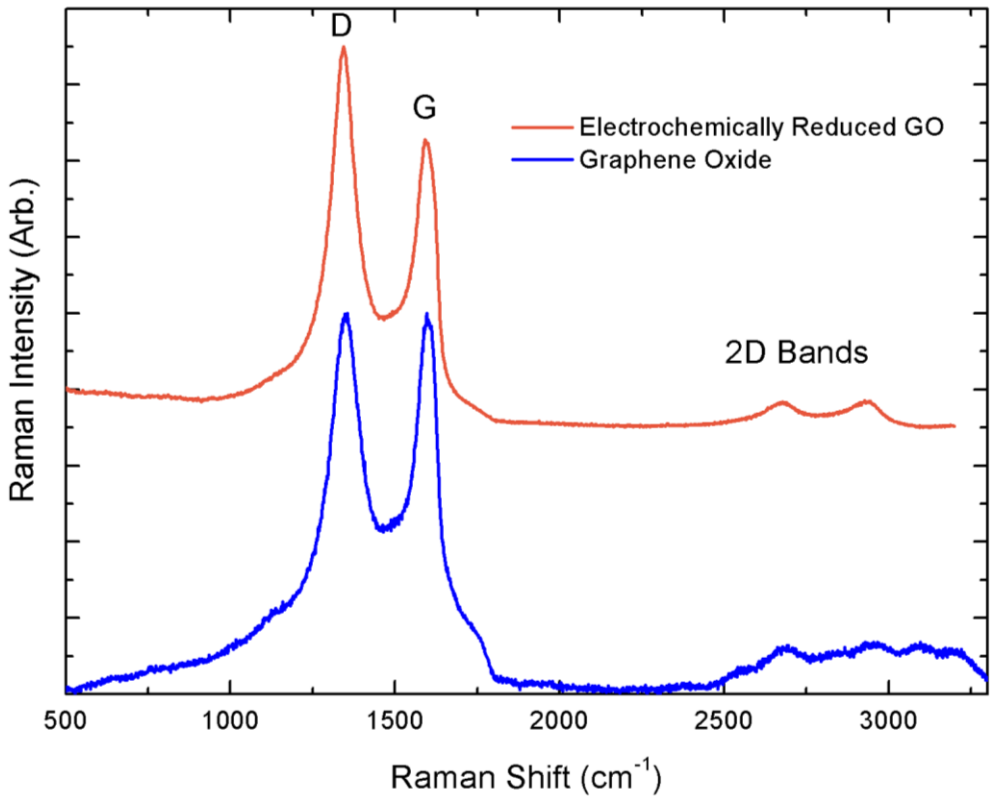

Fig. 3.1.8. Raman Spectra comparison of dropcasted graphene oxide and electrochemically reduced graphene oxide.

3.1.3.2. Electrochemical Characterization

It is well known that the electrochemical response of energy storage materials is closely related to their active surface area, their capacity and their conductivity among others. If, as suggested by SEM, the binder-free integration between Er-GO and the double metal hydroxide material is good, the carbon material could provide a good conductive matrix with increased surface area that would support the highly capacitive hydroxides. Thus, an increase in the electrochemical performance of $Ni_xCo_{1-x}(OH)_2$/Er-GO would be expected. Moreover, the interconnection between the nanosheets may prove useful to reinforce the electrode material to resist upon cycling. Materials were tested by means of cyclic voltammetry as shown in Fig. 3.1.9a. Cyclic voltammetry of $Ni_xCo_{1-x}(OH)_2$ and $Ni_xCo_{1-x}(OH)_2$/Er-GO and, for comparison purposes, the individual metal hydroxide $Ni(OH)_2$ and $Co(OH)_2$ are presented. The results, measured in KOH 1M, are shown in a potential range that varies within -0.2V to 0.5V (vs. SCE) for measurements performed at a scan rate of 50 mV/s.

As expected from previously reported literature, all Ni-Co hydroxide-based materials present a couple of peaks corresponding to the cathodic and anodic waves. For Cobalt hydroxide the oxidation peak occurs at approximately 0.016 V (vs. SCE) while reduction happens at -0.028 V (vs. SCE). This is associated to one redox reversible reaction for the couple Co(II)/Co(III) for the redox reaction:

$$Co(OH)_2 + OH^- \leftrightarrow CoOOH + H_2O + e^- \text{ (eq. 3.1.1)}$$

On the other hand, Nickel hydroxide also shows one reversible reaction which is associated to the well-established reaction:

$$Ni(OH)_2 + OH^- \leftrightarrow NiOOH + H_2O + e^- \text{ (eq. 3.1.2)}$$

with an oxidation peak at 0.39 V (vs. SCE) and a reduction peak at around 0.29V (vs. SCE). It is worth noting that both reactions are associated to hydroxyl transfer and, therefore, the KOH electrolyte penetration is expected to play a key role in the rate capabilities of the process and in the overall electrochemical performance. Moreover, there is a phase transition from α-Ni-Co$(OH)_2$ to γ-Ni-Co(OOH) when the sample is charged which is reversed when discharged. Analogous reactions are expected for the double hydroxide material, with intercalation/de-intercalation of hydroxyl anions.

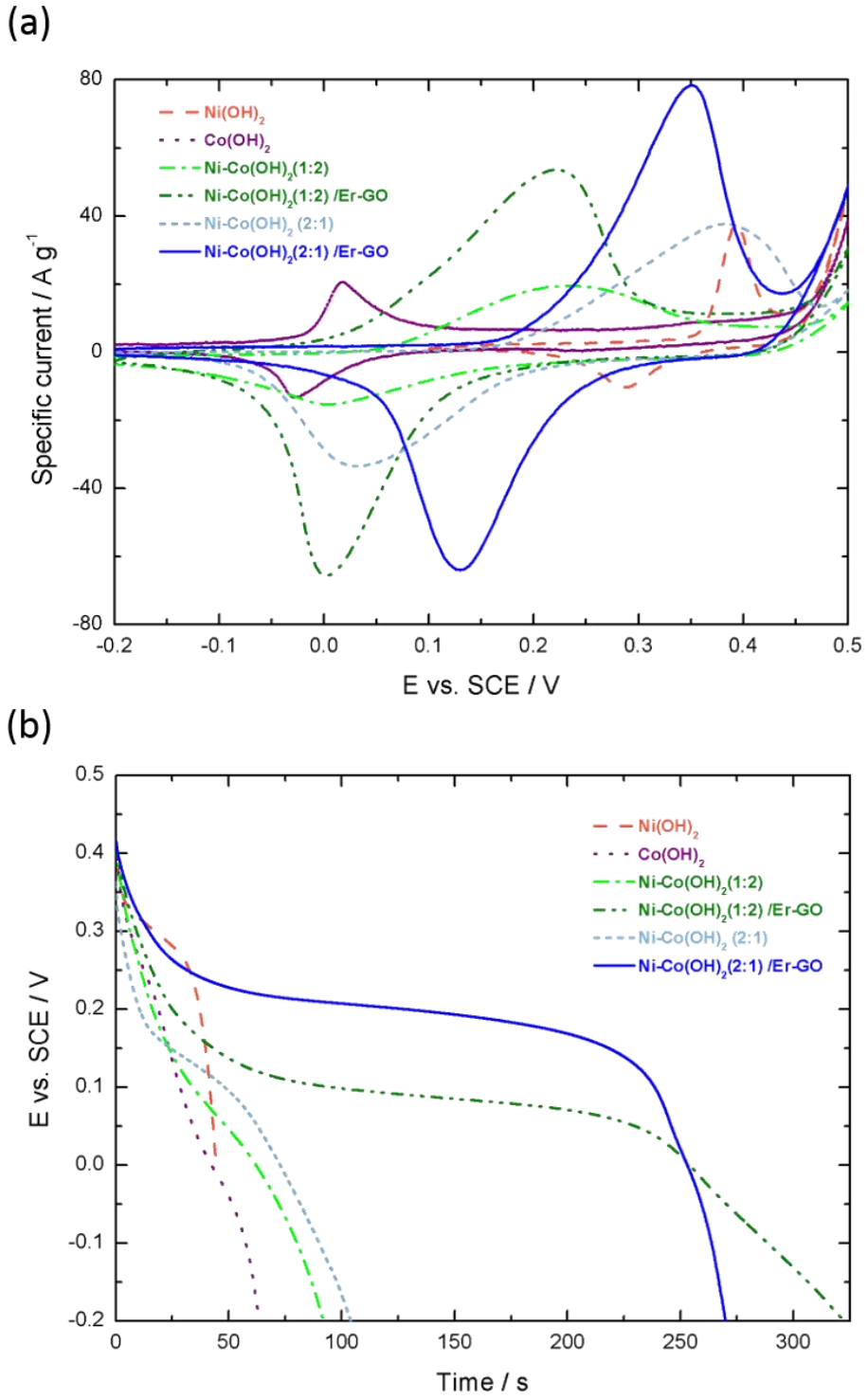

Fig. 3.1.9. (a) Cyclic Voltammetry comparison at 50 mV/s and (b) Galvanostatic Charge Discharge comparison at 1A/g.

When the double-hydroxide material, $Ni_xCo_{1-x}(OH)_2$, is investigated by CV three main features can be observed. First, one pair of redox peaks, associated to the aforementioned reactions. It can be noticed that these peaks are broadened in comparison to those observed for single Nickel and Cobalt Hydroxides, indicating overlapped contributions from both Nickel and Cobalt. Secondly, a displacement of the peaks is also observed according to the quantity of nickel or cobalt introduced in the system. In fact, for Ni-Co$(OH)_2$(1:2) the redox peaks are displayed in a potential region that is closer to single cobalt hydroxide, namely, an oxidation peak at 0.23V and a reduction peak at 0V (vs. SCE); whereas for Ni-Co$(OH)_2$(2:1) the voltammetric waves are closer to the single $Ni(OH)_2$ peak region, this is, 0.38V and 0.03V for the oxidation and reduction reactions respectively. It is also worth mentioning that the ratio between the oxidation and reduction peaks is closer to one in comparison to the individual metal hydroxides, showing a good reversibility of the redox reaction. In fact, while $Ni(OH)_2$ and $Co(OH)_2$ present a maximum current peak ratio ($I_{max,\ cathodic}$/ $I_{max,\ anodic}$) of 3.7 and 1.6 respectively, the composite materials have a value around 1.2 in any case, suggesting a good reversibility of the reaction.

The area under the cyclic voltammograms of the double hydroxide materials is much larger compared to single nickel and cobalt hydroxide. This entails a growth in the capacity behaviour of the material. There is a synergistic addition to their response creating not only an intermediate behaviour but an increased response as a result of a cohesive electrochemical performance. This is in good accordance with previously reported literature [47,64,65].

When Er-GO is integrated into the mixed Ni-Co hydroxides (Fig. 3.1.9a), the voltammetric profile is similar to their analogous carbon-free material showing the presence of a main anodic and cathodic waves. This is attributed to the strong faradaic process that, as expected, contribute more to the capacity than the double-layer charging/discharging of Er-GO. A synergistic effect can again be seen with enlarged capacity response for the composite material. Peaks are maintained although slightly displaced, reducing the anodic/cathodic peak distance to more intermediate values of $Ni(OH)_2$ and $Co(OH)_2$ peaks; 0.22V and 0.35V for the oxidation peaks and 0V and 0.13V for the reduction peaks of Ni-Co$(OH)_2$(2:1)/Er-GO and Ni-Co$(OH)_2$(1:2)/Er-GO respectively.

Capacity values are calculated for these composites from discharge curves presented in Fig. 3.1.9b. As it can be observed, GCD curves present a plateau at around 0.1-0.2 V making the response voltage dependent. While Ni-Co$(OH)_2$(1:2) and Ni-Co$(OH)_2$(2:1) present values of only 30 and 34 mA·h/g at 1A/g; Ni-Co$(OH)_2$(1:2)/Er-GO and Ni-Co$(OH)_2$(2:1)/Er-GO present an increase of around a 250% in their capacity response, with values of 96 mA·h/g for the first and 74 mA·h/g for the latter. Nickel-Cobalt hydroxides have been previously reported in literature, also combined with graphene derivatives. Kulkarni et al. presented a similar result for the Ni-Co hydroxides by studying the potentiodynamic deposition of Co-Ni LDH on top of Stainless Steel. The results reported capacitance values of 1164 F/g at 100mV/s with 77% retention after 10000 cycles in KOH 2M with similar discharge values to the ones obtained in the present report [66]. Other synthesis techniques have also been investigated, like the one used by Meng et al., a solvothermal synthesis to produce an analogous material with values up to 855.4 C/g in 6M KOH in a 0.5V range and an 80% retention after 1000 cycles [67].

Several groups have focused in increasing the specific capacity by introducing another substrate. For instance, Zhang et al. published Ni-Co LDH on top of Nickel Foam on a

zeolitic imidazolate framework with a specific capacity of 894 C/g at 2A/g for a 0.45V potential range [68].

Araki et al. reported stabilized sol-gel alpha-$NiCo(OH)_2$ at different molar ratios with specific capacity ranging from 355 to 714 C/g and a 700 cycle stability of the system [69]. The same group recently reported a mixture of Ni-Co alpha hydroxides mixed with reduced graphene oxide, achieving values analogous to the present work as high as 1348 F/g and a 96% retention after 5000 cycles while Ni-Co hydroxides on their own delivered an specific capacitance of 1036 F/g with a similar capacitance retention [70].

Other examples with graphene include the work of Bai et al. that describes a reduced graphene oxide skeleton on top of a nickel foam that was consecutively dip-coated with Ni-Co double hydroxide achieving a capacitance of 1054 F/g in a 0.5V potential range and 70% retention after 4000 cycles [41] or the one presented by Wang et al. that wrapped nanohexagons of the double hydroxide with reduced graphene oxide with a maximum capacitance of 1292.79 F/g and an 85.9% retention after 2500 cycles [71]. In any case, when graphene derivatives are introduced, aggregation is reduced and electron transport is increased.

In this study, the individual response of the material, by selecting an electrochemically inert substrate, and the effect that electrochemically reduced graphene oxide produces in the double hydroxide and its electrochemical cycling degradation are investigated. The increased capacity when Er-GO is incorporated is associated to a synergistic effect that can be attributed to several reasons. First of all, the network of the composite material provides more anchor sites compared to double metal hydroxides deposited directly on top of stainless steel. This is a more extensive active surface area that will reduce aggregation and increase the total deposited active material.

On second place, increased efficiency in both charge transport and ion mobility is achieved due to the intimate contact between the carbon conductive material and the metal hydroxide capacitive material. Graphene is known to be an excellent electronic conductor, thus, a sustained matrix for an enhanced electron transfer is created with this approach. An increased active surface area can be related to a major electrolyte/electrode interaction, leading to a better hydroxyl ion mobility, which is responsible for the faradaic reactions. Finally, the nanostructured nature of the flakes of graphene-derivative composite material lead to an increased porosity and active surface area as observed by SEM. This is opposed to the compact double hydroxides material and may also contribute to the accessibility of the electrolyte and ion mobility enhancing the electrochemical response [22].

Fig. 3.1.10a, 3.1.10c, 3.1.11a and 3.1.11c show the evolution of the composite materials with different scan rates, ranging from 20 mV/s up to 2000 mV/s depending on the material. The two characteristic peaks are always present when increasing the scan rate up to 200 mV/s. As the scan rate increases, there is a shift of the anodic peak towards more positive potentials while cathodic peaks behave in the opposite manner. This is related to an increase in polarization effects and evidences the reversible nature of the redox process present in the system. The peak current density also increases with increasing scan rates, phenomenon associated to smaller diffusion layers [35,41].

For Ni-$Co(OH)_2$(1:2) and Ni-$Co(OH)_2$(2:1) the curve shape is lost when higher scan rates are used, while for Er-GO based composites higher scan rates can be achieved. The slower nature of redox reactions, so as the difficulties for the hydroxyl ion to mobilise and access the surface area reduce the reversibility of the process, which is translated in a deformation of the cyclic voltammogram shape at high scan rates. The increment in the

oxidation peak potential is associated with a diffusion controlled mechanism for the hydroxyl ions [72].

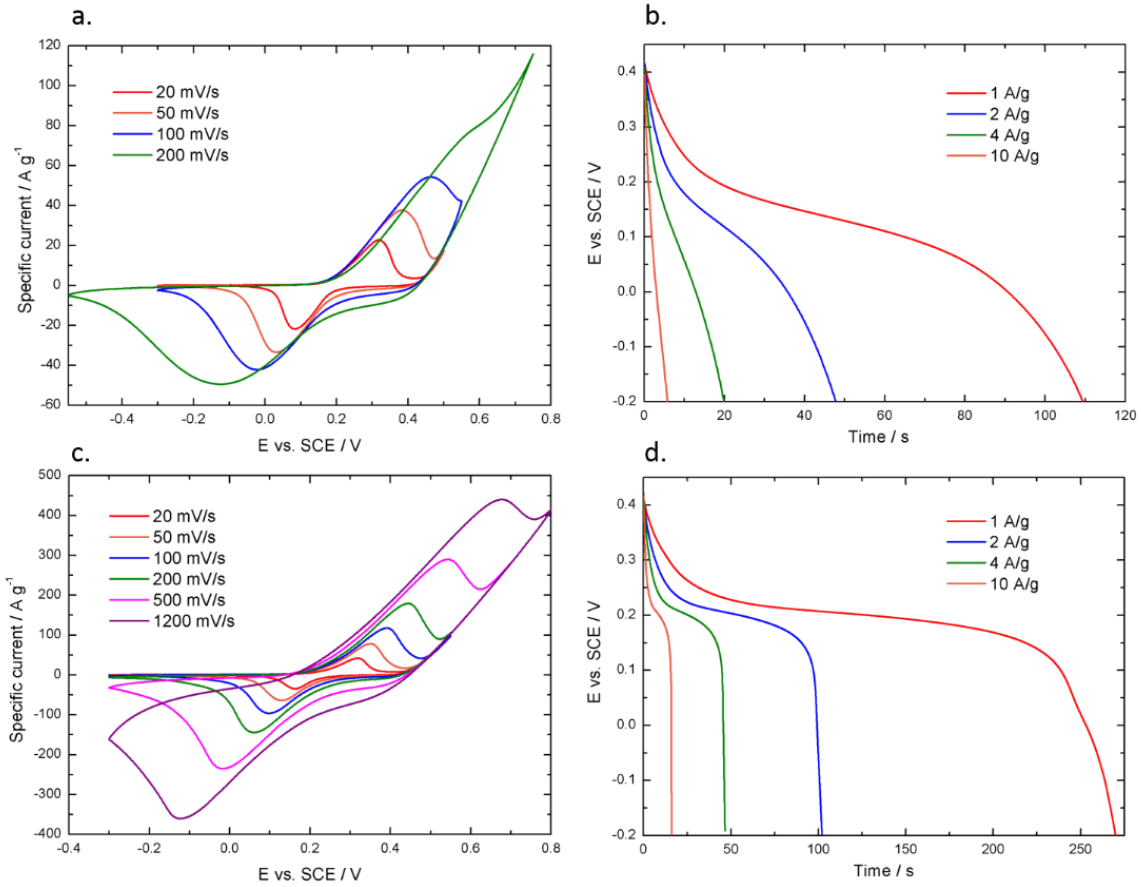

Fig. 3.1.10. Cyclic Voltammetry at different scan rates and Galvanostatic Charge-Discharge Curves at different current densities for (a,b) Ni-$Co(OH)_2$(2:1) and (c,d) Ni-$Co(OH)_2$(2:1)/Er-GO.

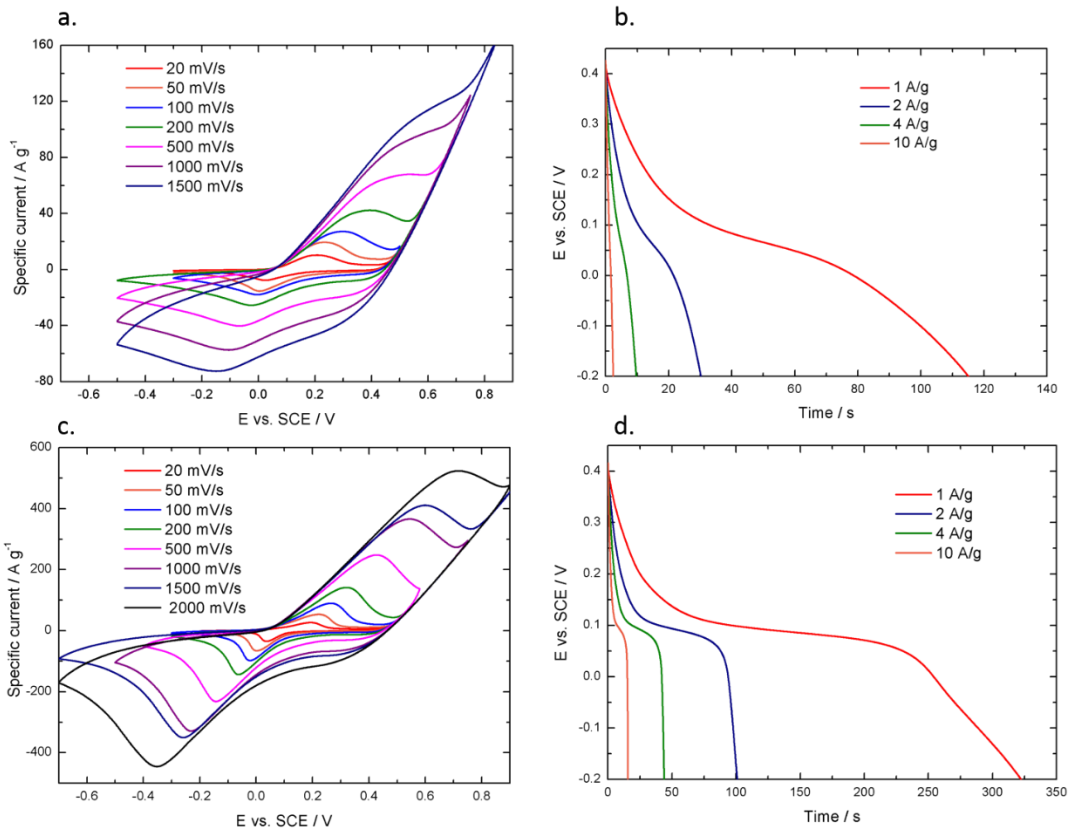

Fig. 3.1.11. Cyclic Voltammetry at different scan rates and Galvanostatic Charge-Discharge Curves at different current densities for (a,b) Ni-Co(OH)$_2$(1:2) and (c,d) Ni-Co(OH)$_2$(1:2)/Er-GO.

When Er-GO is introduced, the system can reach scan rates as high as 1200 mV/s for Ni-Co(OH)$_2$(2:1)/Er-GO and 2000 mV/s for Ni-Co(OH)$_2$(1:2)/Er-GO, without losing their well-defined electrochemical response. Such achievable high scan rates without distorting the CV response is associated to the high rate capabilities obtainable for these materials. To our knowledge, this is the first time that such high scan rates are being used for a Nickel-Cobalt composite material for energy storage purposes. The achievement of these high-rate capabilities is correlated to the inclusion of electrochemically reduced graphene oxide and its intrinsic properties. When the scan rate increases, reactions are subjected to much faster processes. This is associated with the hydroxyl flux, hence good electrolyte penetration and accessible active surface area so as good ionic and electron conductivity of the material. There is less aggregation, which entails more accessibility of the electrolyte and therefore more ion mobility.

When the applied current is increased in galvanostatic charge-discharge measurements, a drop in current values is expected. These results are presented in Fig. 3.1.10b, 3.1.10d, 3.1.11b and 3.1.10d and their capacity retentions are presented in Fig. 3.1.12. When higher current densities are applied, a larger number of hydroxyl atoms are required to conduct the faradaic reactions. For that reason, current densities values of 1, 2, 4 and 10A/g were studied and the values of capacity are presented in table 3.1.3. A higher retention is expected when porosity, exposed active surface area and conductivity are augmented. Capacity retentions are 21, 45, 51 and 58% for Ni-Co(OH)$_2$(2:1), Ni-Co(OH)$_2$(2:1)/Er-GO, Ni-Co(OH)$_2$(1:2) and Ni-Co(OH)$_2$(1:2)/Er-GO respectively.

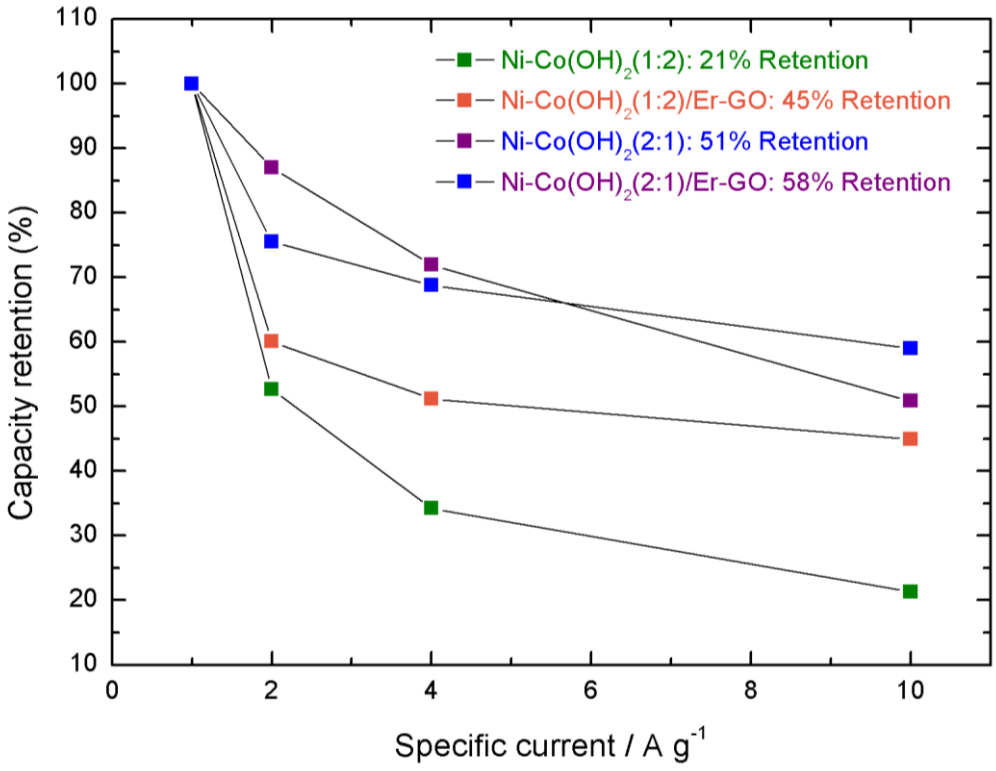

Fig. 3.1.12. Capacity Retention for different Current Densities for the Ni-Co(OH)$_2$ and Ni-Co(OH)$_2$/Er-GO composite materials.

Table 3.1.3
Capacity values for different current densities for Ni-Co(OH)$_2$/Er-GO composite materials.

Current Density ($A \cdot g^{-1}$)	$C_{Ni\text{-}Co(OH)2(1:2)}$ ($mA \cdot h \cdot g^{-1}$)	$C_{Ni\text{-}Co(OH)2(1:2)/Er\text{-}GO)}$ ($mA \cdot h \cdot g^{-1}$)	$C_{Ni\text{-}Co(OH)2(2:1)}$ ($mA \cdot h \cdot g^{-1}$)	$C_{Ni\text{-}Co(OH)2(2:1)/Er\text{-}GO}$ ($mA \cdot h \cdot g^{-1}$)
1	30	96	35	75
2	26	58	18	57
4	22	49	12	52
10	15	43	7	44

3.1.3.3. Electrochemical Impedance Spectroscopy and Cycling Behaviour

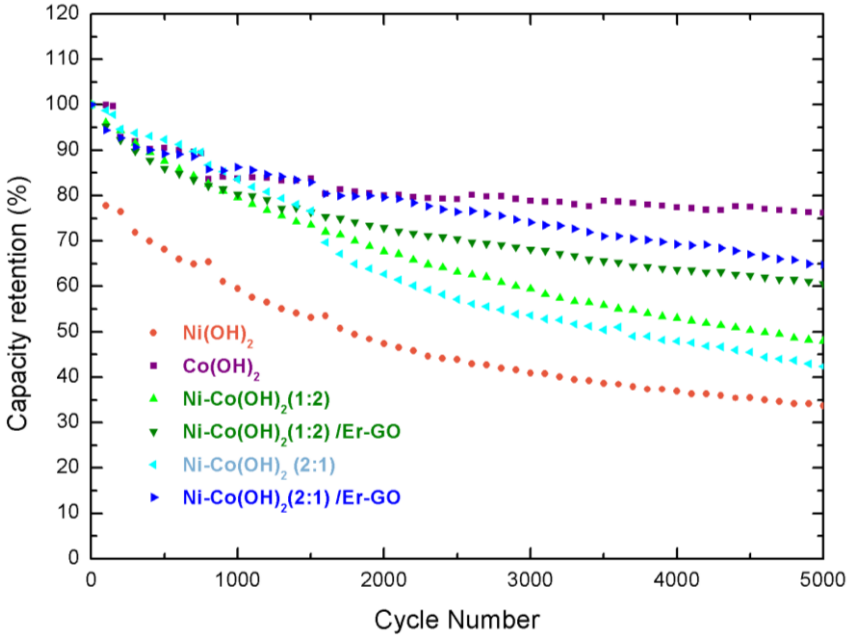

Fig. 3.1.13. Capacity Retention comparison at 10A/g for $Ni(OH)_2$, $Co(OH)_2$, Ni-$Co(OH)_2$ (1:2), Ni-$Co(OH)_2$ (1:2)/Er-GO, Ni-$Co(OH)_2$ (2:1) and Ni-$Co(OH)_2$ (2:1)/Er-GO.

Cycle life is key in the performance and stability evaluation of an energy storage material. The stability of all the composite materials was evaluated by applying a 10A/g charge-discharge current during 5000 cycles and their capacity retention was evaluated, as presented in Fig. 3.1.13. Capacity retentions of 48, 42, 60 and 62% were obtained for Ni-$Co(OH)_2$(1:2), Ni-$Co(OH)_2$(2:1), Ni-$Co(OH)_2$(1:2)/Er-GO and Ni-$Co(OH)_2$(2:1)/Er-GO respectively. The decay in the capacity with cycling is attributed to irreversible reactions, blocking of active sites and formation of resistive diffusion paths and the mechanical degradation of the sample due to swelling during the charge-discharge process. There is an increase in the capacity retention directly related to the presence of Er-GO. This material increases the chemical stability in the charge-discharge process of the film. When the carbon material is present, the composite's stability may be reinforced resisting collapse, surface detachment and degradation upon cycling.

The improvement of electron transport may be another cause of electrochemical enhancement and is closely related to a better transportation from the active material to the current collector. This can only be confirmed if the equivalent series resistance is reduced. For that reason, and to obtain a better electrochemical characterization, electrochemical impedance spectroscopy was performed and evaluated for all samples. EIS for the different electrodeposited films is presented in Fig. 3.1.15 and 3.1.16 for the composite materials along with the cyclic voltammetry response effect for the samples when cycled, presented in Fig. 3.1.14.

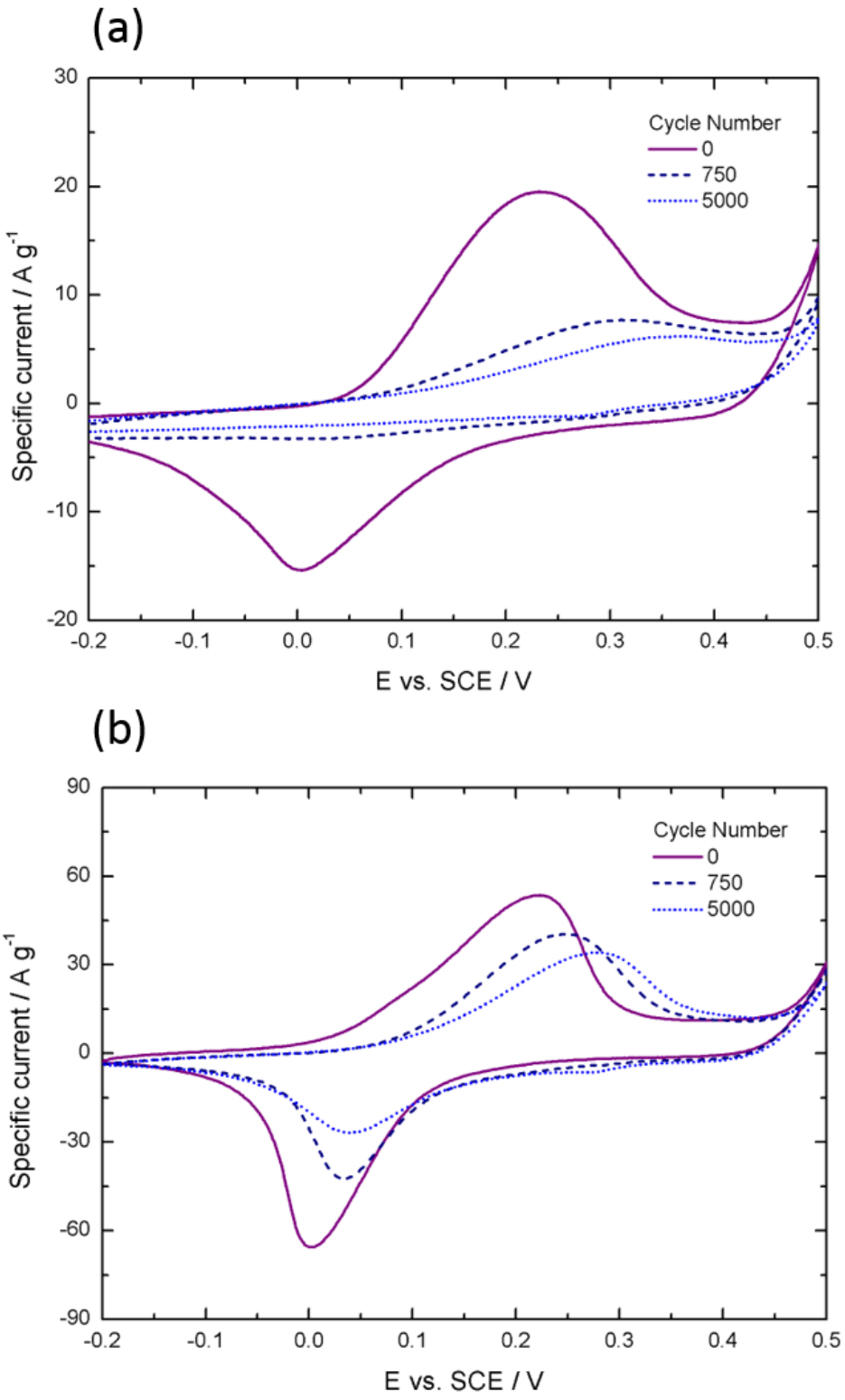

Fig. 3.1.14. Cyclic Voltammetry response degradation with cycling for the samples (a) Ni-Co(OH)$_2$ (2:1) and (b) Ni-Co(OH)$_2$(2:1)/Er-GO composite materials.

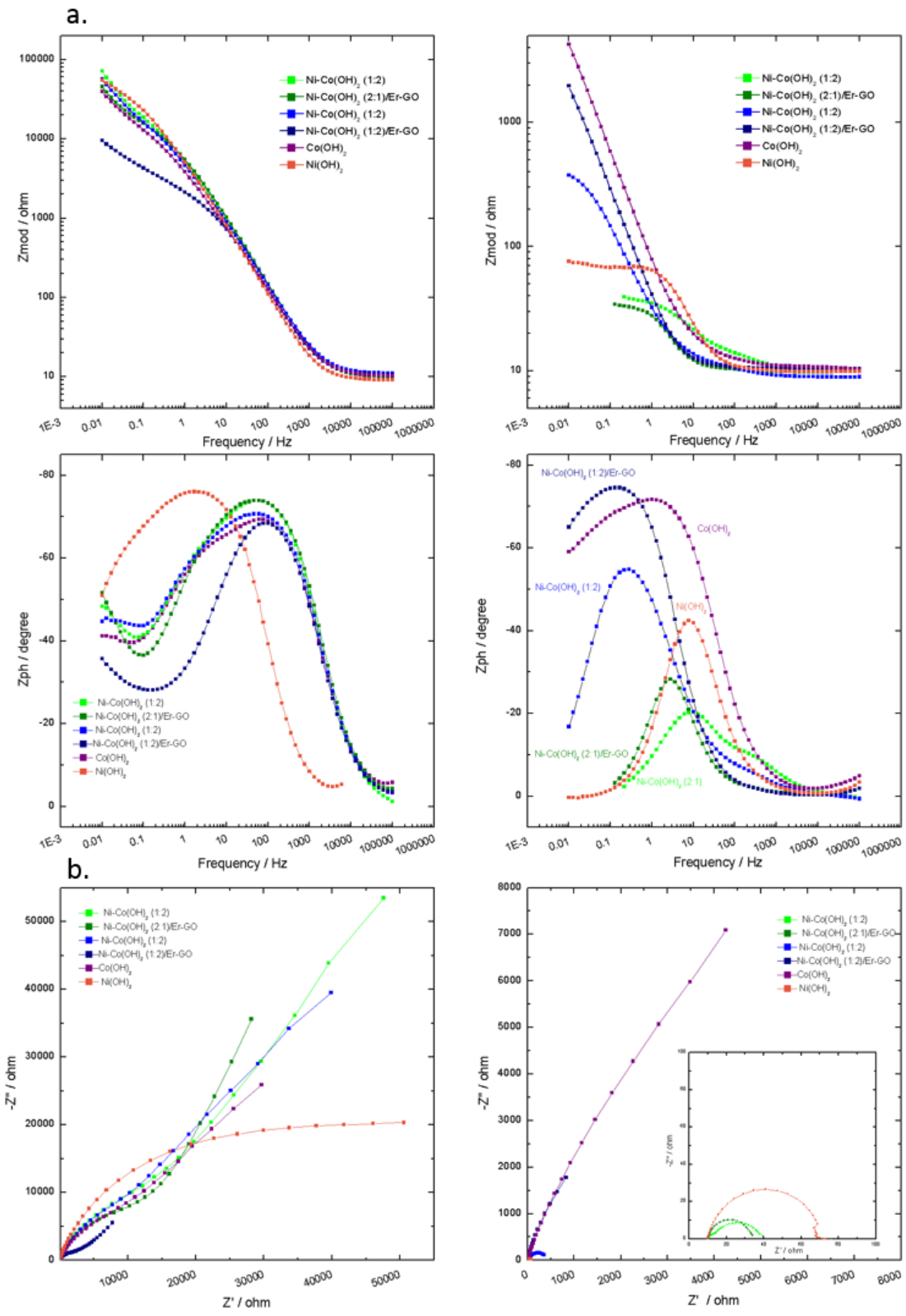

Fig. 3.1.15. (a-b) Bode and (c-d) Nyquist Electrochemical Impedance Spectra of $Co(OH)_2$, $Ni(OH)_2$, Ni-$Co(OH)_2$(1:2), Ni-$Co(OH)_2$(1:2)/Er-GO, Ni-$Co(OH)_2$(2:1) and Ni-$Co(OH)_2$(2:1)/Er-GO composite materials.

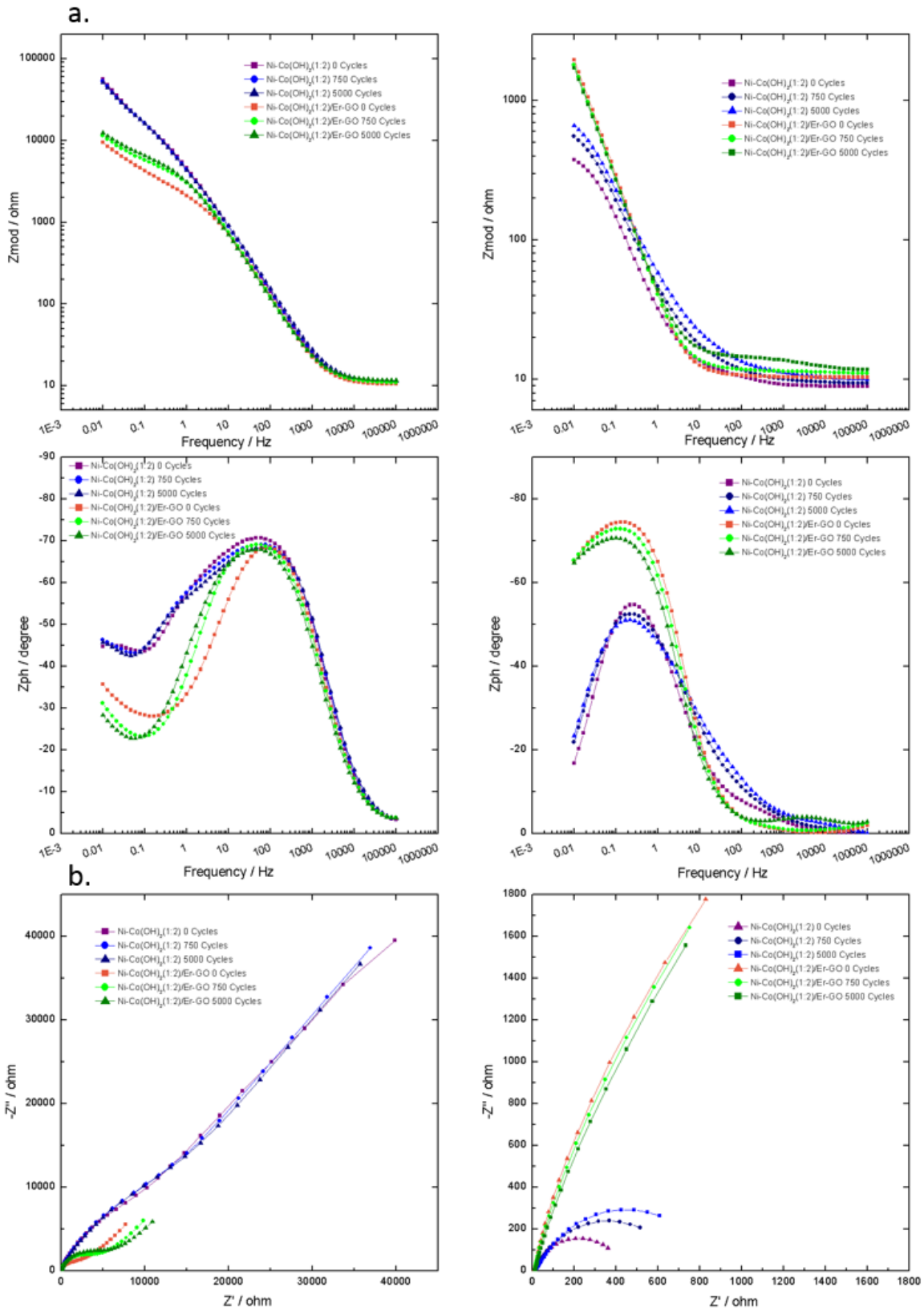

Fig. 3.1.16. (a-b) Bode and (c-d) Nyquist Electrochemical Impedance Spectra of the Ni-$Co(OH)_2$(1:2) and Ni-$Co(OH)_2$(1:2)/Er-GO composite materials at 0, 750 and 5000 cycles of Galvanostatic Charge Discharge at 10 A/g for both discharged (left) and charged (right) potentials of the sample.

Electrochemical Impedance Spectroscopy is proven to be a very powerful technique to understand electrochemical processes and mechanisms, providing useful information regarding Equivalent Series Resistance and how ideal and relevant a material's capacitive behaviour is. Two different bias were studied for each sample corresponding to different state-of-charge: a cathodic potential corresponding to the discharged state (-0.2V for Ni-$Co(OH)_2$(2:1) composites and -0.1V for Ni-$Co(OH)_2$(1:2) materials); and an anodic potential corresponding to the charged state (0.45V for Ni-$Co(OH)_2$(2:1) and Ni-$Co(OH)_2$(2:1)/Er-GO and 0.4V for Ni-$Co(OH)_2$(1:2) and Ni-$Co(OH)_2$(1:2)/Er-GO).

To understand the EIS response of the materials and their degradation from a chemical view point, charge-discharge processes must be born in mind so as the potential degradation mechanisms that may affect the sample. As aforementioned, Nickel hydroxide can be obtained in two different well-known polymorphs, α and β. On one hand, β phases are based on brucite-type layers with good order along the c-axis and an inter-slab distance of 4.8Å. On the other hand, the α structure also has a brucite-type structure derived from the other but with water molecules and anionic species intercalated between the randomly stacked layers of nickel hydroxide resulting in a d-spacing of 7.5-8.5 Å. When an α phase is charged, it transitions into a γ phase. Due to the instability of α/ γ phases, discussed later and summarized in Fig. 3.1.17a, the former β/β transition has traditionally been used in Nickel-Metal hydride batteries although studies show that the latter has a better capacity response since it can exchange a greater number of electrons per reaction. This is due to the higher valences achieved in their charged state for the γ structures (average oxidation degree of nickel ions is 3.5) producing a theoretical average electron exchange of 1.5 in the reduction to α phases compared to 1 from the β(III) to β(II) system [73].

Bode et al. [74] first established that α-$Ni(OH)_2$ transforms into γ-NiOOH whereas β-$Ni(OH)_2$ does to β-NiOOH. Also, α-$Ni(OH)_2$ dehydrates into β -$Ni(OH)_2$ in alkali media and β-NiOOH transforms into γ-NiOOH when overcharged as seen in Fig. 3.1.17.

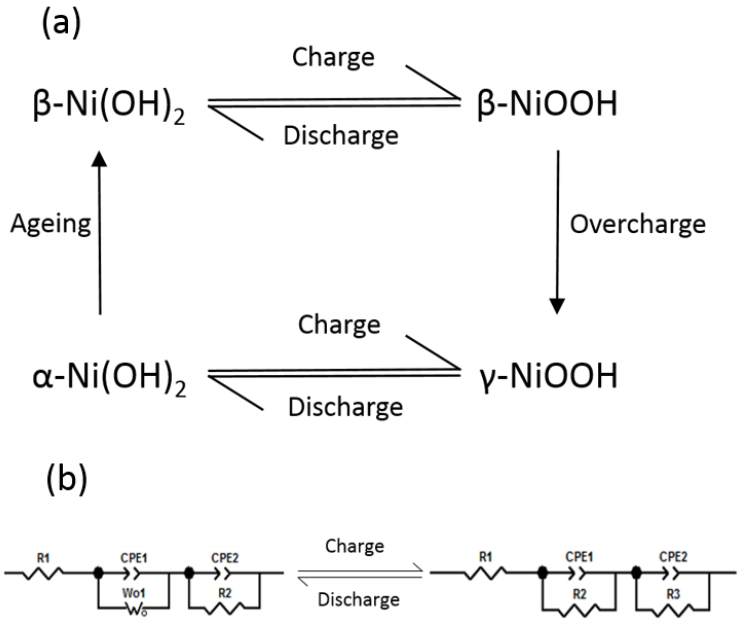

Fig. 3.1.17. (a) Reaction diagram first presented by Bode et al. for the Nickel hydroxide charge-discharge reaction. (b) Equivalent circuit used in the fitting of the charge-discharge process [74].

The charge and discharge process of Nickel hydroxide has been widely studied and a solid-state diffusion of protons (and associated hydroxyl ion diffusion in the alkali media of the electrolyte) has been proposed. During charge, the proton diffuses to the film/electrolyte interface to react with a hydroxyl ion to form water. Then, during discharge, a proton diffuses from the film/electrolyte interface into the active material and an electron enters the conducting substrate/film interface [75]. As suggested by Barnard, Randell and Tye [76], both α-$Ni(OH)_2$ and β-$Ni(OH)_2$ are relatively good proton conductors but, in pure state, p-type semiconductors. When Cobalt is added, conductivity is increased. Simplifying, when the charge process begins, localized homogeneous areas of an intermediate higher oxidation phase appears ($Ni^{II}_xNi^{III}_{1-x}(OH)_2$) creating a phase boundary that grows continuously by charge transfer and diffusion. A second analogous $Ni^{II}_{1-x}Ni^{III}_x(OH)_2$ phase is produced until it is completely transformed to γ-NiOOH, which is electronically conducting [76]. Similar intermediate oxidation phases are expected for cobalt hydroxide composites (an intermediate phase with an oxidation degree of about 20% is formed [77]). Nickel-Cobalt hydroxide layers behave analogously to Nickel hydroxide.

Thus, the electrodeposited layer changes from a semiconductor to a relatively good conductor in the charging process. As defined by Armstrong and co-workers, this change in conductivity will affect the impedance spectra. Four sources of impedance would be present, namely: bulk electrolyte, KOH 1M; the electrodeposited (ED) film bulk impedance; the electrolyte/ED film interface and, finally, the ED film/Stainless Steel interface; as illustrated in Fig. 3.1.18 [78].

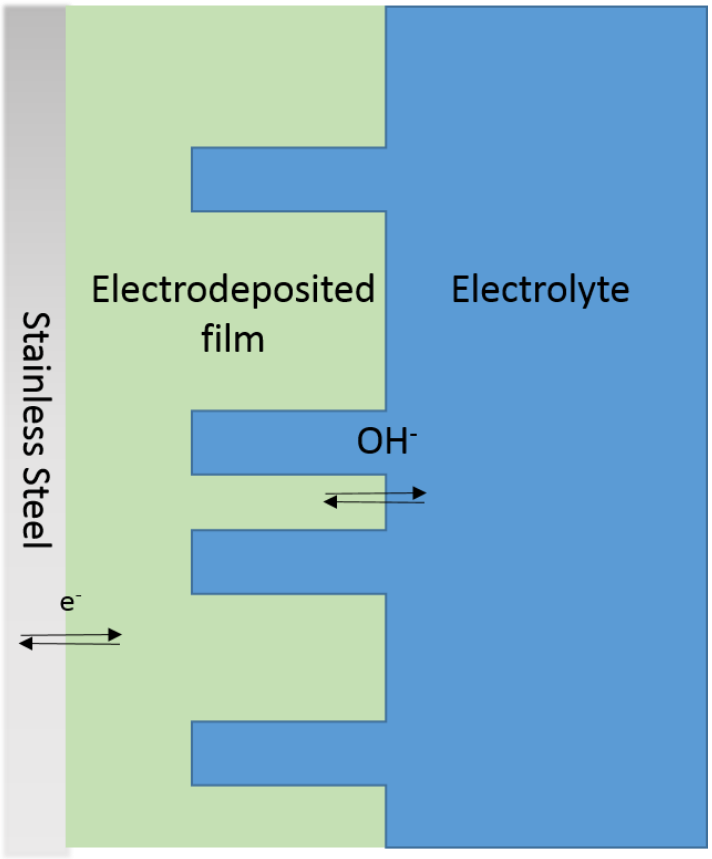

Fig. 3.1.18. Representation of the reactions in a Ni-$Co(OH)_2$ /Er-GO film in KOH 1M electrolyte as presented by Armstrong et al. [78].

When looking at the response obtained for the module of the resistance there is always a resistive plateau at high frequencies (HF) that is followed by a capacitive slope at low frequencies (LF). The HF resistive plateau is constant regardless the sample. This resistance is associated to the KOH electrolyte resistance of a three-electrode system, thus, it shall remain constant in every experiment. At high frequencies only large geometrical features can be considered for the impedance response since ion migration is out of them. Then, at lower frequencies, smaller features begin to contribute to interfacial capacitance. The capacity slope does depend on the applied bias and shows an incipient second resistive plateau that seems to be incomplete for discharged samples. This plateau is associated to an electrochemical process that requires high relaxation times. In accordance with the cyclic voltammetry response obtained, it is intrinsically related to hydroxyl ion diffusion processes in charge of the redox reactions of the system, being the process at the $Ni(OH)_2$/KOH interface the determining step. This is a Warburg-type impedance with finite diffusion effects in the Ni-$Co(OH)_2$ phases.

Although similar capacity slopes are present for the discharged samples, with and without Er-GO, and a similar value for the phase-angle is obtained, when the sample is charged both the slope and phase angle modulus obtained for the Er-GO based composite have a higher absolute value, indicating a higher charge storage capacity. It is worth mentioning that the ideal value of -90^o is never achieved as it usually occurs for faradaic reactions. For the Nyquist plots, a semicircle was expected due to a charge-transfer reaction in a completely charged sample where oxygen evolution potentials are nearly used for nickel samples. However, the inclusion of cobalt lowers the oxygen evolution reaction effect, giving a capacitive response again with the presence of Warburg diffusion-controlled processes since the mechanism is, again, controlled by proton diffusion. It is worth noticing that this is only present in the samples with higher content of Cobalt whereas the samples with more Nickel content behave similarly to $Ni(OH)_2$.

Accordingly, the resistance observable at the Nyquist plots is much lower for compounds with Er-GO integrated on them. This can be qualitatively evaluated by the smaller semicircle of the Nyquist plot, associated to a smaller inner resistance of the sample. This would explain a facilitated charge transfer and lowered series resistance, thus, higher electron transport. Similarly, it can be correlated to the previously reported improved electrochemical cycling stability, the smoother the charge transfer the less degradation of the sample in continuous measurements. Finally, the fact that Er-GO based samples have also a higher slope in any case than the individual Ni-Co hydroxide materials at low frequencies of the Nyquist plot also indicates a smaller charge-transfer and diffusion resistance, correlated to a higher capacity of the carbon-based samples.

Higher capacitance values are obtained when the sample is fully charged in comparison to when discharged. Thus, only when the sample is completely oxidized it will show a capacitive response from the entire film/electrolyte interface allowing faster electron exchange with the substrate and a response less dominated by proton diffusion but from the capacitance response of the film material. Thus, in an equivalent circuit presented in this paper, shown in Fig. 3.1.17b, the two phenomena of diffusion and film capacity are separated. In the discharge state of the sample diffusion will take priority while in the charged condition the capacity response will be much higher.

When more cobalt is incorporated into the sample, the conductivity improves, reducing the difference in capacity between the charged and discharged state of the sample and reducing the effect of diffusion processes as main determining step. This is observable by the higher slope in the modulus of impedance at low frequencies, closer values to -90^o at the phase angle and a more capacity-type response in the Nyquist plot instead of the

expected semicircle. Moreover, when Er-GO is integrated, this difference becomes more apparent since the impedance response is closer to $Co(OH)_2$, this is, where diffusion processes are less relevant, and less resistance is present in the samples.

Summarizing, lower resistance is found for materials with reduced graphene oxide integrated and more cobalt is present, leading to higher capacities as shown by angles closer to -90º for charged samples that correlate to a more ideal behaviour and smaller semicircles at high frequencies.

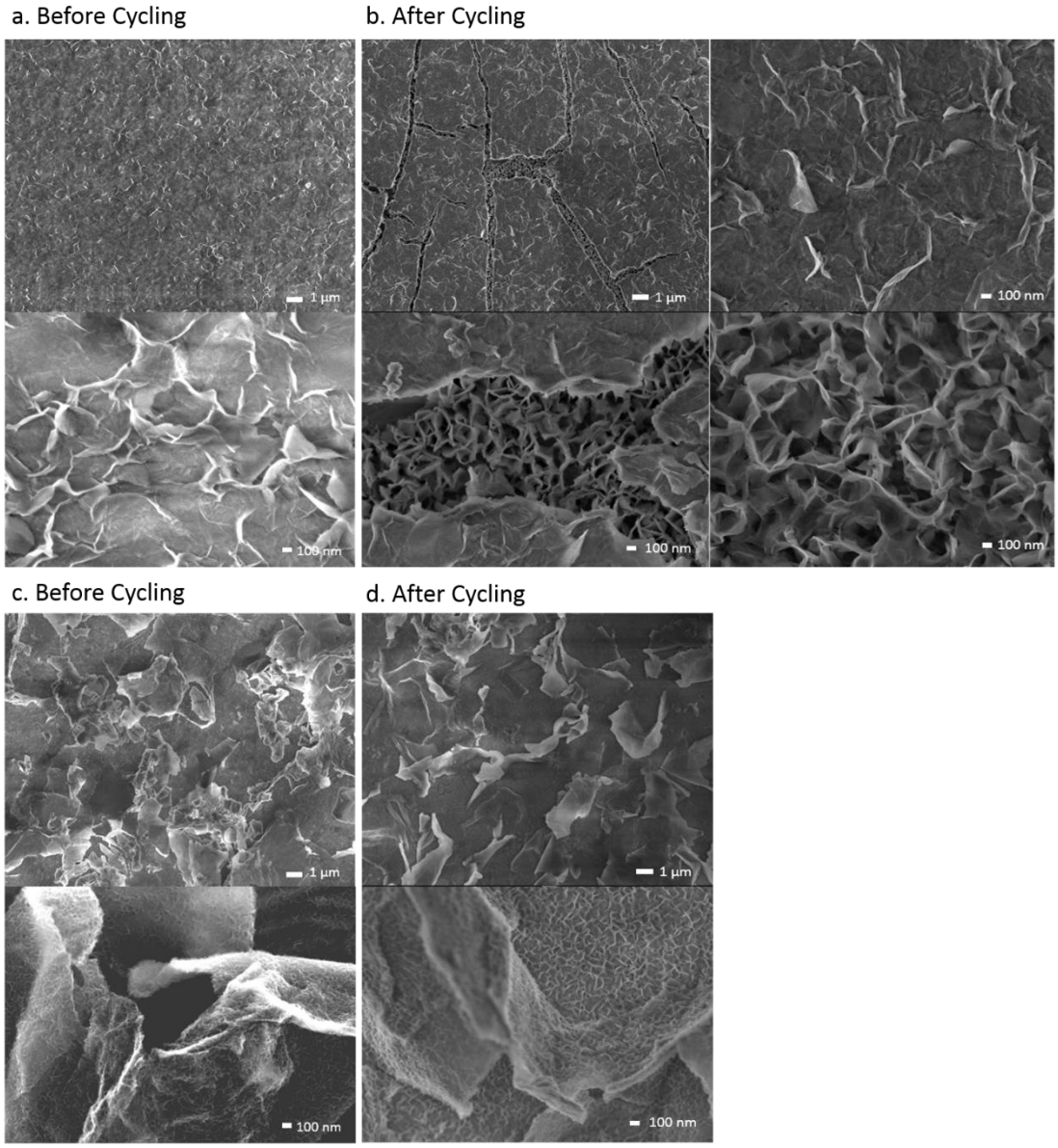

Fig. 3.1.19. Scanning Electron Microscopy images of the samples (a), (b) Ni-$Co(OH)_2$ (1:2) and (c), (d) Ni-$Co(OH)_2$/Er-GO before and after cycling.

Cycling of $Ni(OH)_2$ was studied in-depth by McBreen, Zimmerman and others. As it can be worked out from the reaction diagram, in the cycling of α-$Ni(OH)_2$, a parasitic reaction may appear. α-$Ni(OH)_2$ may transform along the time into β -$Ni(OH)_2$ since the presented media is basic. However, the experimental conditions (KOH 1M at room temperature) are mild, minimizing the aging effect. For instance, Tye et al. used 7M KOH at 22ºC for over 16h and fully α to β conversion was not yet achieved [76]. Thus, it is expected that this conversion may be partially minimized but still a crucial effect in the degradation

process. In a similar fashion, α phases of Cobalt transform into β phases upon aging [77] although their polymorphs are not as well studied. Since the materials presented in this work are either based on a majority of Nickel or Cobalt hydroxide, mechanisms can be assumed to be identical.

Nonetheless, there are more sources of potential degradation mechanisms of the sample. One being swelling and blistering of γ-NiOOH phases when converted from β -$Ni(OH)_2$. This is one of the main limitations for commercial nickel-based batteries [79]. They reported that swelling and blistering are caused by the volumetric expansion of this material due to its 23% lower density compared to β-NiOOH. If, as expected during cycling, the conversion from α to β occurs, also the transformation from β to γ by overcharge may happen. As a consequence, this swelling would lead to substrate detachment of the material from the substrate since great mechanical stresses are produced.

Although swelling may be partially mitigated by the inclusion of Cobalt phases within the nickel hydroxide structures it is still expected to happen in the double hydroxide films. This is confirmed by SEM. SEM images of Ni-$Co(OH)_2$ (1:2) and Ni-$Co(OH)_2$ (1:2)/Er-GO after being cycled are presented in Fig. 3.1.19. Analogous results are obtained for Ni-$Co(OH)_2$ (2:1) and Ni-$Co(OH)_2$ (2:1)/Er-GO.

As observed, when Ni-$Co(OH)_2$ (1:2) undergoes charge-discharge cycling, the superficial structure collapses due to poor strain accommodation, creating breaches that reveal an inner less dense structure. There is a degradation of the materials' surface that leads to an early decay in capacity when cycling. Besides, the inner structure has a reduced density and greater porosity that may be correlated to an increase in equivalent series resistance, observed by impedance spectroscopy. Like all porous electrodes, electrolyte exhaustion within the pores eventually produces mass transport and ohmic overpotential losses and power reduction may also happen. On the other hand, when Er-GO is introduced, the carbon material accommodates the metal double hydroxide on top of its surface, reducing strain forces that inhibit the collapse of the structure and avoid surface modification, maintaining its porosity. This increased surface stability can be associated to the higher material capacity retention.

Finally, cycle and temperature dependent parasitic processes affect the system, for instance, Oxygen evolution [80]. Oxygen evolution leads to oxygen bubbling that contributes to the degradation of the material by increasing the internal resistance. This is particularly interesting for $Ni(OH)_2$ cycling reactions since their potential is quite similar to that of the oxygen evolution reaction. Nonetheless, by integrating cobalt into the system the α/γ redox voltage couple is lowered, reducing the probability of oxygen evolution to occur [75,81].

Three main effects are hence considered the cause of degradation of the capacitive behaviour of the sample, α to β phase transformation and pore exhaustion leading to mechanical stress and structure degradation. This is corroborated by both electrochemical (EIS) and morphological (SEM) characterization. This is translated in a less ideal capacitive-like behaviour, increasing resistance and lowering the absolute value of the phase angle plotted against frequency when cycling. If these phenomena, along with the two main charge-discharge mechanisms, diffusion and layer capacitance, are considered, the equivalent circuit model may be applied. Results obtained from the fitting of experimental data and their variation with cycling are also presented in tables 3.1.4 and 3.1.5.

Table 3.1.4
Fitting results for the equivalent circuits shown in Fig. 3.1.17 for the impedance spectroscopy done in Ni-$Co(OH)_2$ electrodeposited layers.

	Discharged			Charged		
Cycle number	0	750	5000	0	750	5000
$R_1(\Omega \cdot cm^2)$	10.46	10.64	10.92	8.76	9.24	9.95
$Y_{oCPE1}(Ss^n \cdot cm^{-2})$	7.98E-05	1.05E-04	1.10E-04	2.74E-02	2.40E-02	1.68E-02
N_{CPE1}	0.52	0.57	0.57	0.45	0.43	0.42
$R_{Wo1}/R_2(\Omega \cdot cm^2)$	1.61	0.88	0.69	7.36	46.1	128.1
$Y_{Wo1}(Ss^n \cdot cm^{-2})$	1.89E-05	1.30E-05	9.88E-06			
N_{Wo1}	0.46	0.5	0.51			
$Y_{oCPE2}(Ss^n \cdot cm^{-2})$	1.16E-04	1.25E-04	1.40E-04	9.09E-03	7.63E-03	7.27E-03
N_{CPE2}	0.78	0.74	0.72	0.82	0.8	0.8
$R_3(\Omega \cdot cm^2)$	4674	7839	8063	414.8	636.4	745.3
Chi-Squared	3.18E-04	3.45E-04	3.26E-04	4.61E-04	1.35E-04	9.82E-05

Table 3.1.5
Fitting results for the equivalent circuits shown in Fig. 3.1.17 for the impedance spectroscopy done in Ni-$Co(OH)_2$/Er-GO electrodeposited layers.

	Discharged			Charged		
Cycle number	0	750	5000	0	750	5000
R_1 ($\Omega \cdot cm^2$)	10.1	10.66	11.22	10.35	11.34	11.31
$Y_{oCPE1}(Ss^n \cdot cm^{-2})$	3.99E-04	4.18E-04	3.66E-04	5.22E-03	5.52E-03	5.56E-03
N_{CPE1}	0.43	0.45	0.42	0.88	0.86	0.85
R_{Wo1}/R_2 ($\Omega \cdot cm^2$)	0.25	0.55	1.18	7129	7479	7751
$Y_{Wo1}(Ss^n \cdot cm^{-2})$	1.43E-05	5.68E-05	5.23E-05			
N_{Wo1}	0.57	0.54	0.48			
$Y_{oCPE2}(Ss^n \cdot cm^{-2})$	9.24E-05	5.90E-05	7.20E-05	7.53E-03	8.89E-03	9.50E-04
N_{CPE2}	0.76	0.79	0.79	0.84	0.77	0.58
$R_3(\Omega \cdot cm^2)$	1422	3409	4066	0.29	0.43	3.28
Chi-Squared	1.64E-04	2.41E-04	2.93E-04	6.33E-04	3.01E-04	2.33E-04

There are several relevant features that can be obtained from the equivalent circuit and fitted data interpretation. First of all, the transition from a Warburg diffusion process when the sample is discharge to a double layer capacitance when charged. When the sample is discharged, the poorer conductivity of the Ni-Co hydroxide layer and its transition to a higher oxidation state is dominated by a diffusion-controlled process. As explained, this will dominate the entire charging process. Once the sample is completely charged and due to the increased conductivity of the material, the γ phase, the system is no longer governed by diffusion effects and a capacitive response is to be expected

Warburg lines become no longer relevant, thus, the observable semicircle at the Nyquist plot, not observable in some cases due to its big radius, is associated to charge transfer processes at the electrode surface [82].

Then, capacitance increases remarkably for the charged samples for both the carbon-based layers and the electrodeposited layers without carbon. Also, diffusion processes disappear producing a highly resistive layer. As expected, while there is an increase in the diffusion process resistance, there is a drop in the resistance of the capacitive process, pointing out its greater relevance. Films in which electrochemically reduced graphene oxide are included present much lower values of resistance for similar capacitance values. The increase in resistance for the diffusion process reflects the independence of the system from it, especially when Er-GO is integrated since they present higher values for the resistance.

Finally, if the degradation process is evaluated, resistance values always increase with cycling. The most relevant feature is the increase in resistance for the diffusion associated process. While Ni-Co$(OH)_2$ films present a remarkable increase in the resistance values and decrease in the capacitance values with the increase of the cycle number, the same values remain more constant for the Er-GO integrated samples. This may be associated to a better proton diffusion process, this is, a more effective charge in which there is less degradation of the materials in the charge-discharge process. There is also a decrease in the capacitance values with cycling, as expected from the degradation of the material.

If, as expected, the degradation mechanism is greatly influenced by the transformation from α to β phases, which are associated to a less capacitance process, when Er-GO is introduced, this phase transformation would be somehow inhibited and α phases stabilised. At the same time, if this process is inhibited, so is the β/γ charge process leading to swelling a detachment issues. The complete change in the morphology of the film by integrating Er-GO compared to the carbon-free material leads to a more accessible, hence, more stable surface that avoids collapse and degradation by strain accommodation, which is reflected in a bigger increase of the resistance values for the samples without the graphene derivative. This would also explain the decrease in the capacity signal obtained for the cyclic voltammetry with cycling, which is much more relevant for the samples without the carbon-based material. Nonetheless, the most influential effect explaining the degradation would be, apart from structural collapse, the exhaustion of pores with the electrolyte, which would lead to localized shortcuts and, as a consequence, an increase in the overall resistance. Since Er-GO creates a conductive and more accessible network, in which greater contact with the electrolyte is achieved, porosity exhaustion is minimized. The fact that the surface does not fracture and is more homogeneous (in comparison to the inner structure revealed in the Ni-Co$(OH)_2$ electrodeposited samples) leads to reduced pore exhaustion and morphological differences that ultimately affect capacity retention.

3.1.4. Conclusions

In summary, α-Cobalt-Nickel hydroxides were electrodeposited with Electrochemically Reduced Graphene Oxide to study the influence of this carbon-based material in both morphology and the electrochemical response of the materials. The composite consists of metal flakes that embed the spike-like structure of nickel and cobalt hydroxide, optimizing the interaction between the two materials and creating a network that produces a synergistic effect to the electrochemical response measured.

Two different Nickel-Cobalt ratios are used. Cobalt has traditionally been used to improve Nickel conductivity. By studying two different ratios along with the inclusion of electrochemically reduced graphene oxide (Er-GO) the great dependence of the electrochemical capacity from conductivity is evidenced. Creating a network with overall increased conductivity may play a role as relevant as, in this case, the improvement of the intrinsic capacity response of the material. In principle, a greater influence from the capacity was expected from the nickel inclusion, however, values with increased cobalt concentration were found to show a better electrochemical response. This would entail that charge-transfer resistance processes are fundamental in the electrochemical behaviour of a material for energy storage application and shall be evaluated and optimized. EIS spectra may be an excellent technique in this evaluation.

The inclusion of electrochemically reduced graphene oxide into a double nickel-cobalt hydroxide system has greatly improved the electrochemical properties of the system; increasing their capacity in approximately a 250% and their capacity retention after 5000 cycles at 10A/g by around a 20%. This is achieved, among others, by increasing the active surface area and electrolyte accessibility while reducing graphene monolayers stacking and metal agglomeration. As a consequence, the graphene derivative material also provides a conductive network in which metal hydroxides can be anchored becoming more accessible for ion exchange, thus enhancing capacitive faradaic reactions, and improving the charge transfer and electron mobility within the sample. Moreover, it reinforces the material, improving their cycling stability.

Values up to 96mA·h/g with a 62% capacity retention after 5000 cycles at 10A/g are obtained for Ni-Co$(OH)_2$/Er-GO with a nickel:cobalt molar ratio of 1:2. This loss in capacity retention is associated to mechanical degradation, pore exhaustion and α to β hydroxide phase transitions. An exhaustive analysis by SEM and EIS has been done in order to further understand the ageing and degradation mechanisms of the sample and the effect of Er-GO in these processes. When Er-GO is included, the strain forces present in the metal hydroxide composites are accommodated, resulting in the reduction of structure degradation and collapse of the pores. Besides, it provides a conductive matrix that greatly interacts with the electrolyte. This avoids increased resistance in the electron transfer process associated to that mechanical degradation. It is also remarkable that scan rates as high as 2000 mV/s could be used without deforming the cyclic voltammetry electrochemical response, proving its excellent rate capability and the potential suitability of the material as electrode for energy storage. Besides it proves that carbon-based materials, in particular graphene derivatives, mixed with metal hydroxides are an interesting option towards next-generation energy storage devices. Finally, electrodeposition technique has proven to be a simple yet effective way to integrate carbon/metal hydroxides in what may be a scalable-up process.

Acknowledgements

This work has been performed in scope of International Doctoral Program in Functional Materials (IDS-FunMat, Erasmus Mundus) and funded by the European Union. We would like to express our gratitude to the Fundação para a Ciência e Tecnologia (FCT) for the funding under the contracts M-ERA.NET/0002/2012 and UID/QUI/00100/2013. We would also like to acknowledge Sabine Gomes for performing the GIXD experiments, Catherine Denage and Philippe Dagault for their general assistance, Stephane Le Blond de Plouy and Philipe Legros and their respective centers (Centre de MicroCaractérisation Raimond Castaing and Plateforme Aquitane de Caractérisation des Matériaux, PLACAMAT) for their SEM images, François Weill and Marion Gayot also from PLACAMAT for their insights on TEM and, finally, Christine Labrugere from PLACAMAT for her assistance on XPS.

Chapter 3.1 references

[1] A. Manthiram, Y. Fu, Y.S. Su, In Charge of the World: Electrochemical Energy Storage, J. Phys. Chem. Lett. 4 (2013) 1295–1297.

[2] M. Miroshnikov, K.P. Divya, G. Babu, A. Meiyazhagan, L. Mohana, R. Arava, P.M. Ajayan, G. John, Power from nature: designing green battery materials from electroactive quinone derivatives and organic polymers, J. Mater. Chem. A Mater. Energy Sustain. 4 (2016) 12370–12386. doi:10.1039/c6ta03166h.

[3] J. Vatamanu, D. Bedrov, Capacitive Energy Storage: Current and Future Challenges, J. Phys. Chem. Lett. 6 (2015) 3594–3609. doi:10.1021/acs.jpclett.5b01199.

[4] P. Simon, Y. Gogotsi, B. Dunn, Where Do Batteries End and Supercapacitors Begin?, Science (80-.). 343 (2014) 1210–1211. doi:10.1126/science.1249625.

[5] B.E. Conway, Transition from "supercapacitor" to "battery" behavior in electrochemical energy storage., J. Electrochem. Soc. 138 (1991) 1539–1548. doi:10.1149/1.2085829.

[6] J.H. Chae, X. Zhou, G.Z. Chen, From electrochemical capacitors to supercapatteries, Green. 2 (2012) 41–54. doi:10.1515/green-2011-0007.

[7] V. Augustyn, J. Come, M.A. Lowe, J.W. Kim, P.-L. Taberna, S.H. Tolbert, H.D. Abruña, P. Simon, B. Dunn, High-rate electrochemical energy storage through Li+ intercalation pseudocapacitance., Nat. Mater. 12 (2013) 518–22. doi:10.1038/nmat3601.

[8] M. Okubo, E. Hosono, J. Kim, M. Enomoto, N. Kojima, T. Kudo, H. Zhou, I. Honma, Nanosize effect on high-rate Li-ion intercalation in LiCoO2 electrode, J. Am. Chem. Soc. 129 (2007) 7444–7452. doi:10.1021/ja0681927.

[9] M. Sathiya, a S. Prakash, K. Ramesha, J. Tarascon, a K. Shukla, V2O5-Anchored Carbon Nanotubes for Enhanced Electrochemical Energy Storage, J. Am. Chem. Soc. 133 (2011) 16291–16299. doi:10.1021/ja207285b.

[10] T. Brousse, D. Belanger, J.W. Long, To Be or Not To Be Pseudocapacitive?, J. Electrochem. Soc. 162 (2015) A5185–A5189. doi:10.1149/2.0201505jes.

[11] A.D. Su, X. Zhang, A. Rinaldi, S.T. Nguyen, H. Liu, Z. Lei, L. Lu, H.M. Duong, Hierarchical porous nickel oxide – carbon nanotubes as advanced pseudocapacitor materials for supercapacitors, 562 (2013) 68–73. doi:10.1016/j.cplett.2013.01.023.

[12] S. Dong, A.Q. Dao, B. Zheng, Z. Tan, C. Fu, H. Liu, F. Xiao, One-step electrochemical synthesis of three-dimensional graphene foam loaded nickel–cobalt hydroxides nanoflakes and its electrochemical properties, Electrochim. Acta. 152 (2015) 195–201. doi:10.1016/j.electacta.2014.09.061.

[13] T.A. Han, J.P. Tu, J.B. Wu, Y.F. Yuan, Y. Li, Influence of Nanosized α-Ni(OH)2 Addition on the Electrochemical Performance of β-Ni(OH)2 Electrode, Solid State Phenom. 121–123 (2007) 1265–1268. doi:10.4028/www.scientific.net/SSP.121-123.1265.

[14] G. Wang, L. Zhang, J. Zhang, A review of electrode materials for electrochemical supercapacitors., Chem. Soc. Rev. 41 (2012) 797–828. doi:10.1039/c1cs15060j.

[15] W. Zhou, M. Xu, D. Zhao, C. Xu, H. Li, Electrodeposition and characterization of ordered mesoporous cobalt hydroxide films on different substrates for

supercapacitors, Microporous Mesoporous Mater. 117 (2009) 55–60. doi:10.1016/j.micromeso.2008.06.004.

[16] X. Wang, T. Song, Buckypaper templating Ni-Co hydroxide nanosheets as free-standing electrode for ultrathin and flexible supercapacitors, New J. Chem. 40 (2016) 8006–8011. doi:10.1039/C6NJ01470D.

[17] T. Nguyen, M. Boudard, M.J. Carmezim, M.F. Montemor, Layered Ni(OH)2-Co(OH)2 films prepared by electrodeposition as charge storage electrodes for hybrid supercapacitors, Sci. Rep. (2017) 1–10. doi:10.1038/srep39980.

[18] V. Gupta, S. Gupta, N. Miura, Potentiostatically deposited nanostructured CoxNi1−x layered double hydroxides as electrode materials for redox-supercapacitors, J. Power Sources. 175 (2008) 680–685. doi:10.1016/j.jpowsour.2007.09.004.

[19] M. Zhi, C. Xiang, J. Li, M. Li, N. Wu, Nanostructured carbon-metal oxide composite electrodes for supercapacitors: a review., Nanoscale. 5 (2013) 72–88. doi:10.1039/c2nr32040a.

[20] A.K. Mishra, S. Ramaprabhu, Functionalized Graphene-Based Nanocomposites for Supercapacitor Application, (2011) 14006–14013.

[21] A.G. Pandolfo, A.F. Hollenkamp, Carbon properties and their role in supercapacitors, J. Power Sources. 157 (2006) 11–27. doi:10.1016/j.jpowsour.2006.02.065.

[22] K.S. Novoselov, V.I. Fal'ko, L. Colombo, P.R. Gellert, M.G. Schwab, K. Kim, A roadmap for graphene., Nature. 490 (2012) 192–200. doi:10.1038/nature11458.

[23] Y. Si, E.T. Samulski, Exfoliated Graphene Separated by Platinum Nanoparticles, Chem. Mater. 20 (2008) 6792–6797. doi:10.1021/cm801356a.

[24] Y. Huang, J. Liang, Y. Chen, An overview of the applications of graphene-based materials in supercapacitors., Small. 8 (2012) 1805–34. doi:10.1002/smll.201102635.

[25] J. Zhang, J. Jiang, X.S. Zhao, Synthesis and Capacitive Properties of Manganese Oxide Nanosheets Dispersed on Functionalized Graphene Sheets, J. Phys. Chem. C. 115 (2011) 6448–6454.

[26] C. Ge, Z. Hou, B. He, F. Zeng, J. Cao, Y. Liu, Y. Kuang, Three-dimensional flower-like nickel oxide supported on graphene sheets as electrode material for supercapacitors, J. Sol-Gel Sci. Technol. 63 (2012) 146–152. doi:10.1007/s10971-012-2778-7.

[27] X. Zhu, H. Dai, J. Hu, L. Ding, L. Jiang, Reduced graphene oxide–nickel oxide composite as high performance electrode materials for supercapacitors, J. Power Sources. 203 (2012) 243–249. doi:10.1016/j.jpowsour.2011.11.055.

[28] Y. Jiang, D. Chen, J. Song, Z. Jiao, Q. Ma, H. Zhang, L. Cheng, B. Zhao, Y. Chu, A facile hydrothermal synthesis of graphene porous NiO nanocomposite and its application in electrochemical capacitors, Electrochim. Acta. 91 (2013) 173–178. doi:10.1016/j.electacta.2012.12.032.

[29] S.I. Kim, J.S. Lee, H.J. Ahn, H.K. Song, J.H. Jang, Facile route to an efficient NiO supercapacitor with a three-dimensional nanonetwork morphology., ACS Appl. Mater. Interfaces. 5 (2013) 1596–603. doi:10.1021/am3021894.

[30] X. Su, H. Chai, D. Jia, S. Bao, W. Zhou, M. Zhou, Effective microwave-assisted synthesis of graphene nanosheets/NiO composite for high-performance supercapacitors, New J. Chem. 37 (2013) 439. doi:10.1039/c2nj40785j.

[31] X. Xia, J. Tu, Y. Mai, R. Chen, X. Wang, C. Gu, X. Zhao, Graphene sheet/porous NiO hybrid film for supercapacitor applications., Chemistry. 17 (2011) 10898–905. doi:10.1002/chem.201100727.

[32] Y. Chen, X. Zhang, P. Yu, Y. Ma, Electrophoretic deposition of graphene nanosheets on nickel foams for electrochemical capacitors, 195 (2010) 3031–3035. doi:10.1016/j.jpowsour.2009.11.057.

[33] H. Zhang, X. Zhang, D. Zhang, X. Sun, H. Lin, C. Wang, One-Step Electrophoretic Deposition of Reduced Graphene Oxide and Ni(OH)2 Composite Films for Controlled Syntheses Supercapacitor Electrodes, J. Phys. Chem. B. 117 (2013) 1616–1627.

[34] A. García-Gómez, R.G. Duarte, S. Eugénio, T.M. Silva, M.J. Carmezim, M.F. Montemor, Fabrication of electrochemically reduced graphene oxide/cobalt oxide composite for charge storage electrodes, J. Electroanal. Chem. 755 (2015) 151–157. doi:10.1016/j.jelechem.2015.07.053.

[35] R.P. Silva, S. Eugénio, R. Duarte, T.M. Silva, M.J. Carmezim, M.F. Montemor, Co-Electrochemical Response of 70Co-30Ni Highly Branched 3D-Dendritic Structures for Charge Storage Electrodes, Electrochim. Acta. 167 (2015) 13–19. doi:10.1016/j.electacta.2015.03.083.

[36] T. Zhao, H. Jiang, J. Ma, Surfactant-assisted electrochemical deposition of α-cobalt hydroxide for supercapacitors, J. Power Sources. 196 (2011) 860–864. doi:10.1016/j.jpowsour.2010.06.042.

[37] J.S. Lee, D.H. Shin, W. Kim, J. Jang, Highly ordered, polypyrrole-coated Co(OH)2 architectures for high-performance asymmetric supercapacitors, J. Mater. Chem. A. 4 (2016) 6603–6609. doi:10.1039/C6TA01419D.

[38] C. Zhao, X. Wang, S. Wang, Y. Wang, Y. Zhao, W. Zheng, Synthesis of Co(OH)2/graphene/Ni foam nano-electrodes with excellent pseudocapacitive behavior and high cycling stability for supercapacitors, Int. J. Hydrogen Energy. 37 (2012) 11846–11852. doi:10.1016/j.ijhydene.2012.05.138.

[39] M. Li, J.P. Cheng, J. Wang, F. Liu, X.B. Zhang, The growth of nickel-manganese and cobalt-manganese layered double hydroxides on reduced graphene oxide for supercapacitor, Electrochim. Acta. 206 (2016) 108–115. doi:10.1016/j.electacta.2016.04.084.

[40] F. Grote, Z.Y. Yu, J.L. Wang, S.H. Yu, Y. Lei, Self-Stacked Reduced Graphene Oxide Nanosheets Coated with Cobalt-Nickel Hydroxide by One-Step Electrochemical Deposition toward Flexible Electrochromic Supercapacitors, Small. 11 (2015) 4666–4672. doi:10.1002/smll.201501037.

[41] X. Bai, Q. Liu, H. Zhang, J. Liu, Z. Li, X. Jing, Y. Yuan, L. Liu, J. Wang, Nickel-Cobalt Layered Double Hydroxide Nanowires on Three Dimensional Graphene Nickel Foam for High Performance Asymmetric Supercapacitors, Electrochim. Acta. 215 (2016) 492–499. doi:10.1016/j.electacta.2016.08.134.

[42] X. Zang, C. Sun, Z. Dai, J. Yang, X. Dong, Nickel hydroxide nanosheets supported on reduced graphene oxide for high-performance supercapacitors, J. Alloys

Compd. 691 (2017) 144–150. doi:10.1016/j.jallcom.2016.08.233.

[43] H. Xie, S. Tang, D. Li, S. Vongehr, X. Meng, Flexible Asymmetric Supercapacitors Based on Nitrogen-Doped Graphene Hydrogels with Embedded Nickel Hydroxide Nanoplates, ChemSusChem. (2016) 1–9. doi:10.1002/cssc.201600150.

[44] Z. Hu, Y. Xie, Y. Wang, H. Wu, Y. Yang, Z. Zhang, Synthesis and electrochemical characterization of mesoporous CoxNi1−x layered double hydroxides as electrode materials for supercapacitors, Electrochim. Acta. 54 (2009) 2737–2741. doi:10.1016/j.electacta.2008.11.035.

[45] X. Tian, C. Cheng, L. Qian, B. Zheng, H. Yuan, S. Xie, D. Xiao, M.M.F. Choi, Microwave-assisted non-aqueous homogenous precipitation of nanoball-like mesoporous α-Ni(OH)2 as a precursor for NiOx and its application as a pseudocapacitor, J. Mater. Chem. 22 (2012) 8029–8035. doi:10.1039/c2jm16057a.

[46] W.C. Fang, Synthesis and Electrochemical Characterization of Vanadium Oxide/Carbon Nanotube Composites for Supercapacitors, J. Phys. Chem. C. 112 (2008) 11552–11555. doi:10.1021/jp8011602.

[47] J. Pu, Y. Tong, S. Wang, E. Sheng, Z. Wang, Nickel-cobalt hydroxide nanosheets arrays on Ni foam for pseudocapacitor applications, J. Power Sources. 250 (2014) 250–256. doi:10.1016/j.jpowsour.2013.10.108.

[48] R.R. Salunkhe, K. Jang, S. Lee, H. Ahn, Aligned nickel-cobalt hydroxide nanorod arrays for electrochemical pseudocapacitor applications, RSC Adv. 2 (2012) 3190. doi:10.1039/c2ra01220k.

[49] D.S. Hall, D.J. Lockwood, C. Bock, B.R. MacDougall, Nickel hydroxides and related materials: a review of their structures, synthesis and properties., Proc. Math. Phys. Eng. Sci. 471 (2015) 20140792. doi:10.1098/rspa.2014.0792.

[50] Z. Liu, R. Ma, M. Osada, K. Takada, T. Sasaki, Selective and controlled synthesis of alpha- and beta-cobalt hydroxides in highly developed hexagonal platelets, J. Am. Chem. Soc. 127 (2005) 13869–13874. doi:10.1021/ja0523338.

[51] C. Delmas, Y. Borthomieu, A new route to obtain well crystallized layer double hydroxides, J. Solid State Chem. 104 (1993) 345–352. doi:10.1006/jssc.1993.1169.

[52] L. Bing, Y. Huatang, Z. Yunshi, Z. Zuoxiang, S. Deying, Cyclic voltammetric studies of stabilized α-nickel hydroxide electrode, J. Power Sources. 79 (1999) 277–280. doi:10.1016/S0378-7753(99)00053-1.

[53] L. Guerlou-Demourgues, C. Denage, C. Delmas, New manganese-substituted nickel hydroxides Part 1. Crystal chemistry and physical characterization, 52 (1994) 269–274.

[54] G.K. Ramesha, N.S. Sampath, Electrochemical Reduction of Oriented Graphene Oxide Films: An in Situ Raman Spectroelectrochemical Study, J. Phys. Chem. C. 113 (2009) 7985–7989.

[55] R. Wang, A. Jayakumar, C. Xu, J. Lee, Ni(OH)2 Nanoflowers/Graphene Hydrogels: A New Assembly for Supercapacitors, ACS Sustain. Chem. Eng. 4 (2016) 3736–3742. doi:10.1021/acssuschemeng.6b00362.

[56] X. Díez-Betriu, S. Álvarez-García, C. Botas, P. Álvarez, J. Sánchez-Marcos, C.

Prieto, R. Menéndez, A. de Andrés, Raman spectroscopy for the study of reduction mechanisms and optimization of conductivity in graphene oxide thin films, J. Mater. Chem. C. 1 (2013) 6905. doi:10.1039/c3tc31124d.

[57] M. Hilder, B. Winther-Jensen, D. Li, M. Forsyth, D.R. MacFarlane, Direct electro-deposition of graphene from aqueous suspensions., Phys. Chem. Chem. Phys. 13 (2011) 9187–9193. doi:10.1039/c1cp20173e.

[58] J. Yang, H. Liu, W.N. Martens, R.L. Frost, Synthesis and Characterization of Cobalt Hydroxide , Cobalt Oxyhydroxide , and Cobalt Oxide Nanodiscs, J. Phys. Chem. C. 114 (2010) 111–119.

[59] R. Della Noce, S. Eugénio, T.M. Silva, M.J. Carmezim, M.F. Montemor, α-Co(OH)2/carbon nanofoam composite as electrochemical capacitor electrode operating at 2 v in aqueous medium, J. Power Sources. 288 (2015) 234–242. doi:10.1016/j.jpowsour.2015.04.131.

[60] M. Vidotti, R.P. Salvador, E. a Ponzio, S.I. Córdoba de Torresi, Mixed Ni/Co hydroxide nanoparticles synthesized by sonochemical method., J. Nanosci. Nanotechnol. 7 (2007) 1–6. doi:10.1166/jnn.2007.651.

[61] L. Ye, L. Zhao, H. Zhang, B. Zhang, H. Wang, One-pot formation of ultra-thin Ni/Co hydroxides with a sheet-like structure for enhanced asymmetric supercapacitors, J. Mater. Chem. A Mater. Energy Sustain. 4 (2016) 9160–9168. doi:10.1039/C6TA02436J.

[62] J. Desilvestro, D.A. Corrigan, M.J. Weaver, Characterization of Redox States of Nickel Hydroxide Film Electrodes by In Situ Surface Raman Spectroscopy, J. Electrochem. Soc. 135 (1988) 885–892.

[63] S. Deabate, F. Fourgeot, F. Henn, X-ray diffraction and micro-Raman spectroscopy analysis of new nickel hydroxide obtained by electrodialysis, J. Power Sources. 87 (2000) 125–136. doi:10.1016/S0378-7753(99)00437-1.

[64] H. Chen, L. Hu, M. Chen, Y. Yan, L. Wu, Nickel-cobalt layered double hydroxide nanosheets for high-performance supercapacitor electrode materials, Adv. Funct. Mater. 24 (2014) 934–942. doi:10.1002/adfm.201301747.

[65] M. Vidotti, M.R. Silva, R.P. Salvador, S.I.C. de Torresi, L.H. Dall'Antonia, Electrocatalytic oxidation of urea by nanostructured nickel/cobalt hydroxide electrodes, Electrochim. Acta. 53 (2008) 4030–4034. doi:10.1016/j.electacta.2007.11.029.

[66] S.B. Kulkarni, a. D. Jagadale, V.S. Kumbhar, R.N. Bulakhe, S.S. Joshi, C.D. Lokhande, Potentiodynamic deposition of composition influenced Co 1-xNix LDHs thin film electrode for redox supercapacitors, Int. J. Hydrogen Energy. 38 (2013) 4046–4053. doi:10.1016/j.ijhydene.2013.01.047.

[67] X. Meng, M. Feng, H. Zhang, Z. Ma, C. Zhang, Solvothermal synthesis of cobalt / nickel layered double hydroxides for energy storage devices, J. Alloys Compd. 695 (2017) 3522–3529. doi:10.1016/j.jallcom.2016.11.419.

[68] J. Zhang, K. Xiao, T. Zhang, G. Qian, Y. Wang, Y. Feng, Porous nickel-cobalt layered double hydroxide nano fl ake array derived from ZIF-L-Co nano flake array for battery-type electrodes with enhanced energy storage performance, Electrochim. Acta. 226 (2017) 113–120. doi:10.1016/j.electacta.2016.12.195.

[69] P.R. Martins, A. Luis, A. Parussulo, S.H. Toma, M.A. Rocha, H.E. Toma, K.

Araki, Highly stabilized alpha-NiCo (OH) 2 nanomaterials for high performance device application, J. Power Sources. 218 (2012) 1–4. doi:10.1016/j.jpowsour.2012.06.065.

[70] J.M. Gonçalves, R.R. Guimar, Electrode materials based on a-NiCo(OH)2 and rGO for high performance energy storage device, RSC Adv. (2016) 102504–102512. doi:10.1039/C6RA20317E.

[71] X. Su, C. Gao, M. Cheng, R. Wang, Controllable synthesis of Ni(OH)2 /Co(OH)2 hollow nanohexagons wrapped in reduced graphene oxide for supercapacitors, RSC Adv. 6 (2016) 97172–97179. doi:10.1039/C6RA20361B.

[72] D. Pech, M. Brunet, H. Durou, P. Huang, V. Mochalin, Y. Gogotsi, P.-L. Taberna, P. Simon, Ultrahigh-power micrometre-sized supercapacitors based on onion-like carbon., Nat. Nanotechnol. 5 (2010) 651–4. doi:10.1038/nnano.2010.162.

[73] C. Tessier, C. Faure, L. Guerlou-Demourgues, C. Denage, G. Nabias, C. Delmas, Electrochemical Study of Zinc-Substituted Nickel Hydroxide, J. Electrochem. Soc. 149 (2002) A1136. doi:10.1149/1.1495496.

[74] H. Bode, J. Witte, K. Dehmelt, Zur Kenntnis der Nickelhydroxidelektrode - I. Über das Nickel (II)-Hydroxidhydrat, Electrochim. Acta. 11 (1966) 1079–1087.

[75] J.W. Montupally, S., Streinz, C.C., Weidner, Proton Diffusions in Nickel Hydroxide Films: Measurement of the Diffusion Coefficient as a Function of State of Charge, J. Electrochem. Soc. 142 (1995) 1401–1408.

[76] R. Barnard, C.F. Randell, F.L. Tye, Studies concerning charged nickel hydroxide electrodes I. Measurement of reversible potentials, J. Appl. Electrochem. 10 (1980) 109–125. doi:10.1007/BF00937345.

[77] R.M.A. Lieth, Preparation and crystal growth of materials with layered structures, Springer Science + Business Media, B.V., 1977. doi:10.1007/978-94-017-2750-1_4.

[78] R.D. Armstrong, E.A. Charles, Some Aspects of the A.C. Impedance Behaviour of Nickel Hydroxide and Nickel/Cobalt Hydroxide Electrodes in Alkaline Solution, J. Power Sources. 27 (1989) 15–21.

[79] M. Oshitani, T. Takayama, K. Takashima, S. Tsuji, A study on the swelling of a sintered nickel hydroxide electrode, J. Appl. Electrochem. 16 (1986) 403–412. doi:10.1007/BF01008851.

[80] and B.G.P. S. J. Lenhart, *'l D. D. Macdonald, An AC Impedance Study of the Degradation of Porous Nickel Battery Electrodes, J. Electrochem. Soc. 135 (1988) 1063–1071.

[81] J. McBreen, The Nickel Oxide Eletrode, in: R.E. Bockris, John O'M., Conway, Brian E., White (Ed.), Mod. Asp. Electrochem., 1990: pp. 29–63.

[82] Y. Xu, The electrochemical behavior of Ni-MH battery, Ni(OH)2 electrode and metal hydride electrode, Int. J. Hydrogen Energy. 29 (2004) 749–757. doi:10.1016/j.ijhydene.2003.08.013.

3.2 Ni-Co hydroxides for Energy Storage Applications: Using Mott-Schottky to support potential selection in Impedance Spectroscopy.

Alberto Adán-Más[a,b,*] , Teresa M. Silva[a,c], Liliane Guerlou-Demourgues[b,d], Maria Fátima G. Montemor[a,*]

[a] Centro de Química Estrutural-CQE, DEQ, Instituto Superior Técnico, Universidade de Lisboa, 1049-001, Lisboa, Portugal

[b] CNRS, University of Bordeaux, Bordeaux INP, ICMCB UPR 9048, 33600 Pessac, France

[c] ADEM, GI-MOSM, ISEL-Instituto Superior de Engenharia de Lisboa, Instituto Politécnico de Lisboa, Lisboa, Portugal

[d] RS2E, Réseau Français sur le Stockage Electrochimique de l'Energie, FR CNRS 3459, France.

Keywords: Nickel-Cobalt Hydroxide; Energy Storage; Electrochemical Impedance Spectroscopy; Mott-Schottky.

Abstract

Electrochemical Impedance Spectroscopy (EIS) is a powerful technique to understand the electrode-electrolyte interaction and to evaluate degradation, resistive behavior and electrochemical activity of energy storage materials. However, it can sometimes be misused or under-interpreted. To effectively acquire EIS results, the voltages imposed to the working electrode, at which EIS spectra are obtained, shall be critically selected. This work follows a previous study on the EIS response of Nickel-Cobalt hydroxide, and highlights the Mott-Schottky approach as a complementary tool to explain the behavior of the Impedance Spectroscopy results obtained at different potentials. Moreover, Mott-Schottky is used to further understand the fundamental processes occurring at the electrode-electrolyte interface of Nickel-Cobalt hydroxide in alkali media and to explain the changes in conductivity of the material that ultimately determine the electrode electrochemical activity.

3.2.1. Introduction

Energy storage electrode materials are greatly influenced by their electrode-electrolyte interaction. Evaluating the most relevant parameters affecting it is crucial. In the particular case of energy storage materials, the specific surface area of the electrode material or the ionic conductivity of the electrolyte are two of the most interesting properties to study. When designing an energy storage device, all the integrating materials must be considered, being the electrolyte one of the components with greater relevance. The electrolyte affects the final electrochemical response in a number of different ways. For example, it limits the ionic conductivity of the system and determines the potential range at which it can be used [1–3]. As a matter of fact, several groups have been working on developing redox electrolytes as a manner to increase the electrochemical performance and charge storage processes of supercapacitors [4].

On the other hand, one of the greatest challenges in developing new energy storage materials is to overcome their degradation and increase their cycle stability. Again, the cycle-life and lifetime of an electrode material is dependent on the electrode-electrolyte interaction. Thus, selecting an appropriate electrode-electrolyte interface system is key for an optimal performance with minimized degradation phenomena [5]. Not only that, once a system is optimized, it is interesting to obtain as much information about the reactivity and events occurring as possible to elucidate, and potentially solve, the issues that may rise. Hence, it seems critical to understand and study the processes occurring at the electrode-electrolyte interface.

Therefore, to further comprehend the electrode-electrolyte interaction, have a deeper understanding of the processes occurring and the extent to which a capacity or capacitance and their fading are affected by the interface, it is interesting to explore techniques that may reveal novel and useful information about the system.

Several techniques are being applied, such as cyclic voltammetry, hydrodynamic voltammetry, chronoamperometry and electrochemical impedance spectroscopy (EIS) [6]. EIS is often used to evaluate the different sources of resistance (and conductivity of the components of the electrode) found in an energy storage device, and usually serves as an additional technique to evaluate the electrode-electrolyte interaction and charge transport phenomena [7,8,17–21,9–16]. However, it is commonly found that the measurement was done at open circuit potential or that it was performed at a single potential although the electrode electrochemical response is voltage dependent [13–21].

In the case of those supercapacitive materials that are purely based on electrostatic interactions, their response is voltage independent and the latter may be possible. However, when a faradaic response is present in the system, the response of the system will vary if the voltage is changed. Thus, the chemical condition of the system and the reactions occurring at a particular potential must be born in mind since they will greatly affect the results, and therefore, the conclusions that may be obtained. This can also be applied to pseudocapacitive materials that do not have a perfect squared response in their cyclic voltammetries, given the fact that they are likely to have voltage-dependent redox reactions. Many groups have studied the electrochemical impedance response at a single potential although their pseudocapacitive material presents a slight peak. It may be possible that performing EIS at a lower and higher potentials would produce different responses that would bring more insights in the reaction evolution [22–27].

For that reason, Mott-Schottky can be suggested as a complementary technique to evaluate the key potentials at which EIS shall be performed in faradaic-type energy storage electrochemical systems. This will ensure that EIS is performed at a critically-

selected voltage and that it will provide meaningful information. It also serves as a tool to further understand the mechanisms for a given faradaic reaction. Due to its fundamental principles, Mott-Schottky can be used in the explanation of the electrode reactivity and the changes in conductivity of the material.

Mott-Schottky is traditionally used as a technique to measure the flatband potential of a semiconductor material and the charge carrier densities of bulk semiconductors in contact with electrolytes [28]. This is intrinsically related to the phase present in the electrode and, as a consequence, serves as a mean to evaluate the conductivity and enables a better understanding of the electron and ion transfer processes at the electrode-electrolyte interface [29].

By varying the potential at the electrode-electrolyte interface, the space-charge capacitance within the semiconductor is measured. As a consequence, the location of the energy levels in the electrode-electrolyte junction, namely, the flat band potential E_{FB}, the conduction band edge E_c and the valence band edge E_V can be studied. This technique is, then, a trustworthy measurement of the energetic distance between the Fermi level and the nearest characteristic level of the semiconductor [28].

In the present work, an energy storage material displaying semiconductor behaviour has been selected as subject of study: Ni-Co$(OH)_2$ with a nickel-cobalt ratio of 1:2. This material was studied in our previous work together with the evaluation of its degradation analysis by means of electrochemical impedance spectra [30].

Mott-Schottky is here presented as a mean to critically evaluate the voltages at which EIS shall be performed and as a tool to understand changes in the conductivity of the sample, during the charge process, at a more fundamental level. By means of this technique, it is possible to understand the cause by which Electrochemical Impedance Spectra vary with voltage and it is also possible to further comprehend the phenomena occurring at the interface of Ni-Co$(OH)_2$ with alkali media. Nickel-Cobalt based materials are often subject of research in energy storage applications and the correct evaluation of EIS spectra shall be done to not provide misleading information [31].

3.2.2. Experimental

3.2.2.1. Materials

To deposit the double hydroxide material, $Ni(NO_3)_2 \cdot 6H_2O$ and $Co(NO_3)_2 \cdot 6H_2O$ were obtained from Sigma-Aldrich and used in the preparation of electrode materials as received. Plates of AISI 304 (Goodfellow) 0.914mm thick stainless-steel were used as current collector and substrate for the electrodeposition. They were polished with emery paper with 2500 grit SiC paper to a rough finish and double-rinsed with water and acetone to eliminate abrasive particles. They were then air-dried. Potassium hydroxide was used as received from Sigma-Aldrich and used to prepare a 1M KOH electrolyte solution.

3.2.2.2. Synthesis of electrodeposited $Ni_xCo_{1-x}(OH)_2$ on Stainless Steel.

Electrodeposition was carried out following the procedure described in [30]. Summarizing, a three-electrode cell (Stainless steel substrate as working electrode, SCE reference electrode and a Platinum wire as counter electrode) and an Interface IFC1000-07087 Potentiostat (Gamry Instruments) were used to deposit the material in a limited circular area of $1cm^2$. The electrodeposition electrolyte was prepared by dissolving 0.0872g of $Ni(NO_3)_2 \cdot 6H_2O$ and 0.1746 $Co(NO_3)_2 \cdot 6H_2O$ with 100mL of distilled water. Then, thirty 20-second symmetric pulse between two cathodic potentials (-0.9V and -

1.2V vs SCE) were applied to complete the electrodeposition process. The electrodes were washed with distilled water and ethanol and dried for 24-48h before electrochemical measurements. The resulting thin film is designated as Ni-Co$(OH)_2$ (1:2).

The deposited mass, which was determined by means of a micro-balance Sartorius MC5-0CE with an accuracy of 0.01mg, varied between 0.1 and 0.2 mg.

3.2.2.3. Electrochemical Study of $Ni_xCo_{1-x}(OH)_2$ composites.

All electrochemical characterization was performed using the aforementioned equipment and a three-electrode electrochemical cell with KOH 1M as electrolyte. Cyclic Voltammetry was carried out at 50 $mV \cdot s^{-1}$ in a potential window ranging from -0.2V to 0.5V vs SCE electrode.

Prior to the Electrochemical Impedance Spectroscopy (EIS) measurement, a conditioning at the desired measuring voltage for 1000 seconds was done. EIS measurements were carried out at different applied potentials (corresponding to partially charged, 0.1V, charged, 0.4V, and discharged conditions, -0.2V) by applying a sinusoidal perturbation with 10 mV of amplitude (RMS) in the frequency range of 0.01 to 10^5 Hz. Mott-Schottky measurements were performed in a potential range from -0.2V to 0.5V vs SCE with an AC frequency of 10 mV·ms at 1000Hz.

3.2.2.4. Physico-chemical Characterization

The Scanning Electron Microscopy (SEM) direct imaging (FEG-SEM JEOL JSM 7800F Prime) presented in this work was used to observe the morphological characteristics of the sample.

3.2.3. Results and Discussion

3.2.3.1. Physico-chemical Characterization

Results in the present manuscript are a follow-up of Ni-Co hydroxides for energy storage previously introduced in [30], where a detailed physico-chemical characterization can be found. Summarizing, the energy-storage material is an alpha Ni-Co$(OH)_2$ phase with a Nickel-Cobalt ratio of 1:2. The morphological features obtained by Scanning Electron Microscopy are evidenced in Fig. 3.2.1. The Ni-Co$(OH)_2$ (1:2) material shows a nanosheet-like structure with no apparent order deposited on top of the stainless-steel substrate. The material forms a percolation network that is densely-packed, which is in accordance to previously reported literature [32,33].

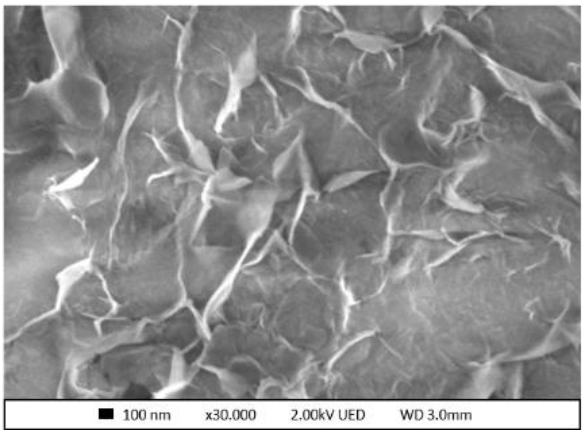

Fig. 3.2.1. Scanning Electron Microscopy image of (a) Ni-Co$(OH)_2$ (1:2).

3.2.3.2. Electro-chemical Characterization

Fig. 3.2.2 shows the cyclic voltammetry response obtained for Ni-$Co(OH)_2$ (1:2) [30]. The charge-discharge reaction corresponds to either proton diffusion or hydroxyl intercalation, reactions exemplified in eq. (3.2.1) and eq. (3.2.2):

$$\alpha\text{-}Ni_xCo_{1-x}(OH)_2 + OH^- \longleftrightarrow \gamma\text{-}Ni_xCo_{1-x}OOH + H_2O + e^- \quad (eq.\ 3.2.1)$$

$$\alpha\text{-}Ni_xCo_{1-x}(OH)_2 \longleftrightarrow \gamma\text{-}Ni_xCo_{1-x}OOH_{2-x} + xH^+ + xe^- \quad (eq.\ 3.2.2)$$

It shall be taken into account that these are not the exact formulae of the phases involved since carbonate, nitrate and water ions are intercalated in the interslab space of nickel-cobalt hydroxide layers. The resulting ideal formula would be $Ni_xCo_{1-x}(OH)_2(H_2O)_{1.2}(2\cdot NO_3^-, CO_3^{2-})_{0.10}$ and, therefore, eq.3.2.1 and eq.3.2.2 are only a simplified reaction that intent to exemplify the charge-discharge process from an electrochemical point of view since the exact mechanism is still unclear [34–37]. Nonetheless, this reaction was studied in-depth by Bode et al. for nickel hydroxide. They determined that an α-nickel-hydroxide phase transforms into a γ-oxyhydroxide phase when charged [38].

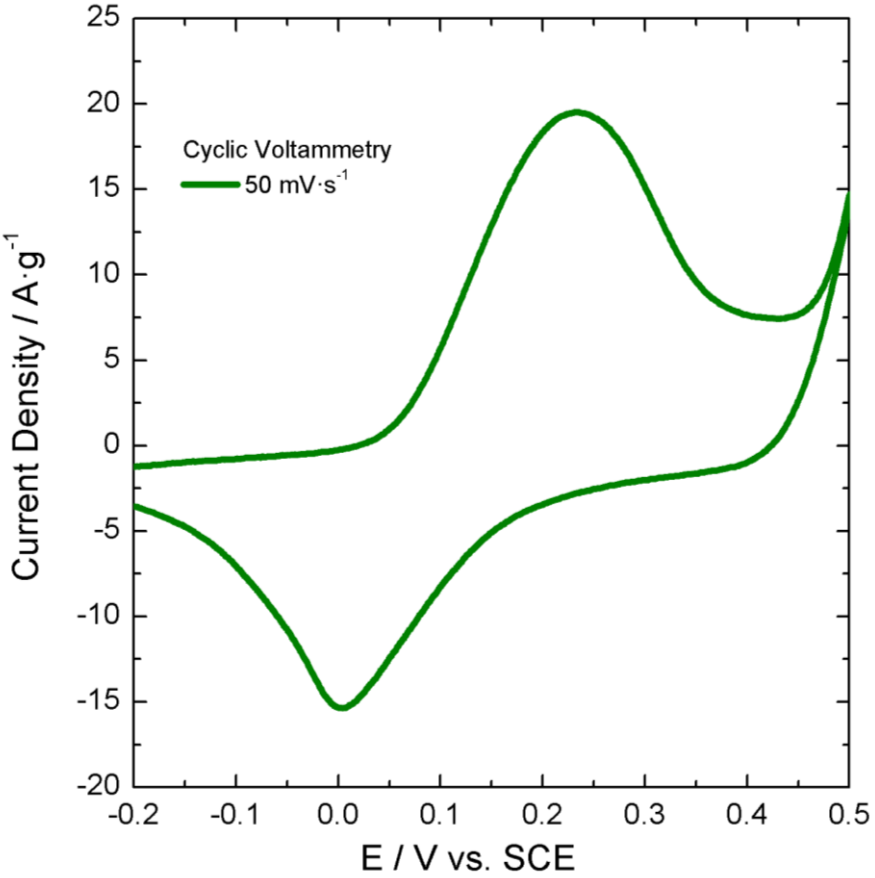

Fig. 3.2.2. Cyclic Voltammetry at 50 $mV\cdot s^{-1}$ plot for Ni-$Co(OH)_2$ (1:2) [30].

That transformation entails an average electron exchange of 1.5 for nickel hydroxide, since the oxidation degree of the charged form of the nickel ions is 3.5 [39]. In the case of cobalt doped nickel hydroxide, the average electron exchange varies according to the oxidation state of Cobalt and the number of exchanged electrons may vary. For instance, when it is stabilized as Co^{3+}, this number is decreased [40]. The mechanism associated is a hydroxyl diffusion or solid-state diffusion of protons as introduced by Weider et al. and Tye et al. [38,41–43]. As explained by Tye et al. [43], localized homogeneous areas of an intermediate oxidation state ($Ni_x^{II}Ni_{1-x}^{III}$- $Co_x^{II}Co_{1-x}^{III}(OH)_2$) appear in the

charging process. If the material keeps being under charge, a second phase is developed. In this phase there is a majority of the higher oxidation state present until the material is fully converted to the gamma structure.

Armstrong and co-workers [42] already established that the state of charge of this sample will affect the impedance spectra response of the material. There are three main potential ranges of interest in the charging process of the sample. The first one is at very cathodic potentials, when the hydroxide material is completely discharged. The second voltage of interest for EIS is an intermediate charge state, as it will be seen, at a potential that corresponds to the flatband potential. This is the intermediate point in between the cathodic and anodic faradaic peaks, which correspond to the charge and discharge reaction respectively, present at the cyclic voltammetry. The last is at very anodic potentials, at which the reaction has been completed and the sample is fully charged. Thus, EIS results are expected to be very different, depending on the selected potential. This voltage-dependent response is noticed in Fig. 3.2.3, where EIS spectra obtained at different imposed potentials are presented.
Moreover, to fully understand these results, the experimental data was fitted with the equivalent circuit presented in Fig. 3.2.3d. The corresponding fitting parameters are depicted in Table 3.2.1.

As seen in the equivalent circuit, the energy-storage mechanism is here modelled considering two different processes: diffusion-controlled phenomena and capacitive response. These are considered, for interpretation purposes, independent one from the other. Regarding the diffusion processes, which can be associated with proton intercalation, the fitting parameters reveal a notable decay in the resistance to diffusion, which can be related, as later considered, to a change in conductivity of the material. This is observed when the applied potential moves from cathodic (-0.2V vs SCE) to an intermediate value (0.1V vs SCE). Therefore, the diffusion transport phenomena are facilitated. Once the material is completely charged (0.4V vs SCE), diffusion-controlled processes are hindered and fitting with a Warburg element is no longer possible, due to the fact that once the reaction is finished, the associated proton diffusion is also finished. As a consequence, the time constant observed in the range 100-1000Hz in the Bode plot vanishes (Fig. 3.2.3b). Thus, the intermediate potential is the potential at which the proton diffusion and, therefore, the reaction, starts. Moreover, as long as the phase transition evolves, diffusion-controlled processes become less and less relevant until they disappear as soon as the charged potential is attained.

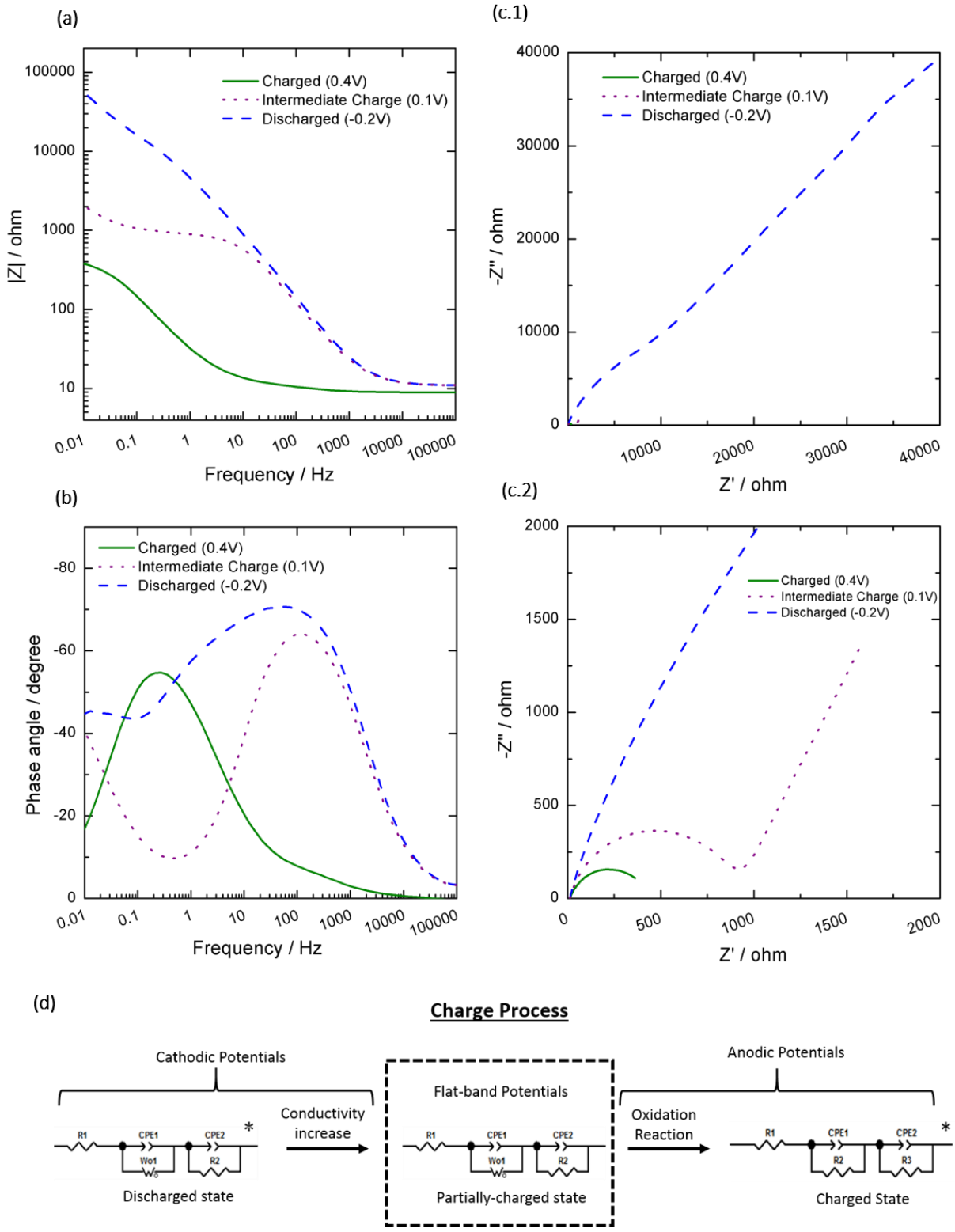

Fig. 3.2.3 Bode (a-b) and Nyquist plots, at different magnifications, (c.1 - c.2) of Impedance Spectroscopy for Ni-Co(OH)$_2$ (1:2) at discharged (-0.2V), intermediate charge (0.1V) and charged condition (0.4V) of the sample. (d) EIS Equivalent circuit employed to fit the variation of impedance spectra obtained for Ni-Co(OH)$_2$ (1:2) in the charge process. EIS spectra for the charged and discharged condition of the sample and the equivalent circuits marked with * are equivalent to those discussed in [30].

Concerning the capacitive component, the fitting parameters suggest that during the reaction, the capacitance value of the material is slightly changed and increases for the charged sample, as expected. However, the most relevant feature is the drastic reduction on the resistance values. When the material is completely discharged, at cathodic potentials, the resistance value is much higher. Once more anodic potentials are applied, this resistance drops significantly. This can easily be observed in Fig. 3.2.3a. At this potential, as later explained, the material behaves as a degenerated semiconductor, the intercalation/de-intercalation processes are favoured, and the energy storage reaction starts. When this happens, energy is stored by means of a phase transformation. This new phase is, consequently, more capacitive, hence the increase observed in the Y_{oCPE2} value. Finally, once the reaction is completed, the material is fully transformed into γ-$Ni_xCo_{1-x}OOH$, which is conductive. Consequently, the resistance values decrease up to 10 times as compared to the initial hydroxide material.

Table 3.2.1.
Values obtained for the fitting results of the impedance spectra of Ni-$Co(OH)_2$ (1:2) according to the equivalent circuits presented in Fig. 3.2.3. Results marked with * are equivalent to those presented in [30].

	Ni-Co(OH)2 (1:2)		
	Discharged*	**Intermediate State**	**Charged***
$R_1(\Omega \cdot cm^2)$	10.46	10.94	8.76
$Y_{oCPE1}(Ss^n \cdot cm^{-2})$	7.98E-05	5.07E-03	2.74E-02
N_{CPE1}	0.52	0.72647	0.45
$R_{Wo1}/R_2(\Omega \cdot cm^2)$	1.61	0.0035365	7.36
$Y_{Wo1}(Ss^n \cdot cm^{-2})$	1.89E-05	5.55E-04	
N_{Wo1}	0.46	0.85502	
$Y_{oCPE2}(Ss^n \cdot cm^{-2})$	1.16E-04	3.69E-05	9.09E-03
N_{CPE2}	0.78	0.8372	0.82
$R_3(\Omega \cdot cm^2)$	4674	936.8	414.8
Chi-Squared	3.18E-04	2.40E-04	4.61E-04

As expected, the impedance response and the evolution of the impedance parameters is greatly dependent on the applied voltage and the electronic state at which the sample is. Nonetheless, there are many examples in literature where this effect is not considered and the selection of potential is not consistently reasoned, resulting in EIS done either at open circuit potentials or at randomly selected potentials. This leads to inconclusive or uncompleted results found for various materials [13–21].

It is worth mentioning that this reasoning could also be extended to pseudocapacitive materials with very small peaks being observed in the voltammograms. Considering that EIS carried out at different potentials leads to different responses that provide useful information about the reactivity of the system, it is extremely important to accurately select such potentials [22–27]. Mott-Schottky can be a powerful tool to support this selection, to understand the electronic evolution of the material during the charge process and to explain the changes in conductivity. Thus, in this work, Mott-Schottky is applied and a proposed model for the electronic structure of Ni-Co hydroxide films is presented, which enables the evaluation of the exact potentials at which EIS shall be performed to obtain more precise information on the different states of the material.

The variation of the capacitive response with potential in the Mott-Schottky form (C^{-2} vs. E) is presented in Fig. 3.2.4. As it can be seen, high C^{-2} values are recorded for the sample when the potential is in the cathodic range, below 0.04V. Then, a strong decay in the 0.04 to 0.12V range is observed. Since this decrease in the C^{-2} value is linear, the Mott-Schottky relation (eq.3.2.3) is applicable. Moreover, the fact that the C^{-2} vs. E follows a straight line with a negative slope indicates a p-type behaviour, being possible to state that Ni-Co$(OH)_2$ presents a p-type semiconducting nature.

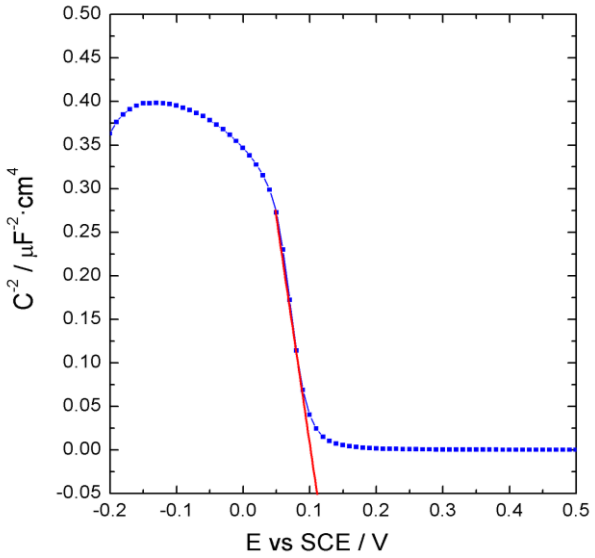

Fig. 3.2.4. Mott-Schottky at 1000Hz (blue) and fitting of the linear region of the Mott-Schottky plots (red) of Ni-Co$(OH)_2$ (1:2).

According to the semiconductor theory, the space-charge capacitance of a p-type semiconductor is given by:

$$\frac{1}{{C_{SC}}^2} = \frac{2}{\varepsilon_{SC}\varepsilon_0 e A^2 N_A}\left(E - E_{FB} - \frac{kT}{e}\right) \quad (eq.3.2.3)$$

where ε refers to the relative permitivity (dielectric constant), ε_0 is the vacuum permittivity, e is the charge of the electron, N_A is the acceptor concentration, E is the applied potential and E_{FB} is the flatband potential. This relationship describes the behavior of the space-charge region, when depleted, and an external polarization potential E is applied: $\emptyset_{SC} = E - E_{FB}$ [44]. By means of this equation, the flatband potential of the material can be determined by evaluating the interception of the linear region with the axis. Also, the doping agent concentration, N_A, can be worked out from the slope of that linear relation.

It is worth mentioning that, when applying Mott-Schottky, there are two main sources of capacitance that could be measured, namely, Helmholtz capacitance and space-charge capacitance. Nonetheless, in Mott-Schottky measurements it is assumed that the space-charge capacitance is much larger in comparison to the contribution of the Helmholtz one. Thus, it is assumed that the measured junction capacitance reflects the space-charge capacitance since it is much larger than the Helmholtz or diffusion layer capacitance. It is worth noting that this is only true when the variation of capacitance with potential is linear, as shown in the Mott-Schottky plots. Otherwise, it would be erroneous to make such an assumption [45].

Applying eq. 3.2.3 to the experimental data, it is possible to determine a value of 0.102V for the flatband potential, which coincides with the beginning of the main voltammetric peak. Since the material begins its energy storage reaction at a potential value near the flatband potential the decrease in the resistance with the applied potential of the Ni-$Co(OH)_2$ observed by impedance measurements can be explained in terms of the electronic structure on the material. This is schematically shown in Fig. 3.2.5 where the electronic model for a p-type semiconductor, superimposed with the voltammetric profile of Ni-Co hydroxide and the charging phase changes are depicted.

As it is well known, when an electrolyte and an electrode get in contact, their Fermi levels get balanced. When this occurs, the displacement of the Fermi level induces bending of the valence and the conduction energy bands, which is done in reference to the electrolyte and translates into charge separation, producing charged zones at both sides of the interface [46]. This charge separation is negligible when the material is conductive but becomes of relevant extension (100-1000Å) for semiconductors. This charged region is known as the space-charge region [47]. In the electrolyte, this region is placed at the Helmholtz layer and the Gouy-Chapman diffusion plane (which is despicable for electrolytes with concentration above 0.1M).

Since the Fermi level is directly related with the electrochemical potential, when an external potential is applied, the Fermi level can be artificially modified giving rise to three different electronic situations for a p-type semiconductor, schematically depicted in Fig. 3.2.5a-c

The first electronic situation is when nickel-cobalt energy storage material is at its discharged state. In this case, cathodic polarizations are applied, induced by the imposition of potentials lower than the flatband potential (E_{FB}). Thus, the Fermi level of the semiconductor is forced to be raised. The bands, to accommodate to the Fermi level of the electrolyte caused by the external injection of electrons, bend downwards, as seen in Fig. 3.2.5a. Consequently, electrons occupy the vacancies of the valence band and create an inner negative charge in the semiconductor. This negative region is depleted of vacancies, which are the main charge carriers in a p-type semiconductor. For that reason, it is known as the space-charge or depletion region. The formation of a depletion layer is associated to the higher value observed in the C^{-2} vs. E plot and the formation of an insulating Schottky barrier. This explains the high resistance values extracted from EIS for the material in its discharged condition.

As long as the potential increases in the anodic direction, the Fermi level of the semiconductor is forced to decrease until the flatband potential is reached. This reduces the space-charge capacitance with the resultant decay of C^{-2} vs. E observed in Fig. 3.2.4. Once E_{FB} is reached there is no electron transfer and there is no space-charge region (Fig. 3.2.5b). In this case, there is no accumulated charge in the semiconductor and the bands are flat from the inner side to the external part of the semiconductor. Since there is no charge in the electrode-electrolyte interface, the Shottky barrier is no longer present. That is observed in EIS results by the drastic reduction of diffusion-related resistance at the intermediate charge state of the sample.

Once the material is polarized anodically, this is, at applied potentials is higher than the flatband potential, the Fermi level of the electrolyte is positioned above the Fermi level of the semiconductor (Fig. 3.2.5c). This produces upward band bending and an accumulation layer of vacancies in the valence band emerges. Since vacancies are accumulated at the surface, a positively charged region appears. Moreover, if the polarization of the material is such that the Fermi level is displaced down enough to

cross the edge of the valence band, the semiconductor then becomes degenerate in the space charge region, and the material behaves as a metallic conductor [48].

It is worth noting that, since the doping concentration for nickel and cobalt hydroxides and oxides is typically high, in the order of ~10^{20} [49,50], the Fermi level is positioned very near the edge of the valence band. As a consequence, for the studied material, the degenerate condition can be achieved even for very small anodic polarisations (Fig. 3.2.5c). In these conditions the hydroxide behaves as a metallic conductor, which explains the low resistance values observed by EIS for charged condition of the material.

The band model proposed in Fig. 3.2.5 can also explain the charging mechanism of the material. In fact, the flow of electrons that go from the semiconductor to the electrolyte interface interact with the protons present in the solution, leading to the proton diffusion reaction and the oxidation reaction of the metal ions. Accordingly, the phase transition, exemplified in Fig. 3.2.5(d-h), is only possible in this potential range above the flatband potential.

Therefore, in the potential range from-0.2V to 0.5V the material changes from a depleted semiconductor to a degenerated semiconductor (nickel-cobalt hydroxide at a potential higher than the flatband potential). Then, the energy storage reaction becomes possible giving rise to the transition to the oxyhydroxide phase (γ-$Ni_xCo_{1-x}OOH$) which is conductive. For conductive materials, the space-charge region is negligible and, for that reason, no space-charge capacitance is observable in the Mott-Schottky plot at cathodic potentials. Finally, the new phase is conductive and, consequently, there is a dramatic decrease in the resistivity values observed in EIS.

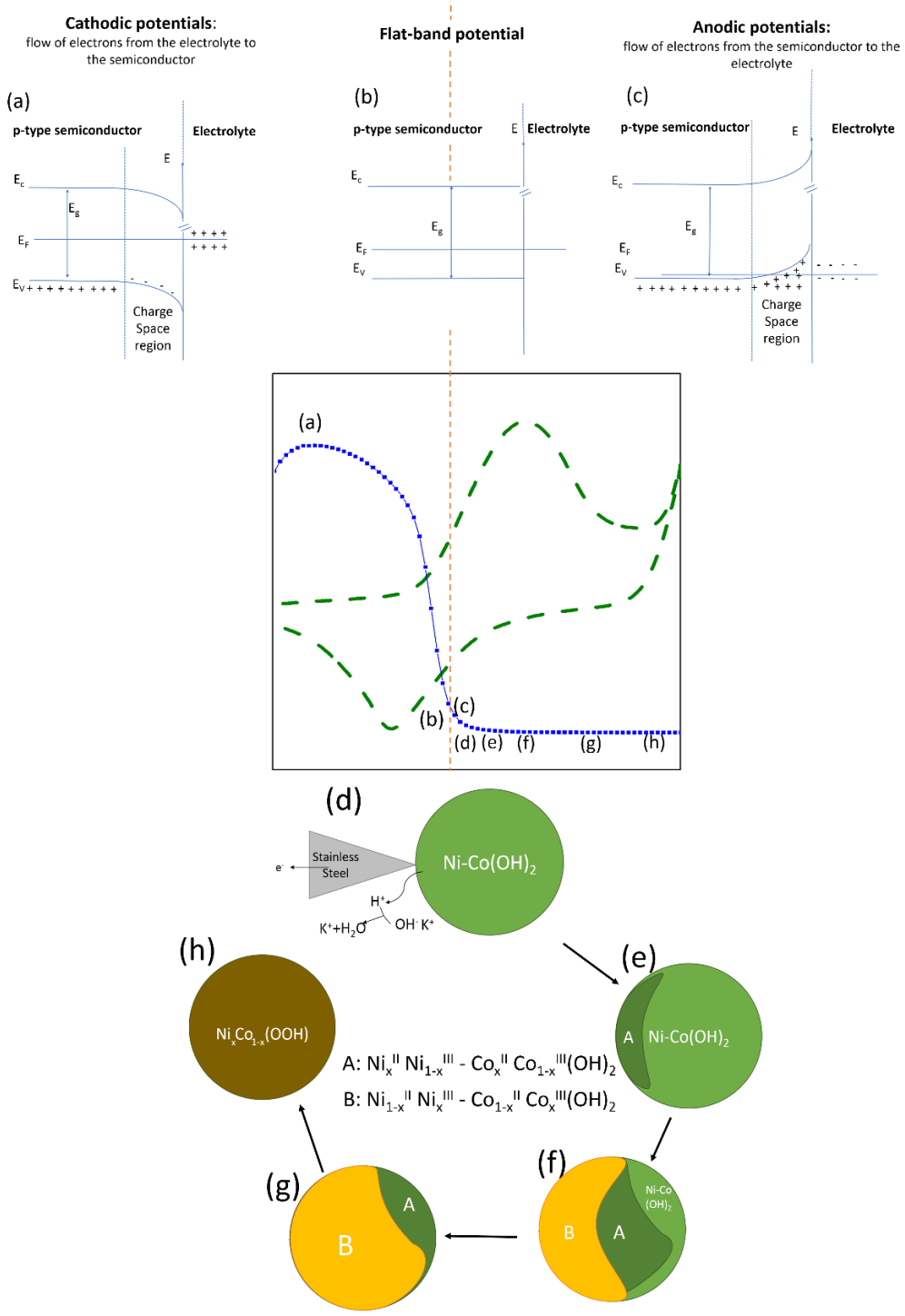

Fig. 3.2.5. Electronic and Phase model of the Charging process of Nickel-Cobalt hydroxide based on the current density (cyclic voltammetry) and charge-space capacitance (Mott-Schottky) as a function of the applied potential. (a) Illustration of the band bend occurring when the Fermi level of the semiconductor is placed higher than that of the electrolyte for a p-type semiconductor. (b) Illustration of the equilibrium state of bands when the Fermi level of the semiconductor is the same of the electrolyte. (c) Illustration of the band bend happening when the Fermi level of the semiconductor is placed lower than that of the electrolyte for a p-type semiconductor. (d-e) Modification of the phase transformations occurring during the charging process for the Ni-Co double hydroxide materials first presented by Barnard, Randell and Tye [43].

Summarizing, Mott-Schottky can be very useful to evaluate the depletion state of the material, which is correlated to its conductivity. At cathodic potentials, there is a depletion region and, as a consequence, the material is non-conductive, and no reaction is possible. Once the potential is increased, the Fermi level of the semiconductor decreases until it reaches a degenerate state and the material behaves as a conductor. Once more anodic potentials are applied, the semiconductor acts as an electron donor and gets oxidised to higher oxidation states of Nickel and Cobalt. Consequently, the faradaic reaction becomes possible and the solid-state proton diffusion begins. This is the charge reaction, where there is a phase transition from nickel-cobalt hydroxide to nickel-cobalt oxyhydroxide, with the consequent stabilization of the conductive phase.

Thus, Mott-Schottky combined with cyclic voltammetry proves to be a very useful tool to evaluate the potentials at which EIS should be studied and provides complementary information to understand EIS results and the respective charging mechanism. This tool, first used for energy storage applications to our best knowledge, suggests that the potentials at which EIS is carried out shall be wisely selected and that is very useful to perform EIS not only at one potential, but at least at two, in charged and discharged conditions. Moreover, to further understand the reaction evolution processes, a third potential that corresponds to a degenerate semiconductor condition, the flatband potential, shall also be considered.

3.2.4. Conclusions

Impedance Spectroscopy is a very powerful technique that can provide in-depth information about resistance, porosity, degradation and charge-transport phenomena of a system. In the present work, EIS is used to comprehend the charge mechanism of nickel-cobalt hydroxide. Results evidence that for charge storage materials, EIS spectra are voltage-dependent and that it relies on the charge-state of the sample and its conductivity at a given potential. Furthermore, Mott-Schottky has been successfully implemented to explain the electronic-band evolution of Nickel-Cobalt hydroxide and to provide complementary information to critically select the potential values at which EIS measurements shall be performed. Finally, Mott-Schottky has also aid in understanding the variation of the Fermi levels at the interface of Nickel-Cobalt hydroxide in alkali media during the charge mechanism.

Acknowledgments

This work has been performed in scope of International Doctoral Program in Functional Materials (IDS-FunMat, Erasmus Mundus) and funded by the European Union. We would like to express our gratitude to the Fundação para a Ciência e Tecnologia (FCT) for the funding under the contracts M-ERA.NET/0004/2014 and UID/QUI/00100/2013t. We would also like to acknowledge the team at Plateforme Aquitaine de Caractérisation des Matériaux, PLACAMAT for their general assistance and, finally, Stephane Le Blond de Plouy (Centre de MicroCaractérisation Raimond Castaing) for the SEM image.

Chapter 3.2 references

[1] V. Palomares, P. Serras, I. Villaluenga, K.B. Hueso, J. Carretero-Gonzalez, T. Rojo, Na-ion batteries , recent advances and present challenges to become low cost energy storage systems, Energy Environ. Sci. 5 (2012) 5884–5901. doi:10.1039/c2ee02781j.

[2] D. Aurbach, Y. Talyosef, B. Markovsky, E. Markevich, E. Zinigrad, L. Asraf, J.S. Gnanaraj, H. Kim, Design of electrolyte solutions for Li and Li-ion batteries : a review, Electrochim. Acta. 50 (2004) 247–254. doi:10.1016/j.electacta.2004.01.090.

[3] Lan Xia, L. Yu, D. Hua, G.Z. Chen, Electrolytes for electrochemical energy storage, Mater. Chem. Front. 1 (2017) 584. doi:10.1039/C6QM00169F.

[4] B. Akinwolemiwa, C. Peng, G.Z. Chen, Redox Electrolytes in Supercapacitors, J. Electrochem. Soc. 162 (2015) 5054–5059. doi:10.1149/2.0111505jes.

[5] J.M. Tarascon, M. Armand, Issues and challenges facing rechargeable lithium batteries., Nature. 414 (2001) 359–367. http://www.ncbi.nlm.nih.gov/pubmed/11713543.

[6] W. Sugimoto, K. Yokoshima, Y. Murakami, and Y. Takasu, Charge Storage Mechanism of Nanostructured Anhydrous and Hydrous Ruthenium-Based Oxides, Electrochim. Acta. 52 (2006) 1742–1748.

[7] X. Xia, W. Lei, Q. Hao, W. Wang, X. Wang, One-step synthesis of CoMoO4 / graphene composites with enhanced electrochemical properties for supercapacitors, Electrochim. Acta. 99 (2013) 253–261. doi:10.1016/j.electacta.2013.03.131.

[8] D. Pech, M. Brunet, H. Durou, P. Huang, V. Mochalin, Y. Gogotsi, P.-L. Taberna, P. Simon, Ultrahigh-power micrometre-sized supercapacitors based on onion-like carbon., Nat. Nanotechnol. 5 (2010) 651–4. doi:10.1038/nnano.2010.162.

[9] M. Beidaghi, C. Wang, Micro-Supercapacitors Based on Interdigital Electrodes of Reduced Graphene Oxide and Carbon Nanotube Composites with Ultrahigh Power Handling Performance, (2012) 4501–4510. doi:10.1002/adfm.201201292.

[10] X. Xia, Z. Zeng, X. Li, J. Yongqi Zhang, I. Tu, N.C. Fan, H. Zhangc, H.J. Fan, Fabrication of metal oxide nanobranches on atomic-layer-deposited TiO2 nanotube arrays and their application in energy storage, Nanoscale. 5 (2013) 6040–6047. doi:10.1039/c3nr01606d.

[11] Z. Li, Z. Zhou, G. Yun, K. Shi, X. Lv, B. Yang, High-performance solid-state supercapacitors based on graphene-ZnO hybrid nanocomposites, Nanoscal. 8 (2013) 1–9.

[12] A. Ramadoss, G.-S. Kim, S.J. Kim, Fabrication of reduced graphene oxide/TiO2 nanorod/reduced graphene oxide hybrid nanostructures as electrode materials for supercapacitor applications., CrystEngComm. 15 (2013) 10222–10229. doi:10.1039/c3ce41517a.

[13] W. Shi, J. Zhu, H. Sim, Y. Tay, Z. Lu, X. Zhang, Y. Sharma, M. Srinivasan, H. Zhang, H. Hng, Q. Yan, Achieving high specific charge capacitances in Fe3O4 / reduced graphene oxide nanocomposites, (2011) 3422–3427. doi:10.1039/c0jm03175e.

[14] D. Cai, S. Xiao, D. Wang, B. Liu, L. Wang, Y. Liu, H. Li, Y. Wang, Q. Li, T. Wang, Morphology controlled synthesis of NiCo2O4 nanosheet array nanostructures on nickel foam and their application for pseudocapacitors., Electrochim. Acta. 142 (2014) 118–124. doi:10.1016/j.electacta.2014.06.119.

[15] E. Umeshbabu, G. Rajeshkhanna, G.R. Rao, Urchin and sheaf-like NiCo2O4 nanostructures: Synthesis and electrochemical energy storage application., Int. J. Hydrogen Energy. 39 (2014) 15627–15638. doi:10.1016/j.ijhydene.2014.07.168.

[16] V. Gupta, S. Gupta, N. Miura, Potentiostatically deposited nanostructured CoxNi1−x layered double hydroxides as electrode materials for redox-supercapacitors, J. Power Sources. 175 (2008) 680–685. doi:10.1016/j.jpowsour.2007.09.004.

[17] K. Xie, J. Li, Y. Lai, W. Lu, Y. Liu, L. Zhou, H. Huang, Highly ordered iron oxide nanotube arrays as electrodes for electrochemical energy storage, Electrochem. Commun. 13 (2011) 657–660. doi:10.1016/j.elecom.2011.03.040.

[18] M. Li, Y. Wang, D. Wu, L. Wang, H. Yang, Hierarchical grass like NiCo2O4 nanoflakes on 3-dimensional microporous electrically conductive network with Superior Electrochemical Performance, Energy Procedia. 105 (2017) 4848–4853. doi:10.1016/j.egypro.2017.03.960.

[19] X. Xia, Q. Hao, W. Lei, W. Wang, D. Sun, X. Wang, Nanostructured ternary composites of graphene/Fe2O3/polyaniline for high-performance supercapacitors, J. Mater. Chem. (2012) 16844–16850. doi:10.1039/c2jm33064d.

[20] Z. Wang, X. Zhang, Y. Li, Z. Hao, Synthesis of graphene–NiFe2O4 nanocomposites and their electrochemical capacitive behavior, J. Mater. Chem. A. 1 (2013) 6393–6399. doi:10.1039/c3ta10433h.

[21] D.T. Dam, J. Lee, T. Huang, Ultra-small and low crystalline CoMoO4 nanorods for electrochemical capacitors, Sustain. Energy Fuels. 1 (2017) 324–335. doi:10.1039/C6SE00025H.

[22] M.-H. Bai, L.-J. Bian, Y. Song, X.-X. Liu, Electrochemical Codeposition of Vanadium Oxide and Polypyrrole for High-Performance Supercapacitor with High Working Voltage., ACS Appl. Mater. Interfaces. 6 (2014) 12656–12664. doi:10.1021/am502630g.

[23] X. Xiao, T. Ding, L. Yuan, Y. Shen, Q. Zhong, X. Zhang, Y. Cao, B. Hu, T. Zhai, L. Gong, J. Chen, Y. Tong, J. Zhou, Z.L. Wang, WO3-x/MoO3-x core/shell nanowires on carbon fabric as an anode for all-solid-state asymmetric supercapacitors., Adv. Energy Mater. 2 (2012) 1328–1332. doi:10.1002/aenm.201200380.

[24] H. Wu, C. Xu, J. Xu, L. Lu, Z. Fan, X. Chen, Y. Song, D. Li, Enhanced supercapacitance in anodic TiO2 nanotube films by hydrogen plasma treatment., Nanotechnology. 24 (2013) 455401/1-455401/7. doi:10.1088/0957-4484/24/45/455401.

[25] C. Johnston, P.S. Grant, X. Zhao, C. Johnston, P.S. Grant, A novel hybrid supercapacitor with a carbon nanotube cathode and an iron oxide / carbon nanotube composite anode oxide / carbon nanotube composite anode, J. Mater. Chem. 19 (2009) 8755–8760. doi:10.1039/b909779a.

[26] F. Tao, Y. Shen, Y. Liang, H. Li, Synthesis and characterization of Co(OH)2/TiO2 nanotube composites as supercapacitor materials, J Solid State Electrochem. 11 (2007) 853–858. doi:10.1007/s10008-006-0232-x.

[27] T. Hsieh, C. Chuang, W. Chen, J. Huang, Hydrous ruthenium dioxide / multi-walled carbon-nanotube / titanium electrodes for supercapacitors, Carbon N. Y. 50 (2011) 1740–1747. doi:10.1016/j.carbon.2011.12.017.

[28] G. Natu, P. Hasin, Z. Huang, Z. Ji, M. He, Y. Wu, Valence Band-Edge Engineering of Nickel Oxide Nanoparticles via Cobalt Doping for Application in p - Type Dye-Sensitized Solar Cells, (2012).

[29] F. La Mantia, H. Habazaki, M. Santamaria, F. Di Quarto, A Critical Assessment of the Mott – Schottky Analysis for the Characterisation of Passive Film Electrolyte Junctions 1 , 2, 46 (2010) 1306–1322. doi:10.1134/S102319351011011X.

[30] A. Adán-más, R.G. Duarte, T.M. Silva, L. Guerlou-demourgues, M. Fátima, G. Montemor, Enhancement of the Ni-Co hydroxide response as Energy Storage Material by Electrochemically Reduced Graphene Oxide, Electrochim. Acta. 240 (2017) 323–340. doi:10.1016/j.electacta.2017.04.070.

[31] M.G. Ortiz, S.G. Real, E.B. Castro, Preparation and characterization of positive electrode of Ni-MH batteries with cobalt additives, Int. J. Hydrogen Energy. 39 (2014) 8661–8666. doi:10.1016/j.ijhydene.2013.12.065.

[32] T. Nguyen, M. Boudard, M.J. Carmezim, M.F. Montemor, Layered Ni(OH)2-Co(OH)2 films prepared by electrodeposition as charge storage electrodes for hybrid supercapacitors, Sci. Rep. (2017) 1–10. doi:10.1038/srep39980.

[33] T. Nguyen, M. Boudard, M. João Carmezim, M. Fátima Montemor, NixCo1-x(OH)2 nanosheets on carbon nanofoam paper as high areal capacity electrodes for hybrid supercapacitors, Energy. 126 (2017) 208–216. doi:10.1016/j.energy.2017.03.024.

[34] M. Paszkiewicz, I. Walas, The potentiodynamic investigations of the overcharge and self-discharge of nickel hydroxide electrode, Electrochim. Acta. 24 (1979) 629–631. doi:10.1016/0013-4686(79)87043-7.

[35] G. Feuillade, R. Jacoud, Transferts ioniques durant l'oxydation anodique d'un hydroxyde de nickel, Electrochim. Acta. 14 (1969) 1297–1311. doi:10.1016/0013-4686(69)87023-4.

[36] P. Oliva, J. Leonardi, J.F. Laurent, C. Delmas, J.J. Braconnier, M. Figlarz, F. Fievet, A. de Guibert, Review of the structure and the electrochemistry of nickel hydroxides and oxy-hydroxides, J. Power Sources. 8 (1982) 229–255. doi:10.1016/0378-7753(82)80057-8.

[37] C. Faure, C. Delmas, M. Fouassier, P. Willmann, Preparation and characterization of cobalt-substituted α-nickel hydroxides stable in KOH medium Part I. α′-hydroxide with an ordered packing, J. Power Sources. 35 (1991) 249–261. doi:http://dx.doi.org/10.1016/0378-7753(91)80110-J.

[38] J.W. Montupally, S., Streinz, C.C., Weidner, Proton Diffusions in Nickel Hydroxide Films: Measurement of the Diffusion Coefficient as a Function of State of Charge, J. Electrochem. Soc. 142 (1995) 1401–1408.

[39] C. Tessier, C. Faure, L. Guerlou-Demourgues, C. Denage, G. Nabias, C. Delmas,

Electrochemical Study of Zinc-Substituted Nickel Hydroxide, J. Electrochem. Soc. 149 (2002) A1136. doi:10.1149/1.1495496.

[40] C. Delmas, C. Faure, Y. Borthomieu, The effect of cobalt on the chemical and electrochemical behaviour of the nickel hydroxide electrode, Mater. Sci. Eng. B. 13 (1992) 89–96. doi:10.1016/0921-5107(92)90147-2.

[41] A.N. Dey, U.S. Pat, D.L. Foster, H.C. Kuo, C.R. Schlaikjer, M. Kalliandis, An AC Impedance Study of the Degradation of Porous Nickel Battery Electrodes, 135 (1986).

[42] R.D. Armstrong, E.A. Charles, Some Aspects of the A.C. Impedance Behaviour of Nickel Hydroxide and Nickel/Cobalt Hydroxide Electrodes in Alkaline Solution, J. Power Sources. 27 (1989) 15–21.

[43] R. Barnard, C.F. Randell, F.L. Tye, Studies concerning charged nickel hydroxide electrodes I. Measurement of reversible potentials, J. Appl. Electrochem. 10 (1980) 109–125. doi:10.1007/BF00937345.

[44] T.M. Silva, a. M.P. Simões, M.G.S. Ferreira, M. Walls, M. Da Cunha Belo, Electronic structure of iridium oxide films formed in neutral phosphate buffer solution, J. Electroanal. Chem. 441 (1998) 5–12. doi:10.1016/S0022-0728(97)00300-8.

[45] G. Hodes, Electrochemistry of Nanomaterials, Wiley, 2008. http://eu.wiley.com/WileyCDA/WileyTitle/productCd-3527612793.html.

[46] J.O. Bockris, A.K.N. Reddy, Modern Electrochemistry: An Introduction to an Interdisciplinary Area, Plenum Press, N.Y., 1970.

[47] A.K. Vijh, Electrochemistry of metals and semiconductors: The application of solid state science to electrochemical phenomena, M. Dekker, 1973.

[48] Y.V. Pleskov, Y.Y. Gurevich, Semiconductor Photoelectrochemistry, Consultants Bureau,New York, NY, 1986. doi:10.1016/0022-0728(88)80185-2.

[49] G. Barral, S. Maximovitch, F. Njanjo-Eyoke, Study of electrochemically formed Ni(OH)2 layers by EIS, Electrochim. Acta. 41 (1996) 1305–1311. doi:10.1016/0013-4686(95)00451-3.

[50] E. Sikora, D.D. Macdonald, Nature of the passive film on nickel, Electrochim. Acta. 48 (2002) 69–77. doi:10.1016/S0013-4686(02)00552-2.

3.3 In-situ localized pH, pNa and dissolved O_2 measurements during charge-discharge of $Ni_xCo_{1-x}(OH)_2$ film electrode.

Alberto Adán-Más[a,b,*] , Maryna G. Taryba[a], Teresa M. Silva[a,c], Liliane Guerlou-Demourgues[b,d], M. F. Montemor[a,*]

[a] Centro de Química Estrutural-CQE, DEQ, Instituto Superior Técnico, Universidade de Lisboa, 1049-001, Lisboa, Portugal

[b] CNRS, University of Bordeaux, Bordeaux INP, ICMCB UPR 9048, 33600 Pessac, France

[c] ADEM, GI-MOSM, ISEL-Instituto Superior de Engenharia de Lisboa, Instituto Politécnico de Lisboa, Lisboa, Portugal

[d] RS2E, Réseau Français sur le Stockage Electrochimique de l'Energie, FR CNRS 3459, France.

Keywords: Nickel-Cobalt Hydroxide; Energy Storage; Localized micro-potentiometry; NiMH batteries; Charge mechanism

Abstract

Nickel hydroxide, usually stabilized with cobalt, has been widely studied for energy storage applications. Although its charge-discharge mechanism seems to be simple, there is a lot of controversy regarding species involved in the process. To highlight such mechanism, this work discusses, for the first time, localized in-situ measurements of pH, pNa and dissolved O_2 carried out during cyclic voltammetry of nickel-cobalt hydroxide electrodes in Na_2SO_4 0.05M. Local pH and pNa distributions were recorded using micro-potentiometric sensors with liquid membrane, while dissolved O_2 was monitored using a fiber-optic microsensor. Although widely used in corrosion and biology, ion-selective localized techniques had not yet been reported for studying energy storage materials. Thus, this work evidences how these tools can bring further insights and understanding about the charge processes in metal hydroxide electrodes by direct measuring the gradients of relevant species at the electrode-electrolyte interface.

3.3.1. Introduction

Nickel hydroxide has been used in different applications such as electrochromic devices or water electrolysers [1,2], and it is intensively used in energy storage applications such as nickel batteries [3] due to its high theoretical capacity, low cost, accessibility and simple synthesis [4–8]. In recent years, it has resurged as a potential material for the next-generation of energy storage devices, particularly when combined with other materials [9–11]. For example, cobalt can improve the electrochemical response, conductivity and stability of nickel oxides and hydroxides, extending its stability [12,13].

Studies to understand the oxidation-reduction mechanism of nickel hydroxide based materials and the different phases involved in the charge storage process have been performed since 1966, when Bode et al. proposed a diagram elucidating the possible phase transformations occurring in the material [14]. Although the charge storage mechanisms are considered quite simple, there are several models proposed in literature. In general, reports consider either solid-state H^+ transport mechanism [15–17] , as exemplified by equations 3.3.1 and 3.3.2, or OH^- transport model [15,18–20]. If cobalt (III) and ion contributions are considered, the mechanism proposed in equation 3.3.1 has been applied:

$$\alpha\text{-}Ni_xCo_{1-x}(OH)_2(2NO_3^-, CO_3^{2-})_{(1-x)/2}(H_2O)_{0.5} + (0.5\text{-}y)(Na^+, K^+) \longleftrightarrow \gamma\text{-}Ni_xCo_{1-x}OO(H^+)_y(Na^+,K^+)_{(0.5-y)}(H_2O)_{0.5} + (2\text{-}y)H^+ + (1-x)/2\ (2NO_3^-, CO_3^{2-}) + (0.5+x)e^- \quad \text{eq. (3.3.1)}$$

If cobalt (II) is considered, equation 3.3.2 has been proposed:

$$\beta\text{-}Ni_xCo_{1-x}O_2H_{1+x} \longleftrightarrow \beta\text{-}Ni_xCo_{1-x}OOH + xH^+ + xe^- \quad \text{eq. (3.3.2)}$$

On the one hand, when H^+ transport is considered, three different submodels have been proposed, depending on the contribution of cations from the solution, the hydration of metal ions and the extent of hydration of reactants and reaction products [15–17]. On the other hand, a mechanism based on OH^- was first considered in basis of oxygen and hydrogen isotopic studies [20]. Moreover, results also differ on the role of cations in the mechanism [17–19]. Thus, although the final phases are well known, the exact mechanism is yet to be completely understood [2,21].

The understanding of the process also requires to include the effect of the oxygen evolution reaction (OER), a parasitic reaction which induces hysteresis along the whole nickel hydroxide oxidation-reduction reaction [22,23]. However, the extent of this phenomena has yet to be determined [24]. Pandolfo [25] et al. reported that OER on $Ni(OH)_2$ occurs at 0.55V vs. Hg/HgO in KOH 1M, while Ta [26] et al. reported similar results at 0.5V vs. Hg/HgO. In principle, OER is fuelled by part of the current used during oxidation of the electrode and produces a slowly steady decrease of the oxidation state in nickel oxyhydroxide (self-discharge) at open circuit, as demonstrated by Conway [24,26,27].

A wide range of techniques have been applied to investigate the charge mechanism in Ni hydroxide-based materials. In particular, electrochemical quartz crystal microbalance (EQCM) [18,19,28], but also x-ray adsorption near edge structure (XANES) combined with extended x-ray absorption fine structure (EXAFS) [29], Raman [30,31], UV [32] or scanning electron microscopy [33] provided relevant data. Recently, the combination of EQCM with probe laser beam (PLB) was proposed as *in situ* characterization tool, to determine, more precisely, the oxidation-reduction

mechanism. EQCM accurately quantifies mass changes [22], while PLB allows determination of the direction of the net ionic flux across the electrode-electrolyte interface [28]. However, it is rather challenging to separate the contribution of cations, anions and solvent molecules and to precisely understand the nature of the charge-compensation processes [21].

Thus, localized measurements to determine local pH, concentration of the cations involved in the process at the vicinity of the electrode-electrolyte interface and the dissolved oxygen content in the electrolyte can bring key data to unveil the charge storage mechanisms. For that reason, in this work, local micro-potentiometry has been applied. To the best of authors' knowledge, such technique has never been applied before in the field of energy storage materials and the results obtained in this work bring relevant novelty.

Local micro-potentiometry, also known as scanning ion-selective electrode technique (SIET), has been widely used in biology, physiology and, over the last years in corrosion science [34–42] too. It enables the measurement of specific ions activity, at a quasi-constant micro-distance, over an active surface in an electrolyte. SIET measurements require a potentiometric cell that contains the active material, a reference electrode and an ion-selective microelectrode assembled in such a way that it allows accurate positioning of the microelectrode over the sample and the evaluation of ion-selective differences in the electrolyte nearby the surface-electrolyte interface at localized micro-scale. There is a significant difference between measurements of bulk and localized ions' concentrations/ activities. Measurements in bulk electrolyte provide important insights, however the results reflect an average concentration of species present in solution. It is known that distribution of particular ions in solution, in the close vicinity of the surface of the electrode, may change during oxidation-reduction processes, thus involving species from the medium and the active material. These changes in ions' distributions vanish when progressing into bulk solution, and, hence, they can only be detected at the vicinity of the active surface. The spatially resolved in-situ localized techniques employed in this work enable to record key chemical information at a micro-distance from the active materials' surface and how the concentration of relevant species changes during polarization of the electrode. This provides better understanding of the redox processes that may occur during charge-discharge of the active material, highlighting the mechanisms contributing to energy storage. Thus, the present work discusses the results of pH, pNa and dissolved O_2 localized measurements during charge-discharge of electrodeposited nickel-cobalt hydroxide in aqueous media (0.05M Na_2SO_4 and K_2SO_4), and how these bring new light into the proposed mechanisms.

3.3.2. Experimental

3.3.2.1 Synthesis of Ni-Co hydroxide film.

Ni-Co hydroxide was deposited by means of cathodic electrodeposition using a potentiostat/galvanostat Gamry Interface 1000E. A pulsed potential between -0.9V and -1.2V was applied to a three-electrode cell containing a 100 mL solution containing 0.11g of $Co(NO_3)_2$, 0.21g of $Ni(NO_3)_2$ and 0.11g of $NaNO_3$. The duration of each pulse was 10 seconds, resulting in a total of 400 seconds for the electrodeposited layer. Longer deposition times would lead to thicker samples that would lead to interferences in the localized measurements. Platinum wire was used as counter electrode, SCE as reference electrode and Stainless Steel (AISI 304, Goodfellow) embedded in epoxy resin as substrate. The dimensions of the sample tested were 4mm x 4mm x 4mm. Stabilization

of the electrode material was undergone prior to the sample analysis. For that, the sample was cycled between -0.2V and 0.9V for an average of 20 cycles at 10 $mV \cdot s^{-1}$.

Electrodeposited thin-film are used since they are not affected by the influence of binders, carbonaceous additives, current-collector geometry or other components typically utilized in a commercially prepared nickel hydroxide electrode [27].

3.3.2.2 Materials characterization.

To study the material morphology, field emission scanning electron microscope coupled with EDS was used (FEG-SEM JEOL JSM7001F with Oxford light elements EDS detector INCA 250) and a Hitachi 8100 transmission electron microscope with LaB_6 filament at a working voltage of 200kV coupled with a ThermoNoran SystemSix EDS detector.

X-Ray Diffraction patters were obtained using an X'Pert Philips PMD diffractometer with a Panalytical X'celerator detector, using graphite-monochromized Cu K_α radiation (λ=1.54056Å).

Raman spectra were collected by means of an i-Raman® spectrometer from B&W Tek with an excitation laser beam of 532nm. The spectra were obtained with an acquisition time of 60 seconds and 2 accumulations.

3.3.2.3 Electrochemical evaluation.

The electrochemical evaluation was performed by means of a potentiostat/galvanostat Gamry Interface 1000E coupled with Pt as reference and as counter electrode. Cyclic voltammetry was carried out at two scan rates, 3 and 5$mV \cdot s^{-1}$ in a potential window ranging from -0.2V to 1.1V vs Pt or -0.3V to 1.1V vs Pt according to the electrolyte used, K_2SO_4 0.05M or Na_2SO_4 0.05M respectively. Neutral electrolytes were employed due to the requirements imposed by micro-potentiometry equipment, in particular microelelctrode stability. It is worth mentioning that all the measurements are recorded on the second cycle at the designated scan rate after the initial conditioning of 20 cycles and 2 more cycles at 10$mV \cdot s^{-1}$.

3.3.2.4 Micro-potentiometry.

Micro-potentiometric pH and pNa (i.e. pNa=-lg[Na+]) measurements were performed using the equipment and corresponding software from Applicable Electronics™ and Science Wares™. pH-selective glass-capillary microelectrodes were employed. Silanized glass micropipettes were back-filled with the inner filling solution and tip-filled with the corresponding ion-selective membrane with extended pH working range, based on [43] and Na^+ selective membrane developed according to requirements of corrosion studies for avoiding IR-drop effect and pH sensitivity [44]. The glass-capillary micro-electrodes were prepared as described elsewhere [43,45].

The tip orifice diameter of the glass-capillary microelectrodes was (1.8±0.2) µm. A homemade Ag/AgCl/0.05M NaCl mini-electrode was used as an external reference electrode for micro-potentiometric measurements. The ion-selective microelectrodes were calibrated prior each measurement. The micro-potentiometric probes were positioned (30±5) µm above the surface. Measurements were obtained, at least, by triplicate.

3.3.2.5 Fiber-optic oxygen micro-sensor.

The concentration of dissolved oxygen was measured using FireStingO2 fibre-optic oxygen meter (Pyroscience™). The micro-sensor employs an O_2-sensitive indicator immobilized on the tip of the sensor. The indicator is excitable with orange-red light at a wavelength of 610–630 nm and demonstrates an oxygen dependent luminescence at 760–790 nm. The measuring principle is based on a sinusoidally modulated red excitation light causing a phase-shifted sinusoidally modulated emission in the NIR. The detection limit of the micro-optode is 0.01 ppm. The needle-type retractable micro-sensor OXR50 with 50 µm tip diameter was used for experiments. The optode was positioned (70±10) µm over the sample surface. This sensor provides response time of less than 1 s, reduced interference on medium and high stability of the signal. The calibration of the micro-optode was performed using N2 (0%DO) and air (20.9% DO) saturated solutions [46].

3.3.3. Results

3.3.3.1 Physico-chemical characterization

Nickel-cobalt hydroxides were deposited on stainless steel collectors. Scanning electron microscopy (SEM) and transmission electron microscopy (TEM) were used to disclose the morphology and microstructural characteristics of the electrode material, while X-ray diffraction (XRD), Raman spectroscopy and electron diffraction spectroscopy (EDS) were performed to elucidate the chemical composition. As exhibited in Fig. 3.3.1a, nickel-cobalt hydroxide presented a nanosheet-like structure, with nearly vertical alignment that forms a percolation network, in good agreement with literature [47]. TEM microscopy, depicted in Fig. 3.3.1b, revealed the thin nature and random orientation of the electrodeposited nanosheets. The electron diffraction pattern obtained for selected areas (SAED) evidenced the presence of blurred diffraction peaks, as result of the nano-structural nature or low degree of crystallinity of the material.

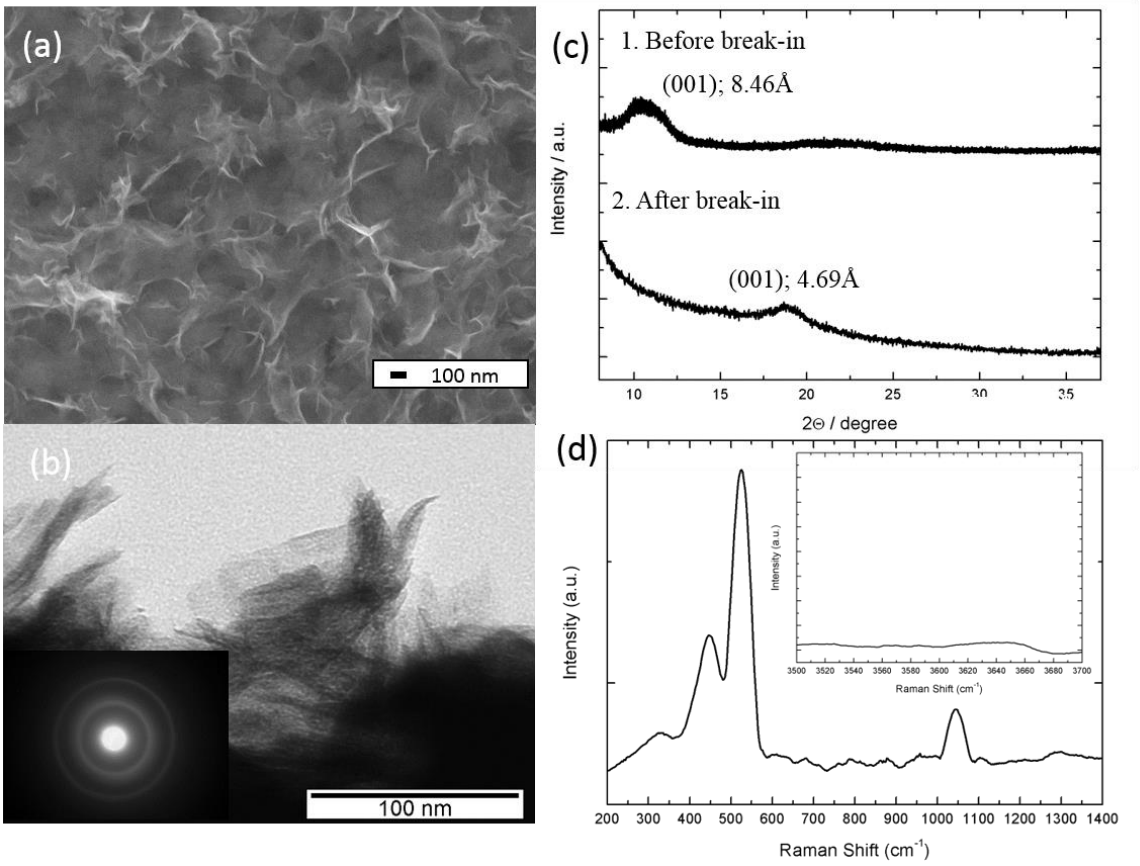

Fig. 3.3.1. Physico-chemical characterization of the surface film: **a)** Scanning Electron Microscopy image. **b)** Transmission Electron Microscopy with diffraction rings inset. **c)** XRD Spectra and **d)** Raman Spectra of $Ni_xCo_{1-x}(OH)_2$.

XRD, depicted in Fig. 3.3.1c, initially presented a peak at 10.32º, indicating an interslab distance of approximately 8.46Å. However, after a 20-cycle break-in, the peak shifted to 18.70 º, which corresponds to an insterslab distance of 4.69Å for the (001) line. Nickel-cobalt hydroxide materials consist of $Ni_xCo_{1-x}(OH)_2$ slabs that may incorporate H_2O, NO_3^- and CO_3^{2-} into the interlayer distance. Depending on the extent of these intercalated molecules, two different phases can be formed, α or β. For β nickel-cobalt hydroxide materials, there are no intercalated species in the interslab space, resulting in an interplanar distance of approximately 4.8Å, while this distance is enlarged to 7.5-8.5Å for the α phase, depending on the intercalated species [48]. In this work, XRD results evidenced an interslab distance of 8.46 Å, a fact that allows to conclude that original electrodeposited phase can be unequivocally classified as α-$Ni_xCo_{1-x}(OH)_2$. Moreover, results obtained by XRD showed that, after break-in, this material is transformed into the β phase due to the known instability of the α phase [12,49].

Raman spectroscopy was performed in the 200-3700 cm^{-1} range. The single peak at 329.5 cm^{-1}, and the double peak at 445.54 and 522.81 cm^{-1} are characteristic of E_g mode, O-M-O bending and M-O A_g vibrations modes, respectively. Moreover, there are two main characteristics that can differentiate the α phase from the β phase by means of Raman spectroscopy: first, the peak at 1048.35 cm^{-1} is associated to NO_3^- ions intercalated in the interslab space; secondly, Raman spectra present a shoulder at 3658 cm^{-1} that disappears in the β structure. Besides these, β structures also display a relatively intense peak at around 3580 cm^{-1} [50]. Therefore, Raman spectra confirm the presence of an α Nickel-Cobalt phase.

Electron diffraction spectroscopy and mapping were performed to evaluate the nickel-cobalt ratio electrodeposited in the sample and to study the homogeneity and dispersion of nickel and cobalt in the electrodeposited material. Results are shown in Fig. 3.3.2. The Ni:Co atomic ratio obtained was 1.8, which is close to the electrolyte composition used in the synthesis process and is in good accordance with previous reports [11].

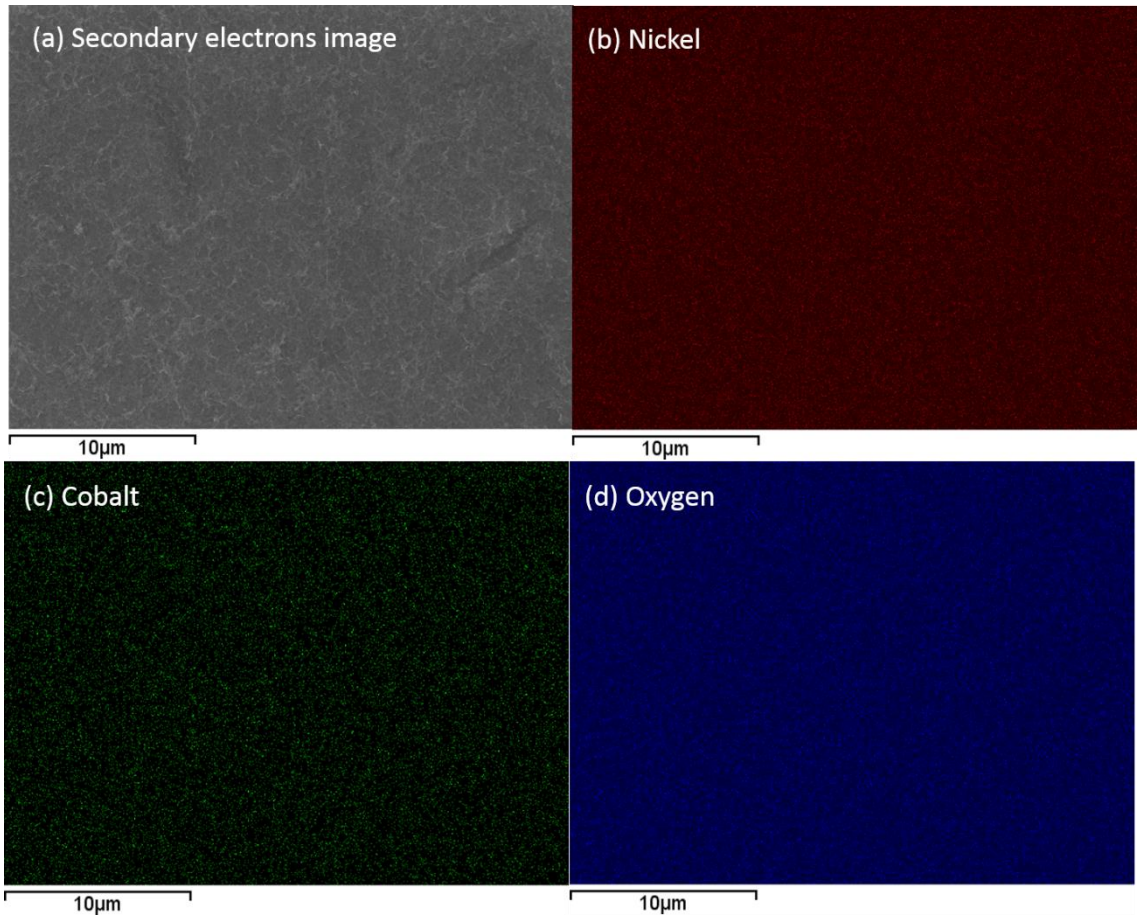

Fig. 3.3.2. Geometry of the analyzed samples used in the set-up: Stainless steel substrate embedded in epoxy

3.3.3.2 Electrochemical and localized measurements

The electrochemical response of nickel-cobalt hydroxide was evaluated in K_2SO_4 and Na_2SO_4 0.05M at the same time as localized pH and dissolved O_2 were monitored in-situ. It is worth mentioning that measurements could not be performed in KOH due to accelerated deterioration of the micro electrodes used in SIET. For increased accuracy in SIET measurements, a special experimental methodology was used. First, the response of polarized stainless steel substrates was investigated; the results evidenced a profile identical to that of inert polarized metals [46], when pH is pre-defined by the applied current and by the distance of the measuring electrode to the polarized surface. Secondly, possible pitfalls due to IR-drop were considered too. This is critical to ensure the reliability of data recorded using ion-selective microelectrodes, especially under external polarization conditions. To this end, two experimental setups were designed: (1) measurements in dilute electrolytes, 0.005M K_2SO_4 and 0.005M Na_2SO_4; (2) measurements using an ion-selective microelectrode prepared with a longer membrane (x15), in the range of 800-1000 µm.

The IR-drop effect is known to be more pronounced in solutions with low conductivity (i.e. less concentrated). However, in the present case, the recorded profile of the pH and pNa changes were essentially the same in the tested solutions with different conductivity (0.5M, 0.05M, 0.005M K_2SO_4 and Na_2SO_4, respectively for pH and pNa). This result proved the negligible influence of the IR-drop influence on the data obtained. The second experiment was supposed to reveal the IR-drop, if present, due to the higher resistivity of the 15x longer ion-selective membrane. The microelectrodes with membrane length in the range of 800-1000 µm (around 15 times longer than the regular membrane length) were tested under reproducible conditions. The results confirmed absence/negligible IR-drop effects.

$Ni_xCo_{1-x}(OH)_2$ produces a meaningful signal as evidenced by the results presented in Fig. 3.3.3 and 3.3.4. Due to limited time-response of the ion-selective electrode (2-3 seconds), cyclic voltammetry was performed at scan rates of 3 and 5 $mV \cdot s^{-1}$ in a potential range from -0.2V to 1.1V (vs. Pt). It is worth mentioning that an extended potential window for nickel hydroxide in sulphate electrolytes, like Na_2SO_4, is obtained as already reported [51,52].

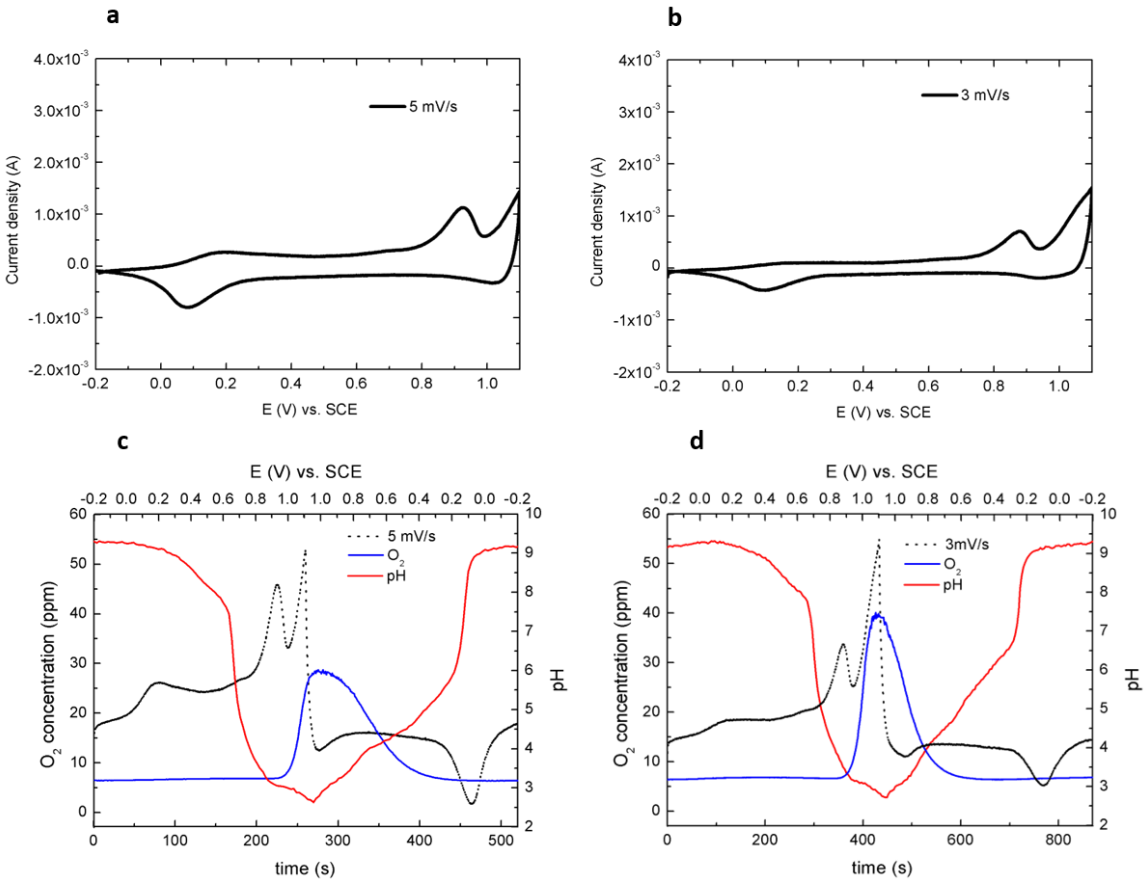

Fig. 3.3.3. Cyclic voltammetry at: **a)** 5 $mV \cdot s^{-1}$ and **b)** 3 $mV \cdot s^{-1}$ and their expanded version in time **c)** and **d)** with the corresponding measurements of pH and dissolved O_2 content variation measured in-situ within a potential range from -0.2V to 1.1V in K_2SO_4 0.05M.

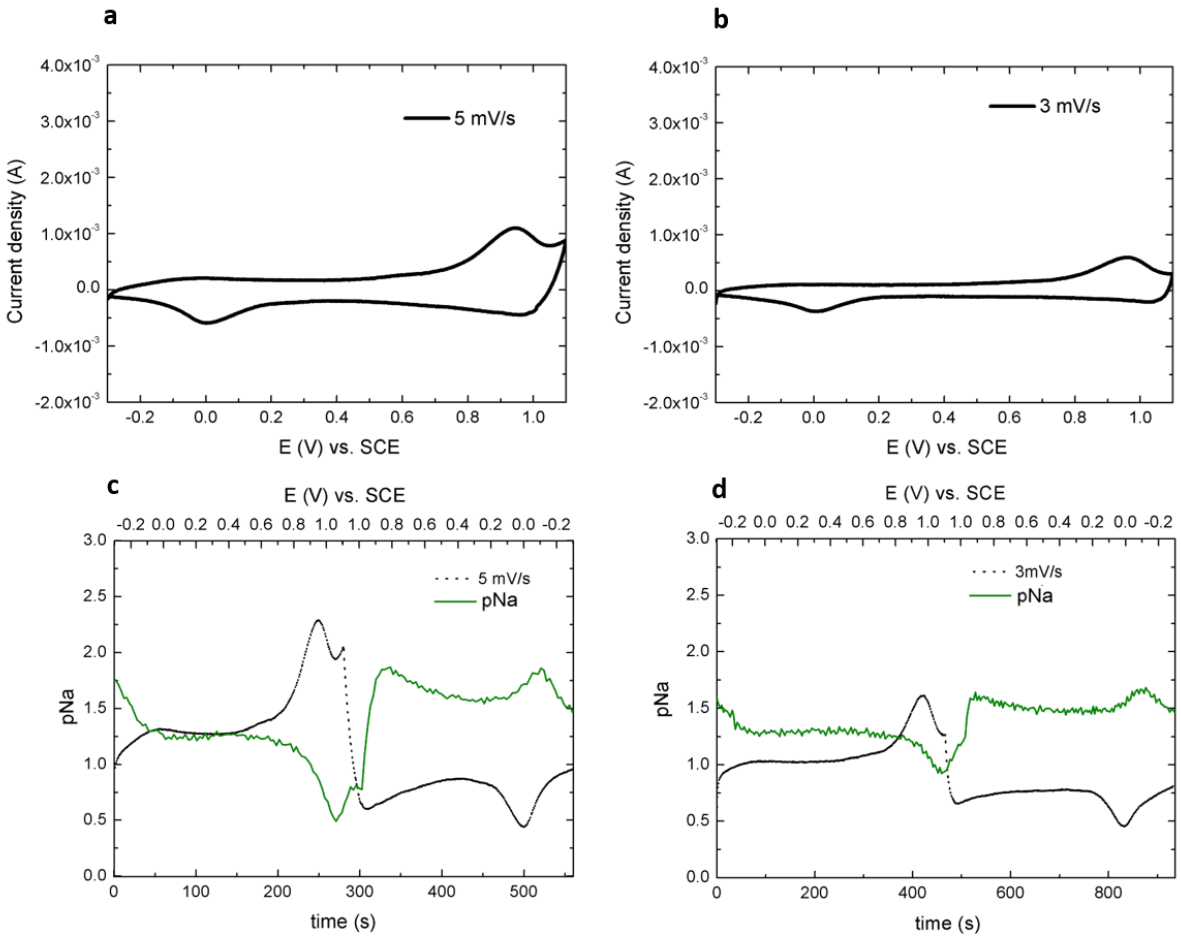

Fig. 3.3.4. Cyclic voltammetry at: **a)** 5 $mV \cdot s^{-1}$and **b)** 3 $mV \cdot s^{-1}$ and their expanded version in time **c)** and **d)** with the corresponding in-situ measurements of pNa within a potential ranging from -0.3V to 1.1V in Na_2SO_4 0.05M.

3.3.3.2.1 Anodic scan

When the sample was anodically polarized after 20 previous cycles in the potential window from -0.2V to 1.1V, a peak at 0.9V was clearly observed in the voltammetric profiles (Fig. 3.3.3). According to pH variations, the potential window can be divided in four regions: (1) Potential range from -0.2V to 0.3V: evidenced stable pH around 9.2 and decreasing pNa from 1.75 to 1.25 at 5 $mV \cdot s^{-1}$ (increased activity of sodium ions in solution, $pNa \approx -\log[Na^+]$). (2) Potential range from 0.3V to 0.65V: slight decrease of pH and stable pNa. (3) Scan throughout the anodic peak: large diminution of pH and pNa. (4) For polarizations over 1 V: the OER started.

In the potential range from -0.2V to 0.3V, the charge mechanism did not induce variations of pH but caused a diminution and posterior stabilization of pNa. As the oxidation-reduction reaction had not started, and sodium ions could not intercalate into β nickel-cobalt hydroxide due to structural constraints, the increased number of sodium ions might be induced by cations diffusion from bulk electrolyte to the interface, where they accumulate. Surface positive polarization during the anodic scan results in sulphate attraction for excess charge neutralization. Sulphate ions create a negatively charged layer on top of the active material that consequently attracts sodium ions in the vicinity of the interface, causing their accumulation (decrease in pNa). However, this phenomenon is not fully understood yet and further investigation is required.

In the potential range from 0.2V to 0.64V, pNa was nearly stable and there was a progressive pH decrease from 9 to 7.44 at $5mV \cdot s^{-1}$. Since pH was initially basic, such decrease could be caused by: (1) de-intercalation of protons from the active material, (2) depletion of hydroxyl ions in the electrolyte layer over the surface or (3) production/expulsion of solvent molecules at the interface.

Two possible explanations for this phenomenon can be proposed, considering whether the faradic reaction had started or not. On the one hand, if no faradaic reaction is considered to occur, supported by the unchanged current density as observed in cyclic voltammetry, and since proton de-intercalation would be associated to a change in the oxidation state of nickel, pH variation cannot be caused by proton de-intercalation. In fact, given the pH decrease profile in this potential range, it probably accounts for electrolyte diffusion-controlled processes. Moreover, the faster the scan rate, the more pronounced is the pH change. If pNa and pH variations are considered altogether, sodium ions may accumulate at the interface, reducing pNa, with increasing applied potential due to the aforementioned surface polarization, which is sensible to the applied current and is therefore affected by the scan rate. Due to excess of negative charge, both Na^+ and H^+ cations may be attracted, to reduce the excess of charge from SO_4^{2-}, thus decreasing pH. Results could also be explained considering a change in the coordination state of nickel atoms in the surface of the material caused by the excess of sodium ions may occur. A change in the hydration shell would not produce a visible response in current density, while potentially it would induce pH variations.

On the other hand, if it is assumed that the faradaic reaction starts at 0.3V and evolves until the main anodic peak, either hydroxyl injection or proton de-intercalation could be possible. Considering the first possibility, generation of water inside the material, that would be expelled due to volume constrains imposed by the structure, may occur, aiding the pH decrease. If proton expulsion is considered, a solid-state proton transport model is also a plausible mechanism within this potential range. Considering this case, sodium ions would initially accumulate at the interface due to surface polarization and its activity would remain unchanged until the anodic peak.

In the potential range from 0.64V to 0.97V, the faradaic reaction occurred, as evidenced by the peak in the cyclic voltammogram. This region is slightly deviated in Na_2SO_4 electrolyte and an identical behaviour is observed in the 0.7V to 1V range, where an abrupt decrease of both pH and pNa was noticed. pH decreased from 7.76 to 3.15 and from 7.44 to 3.14 and pNa decreased from 1.25 to 0.93 and from 1.25 to 0.49, respectively at scan rates of 3 and $5mV \cdot s^{-1}$. Thus, within this potential range a much sharper pH decrease was noticed comparatively to the previous potential range. This behaviour can be explained by assuming two different regimes: electrolyte-diffusion-controlled mechanism in the previous potential range, while another mechanism dominates in the current potential range. In fact, this abrupt pH acidification allows, in principle, to exclude a diffusion-controlled process in the electrolyte, which would induce a lower slope in the variation of pH. Moreover, at these scan rates, the material may be considered to be fully charged when the reaction is finished, explaining why the same pH value is obtained after charge in both cases. In principle, the pH drop can be consequence of either hydroxyl intercalation, which would locally reduce its concentration at the interface, leading to pH decrease, or proton transport and proton release during the charging process. However, while the latter is only limited by the mobility of the ions within the electrode material (solid state diffusion of protons) and its response would not be limited by diffusion in the electrolyte, hydroxide intercalation would be dominated by hydroxyl ions diffusion from the electrolyte to the electrode

material and the solid-state hydroxyl mobility in nickel-cobalt hydroxide. Therefore, an abrupt pH decrease indicates that the process is not hydroxyl diffusion-limited in the electrolyte, but mainly controlled by the transformation of the material. The most likely mechanism for the faradaic process should therefore involve solid-state transport of protons and their de-intercalation.

On the other hand, there is an accumulation of sodium ions at the interface during the charging reaction. Given solid-state structural limitations, sodium ions cannot be intercalated in β phases. Therefore, it is possible that during the redox reaction there is an excess of negative charge at the surface of the material due to limited proton de-intercalation and kinetics that produces sulphate diffusion for charge compensation. To compensate that excess of negative charge, sodium ions diffuse to the vicinity of the surface, decreasing pNa at the interface during the redox reaction. Moreover, the pNa variations are larger with increased scan rate, corroborating that the mechanism is affected by the magnitude of polarization and kinetics of the faradaic reaction. For higher applied currents (higher scan rates) there is a greater variation of pNa since de-intercalation of protons is not favoured and the system do not have enough time to compensate surface charge and sodium ions accumulate at the surface of the material. Intercalation processes are greatly dependent on the reaction kinetics, being enhanced for slower scan rates [4]. Therefore, sodium ions' transportation is driven to maintain surface electroneutrality.

Within the previous potential ranges, the variation of O_2 in solution during the redox reaction was negligible and its concentration was maintained around 7.4 -7.6 ppm (Fig. 3.3.3), which is within the normal range for dissolved oxygen in aqueous solutions.

The final step in the anodic scan is the oxygen evolution reaction (1.0V to 1.1V). Once the oxygen evolution reaction potential is reached, there was a substantial increase of the DO signal and an extra decrease of the pH that corresponds to the release of protons during OER according to the reaction exemplified in equation 3.3.3:

$$2H_2O \rightarrow 4H^+ + 4e^- \qquad \text{eq. (3.3.3)}$$

Regarding pNa, there was an increase of its value, which can be associated to a decrease in the concentration of sodium ions. This has been previously explained by Lamaka et al. [45] as consequence of excess of positive charge due to the proton production that generates a localized repulsion of sodium ions resulting in Na^+ depletion.

3.3.3.2.2 Cathodic scan

Once the polarization is reversed 4 different regions were noticed: (1) Oxygen reduction reaction (1.1V-1.0V), with the consequent increase in pH, decrease in dissolved oxygen and constant pNa value; (2) progressive pH raise and sharp change of pNa followed by stabilization in the 1V to 0.2V range; (3) sharp increase of pH and pNa, coincident with the cathodic peak and (4) pH and pNa stabilization around values of 9 and 1.5, respectively, after the reaction.

In the potential range from 1.0V to 0.20V, the pH increased almost linearly from 2.9 to 5.96 at 5 $mV \cdot s^{-1}$. On the other hand, pNa increased dramatically in the 1.0V to 0.8V potential range at 5 $mV \cdot s^{-1}$, reaching a value of 1.8 and then slowly decreased to 1.6 at the same scan rate in the 0.8V to 0.2V range. Similar values were obtained at 3$mV \cdot s^{-1}$. Once the potential was reversed, sodium ion accumulation at the interface is no longer required and sodium concentration is re-stablished to bulk levels, resulting in the drastic increase of pNa. There are no peaks in the cyclic voltammetry and a diffusion-controlled

regime (progressive increase) in the pH response was observed. Again, there are two possible explanations. On the one hand, assuming that the reaction had begun at this potential, diffusion of protons in the electrolyte and their intercalation inside the active material occurred. This process is controlled by both diffusion in the electrolyte and solid-state proton transport. Given the fact that pH at the beginning of this process was acid, de-intercalation of hydroxyl ions would produce a more drastic change in pH and thus it is unfeasible. On the other hand, considering that the reaction did not start, an equilibration between the interface and bulk electrolyte would be expected, progressively raising the pH and pNa.

Finally, during the cathodic peak there was again an increase of pNa up to 1.9 and 1.7 for $5mV \cdot s^{-1}$and $3mV \cdot s^{-1,}$ respectively. After the cathodic peak pNa returned to the initial value of 1.5. Simultaneously, the pH increased drastically to 9.0. Again, the nature of the 3-unit pH variation indicates a reaction-controlled mechanism that is not subjected to electrolyte diffusion-controlled phenomena. Given the results obtained during the oxidation reaction, it is likely that the reaction occurs in the same manner during reduction. Protons, which are provided by the solvent, intercalate and proceed to a solid-state proton transport. Solvent can be assumed to be easily accessible by the surface of the active material, being de-protonated to generate OH^-, and therefore, is not considered as a diffusion-limiting factor. In this case, sodium ions depletion starts the maximum of the cathodic peak, corresponding to a major change in the conductivity of the material from NiOOH, conductive, to $Ni(OH)_2$, semiconductor. This pNa increase may be therefore associated to a change in conductivity of the material and, consecutively, to surface charge compensation phenomena. Another possibility is that the observed pNa increase is due to a strong flux of hydroxyl ions, repelled by the negative polarization of the surface, that affect sodium ions. It is worth mentioning that the exact mechanism is not fully understood and requires further analysis; however, the role of Na^+ may be associated in maintaining electroneutrality in any case. Once the reaction is finished, after complete transformation to $Ni(OH)_2$, there is no need for further charge compensation and pNa returns to bulk levels.

3.3.4. Discussion

As aforementioned, there are several possible mechanisms that may explain the charge-discharge reaction [15], which can be divided in either proton or hydroxyl transport models. These reactions are exemplified in equations 3.3.1 and 3.3.2 (proton transport model) or 3.3.4 and 3.3.5 (hydroxyl transport model):

$$\alpha\text{-}Ni_xCo_{1-x}(OH)_2(2NO_3^-, CO_3^{2-})_{(1-x)/2}(H_2O)_{0.5} + (0.5\text{-}y)(Na^+, K^+) + (2\text{-}y)OH^- \longleftrightarrow \gamma\text{-}Ni_xCo_{1-x}OO(H^+)_y(Na^+,K^+)_{(0.5-y)}(H_2O)_{0.5} + (2\text{-}y)H_2O + (1\text{-}x)/2\ (2NO_3^-, CO_3^{2-}) + (0.5+x)e^- \quad \text{eq. (3.3.4)}$$

$$\beta\text{-}Ni_xCo_{1-x}O_2H_{1+x} + xOH^- \longleftrightarrow \beta\text{-}Ni_xCo_{1-x}OOH + xH_2O + xe^- \quad \text{eq. (3.3.5)}$$

Since cobalt ions are stabilized in the +3 oxidation state in the β phase, there must be proton deficiency to achieve charge compensation in accordance to Barnard et al. [53].

Several groups have reported mass changes during charge of $\alpha\text{-}Ni(OH)_2$, a phenomenon generally assigned to cation insertion [1,2,17,18,54–56]. Considering the non-stoichiometric model developed by Weidner et al. [22], there is a continuous change in the composition of the material between the fully charged and discharged composition

[57], this is, NiOOH and $Ni(OH)_2$ do not exist as separate solid phases, but rather as one non-stoichiometric solid phase [27]. According to this model, during oxidation protons are removed from vacancies (and from the interslab space) and diffuse to the electrode-electrolyte interface [58] where they react with OH^- to form water [2,26], with the consequent oxidation of Ni^{2+} into Ni^{3+} . To maintain electroneutrality, the transport of electrons and ions has to proceed at the same rate [59]. Alkali cations are simultaneously intercalated increasing mass, as suggested by Bernard et al. [16,60]. For that matter, there is an insertion of alkali ions in some prismatic sites of the γ phases [23]. Eventually, the mass variation reverses, as consequence of the instability of the α phase and its transformation into β phase [55]. Moreover, there is an increase of water content with cycling, with water expulsion during charge and incorporation during discharge, to maintain electroneutrality [15,56] regardless the counter-ion [17,21]. Therefore, this corresponds to as solid-state proton diffusion model, with proton transport and expulsion during charge and proton insertion during discharge.

The dynamics of (de-)intercalation and the interface transfer rates were studied by means of probe beam deflection (PBD) in combination with EQCM. Employing these techniques, the authors suggested that the contribution of individual species is dominated by OH^- with H_2O expulsion during oxidation. There has been little direct evidence of significant transfer of cations across the interface. Thus, it was proposed that cations are expulsed from the film material at a more negative potential than peak potential (E_p) and, once the material is polarized above E_p, either hydroxide insertion or de-intercalation of protons (producing water, which would not be detected by EPB since they would rapidly recombine with hydroxyl ions) would occur [1,2]. As a result, some authors support the hydroxyl transport model.

Based on EQCM studies, two ionic species shall concurrently move in opposing directions to maintain electroneutrality. Thus, it is reported that if OH^- ions are inserted during oxidation, with the consequent increase in mass, there must be a counterflux of ions [2,61]. Moreover, the rigid nature of the nickel hydroxide lattice imposes volume constraints, thus, while hydroxyl ions enter the structure, water molecules must leave at the same rate [15,60,62]. This results in H_2O moving on the same time scale as ionic hydroxide and is not controlled by diffusion [1]. It is also worth mentioning that mass increase occurs during the first cycles, but then mass change inversion occurs in extended redox cycles, which has been assigned to formation of beta phase [55]. During early immersion and first cycles, the material suffers a "break-in" in which cations and water molecules get de-intercalated and the species trapped in the interlayer space during electrodeposition are expelled [54,55,61]. Therefore, the increase in mass is likely to result from the incorporation of another species rather than protons or cations.

Cobalt and nickel-cobalt hydroxides are not as studied as nickel hydroxide. The oxidation of cobalt hydroxide is considered to occur in a sequential process. It was proposed that cobalt hydroxide first undergoes dissolution in alkaline electrolytes and then diffuses to the electrode surface where it suffers de-protonation to produce the oxyhydroxide material [63]. Tarascon et al., suggested a two-step mechanism involving dissolution followed by a solid state reaction [64–66]. When cobalt is incorporated into nickel hydroxide, the oxygen overpotential is raised, there is an apparent increase in the depth of discharge, conductivity and mechanical resistance are enhanced and the alpha structure of nickel-cobalt hydroxide is stabilized [67,68].

Based on a concise literature revision, the main conclusions to consider from previous reports are: 1) Mass increases during charge in α-$Ni(OH)_2$; behaviour that, eventually,

may invert due to α to β transformation; 2) reduced contribution from cations and great contribution of OH^-; 3) Electroneutrality shall be maintained; 4) Water content in the sample changes due to expulsion during charge, insertion during discharge, being limited by volume constraints; 5) thanks to solid-state chemistry there is evidence of sodium and potassium ions in γ-$Ni_xCo_{1-x}OOH$, while none in the α structure. Thus, cations shall be intercalated during charge and de-intercalated during discharge [69]; 6) possible "break-in" process during the first cycles; 7) transfer of ions and electrons shall be simultaneous; 8) the reaction evolves in a non-stoichiometric manner with intermediate states; 9) OER may affect the entire charge-discharge reaction and is affected by the addition of cobalt; 10) two-step mechanisms may be considered for both nickel and cobalt hydroxide; 11) KOH is usually used, while neutral electrolyte is employed in the present work.

Summarizing, for the charging process, and bearing in mind these considerations, the material required nearly 20 cycles to be stabilized, as stated in the experimental section, a process that resulted in a pH of 9 and bulk pNa value of 1.5. Thus, the results evidence that "break-in" occurs during the first cycles, period during which anions initially intercalated in the interlayer space during electrodeposition are expelled, and the initial α phase is transformed into the β phase. This would result in a mass decrease after which electrochemical stabilization would be achieved.

The pNa results evidence sodium ions mobility during the reaction and indicate that they play a main role in maintaining surface electroneutrality but, have less relevant contribution in the phase transformation occurring during charge than proton ions, as expected for β nickel-cobalt hydroxide. Alkali ions are not likely to be inserted/de-intercalated during charge-discharge. However, alkali ions accumulate at the interface during charge in a greater extent for faster scan rates, which suggests a process kinetically controlled by solid-state de-intercalation of proton ions and surface charge compensation by alkali ions.

pH evolution suggests two main stages during the oxidation reaction, dominated by different processes. The first is characterised by a steady decrease of pH and may correspond to a diffusion-controlled process, in which electrolyte diffusion plays the most important role, in particular, diffusion of the most abundant species (hydroxyl ions during oxidation and protons during reduction, considering the weak basic nature of the electrolyte). That would explain the results observed by PBD [2] in which hydroxyl ions were the main contributors to the signal in the potential range before the anodic peak. This stage is followed by a drastic decrease of pH during the anodic peak. This has been related to a solid-state transport of protons as charge mechanism, as opposed to hydroxyl intercalation which was also considered.

Regarding the effect of OER, it has been observed that the process of charge is affected by this parasitic reaction if the potential range is extended beyond the main anodic peak, while no relevant variation is observed in the -0.2V to 1.0V (vs. Pt) potential range. Nonetheless, further studies shall be performed to establish the effect of OER in the self-discharge of the material. The entire process is exemplified in Fig. 3.3.5.

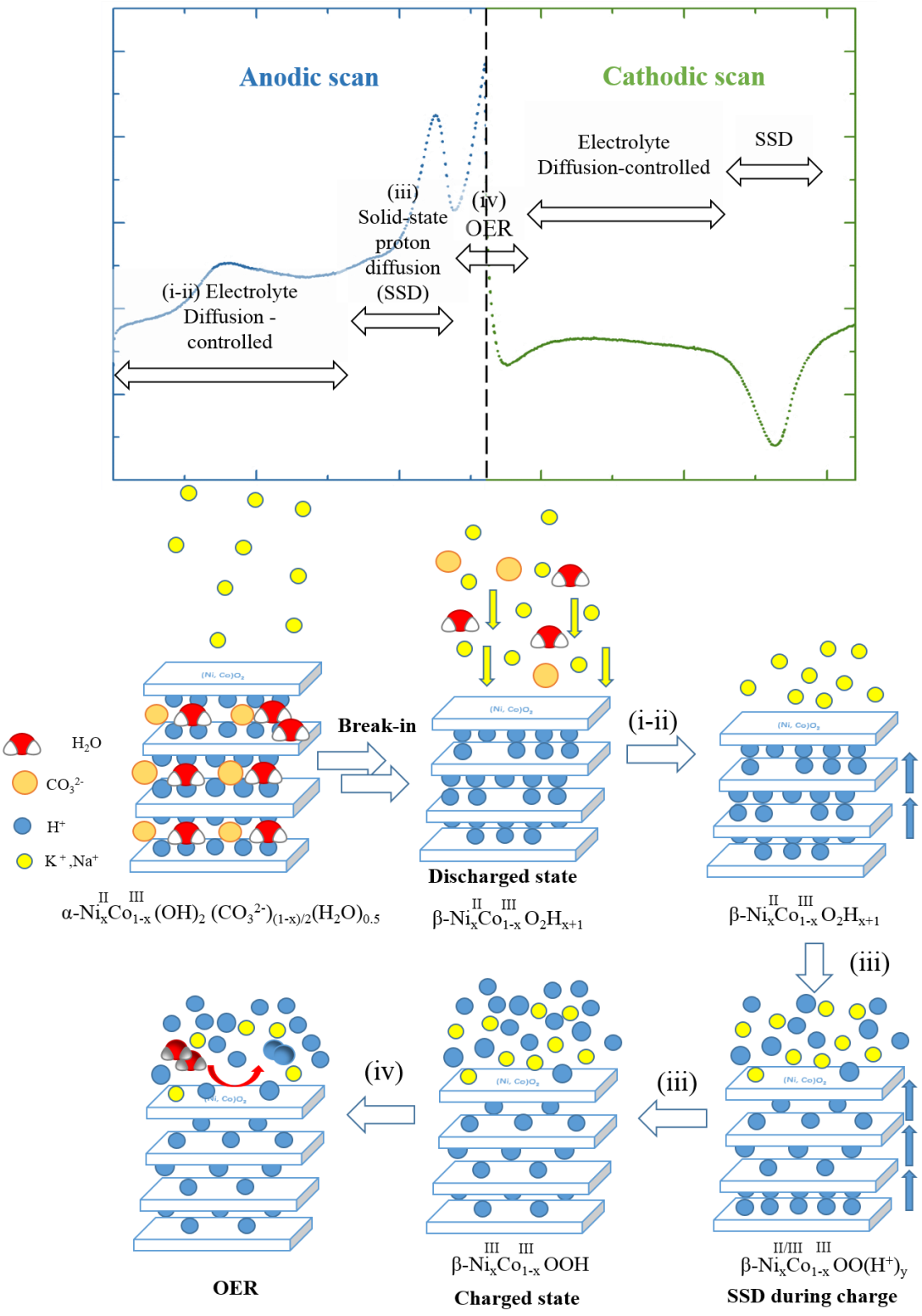

Fig. 3.3.5. Schematic representation of the processes occurring during oxidation-reduction of $Ni_xCo_{1-x}(OH)_2$ in K_2SO_4/ Na_2SO_4 0.05M.

3.3.5. Conclusions

In conclusion, the application of localized potentiometry enables the measurement of pH, dissolved oxygen and pNa at the electrode-electrolyte interface for nickel-cobalt hydroxides films used as charge storage electrodes. As Mousty et al. [21] indicated, the understanding of the ion motion in the electron transport mechanism and surface reaction is very challenging. Conventional electrochemical techniques, even when coupled with *in-situ* characterization techniques, are not always sufficient. The use of localized techniques has enabled to obtain more information on the charge-discharge reaction, which has been intensively discussed for many years. These techniques are applied, for the first time, to understand the energy storage mechanism in nickel-cobalt hydroxides and may be extremely useful, in combination with other tools, to elucidate materials' reactivity, oxidation mechanism of LDH materials and other energy storage materials, especially in those involving intercalation. The participation of alkali ions in surface charge neutralization and the appearance of OER close to anodic peak potential have been confirmed, although further studies regarding the oxidation and cycling behaviour, the role of cobalt in the nickel-hydroxide structure, the effect of the solvent and the self-discharge of the material shall be done by means of these techniques to achieve a more complete understanding of the oxidation-reduction reactions of nickel-cobalt hydroxide as charge storage materials.

Acknowledgments

This work has been performed in scope of International Doctoral Program in Functional Materials (IDS-FunMat, Erasmus Mundus) and funded by the European Union. We would like to express our gratitude to the Fundação para a Ciência e Tecnologia (FCT) for the funding under the contracts M-ERA.NET/0004/2014 and UID/QUI/00100/2013t. We would also like to acknowledge Tuyen Nguyen, Sonia Eugénio and Isabel Dias Nogueira for their assistance during characterization.

Chapter 3.3 references

[1] H.M. French, M.J. Henderson, A.R. Hillman, E. Vieil, Temporal resolution of ion and solvent transfers at nickel hydroxide films exposed to LiOH, Solid State Ionics. 150 (2002) 27–37. doi:10.1016/S0167-2738(02)00261-8.

[2] H.M. French, M.J. Henderson, A.R. Hillman, E. Vieil, Ion and solvent transfer discrimination at a nickel hydroxide film exposed to LiOH by combined electrochemical quartz crystal microbalance (EQCM) and probe beam deflection (PBD) techniques, J. Electroanal. Chem. 500 (2001) 192–207. doi:10.1016/S0022-0728(00)00373-9.

[3] A. Taniguchi, N. Fujioka, M. Ikoma, A. Ohta, Development of nickel / metal-hydride batteries for EVs and HEVs, J. Power Sources. 100 (2001) 117–124.

[4] G. Wang, L. Zhang, J. Zhang, A review of electrode materials for electrochemical supercapacitors., Chem. Soc. Rev. 41 (2012) 797–828. doi:10.1039/c1cs15060j.

[5] Y. Chuminjak, S. Daothong, A. Kuntarug, High-performance Electrochemical Energy Storage Electrodes Based on Nickel Oxide-coated Nickel Foam Prepared by Sparking Method, Electrochim. Acta. 238 (2017) 298–309. doi:10.1016/j.electacta.2017.03.190.

[6] P. Sirisinudomkit, P. Iamprasertkun, A. Krittayavathananon, T. Pettong, P. Dittanet, P. Kidkhunthodc, M. Sawangphruk, Hybrid energy storage of battery-type nickel hydroxide and supercapacitor-type graphene: redox additive and charge storage mechanism, Sustain. Energy Fuels. 1 (2017) 275–279. doi:10.1039/C7SE00052A.

[7] H. Chen, L. Hu, M. Chen, Y. Yan, L. Wu, Nickel-cobalt layered double hydroxide nanosheets for high-performance supercapacitor electrode materials, Adv. Funct. Mater. 24 (2014) 934–942. doi:10.1002/adfm.201301747.

[8] X. Cai, X. Shen, L. Ma, Z. Ji, C. Xu, A. Yuan, Solvothermal synthesis of NiCo-layered double hydroxide nanosheets decorated on RGO sheets for high performance supercapacitor, Chem. Eng. J. 268 (2015) 251–259. doi:10.1016/j.cej.2015.01.072.

[9] H. Chen, L. Hu, Y. Yan, R. Che, M. Chen, L. Wu, One-Step Fabrication of Ultrathin Porous Nickel Hydroxide-Manganese Dioxide Hybrid Nanosheets for Supercapacitor Electrodes with Excellent Capacitive Performance., Adv. Energy Mater. 3 (2013) 1636–1646. doi:10.1002/aenm.201300580.

[10] L.G. Beka, X. Li, W. Liu, Nickel Cobalt Sulfide core/shell structure on 3D Graphene for supercapacitor application, Sci. Rep. 7 (2017) 1–11. doi:10.1038/s41598-017-02309-8.

[11] A. Adán-más, R.G. Duarte, T.M. Silva, L. Guerlou-demourgues, M. Fátima, G. Montemor, Enhancement of the Ni-Co hydroxide response as Energy Storage Material by Electrochemically Reduced Graphene Oxide, Electrochim. Acta. 240 (2017) 323–340. doi:10.1016/j.electacta.2017.04.070.

[12] C. Delmas, C. Faure, Y. Borthomieu, The effect of cobalt on the chemical and electrochemical behaviour of the nickel hydroxide electrode, Mater. Sci. Eng. B. 13 (1992) 89–96. doi:10.1016/0921-5107(92)90147-2.

[13] R.D. Armstrong, E.A. Charles, Some Aspects of the A.C. Impedance Behaviour of Nickel Hydroxide and Nickel/Cobalt Hydroxide Electrodes in Alkaline

Solution, J. Power Sources. 27 (1989) 15–21.

[14] H. Bode, J. Witte, K. Dehmelt, Zur Kenntnis der Nickelhydroxidelektrode - I. Über das Nickel (II)-Hydroxidhydrat, Electrochim. Acta. 11 (1966) 1079–1087.

[15] M. Wehrens-Dijksma, P.H.L. Notten, Electrochemical Quartz Microbalance characterization of Ni(OH)2-based thin film electrodes, Electrochim. Acta. 51 (2006) 3609–3621. doi:10.1016/j.electacta.2005.10.022.

[16] P. Bernard, C. Gabrielli, M. Keddam, H. Takenouti, AC quartz crystal microbalance applied to the studies of the nickel hydroxide behaviour in alkaline solutions, Electrochim. Acta. 36 (1991) 743–746.

[17] G.T. Cheek, W.E. O'Grady, Redox behavior of the nickel oxide electrode system: quartz crystal microbalance studies, J. Electroanal. Chem. 421 (1997) 173–177. doi:10.1016/S0022-0728(96)04821-8.

[18] Y. Mo, E. Hwang, D.A. Scherson, In Situ Quarlz Crystal Microbalance Studies of Nickel Hydrous Oxide Films in Alkaline Electrolytes, J. Electrochem. Soc. 143 (1996) 5–11.

[19] S.I. Cordoba-Torresi, A. A. Hugot-Le Gaff, S. Joiret, Electrochromic Behavior of Nickel Oxide Electrodes II . Identification of the Bleached State by Raman Spectroscopy and Nuclear Reactions, J. Electrochem. Soc. 138 (1991) 1554–1559.

[20] G. Feuillade, R. Jacoud, Transferts ioniques durant l'oxydation anodique d'un hydroxyde de nickel, Electrochim. Acta. 14 (1969) 1297–1311. doi:10.1016/0013-4686(69)87023-4.

[21] C. Taviot-Guého, P. Vialat, F. Leroux, F. Razzaghi, H. Perrot, O. Sel, N.D. Jensen, U.G. Nielsen, S. Peulon, E. Elkaim, C. Mousty, Dynamic Characterization of Inter- and Intralamellar Domains of Cobalt-Based Layered Double Hydroxides upon Electrochemical Oxidation, Chem. Mater. 28 (2016) 7793–7806. doi:10.1021/acs.chemmater.6b03061.

[22] V. Srinivasan, B.C. Cornilsen, J.W. Weidner, A nonstoichiometric structural model to characterize changes in the nickel hydroxide electrode during cycling, J. Solid State Electrochem. 9 (2005) 61–76. doi:10.1007/s10008-004-0525-x.

[23] V. Srinivasan, J.W. Weidner, R.E. White, Mathematical models of the nickel hydroxide active material, J. Solid State Electrochem. 4 (2000) 367–382. doi:10.1007/s100080000107.

[24] P.L. Bourgault, B.E. Conway, The Electrochemical Behavior of the Nickel Oxide Electrode: Part II. Quasi-Equilibrium Behavior, Can. J. Chem. 38 (1960) 1557–1575. doi:10.1139/v60-216.

[25] G.A. Snook, N.W. Duffy, A.G. Pandolfo, Detection of Oxygen Evolution from Nickel Hydroxide Electrodes Using Scanning Electrochemical Microscopy, J. Electrochem. Soc. 155 (2008) A262. doi:10.1149/1.2830837.

[26] K.P. Ta, Mass Transfer and Kinetic Phenomena at the Nickel Hydroxide Electrode, J. Electrochem. Soc. 145 (1998) 3860. doi:10.1149/1.1838886.

[27] K.P. Ta, Proton Intercalation Hysteresis in Charging and Discharging Nickel Hydroxide Electrodes, J. Electrochem. Soc. 146 (1999) 2769. doi:10.1149/1.1392007.

[28] K.-W. Nam, K.-B. Kim, A Study of the Preparation of NiOx Electrode via Electrochemical Route for Supercapacitor Applications and Their Charge Storage Mechanism, J. Electrochem. Soc. 149 (2002) A346. doi:10.1149/1.1449951.

[29] W. O'Grady, K. Pandya, K. Swider, D. Corrigan, In Situ X-Ray Absorption Near-Edge Structure Evidence for Quadrivalent Nickel in Nickel Battery Electrodes, J. Electrochem. Soc. 143 (1996) 1613. doi:10.1149/1.1836687.

[30] J. Desilvestro, D.A. Corrigan, M.J. Weaver, Characterization of Redox States of Nickel Hydroxide Film Electrodes by In Situ Surface Raman Spectroscopy, J. Electrochem. Soc. 135 (1988) 885–892.

[31] R. Kostecki, F. McLarnon, Electrochemical and In Situ Raman Spectroscopic Characterization of Nickel Hydroxide Electrodes, J. Electrochem. Soc. 144 (1997) 485–493. doi:10.1149/1.1837437.

[32] D.A. Corrigan, S.L. Knight, Electrochemical and Spectroscopic Evidence on the Participation of Quadrivalent Nickel in the Nickel Hydroxide Redox Reaction, J. Electrochem. Soc. 136 (1989) 613. doi:10.1149/1.2096697.

[33] Y. Zhang, X. Cao, H. Yuan, W. Zhang, Z. Zhou, Oxygen evolution reaction on Ni hydroxide film electrode containing various content of Co, Int. J. Hydrogen Energy. 24 (1999) 529–536. doi:10.1016/S0360-3199(98)00086-X.

[34] I.A. Newman, Ion transport in roots: Measurement of fluxes using ion-selective microelectrodes to characterize transporter function, Plant, Cell Environ. 24 (2001) 1–14. doi:10.1046/j.1365-3040.2001.00661.x.

[35] M. Marenzana, A.M. Shipley, P. Squitiero, J.G. Kunkel, A. Rubinacci, Bone as an ion exchange organ: Evidence for instantaneous cell-dependent calcium efflux from bone not due to resorption, Bone. 37 (2005) 545–554. doi:10.1016/j.bone.2005.04.036.

[36] A. Alvarez-Pampliega, M.G. Taryba, K. Van Den Bergh, J. De Strycker, S. V. Lamaka, H. Terryn, Study of local Na+ and Cl- distributions during the cut-edge corrosion of aluminum rich metal-coated steel by scanning vibrating electrode and micro-potentiometric techniques, Electrochim. Acta. 102 (2013) 319–327. doi:10.1016/j.electacta.2013.03.186.

[37] M. Taryba, S. V. Lamaka, D. Snihirova, M.G.S. Ferreira, M.F. Montemor, W.K. Wijting, S. Toews, G. Grundmeier, The combined use of scanning vibrating electrode technique and micro-potentiometry to assess the self-repair processes in defects on "smart" coatings applied to galvanized steel, Electrochim. Acta. 56 (2011) 4475–4488. doi:10.1016/j.electacta.2011.02.048.

[38] A.C. Bastos, O. V. Karavai, M.L. Zheludkevich, K.A. Yasakau, M.G.S. Ferreira, Localised measurements of pH and dissolved oxygen as complements to SVET in the investigation of corrosion at defects in coated aluminum alloy, Electroanalysis. 22 (2010) 2009–2016. doi:10.1002/elan.201000076.

[39] K. Ogle, S. Morel, D. Jacquet, Observation of Self-Healing Functions on the Cut Edge of Galvanized Steel Using SVET and pH Microscopy, J. Electrochem. Soc. 153 (2006) B1. doi:10.1149/1.2126577.

[40] J. Izquierdo, L. Nagy, Á. Varga, J.J. Santana, G. Nagy, R.M. Souto, Spatially resolved measurement of electrochemical activity and pH distributions in

corrosion processes by scanning electrochemical microscopy using antimony microelectrode tips, Electrochim. Acta. 56 (2011) 8846–8850. doi:10.1016/j.electacta.2011.07.076.

[41] M.F. Montemor, D. V. Snihirova, M.G. Taryba, S. V. Lamaka, I.A. Kartsonakis, A.C. Balaskas, G.C. Kordas, J. Tedim, A. Kuznetsova, M.L. Zheludkevich, M.G.S. Ferreira, Evaluation of self-healing ability in protective coatings modified with combinations of layered double hydroxides and cerium molibdate nanocontainers filled with corrosion inhibitors, Electrochim. Acta. 60 (2012) 31–40. doi:10.1016/j.electacta.2011.10.078.

[42] H. Ding, L.H. Hihara, Localized Corrosion Currents and pH Profile over B4C, SiC, and Al2O3 Reinforced 6092 Aluminum Composites, J. Electrochem. Soc. 152 (2005) B161–B167. doi:10.1149/1.1870873.

[43] E.A. Zdrachek, A.G. Karotkaya, V.A. Nazarov, K.A. Andronchyk, L.S. Stanishevskii, V. V. Egorov, M.G. Taryba, D. Snihirova, M. Kopylovich, S. V. Lamaka, H+-selective microelectrodes with optimized measuring range for corrosion studies, Sensors Actuators, B Chem. 207 (2015) 967–975. doi:10.1016/j.snb.2014.07.106.

[44] V.A. Nazarov, M.G. Taryba, E.A. Zdrachek, K.A. Andronchyk, V. V. Egorov, S. V. Lamaka, Sodium- and chloride-selective microelectrodes optimized for corrosion studies, J. Electroanal. Chem. 706 (2013) 13–24. doi:10.1016/j.jelechem.2013.07.034.

[45] S. V. Lamaka, R.M. Souto, M.G.S. Ferreira, In-situ visualization of local corrosion by Scanning Ion-selective electrode technique (SIET) - Chapter in Microscopy: Science, Technology, Applications and Education., FORMATEX 2010, 2010.

[46] S. V. Lamaka, M. Taryba, M.F. Montemor, H.S. Isaacs, M.G.S. Ferreira, Quasi-simultaneous measurements of ionic currents by vibrating probe and pH distribution by ion-selective microelectrode, Electrochem. Commun. 13 (2011) 20–23. doi:10.1016/j.elecom.2010.11.002.

[47] T. Nguyen, M. Boudard, M.J. Carmezim, M.F. Montemor, Layered Ni(OH)2-Co(OH)2 films prepared by electrodeposition as charge storage electrodes for hybrid supercapacitors, Sci. Rep. (2017) 1–10. doi:10.1038/srep39980.

[48] C. Delmas, Y. Borthomieu, A new route to obtain well crystallized layer double hydroxides, J. Solid State Chem. 104 (1993) 345–352. doi:10.1006/jssc.1993.1169.

[49] P. Oliva, J. Leonardi, J.F. Laurent, C. Delmas, J.J. Braconnier, M. Figlarz, F. Fievet, A. de Guibert, Review of the structure and the electrochemistry of nickel hydroxides and oxy-hydroxides, J. Power Sources. 8 (1982) 229–255. doi:10.1016/0378-7753(82)80057-8.

[50] M.C. Bernard, P. Bernard, M. Keddam, S. Senyarich, H. Takenouti, Characterisation of new nickel hydroxides during the transformation of α Ni(OH)2 to β Ni(OH)2 by ageing, Electrochim. Acta. 41 (1996) 91–93. doi:10.1016/0013-4686(95)00282-J.

[51] C.-C. Hu, K.-H. Chang, T.-Y. Hsu, The Synergistic Influences of OH- Concentration and Electrolyte Conductivity on the Redox Behavior of

Ni(OH)2/NiOOH, J. Electrochem. Soc. 155 (2008) F196. doi:10.1149/1.2945911.

[52] P.K. Nayak, N. Munichandraiah, Cobalt Hydroxide as a Capacitor Material: Tuning Its Potential Window, J. Electrochem. Soc. 155 (2008) A855. doi:10.1149/1.2977976.

[53] R. Barnard, G.T. Crickmore, J.A. Lee, F.L. Tye, The cause of residual capacity in nickel oxyhydroxide electrodes, J. Appl. Electrochem. 10 (1980) 61–70. doi:10.1007/BF00937339.

[54] J.W. Lee, J.N. Han, M. Seo, S. Il Pyun, Transport of alkaline cation and neutral species through the α-Ni(OH)2/γ-NiOOH film electrode, J. Solid State Electrochem. 5 (2001) 459–465. doi:10.1007/s100080100198.

[55] R. Etchenique, E.J. Calvo, Electrochemical Quartz Crystal Microbalance Gravimetric and Viscoelastic Studies of Nickel Hydroxide Battery Electrodes, J. Electrochem. Soc. 148 (2001) A361. doi:10.1149/1.1357170.

[56] S. Il Pyun, K.H. Kim, J.N. Han, Analysis of stresses generated during hydrogen extraction from and injection into Ni(OH)2/NiOOH film electrode, J. Power Sources. 91 (2000) 92–98. doi:10.1016/S0378-7753(00)00464-X.

[57] P.J. Tsai, S.L.I. Chan, Nickel-based batteries: materials and chemistry, Woodhead Publishing Limited, 2013. doi:10.1533/9780857097378.3.309.

[58] S. Motupally, Proton Diffusion in Nickel Hydroxide Films, J. Electrochem. Soc. 142 (1995) 1401. doi:10.1149/1.2048589.

[59] U. Schröder, K.B. Oldham, J.C. Myland, P.J. Mahon, F. Scholz, Modelling of solid state voltammetry of immobilized microcrystals assuming an initiation of the electrochemical reaction at a three-phase junction, J. Solid State Electrochem. 4 (2000) 314–324. doi:10.1007/s100080000130.

[60] Min-Seuk Kim and Kwang-Bum Kim, A Study of the Electrochemical Redox Behavior of Electrochemically Precipitated Nickel Hydroxides Using Electrochemical Quartz Crystal Microbalance, J. Electrochem. Soc. 144 (1997) 1537–1543.

[61] M. Gonsalves, A. Robert Hillman, Effect of time scale on redox-driven ion and solvent transfers at nickel hydroxide films in aqueous lithium hydroxide solutions, J. Electroanal. Chem. 454 (1998) 183–202. doi:10.1016/S0022-0728(98)00262-9.

[62] M. Aia, Structure and Stoichiometry of Nickel Hydroxides in Sintered Nickel Positive Electrodes, J. Electrochem. Soc. 114 (1967) 418–423. doi:10.1149/1.2426619.

[63] P. Elumalai, H.N. Vasan, N. Munichandraiah, Electrochemical studies of cobalt hydroxide - an additive for nickel electrodes, J. Power Sources. 93 (2001) 201–208. doi:10.1016/S0378-7753(00)00572-3.

[64] P. Benson, G.W.D. Briggs, W.F.K. Wynne-Jones, The cobalt hydroxide electrode—II. Electrochemical behaviour, Electrochim. Acta. 9 (1964) 281–288. doi:http://dx.doi.org/10.1016/0013-4686(64)80017-7.

[65] V. Pralong, A. Delahaye-Vidal, B. Beaudoin, B. Gérand, J.-M. Tarascon, Oxidation mechanism of cobalt hydroxide to cobalt oxyhydroxide, J. Mater.

Chem. 9 (1999) 955–960. doi:10.1039/a807689h.

[66] V. Pralong, A. Delahaye-Vidal, B. Beaudoin, J.-B. Leriche, J.-M. Tarascon, Electrochemical Behavior of Cobalt Hydroxide Used as Additive in the Nickel Hydroxide Electrode, J. Electrochem. Soc. 147 (2000) 1306. doi:10.1149/1.1393355.

[67] B.C. Cornilsen, X. Shan, P.L. Loyselle, Structural comparison of nickel electrodes and precursor phases, J. Power Sources. 29 (1990) 453–466. doi:10.1016/0378-7753(90)85018-8.

[68] R.D. Armstrong, G.W.D. Briggs, E.A. Charles, Some effects of the addition of cobalt to the nickel hydroxide electrode, J. Appl. Ele. 18 (1988) 215–219.

[69] C. Faure, C. Delmas, P. Willmann, Preparation and characterization of cobalt-substituted α-nickel hydroxide stable in KOH medium Part II. α-Hydroxide with a turbostratic structure, J. Power Sources. 35 (1991) 263–277. doi:http://dx.doi.org/10.1016/0378-7753(91)80111-A.

3.4 Reduced graphene oxide modified Nickel-Cobalt oxide performance and degradation for energy storage applications.

Alberto Adán-Más[a,b,*], T. M. Silva[a,c], L. Guerlou-Demourgues[b,d], Lydie Bourgeois[e,f], M. F. Montemor[a,*]

[a] Centro de Química Estrutural-CQE, DEQ, Instituto Superior Técnico, Universidade de Lisboa, 1049-001, Lisboa, Portugal

[b] CNRS, University of Bordeaux, Bordeaux INP, ICMCB UPR 9048, 33600 Pessac, France

[c] ADEM, GI-MOSM, ISEL-Instituto Superior de Engenharia de Lisboa, Instituto Politécnico de Lisboa, Lisboa, Portugal

[d]RS2E, Réseau Français sur le Stockage Electrochimique de l'Energie, FR CNRS 3459, France.

[e]Université de Bordeaux, ISM, Groupe de Spectroscopie Moléculaire, F-33405, Talence, France.

[f]Bordeaux INP, ISM, CNRS UMR 5255, F-33405, Talence, France.

Keywords: Electrochemically reduced graphene oxide; Nickel-cobalt oxide; Energy storage; Electrode degradation; Electrochemical impedance spectroscopy

Abstract

Nickel-cobalt oxide was synthesized in combination with electrochemically reduced graphene oxide (Er-GO) by one-step electrodeposition on stainless steel followed by thermal treatment. The presence of reduced graphene oxide led to enhanced electrochemical response, with a capacity increase from 113 $mA \cdot h \cdot g^{-1}$ to 180 $mA \cdot h \cdot g^{-1}$, and to increased faradaic efficiency and rate capability. Compared to Ni-Co oxide, the addition of reduced graphene oxide increased capacity retention from 58% to 83% after 5000 cycles. The material fade during cycling was studied by means of electrochemical impedance spectroscopy, electron diffraction spectroscopy and scanning electron microscopy. As a result, different degradation mechanisms were identified as source of the capacity decay, such as microstructural cracking, phase transformation and parasitic reactions.

3.4.1. Introduction

High-performance, cost-effective and environmentally-friendly electrode materials play a pivotal role in the development of more effective electrochemical energy storage solutions. Electrode materials are classified in different groups according to their electrochemical response, namely: battery-like electrodes, capacitive electrodes and electrodes with an intermediate response (pseudocapacitive, supercapattery, etc.) [1–3].

Many materials are being studied as potential candidates for the next-generation of electrochemical energy storage devices. For instance, for supercapacitor/pseudocapacitor applications, electrodes can be composed of materials as different in nature as carbon-based materials and manganese oxides [4,5]. An alternative is to produce composites consisting of materials that have complementary properties. This is the case of carbon-based materials mixed with polymers and single or mixed transition metal oxides/hydroxides [6–10].

Mixed metal oxides and hydroxides are commonly studied as feasible electrode materials. Examples of that are $Ni_xMn_{1-x}O_y$, $MnCo_2O_4$, Zn_2SnO_4 or $CuFe_2O_4$ amongst many others[11–15]. Of particular interest are nickel-cobalt oxides due to their relative low cost and toxicity, strong redox activity and stable electrochemical response [16]. For instance, one of the most interesting properties of $NiCo_2O_4$ is low proton/cation diffusion resistance and easy electrolyte penetration [17]. Thus, this material is often selected as electrode for charge storage applications.

Several approaches have been used to synthesize nickel-cobalt oxides, such as liquid-phase co-precipitation, sol-gel routes or microwave-assisted synthesis [18–21]. Among all possible techniques, electrodeposition is considered as a flexible and cost-effective route to produce this material. This route enables the tailoring of electrode properties, by adjusting the deposition parameters to create distinct film morphologies, with different composition and porosity, and to achieve optimal electrochemical response. For that reason, electrodeposition is a promising technique for the scale up of such materials [22]. Besides, since no binders are required, which would decrease the overall electrochemical response, the electron transport to the substrate is facilitated. Moreover, resistances are generally low since most of the active material can be easily exposed to the electrolyte [23]. Nickel-cobalt oxides can be obtained by direct electrodeposition of the parent hydroxide followed by thermal treatment at 300^{o}C for 2 hours [23–25].

To further improve the electrochemical response of nickel-cobalt compounds, its combination with carbon-based materials has been proposed. Several different composites have been studied such as $NiCo_2O_4$ with flexible carbon fabric [26], graphite oxide [27], carbon nanotubes [28] or activated carbon [29]. More recently, graphene and its derivatives have attracted attention for fabricating composites with metal oxides. Due to their attractive properties, *graphenes* have been combined with transition metal oxides and used in different applications, such as drug delivery, catalysis or sensors [30]. Energy storage applications can also greatly benefit from the synergistic combination of the two materials by taking advantage of the large surface area and good conductivity of graphene derivatives. Recent work reports the synthesis of nickel-cobalt oxides and graphene composites by several techniques such as hydrothermal and solvothermal routes [30,31], self-assembly of exfoliated nanosheets with posterior thermal treatment [32], chemical vapour deposition and thermal treatment [33], microwave-assisted synthesis [34] or electrochemical deposition [35]. In some cases, graphene derivatives were used as substrate in the electrodeposition process. For example, Lee et al. prepared a graphene foam by chemical vapour deposition that was covered with double metal

oxides by electrodeposition [36]. Shim et al. decorated a nickel foam by electrodepositing GO and then proceeded to the two-step oxide electrodeposition process followed by thermal reduction [37].

In the present work, a composite containing reduced graphene oxide and mixed cobalt-nickel oxide was prepared, by means of a one-step electrodeposition followed by thermal treatment. The results have shown that presence of reduced graphene oxide (Er-GO)/nickel-cobalt oxide induced relevant changes on the electrochemical activity of the mixed metal oxide. Additionally, the degradation of the composite was studied by means of electrochemical impedance spectroscopy, electron diffraction spectroscopy, cyclic voltammetry and scanning electron microscopy. These measurements revealed important insights to understand the capacity fade that the material suffers in long term use. To the best of the author's knowledge, this is the first time that an in-depth study of the degradation of electrochemically reduced graphene oxide in combination with nickel-cobalt oxide by means of electrochemical impedance spectroscopy together with its physico-chemical characterization after cycling is discussed.

3.4.2. Experimental

3.4.2.1. Materials

Stainless steel, AISI 304 (Goodfellow) 0.914mm thick, was used as current collector. To ensure homogeneous electrodeposition and absence of contaminants, steel was first polished with emery paper to a rough finish, then cleaned with water and acetone and, finally, air-dried. $Ni(NO_3)_2 \cdot 6H_2O$ and $Co(NO_3)_2 \cdot 6H_2O$ (pro-analysis grade) were obtained from Sigma-Aldrich. A commercial graphene oxide (GO) aqueous solution from Graphenea Tech. Co, with a concentration of $4 g \cdot L^{-1}$ was used. Finally, KOH 1M was used as testing electrolyte. For that purpose, potassium hydroxide purchased from Sigma-Aldrich was used.

3.4.2.2. Synthesis of electrodeposited $Ni_xCo_{1-x}O_y$ and $Ni_xCo_{1-x}O_y$/Er-GO composites on stainless steel.

The synthesis of the nickel-cobalt oxide and its composite with electrochemically reduced graphene oxide (Er-GO) follows a simple two-step process of electrodeposition followed by thermal treatment. Typically, a 50 mL aqueous solution with a concentration of $2 g \cdot L^{-1}$ of nickel hexahydrate nitrate and $1 g \cdot L^{-1}$ of hexahydrate cobalt nitrate was prepared as electrodeposition electrolyte. For the composite including electrochemically reduced graphene oxide, water was substituted as solvent by a suspension of GO commercial solution diluted to $1 g \cdot L^{-1}$. To ensure good dispersion and layer separation of the aqueous suspension of graphene oxide, it was ultrasonicated for 30 minutes prior to dissolution of the metal nitrates.

Electrodeposition was conducted in a three-electrode electrochemical cell by means of an Interface IFC1000-07087 Potentiostat (Gamry Instruments) in a limited circular area of 1.6 cm^2. To simplify, the synthesized materials will be designated throughout the paper as NCOx (from *n*ickel-*c*obalt *ox*ide) and NCOx/Er-GO.

A platinum foil of 2.5x2.5 cm^2 was used as counter electrode and saturated calomel electrode (SCE) as reference electrode. The pulsed potentiostatic electrodeposition was carried out by means of two cathodic potentials, -0.9V and -1.2V, applied in a 10 second pulse for 40 cycles. After electrodeposition, the electrodes were washed with distilled water and dried at room temperature for 24-48h. Finally, thermal treatment was performed by heating the composite materials at 300ºC for 3 hours in normal

atmosphere, as it is reported in literature that it is sufficient for the complete transformation of hydroxides to oxides and shows and optimal electrochemical response[38,39].

It is worth mentioning that the mass of the samples always varied between 0.15 and 0.2 mg, which was determined by means of a micro-balance Sartorius MC5-0CE with an accuracy of 0.01mg.

3.4.2.3. Electrochemical study of $Ni_xCo_{1-x}O_y$ and $Ni_xCo_{1-x}O_y$/Er-GO composites.

All tests were performed in a three-electrode electrochemical cell with KOH 1M as electrolyte using the same electrochemical equipment as for electrodeposition. Cyclic voltammetry, galvanostatic charge-discharge (GCD), electrochemical impedance spectroscopy (EIS) and capacity retention with GCD cycling were used to study the electrochemical response of the materials. Cyclic voltammetry was performed in the potential range from -0.2V to 0.7V vs. SCE at different scan rates (10-500) $mV \cdot s^{-1}$. GCD was carried out at different current values from 1 to 10 $A \cdot g^{-1}$ in the 0.0V to 0.45V potential range. EIS was carried out at two different potentials, corresponding to two different charge states of the material, this is, discharged at -0.2V and charged at 0.45V. First, a conditioning pre-step was done by applying a voltage of interest for 1000s. Then, EIS was measured by applying a sinusoidal perturbation with 10mV of amplitude (RMS) in the frequency range 0.01 – 10^4 Hz. Finally, capacity retention testing was performed for the nickel-cobalt oxide material by charging and discharging the material 5000 times at a current density of 8 $A \cdot g^{-1}$.

3.4.2.4. Physico-chemical characterization

Surface morphology and chemical composition of the different materials were studied by means of scanning electron microscopy (SEM) direct imaging, energy dispersive X-ray spectroscopy (EDS), transmission electron microscopy (TEM), X-ray photoelectron spectroscopy (XPS) and Raman spectroscopy.

SEM imaging was obtained by means of an FEG-SEM JEOL JSM 7800F Prime coupled with an EDS detector (EDS SDD X-Max 80mm^2 Oxford Instruments AZtecEnergy detector, which is located at the centre of micro-characterization Raimond Castaing, Toulouse). Two detectors were used in the measurement, compositional and upper electron detector.

TEM images and EDS were obtained with a TEM JEOL 2200FS coupled with an EDX JEOL Si-Li working at 200k located at the Platform of Materials Characterization of Aquitaine (PLACAMAT). The image resolution is 0.19nm and the EDS point resolution is 1.5nm. Since the materials were attached to the conductive substrate, a portion of the thin layer had to be scratched and dispersed in ethanol on top of a carbon-coated gold grid.

Raman spectra were recorded using a Jobin Yvon Horiba Labram HR-800 micro-spectrometer with a 514.5 nm excitation wavelength (Ar^+ laser) and a power adjusted to ca. 50µW to avoid any degradation of the sample.

XPS surface analysis was obtained using a ThermoFisher Scientific K-ALPHA spectrometer with a monochromatized Al Kα source (hν = 1486.6 eV) and a 200 microns spot size. Before insertion of samples in the analysis chamber, a pressure of $3 \cdot 10^{-7}$ mbar was always reached in the load lock chamber. High-resolution photoionization spectra were acquired for the elements (C1s, Ca2p, Cl2p, Co2p, Co3p, Cr2p, Fe2p, Fe3p, N1s, Ni2p, Ni3p, O1s, and Si2p) by using a constant pass energy of 40 eV although wider

spectra in the 0 to 100 eV range were first obtained at a constant pass energy of 200 eV. Charge neutralization was applied during analysis. High resolution spectra were fitted and quantified using the AVANTAGE® software provided by ThermoFisher Scientific. Furthermore, XPS was also used to characterize the material and distinguish its surface chemical state and determine the oxidation state of nickel and cobalt. For that reason, the main elements considered were nickel, cobalt and oxygen. The spectra were corrected to obtain a carbon 1s spectral component binding energy at around 284.7 eV. Moreover, a standard Shirley background was generally used except for those cases in which relevant information was lost, in which linear background subtraction was considered.

Grazing incident X-ray diffraction (GIXD) analysis were performed, however, no meaningful signal could be obtained due to the thinness of the deposited layer and its nanostructured nature.

3.4.3. Results and Discussion

3.4.3.1. Physico-Chemical Characterization

3.4.3.1.1 Morphological Characterization

Fig. 3.4.1. shows the morphology of $Ni_xCo_{1-x}O_y$ (NCOx) and $Ni_xCo_{1-x}O_y$/Er-GO (NCOx/Er-GO) obtained by electrodeposition and thermal treatment. They are shown in two different detector modes: upper electron detector, whose signal is obtained at a very close distance from the sample, to enhance morphological details, and compositional (COMPO) mode, that collects secondary electrons and displays a different signal depending on the atomic mass of the elements present in the sample. NCOx shows a relatively porous morphology that seems to be formed by small aggregated areas of nanosheets of approximately 200-500nm. This is similar to the flake-like structure presented in previous work, but with a greater level of agglomeration [40,41]. SEM images of the parent hydroxides have been included for comparison purposes (Fig. 3.4.2). Some spike-like features are still observable although they do not present any compositional difference. Moreover, this aggregated nanosheet-like structure with no apparent order forms a densely-packed percolation network whose pores can be differentiated as darker areas at the compositional image (Fig. 3.4.1b) in accordance with literature [9,10]. This suggests that, in this case, the nanosheet-like structure is aggregated to better accommodate strain, becoming more densely packed, while conserving some of the features at a superficial level.

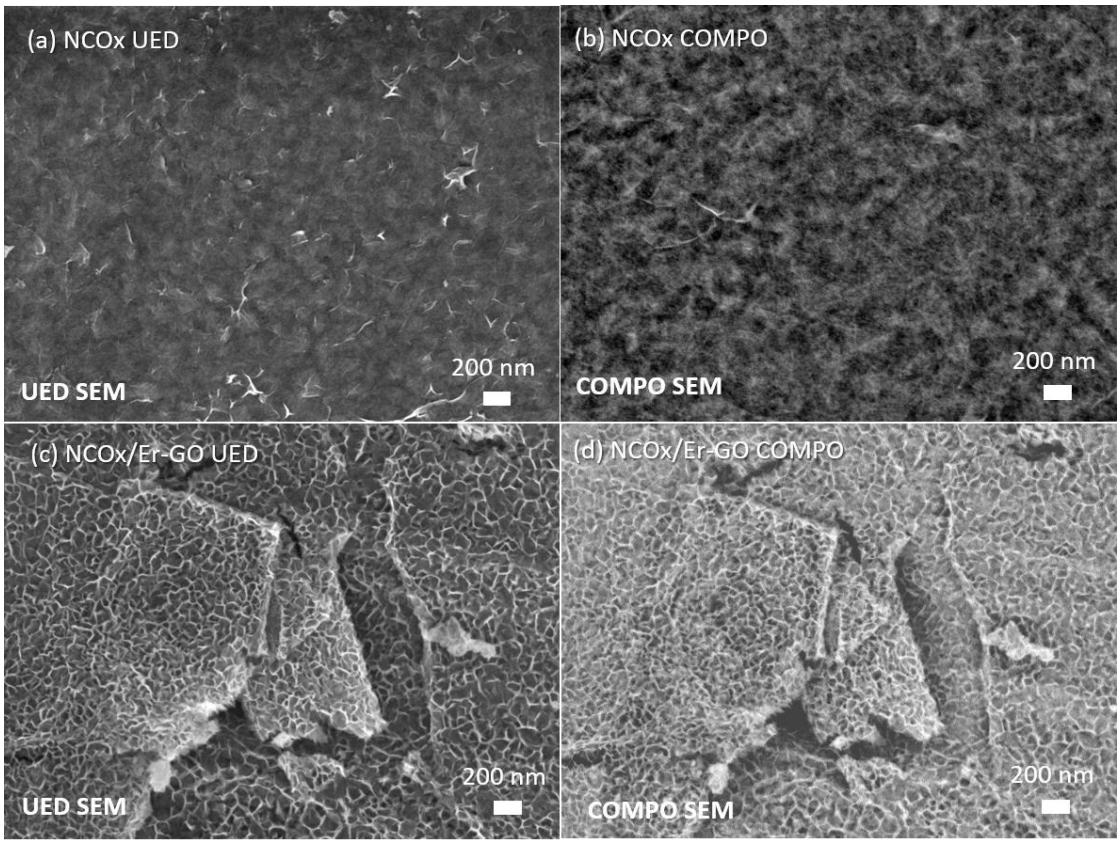

Fig.3.4.1. SEM images of **(a)** NCOx obtained with an upper-electrons detector (UED), **(b)** and a compositional detector (COMPO). **(c)** NCOx/Er-GO obtained with an UED and **(d)** a COMPO detector.

The morphology of the Er-GO containing composite is, as observed by SEM in Fig. 3.4.1, relatively different to that of the material without carbon. In this case, the said aggregation has not occurred, and the material presents the nanosheet-based structure on top of the carbonaceous material. Er-GO presents micrometric wrinkles and defects and seems to cover all the substrate. Then, on top of the carbon-based material, Ni-Co oxides can be found. This structure is similar to other reported Ni-Co oxides [42]. NCOx/Er-GO presents similar morphology to the non-thermally-treated precursor which suggests that, by dispersing the nickel and cobalt nanoflakes on top of the reduced graphene oxide wrinkles, aggregation of said flakes is avoided. In conclusion, when no electrochemically reduced graphene oxide is present, the material presents higher strain that becomes accommodated with thermal treatment by the formation of aggregates. Once Er-GO is introduced, the material remains unchanged during thermal treatment [35].

Pristine graphene has very high conductivity (>3000 $W \cdot mK^{-1}$) [43,44]. Although the properties of graphene oxide and reduced graphene oxide are not comparable to that of pristine graphene, it has been reported that reduction of graphene oxide and thermal treatment enhance the thermal conductivity of the material, in fact, it increased up to 10^6 times as reduction at low temperature (<240^{o}C) progressed [45] and it enhanced the longer the thermal treatment [46]. It is possible that the inclusion of a better thermal conductor inhibits the structural variation of the material by a homogeneous distribution of temperature in the material. Thus, thermal treatment does not have preferential areas while, in the case of NCOx, which in principle has poorer thermal conduction, the

material aggregates as the thermal distribution is inhomogeneous. However, this phenomenon is yet poorly understood and requires further understanding to corroborate this statement.

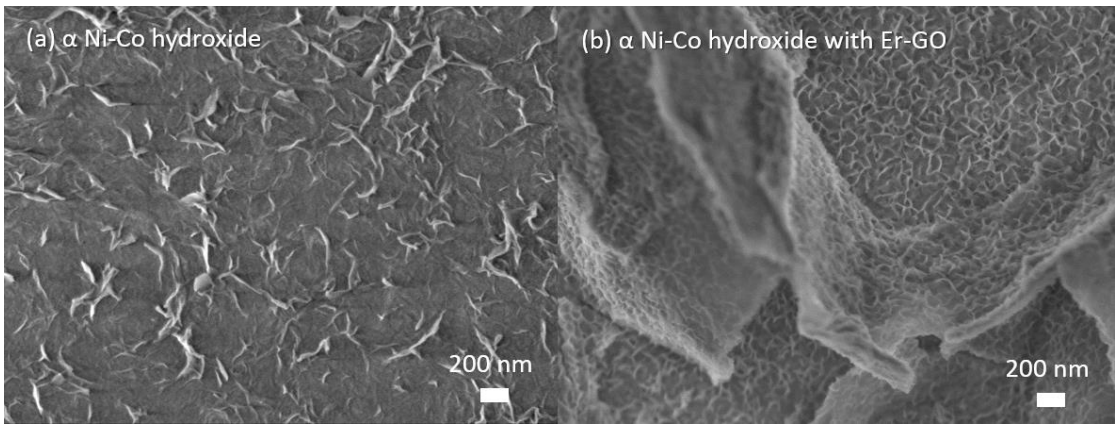

Fig. 3.4.2. Scanning electron microscopy image of **(a)** electrodeposited α Ni-Co hydroxide material and **(b)** electrodeposited α Ni-Co hydroxide material in combination with Er-GO, for the same nickel:cobalt ratio, included for comparison purposes.

The transmission electron microscopy (TEM) images are shown in Fig. 3.4.3 and it can be observed that NCOx consists of randomly oriented grains. These grains have very small coherent domains of approximately 2 to 5 nm. This morphology is also in accordance to previously reported literature [31,47]. Therefore, aggregates of 200-500nm observed by SEM consist of grains with very small coherent domains of 2-5 nm diameter.

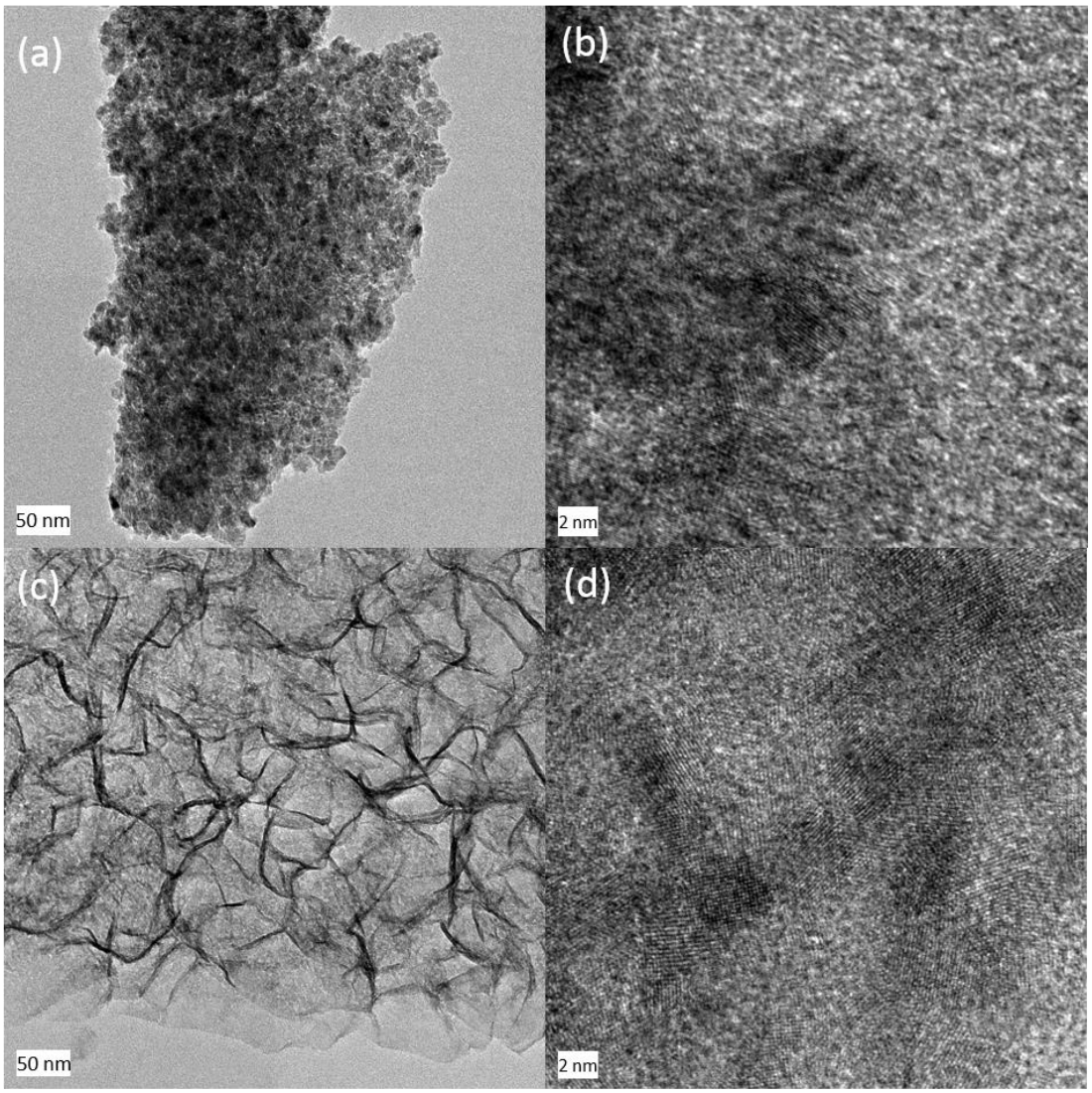

Fig. 3.4.3. Low magnification TEM images of (**a**) NCOx and (**b**) NCOx/Er-GO. HR-TEM images of (**c**) NCOx and (**d**) NCOx/Er-GO.

For the graphene-based material, the wrinkles of the carbon flakes are observed at higher magnification. Nonetheless, if a closer view to the surface morphology is taken, small features with very small coherent domains are present (see Fig. 3.4.4). An image of the FFT obtained for the high-resolution image of the composite material is also included in the supplementary material, which evidences the polycrystalline nature of the synthesized oxide. Thus, it can be deduced that the oxide material is deposited on top of the carbon flakes, in accordance with the SEM results. These small features correspond to the spike-like structures observed by SEM that can be better resolved by HRTEM.

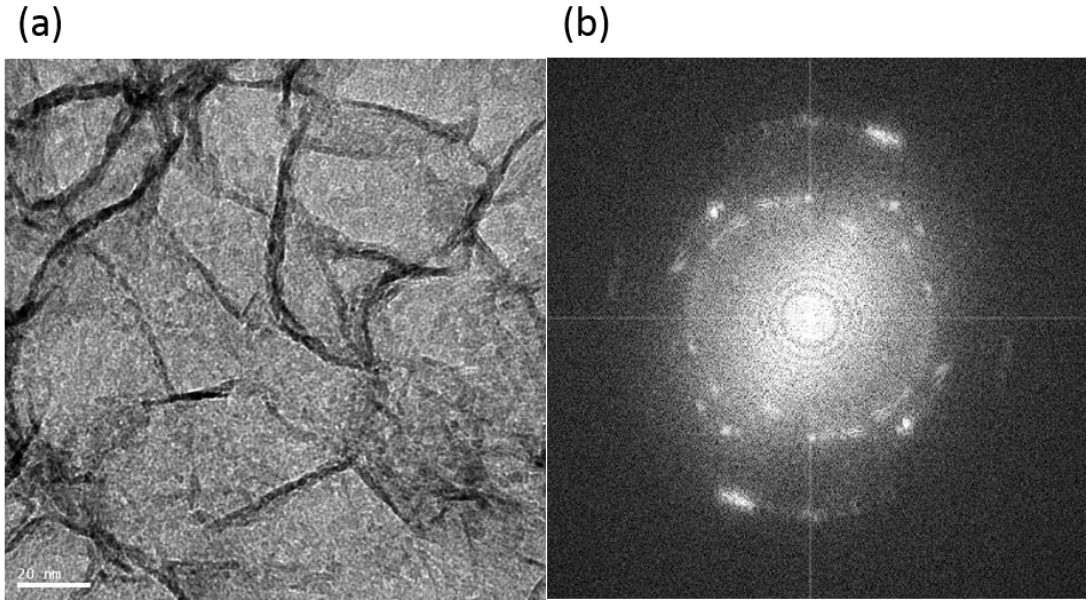

Fig. 3.4.4. Transmission electron microscopy image of **(a)** Ni-Co oxide material on top of electrochemically graphene oxide and **(b)** the corresponding FFT image of the area.

3.4.3.1.2 Chemical Characterization

EDS results, presented in Fig. 3.4.5, show the homogeneous distribution of nickel and cobalt atoms exemplifying the good distribution of both metals that integrate the oxide material. Moreover, the good coverage of the carbon flakes by nickel-cobalt oxide can also be observed for the Er-GO containing composite. If the atomic percentage ratio between nickel and cobalt is considered as a semi-quantitative evaluation for the material analysed by means of EDS, a nearly 2:1 Nickel-Cobalt ratio is found, resulting in an empiric formula of $Ni_{0.63}Co_{0.37}O$ for both the material with and without Er-GO; which is in accordance to the molar ratio used in the electrolyte for electrodeposition. A similar semi-quantitative result is obtained by means of XPS, in which the empiric formula considering the Ni/Co ratio obtained is $Ni_{0.64}Co_{0.36}O$ for NCOx and $Ni_{0.68}Co_{0.32}O$ for NCOx/Er-GO. Thus, this material can be understood as a mixed nickel-cobalt oxide. X-ray photoelectron spectroscopy was done to further elucidate the composition of the material. For that purpose, the photoionizations of Nickel 2p3, Cobalt 2p3, Oxygen 1s and Carbon 1s were investigated. Neither Iron nor Chromium were detected, which evidenced complete coverage of the substrate during the electrodeposition. XPS results are shown in Fig. 3.4.6.

(a)

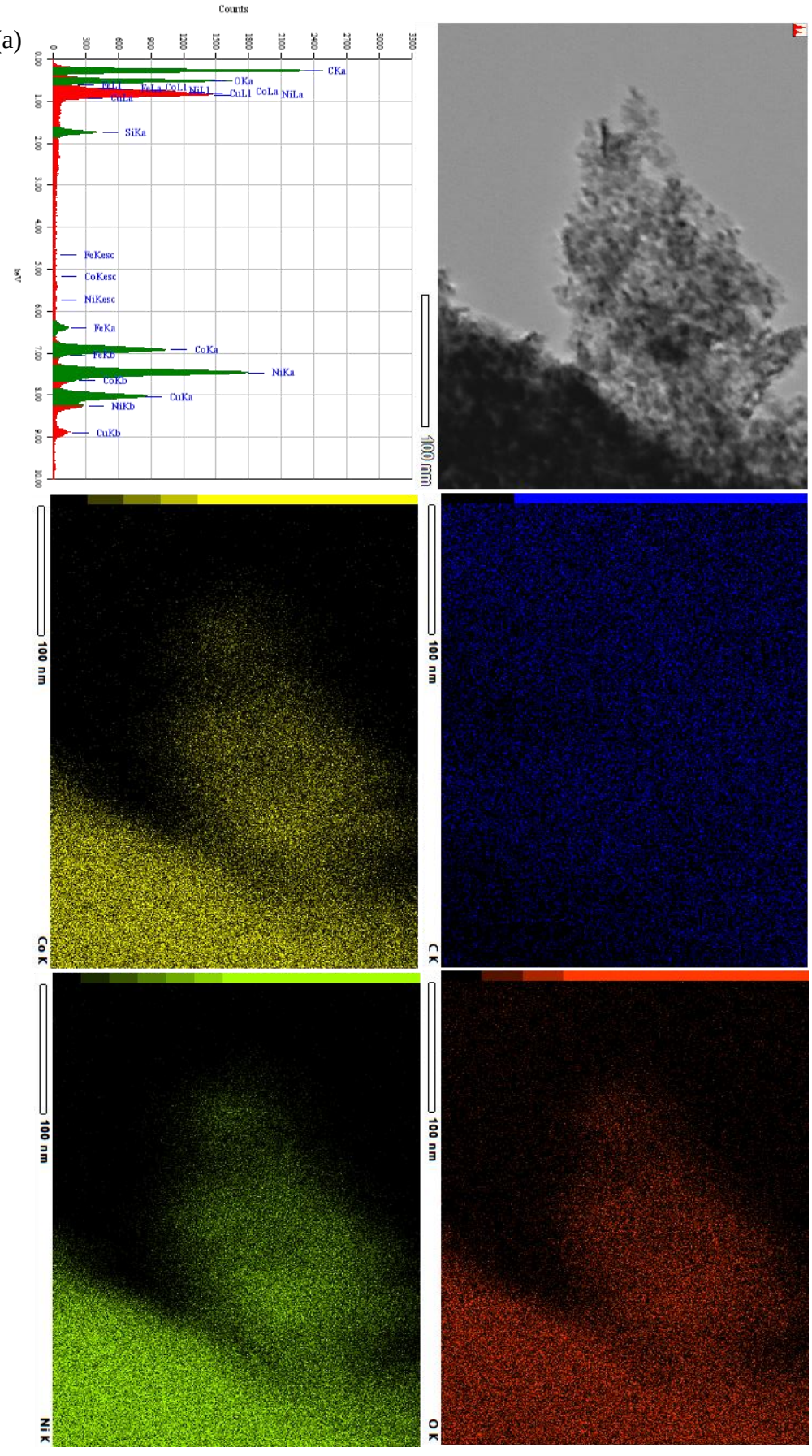
Counts
keV
CKa
OKa
CuLl
CoLa
NiLa
SiKa
FeKesc
CoKesc
NiKesc
FeKa
CoKa
NiKa
CuKa
NiKb
CuKb
100 nm
Co K
C K
Ni K
O K

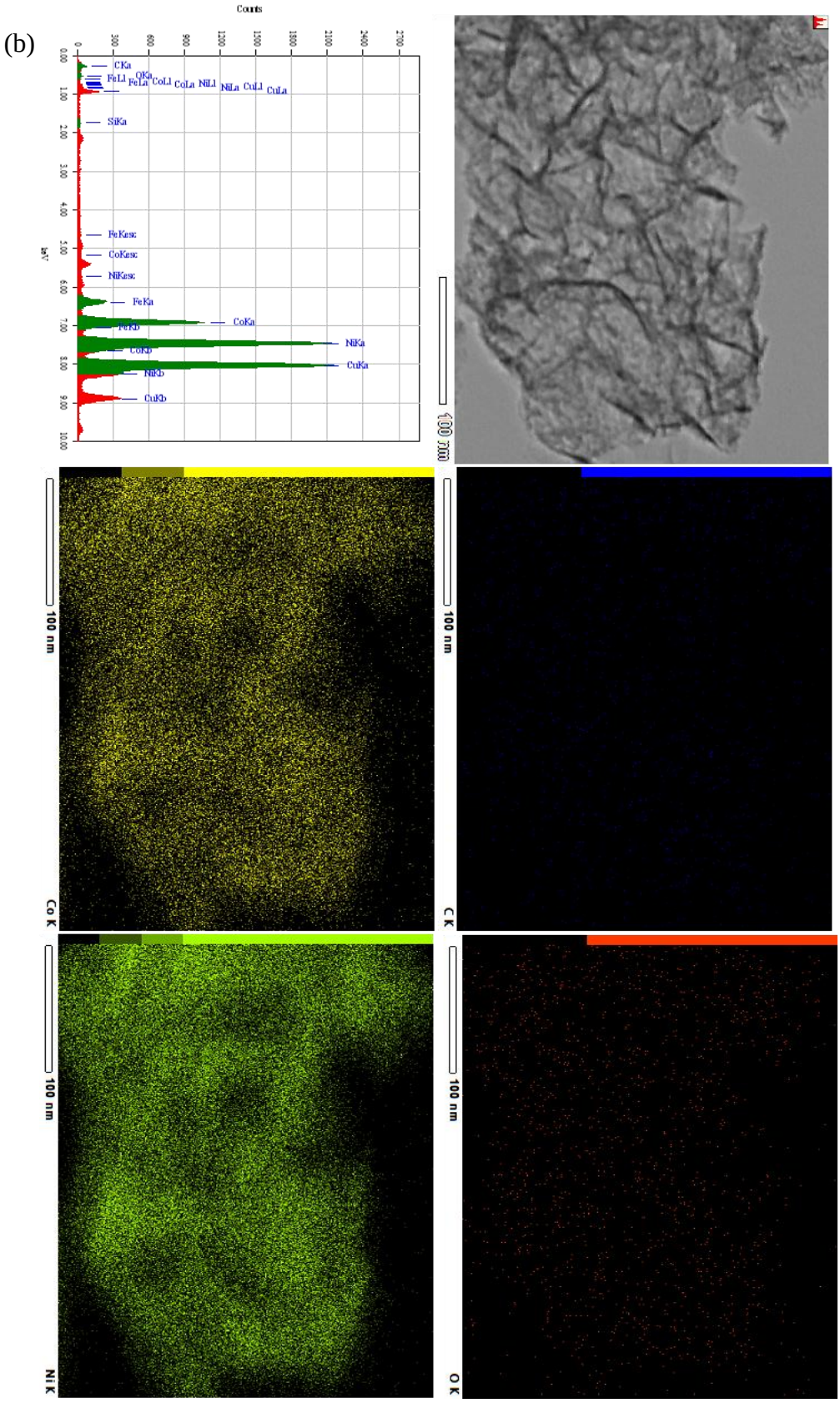

Fig. 3.4.5. Electron diffraction spectroscopy mapping for the elements Carbon (blue), Oxygen (red), Cobalt (yellow) and Nickel (green) for the composites (a) Ni-Co oxide and (b) Ni-Co oxide on top of an electrochemically reduced graphene oxide flake.

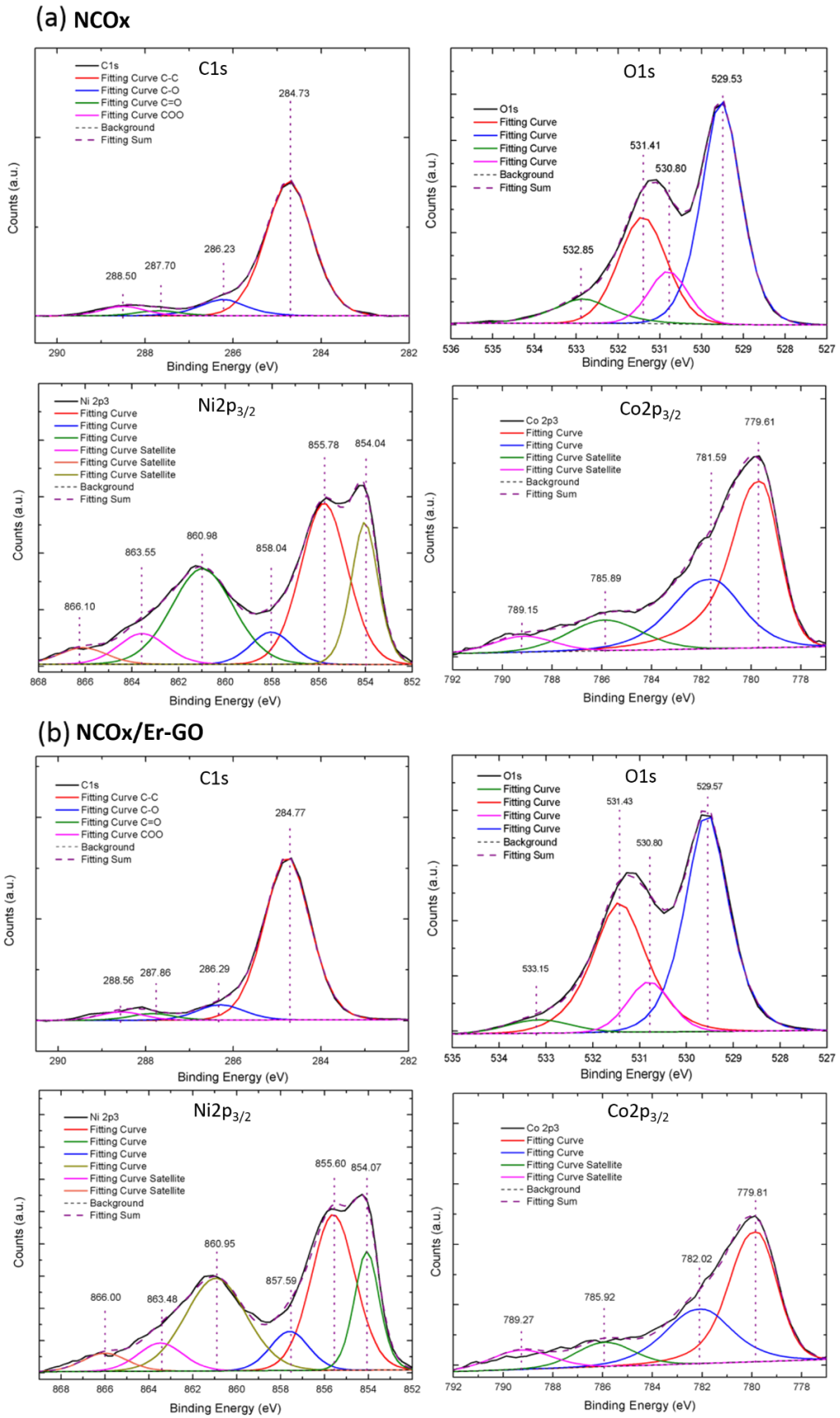

Fig. 3.4.6. X-ray photoelectron spectroscopy results for the elements Carbon 1s, Oxygen 1s, Nickel 2p3 and Cobalt 2p3 for the composites (**a**) NCOx and (**b**) NCOx/Er-GO.

Traditionally, the assignment of discrete binding energy values was done in XPS data treatment to assign different oxidation states for nickel metal and nickel hydroxides, oxides and oxyhydroxides. However, due to the splitting nature into multiplet contributions and the overlaps of the main line and satellite peaks in the most intense Ni 2p spectra, this approach has been substituted by multi-component spectral envelopes. These are done with the minimum possible number of components and their correspondent shake-up and plasmon satellites [48–50].

The main contribution to the primary peak is based on Ni^{2+} and Ni^{3+} chemical states, although their contributions cannot be perfectly resolved, even when there is a main peak as reference. Nonetheless it is observed that Ni^{3+} tends to appear at higher binding energies [50]. Also, a third contribution in the region between the main line multiplet and the related satellites is considered in the fitting and represents the combined losses at 4.3 eV, 6.0 eV and 7.4 eV due to intra- and inter-band transitions allowed by breakdown of dipole selection rules with delocalized electrons in polycrystalline samples, as described by Hagelin-Weaver et al [49,51]. In conclusion, the experimental signal has been reconstructed by fitting to six Voigt peaks that have been assigned to different electronic configurations after the creation of the 2p core-hole upon photoemission [52]. Three main peaks are used in the fitting of the main multiplet for nickel and are assigned to a cluster mode with a final configuration of cd^9L for the peak at lowest BE, d^8:cd^9L configuration from surface-sensitive components for the peak at around 855.6 eV and a cd^9:d^7 for the third component of the multiplet. Besides, three satellite/plasmon peaks are considered to contribute to the final signal. They arise from energy losses corresponding to surface plasmons and bulk plasmons, corresponding to $cd^{10}L^2$ and cd^8 cluster model final state configurations, and weaker shake-up contributions for the component at higher BE. These different configurations come from the overlap of the frozen ground state and the unscreened final state and the effect of neighbouring electrons, and associate charge transfer processes between the ligand anions and the Ni cation, coming from adjacent Ni-O clusters. Both the area and the position are considered in the fitting of nickel [50,52].

In this case, there is a major contribution from Ni (II)/Ni(III) centred at 854.0/855.7 eV and a third component corresponding to combined losses. It can be observed that the main peak becomes partially resolved, showing two decreasing maxima. This is only observed in nickel-oxide configurations. Also, three other peaks, corresponding to shake-up satellites and plasmons at 6, 9 and 12 eV higher binding energies than the main peak, are present. Given these peak positions, and the contribution of each component to the total signal (as seen in supplementary information table 3.4.1, related to XPS identification work performed by Biesinger et al. [49] and the calculations presented by Gupta and Sen [51,53]) nickel can be identified, in this case ,to be coordinated with oxygen atoms in its nickel oxide form.

Cobalt 2p3 is fitted with an asymmetric main peak and two plasmon loss peaks 3eV and 5eV above the main peak, which constitute the surface and bulk plasmons respectively [48]. The main peak, similarly to the case for nickel, is resolved in two main components, associated to different chemical species despite the significant overlap in binding energy that they have. In the de-convolution of the peak there is an intense main peak centred at approximately 779.7 eV. Given the low value for this binding energy, cobalt may be present in its oxide form instead of the oxyhydroxide or hydroxide alternatives [54]. The presence of a wide peak centred at around 781.8 eV evidences the divalent nature of the oxide. Two satellite peaks are present in the case of cobalt related configuration and are associated to either coupling between unpaired electrons

(multiplet splitting) or multiple electron excitation (shake-ups). Although the peak centred at 789.2eV would be present in all the possible configurations, Co(II) oxides are distinguished from Co(III) oxides by the absence of multi-electron excitation satellites in the latter. Given the fact that a peak is centred at 785.9 eV and that lower binding energies to what would be expected for cobalt hydroxide and its contribution to the overall signal, cobalt can be unequivocally identified to be in its oxide form [54].

In addition, four peaks are required to fit the oxygen 1s envelope. The main intense peak is centred at 529.6 eV. This peak is characteristic for both nickel and cobalt oxide and does not have a relevant contribution in isolated nickel/cobalt hydroxide [54]. Then, another three peaks, of lower intensity, are centred at 530.8 eV, 531.4 eV and 532.9 eV. The first peak at lower binding energies is associated to oxygen from hydroxyl ions. The higher binding energy peaks are ascribed to hydroxyl, carbonate ions and other oxygen ions and possible surface contamination. If the contribution to the total signal is analysed and compared to literature, as presented in table 3.4.1, results also agree with Ni-O and Co-O bonding nature. For that reason, it can be concluded that the phase present is a mixed oxide with formula $Ni_xCo_{1-x}O_y$.

Fig. 3.4.7 shows the Raman spectra obtained for the composites. Raman spectroscopy is a powerful technique extensively used in the characterization of graphene derivatives, enabling the evaluation of defects and disorders associated to its structure. As expected for NCOx/Er-GO, two main peaks are present at approximately 1368 cm^{-1} and 1594 cm^{-1}, corresponding to the D and G bands, respectively. The former is associated to local defects and disorders and is originated k point phonon breathing with A_{1g} symmetry; the latter is related to sp^2 carbon atoms E_{2g} vibrational mode [41,55]. Note that the shoulder detected around 1550 cm^{-1} is observed for some other carbon nanostructures [63,64]. The signature obtained for NCOx/Er-GO after thermal treatment is different from graphene oxide and as-synthesised reduced graphene oxide (Fig. 3.4.8) and indicates a successful reduction of the graphene derivative and an effect of thermal treatment on signal intensity on the D and G bands.

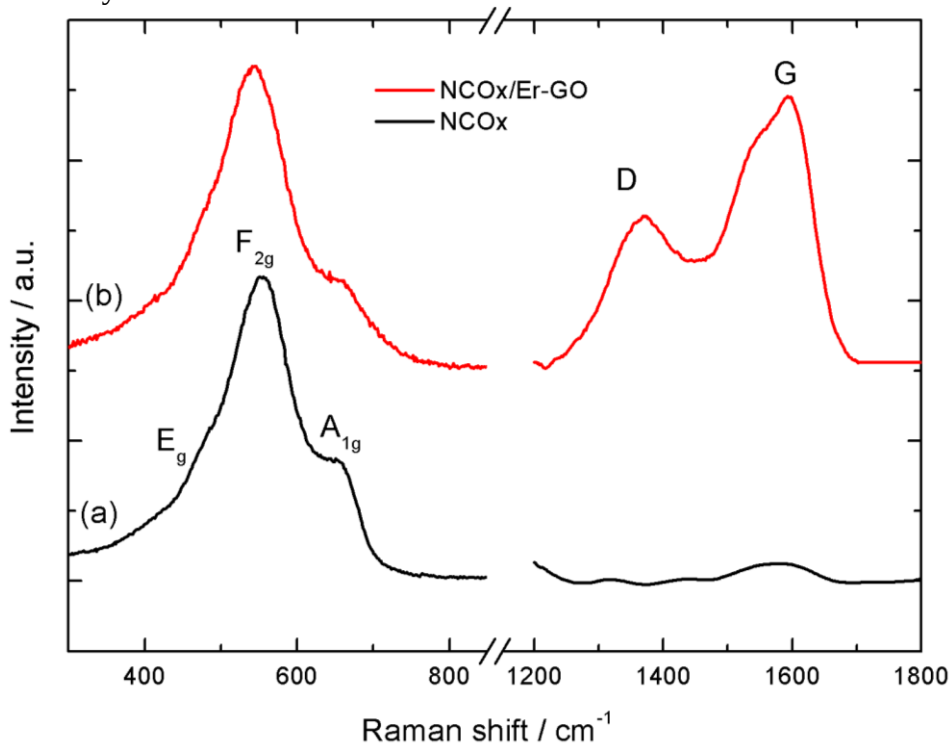

Fig. 3.4.7. Raman spectra for (**a**) NCOx and (**b**) NCOx/Er-GO.

Table 3.4.1

X-ray photoelectron spectroscopy comparison for the fitted results obtained for the nickel-cobalt oxide and the nickel-cobalt oxide combined with electrochemically reduced graphene oxide composites and the XPS data extracted from reference [48] for Oxygen 1s, Cobalt $2p_{3/2}$ and Nickel $2p_{3/2}$. The contribution, in percentage, of each peak to the total signal obtained has also been depicted together with the peak position associated to each component of the fitting spectra. Therefore, each peak of the table corresponds to a component used in the fitting of the spectra for each element, determining its binding energy and areal in percentage.

Selected O1s values									
		Peak 1 Binding energy (eV)	%	Peak 2 Binding energy (eV)	%	Peak 3 Binding energy (eV)	%	Peak 4 Binding energy (eV)	%
Reference [48]	CoO	529.8	62	531.4	34	532.9	4		
	$Co(OH)_2$	-	-	531.1	86	532.3	14		
	Co_3O_4	530.0	53	530.8	41	532.7	6		
	NiO	529.3	69	531.1	29	532.8	2		
	$Ni(OH)_2$	-	-	530.9	100	-	-		
NCOx	Oxygen 1s	529.5	51	531.4	28	532.9	8.49	530.8	11
NCOx / Er-GO	Oxygen 1s	529.6	49	531.4	36	533.2	4.14	530.8	10

Selected Co2p3 values							
		Peak 1 Binding energy (eV)	%	Peak 2 Binding energy (eV)	%	Peak 3 Binding energy (eV)	%
Reference [48]	CoO	780.0	46.6	782.1	11.0	783.1	8.0
	Co(OH)2	780.4	38.1	782.2	26.6	786.0	33.0
	Co3O4	779.6	40.5	780.9	29.1	782.2	15.2
	Co(0)	778.1	81.0	781.1	25.7	785.5	1.6
	CoOOH*	780.1	61.4	781.4	24.5	783.1	5.2
NCOx	Cobalt 2p3	779.6	51.9	781.6	29.5		
NCOx / Er-GO	Cobalt 2p3	779.8	50.4	782.0	29.6		

		Peak 4 Binding energy (eV)	%	Peak 5 Binding energy (eV)	%		
Reference [48]	CoO						
	Co(OH)2	790.4	2.4				
	Co3O4	785.2	8.1	789.5	7.2		
	Co(0)	786.5	26.1				
	CoOOH*	790.1	8.9				
NCOx	Cobalt 2p3	785.9	13.0	789.2	5.7		
NCOx / Er-GO	Cobalt 2p3	785.9	10.9	789.3	9.2		

Selected Ni2p3 values							
		Peak 1 Binding energy (eV)	**%**	**Peak 2 Binding energy (eV)**	**%**	**Peak 3 Binding energy (eV)**	**%**
Reference [48]	NiO	853.7	14.3	855.4	44.2	860.9	34.0
	$Ni(OH)_2$	854.9	7.4	855.7	45.3	857.7	3.0
	Gamma NiOOH	854.6	13.8	855.3	12.4	855.7	9.7
	Beta NiOOH 3+ portion	854.6	9.2	855.3	8.3	855.7	6.4
	Beta NiOOH 2+ portion	854.9	2.5	855.7	15.1	857.7	1.0
NCOx	Nickel $2p_3$	854.0	18.5	855.8	36.1	861.0	28.3
NCOx / Er-GO	Nickel $2p_3$	854.1	15.8	855.6	35.9	861.0	29.6
		Peak 4 Binding energy (eV)	**%**	**Peak 5 Binding energy (eV)**	**%**	**Peak 6 Binding energy (eV)**	**%**
Reference [48]	NiO	864.0	3.6	866.3	3.9		
	$Ni(OH)_2$	860.5	1.4	861.5	39.2	866.5	3.7
	Gamma NiOOH	856.5	20.1	857.8	8.7	861.0	23.3
	Beta NiOOH 3+ portion	856.5	13.8	857.8	5.8	861.0	15.6
	Beta NiOOH 2+ portion	860.5	0.5	861.5	13.1	866.5	1.2
NCOx	Nickel $2p_3$	863.6	7.0	866.1	3.8		
NCOx / Er-GO	Nickel $2p_3$	863.5	6.6	866.0	4.3		
		Peak 7 Binding energy (eV)	**%**				
Reference [48]	NiO						
	$Ni(OH)_2$						
	Gamma NiOOH	864.4	11.4				
	Beta NiOOH 3+ portion	864.4	7.6				
	Beta NiOOH 2+ portion						
NCOx	Nickel $2p_3$						
NCOx / Er-GO	Nickel $2p_3$						

Usually, the ratio between the integrated intensity of the D peak and the G peak offers information regarding the average size of the sp^2 domains and the charge transfer between carbon and other compounds [56]. Then, a higher the I_D/I_G ratio is correlated to smaller sp^2 domains. In our case, this ratio has a value of 0.62, which indicates large sp^2 domains [57]. It has been currently observed in literature that the signal of the D peak is reduced with temperature treatment, indicating either an improved quality of the graphene film [58,59] or an agglomeration of the carbon-based material that induces a recovery of its graphitic nature. This change in the I_D and I_G intensities is shown in Fig. 3.4.8. Thus, during electrodeposition, electrochemically reduced graphene oxide is produced [35] and after the thermal treatment undertaken, graphene layers are likely to improve their quality by the restoration of the Csp^2 matrix [60]. Although an interaction between the different carbon layers is also possible, due to their complete coverage with

nickel-cobalt oxide, as observed by EDS results presented in Fig. 3.4.5, re-stacking is unlikely and a restoration of the Csp^2 is considered.

In addition, there are three signals at ca. 480, 550 and 655 cm^{-1}, associated to nickel-cobalt oxide. These bands correspond to Ni-O and Co-O vibrations and can be assigned, by analogy, to the E_g, F_{2g} and A_{1g} Raman-active modes of the ideal cubic spinel $NiCo_2O_4$ [61,62]. It is worth mentioning that there is a small band shift for NCOx/Er-GO that is related to the direct charge transfer between rGO and (Ni-Co)O [56]. Only Co-O and Ni-O vibrational modes are observed, this is, no -OH signal is detected between 3000 and 4000 cm^{-1}, indicating successful de-hydroxylation of the materials. This is in accordance with previously reported literature [61,62]. Thus, Raman spectra confirm the presence of a cobalt-substituted nickel oxide phase on top of thermally treated highly reduced graphene oxide with a restored 2D lattice.

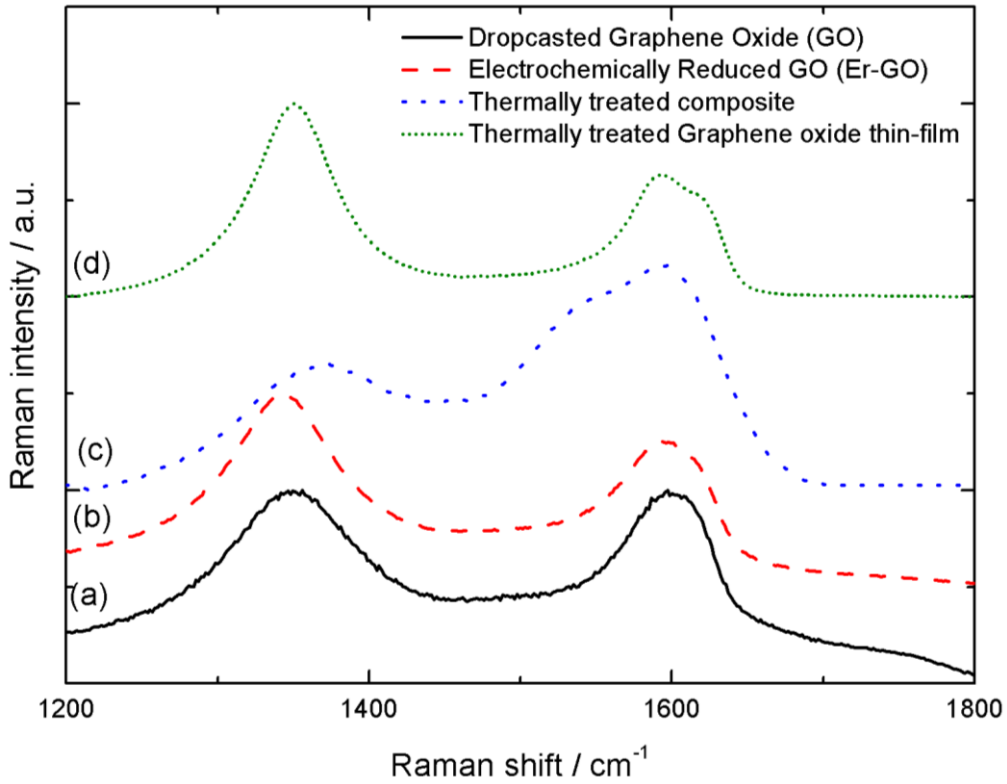

Fig. 3.4.8. Raman spectra comparison for the signal obtained for (a) dropcasted graphene oxide with no electrochemical reduction, (b) graphene oxide after electrochemical reduction, (c) graphene oxide in the composite material after electrochemical reduction and thermal treatment, (d) pure GO thin-film after thermal treatment. (a) and (b) were previously reported in Chapter 3.1 and were acquired at different excitation wavelength.

3.4.3.2. Electrochemical Characterization

Results for cyclic voltammetry obtained at 50 $mV \cdot s^{-1}$ in the -0.2 V to 0.5 V (vs. SCE) potential range and galvanostatic charge-discharge obtained at 1 $A \cdot g^{-1}$ in the 0.0 V to 0.45 V (vs. SCE) range for NCOx and NCOx/Er-GO obtained in KOH 1M are presented in Fig. 3.4.9.

As expected for a nickel-cobalt oxide-based material, the voltammogram presents a peak in the anodic wave, centred at 0.33 V and 0.30 V for the material without and with reduced graphene oxide respectively, and a counter-peak in the cathodic wave centred at 0.23V and 0.20V for NCOx and NCOx /Er-GO respectively.

The reported charge-discharge reaction for nickel oxide is [63]:

$$NiO + OH^- \leftrightarrow NiO(OH) + H_2O + e^- \quad \text{(eq. 3.4.1)}$$

Given that reaction, the charge-discharge reaction for the present material can be considered to be as exemplified in eq. 3.4.2:

$$Ni_{1-x}Co_xO_y + 2OH^- \leftrightarrow Ni_{1-x}Co_xO(OH) + H_2O + e^- \quad \text{(eq. 3.4.2)}$$

It is also worth noting that these reactions do not show the exact stoichiometry and are only intended to exemplify the oxidation state variation of nickel and cobalt during the charge-discharge process.

As far as the maximum current peak ratio ($I_{max,\ anodic}/I_{max,\ cathodic}$) is concerned, if the ratio of the intensity of the cathodic peak against the intensity of the anodic peak is calculated, it is approximately 1.4 in both cases, indicating a similar and partial irreversibility of the reaction. Again, this difference may result in the lowering of capacity efficiency with continuous charge-discharge.

Nonetheless, the most relevant feature is the increase in the total area of the voltammogram when Er-GO is introduced. This is consequence of the increase in capacity due to the synergistic response of Ni-Co oxides and Er-GO [34,35].

The cyclic voltammetry response with the scan rate is presented in Fig. 3.4.10a,c, in the scan rate range from 10 $mV \cdot s^{-1}$ to 500 $mV \cdot s^{-1}$, and the results show that both materials present very good scan rate capabilities. The two characteristic peaks are always present and the form of both the cathodic and the anodic wave is kept for a wide range of scan rates. Very high scan rates can be achieved for a nickel-cobalt oxide material by means of electrodeposition. This has been observed in other films for energy storage applications obtained by means of electrophoresis or electrodeposition [35,64], however, this is rarely seen in nickel-cobalt metal oxides where the highest reported scan rates are usually 100 $mV \cdot s^{-1}$ or lower [24,25,65,66]. This may be the result of a combination between good substrate-electrode contact and enhanced electrode-electrolyte interaction because of morphology tailoring and absence of binders.

Finally, when the scan rate is increased, a shift of the anodic peak towards more positive potentials is observed, while the cathodic counterpart is displaced towards more negative potentials. Furthermore, the current density increases with faster scan rates. This is a consequence of the polarization effects, evidencing the quasi-reversible nature of the redox processes in the system and smaller diffusion layers associated to faster redox reactions with increased scan rate [67,68].

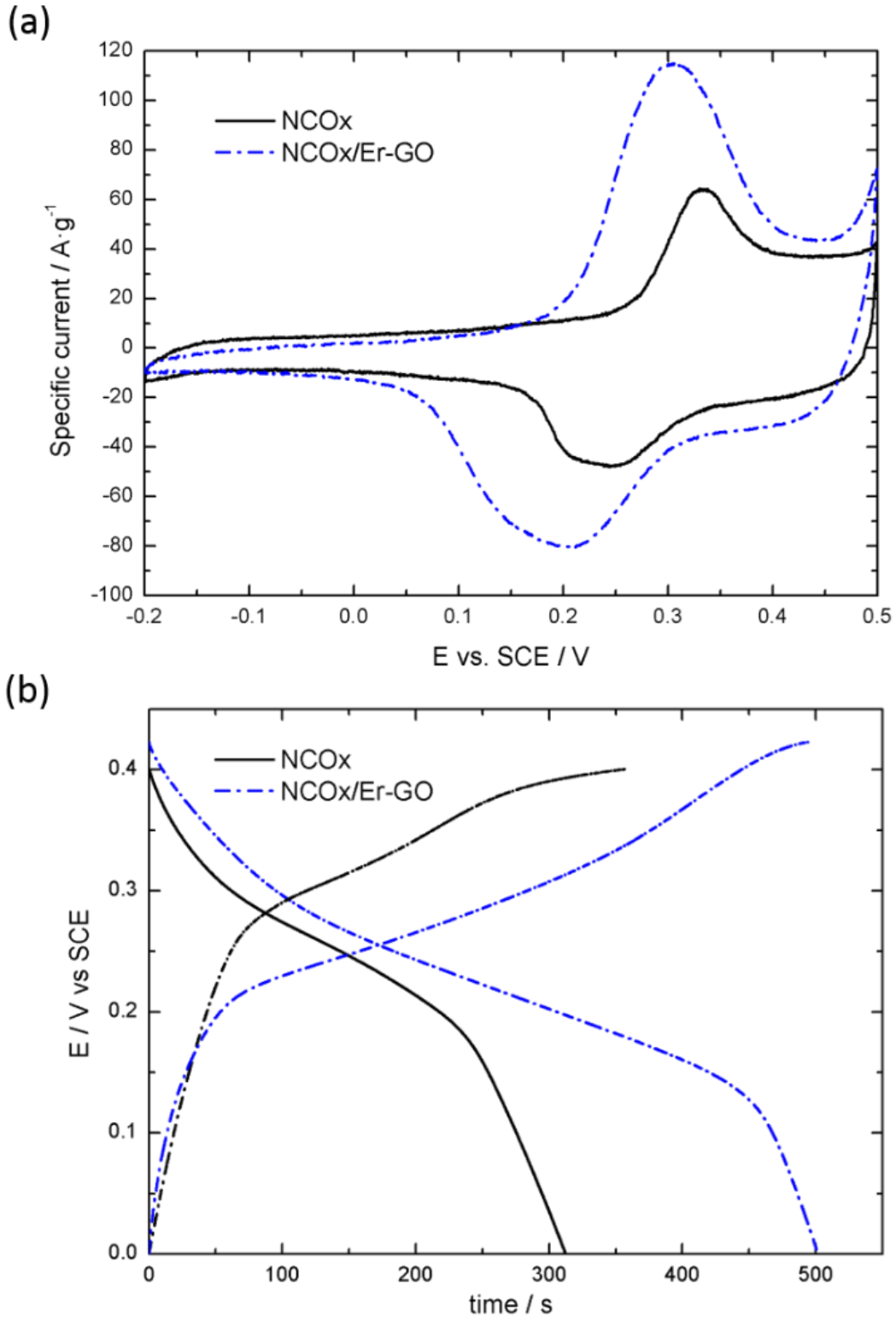

Fig. 3.4.9. Cyclic Voltammetry and Galvanostatic charge-discharge results comparison at 50 mV/s and 1A/g respectively for (**a**) NCOx and (**b**) NCOx/Er-GO measured in KOH 1M.

In conclusion, introducing the graphene derivative does not alter the electrochemical response of the material but does enhance the electrochemical response, resulting in an augmentation of the capacity due to a synergistic effect between the two components. This is also observable in the galvanostatic charge-discharge curve (Fig. 3.4.9b).

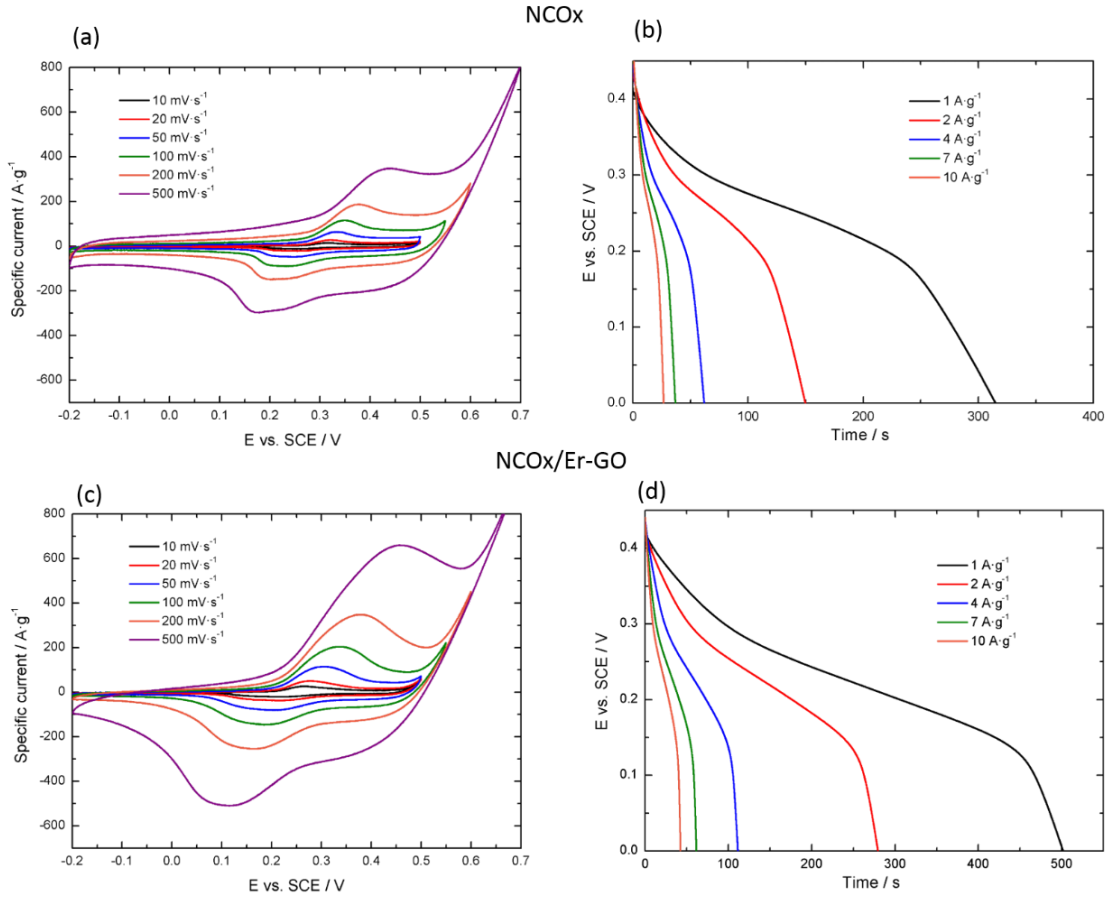

Fig. 3.4.10. Cyclic Voltammetry for (**a**) NCOx and (**c**) NCOx/Er-GO at scan rates from 10-500 $mV \cdot s^{-1}$ and Galvanostatic Charge-Discharge Curves at current densities from 1-10 $A \cdot g^{-1}$ for (**b**) NCOx and (**d**) NCOx/Er-GO measured in KOH 1M.

On the one hand, the capacity values obtained from the discharge curves in KOH 1M (curves presented in Fig. 3.4.10.b,d and values shown in table 3.4.2) go from 113.4 $mA \cdot h \cdot g^{-1}$ at $1A \cdot g^{-1}$ to 95.5 $mA \cdot h \cdot g^{-1}$ at an applied specific current of 10 $A \cdot g^{-1}$ for NCOx. On the other hand, the values obtained for NCOx/Er-GO range from 180.6 $mA \cdot h \cdot g^{-1}$ to 152.6 $mA \cdot h \cdot g^{-1}$ at 1 and 10 $A \cdot g^{-1}$ respectively. Indeed, an increased capacity of approximately 159% of the initial value is obtained, together with a better capacity rate when thermally treated electrochemically reduced graphene oxide in introduced.

Several groups have studied the electrochemical performance of Ni and Co oxides before, although sometimes wrongly reported as capacitance despite their redox reaction based on a phase transformation and a voltage-dependent response in their galvanostatic charge-discharge curves as explained by Brousse et al. [69]. Li et al. have reported 1523.0 $F \cdot g^{-1}$ at 2 $A \cdot g^{-1}$ in the 0.05V to 0.55V potential range (vs. SCE) in KOH 2M, excellent rate capability and cycling stability for electrodeposited $Ni_{0.61}Co_{0.39}$ oxide [25] while Gong et al. reported 1479 $F \cdot g^{-1}$ at $1A.g^{-1}$ in the 0.0V to 0.5V potential range in the same electrolyte [70]. Various nickel-cobalt oxide/carbon composite materials have also been prepared, for instance, Wang et al. prepared Ni-Co oxide nanocages on top of graphene nanoribbons by chemical precipitation followed by hydrothermal reaction

resulting in 937.8 $F \cdot g^{-1}$ at $1A \cdot g^{-1}$ in the 0.00V to 0.45V potential range (vs. RHE) in 2M KOH [71]. Another example is that of Lu-Yin et al., who prepared a mixture of nickel-cobalt hydroxide, nickel-cobalt oxide and reduced graphene oxide by a one-step hydrothermal method followed by thermal treatment. Their material displayed $1.25mA \cdot h \cdot cm^{-2}$ at $5mA \cdot cm^{-2}$ and approximately 60% capacity retention after 10.000 cycles in 5M KOH [72].

Table 3.4.2
Values of capacity calculated at current densities ranging from 1 to 10 $A \cdot g^{-1}$ for NCOx and NCOx/Er-GO.

Current Density ($A \cdot g^{-1}$)	C_{NCOx} ($mA \cdot h \cdot g^{-1}$)	$C_{NCOx/Er\text{-}GO}$ ($mA \cdot h \cdot g^{-1}$)
1	113.4	180.6
2	107.7	201.2
4	88.9	160.2
7	92.5	154.8
10	95.5	152.6

Both materials display excellent rate capability, with a minimum capacity retention of 78% in the case of NCOx and of 84% in the case of NCOx/Er-GO when 10 $A \cdot g^{-1}$ are applied. Again, it is worth noticing the overall better rate capability of the material in the presence of electrochemically reduced graphene oxide, in accordance with literature [32,73]. This may be the result of a better electron transport induced by the Er-GO matrix, in which the nickel-cobalt oxide is sustained as observed by SEM and TEM.

Faradaic efficiency is also an important characteristic that shall be studied. If the charge versus discharge time for the composite materials is evaluated ($t_{discharge}/t_{charge}$) at 1 $A \cdot g^{-1}$, a ratio of 0.88 is obtained for NCOx while a value of 1.01 is obtained for NCOx/Er-GO. This shows better faradaic efficiency when Er-GO is integrated. While the pure nickel-cobalt oxide material shows relevant faradaic losses in the charge-discharge process, it is optimized for NCOx /Er-GO. This may be the result of a better electron transfer since Er-GO may create a matrix that acts as a secondary substrate and enhances the conduction of electrons and, therefore, better reversibility of the reaction [74].

Finally, another relevant feature that can be observed in the charge-discharge curves is the progressively descending plateau. If the discharge curve of NCOx is considered, a nearly linear descending plateau begins at 0.30V that ends at approximately 0.2 V whereas, in the case of NCOx/Er-GO, the plateau is prolonged from 0.29 V to 0.14 V. Thus, the response, which is voltage dependent, extends its effective potential range in the presence of Er-GO.

3.4.3.3. Cycling Degradation Mechanism

One of the main goals when synthesizing a new material for energy storage applications is to obtain increased durability in their charge-discharge cycling. In fact, end-of-life criteria for both supercapacitors and batteries is generally considered when their capacity/capacitance is reduced in a 20-30% or there is an increase of a 100% in the equivalent series resistance [75,76].

To evaluate the sources of capacity and degradation phenomenon in NCOx and NCOx/Er-GO, different techniques were applied. First, a durability test during 5000

cycles of charge-discharge at 8 $A \cdot g^{-1}$ (Fig. 3.4.11). EIS and cyclic voltammetry were performed after 0, 150, 750, 1500 and 5000 cycles together with the physico-chemical evaluation by means of SEM/EDS before and after cycling.

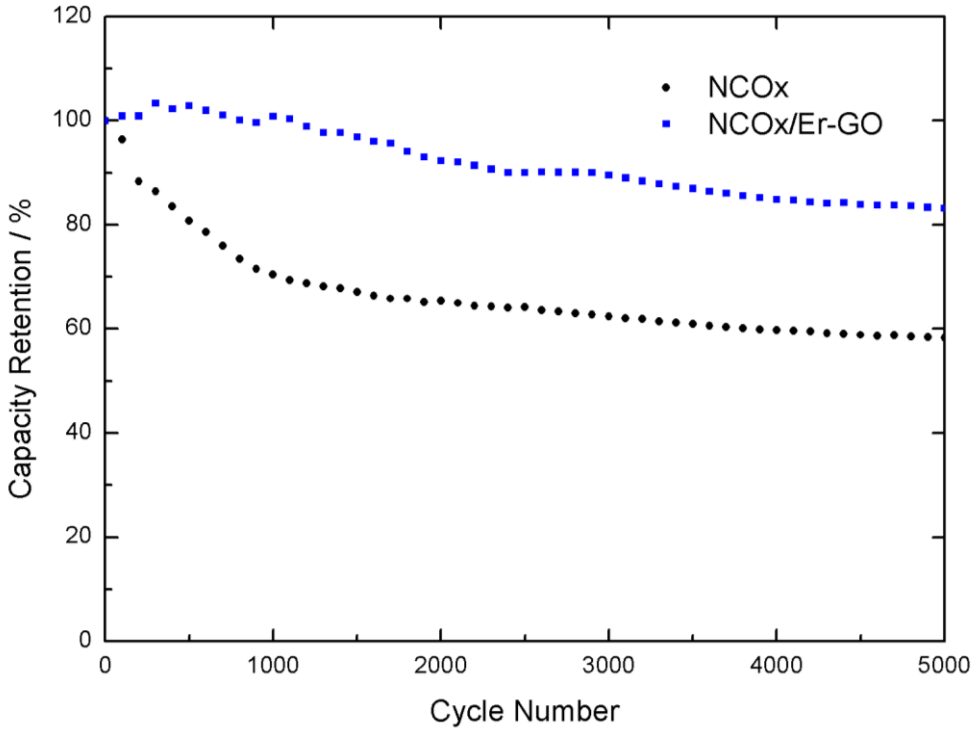

Fig. 3.4.11. Capacity Retention comparison obtained during cycling at 8 $A \cdot g^{-1}$ during 5000 cycles measured in KOH 1M.

NCOx has a capacity retention of 58% after 5000 cycles, while a 70% and 80% end-of-life criterion occurs after 1059 and 563 cycles respectively. On the other hand, NCOx/Er-GO maintains a capacity retention of 83.2% even after 5000 cycles, showing its excellent cycle durability and increased performance as compared to its analogous material without electrochemically reduced graphene oxide. Also, an initial increase in capacity is observed.

Results for SEM before and after cycling are depicted in Fig. 3.4.12. It is clearly visible that NCOx/Er-GO remains unchanged, while NCOx suffers from structural cracking. During the charging reaction of NCOx, there is a phase transition. This is generally associated to volume changes due to the nature of the reaction [77], increasing electrode swelling and therefore mechanical degradation. The mechanical stress, given volume variation during charge and discharge, cannot be accommodated and results in cracking. When Er-GO is introduced, nickel-cobalt oxide is homogeneously distributed on top of the carbon surface in homogeneously-distributed and smaller particles, as observed by SEM and TEM. Volume variations therefore affect smaller particles, as compared to the aggregates in NCOx. Consequently, the volume variation that nickel-cobalt oxide on top of reduced graphene oxide endure during charge-discharge is accommodated by the carbon matrix and cracking is inhibited.

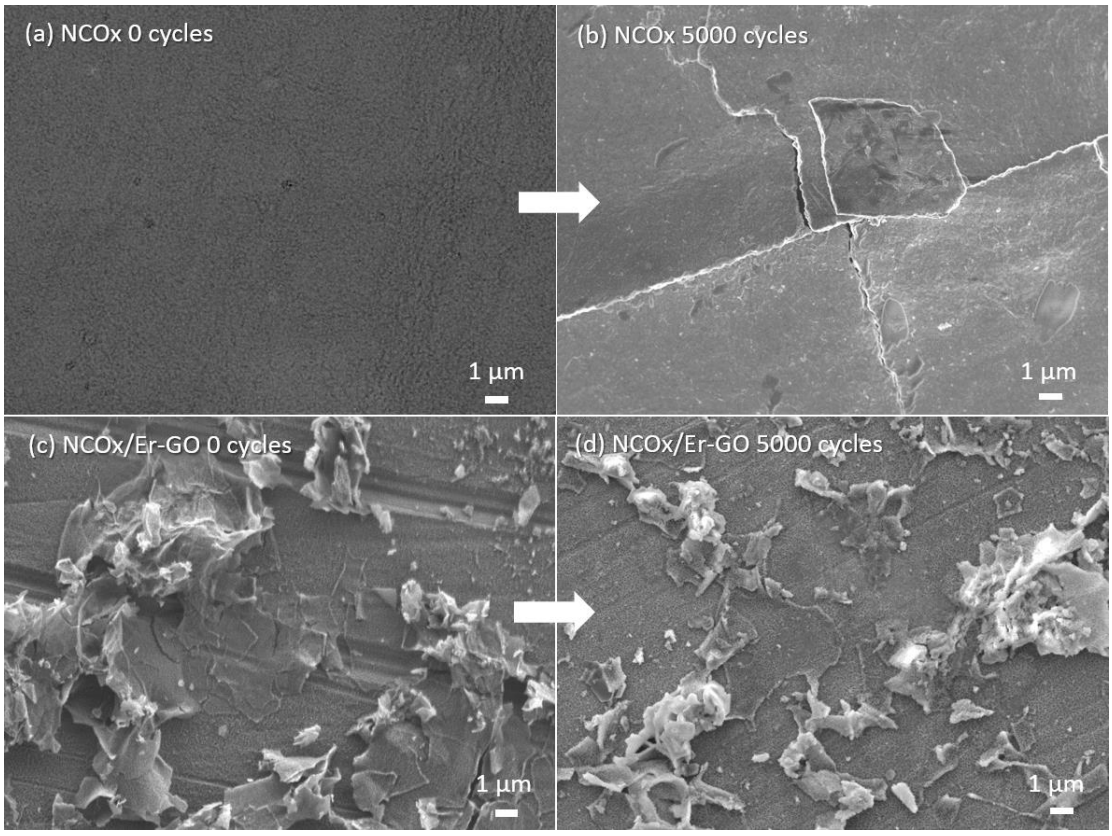

Fig. 3.4.12. Scanning electron microscopy images showing the degradation effects in the initial composites (**a**) NCOx and (**c**) NCOx/Er-GO after 5000 cycles of charge-discharge at a current density of 8 A/g for (**b**) NCOx and (**d**) NCOx/Er-GO.

The change in the composition is also reflected in the electrochemical response by means of cyclic voltammetry and impedance spectroscopy after 0, 150, 750, 1500 and 5000 cycles, which are depicted in Fig. 3.4.13 to 3.4.16. A displacement of the peak towards more anodic values is observed in cyclic voltammetry during cycling.

When the atomic ratios obtained by EDS are considered, initially a Ni:Co ratio of 0.63:0.37 is obtained for both. However, after cycling, the chemical composition evolves to a ratio of 0.60:0.40 in the case of NCOx, while resulting in a value of 0.64:0.36 for NCOx /Er-GO. This would indicate a loss of nickel during the durability test for the former composite while the composition for the Er-GO based composite is maintained. From EDS it can be concluded that chemical dissolution and variation of the composition of the electrode material occurs. However, this behaviour is not completely understood. Normally, the instability of Ni-Co LDH materials arises from dissolution of cobalt ions, resulting in composites with greater nickel concentration [78–81]. Consequently, the peaks tend to vary to more anodic values, where the potential of NiO is located. This is also observed in the present cyclic voltammetry but is contradictory with the present EDS results. Thus, as a result of the semi-quantitative nature of EDS and the anomaly in the results, further analysis in this regard shall be done.

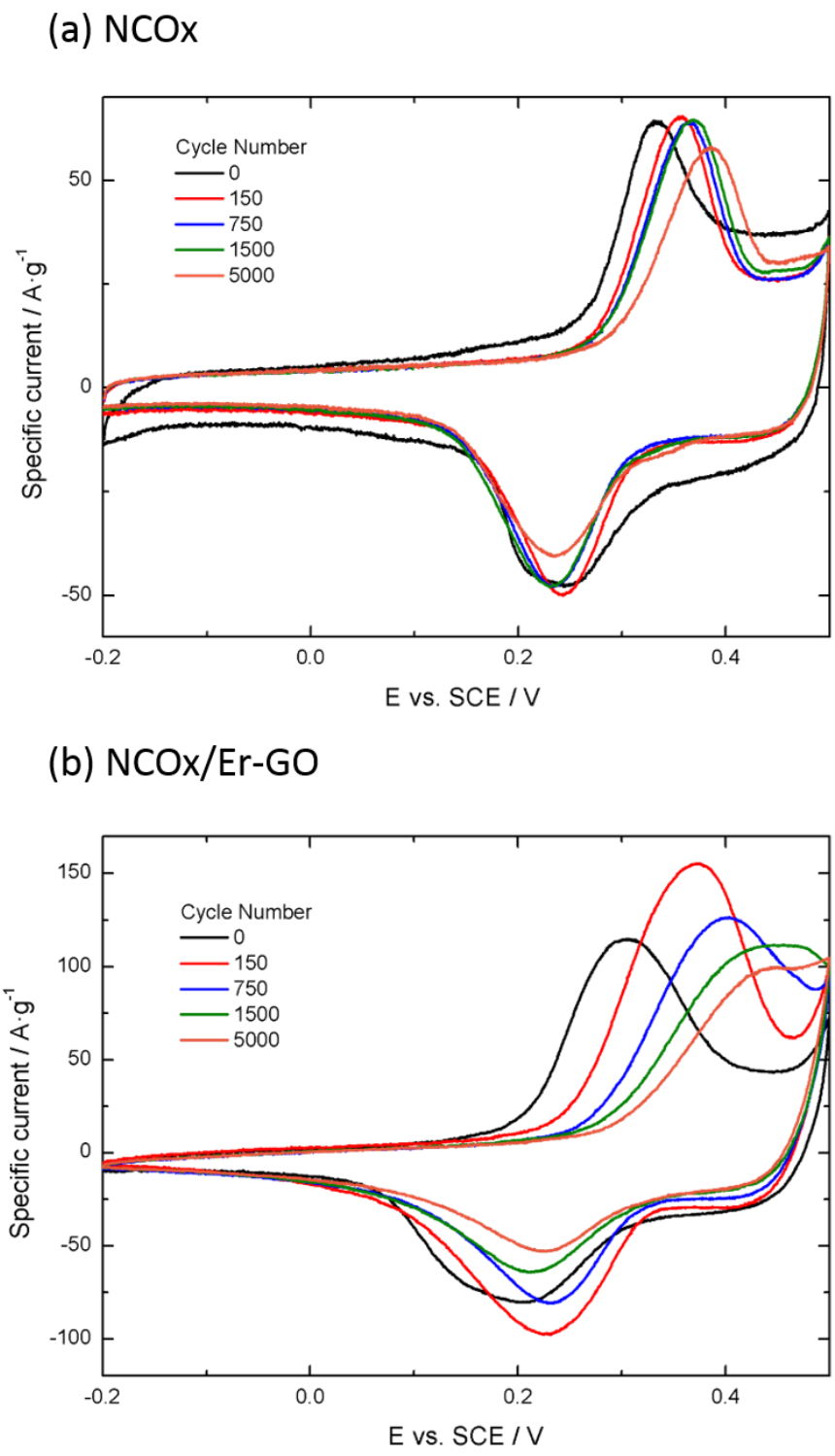

Fig. 3.4.13. Cyclic Voltammetry response degradation at 50 $mV \cdot s^{-1}$ with cycling for (**a**) NCOx and (**b**) NCOx/Er-GO measured in KOH 1M.

For energy storage materials with faradaic response, it is important to evaluate their EIS response at least in two different potentials, charged and discharged conditions, since different and relevant information can be obtained from both. For that reason, the EIS spectra were obtained at -0.2 V and 0.45 V (vs. SCE). The direct comparison of the EIS response during the first cycle is depicted in Fig. 3.4.14, although the evolution of the EIS spectra after 0, 150, 750, 1500 and 5000 cycles of galvanostatic charge-discharge cycling at $8A \cdot g^{-1}$ is depicted in Fig.3.4.15 and Fig.3.4.16.

The charge mechanism involves the transformation of semi-conductive nickel-cobalt oxide into a conductive oxyhydroxide [82]. Thus, a reduction in the film charge-transfer resistance from the discharged to charged condition is expected. This is visible by the appearance of a second plateau with lower resistance at low frequencies in the modulus of resistance vs. frequency plot and the decrease in the diameter of the semi-circle of Nyquist plots. Moreover, in the discharged condition, a less kinetically favoured process at low frequencies is present that disappears when the material is charged. The material's behaviour is, as usually reported for impedance spectroscopy [41,83,84], separated in the contribution of two time-constants, namely, double layer capacitance (superficial charges and resistance associated in the charge transfer change from ionic conductor to electron conduction in a solid) and film capacitance. This is reflected in the equivalent circuit presented in Fig. 3.4.17. With cycling, the material becomes more resistive for both charge-states of the material, which leads to increased values of the second resistive plateau in the modulus vs. frequency plot and an increasing semi-circle in Nyquist plots. Moreover, low-frequency resistive phenomena become more relevant with cycling when the electrode is discharged, at -0.2V, as observed in the phase angle plot.

A graphic analysis of the results obtained for the mathematical fitting of impedance results is presented in Fig. 3.4.18. Considering the values obtained for NCOx, three main features can be observed. First, the increase in the admittance of the constant phase element (CPE) assigned to the double-layer when the electrode is charged. Second, the drastic reduction of film resistance when the material is converted from oxide to oxyhydroxide (and an associated increase in film admittance). Third, the overall increase in resistance with cycling. The variation of film admittance and resistance for the material at -0.2 V and at 0.45 V is expected and associated to the oxidation state change for nickel and cobalt and change in conductivity when the phase is transformed from oxide to oxyhydroxide.

There are several potential explanations for the evolution/degradation of these materials with cycling. In the case of NCOx it shall be considered that: 1) There is a progressive decay of capacity, more intense during the first cycles. 2) Double layer and equivalent series resistance are maintained (with a very small increase) throughout cycling. 3) Film resistance increases with cycling. 4) There is an evident material degradation as observed by SEM. Thus, the increase in resistance may be related to the increased strain induced by the collapse of the superficial structure. 5) There is a variation in the chemical composition, which is reflected by EDS and the peak potential variation in cyclic voltammetry. 6) Oxygen evolution reaction is close to the maximum charge potential and may contribute as a parasitic reaction inducing capacity decay. Also, OER could mechanically degrade the material, if O_2 is produced. 7) Cycling displaces the anodic peak to higher potentials as observed by cyclic voltammetry. Thus, the electrochemical reaction is closer to the OER potentially being more affected by it as long as the cycling evolves. 8) Low-frequency phenomena obtained at -0.2 V becomes intensified with cycling.

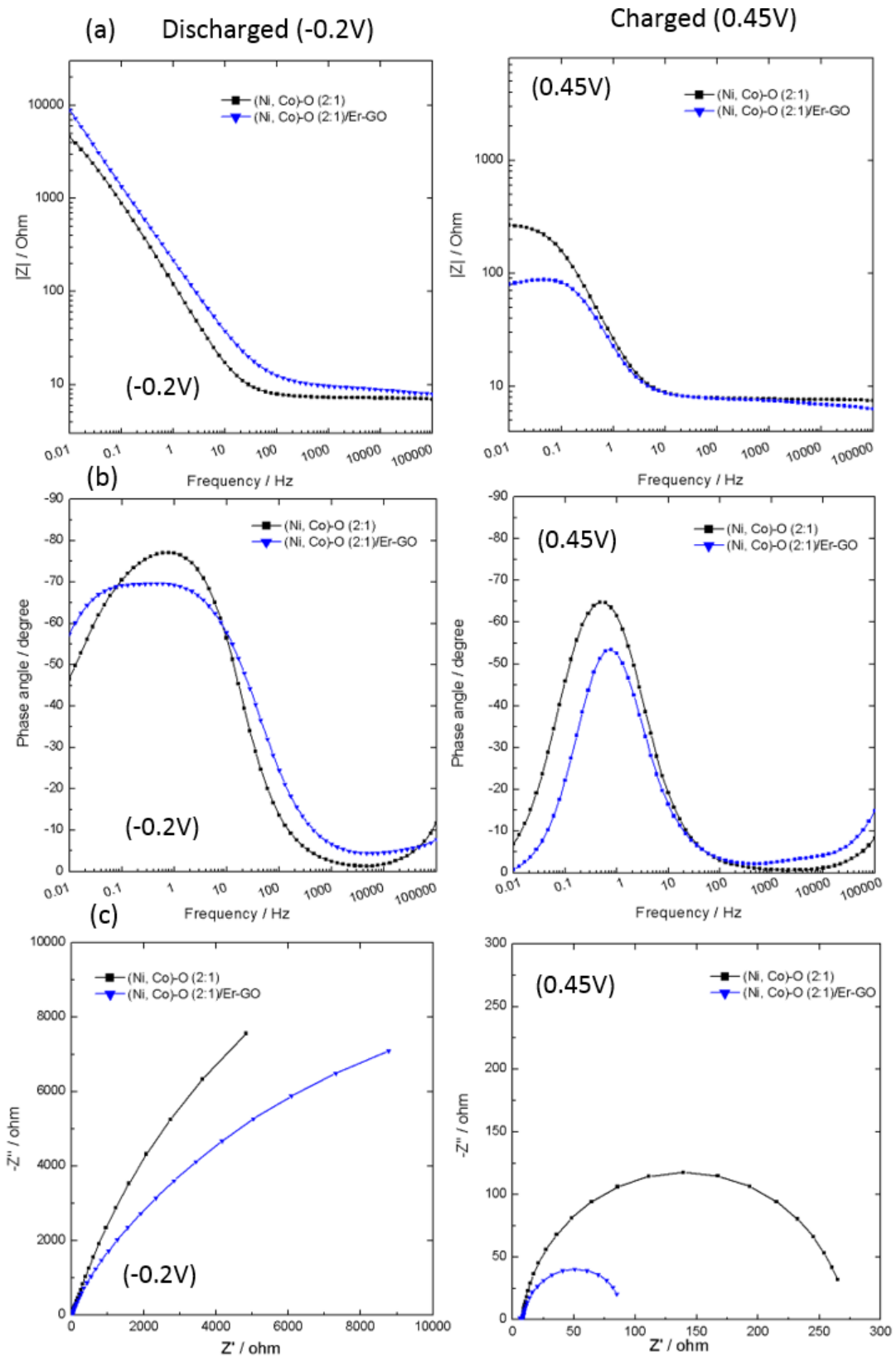

Fig. 3.4.14. Electrochemical impedance spectra comparison for electrodeposited Ni-Co oxide and Ni-Co oxide measured in KOH 1M in combination with electrochemically reduced graphene oxide in the form of (a) impedance modulus versus frequency (b) phase angle versus frequency and (c) Nyquist plots obtained at two different potentials, namely -0.2V, discharged condition, and 0.45V, charged condition.

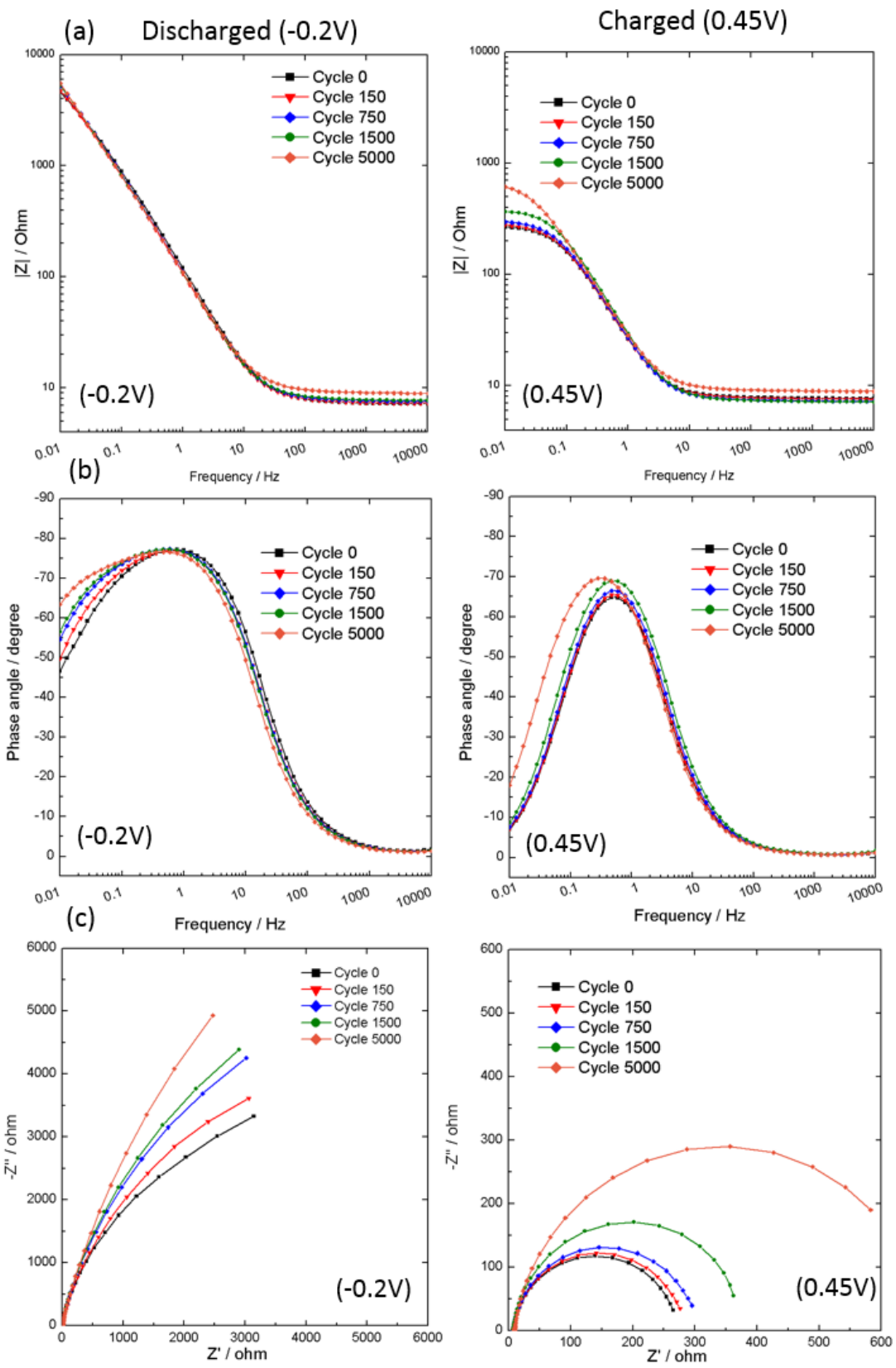

Fig. 3.4.15. (**a**) and (**b**) Bode and (**c**) Nyquist Electrochemical Impedance Spectra for NCOx composite material after 0, 150, 750, 1500 and 5000 cycles of Galvanostatic Charge Discharge at 8 A/g for both discharged (-0.2V, left) and charged (0.45V, right) potentials.

When reduced graphene oxide is included, a similar behaviour to that of NCOx is observed. Nonetheless, there are several features that are different and shall be considered: 1) ESR is slightly lower than for NCOx. 2) Double layer resistance has significantly lower values. The measured resistance is normalized to the apparent experimental area (1 cm^2) but the real area includes a much more extensive surface area, as a consequence of the Er-GO matrix. Thus, these calculated values are apparent resistance values that should be multiplied by the real active area of the material, which would probably lead to similar values to those obtained for NCOx. 3) Double layer resistance is maintained at both charge-states of the material. 4) Film resistance is much higher for the discharged condition while lower for the charged condition as compared to NCOx. This may be related to a greater exposure of the nickel-cobalt material to the electrolyte induced by Er-GO and the change in the conductivity in the charging process. In a similar manner, there is a greater variance of the CPE admittance assigned to the film for NCOx/Er-GO, with higher conductivity for NCOx/Er-GO compared to NCOx when the electrode is charged, while lower when the electrode is discharged. 5) An additional time constant is developed in the discharged form (-0.2V) with cycling at mid-frequencies, more evidenced when the material is cycled 750 times. This new time constant separates the capacitive contribution of the material in two components and is not as visible when the material is fully charged. This new time constant is included in the equivalent circuit for the fitting in the discharged condition after 750 cycles. 6) There is an initial decrease in film resistance when the material is charged during the first 1000 cycles. Accordingly, there is an increase in the CPE admittance as observed in the cycling test performed at 8 $A \cdot g^{-1}$. 7) No mechanical degradation or strain is visible by SEM for NCOx/Er-GO. However, the variation in the electrochemical response observed by cyclic voltammetry is much more evident than in the case of NCOx, with initial increased capacity. A variation in chemical composition of the material shall also be taken into account since it is observed by EDS.

Thus, it can be considered that Er-GO acts as a matrix that accommodates strain, reducing the mechanical degradation observed by SEM. Moreover, given its increased active surface area, Er-GO induces more exposure of nickel-cobalt oxide deposited on top of it, leading to increased number of active sites. It also serves as a conductive matrix, reducing overall resistance. During the first cycles, electrolyte penetration may reach initially inaccessible pores that later become active sites, leading to an initial increase in capacity. Besides, the observed increase in resistance with cycling is much smaller in absolute terms in the case of the Er-GO containing material. While Ni-Co oxide is affected by mechanical degradation, increasing the measured resistance, NCOx/Er-GO initially increases its capacity by electrolyte penetration during the first 1000 cycles and inhibits mechanical stress.

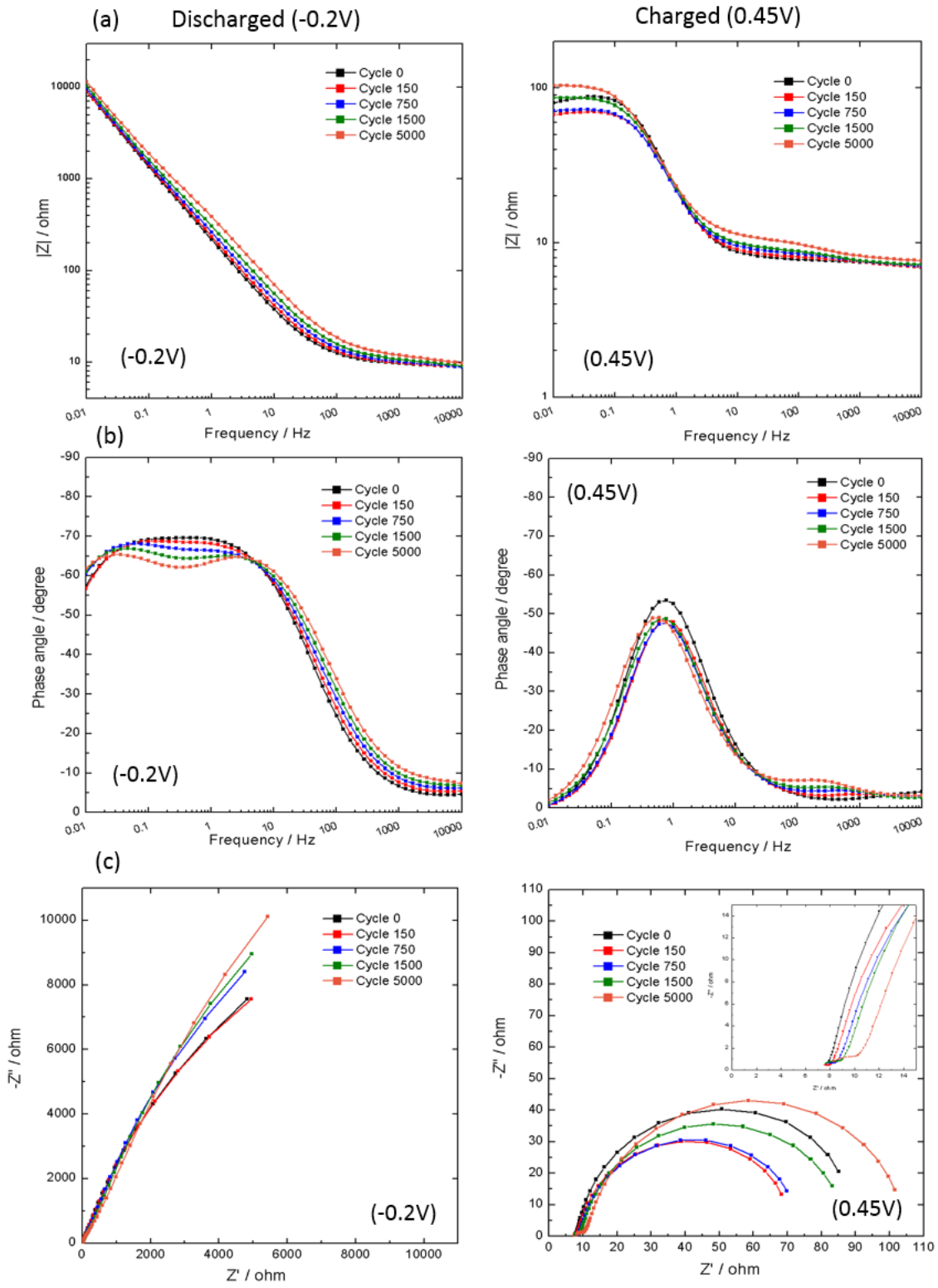

Fig. 3.4.16. (**a**) and (**b**) Bode and (**c**) Nyquist Electrochemical Impedance Spectra for NCOx/Er-GO composite material after 0, 150, 750, 1500 and 5000 cycles of Galvanostatic Charge Discharge at 8 A/g for both discharged (-0.2V, left) and charged (0.45V, right) potentials.

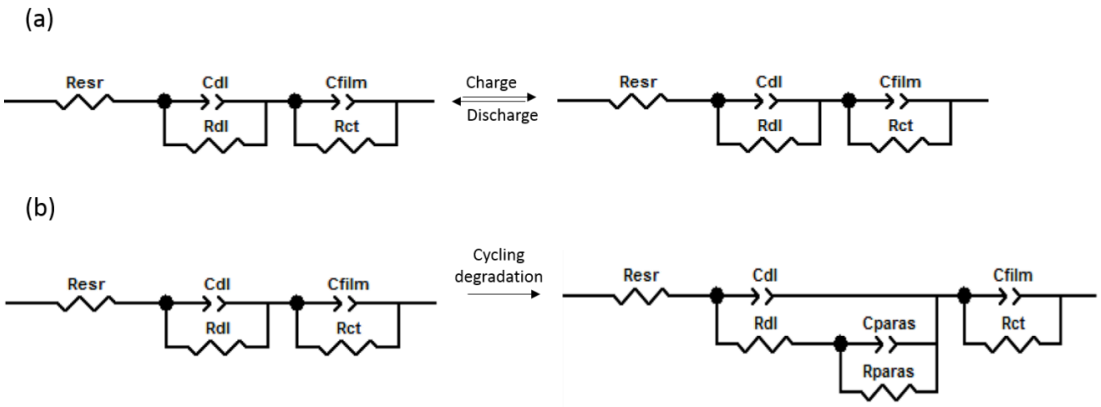

Fig. 3.4.17. (**a**) General equivalent circuit model used in the fitting of the impedance spectra acquired for NCOx and NCOx/Er-GO for the results obtained at -0.2V (discharged) and 0.45V (charged) and (**b**) Equivalent circuit model used in the fitting of impedance spectra acquired for NCOx/Er-GO at -0.2V with cycling after 750, 1500 and 5000 cycles.

However, the increased exposure to the electrolyte leads to the formation and stabilization of a secondary parasitic phase, as observed by the new time constant by EIS. This parasitic reaction, considering previous reports, is likely to be the formation of a nickel-cobalt hydroxide phase. When material is charged, an oxyhydroxide phase is formed and, when this reaction is reversed, it may generate a hydroxide phase considering that the reaction takes place in alkali media and taking into account that nickel-cobalt hydroxide is also transformed into an oxyhydroxide phase during charging, as exemplified in equations 3.4.3 and 3.4.4 [85]:

$$\alpha\text{-}Ni_xCo_{1-x}(OH)_2(2NO_3^-,\ CO_3^{2-})_{(1-x)/2}(H_2O)_{0.5} + (0.5\text{-}y)(\ Na^+,\ K^+) \longleftrightarrow \gamma\text{-}Ni_xCo_{1-x}OO(H^+)_y(Na^+,K^+)_{(0.5-y)}(H_2O)_{0.5} + (2\text{-}y)H^+ + (1\text{-}x)/2\ (2NO_3^-,\ CO_3^{2-}) + (0.5+x)e^-$$

(eq. 3.4.3)

$$\beta\text{-}Ni_xCo_{1-x}O_2H_{1+x} \longleftrightarrow \beta\text{-}Ni_xCo_{1-x}OOH + xH^+ + xe^- \qquad \text{(eq. 3.4.4)}$$

When Er-GO is introduced, the reaction presented in equation 3.4.4 is promoted, leading to the formation of $Ni_{1-x}Co_xO_y$ together with $Ni_xCo_{1-x}(OH)_2$. This would explain the shift in the peaks of cyclic voltammetry. Moreover, when charged, the material transforms into the oxyhydroxide form in any case and, for that reason, mid-frequency EIS response is less affected in the charged state. When discharged, given the fact that the conductivity of the oxide is higher than of the hydroxide [86–88], this phenomenon increases mid-frequency resistance.

Finally, a similar decay in capacity of NCOx to NCOx/Er-GO (once the material is stabilized) is observed, associated to similar degradation processes. In fact, the low-frequency evolution in the discharged potential for NCOx and the variation observed by cyclic voltammetry with cycling suggests that this second phase may be also formed for NCOx, although due to the reduced electrolyte accessibility of the material and lower active surface area, it is not as relevant. Summarizing, mechanical degradation, formation of a secondary phase and OER parasitic reaction are pin-pointed as the main sources of NCOx degradation, while an initial activation, produced by electrolyte penetration when Er-GO is present, leads to an initial increase of material's capacity. When Er-GO is introduced, mechanical degradation is reduced, while the formation of a secondary phase is promoted.

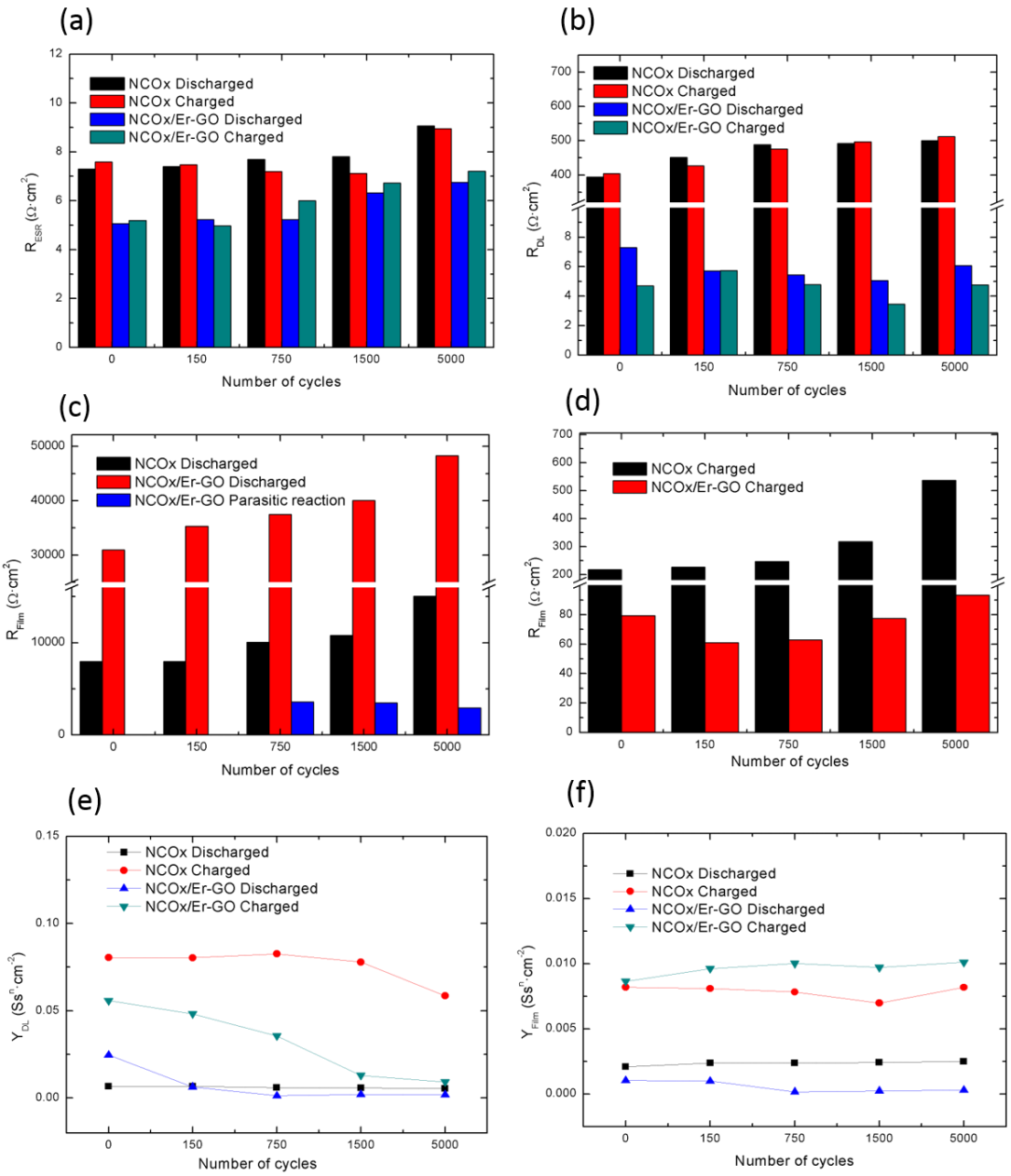

Fig. 3.4.18. Graphic analysis of the results obtained for the fitting of EIS spectra. Data table not presented.

3.4.4. Conclusions

Cobalt-nickel oxide in combination with electrochemically reduced graphene oxide was successfully prepared by electrodeposition followed by thermal treatment. The inclusion of reduced graphene oxide to the mixed oxide greatly improved its energy storage capability that increases from 113 $mA \cdot h \cdot g^{-1}$ to 180 $mA \cdot h \cdot g^{-1}$. Cycling stability after 5000 cycles, and subsequent capacity retention, increased from 58% to 83%. The faradaic efficiency was improved from 0.88 to 1.01 and the rate capability of the composite raised from 78% to 84%. Finally, a detailed study on the degradation mechanism by means of electrochemical impedance spectroscopy was performed in combination with cyclic voltammetry, scanning electron microscopy and electron diffraction spectroscopy. EIS evidenced the change in conductivity in the oxidation process of the material and the appearance of a second time constant for NCOx/Er-GO at -0.2V after cycling that is associated to a new phase that may be nickel-cobalt hydroxide. Thus, there are three main key observations related to the cycling stability of the material: 1) Variation in peak potential by cyclic voltammetry. 2) Mechanical degradation observed by SEM. 3) New time mid-frequency constant in EIS spectra. These results suggest that degradation mechanisms, and consequent capacity fade, can be attributed to cracking caused by strain during charge and discharge, phase transformations that result in a parasitic phase and side reactions such as oxygen evolution. Electrochemically reduced graphene oxide serves as a conductive matrix that accommodates strain and increases the number of active sites, leading to increased electrochemical performance. Thus, a synergistic carbon-transition metal composite material is produced by means of a very simple route that has enhanced performance as compared to its analogous material without electrochemically reduced graphene oxide, serving as an example of the potential that reduced graphene oxide has for energy storage applications.

Acknowledgements

This work has been performed in scope of International Doctoral Program in Functional Materials (**IDS-FunMat, Erasmus Mundus**) and funded by the European Union. We would like to express our gratitude to the Fundação para a Ciência e Tecnologia (FCT) for the funding under the contracts M-ERA.NET/0002/2012 and UID/QUI/00100/2013. We would also like to acknowledge Mª Joao Carmezim, Sabine Gomes for performing the GIXD experiments, Catherine Denage and Philippe Dagault for their general assistance, Stephane Le Blond de Plouy for performing SEM images at the Centre de MicroCaractérisation Raimond Castaing (UMS 3623, 3 rue caroline Aigle, 31400 Toulouse, FRANCE), Marion Gayot for performing TEM images at PLACAMAT (Plateforme Aquitane de Caractérisation des Matériaux UMS 3626 CNRS-Université de Bordeaux, 33600 Pessac, FRANCE), Philipe Legros and François Weill (PLACAMAT) for their SEM and TEM assistance respectively and, finally, Christine Labrugere (PLACAMAT) for performing XPS and assisting in the data interpretation.

Chapter 3.4 References

[1] P. Simon, Y. Gogotsi, B. Dunn, Where Do Batteries End and Supercapacitors Begin?, Science (80-.). 343 (2014) 1210–1211. doi:10.1126/science.1249625.

[2] B.E. Conway, Transition from "supercapacitor" to "battery" behavior in electrochemical energy storage., J. Electrochem. Soc. 138 (1991) 1539–1548. doi:10.1149/1.2085829.

[3] J.H. Chae, X. Zhou, G.Z. Chen, From electrochemical capacitors to supercapatteries, Green. 2 (2012) 41–54. doi:10.1515/green-2011-0007.

[4] W. Wei, X. Cui, W. Chen, D.G. Ivey, Manganese oxide-based materials as electrochemical supercapacitor electrodes, Chem. Soc. Rev. 40 (2011) 1697–1721. doi:10.1039/C0CS00127A.

[5] M. Pumera, Graphene-based nanomaterials for energy storage, (2011) 668–674. doi:10.1039/c0ee00295j.

[6] G. Wang, Z. Lei, Z. Jiujun, A review of electrode materials for electrochemical supercapacitors, ChemsucChem. 5 (2012) 797. doi:10.1039/c1cs15060j.

[7] Y. Xie, X.W. Lou, C. Yuan, H. Bin Wu, Y. Xie, X. Wen, D. Lou, Mixed Transition-Metal Oxides : Design , Synthesis , and Energy-Related Applications, Angew. Chem. Int. Ed. Engl. 53 (2014) 1488–1504. doi:10.1002/anie.201303971.

[8] R. Della Noce, a-Co (OH) 2 / carbon nanofoam composite as electrochemical capacitor electrode operating at 2 V in aqueous medium, (2015). doi:10.1016/j.jpowsour.2015.04.131.

[9] T. Nguyen, M. Boudard, M. João Carmezim, M. Fátima Montemor, NixCo1-x(OH)2 nanosheets on carbon nanofoam paper as high areal capacity electrodes for hybrid supercapacitors, Energy. 126 (2017) 208–216. doi:10.1016/j.energy.2017.03.024.

[10] T. Nguyen, M. Boudard, M.J. Carmezim, M.F. Montemor, Layered Ni(OH)2-Co(OH)2 films prepared by electrodeposition as charge storage electrodes for hybrid supercapacitors, Sci. Rep. (2017) 1–10. doi:10.1038/srep39980.

[11] V.A. Online, T. Nguyen, M. Boudard, L. Rapenne, Morphological changes and electrochemical response of mixed nickel manganese oxides as charge storage electrodes, (2015) 10875–10882. doi:10.1039/C5TA01453K.

[12] T. Nguyen, M. Boudard, L. Rapenne, O. Chaix-pluchery, Structural evolution, magnetic properties and electrochemical response of MnCo2O4 nanosheeet films, (2015) 27844–27852. doi:10.1039/C5RA03047A.

[13] Y. Nuli, Q. Qin, Nanocrystalline transition metal ferrite thin films prepared by an electrochemical route for Li-ion batteries, J. Power Sources. 142 (2005) 292–297. doi:10.1016/j.jpowsour.2004.10.015.

[14] K. Karthikeyan, D. Kalpana, N.G. Renganathan, Synthesis and characterization of ZnCo2O4 nanomaterial for symmetric supercapacitor applications, Ionics (Kiel). 15 (2009) 107–110. doi:10.1007/s11581-008-0227-y.

[15] A. Rong, X.P. Gao, G.R. Li, T.Y. Yan, H.Y. Zhu, J.Q. Qu, D.Y. Song, Hydrothermal Synthesis of Zn2SnO4 as Anode Materials for Li-Ion Battery, J. Phys. Chem. B. 110 (2006) 14754–14760. doi:10.1021/jp062875r.

[16] G. He, L. Wang, H. Chen, X. Sun, X. Wang, Preparation and performance of NiCo2O4 nanowires-loaded graphene as supercapacitor material, Mater. Lett. 98 (2013) 164–167. doi:10.1016/j.matlet.2013.02.035.

[17] Z. Gao, W. Yang, J. Wang, N. Song, X. Li, Flexible all-solid-state hierarchical NiCo2O4/porous graphene paper asymmetric supercapacitors with an exceptional combination of electrochemical properties, Nano Energy. 13 (2015) 306–317. doi:10.1016/j.nanoen.2015.02.036.

[18] M. Li, Y. Wang, D. Wu, L. Wang, H. Yang, Hierarchical grass like NiCo2O4 nanoflakes on 3-dimensional microporous electrically conductive network with Superior Electrochemical Performance, Energy Procedia. 105 (2017) 4848–4853. doi:10.1016/j.egypro.2017.03.960.

[19] C. Yuan, J. Li, L. Hou, L. Yang, L. Shen, X. Zhang, Facile template-free synthesis of ultralayered mesoporous nickel cobaltite nanowires towards high-performance electrochemical capacitors, J. Mater. Chem. 22 (2012) 16084–16090. doi:10.1039/c2jm32351f.

[20] Y. Lei, J. Li, Y. Wang, L. Gu, Y. Chang, H. Yuan, D. Xiao, Rapid Microwave-Assisted Green Synthesis of 3D Hierarchical Flower-Shaped NiCo2O4 Microsphere for High-Performance Supercapacitor, ACS Appl. Mater. Interfaces. 6 (2014) 1773–1780.

[21] T.Y. Wei, C.H. Chen, H.C. Chien, S.Y. Lu, C.C. Hu, A cost-effective supercapacitor material of ultrahigh specific capacitances: spinel nickel cobaltite aerogels from an epoxide-driven sol-gel process, Adv. Mater. 22 (2010) 347–351. doi:10.1002/adma.200902175.

[22] R. Della Noce, S. Eugénio, T.M. Silva, M.J. Carmezim, M.F. Montemor, α-Co(OH)2/carbon nanofoam composite as electrochemical capacitor electrode operating at 2 v in aqueous medium, J. Power Sources. 288 (2015) 234–242. doi:10.1016/j.jpowsour.2015.04.131.

[23] L. Qian, L. Gu, L. Yang, H. Yuan, D. Xiao, Direct growth of NiCo2O4 nanostructures on conductive substrates with enhanced electrocatalytic activity and stability for methanol oxidation, Nanoscale. 3 (2013) 7388–7396. doi:10.1039/c3nr01104f.

[24] C. Yuan, J. Li, L. Hou, X. Zhang, L. Shen, X.W. Lou, Ultrathin mesoporous NiCo 2O 4 nanosheets supported on Ni foam as advanced electrodes for supercapacitors, Adv. Funct. Mater. 22 (2012) 4592–4597. doi:10.1002/adfm.201200994.

[25] Y.-M. Wang, X. Zhang, C.-Y. Guo, Y.-Q. Zhao, C.-L. Xu, H.-L. Li, Controllable synthesis of 3D NiχCo1-χ oxides with different morphologies for high-capacity supercapacitors., J. Mater. Chem. A Mater. Energy Sustain. 1 (2013) 13290–13300. doi:10.1039/c3ta12713c.

[26] J. Du, G. Zhou, H. Zhang, C. Cheng, J. Ma, W. Wei, L. Chen, T. Wang, Ultrathin Porous NiCo2O4 Nanosheet Arrays on Flexible Carbon Fabric for High-Performance Supercapacitors, (2013) 7405–7409.

[27] X. Wang, W.S. Liu, X. Lu, P.S. Lee, Dodecyl sulfate-induced fast faradic process in nickel cobalt oxide–reduced graphite oxide composite material and its application for asymmetric supercapacitor device, J. Mater. Chem. 22 (2012)

23114. doi:10.1039/c2jm35307e.

[28] Z. Fan, J. Chen, K. Cui, F. Sun, Y. Xu, Y. Kuang, Preparation and capacitive properties of cobalt – nickel oxides / carbon nanotube composites, Electrochim. Acta. 52 (2007) 2959–2965. doi:10.1016/j.electacta.2006.09.029.

[29] Q. Li, J. Cheng, B. Wang, L. Zhang, Activated carbon modified by CNTs/Ni-Co oxide as hybrid electrode materials for high performance supercapacitors., IEEE Trans. Nanotechnol. 13 (2014) 557–562. doi:10.1109/TNANO.2014.2310512.

[30] M. Wu, S. Meng, Q. Wang, W. Si, W. Huang, X. Dong, Nickel-Cobalt Oxide Decorated 3D Graphene as an Enzyme Mimic for Glucose and Calcium Detection Nickel-Cobalt Oxide Decorated 3D Graphene as an Enzyme Mimic for Glucose and Calcium Detection, Appl. Mater. Interfaces. (2015). doi:10.1021/acsami.5b06299.

[31] E. Umeshbabu, G. Rajeshkhanna, G.R. Rao, Effect of solvents on the morphology of NiCo 2 O 4 / graphene nanostructures for electrochemical pseudocapacitor application, J. Solid State Electrochem. (2016) 1837–1844. doi:10.1007/s10008-015-3022-5.

[32] H.-W. Wang, Z.-A. Hu, Y.-Q. Chang, Y.-L. Chen, H.-Y. Wu, Z.-Y. Zhang, Y.-Y. Yang, Design and synthesis of NiCo2O4–reduced graphene oxide composites for high performance supercapacitors, J. Mater. Chem. 21 (2011) 10504. doi:10.1039/c1jm10758e.

[33] M. Yu, J. Chen, J. Liu, S. Li, Y. Ma, J. Zhang, J. An, Mesoporous NiCo2O4 nanoneedles grown on 3D graphene-nickel foam for supercapacitor and methanol electro-oxidation, Electrochim. Acta. 151 (2015) 99–108. doi:10.1016/j.electacta.2014.10.156.

[34] D. Carriazo, J. Patiño, M.C. Gutiérrez, M.L. Ferrer, F. del Monte, Microwave-assisted synthesis of NiCo2O4–graphene oxide nanocomposites suitable as electrodes for supercapacitors, RSC Adv. 3 (2013) 13690. doi:10.1039/c3ra42610f.

[35] A. Adán-más, R.G. Duarte, T.M. Silva, L. Guerlou-demourgues, M. Fátima, G. Montemor, Enhancement of the Ni-Co hydroxide response as Energy Storage Material by Electrochemically Reduced Graphene Oxide, Electrochim. Acta. 240 (2017) 323–340. doi:10.1016/j.electacta.2017.04.070.

[36] C. Zhang, T. Kuila, N.H. Kim, S. Hee, J.H. Lee, Facile preparation of flower-like NiCo2O4 / three dimensional graphene foam hybrid for high performance supercapacitor electrodes, Carbon N. Y. 89 (2015) 328–339. doi:10.1016/j.carbon.2015.03.051.

[37] V.H. Nguyen, J. Shim, Three-dimensional nickel foam/graphene/NiCo2O4 as high- performance electrodes for supercapacitors, J. Power Sources. 273 (2015) 110–117. doi:10.1016/j.jpowsour.2014.09.031.

[38] J. Zhang, F. Liu, J.P. Cheng, X.B. Zhang, Binary Nickel-cobalt Oxides Electrode Materials for High-performance Supercapacitors : Influence of its Composition and Porous Nature, ACS Appl. Mater. Interfaces. 7 (2015) 17630–17640.

[39] V. Srinivasan, J.W. Weidner, Studies on the capacitance of nickel oxide films: effect of heating temperature and electrolyte concentration, J. Electrochem. Soc. 147 (2000) 880–885. doi:10.1149/1.1393286.

[40] D.P. Lapham, a C.C. Tseung, The effect of firing temperature, preparation technique and composition on the electrical properties of the nickel cobalt oxide series NixCo1-xOy, J. Mater. Sci. 39 (2004) 251–264. doi:10.1023/B:JMSC.0000007751.14703.4b.

[41] A.N. Naveen, S. Selladurai, Novel low temperature synthesis and electrochemical characterization of mesoporous nickel cobaltite-reduced graphene oxide (RGO) composite for supercapacitor application., Electrochim. Acta. 173 (2015) 290–301. doi:10.1016/j.electacta.2015.05.072.

[42] G. Ma, M. Yang, C. Li, H. Tan, L. Deng, S. Xie, F. Xu, L. Wang, Y. Song, Preparation of spinel nickel-cobalt oxide nanowrinkles/reduced graphene oxide hybrid for nonenzymatic glucose detection at physiological level, Electrochim. Acta. 220 (2016) 545–553. doi:10.1016/j.electacta.2016.10.163.

[43] K.S. Novoselov, V.I. Fal'ko, L. Colombo, P.R. Gellert, M.G. Schwab, K. Kim, A roadmap for graphene., Nature. 490 (2012) 192–200. doi:10.1038/nature11458.

[44] A. Adán-Más, D. Wei, Photoelectrochemical Properties of Graphene and Its Derivatives, Nanomaterials. 3 (2013) 325–356. doi:10.3390/nano3030325.

[45] I. Jung, D.A. Dikin, R.D. Piner, R.S. Ruoff, Tunable Electrical Conductivity of Individual Graphene Oxide Sheets Reduced At "Low" Temperatures, Nano Lett. 8 (2008) 4283.

[46] T. Schwamb, B.R. Burg, N.C. Schirmer, D. Poulikakos, An electrical method for the measurement of the thermal and electrical conductivity of reduced graphene oxide nanostructures, Nanotechnology. 20 (2009). doi:10.1088/0957-4484/20/40/405704.

[47] L. Ma, X. Shen, Z. Ji, X. Cai, G. Zhu, K. Chen, Porous NiCo2O4 nanosheets/reduced graphene oxide composite: Facile synthesis and excellent capacitive performance for supercapacitors, J. Colloid Interface Sci. 440 (2015) 211–218. doi:10.1016/j.jcis.2014.11.008.

[48] M.C. Biesinger, B.P. Payne, A.P. Grosvenor, L.W.M. Lau, A.R. Gerson, R.S.C. Smart, Resolving surface chemical states in XPS analysis of first row transition metals, oxides and hydroxides: Cr, Mn, Fe, Co and Ni, Appl. Surf. Sci. 257 (2011) 2717–2730. doi:10.1016/j.apsusc.2010.10.051.

[49] M.C. Biesinger, B.P. Payne, L.W.M. Lau, A. Gerson, R.S.C. Smart, X-ray photoelectron spectroscopic chemical state Quantification of mixed nickel metal, oxide and hydroxide systems, Surf. Interface Anal. 41 (2009) 324–332. doi:10.1002/sia.3026.

[50] A.P. Grosvenor, M.C. Biesinger, R.S.C. Smart, N.S. McIntyre, New interpretations of XPS spectra of nickel metal and oxides, Surf. Sci. 600 (2006) 1771–1779. doi:10.1016/j.susc.2006.01.041.

[51] H.A.E. Hagelin-Weaver, J.F. Weaver, G.B. Hoflund, G.N. Salaita, Electron energy loss spectroscopic investigation of Ni metal and NiO before and after surface reduction by Ar+bombardment, J. Electron Spectros. Relat. Phenomena. 134 (2004) 139–171. doi:10.1016/j.elspec.2003.10.002.

[52] A.G. Marrani, V. Novelli, S. Sheehan, D.P. Dowling, D. Dini, Probing the Redox States at the Surface of Electroactive Nanoporous NiO Thin Films, (2014).

[53] R.P. Sen, G.S. K., Calculation of multiplet structure of core p-vacancy levels. II, Phys. Rev. B. 12 (1975).

[54] J. Yang, H. Liu, W.N. Martens, R.L. Frost, Synthesis and Characterization of Cobalt Hydroxide , Cobalt Oxyhydroxide , and Cobalt Oxide Nanodiscs, J. Phys. Chem. C. 114 (2010) 111–119.

[55] L. Ma, X. Shen, H. Zhou, Z. Ji, K. Chen, G. Zhu, High performance supercapacitor electrode materials based on porous NiCo2O4 hexagonal nanoplates/reduced graphene oxide composites, Chem. Eng. J. 262 (2015) 980–988. doi:10.1016/j.cej.2014.10.079.

[56] W. Huang, S. Ding, Y. Chen, W. Hao, X. Lai, J. Peng, J. Tu, Y. Cao, X. Li, 3D NiO hollow sphere/reduced graphene oxide composite for high-performance glucose biosensor, Sci. Rep. 7 (2017) 5220. doi:10.1038/s41598-017-05528-1.

[57] S.P. Lim, N.M. Huang, H.N. Lim, Solvothermal synthesis of SnO2/graphene nanocomposites for supercapacitor application., Ceram. Int. 39 (2013) 6647–6655. doi:10.1016/j.ceramint.2013.01.102.

[58] H. Wang, H. Yi, X. Chen, X. Wang, Asymmetric supercapacitors based on nano-architectured nickel oxide/graphene foam and hierarchical porous nitrogen-doped carbon nanotubes with ultrahigh-rate performance, J. Mater. Chem. A. 2 (2014) 3223–3230. doi:10.1039/C3TA15046A.

[59] J. Hong, M.K. Park, E.J. Lee, D. Lee, D.S. Hwang, S. Ryu, Origin of New Broad Raman D and G Peaks in Annealed Graphene, Sci. Rep. 3 (2013) 1–5. doi:10.1038/srep02700.

[60] R. Kumar, B.R. Mehta, M. Bhatnagar, R. S, S. Mahapatra, S. Salkalachen, P. Jhawar, Graphene as a transparent conducting and surface field layer in planar Si solar cells, Nanoscale Res. Lett. 9 (2014) 349. doi:10.1186/1556-276X-9-349.

[61] J.-H. Zhong, A.-L. Wang, G.-R. Li, J.-W. Wang, Y.-N. Ou, Y.-X. Tong, Co3O4/Ni(OH)2 composite mesoporous nanosheet networks as a promising electrode for supercapacitor applications, J. Mater. Chem. 22 (2012) 5656. doi:10.1039/c2jm15863a.

[62] Z. Liu, K. Xiao, Q. Xu, N. Li, Y. Su, H. Wang, S. Chen, Fabrication of hierarchical flower-like super-structures consisting of porous NiCo2O4 nanosheets and their electrochemical and magnetic properties, RSC Adv. 3 (2013) 4372. doi:10.1039/c3ra23084h.

[63] Y. Chuminjak, S. Daothong, A. Kuntarug, High-performance Electrochemical Energy Storage Electrodes Based on Nickel Oxide-coated Nickel Foam Prepared by Sparking Method, Electrochim. Acta. 238 (2017) 298–309. doi:10.1016/j.electacta.2017.03.190.

[64] H. Zhang, X. Zhang, D. Zhang, X. Sun, H. Lin, C. Wang, One-Step Electrophoretic Deposition of Reduced Graphene Oxide and Ni(OH)2 Composite Films for Controlled Syntheses Supercapacitor Electrodes, J. Phys. Chem. B. 117 (2013) 1616–1627.

[65] Y. Bai, M. Liu, J. Sun, L. Gao, Fabrication of Ni-Co binary oxide/reduced graphene oxide composite with high capacitance and cyclicity as efficient electrode for supercapacitors, Ionics (Kiel). 22 (2016) 535–544. doi:10.1007/s11581-015-1576-y.

[66] X. Lu, X. Huang, S. Xie, T. Zhai, C. Wang, P. Zhang, M. Yu, W. Li, C. Liang, Y. Tong, Controllable synthesis of porous nickel–cobalt oxide nanosheets for supercapacitors, J. Mater. Chem. 22 (2012) 13357. doi:10.1039/c2jm30927k.

[67] R.P. Silva, S. Eugénio, R. Duarte, T.M. Silva, M.J. Carmezim, M.F. Montemor, Co-Electrochemical Response of 70Co-30Ni Highly Branched 3D-Dendritic Structures for Charge Storage Electrodes, Electrochim. Acta. 167 (2015) 13–19. doi:10.1016/j.electacta.2015.03.083.

[68] G. Wang, L. Zhang, J. Zhang, A review of electrode materials for electrochemical supercapacitors, Chem. Soc. Rev. 41 (2012) 797–828. doi:Doi 10.1039/C1cs15060j.

[69] T. Brousse, D. Belanger, J.W. Long, To Be or Not To Be Pseudocapacitive?, J. Electrochem. Soc. 162 (2015) A5185–A5189. doi:10.1149/2.0201505jes.

[70] X. Wang, C. Yan, A. Sumboja, P. See, High performance porous nickel cobalt oxide nanowires for asymmetric supercapacitor, Nano Energy. 3 (2014) 119–126. doi:10.1016/j.nanoen.2013.11.001.

[71] X. Zhao, X. Li, Y. Huang, Z. Su, J. Long, S. Zhang, J. Sha, T. Wu, R. Wang, Electrochemical performances of graphene nanoribbons interlacing hollow NiCo oxide nanocages, J. Nanoparticle Res. 19 (2017). doi:10.1007/s11051-017-4078-1.

[72] S.S. Yang, L.Y. Lin, X. Li, C.W. Ma, H.X. Lai, L.Y. Lin, Methodology for synthesizing the nickel cobalt hydroxide/oxide and reduced graphene oxide complex for energy storage electrodes, J. Energy Storage. 14 (2017) 112–124. doi:10.1016/j.est.2017.09.015.

[73] M. Yu, J. Chen, J. Liu, S. Li, Y. Ma, J. Zhang, J. An, Mesoporous NiCo2O4nanoneedles grown on 3D graphene-nickel foam for supercapacitor and methanol electro-oxidation, Electrochim. Acta. 151 (2015) 99–108. doi:10.1016/j.electacta.2014.10.156.

[74] M. Rajkumar, C.T. Hsu, T.H. Wu, M.G. Chen, C.C. Hu, Advanced materials for aqueous supercapacitors in the asymmetric design, Prog. Nat. Sci. Mater. Int. 25 (2015) 527–544. doi:10.1016/j.pnsc.2015.11.012.

[75] D.B. Murray, J.G. Hayes, Cycle testing of supercapacitors for long-life robust applications, IEEE Trans. Power Electron. 30 (2015) 2505–2516. doi:10.1109/TPEL.2014.2373368.

[76] S. Saxena, C. Le Floch, J. Macdonald, S. Moura, Quantifying EV battery end-of-life through analysis of travel needs with vehicle powertrain models, J. Power Sources. 282 (2015) 265–276. doi:10.1016/j.jpowsour.2015.01.072.

[77] P.J. Tsai, S.L.I. Chan, Nickel-based batteries: materials and chemistry, Woodhead Publishing Limited, 2013. doi:10.1533/9780857097378.3.309.

[78] V. Pralong, A. Delahaye-Vidal, Y. Chabre, B. Beaudoin, J.-M. Tarascon, The Outcome of Cobalt in the Nickel–Cobalt Oxyhydroxide Electrodes of Alkaline Batteries, J. Solid State Chem. 162 (2001) 270–281. doi:10.1006/jssc.2001.9293.

[79] C. Faure, Y. Borthomieu, C. Delmas, M. Fouassier, Infrared characterization of turbostratic α- and well crystallized α*-cobalted nickel hydroxides, J. Power Sources. 36 (1991) 113–125. doi:http://dx.doi.org/10.1016/0378-7753(91)80008-L.

[80] C. Faure, C. Delmas, P. Willmann, Electrochemical behavior of α-cobalted nickel hydroxide electrodes, J. Power Sources. 36 (1991) 497–506. doi:http://dx.doi.org/10.1016/0378-7753(91)80075-9.

[81] C. Delmas, C. Faure, Y. Borthomieu, The effect of cobalt on the chemical and electrochemical behaviour of the nickel hydroxide electrode, Mater. Sci. Eng. B. 13 (1992) 89–96. doi:10.1016/0921-5107(92)90147-2.

[82] S.P. Mitoff, Electrical conductivity and thermodynamic equilibrium in nickel oxide, J. Chem. Phys. 727 (1961) 882–889. doi:10.1063/1.1701231.

[83] B.K. Kim, V. Chabot, A. Yu, Carbon nanomaterials supported Ni(OH)2/NiO hybrid flower structurefor supercapacitor, Electrochim. Acta. 109 (2013) 370–380. doi:10.1016/j.electacta.2013.07.119.

[84] B. Yan, M. Li, X. Li, Z. Bai, L. Dong, D. Li, Electrochemical impedance spectroscopy illuminating performance evolution of porous core-shell structured nickel/nickel oxide anode materials, Electrochim. Acta. 164 (2015) 55–61. doi:10.1016/j.electacta.2015.02.178.

[85] C. Faure, C. Delmas, M. Fouassier, P. Willmann, Preparation and characterization of cobalt-substituted α-nickel hydroxides stable in KOH medium Part I. α′-hydroxide with an ordered packing, J. Power Sources. 35 (1991) 249–261. doi:http://dx.doi.org/10.1016/0378-7753(91)80110-J.

[86] K. V. Rao, a. Smakula, Dielectric properties of cobalt oxide, nickel oxide, and their mixed crystals, J. Appl. Phys. 36 (1965) 2031–2038. doi:10.1063/1.1714397.

[87] P. Hermet, L. Gourrier, J. Bantignies, D. Ravot, T. Michel, S. Deabate, P. Boulet, F. Henn, Dielectric , magnetic , and phonon properties of nickel hydroxide, Phys. Rev. B. 235211 (2011) 1–10. doi:10.1103/PhysRevB.84.235211.

[88] I. Petousis, D. Mrdjenovich, E. Ballouz, M. Liu, D. Winston, W. Chen, T. Graf, T.D. Schladt, K.A. Persson, F.B. Prinz, High-throughput screening of inorganic compounds for the discovery of novel dielectric and optical materials, Sci. Data. 4 (2017) 160134. doi:10.1038/sdata.2016.134.

3.5 Comparative study of nickel-cobalt hydroxides and oxyhydroxides for energy storage applications during their delamination.

Alberto Adán-Más[a,b,*], Jacob Olchowka [b,c], Cyril Aymonnier [b], Lydie Bourgeois[d,e], Philippe Legros[f], Patrizia Paradiso[g], M. F. Montemor[a], Liliane Guerlou-Demourgues[b,c,*]

[a] Centro de Química Estrutural-CQE, DEQ, Instituto Superior Técnico, Universidade de Lisboa, 1049-001, Lisboa, Portugal

[b] CNRS, University of Bordeaux, Bordeaux INP, ICMCB UPR 9048, 33600 Pessac, France

[c] RS2E, Réseau Français sur le Stockage Electrochimique de l'Energie, FR CNRS 3459, France.

[d] Université de Bordeaux, ISM, Groupe de Spectroscopie Moléculaire, F-33405, Talence, France.

[e] Bordeaux INP, ISM, CNRS UMR 5255, F-33405, Talence, France.

[f] PLACAMAT UMS 3626, CNRS-Université de Bordeaux, F-33608 Pessac Cédex, France

[g] IDMEC – Instituto de Engenharia Mecánica, Universidade de Lisboa, 1049-001, Lisboa, Portugal

Keywords: Nickel-cobalt hydroxides; Nickel-cobalt oxides; Exfoliation; Energy storage

Abstract

Nickel-cobalt hydroxide and nickel-cobalt oxyhydroxide have been respectively delaminated by lactate and tetrabutylammonium (TBA^+) intercalation in aqueous media. The electrochemical performance of the different materials obtained during delamination has been evaluated, with special emphasis on the effect of the intercalated species and their influence on the behaviour of the delaminated material for energy storage applications. On the one hand, it is shown that intercalation of lactate molecules leads to blockage of the electrode-electrolyte interaction, with subsequent capacity fade and hampered electrochemical performance. On the other hand, delamination in TBA^+, reported for the first time for nickel-cobalt oxyhydroxide in aqueous media, serves as an excellent tool to increase the number of electrochemically active sites and enhances the capacity of nickel-cobalt oxyhydroxide. Results show an increase in capacity from 112 $mA{\cdot}h{\cdot}g^{-1}$ in 1M LiOH at 1 $A{\cdot}g^{-1}$ for the non-delaminated precursor to 165 $mA{\cdot}h{\cdot}g^{-1}$ after exfoliation and re-stacking. Thus, carefully designed exfoliation is a promising route to enhance the performance of electrode materials for energy storage applications.

3.5.1. Introduction

The electrochemical performance of energy storage devices depends on the selection of electrode materials, which are usually optimised to obtain maximum capacity/capacitance, specific power or cycling stability, depending upon application. Nonetheless, active surface area is always a critical parameter. Related to charge storage, chemical and morphological stability, electrode-electrolyte interaction and electron and ion transport, a maximized surface area is of extreme importance in the development of novel materials. For that reason, nanostructured materials, in particular, two-dimensional layered materials, have become a field of great interest.

Layered double hydroxides (LDHs), also known as anionic clays, have been pin-pointed as promising pseudocapacitive materials because of their high redox activity, low cost and environmentally friendliness. LDHs are two-dimensional ionic lamellar materials consisting of positively charged brucite-like layers with an interlayer region containing either solvent molecules or anionic species. In general, they have divalent or trivalent metal cations with the generic formula; $M^{2+}_{1-x}M^{3+}_{x}(OH)_2][A^{n-}]_{x/n}\cdot zH_2O$. A part of the divalent metal ions (M^{2+}, for example, Mg^{2+}, Fe^{2+}, Co^{2+}, Cu^{2+}, Ni^{2+} or Zn^{2+}) are coordinated octahedrally by hydroxyl groups and can be replaced by trivalent metals (M^{3+}, for instance, Al^{3+}, Cr^{3+}, Ga^{3+}, Mn^{3+} or Fe^{3+}) with a molar ratio $M^{3+}/(M^{2+}+M^{3+})$ typically between 0.2 and 0.4. The anion is usually CO_3^{2-}, but it can be substituted by SO_4^{2-}, Cl^-, etc. or organic anions such as acetates or dodecyl sulphate, for instance [1].

However, layered double hydroxide materials present a major limitation: reduced accessibility to the inner surface of the host layers by the electrolyte, which leads to reduced active surface area for energy storage applications. For that reason, many efforts have been made to delaminate such materials. In addition, if the material is successfully delaminated, the positively charged layers can work as building blocks to produce functional materials by integrating them with negatively charged species. Consequently, many attempts have been done to exfoliate different types of LDH [1]. The most common procedure consists in the intercalation of molecules/ions in the interlamellar space and the subsequent delamination in the appropriate solvent. Many solvents have been used, such as butanol [2], acrylates[3], toluene[4] or formamide [5,6] among others. However, from an environmental and practical perspective, it is interesting to achieve delamination in water. The first reported aqueous-based delamination was performed by Hibino et al. [7] for Mg-Al-lactate. The method presents three main advantages compared to delamination in organic solvents, namely, the exclusive use of water, the higher concentration achieved in the delaminated colloidal suspension and, finally, the fact that it does not require heat during the process. Henceforward, other materials have been delaminated in a similar fashion, such as Zn-Al-lactate [8].

Nickel hydroxide and cobalt hydroxide exfoliation are of special interest for energy storage applications. On the one hand, nickel is relatively abundant and cheap, it has a well-known electrochemical activity and a high charge-storage capability [9]. However, nickel-based materials for energy storage applications, this is mainly NiO and $Ni(OH)_2$, face several disadvantages, such as high resistivity [10]. Cobalt-based materials (Co_3O_4 and $Co(OH)_2$) are also promising candidates for energy storage applications due to their larger surface area, high conductivity of cobalt oxyhydroxide and excellent reversible redox reactions that translate into good cycling stability [10]. However, they either present low charge-storage capacity values or short potential ranges, for that reason, its combination with nickel (hydr)oxides is of great interest. Consequently, nickel-cobalt

hydroxides and oxyhydroxides were considered for delamination and energy storage electrode applications in this work.

Nickel hydroxide, cobalt hydroxide and nickel-cobalt hydroxides were successfully delaminated in water by the intercalation of lactates by Lang et al. [11–13]. They also investigated the electrochemical activity by cyclic voltammetry, although no in-depth study for energy storage applications was done. Another known route is exfoliation of oxide and oxyhydroxide materials by means of cation intercalation. A common feature of layered oxides is their cation-exchange property, which enables the modification of the interslab space, ultimately leading to exfoliation. As Sasaki and Ma pointed out [14], there is a well-established route for the exfoliation of layered metal oxides, which consists in solid-state calcination synthesis of precursor materials, with posterior acidification to produce their hydrated protonic form. Finally, they are modified with positively-charged bulky organic ions (TMA^+, TBA^+, etc.) that increase the interlayer distance, decrease the electrostatic interaction between the layers and enables their delamination. Several materials have been exfoliated in that manner, such as MnO_2[15], TaO_3 [16] or $HCoO_2$ [17]. However, to the best of the author's knowledge, neither delamination of nickel nor mixed nickel-cobalt oxyhydroxide has been done.

The different materials obtained during the delamination process of nickel-cobalt hydroxide materials in water by means of lactate intercalation are here studied as potential electrode material for charge-storage in alkali media. In addition, we report delamination of nickel-cobalt oxyhydroxide in TBA-OH and study the behaviour of the different phases obtained during the process. Finally, the influence of different cations in the electrolyte, namely K^+ and Li^+, is considered during the charge-discharge of the different active materials.

3.5.2. Experimental

3.5.2.1 Delamination of nickel-cobalt hydroxide in aqueous media.

The process undertaken for delamination of nickel-cobalt hydroxide by lactate intercalation is illustrated in Fig. 3.5.1 and detailed hereafter.

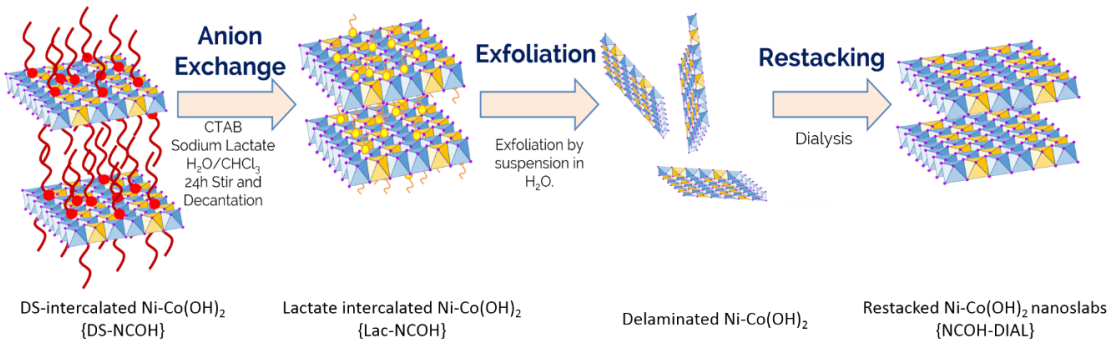

Fig. 3.5.1. Diagram of the delamination process undertaken for nickel-cobalt hydroxide.

3.5.2.1.1 Synthesis of SDS-intercalated nickel-cobalt hydroxide.

Synthesis of lactate intercalated nickel-cobalt hydroxide material proceeded in a modified version to that found in Schneiderová et al. [13] with the addition of a final electrochemical activation step by means of dialysis. First, an SDS-intercalated precursor was synthesized. In a typical experiment, nickel nitrate hexahydrate (2.181 grams, Sigma-Aldrich) and cobalt nitrate hexahydrate (6.543 grams, Alfa Aesar) were diluted in 1 L of distilled water together with 43.257 grams of sodium dodecyl sulfate

(SDS, Sigma-Aldrich) and 25.234 grams of hexamethylenetetramine (HMT, Alfa Aesar). Then, the solution was introduced into a 2 L stainless steel hydrothermal reactor. The temperature was gradually increased up to 120ºC and maintained for 8 hours at a pressure below 2 bars. The system was then gradually cooled down to room temperature and the solid powder was recovered, centrifuged at 4000 rpm and cleaned four times with both water and ethanol. The obtained product is named as DS-NCOH.

3.5.2.1.2 Synthesis of lactate-intercalated nickel-cobalt hydroxide.

0.60 grams of DS-NCOH were dispersed in 50 mL of deionized water containing 0.87 grams of sodium lactate (Sigma-Aldrich) and 2.19 g of cetrimonium bromide (CTAB, Sigma-Aldrich). The suspension was mixed with 150 mL of chloroform (Sigma-Aldrich) and stirred for 24h at room temperature. After separating the phases, the water phase was centrifuged at 4000 rpm for 10 minutes to recover the lactate intercalated nickel-cobalt hydroxide material. The resulting product was washed several times with acetone and ethanol. A green-brown powder was finally obtained, which is denominated as Lac-NCOH.

3.5.2.1.3 Delamination and re-stacking of nickel-cobalt hydroxide nanosheets in water.

When Lac-NCOH is cleaned with water, it delaminates, producing a colloidal suspension. For that, 100 mg of lactate intercalated material were added in 100 mL water. It is worth mentioning that, if the material is not fully delaminated and some suspended particles are obtained, it can be further exfoliated by adding extra 100 mL of solvent, in this case, distilled water. After its suspension, the material is centrifuged at 2000 and 4000 rpm for 4 minutes to remove un-exfoliated material, deposited at the bottom of the vessel. The resulting supernatant solution contains the exfoliated nanosheets. Then, to restack the material, the nanosheet suspension is dialyzed using a 20K MWCO dialysis flask. After dialysis, the material is recovered, washed with ethanol and acetone several times and dried overnight at 40ºC. The material is denominated as Lac-NCOH-DIAL (DIAL as “dialysis”).

3.5.2.2 Delamination of nickel-cobalt oxyhydroxide in aqueous media.

The process undertaken for the delamination of nickel-cobalt oxyhydroxide in tetrabutylammonium hydroxide is exemplified in Fig. 3.5.2 and detailed hereinafter.

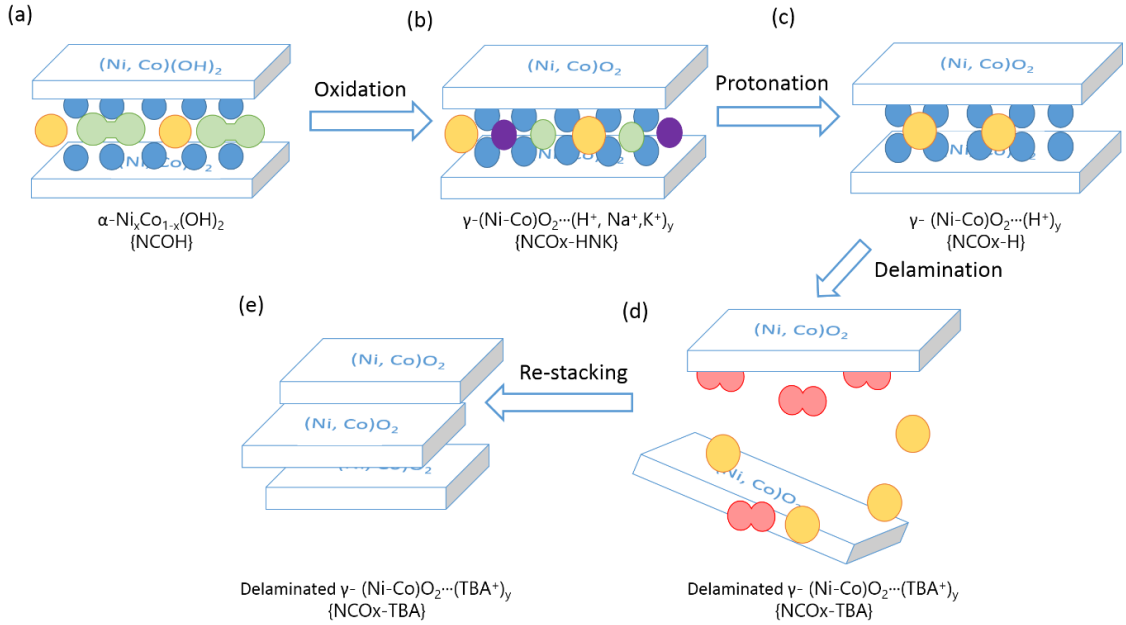

Fig. 3.5.2. Schematic of the exfoliation process for γ-$Ni_xCo_{1-x}O_2$ nanoslabs.

3.5.2.2.1 Synthesis of α-nickel-cobalt hydroxide

Typically, 5 g of nickel nitrate hexahydrate and 10 g of cobalt nitrate hexahydrate were dissolved in 100 mL of distilled water. 40 mL of 2M NaOH containing 1.5 mL of H_2O_2 were quickly poured in the solution forming a green-brown precipitate of α-Ni-Co$(OH)_2\cdot(CO_3^{2-}, 2NO_3^-)_y$. It was then centrifuged at 4000 rpm for 5 minutes and washed with H_2O and ethanol 6 times until neutral pH to remove impurities. Approximately 7 grams of the α phase, named as NCOH, were recovered after the powder was dried at 40ºC for 24h.

3.5.2.2.2 Oxidation reaction to γ-nickel-cobalt oxyhydroxide

2.6 g of NCOH were suspended in a mixture of 20 mL of NaClO 10M (Prolabo) with 80 mL of KOH 5M and kept under stirring for 24h. The resulting suspension was centrifuged at 4000 rpm for 5 minutes. Once the powder was recovered, it was washed 5 times with distilled water and several times with ethanol until neutral pH. 2.2 grams of the resulting γ-phase were recovered and named as NCOx-HNK {as in Nickel-Cobalt OXide intercalated with protons (H), sodium (Na) and potassium (K)}.

3.5.2.2.3 Protonation of γ-nickel-cobalt oxyhydroxide

1.8 grams of NCOx-HNK were suspended in 150 mL of HNO_3 10mM and stirred overnight. The resulting product is a protonated version of the gamma phase in which the sodium and potassium ions intercalated in the interslab distance of material are exchanged by protons. After washing with distilled water and ethanol several times until neutral pH is reached, 1.39 grams of product were recovered and designated as NCOx-H. It is worth mentioning that this step is critical since oxyhydroxides easily dissolve in acid. Higher concentrations and other acids, such as HCl were also tested resulting in the dissolution of the product.

3.5.2.2.4 Delamination and re-stacking of γ-nickel-cobalt oxyhydroxide nanosheets in TBAOH

To maintain a 1:1 H^+:TBA^+ ratio, 0.5 grams of NCOx-H were suspended in a mixture of H_2O: 40% TBAOH (1.5M solution in water, obtained from Acros) containing 2.5mL of TBAOH and 257.5mL of H_2O. The solution was maintained under stirring for 90 days. The resulting black suspension was then centrifuged at 5000 rpm for 10 minutes to remove impurities. Then, the supernatant solution was heated at 50ºC for 10 days to remove the solvent an induce re-stacking of the suspended nanoparticles. The final product is designated as NCOx-TBA.

3.5.2.3 Physico-chemical Characterization

Powder X-Ray Diffraction patterns were obtained using a PANalytical X'Pert Pro Powder Diffractometer in the Brag-Brentano geometry using a monochromator with $K_{\alpha 1}$ line (λ=1.5406 Å) at room temperature, with 2Θ range from 6-80º with a 0.0170º measuring step. The powder was previously grinded to fine powder and measured on a steel powder specimen holder. To avoid signal from the sample holder in the SDS-intercalated and lactate-intercalated samples, capillary X-Ray Diffraction was performed. The powder was introduced in a silicon capillary of 1.0 mm diameter and measured with a PANalytical Empyrean Diffractometer.

Scanning Electron Microscopy direct imaging was performed at the PLateform Aquitaine de Caractérisation des MATériaux (PLACAMAT) by means of a SEM-FEG HR (JEOL 6700F microscope). Transmission Electron Microscopy imaging was performed with a TEM JEOL JEM 1400 Plus microscope, while High-Resolution imaging was obtained by means of a TEM-FEG HR (JEOL 2200FS microscope) working at 200 kV coupled to an EDX JEOL Si-Li detector with an image resolution of 0.19 nm and an EDS point resolution of 1.5 nm. The images for non-exfoliated samples were obtained by suspending a portion of the powder in ethanol and dropping it on top of a carbon coated copper grid. In the case of exfoliated samples, an aliquot was taken of the exfoliated suspension and the carbon-coated grid was simply immersed in the solution.

Fourier-Transform Infrared Spectrometry was performed with a Thermo Electron Corporation Nicolet 5700 equipment in specular mode for wave numbers from 400 cm^{-1} to 4000 cm^{-1}. The powders were previously mixed with KBr at a 1:100 ratio and pressed into disks.

Raman measurements were performed by means of a Yvon Horiba Labram HR-800 micro-spectrometer with a 514.5 nm excitation wavelength (Ar^+ laser) and a power adjusted to ca. 50µW to avoid any degradation of the sample or a LabRAM HR Evolution Raman spectrometer (HORIBA, Jobin Yvon, Edison, NJ) with an operating laser at 532 nm.

Nitrogen adsorption/desorption isotherms were recorded using an ASAP 2020 (Micromeritics) at 377K. Prior the measurements, degasification at 80ºC for 300 minutes and at 110ºC for 200 minutes under high vacuum was performed. The Brunauer-Emmett-Teller specific surface area was computed using adsorption data in the relative pressure (P/P_o) range of 0.18-0.30. The pore size distribution was derived from the amounts adsorbed in the relative pressure range from 0.01-0.99 by means of the adsorption branch using the Barrett-Joyner-Halenda (BJH) method.

Elemental analysis (carbon, hydrogen, nitrogen and sulphur content) were determined by combustion at 920 ºC in a tin foil in excess of oxygen by means of a Thermo Flash

EA 111E Series apparatus. Inductive coupled plasma-optical emission spectroscopy (ICP-OES) was used to obtain the concentration of cobalt, nickel, sodium and potassium. Results were obtained by dissolving 10-20 mg of the powder into HCl, diluted to a concentration in the 1-200 $mg \cdot L^{-1}$ range and analyzed by means of a Varian 720ES ICP-OES spectrometer.

Atomic force microscopy was used to measure the thickness of suspended delaminated nanoparticles. The aqueous suspensions of lactate-intercalated nickel-cobalt hydroxide and tetrabutylammonium-intercalated nickel-cobalt oxyhydroxide were centrifuged at 14600 rpm for 10 minutes. The resulting supernatant solutions were isolated and diluted to double their volume. 1 mL of the diluted solution was dropcasted on top of mica surface and dried at 40ºC for 7 days. A Nanosurf AFM in tapping mode with a silicon pointprobe-plus® Nanosensor cantilever (PPP-NCLAuD-10, gold coated with a resonance frequency of 315 kHz) was used to obtain the delaminated samples topography. The average nanoparticle thickness was determined from at least 4 regions in 2-4 μm^2 AFM images.

3.5.2.4 Electrochemical Characterization

The electrode material consisted of 80% active material, 15% active carbon and 5% of PTFE (Sigma-Aldrich) as binder. The mass of the components was determined by means of a micro-balance Sartorius MC5-0CE with an accuracy of 0.01mg. Once the electrode material was formed, a round area of 1 cm^2 was pressed on a stainless-steel grid by applying 7 tons by means of a hydraulic cylinder press. The mass of active material varied between 1.5 mg to 9.5 mg.

All electrochemical measurements were performed with a three-electrode electrochemical cell by means of an Interface IFC1000-07087 Potentiostat (Gamry Instruments). Platinum foil of 2.5 cm^2 x 2.5 cm^2 was used as counter electrode while SCE electrode was used as reference. LiOH 1M and KOH 1M were used as alkaline electrolytes.

Cyclic voltammetry was carried out at different scan rates (1-20 $mV \cdot s^{-1}$) in a potential window ranging from -0.5V to 0.65V (vs. SCE). Galvanostatic charge-discharge was also carried out at different current densities (1-10 $A \cdot g^{-1}$) in a similar voltage range. Lifetime cycling tests were performed during 5000 charge-discharge cycles at 4 $A \cdot g^{-1}$ for the hydroxide exfoliation route materials and at 10 $A \cdot g^{-1}$ for the oxyhydroxide exfoliation route materials. It is worth mentioning that hydroxide-based cycling tests were performed at lower current density due to poor capacity retention under higher specific currents applied. Also, the materials prepared during the exfoliation of nickel-cobalt hydroxide exhibited an unstable initial performance that was stabilized during the first 1-10 cycles of charge discharge.

3.5.3. Results and Discussion

3.5.3.1. Physico-chemical Characterization

3.5.3.1.1. Nickel-cobalt hydroxide delamination

The synthesis process of nickel-cobalt hydroxide nanosheets is exemplified in Fig. 3.5.1. Essentially, dodecyl sulphate intercalated nickel-cobalt hydroxide is transformed into lactate intercalated nickel-cobalt hydroxide after anion exchange. The lactate intercalated material spontaneously delaminates when dispersed with distilled water. To eliminate lactate residual particles, the material is then subjected to dialysis, after which the material is recovered in its re-stacked form.

3.5.3.1.1.1. X-Ray Diffraction

XRD patterns, presented in Fig. 3.5.3, show the evolution of the phases during the exfoliation process, including α-nickel-cobalt hydroxide obtained by co-precipitation for reference (Fig. 3.5.3a), and confirms the successful intercalation of the large organic anions. From a general point of view, the diagrams were all indexed with a hexagonal cell, as usually reported for this kind of materials. In all cases, the inter-reticular distance of the peak at the lowest angle (001 line) correspond to the interslab, i.e. the distance between two adjacent metal (mixed nickel-cobalt) planes. Normally, this (001) line is accompanied by its subsequent corresponding (002), (003), etc. lines. The inter-reticular distance of the (110) line corresponds to half the distance between two metal (nickel or cobalt) atoms within the slab. It is worth mentioning that these *110* lines, are maintained virtually invariable in all cases, which is proof of the preservation of the nickel-cobalt hydroxide slab, without any variation of the nickel and cobalt oxidation state and composition during all the steps. In addition, the particular asymmetric shape of the (10l) and (110) lines is characteristic of the turbostratic nature of the materials, consisting in a random rotated stacking of the slabs along the hexagonal c axis, while maintaining the interslab space.

In the case of the reference α-nickel-cobalt hydroxide (Fig. 3.5.3a), the first line gives an interslab distance of 7.93 Å, which corresponds to the presence of carbonate anions inserted within the interslab space together with water molecules, as confirmed below by other techniques and already reported [18,19]. When DS^- is intercalated in the interslab distance (Fig. 3.5.3b), 3 lines with inter-reticular distances of 26.48, 12.92 and 8.63 Å appear, attributed to (001), (002) and (003) lines. DS^- is a 12-carbon organic chain that induces expansion of the interslab space up to 26.48 Å when intercalated, distance comparable to previous reports [13]. When lactate material is intercalated (Fig. 3.5.3c), the *001* line shows a distance of 9.42 Å , shorter than for DS^- but longer than in the case of the α structure, which is in accordance with literature [13]. When the material is re-stacked by dialysis (Fig. 3.5.3d), it presents similar peaks to the lactate intercalated material. However, it also presents an extra *001* line, which corresponds to similar values to the α phase. It is possible that, during the re-stacking process in water as solvent, carbonate ions, as exhibiting a strong affinity for this kind of lamellar structures, are incorporated again in the interslab distance to maintain charge electroneutrality between the nickel-cobalt hydroxide slabs. Thus, α-carbonate phase is partially restored. However, lactate molecules are still present in the re-stacked material since its elimination by dialysis is only partial. If lactate removal was complete by dialysis, a peak with an interslab distance of 9.27 Å would not be observed. Therefore, additional purification strategies shall be considered.

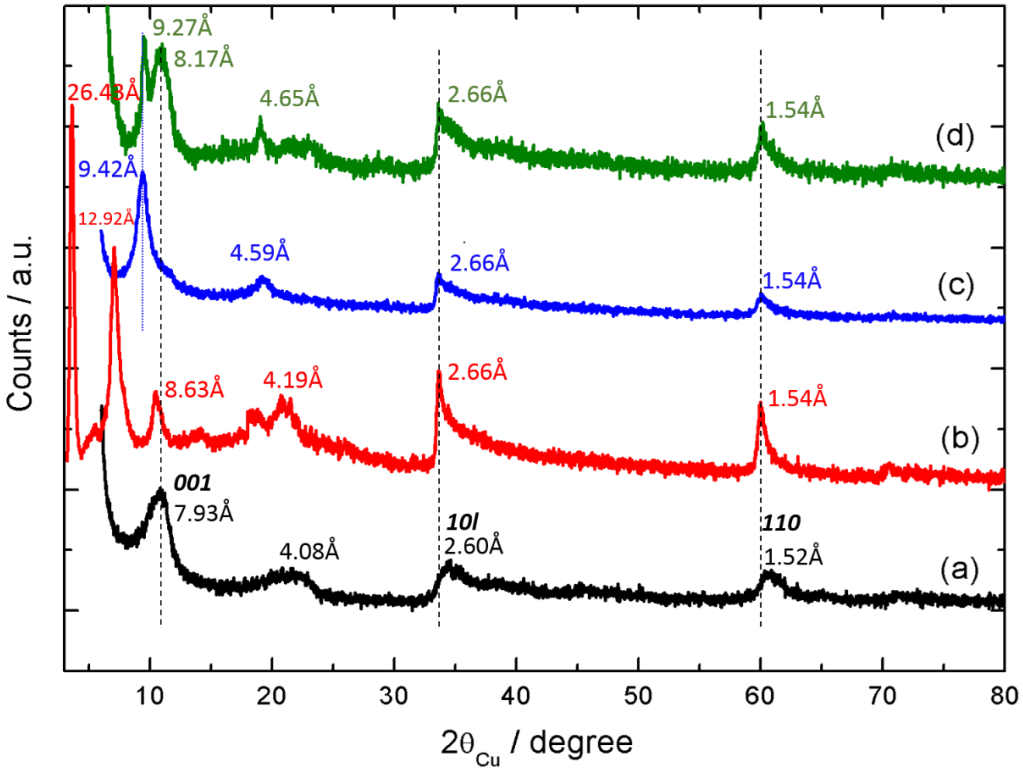

Fig. 3.5.3. X-Ray Diffraction patterns for (a) NCOH taken as reference material, (b) SDS-NCOH, (c) Lac-NCOH and (d) NCOH-DIAL after exfoliation in H_2O and re-stacking by dialysis. Numbers indicate the inter-reticular distances for each assigned peak, they are deduced by indexation with a hexagonal cell.

3.5.3.1.1.2. Elemental analysis

Chemical analysis are provided in table 3.5.1, in weight percent and in molar ratio of each element over (Ni+Co). Nickel and cobalt are in a 0.27/0.73 atomic proportion for all the materials, ratio that is maintained throughout the entire process, which suggests that slab integrity is preserved during delamination. When dodecyl sulphate is intercalated, large carbon amount is present, which is caused by the successful intercalation of the organic molecule. Once the anion exchange for lactate is performed, the carbon value is relatively maintained, indicating a successful anion exchange. Finally, after dialysis, the carbon and hydrogen amounts are significantly reduced but still relevant, which suggests that lactate removal by dialysis is only partially successful. Thus, it will reasonable to observe certain influence of lactate molecules during the evaluation of the electrochemical performance of the material.

Table 3.5.1
Chemical analysis for the materials obtained during the delamination of nickel-cobalt hydroxide by lactate intercalation in weight percentage and their molar ratio in relation to nickel and cobalt content.

	Weight %				Molar ratio : element/(Ni+Co)			
	Co	Ni	C	H	Co	Ni	C	H
DS-NCOH	55.98	21.06	14.36	3.47	0.73	0.27	0.91	2.63
Lac-NCOH	56.5	19.51	17.14	4.32	0.74	0.26	1.1	3.32
NCOH-Dial	68.28	24.79	3.82	1.71	0.73	0.27	0.2	1.07

3.5.3.1.1.3. Scanning and Transmission electron microscopy

Fig. 3.5.4 shows scanning electron microscopy images of DS^- and lactate intercalated and dialysed nickel-cobalt hydroxide. The dodecyl sulphate-intercalated material (Fig. 3.5.4a) consists of randomly-oriented quasi-hexagonal aggregated platelets of different sizes, of generally around 1 μm in diameter. Similar results are obtained for the lactate-intercalated material, in which platelets seem to have better defined hexagonal shape (Fig. 3.5.4b). Finally, when the lactate material is exfoliated in water and then restacked by dialysis (Fig. 3.5.4c), they recover their original morphology of densely-packed agglomerated nanosheets, as in Fig. 3.5.4a, except that the surface seems to be more rugged and poorly defined.

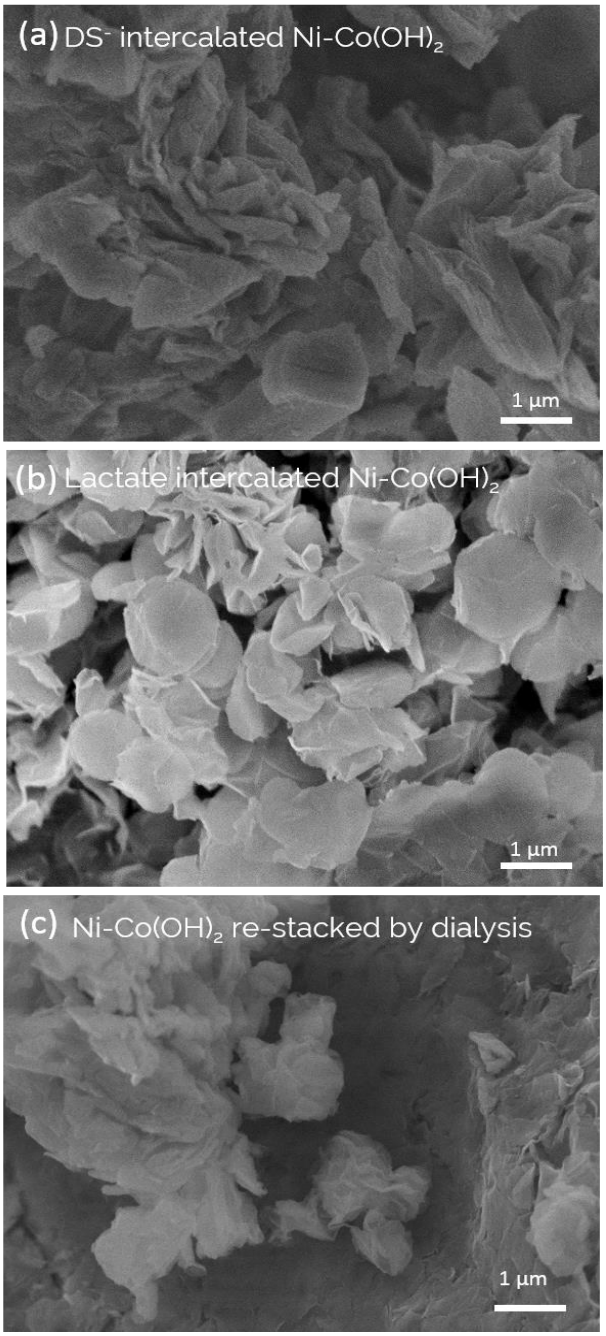

Fig. 3.5.4 Scanning Electron Microscopy images of (a) DS-NCOH, (b) Lac-NCOH and (c) restacked nickel-cobalt hydroxide nanoslabs by dialysis after exfoliation in distilled water (NCOH-DIAL).

Similar results can be observed by Transmission Electron Microscopy (TEM), displayed in Fig. 3.5.5. For the DS-intercalated material, a randomly-oriented agglomerated multi-layered material is obtained. Similar morphology is displayed when lactate is introduced, however, there seems to be a better definition of the few-layer aggregates, suggesting weaker interslab interaction between them. Then, when lactate-intercalated nickel-cobalt hydroxide is introduced in water and delaminated, few-layer Ni-Co$(OH)_2$ aggregated slabs are observed, evidencing the exfoliation process. It must be considered that single monolayers either burn or fold under the electron beam, therefore, no fully extended monolayer image could be obtained. HR-TEM images are presented in Fig. 3.5.6. As shown in HR-TEM, the size of these platelets varies between 500 and 800 nm in diameter. Moreover, between the different hexagonal nanoplatelets, there is a veil-like feature that probably is lactate molecules that fully covers the nanoslabs and interlinks the different nanosheets together. Dodecyl sulphate molecules are bulky molecules that are easily observed by TEM, while lactate molecules, lower in dimension, are likely to cover the surface area of nickel-cobalt hydroxide platelets. Finally, when the delaminated material is centrifuged and restacked, it presents a similar morphology to its precursors.

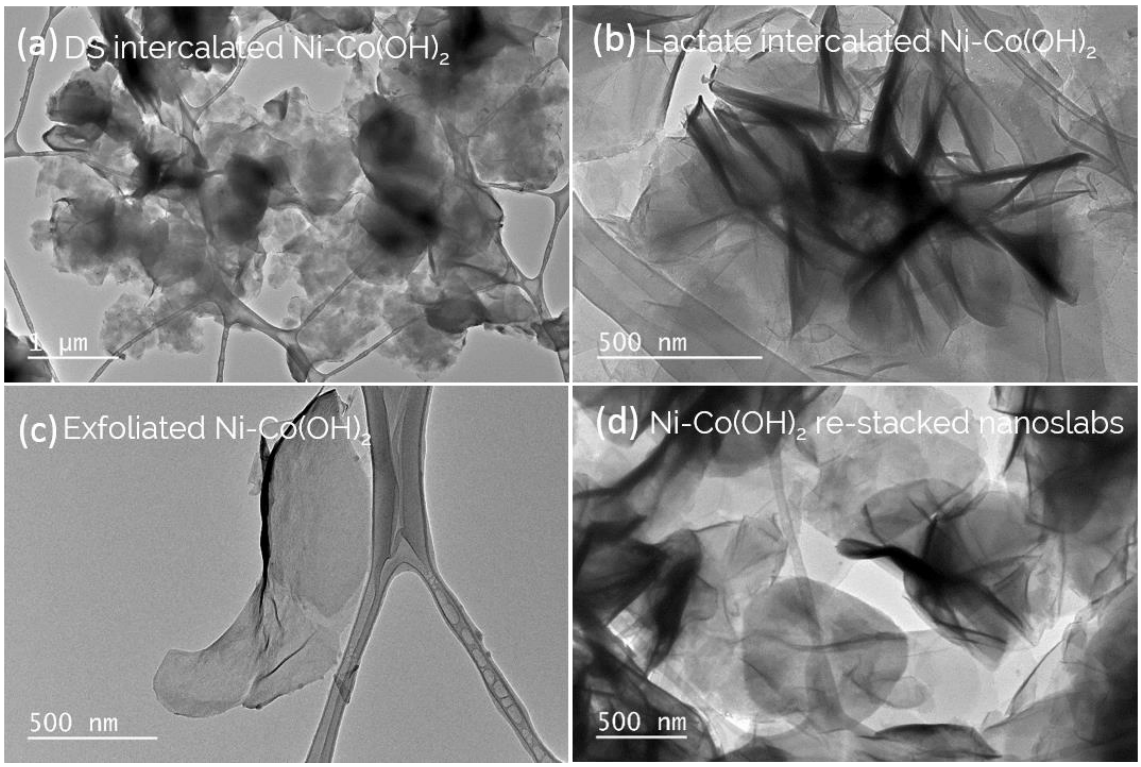

Fig. 3.5.5 Transmission Electron Microscopy images of (a) DS-NCOH, (b) Lac-NCOH, (c) delaminated nanoslabs of lactate intercalated Ni-Co$(OH)_2$ in distilled water and (d) restacked nanoslabs of delaminated Ni-Co$(OH)_2$ slabs obtained by dialysis (NCOH-DIAL).

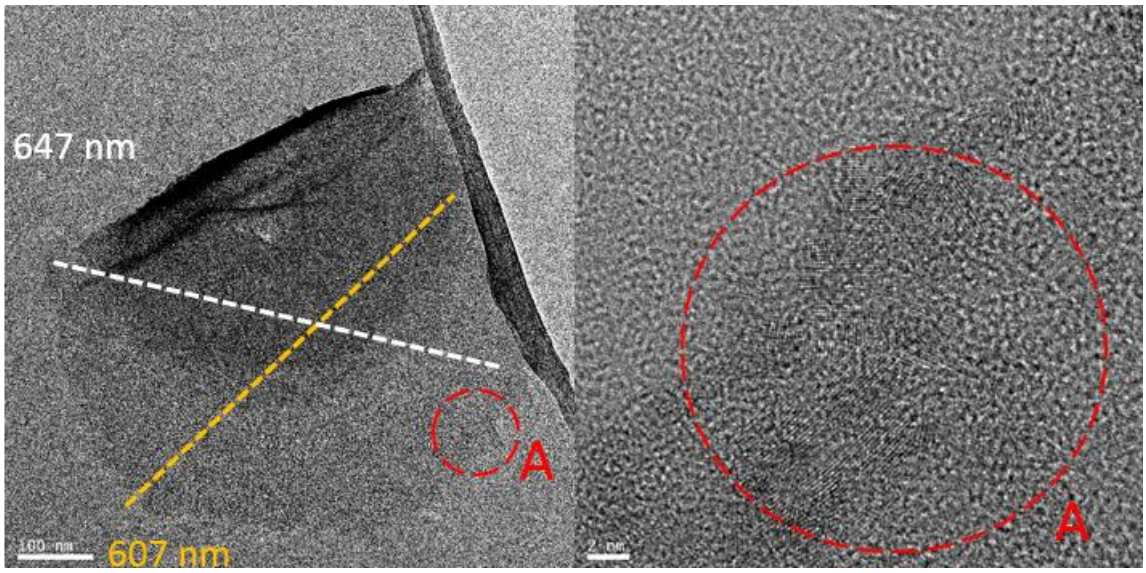

Fig. 3.5.6. HR-TEM images of delaminated lactate-intercalated nickel-cobalt hydroxide in distilled water.

3.5.3.1.1.4. Fourier-transform infrared and Raman spectroscopy

FTIR results for the different materials obtained during delamination are shown in Fig. 3.5.7. NCOH obtained by co-precipitation is also included as reference material. The bands assigned to metal-oxygen Co-O and Ni-O vibrations appear below 700 cm^{-1}[20,21] and, in particular at 665 cm^{-1}. It is worth mentioning that these bands are well-defined for the co-precipitated nickel-cobalt hydroxide while hindered when different intercalated materials are present. Nonetheless, the metal-oxygen signals remain invariable throughout the entire delamination process, confirming that the metal-hydroxide slabs are preserved. Co-precipitated nickel-cobalt hydroxide presents a strong narrow band at 1382 cm^{-1}, corresponding to C-O modes of $-CO_3^{2-}$ at the LDH interlayer. The band at 1639 cm^{-1} is associated to the O-H bending of intercalated water molecules while the major broad band centred at 3442 cm^{-1} is assigned to the stretching vibration of O-H superimposed of structural hydroxyl groups and water molecules [22].

For the DS^- intercalated composite (Fig. 3.5.7b), two bands at 1076 cm^{-1} and 1230 cm^{-1} appear that are associated to S=O antisymmetric stretching of DS^-. Another small band at 1344 cm^{-1} corresponds to traces of HMT that has not reacted. The band at 1465 cm^{-1} is related to the bending vibration of the organic chain of DS^- while the bands at 2917 cm^{-1} and 2848 cm^{-1} are due to the antisymmetric and symmetric $-CH_2$ stretching modes. It is worth mentioning the decrease on the band intensity at 1382 cm^{-1}, associated to carbonate intercalated ions thus confirming their absence, while a similar intensity for the O-H bond signal to the co-precipitated material is obtained.

When lactate is intercalated (Fig. 3.5.7c), sulphate bands (1076, 1230 cm^{-1}) diminish and $-CH_2$ bond signal decreases (2917, 2848 cm^{-1}). However, the H_2O associated bands (1639, 3442 cm^{-1}) become more intense and a band associated to stretching C-OH from lactate appears at 1114 cm^{-1}. COO^- bands, also from lactate, appear at 1583 cm^{-1} and 1382 cm^{-1} [13,22]. After dialysis (Fig. 3.5.7d), the lactate bands at 1382 cm^{-1} and 1583 cm^{-1} are still present, although greatly diminished, while the signal at 1114 cm^{-1}, associated to C-OH, increases its intensity. The H_2O bending and stretching bands gain relevance and a small signal from sulphate, HMT and $-CH_2$ from the intercalation of DS^- are also visible although greatly inhibited. A detail view of the 1390-400 cm^{-1} range is presented in Fig. 3.5.8.

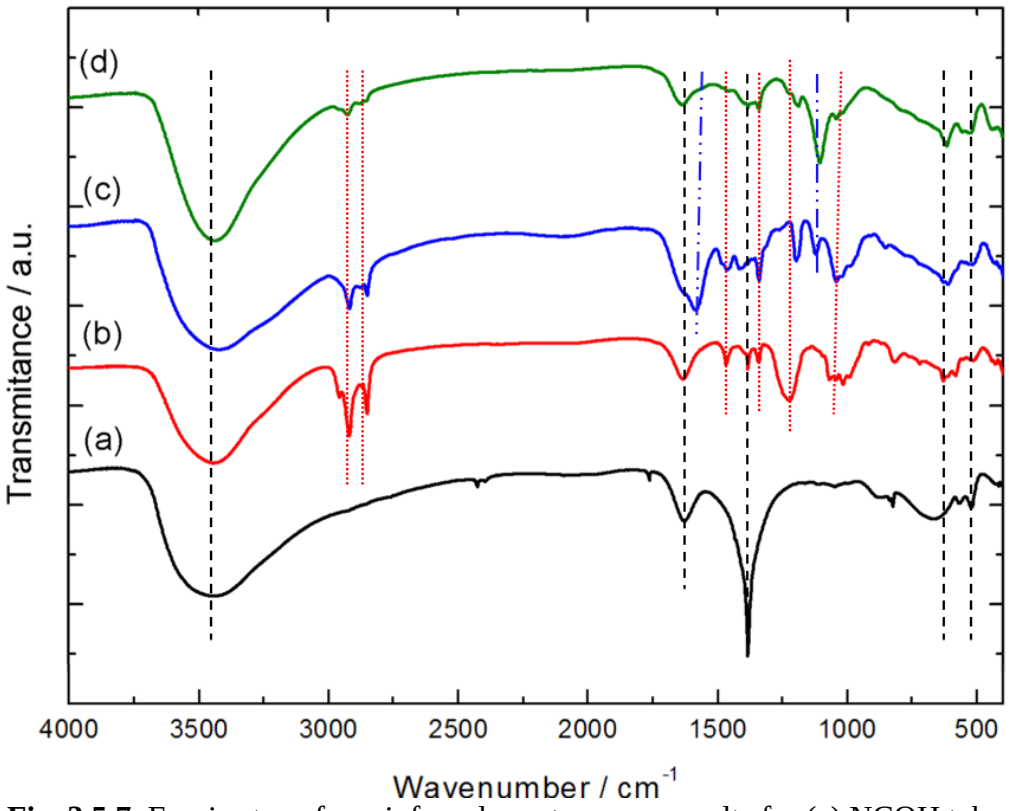

Fig. 3.5.7. Fourier-transform infrared spectroscopy results for (a) NCOH taken as reference material, (b) SDS-NCOH, (c) Lac-NCOH and (d) NCOH-DIAL after exfoliation in H_2O and re-stacking by dialysis.

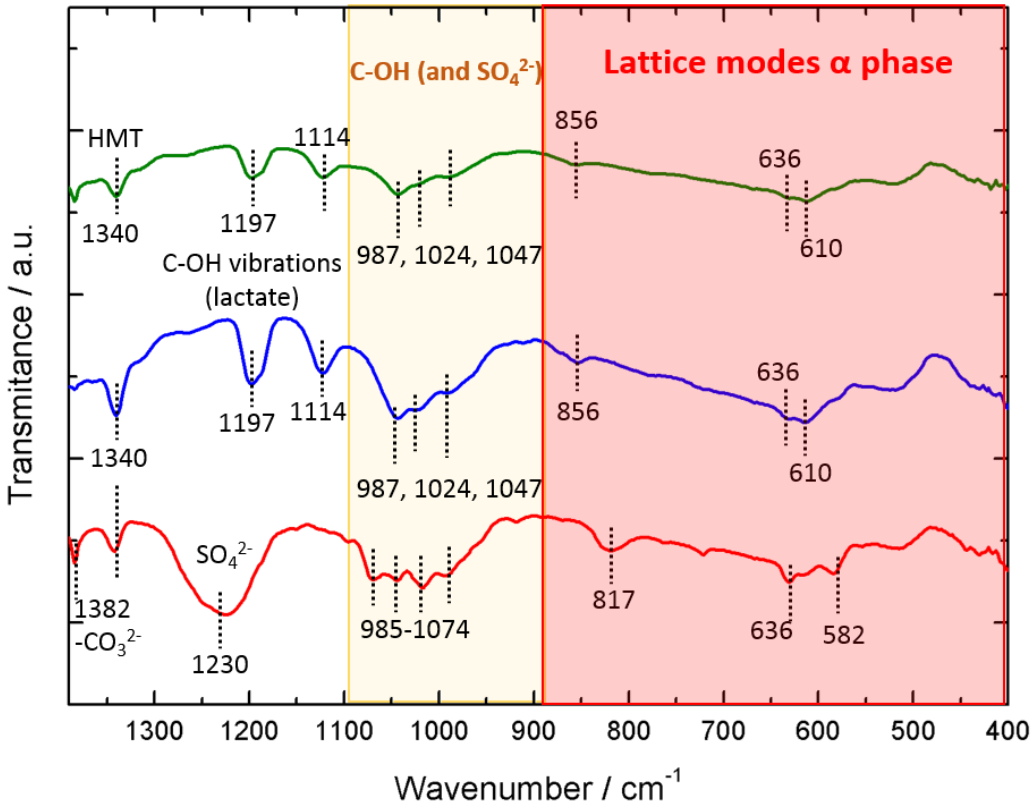

Fig. 3.5.8. Detail of the 400-1390 cm^{-1} section of FTIR spectra for the materials obtained during the delamination of nickel-cobalt hydroxide by lactate intercalation.

Raman results are displayed in Fig. 3.5.9. As it can be seen, the main bands are maintained in all composites throughout the exfoliation process. Two features are, however, different. First, the intensity of the signals in the 2800 to 3060 cm^{-1} range, whose intensity subsequently decreases with each step in the delamination process, agreeing with the theoretical composition of the composites. These bands at 2850 cm^{-1} and 2885 cm^{-1} are assigned to symmetric and anti-symmetric CH_2 stretching modes [22,23]. The organic chain of DS^- is longer than lactate, this is, includes a greater number of -CH_2- groups, resulting in higher intensity of these peaks. When anion exchange for lactate molecules is performed, these lines diminish their intensity. After dialysis, most lactate molecules are removed and, consequently, the signal is hindered.

Second, the band at 1046 cm^{-1} for the co-precipitated material, which is associated to CO_3^{2-} and NO_3^- anions when nickel-cobalt hydroxide is prepared from nitrates, is not present and is substituted by several signals in the 1000-1500 cm^{-1} range [21]. An in-depth evaluation of these peaks is presented in Fig. 3.5.10, which are related to the organic chain of lactate and DS^- [22,24]. It is worth mentioning that the intensity of the lactate-associated peaks become greatly reduced when dialysis is performed. Given these results, the successful intercalation of DS^- and lactate anions and is confirmed, together with dialysis as a purification-restacking method in which lactate is partially removed.

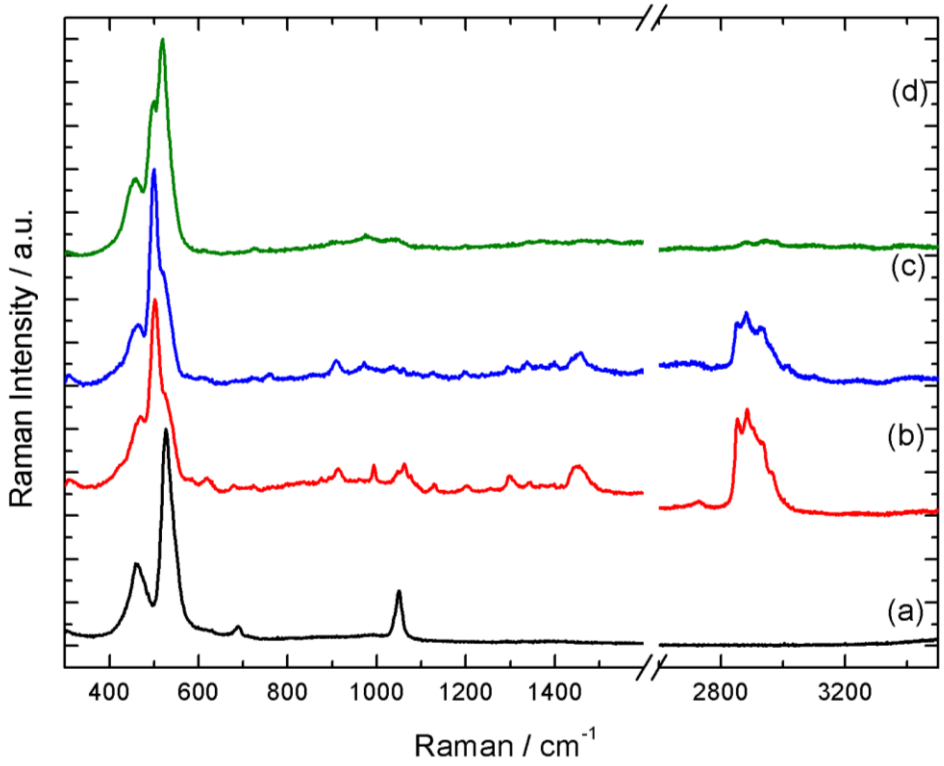

Fig. 3.5.9. Raman results for (a) NCOH taken as reference material, (b) SDS-NCOH, (c) Lac-NCOH and (d) NCOH-DIAL after exfoliation in H_2O and re-stacking by dialysis from 300-1600 cm^{-1} and from 2600 to 3500 cm^{-1}.

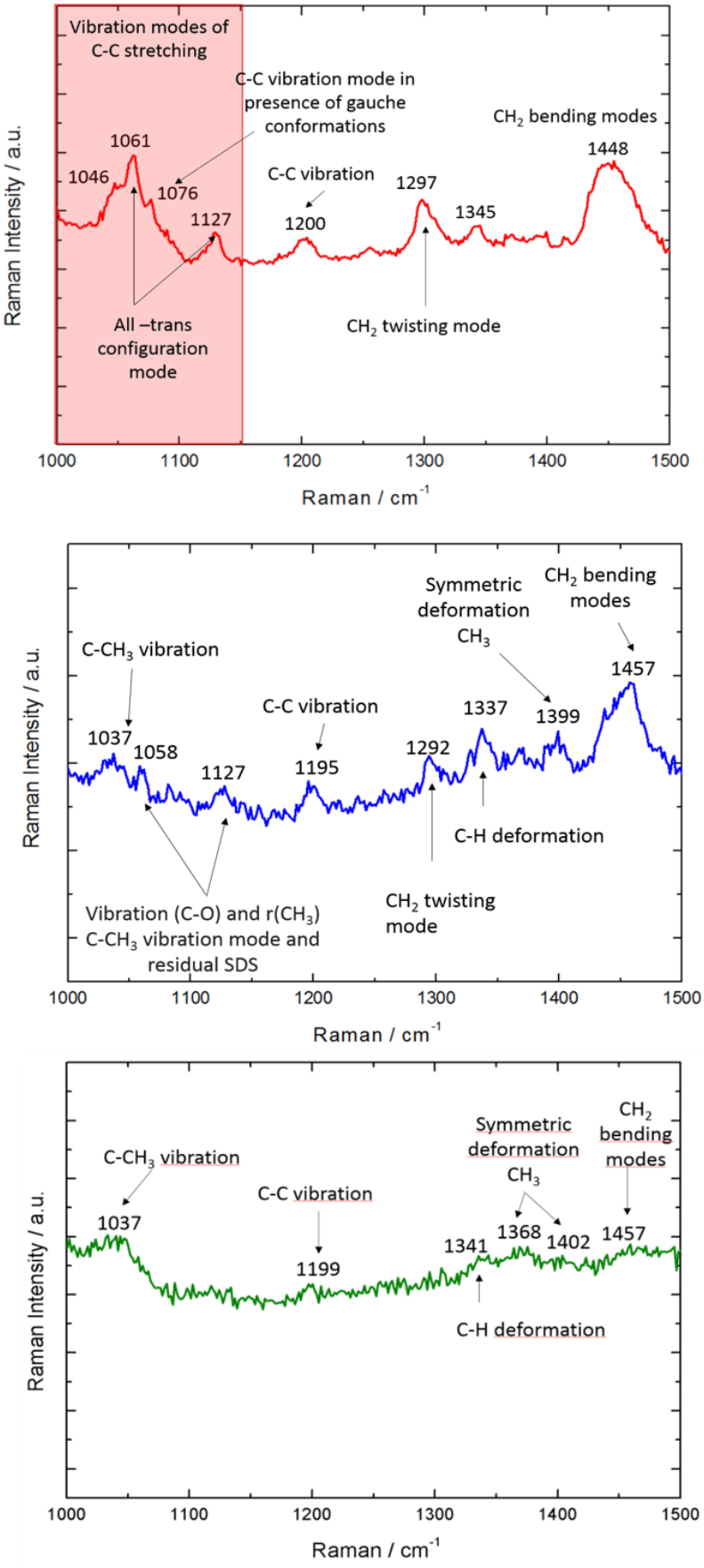

Fig. 3.5.10. Detail of the 1000-1500 cm^{-1} section of Raman spectra for the materials obtained during the delamination of nickel-cobalt hydroxide by lactate intercalation.

3.5.3.1.1.5. Nitrogen adsorption isotherms

Specific surface area of Lac-NCOH was measured by Brunauer-Emmett-Teller (BET) method and the isotherm resulting is included in Fig. 3.5.11. NCOH-DIAL was also analysed, however, results were inconclusive. Lac-NCOH showed an extremely low surface area of only 5 $m^2 \cdot g^{-1}$ in a type II isotherm, indicating the non-porous nature of the material.

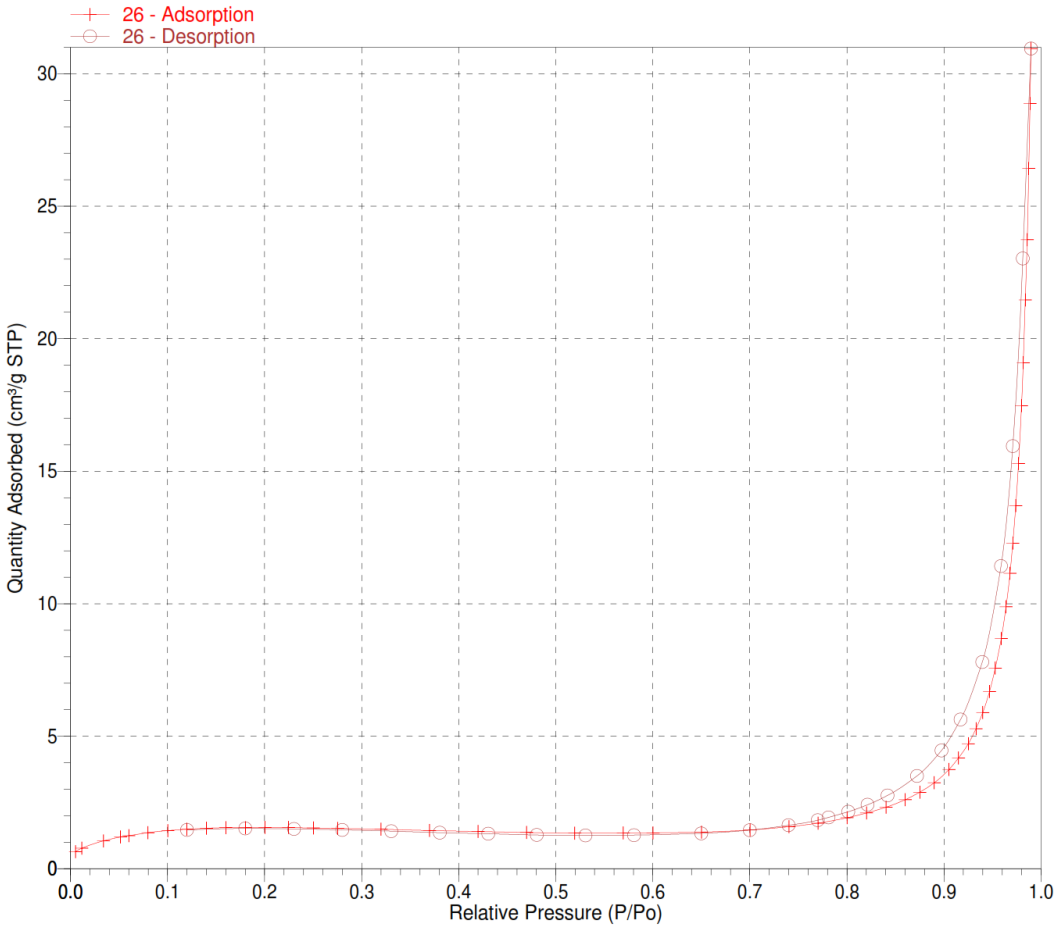

Fig. 3.5.11. BET adsorption-desorption isotherm results for Lac-NCOH.

3.5.3.1.1.6. Atomic force microscopy

AFM results for delaminated lactate intercalated nickel-cobalt hydroxide in distilled water, diluted and dropcasted on top of mica substrate are presented in Fig. 3.5.12. Results display heterogeneous thickness of the few-layer stacks of the sample. The diameter of the particle ranges from approximately 350 nm to 700 nm, in accordance with TEM results, while the height dispersion varies from 5 nm to 70 nm. It is worth noticing that thinner particles of approximately 1 nm are observed, indicated in the circled region of Fig. 3.5.12b, however, their height profile could not be perfectly resolved due to the poor signal/noise ratio obtained. Nonetheless, 5-6nm thick nanolayers can be obtained, that would correspond to 5-7 monolayers, considering the value of a hydrated monolayer of ~0.82 nm, as exemplified in Fig.3.5.12d [14,25–27]. This would indicate that the present exfoliation method successfully produces few-layer nickel-cobalt hydroxide, with a small number of monolayers and a certain number of larger aggregates due to either solvent molecules, attached organic molecules on the surface or few-layer stacks. It is worth mentioning that, during the preparation of the sample for AFM, certain monolayers may aggregate in the drying process. Single

monolayers could be obtained at higher speed centrifugation (~50000 rpm). But this would result in too low yield for feasible electrode preparation for energy storage applications and therefore lower centrifugation rotation speed have been used during the isolation of active material for electrode preparation [27].

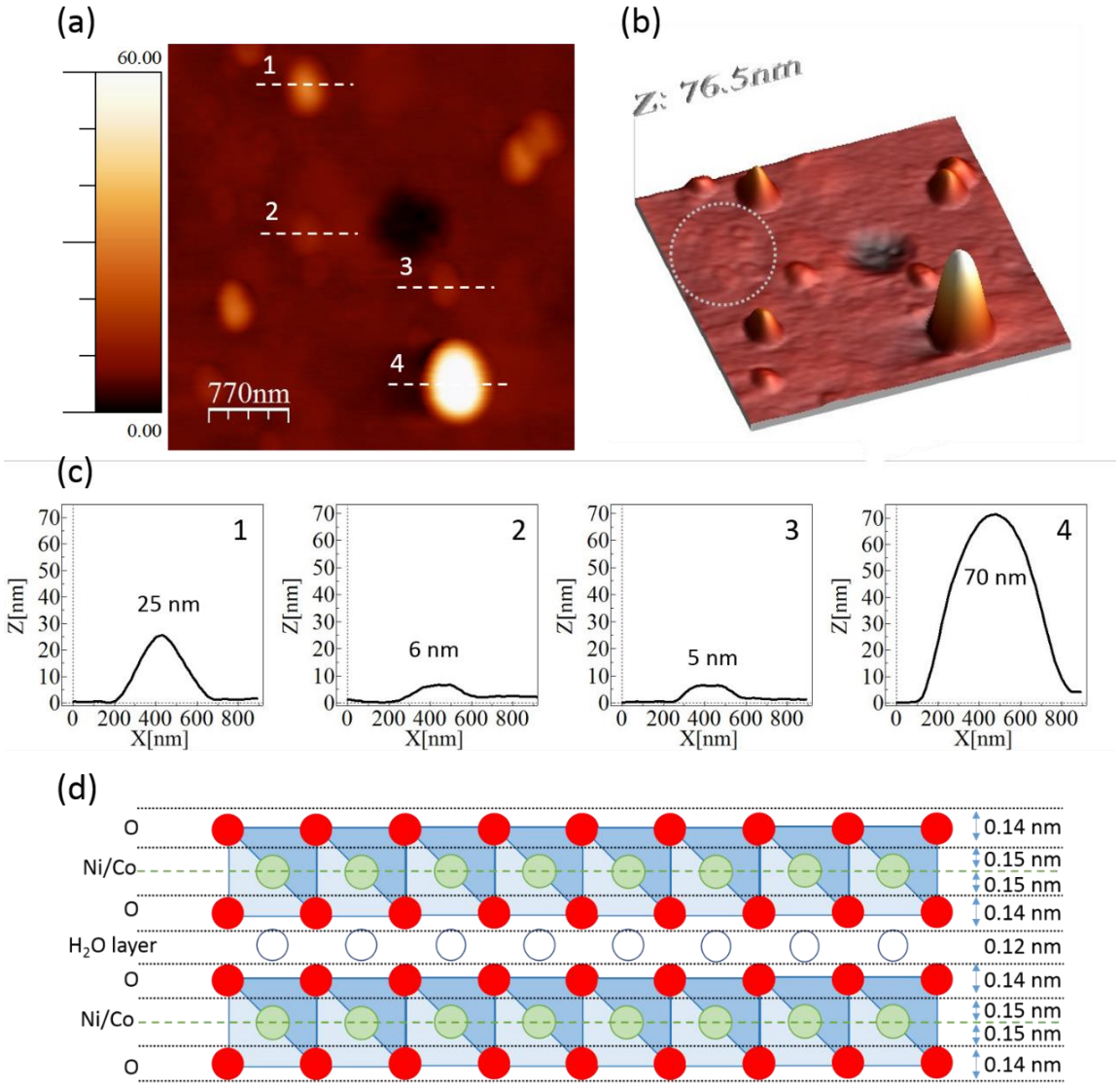

Fig. 3.5.12. Atomic force microscopy topography (a) 2D image, (b) 3D image, and (c) height profiles of delaminated lactate-intercalated nickel-cobalt hydroxide obtained in tapping-mode. Each dotted line corresponds to a height profile with the same numeration. The circled area of the 3D image highlights a region with delaminated nanoslabs whose height profile could not be resolved, (d) schematic representation of theoretic values for a nickel-cobalt oxyhydroxide bilayer.

3.5.3.1.2. Nickel-cobalt oxyhydroxide delamination

The procedure used in the delamination of nickel-cobalt oxide nanosheets is exemplified in Fig. 3.5.2. Essentially, α-Ni-Co$(OH)_2\cdot(CO_3^{2-},2\cdot NO_3^-)_x\cdot(H_2O)_y$ {NCOH} is synthesized by co-precipitation. This is followed by oxidation in NaClO/KOH into γ-(Ni-Co)$O_2\cdot(H^+,Na^+,K^+)_x\cdot(H_2O)_y$ {NCOx-HNK} and protonation into γ-(Ni-Co)$O_2\cdot(H^+)_x\cdot(H_2O)_y$ {H-NCOx-H}. Then, it is suspended in TBA-OH, where it gets exfoliated in small nanoslabs of γ-(Ni-Co)O_2 that are suspended in solution. By means of solvent evaporation the material becomes re-stacked {NCOx-TBA}.

3.5.3.1.2.1. X-Ray Diffraction Spectroscopy

XRD results are presented in Fig. 3.5.13. The patterns were indexed to a hexagonal cell. Again, the line at the lowest angle, indexed as 001, has its inter-reticular distance that corresponds to the interslab distance, i.e. the distance between two adjacent metal planes, while the 001 line corresponds to half the metal-metal distance within the slab [28], and is therefore strongly influenced by the average metal oxidation state. The pristine material presents a peak at 7.93 Å that corresponds to the *001* diffraction line of carbonate/nitrate intercalated α nickel cobalt hydroxide as characterized by Delmas et al. [18]. The metal-metal slab distance (a_{hex} parameter value) obtained for the α phase is 3.04, in accordance with literature, and with the value expected for Ni^{2+} ions coexisting with a certain number of Co^{3+} ions. After oxidation treatment in NaClO/KOH (Fig. 3.5.13 b-d), the 110 line is shifted, and the inter-reticular distance obtained is close to 1.40 Å, which is consistent with the oxidation of nickel and cobalt ions to an average oxidation state of 3.2+, as confirmed by iodometric titration, not reported here. During the subsequent steps, TBA^+ intercalation and exfoliation, the 110 line is almost not shifted, which shows that the metal oxidation state reached is maintained. In the pristine material, carbonate and nitrate anions are intercalated to maintain electroneutrality due to the excess charge caused by Co(III), resulting in an interslab distance close to 7.93 Å. Then, after oxidation with NaClO, the resulting material (Fig. 3.5.13b) γ-(Ni-Co)$O_2\cdot(H^+, Na^+, K^+)_x(H_2O)_y$, exhibits a *001* line with interslab distance of 6.92Å. This interslab distance decrease is due to the modification of the interslab composition resulting from the deprotonation that provokes the intercalation of alkali cations present in the medium (Na^+, K^+) to maintain electroneutrality. The material is then acidified (Fig. 3.5.13c) to substitute the alkali ions in the interslab space for protons, since H^+ ions have better affinity to TBA-OH ions and exfoliation can only be achieved with this intermediate step [29]. The substitution of alkali cations in the interslab space to the smaller protons shortens the interslab distance (*001* line) of NCOx-H to 6.53 Å. Finally, once the material is exfoliated and re-stacked by TBA^+ intercalation and solvent evaporation (Fig. 3.5.13d), the material becomes re-stacked with a higher interslab distance of 7.3 Å.

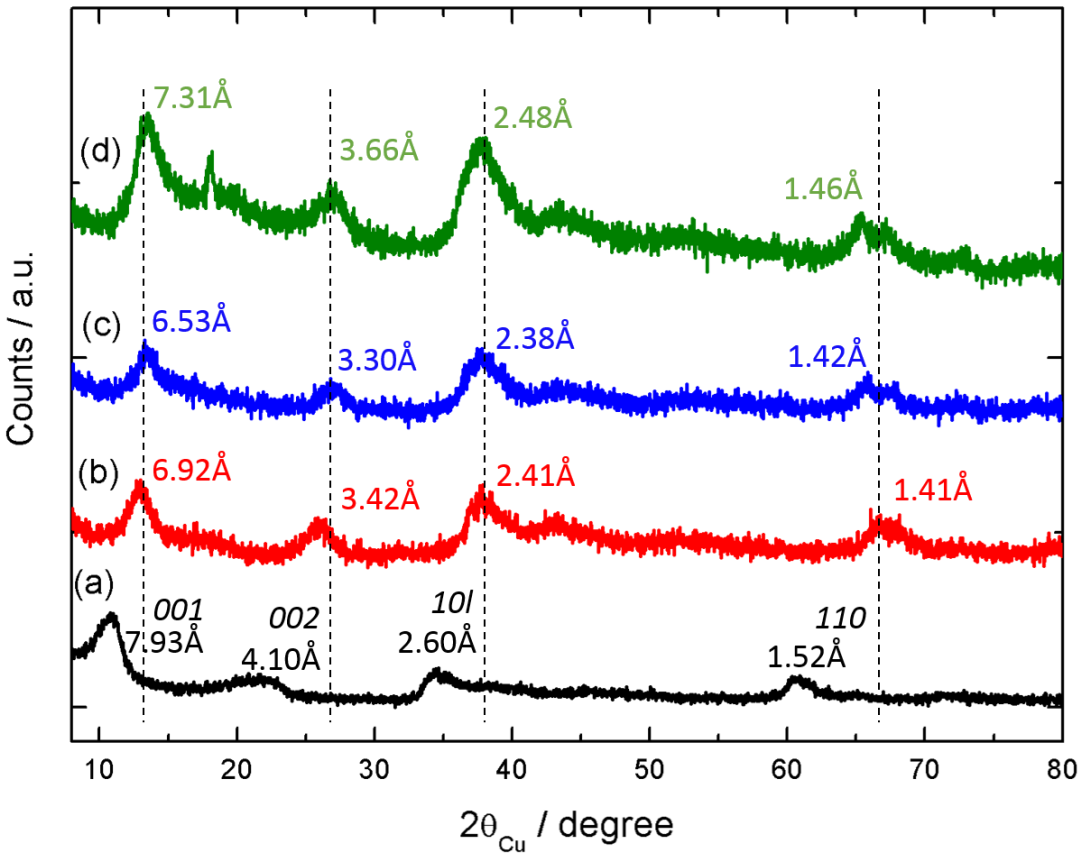

Fig. 3.5.13. X-Ray Diffraction results for (a) NCOH, (b) NCOx-HNK, (c) NCOx-H and (d) restacked NCOx-TBA. The numbers correspond to the inter-reticular distances calculated on the basis of indexation with a hexagonal cell.

3.5.3.1.2.2. Elemental analysis

The results of elemental chemical analysis, displayed in Table 3.5.2, indicate at first that cobalt and nickel are in a 0.65/0.35 atomic ratio, which is maintained during the entire process, exemplifying that the reactions are topotactic and preserve slab integrity. Once the pristine hydroxide material (NCOH) is oxidized to oxyhydroxide (NCOx-HNK) significant amounts of potassium and sodium are present within the material, as expected from literature [18]. During protonation (NCOx-H), the amount of these intercalated cations diminishes overall. Nonetheless, their substitution for proton ions is not complete. Finally, after exfoliation and re-stacking in TBAOH, the carbon signal dramatically augments, nitrogen is still present, while the relative weight percentage of nickel and cobalt diminishes, showing that TBA+ ions are still present within the material. Additional purification steps are therefore required to successfully remove TBA^+ since rinsing with ethanol, acetone and water cannot completely remove the organic material. Thus, it is expected certain influence of TBA^+ in the electrochemical performance of the material.

Table 3.5.2
Chemical analysis for the materials obtained during the delamination of nickel-cobalt oxyhydroxide by tetrabutylammonium intercalation in weight percentage. Note that "Ni to (Ni+Co)" and "Co to (Ni+Co)" are weight ratios.

	Weight %						Molar ratio : element/(Ni+Co)					
	Co	Ni	K	Na	C	N	Co	Ni	K	Na	C	N
NCOH	61.43	32.43	0.18	2.18	0.19	2.24	0.65	0.35	0.003	0.06	0.01	0.1
NCOx-HNK	54.72	29.2	12.31	1.73	0.96	0	0.65	0.35	0.22	0.05	0.05	0
NCOx-H	60.46	33.26	4.64	0.54	0.32	0	0.65	0.35	0.07	0.01	0	0
NCOx-TBA	58.95	31.33	2.84	1.05	3.57	0.09	0.65	0.35	0.05	0.03	0.19	0.004

3.5.3.1.2.3. Scanning and Transmission electron microscopy

The evolution of material's morphology throughout the synthesis procedure is studied by means of SEM and TEM. The size of aggregates is reduced with each step of the synthesis procedure. Initially, NCOH consists of big aggregates of densely-packed particles (>10 µm) (Fig. 3.5.14a). After oxidation, NCOx-NKH presents a very similar morphology (Fig. 3.5.14b). However, the domain size of the particles is slightly reduced. Acidification further decreases the size of the aggregates to particles of 5 µm or smaller size, with a very heterogeneous distribution (Fig. 3.5.14c). After TBAOH exfoliation and re-stacking by evaporation (Fig. 3.5.14d), the particle size distribution becomes more homogeneous and particulates decrease their domain size to approximately 1 µm diameter, although bigger particles can still be found. Thus, porosity and surface area seem to increase at every step of the exfoliation procedure.

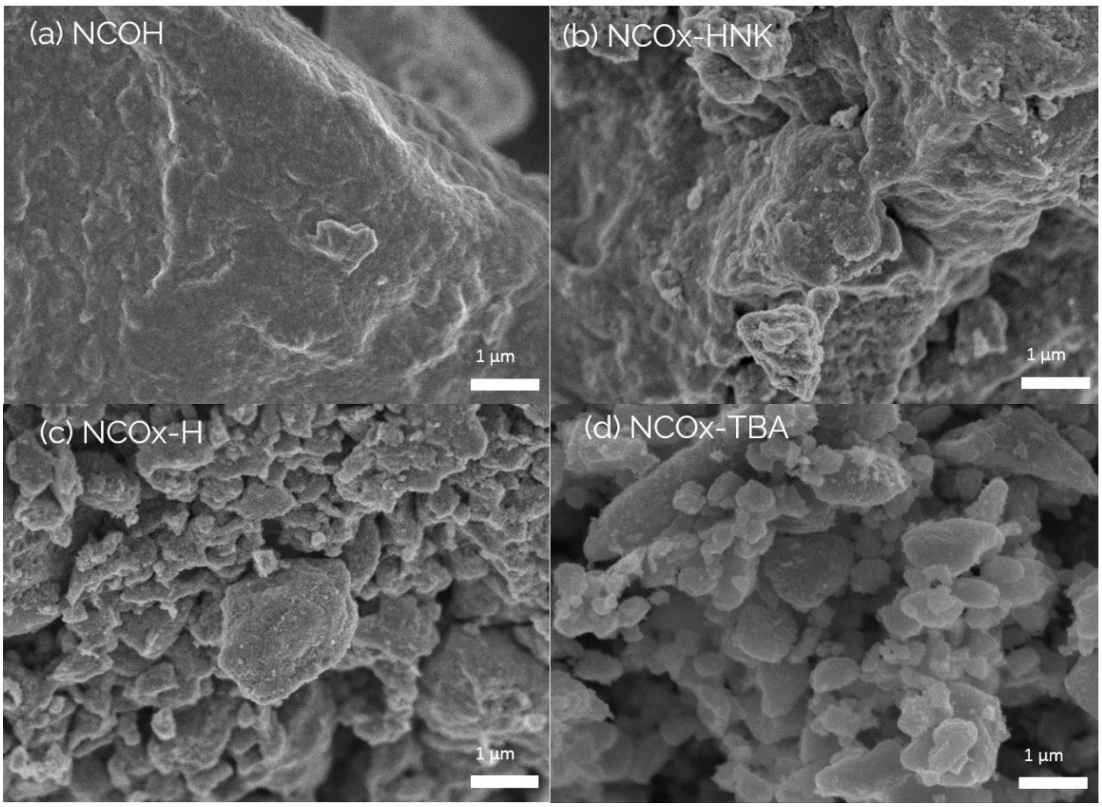

Fig. 3.5.14. Scanning Electron Microscopy images of (a) NCOx-HNK and (b) re-stacked NCOx-TBA after delamination in TBAOH and re-stacking by solvent evaporation.

TEM results, shown in Fig. 3.5.15, provides additional morphological information. NCOx-HKN consists of big aggregates that present randomly oriented nanostructured domains. Thus, nanoparticles of approximately 1-10 nm aggregate in random directions, resulting in the formation of micro-particles. A similar structure can be observed once the material is acidified (Fig. 3.5.15b). However, the coherent domains within the particles are bigger in this case, ranging from 15 to 25 nm size. Once exfoliated by TBA^+ intercalation, dispersed particles of 100-200 nm diameter size are obtained (Fig. 3.5.15c). Given the thin nature of these nanoslabs, it is challenging to obtain TEM images with good resolution. However, it seems that the nanoslabs also consist of smaller coherent domains of 1-20nm, maintaining the nature of the bulk material. It is worth mentioning that the exfoliation also leads to bigger aggregated particles that shall be separated by centrifugation at higher speeds (>15000 rpm). Finally, once the material is re-stacked, a granulated morphology similar to the starting material is obtained (Fig. 3.5.15d).

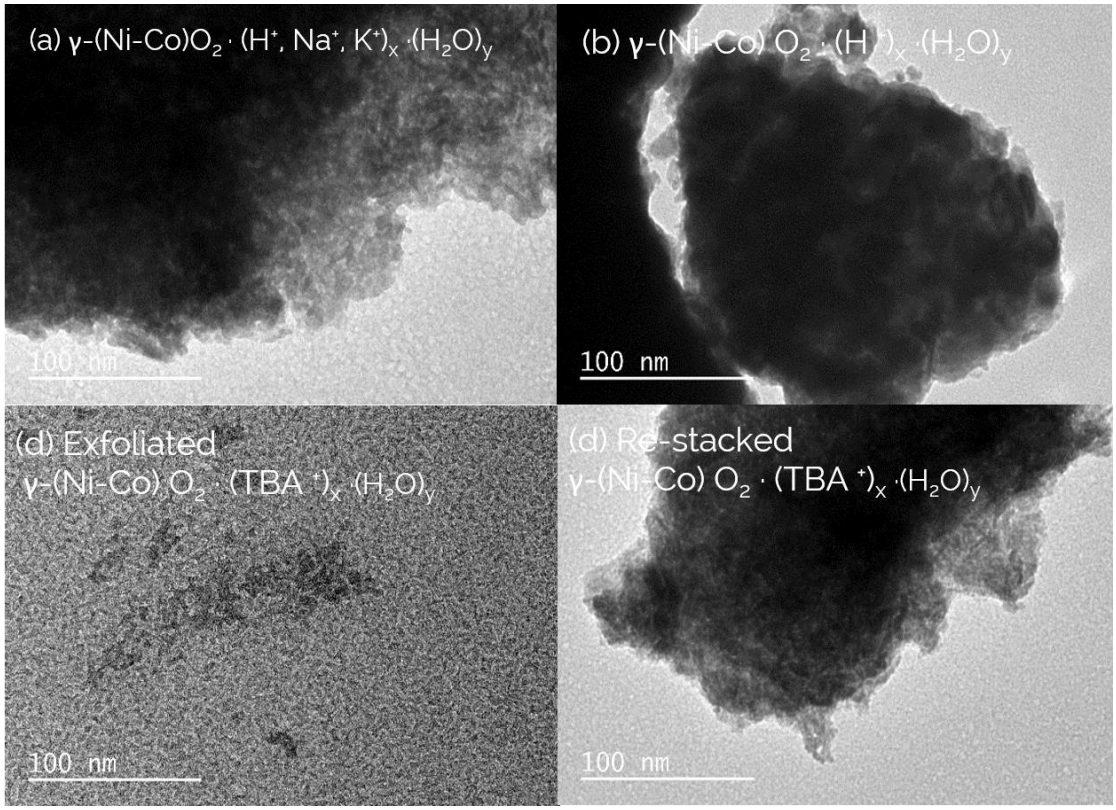

Fig. 3.5.15. Transmission Electron Microscopy images of (a) NCOx-HNK and (b) exfoliated oxide slabs in TBAOH (NCOx-TBA).

3.5.3.1.2.4. Fourier-transform infrared and Raman spectroscopy

When FTIR results are considered, NCOH (Fig. 3.5.16a) is characterized by a large broad signal at 3446 cm^{-1} and a large band and 1646 cm^{-1} (stretching and bending vibrations of water molecules), a strong narrow peak at 1376 cm^{-1} assigned to vibrations of monodentate carbonate anions and, finally, a broad band centred at 673 cm^{-1} and a narrow peak at 522 cm^{-1} that corresponds to stretching vibrations of M-O. When the material is oxidized (Fig. 3.5.16b), the signals associated to vibration modes of water become mitigated while the peaks associated to carbonate anions disappear. On the other hand, a double peak at 570 cm^{-1} and 632 cm^{-1} appears that correspond to M-OH and M-O stretching vibrations. When the sample is protonated (Fig. 3.5.16c), this low-wavenumber peak becomes intensified, while signals associated to water molecules

become weaker. Finally, after exfoliation and re-stacking (Fig. 3.5.16d), FTIR spectrum presents many additional peaks that are associated to TBA^+ molecules since ethanol and acetone rinsing is not enough to eliminate them. There are two main relevant features: (i) the increased signal for the bands associated to water molecules. More water molecules intercalated in the interslab space of the re-stacked material are in accordance with the increased interslab distance observed by XRD, although they could be brought by the residual TBA^+. (ii) M-O and M-OH vibrations, visible at 500-700cm^{-1}, are maintained and become more significant than in the α phase, in which they are barely visible [30–34].

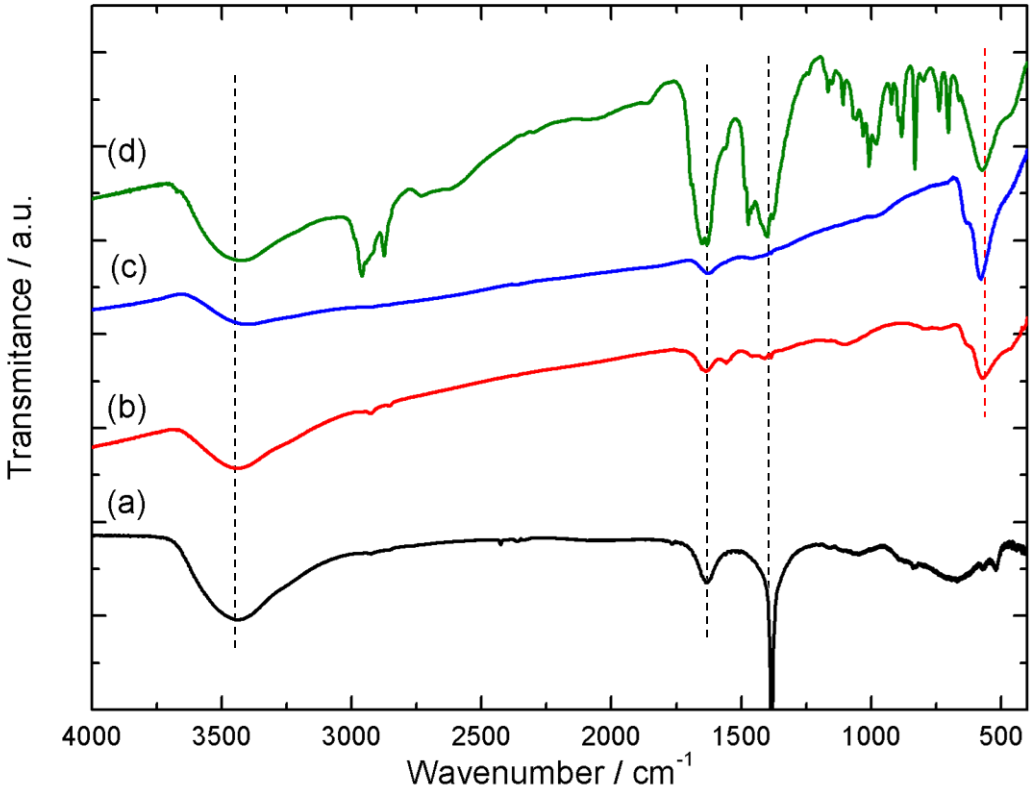

Fig. 3.5.16. FTIR results for (a) NCOH, (b) NCOx-HNK, (c) NCOx-H and (d) restacked NCOx-TBA.

Raman spectra, shown in Fig. 3.5.17, provide additional evidence on the phase transformation process during exfoliation. NCOH presents two main bands, at 464 cm^{-1} and 528 cm^{-1}, assigned to M-OH and M-O vibration modes. When the material is oxidized, these two bands are present at approximately 451 cm^{-1} and 527 cm^{-1} with different relative intensities, and a shoulder is observed around 580 cm^{-1}. This additional signal can also be detected in NCOx-HNK and may be associated to structural defects. Finally, a broad band from 400-700 cm^{-1} with 3-4 peaks is observed when the sample is exfoliated and re-stacked, corresponding to Co-O and Ni-O vibrations influenced by the present of TBA^+ and that require further studies to comprehend, which is out of the scope of the present work [35,36]. As presented in Fig. 3.5.17a, a band at 1066 cm^{-1} is related to intercalated anions in the interslab space while a signal at 3600 cm^{-1} appears because of OH group stretching vibrations (not shown). As expected, the band associated to interslab anions and the signal associated to OH stretching disappear in the phases obtained after material's oxidation.

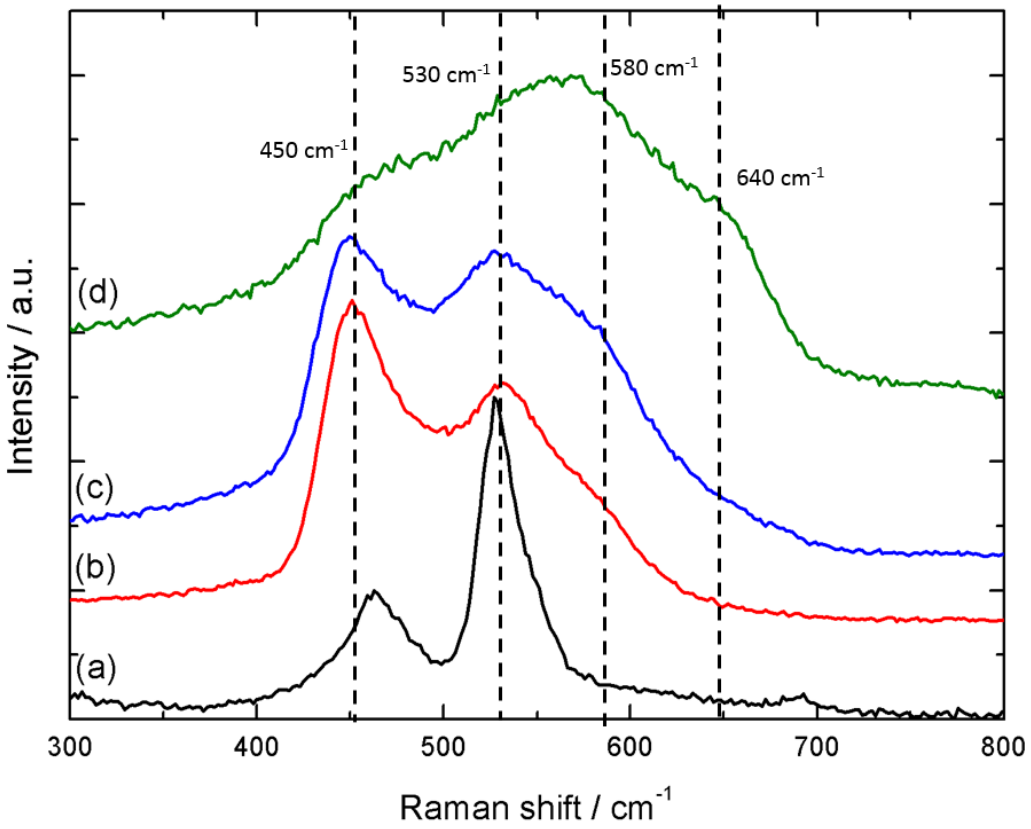

Fig. 3.5.17. Raman results for (a) NCOH, (b) NCOx-HNK, (c) NCOx-H and (d) restacked NCOx-TBA.

3.5.3.1.2.5. Nitrogen adsorption isotherms

The specific surface area of NCOx-H and NCOx-TBA was analysed by BET. Results, presented in Fig. 3.5.18 and 3.5.19, show that both materials display a type IIB isotherm, characteristic of non-porous or macro-porous materials, with a narrow hysteresis cycle; which indicates the presence of some mesopores. NCOx-H presents a specific surface area of 190 $m^2 \cdot g^{-1}$ with a relevant number of mesopores while NCOx-TBA displays a specific surface area of only 94 $m^2 \cdot g^{-1}$. Results suggest that the intercalation with TBA^+ molecules and subsequent re-stacking by solvent evaporation leads to TBA^+ molecules present in the sample, as clearly observed by FTIR, that reduce the N_2 adsorption surface area, which may result in a lower active surface area and worsened electrode-electrolyte interaction in their evaluation as energy storage materials. In any case, certain effect in the electrochemical behaviour is expected from BET results.

3.5.3.1.2.6. Atomic force microscopy

AFM results for delaminated TBA^+ intercalated nickel-cobalt oxide in distilled water, diluted and dropcasted on top of mica are presented in Fig. 3.5.20. Results display a homogeneous dispersion of nanoparticles with different diameters, ranging from 30 to 175 nm. On the other hand, smaller particles present thickness around 1.5-3 nm, while the biggest ones reach values up to 85.6 nm. Similar to the hydroxide exfoliation route, solvent molecules, aggregation during sample preparation for AFM measurements and trapped TBA^+ may increase the expected thickness of the nanolayers. Nonetheless, results present a great number of nanoparticles with a thickness of ~3nm, associated to a 2-3 monolayer stacks of nickel-cobalt oxyhydroxide, when compared to the theoretical value for a nickel-cobalt oxyhydroxide monolayer (0.52nm) with adsorbed TBA^+ molecules on its surface (0.84nm) [25–27].

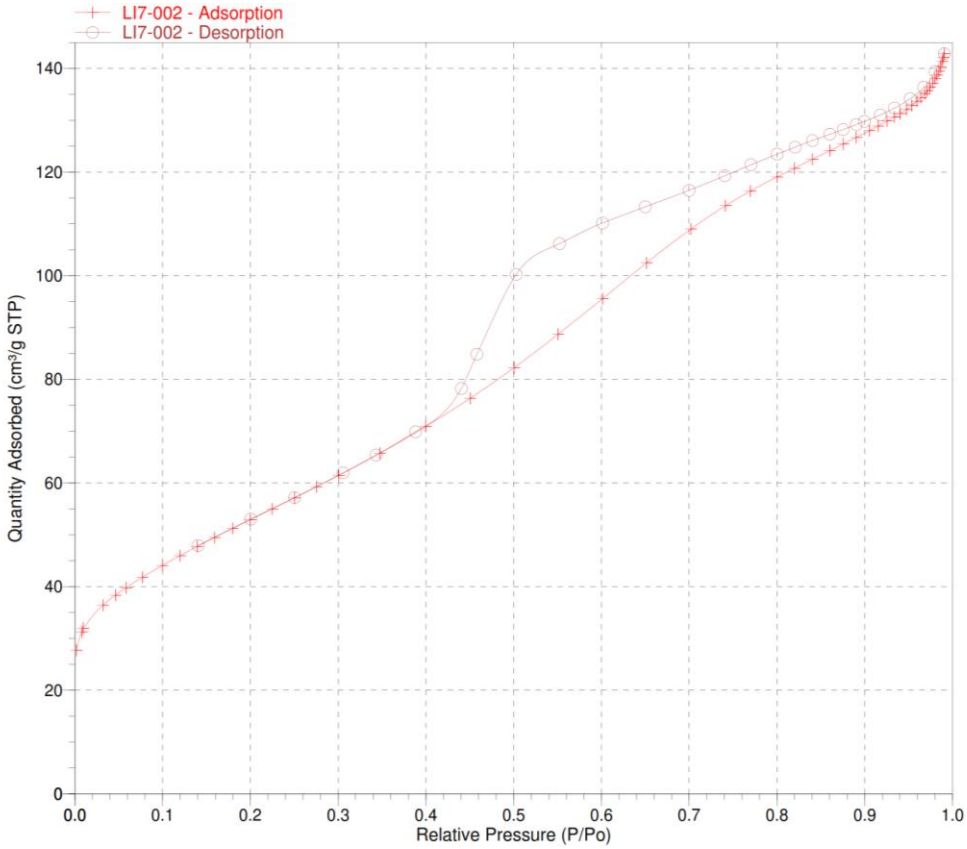

Fig. 3.5.18. BET adsorption-desorption isotherm results for NCOx-H.

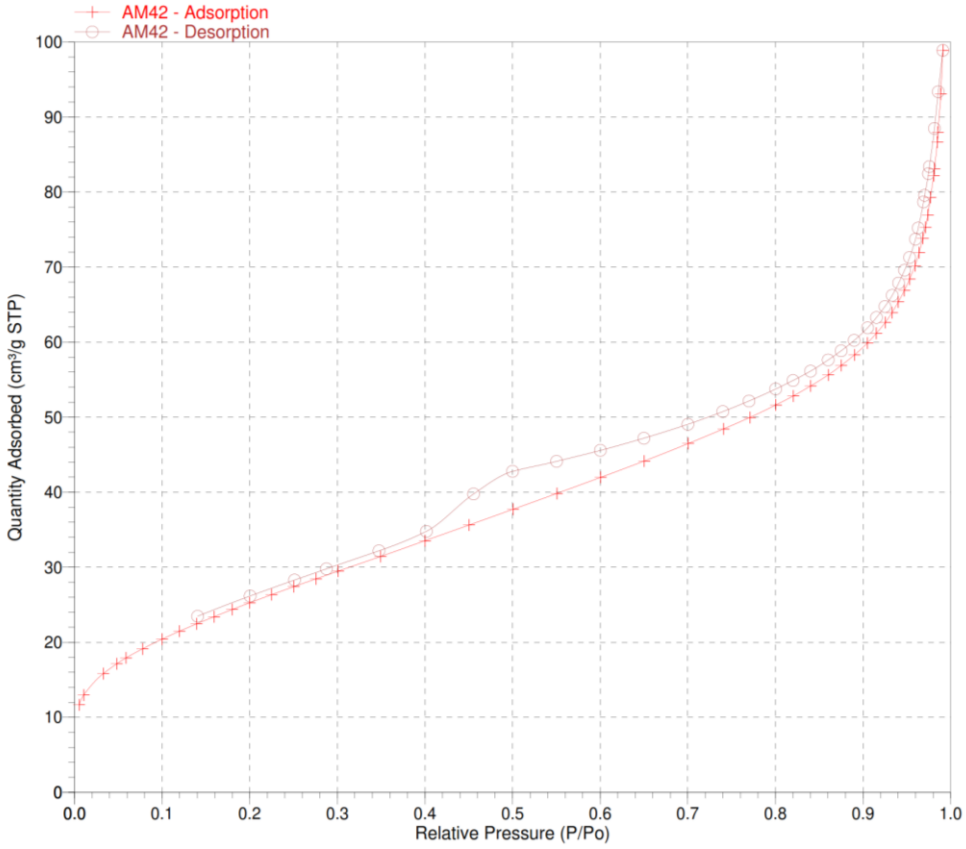

Fig. 3.5.19. BET adsorption-desorption isotherm results for NCOx-TBA.

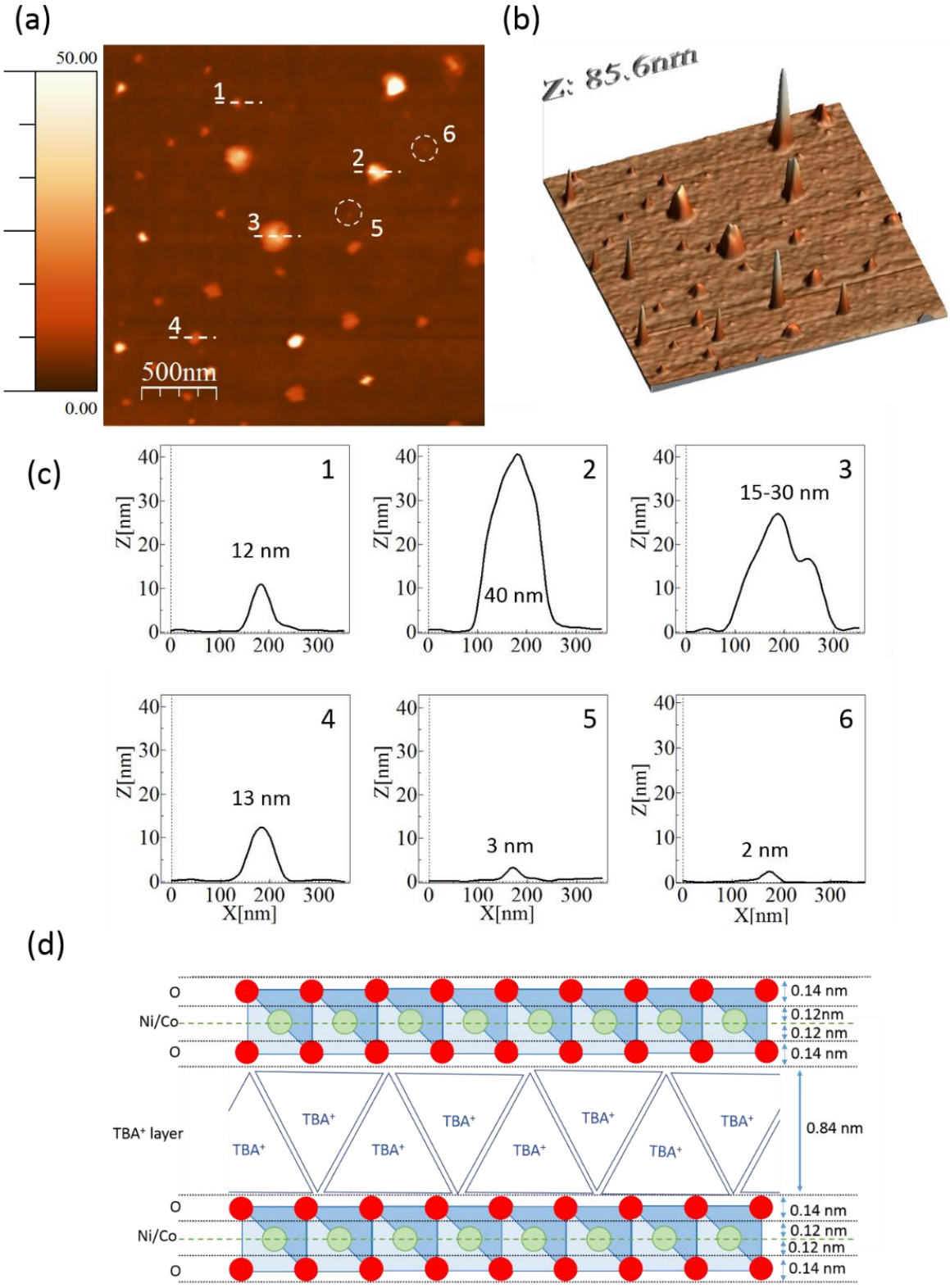

Fig. 3.5.20. Atomic force microscopy topography (a) 2D image, (b) 3D image, and (c) height profiles of delaminated tetrabutylammonium-intercalated nickel-cobalt oxyhydroxide obtained in tapping-mode. Each dotted line corresponds to a height profile with the same numeration, (d) schematic representation of theoretic values for a nickel-cobalt oxyhydroxide bilayer.

3.5.3.2. Electrochemical Characterization

This section aims at comparing the electrochemical behaviour of nickel-cobalt hydroxides and nickel-cobalt oxyhydroxides that were delaminated with two different routes and to determine the effect of the intercalated species on their performances.

3.5.3.2.1. Nickel-cobalt hydroxide delamination.

Results presented are based on the performance after a pre-activation step of 1-10 cycles, exemplified in Fig. 3.5.21.

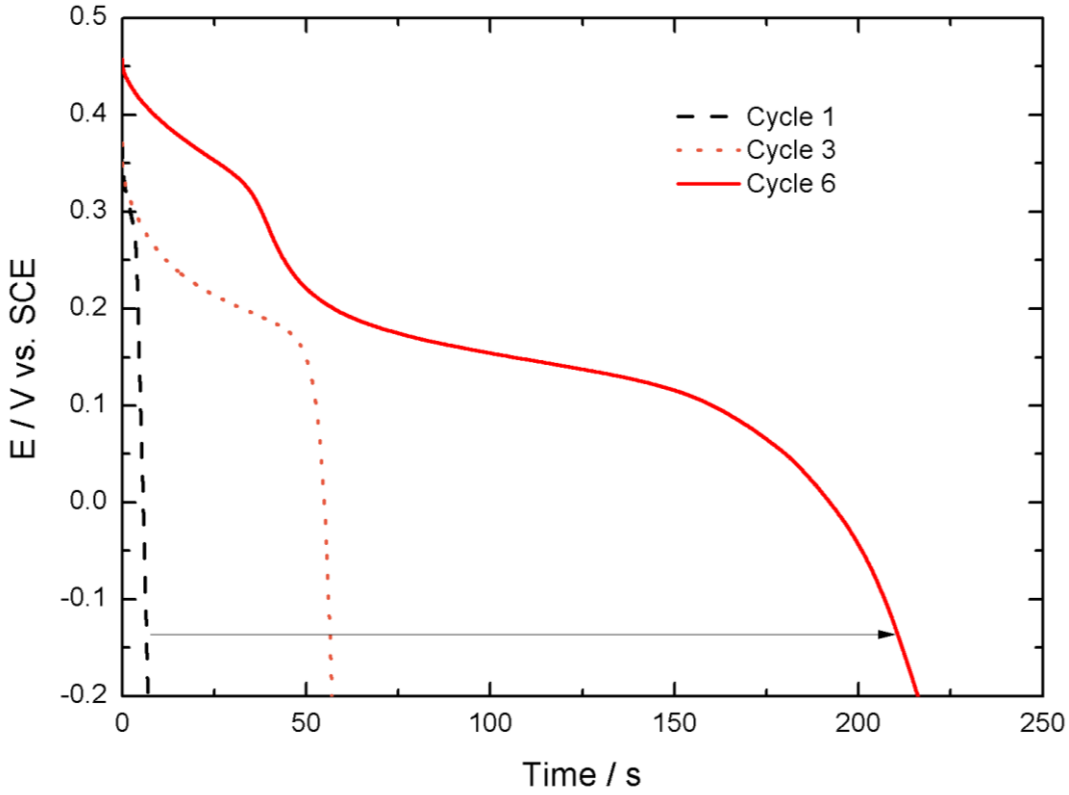

Fig. 3.5.21. Exemplification of the evolution of the discharge curves during the activation process for DS-intercalated nickel-cobalt hydroxide (DS-NCOH) measured at $1A \cdot g^{-1}$ in 1M KOH.

3.5.3.2.1.1 Study in 1M KOH electrolyte

The charge storage performances of the materials involved during the delamination in aqueous media of nickel-cobalt hydroxide by means of lactate intercalation were evaluated in 1M KOH. The results are shown in Fig. 3.5.22. From a general point of view, the shape of the cyclic voltammetry and of the galvanostatic curves are characteristic of faradaic processes.

As far as cyclic voltammetry is concerned (Fig. 3.5.22a), the most relevant feature is the bigger area of the DS-intercalated material (DS-NCOH) compared to the lactate-intercalated material (Lac-NCOH) and the re-stacked material obtained by dialysis (NCOH-DIAL). The cyclic voltammetry for DS-NCOH at a scan rate of $5\ mV \cdot s^{-1}$ in the -0.2 V to 0.55 V potential range (vs. SCE), presented in Fig. 3.5.22a, displays a couple of redox peaks. While the anodic wave is vaguely defined and centred at approximately 0.38V, the cathodic wave is much better defined and centred at 0.23V. Response resembles the shape of classical carbonate intercalated α nickel-cobalt hydroxide in which the anodic wave is inhibited with a very resistive signal (NCOH, see next section

Fig 3.5.26). The maximum current peak ratio ($I_{max,anodic}/I_{max,\ cathodic}$) of 0.8 and different area under both waves evidences the limited reversibility of the reaction. It is worth mentioning that oxygen evolution reaction is always present as a parasitic reaction that produces hysteresis during the oxidation reaction and lowers coulombic efficiency [37,38].

When anion exchange is undertaken, and lactate anions intercalated (Lac-NCOH), the electrochemical signal becomes extremely hampered. The active potential range is, consequently, limited to 0.0V - 0.48V (vs. SCE); the cathodic wave is practically inhibited, with a very small cathodic peak centred at 0.31V while a resistive signal during the anodic wave, which is centred at 0.45V, is obtained. A maximum current peak ratio for Lac-NCOH over 5 reveals the extremely poor reversibility of the reaction. Finally, when the material is delaminated in distilled water and dialyzed, and lactate molecules are partially removed from the material (NCOH-DIAL), it exhibits a better electrochemical signal by means of cyclic voltammetry. Consequently, the signal initially obtained for the lactate intercalated material is enhanced and the peaks become better defined and centred at 0.55V and 0.33V. Nonetheless, although the signal is greatly improved from the lactate-intercalated precursor, it is extremely deficient when compared to the parent DS-intercalated material. Moreover, the maximum current ratio for NCOH-DIAL becomes further intensified with a value over 7, as a result of the irreversibility of the electrochemical reaction.

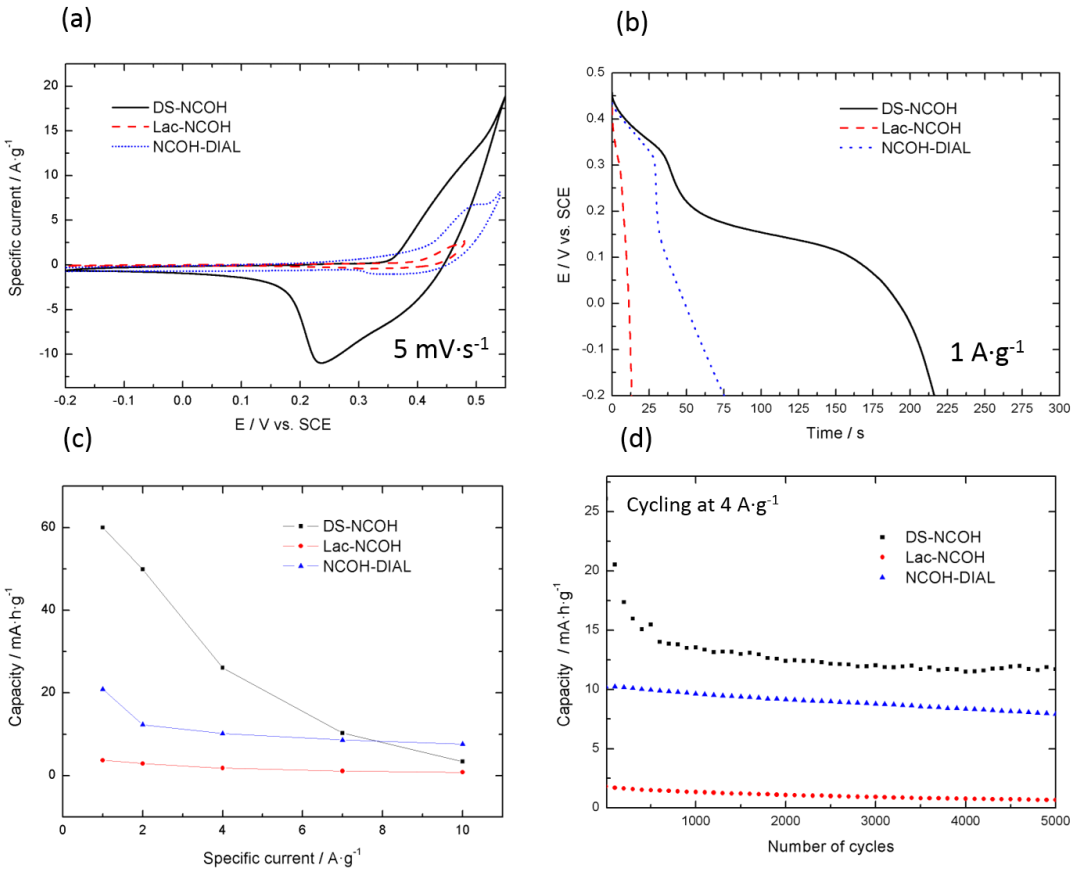

Fig. 3.5.22. Comparison of the electrochemical response by (a) cyclic voltammetry, (b) galvanostatic discharge, (c) capacity at different applied current densities and (d) capacity evaluated by galvanostatic continuous charge-discharge cycling during 5000 cycles at 4 $A \cdot g^{-1}$ for the different composites obtained during delamination by lactates route of nickel-cobalt hydroxide in 1M KOH.

When galvanostatic charge-discharge curves are compared, a maximum discharge time of 216 seconds is obtained for the DS-intercalated material in the 0.46V to -0.2V potential range, while only 13 seconds for Lac-NCOH and 75 seconds for NCHO-DIAL were achieved. These values correspond to a total capacity of 60.0, 3.7 and 20.9 $mA \cdot h \cdot g^{-1}$ for DS-NCOH, Lac-NCOH and NCOH-DIAL, respectively. Compared to co-precipitated nickel-cobalt hydroxide, NCOH (Fig. 3.5.26) that displays a capacity greater than $100mA \cdot h \cdot g^{-1}$, later shown, these values are considerably lower. If the coulombic efficiency is calculated (discharge time/charge time ratio, in percentage), DS-NCOH displays a coulombic efficiency of only a 78%. It is further reduced for Lac-NCOH, which displays 64% coulombic efficiency. When the material is dialyzed, it increases until 91%, suggesting that the organic molecules are responsible for lowering the current efficiency, promoting either side-reactions related to these organic chains or, possibly, oxygen evolution reactions.

Moreover, as shown in Fig. 3.5.22c, if the discharge times are evaluated at different applied current densities, the three composites exhibit a capacity lower than the 50% of their initial capacity at $4\ A \cdot g^{-1}$. It is worth noticing that, at the highest applied current of $10A \cdot g^{-1}$, the dialyzed material displays a higher capacity value than the precursor materials. These results show how the charge-discharge mechanism is extremely dependent on the electrode-electrolyte interaction and how the organic intercalated molecules can limit it. In this case, they lower the overall electrochemical response and extremely affect the kinetics of the reaction. At lower current densities, the interaction between the active material and the electrolyte is favoured due to lower kinetic restrictions, yielding increased capacity responses. When higher current densities are applied, the electrode-electrolyte interaction is greatly inhibited and confined to more superficial reactions, in which the presence of organic molecules plays a major role. DS-NCOH and Lac-NCOH display a major decay of the electrochemical performance, while NCOH-DIAL, with less contribution from organic molecules, exhibits a higher active surface area and better capacity retention at higher currents. Results at different scan rates and different current densities are displayed in Fig. 3.5.23.

Finally, if cycling stability is evaluated at $4\ A \cdot g^{-1}$ during 5000 cycles, due to the initially poor performance of Lac-NCOH and NCOH-DIAL, their capacity seems apparently maintained. Nonetheless, they suffer from a capacity fade of 53% and 25% respectively. However, the initial DS-NCOH capacity, clearly superior, becomes greatly diminished during the first 600 cycles, after which the material's response becomes stabilized. During charge-discharge, the interaction of DS^- anions with the electrolyte probably intensifies the blockage of the active material due to agglomeration or degradation of the organic molecules, resulting in 56% decay of capacity.

It is worth mentioning that the route here presented was first reported by Lang et al. [13], who also evaluated the instability of nickel-cobalt hydroxide peaks by cyclic voltammetry in 1M KOH of spin-coated exfoliated lactate-intercalated material on top of HOPG, and assigned it to layer reorganization upon redox sweeping and charge transfer kinetics dominated by counter-ion diffusion phenomena.

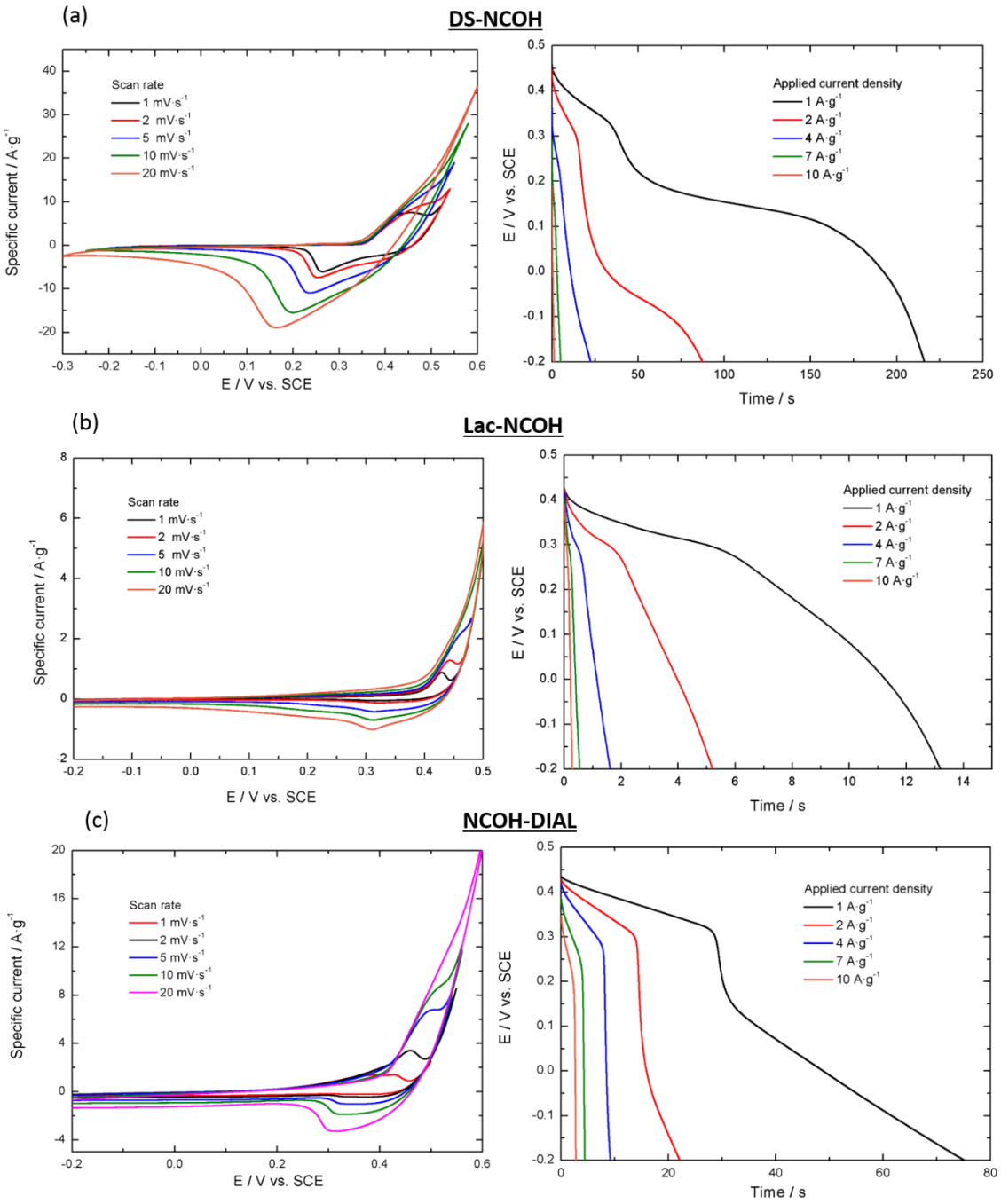

Fig. 3.5.23. Cyclic voltammetries at different scan rates and galvanostatic discharge curves at different applied current densities for the materials obtained during the delamination of nickel-cobalt hydroxide by lactate intercalation evaluated in 1M KOH.

3.5.3.2.1.2 Study in 1M LiOH electrolyte

The electrochemical charge-discharge reaction of α nickel-cobalt hydroxide is dependent on insertion of alkali cations into the interlayer region [39]. Thus, to study the effect of alkali cation in the electrolyte the electrochemical performance of these materials was investigated in 1M LiOH.

It was reported that different alkali cations and electrolyte conductivity can vary the performance of nickel hydroxide [40], with maximum capacities for sodium and lithium hydroxide as electrolyte. Thus, depending on the ionic radii, charge and hydration shell of the alkali cation, amongst many others, different electrochemical charge-storage performance can be expected [41–43]. Recently, NiO and $Ni(OH)_2$ have been studied under different electrolytes. NiO exhibited better electrochemical performance in NaOH than in KOH due to the higher intercalation rate of sodium ions into the electrode surface material [44,45], while $Ni(OH)_2$ performance was enhanced by the presence of lithium ions. This was related to a favoured faradaic charge-transfer mechanism, the intercalation of lithium ions into the interslab space of nickel hydroxide and the inhibition of the α→β phase transformation [46].

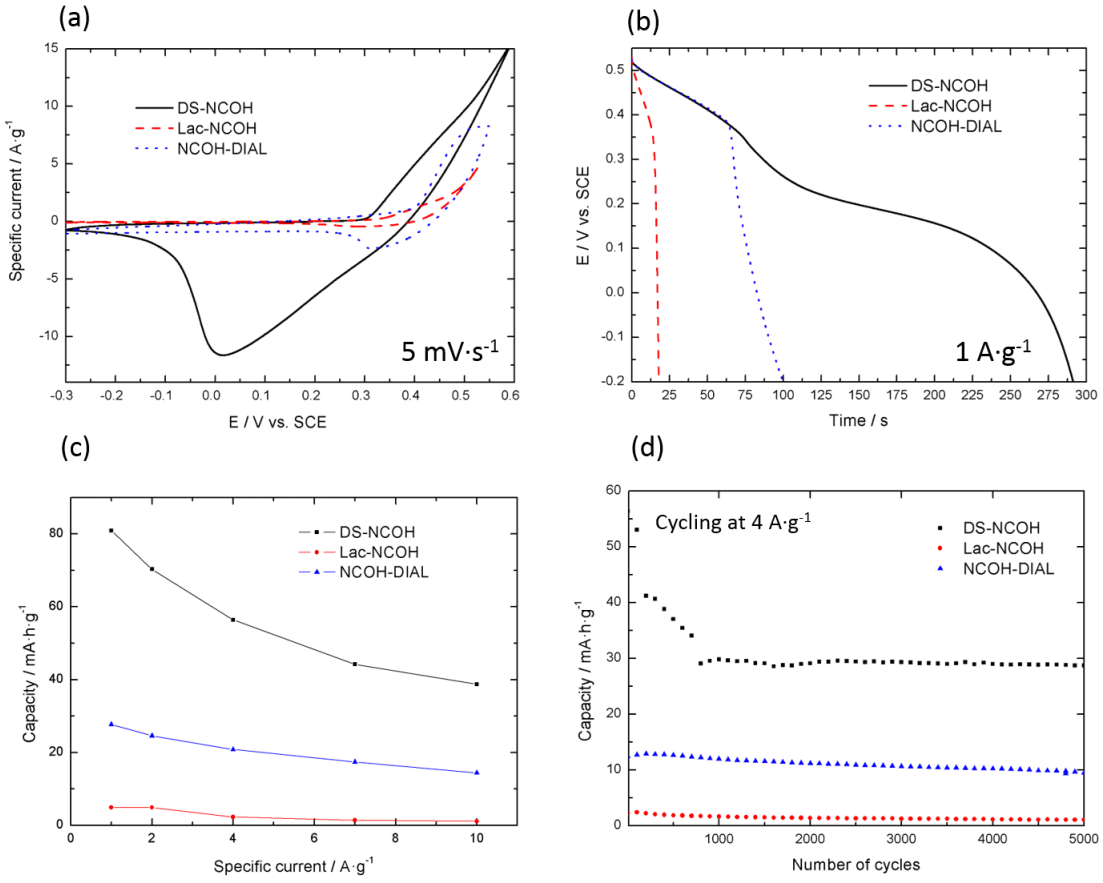

Fig. 3.5.24. Comparison of the electrochemical response by (a) cyclic voltammetry, (b) galvanostatic discharge, (c) capacity at different applied current densities and (d) capacity evaluated by galvanostatic continuous charge-discharge cycling during 5000 cycles at 4 $A \cdot g^{-1}$ for the different composites obtained during delamination by lactates route of nickel-cobalt hydroxide in 1M LiOH.

When nickel-cobalt hydroxide intercalated with dodecyl sulphate or lactate anions are evaluated in 1M LiOH, similar trends to the response in KOH are observed for the three materials in terms of capacity, rate capability and capacity retention with cycling, Fig.

3.5.24. Nonetheless, there are two relevant features observed when LiOH is used instead of KOH. There is a slight increase in capacity, to a value of 80.9, 4.9 and 27.8 $mA \cdot h \cdot g^{-1}$ for DS-NCOH, Lac-NCOH and NCOH-DIAL respectively; and a better capacity retention both at higher applied current densities and during cycling stability tests. This increase in capacity and capacity retention at higher applied currents, in the presence of lithium in the electrolyte, may be caused by better intercalation of Li^+ compared to K^+ and a favoured faradaic charge-transfer mechanism, especially at higher applied current densities. Results at different scan rates and applied current densities are displayed in detail in Fig. 3.5.25.

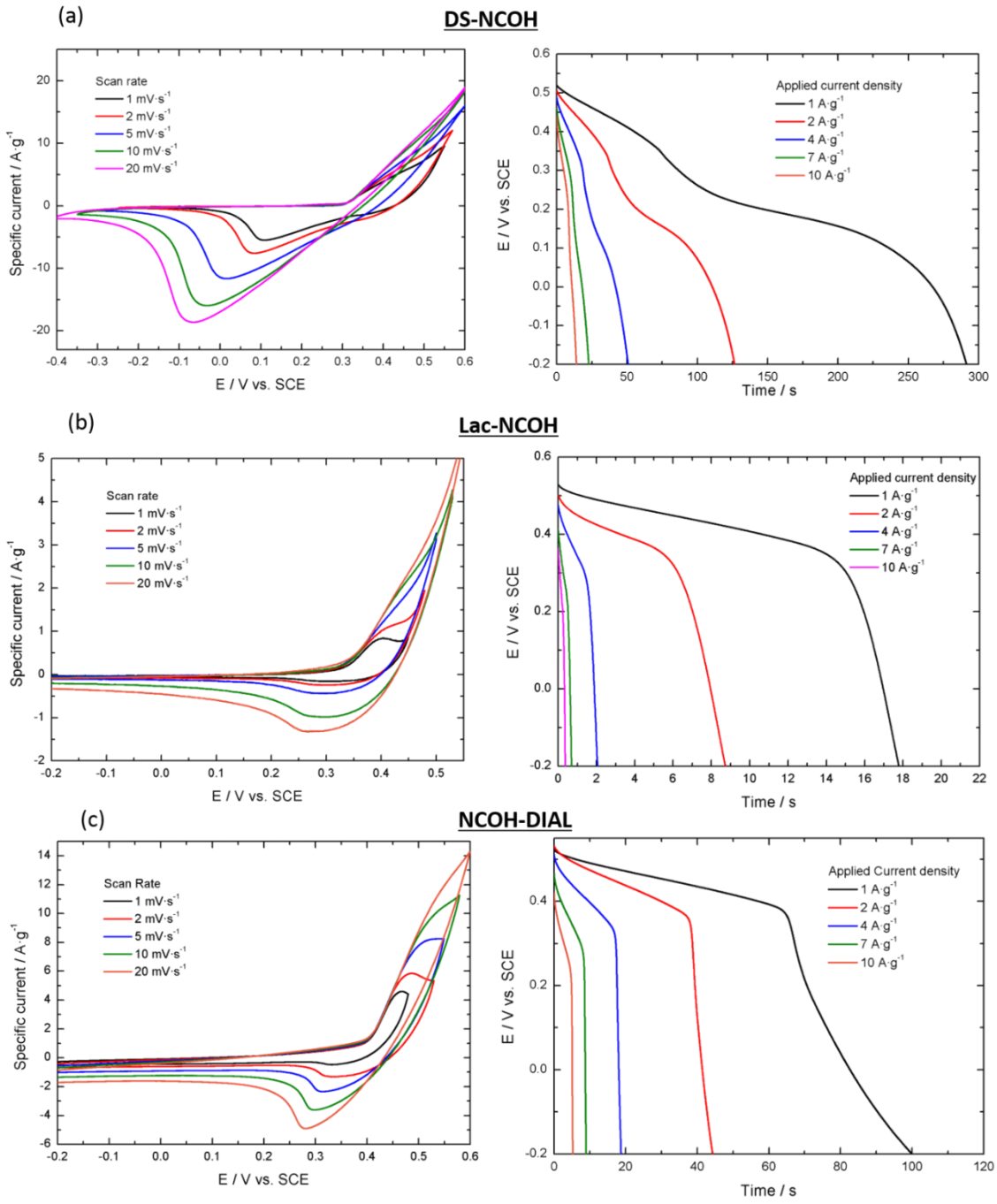

Fig. 3.5.25. Cyclic voltammetries at different scan rates and galvanostatic discharge curves at different applied current densities for the materials obtained during the delamination of nickel-cobalt hydroxide by lactate intercalation evaluated in 1M LiOH.

When the coulombic efficiency is calculated, values of 73, 99 and 89% for DS-NCOH, Lac-NCOH and NCOH-DIAL are obtained. While the current efficiency values are relatively maintained for the DS^- intercalated material and for the dialyzed material, it is extremely increased for the lactate-intercalated material. It has been reported that lithium shifts oxygen evolution reaction to higher values, lowering its effect [26]. In this case, it is likely that the lowering of the coulombic efficiency was caused by oxygen evolution and Li^+ promoted its inhibition, while DS-intercalated material lower coulombic efficiency is likely to be caused by parasitic reactions of the DS^- chains.

In conclusion, the intercalation of poorly conductive organic molecules to achieve the delamination of nickel-cobalt hydroxide greatly suppresses the interaction between the electrolyte and electrochemically active sites. Although dialysis serves as a mean to remove lactate anions, the strongly bonded molecules cannot be totally removed, and inhibition is still present. The use of LiOH relatively improves the electrochemical response and somehow limits the blockage caused by the organic-based anions. However, its effect is insufficient. If maximum electrochemical performance is sought, neither DS^- nor lactate molecules shall be present [47] if a complete activation of the material is sought. For that reason, additional purification routes, or different synthesis strategies for the development of exfoliated nickel-cobalt hydroxide nanoslabs for energy storage applications, shall be developed. In this scope, we present hereafter the results obtained for our alternative and original route concerning the exfoliation of nickel-cobalt oxyhydroxides.

3.5.3.2.2. Nickel-cobalt oxyhydroxide delamination

3.5.3.2.2.1 Study in 1M KOH electrolyte

Cyclic voltammetry curves at 5 $mV \cdot s^{-1}$ are shown in Fig. 3.5.26a in the potential range from -0.3 V to 0.55 V (vs. SCE). For the reference alpha phase (NCOH) an anodic peak with its cathodic counterpart are observed, centred at approximately 0.3 V and -0.05 V respectively), as expected for a mixed nickel-cobalt hydroxide. In the case of the oxyhydroxide (NCOx-HNK), there is a cathodic peak displacement to -0.1 V, while the anodic peak is maintained. Then, for the material after acidification (NCOx-H) the anodic peak is displaced to 0.4V, while the cathodic peak remains at similar values. Finally, in the case of the material exfoliated in TBAOH and re-stacked (NCOx-TBA), both peaks return to similar values to those assigned to the pristine alpha phase, with the anodic peak slightly displaced towards 0.35V. If anodic over cathodic current peak ratios are compared, NCOH presents a ratio of 0.9, while NCOx-HNK and NCOx-H present a ratio 1.0. Finally, the ratio for NCOx-TBA is 1.22, which may be caused by the interference of residual TBA^+ in the material that is being removed from the surface of the nanoobjects. This effect, observed for the first cycles of NCOx-TBA, occurs during reduction and produces a competitive process between discharge and TBA^+ removal that lowers the intensity of the anodic peak.

When galvanostatic charge-discharge curves are compared, best results are obtained for the hydroxide material, displaying 120.2 $mA \cdot h \cdot g^{-1}$. After oxidizing, the capacity of the oxyhydroxide material drops to 105.2 $mA \cdot h \cdot g^{-1}$. Then, when protonated, the material capacity significantly decreases down to 65 $mA \cdot h \cdot g^{-1}$ while, after exfoliation and re-stacking, the capacity increases again to 115 $mA \cdot h \cdot g^{-1}$, which is similar to the parent hydroxide material and slightly higher than the results obtained for NCOx-HNK. It is worth mentioning that all the materials exhibit high coulombic efficiency, with a 98%, 96%, 94% and 98% for NCOH, NCOx-HNK, NCOx-H and NCOx-TBA respectively.

Moreover, if the cycling behavior of these materials is investigated (Fig. 3.5.26d), the capacity for oxyhydroxides is slightly reduced during the first 100 cycles and is henceforth maintained. However, the hydroxide material capacity is greatly reduced during the first 100 cycles and progressively diminishes with cycling, due to the instability of the α phases and their transformation to β phases during continuous charge-discharge. Eventually, the capacity of NCOH diminishes to the point in which the capacity of NCOx-TBA becomes superior. In fact, during the first 100 cycles, NCOx-TBA shows an increase in capacity. This evolution can be explained by the fact that, initially, the interference of TBA^+ impedes an optimized electrode-electrolyte interaction. After activation, TBA^+ is removed from the surface of the active material and there is an increased number of electrochemically active sites. Moreover, once activated, the capacity decay of this material is similar to the performance displayed by the parent oxyhydroxide materials. It is also worth considering the possible tethering of TBA^+ ions to nickel-cobalt nanoslabs preventing the degradation of the material. After 5000 cycles, the capacity retention of the different materials is a 53%, 62%, 74% and 113% for NCOH, NCOx-HNK, NCOx-H and NCOx-TBA respectively. A more detailed view of the first 200 cycles is displayed in Fig. 3.5.27.

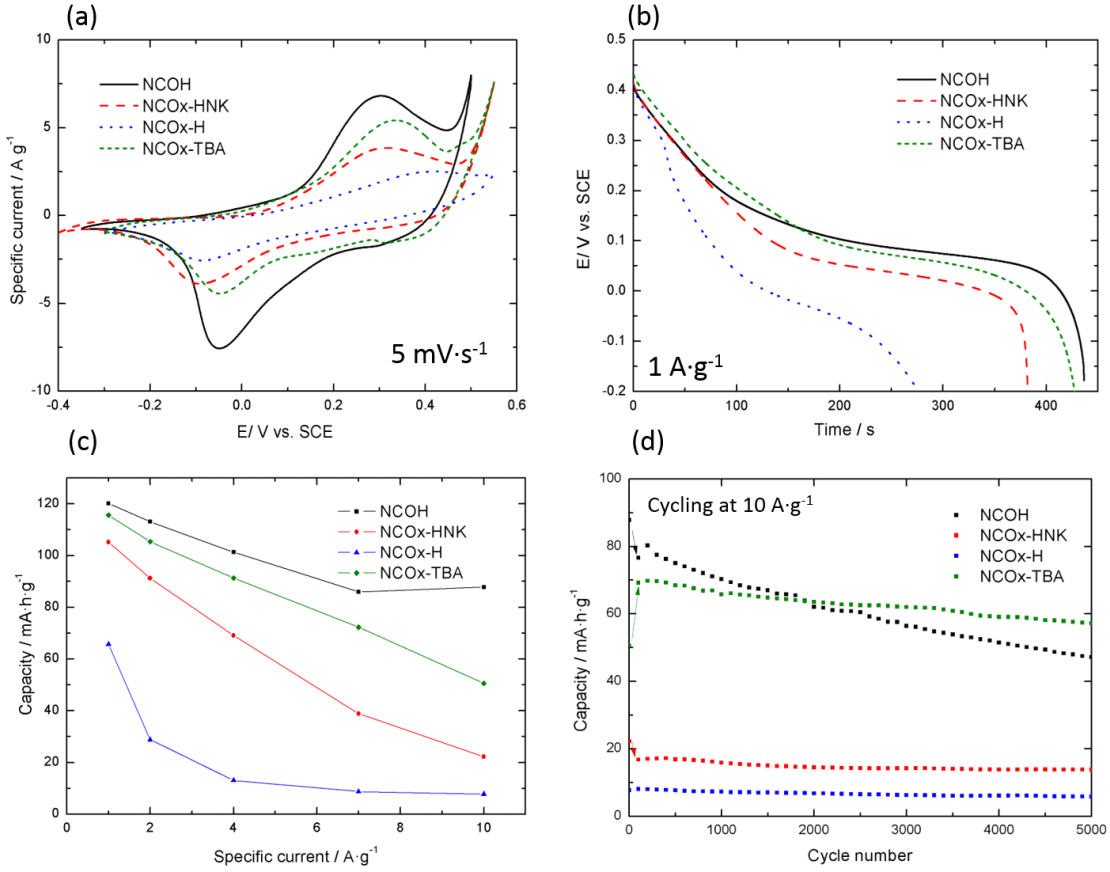

Fig. 3.5.26. Comparison of the electrochemical response by (a) cyclic voltammetry, (b) galvanostatic discharge, (c) capacity retention at different applied current densities and (d) capacity retention evaluated by galvanostatic continuous charge-discharge cycling during 5000 cycles at 10 $A \cdot g^{-1}$ for the different composites obtained during delamination of nickel-cobalt oxyhydroxide by TBA^+ intercalation in 1M KOH.

Finally, when higher current densities are applied (Fig. 3.5.26c), the best rate capability is exhibited by nickel-cobalt hydroxide, that retains up to a 73% of capacity at 10 $A \cdot g^{-1}$. Then, the best performance among the oxyhydroxide group is displayed by NCOx-

TBA, that retains up to a 43% of capacity, while a less promising performance is displayed for NCOx-HNK and NCOx-H with only a 21 and 11% capacity retention respectively at the same applied current density. Results concerning galvanostatic discharges at different applied current densities and cyclic voltammetries at different scan rates are displayed in detail in Fig. 3.5.28.

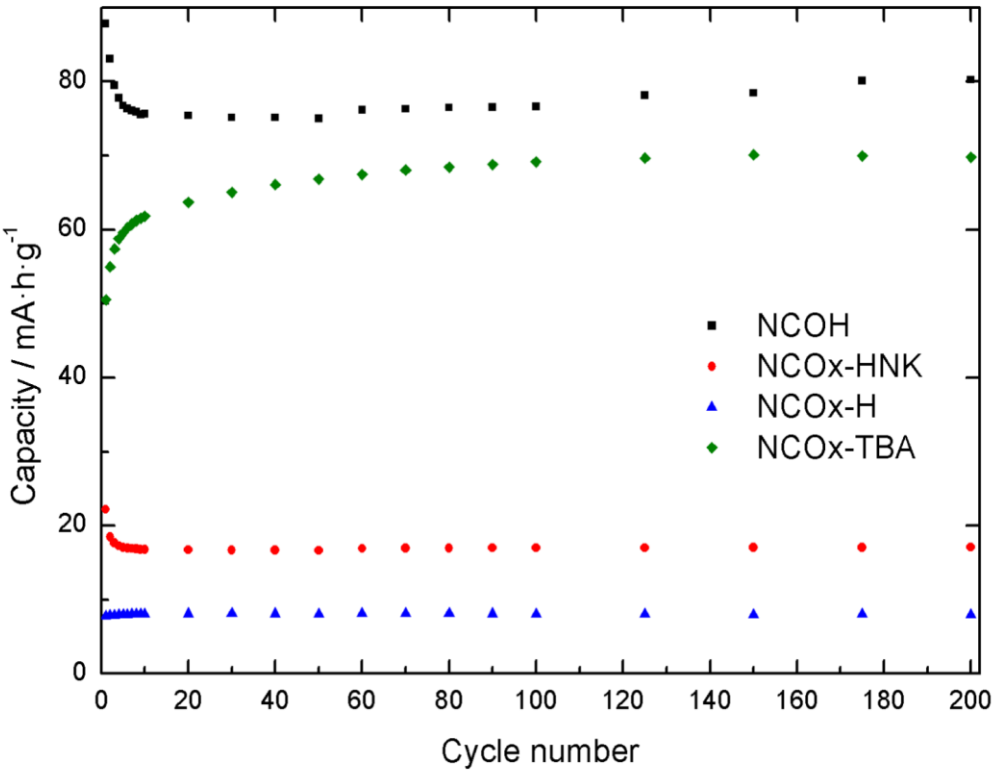

Fig. 3.5.27. Capacity evolution during the first 200 cycles of the materials obtained during the exfoliation in tetrabutylammonium, evaluated at $10A \cdot g^{-1}$ in 1M KOH.

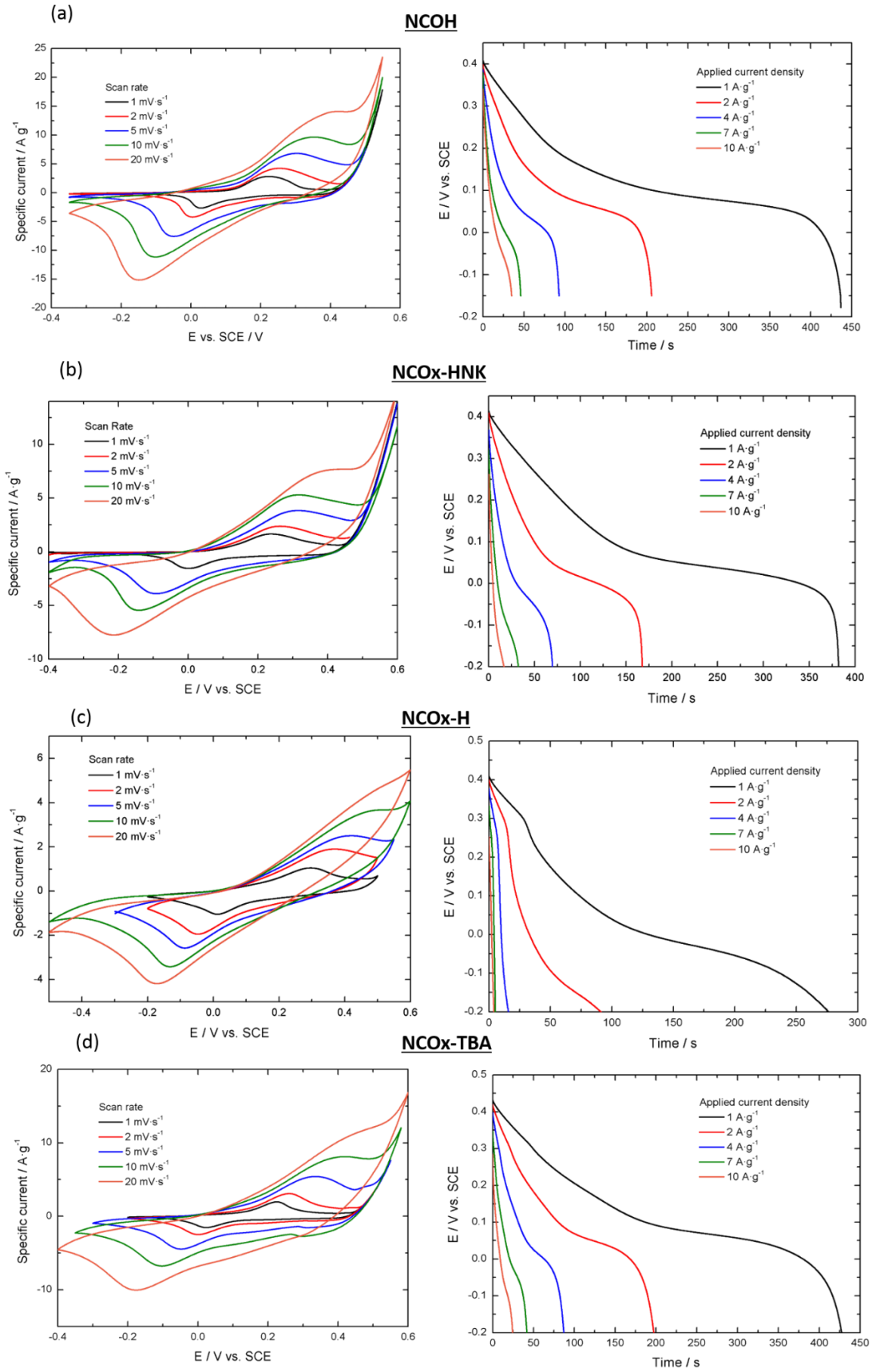

Fig. 3.5.28. Cyclic voltammetries at different scan rates and galvanostatic discharge curves at different applied current densities for the materials obtained during the delamination of nickel-cobalt oxyhydroxide by tetrabutylammonium intercalation evaluated in 1M KOH.

3.5.3.2.2.2 Study in 1M LiOH electrolyte

The electrochemical performance of these materials, shown in Fig. 3.5.29, has also been evaluated in 1M LiOH. The performance of NCOx-HNK and NCOx-H are slightly influenced by the change of electrolyte, with similar cycling performance and capacity values. Values of 112.6 and 79.8 mA·h·g^{-1} are obtained for NCOx-HNK and NCOx-H respectively, with a capacity retention of 38% and 28% after 5000 cycles in 1M LiOH. The main difference resides on the capacity retention values for higher applied current densities, displayed in Fig. 3.5.29c.

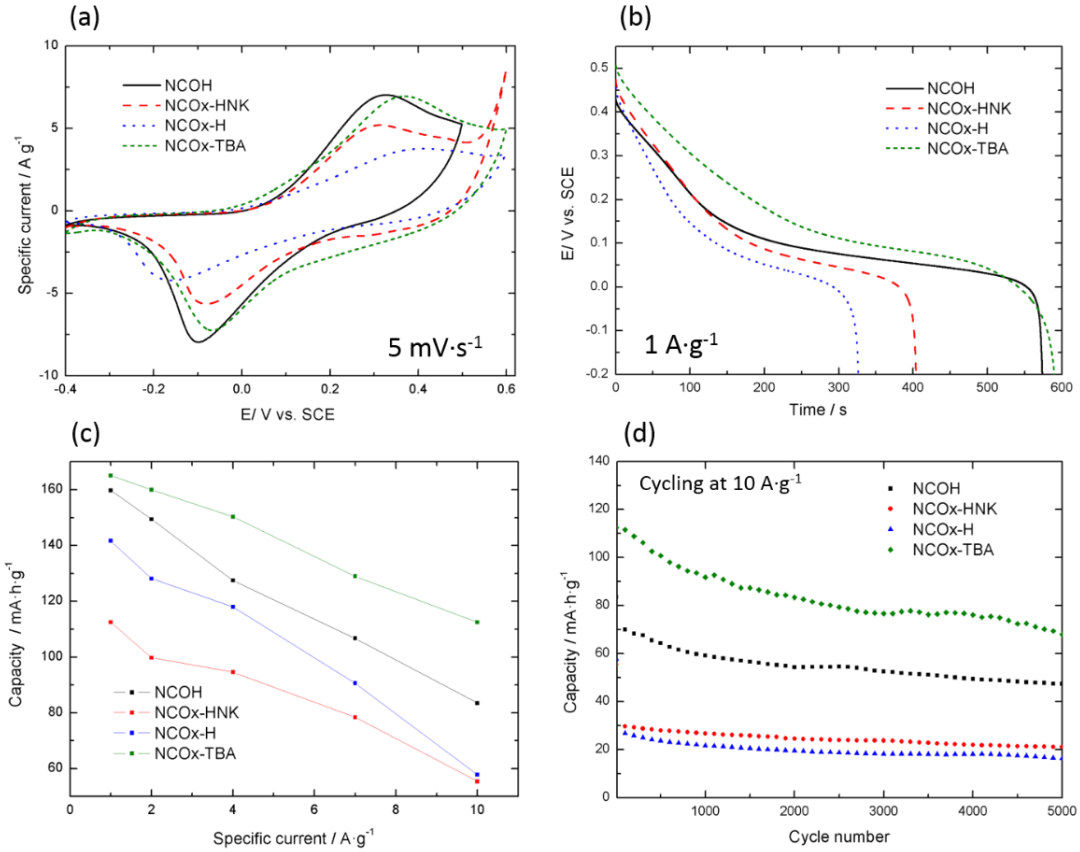

Fig. 3.5.29. Comparison of the electrochemical response by (a) cyclic voltammetry, (b) galvanostatic discharge, (c) capacity retention at different applied current densities and (d) capacity retention evaluated by galvanostatic continuous charge-discharge cycling during 5000 cycles at 10 A·g^{-1} for the different composites obtained during delamination of nickel-cobalt oxyhydroxide by TBA^+ intercalation in 1M LiOH.

There is an evident enhancement in performance for the hydroxide and the re-stacked material when LiOH is used in place of KOH, especially in the case of TBA^+ intercalated nickel-cobalt oxyhydroxide, resulting in a value of 159.8 mA·h·g^{-1} at 1A·g^{-1} and 83.5 mA·h·g^{-1} at 10 A·g^{-1} for NCOH and of 165.1 mA·h·g^{-1} at 1A·g^{-1} and 112.5 mA·h·g^{-1} at 10 A·g^{-1} for NCOx-TBA. Moreover, the behaviour of NCOH in LiOH is similar to KOH and diminishes on a 16% after the first 100 cycles, while the pre-activation step required for NCOx-TBA in KOH is only present for the first 100 cycles, as observed in Fig. 3.5.29d. A capacity retention of 56% and 60% for NCOH and NCOx-TBA is obtained after 5000 cycles at 10A·g^{-1}, respectively. The coulombic efficiency of these materials is similar to results obtained in KOH electrolyte, although overall higher current efficiency for the oxidized materials is obtained, with 98%, 97%, 98% and 98% for NCOH, NCOx-HNK, NCOx-H and NCOx-TBA respectively. In this case, the

electrochemical performance of the exfoliated and re-stacked material slightly surpasses the response of the initial hydroxide parent and is nearly 1.5 times the initial capacity displayed by the non-exfoliated oxyhydroxide. Details on the performance of the different materials at different scan rates and applied current densities are provided in Fig. 3.5.30.

On the one hand, this effect may be explained by the increased electrode-electrolyte interaction and ease for electrolyte penetration within the material once it is exfoliated and re-stacked. Although BET indicates a reduced surface area for NCOx-TBA, this may not correspond to the electrochemically active surface of the material. TBA^+ initially blocks the access to the electrolyte and reduces its surface area. However, when immersed in electrolyte and after a certain activation process, a more intimate contact between active material and electrolyte can be achieved. Moreover, it is observed by TEM and SEM the apparent decrease on the micro-crystalline structure (Fig. 3.5.14 and 3.5.15). It is feasible that, when the material is exfoliated and re-stacked, the interaction between the nanoslabs is reduced, promoting electrolyte penetration and resulting in enhanced capacity response. Therefore, two main factors are considered for the increase in capacity of the material: reduction of the micro-crystalline domain and weakened inter-slab interaction that promotes electrolyte penetration.

On the other hand, the use of LiOH may result in better faradaic charge-transfer phenomenon and better alkali ion penetration. Moreover, LiOH is likely to inhibit oxygen evolution and therefore to favour material oxidation. This is observed in an initially enhanced electrochemical response, with higher capacity, that requires an activation process of only 100 cycles to display maximum capacity. After activation, the cycling behaviour of the material is identical to the non-exfoliated parent material, with increased capacity.

In conclusion, the exfoliation of nickel-cobalt oxyhydroxide by means of TBA^+ intercalation proves delamination as a successful route for the enhancement of the electrochemical properties of the material in which TBA^+ intercalation does not hamper the electrochemical response of the active material. Despite the pre-activation step, especially required in 1M KOH, an optimized performance is observed in which intimate active material-electrolyte contact is achieved. Thus, exfoliation routes of layered materials to obtain few-layer nanostructures may have a positive impact in the production of the next-generation energy storage devices.

In principle, obtaining few-layer nanosheets of a lamellar material by delamination has two expected effects in the electrochemical performance. On the one hand, it serves as a pre-cursor route to create composite materials that interact at an atomic level, combining the benefits of different materials. On the other hand, when a delaminated material is re-stacked, as in this case, an increased active surface area of the material is expected, with the consequent enhanced electrode-electrolyte interaction and better electrochemical performance. However, if strongly-bonded non-conductive molecules are used, such as poorly conductive organic molecules, the electrode-electrolyte interaction is inhibited. Thus, when considering delamination for energy storage applications, careful selection of the molecules to be used during the process is a pre-requisite *sine qua non* to its success.

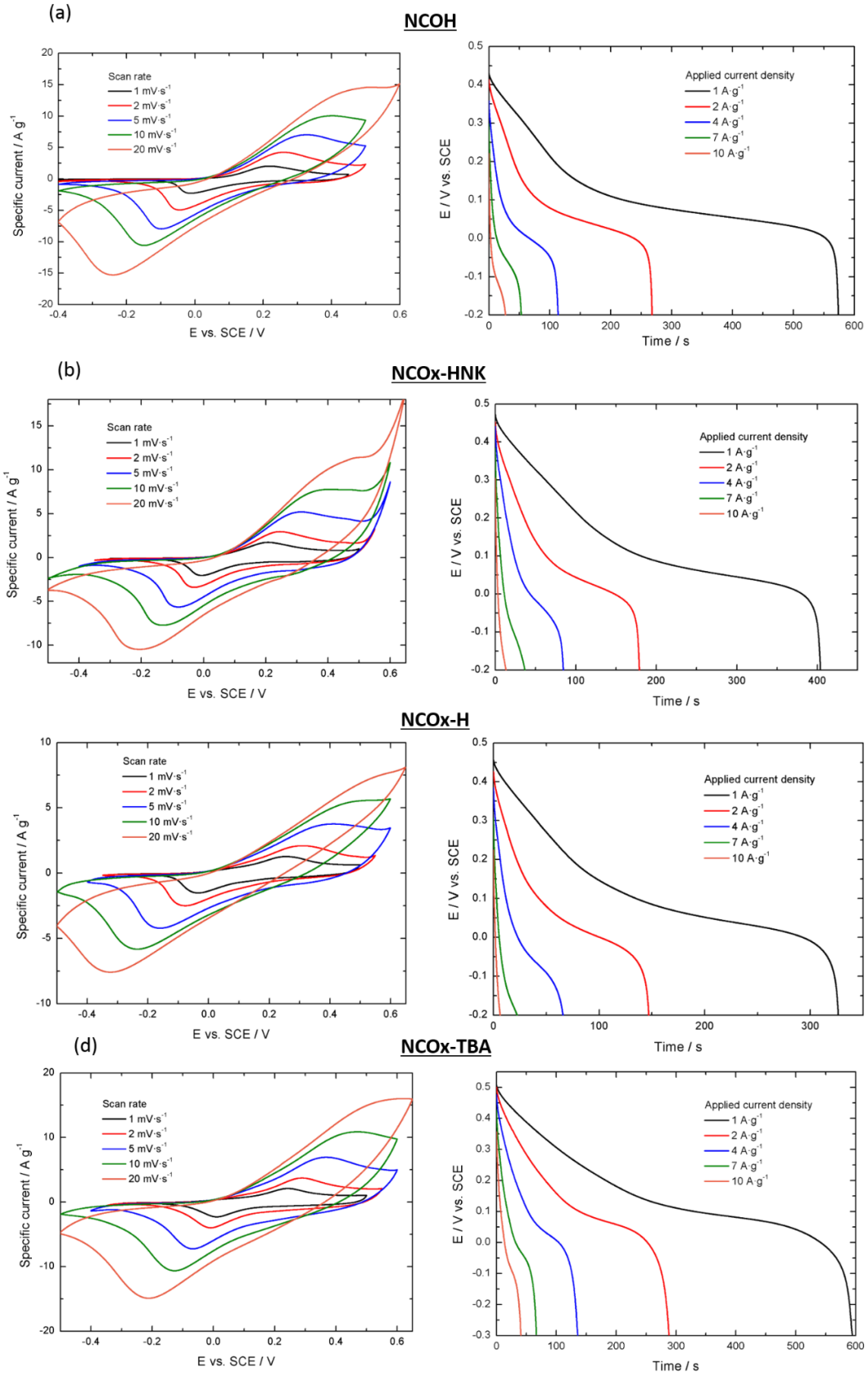

Fig. 3.5.30. Cyclic voltammetries at different scan rates and galvanostatic discharge curves at different applied current densities for the materials obtained during the delamination of nickel-cobalt oxyhydroxide by tetrabutylammonium intercalation evaluated in 1M LiOH.

3.5.4. Conclusions

Two different routes have been evaluated for delamination of nickel-cobalt (oxy)hydroxides and their application for energy storage. On the one hand, the exfoliation of nickel-cobalt hydroxide by lactate-intercalation and re-stacking by dialysis has led to a hindered electrochemical response caused by the blocked interaction between the electrolyte and the electrochemically active sites. This is the result of using poor ionic conductive organic molecules. Dialysis serves as a potential route to remove the residual intercalated material, but the strong bonding of lactate molecules to nickel-cobalt hydroxide nanoslabs requires optimization of the purification routes, or the pursuit of alternative routes, that do not involve non-conductive intercalated species for the delamination of nickel-cobalt hydroxide in aqueous media. On the other hand, delamination of nickel-cobalt oxyhydroxide by intercalation of tetrabutylammonium has proved to work as successful route to enhance the electrochemical performance of nickel-cobalt oxyhydroxide by increasing active surface area and electrode-electrolyte interaction. Therefore, the importance of carefully selecting the intercalated materials during the exfoliation of active layered materials for energy storage purposes has been evidenced and exfoliation in TBA-OH has been pin-pointed as a successful route to enhance the electrochemical activity of nickel-cobalt oxyhydroxide.

Acknowledgements

This work has been performed in scope of International Doctoral Program in Functional Materials (**IDS-FunMat, Erasmus Mundus**) and funded by the European Union. We would like to express our gratitude to the Fundação para a Ciência e Tecnologia (FCT) for the funding under the contracts M-ERA.NET/0002/2012 and UID/QUI/00100/2013. We would also like to acknowledge Laura Ilharco for her assistance in BET measurements and interpretation, Auguste Fernandes in his aid for FTIR spectra acquisition, Kush Kumar Upadhyay for electrochemical discussion, Laetitia Etienne for CHNS and ICP measurements, Eric Lebraud for performing the XRD experiments, Catherine Denage, Sabine Goma and Philippe Dagault for their general assistance and Marion Gayot and Sonia Buffière for performing TEM images at PLACAMAT (Plateforme Aquitaine de Caractérisation des Matériaux UMS 3626 CNRS-Université de Bordeaux, 33600 Pessac, FRANCE).

Chapter 3.5 references

[1] Q. Wang, D.O. Hare, Recent Advances in the Synthesis and Application of Layered Double Hydroxide (LDH) Nanosheets, (2012).

[2] M. Adachi-pagano, C. Forano, J. Besse, M. Inorganiques, C. Esa, U.B. Pascal, A. Cedex, Delamination of layered double hydroxides by use of surfactants, (2000) 91–92.

[3] G. Seeley, S.P. Road, W. Centre, Delamination of layered double hydroxides in polar monomers : new LDH-acrylate nanocomposites †, (2002) 1506–1507.

[4] M. Jobbágy, A.E. Regazzoni, Delamination and restacking of hybrid layered double hydroxides assessed by in situ XRD, 275 (2004) 345–348. doi:10.1016/j.jcis.2004.01.082.

[5] T. Hibino, W. Jones, L. Road, New approach to the delamination of layered double hydroxides, (2001) 1321–1323. doi:10.1039/b101135i.

[6] R. Ma, Z. Liu, K. Takada, N. Iyi, Y. Bando, Synthesis and Exfoliation of Co 2 + - Fe 3 + Layered Double Hydroxides : An Innovative Topochemical Approach, (2007) 5257–5263.

[7] T. Hibino, M. Kobayashi, Delamination of layered double hydroxides in water, (2005) 653–656. doi:10.1039/b416913a.

[8] C. Jaubertie, M.J. Holgado, M.S.S. Roma, V. Rives, U.V. De Salamanca, R. V March, V. Re, M. Recei, V. April, Structural Characterization and Delamination of Lactate-Intercalated Zn , Al-Layered Double Hydroxides, 1 (2006) 3114–3121.

[9] W. Deng, X. Ji, C.E. Banks, RSC Advances Electrochemical capacitors utilising transition metal oxides : an update of recent developments, (2011) 1171–1178. doi:10.1039/c1ra00664a.

[10] G. Wang, Z. Lei, Z. Jiujun, A review of electrode materials for electrochemical supercapacitors, ChemsucChem. 5 (2012) 797. doi:10.1039/c1cs15060j.

[11] B. Schneiderová, J. Demel, J. Pleštil, P. Janda, J. Bohuslav, D. Ihiawakrim, O. Ersen, G. Rogez, K. Lang, Nickel hydroxide ultrathin nanosheets as building blocks for electrochemically active layers, J. Mater. Chem. A. 1 (2013) 11429. doi:10.1039/c3ta12129a.

[12] B. Schneiderová, J. Demel, J. Pleštil, H. Tarábková, J. Bohuslav, K. Lang, Electrochemical performance of cobalt hydroxide nanosheets formed by the delamination of layered cobalt hydroxide in water, Dalt. Trans. 43 (2014) 10484. doi:10.1039/c4dt00141a.

[13] B. Schneiderová, J. Demel, A. Zhigunov, J. Bohuslav, H. Tarábková, P. Janda, K. Lang, Nickel-cobalt hydroxide nanosheets : Synthesis , morphology and electrochemical properties, J. Colloid Interface Sci. 499 (2017) 138–144. doi:10.1016/j.jcis.2017.03.096.

[14] R. Ma, T. Sasaki, Nanosheets of Oxides and Hydroxides: Ultimate 2D Charge-Bearing Functional Crystallites, Adv. Mater. 22 (2010) 5082–5104. doi:10.1002/adma.201001722.

[15] Z.H. Liu, K. Ooi, H. Kanoh, W.P. Tang, T. Tomida, Swelling and delamination behaviors of birnessite-type manganese oxide by intercalation of tetraalkylammonium ions, Langmuir. 16 (2000) 4154–4164. doi:10.1021/la9913755.

[16] K. Fukuda, I. Nakai, Y. Ebina, R. Ma, T. Sasaki, Colloidal unilamellar layers of tantalum oxide with open channels, Inorg. Chem. 46 (2007) 4787–4789. doi:10.1021/ic7004002.

[17] T.W. Kim, E. Oh, A. Jee, T. Lim, H. Park, Soft-Chemical Exfoliation Route to Layered Cobalt Oxide Monolayers and Its Application for Film Deposition and Nanoparticle Synthesis, (2009) 10752–10761. doi:10.1002/chem.200901590.

[18] C. Faure, C. Delmas, P. Willmann, Preparation and characterization of cobalt-substituted α-nickel hydroxide stable in KOH medium Part II. α-Hydroxide with a turbostratic structure, J. Power Sources. 35 (1991) 263–277. doi:http://dx.doi.org/10.1016/0378-7753(91)80111-A.

[19] L. Guerlou-Demourgues, C. Delmas, New manganese-substituted nickel hydroxides, J. Power Sources. 52 (1994) 275–281. doi:10.1016/0378-7753(94)02024-8.

[20] P. Jeevanandam, A. Gedanken, Y. Mastai, Synthesis of alpha-cobalt(II) hydroxide using ultrasound radiation, J. Mater. Chem. 10 (2000) 511–514.

[21] D.S. Hall, D.J. Lockwood, S. Poirier, C. Bock, B.R. MacDougall, Raman and infrared spectroscopy of α and β phases of thin nickel hydroxide films electrochemically formed on nickel, J. Phys. Chem. A. 116 (2012) 6771–6784. doi:10.1021/jp303546r.

[22] L. Deng, H. Zeng, Z. Shi, W. Zhang, J. Luo, Sodium dodecyl sulfate intercalated and acrylamide anchored layered double hydroxides: A multifunctional adsorbent for highly efficient removal of Congo red, J. Colloid Interface Sci. 521 (2018) 172–182. doi:10.1016/j.jcis.2018.03.040.

[23] M. Picquart, Vibrational Mode Behavior of SDS Aqueous Solutions Studied by Raman Scattering, J. Phys. Chem. 90 (1986) 243–250.

[24] M. Pecul, A. Rizzo, J. Leszczynski, Vibrational Raman and Raman optical activity spectra of D-lactic acid, D-lactate, and D-glyceraldehyde: Ab initio calculations, J. Phys. Chem. A. 106 (2002) 11008–11016. doi:10.1021/jp021030m.

[25] Y. Omomo, T. Sasaki, L. Wang, M. Watanabe, Redoxable nanosheet crystallites of MnO2 derived via delamination of a layered manganese oxide, J. Am. Chem. Soc. 125 (2003) 3568–3575. doi:10.1021/ja021364p.

[26] P. Oliva, J. Leonardi, J.F. Laurent, C. Delmas, J.J. Braconnier, M. Figlarz, F. Fievet, A. de Guibert, Review of the structure and the electrochemistry of nickel hydroxides and oxy-hydroxides, J. Power Sources. 8 (1982) 229–255. doi:10.1016/0378-7753(82)80057-8.

[27] C. Tang, Exfoliation and restacking of manganese and cobalt based lamellar oxides for supercapacitor electrodes, Université de Bordeaux, 2017. doi:HAL Id: tel-01696266.

[28] C. Faure, C. Delmas, M. Fouassier, Characterization of a turbostratic α-nickel hydroxide quantitatively obtained from an NiSO4 solution, J. Power Sources. 35 (1991) 279–290. doi:10.1016/0378-7753(91)80112-B.

[29] Q. Gao, O. Giraldo, W. Tong, S.L. Suib, Preparation of Nanometer-Sized Manganese Oxides by Intercalation of Organic Ammonium Ions in Synthetic Birnessite OL-1, Chem. Mater. 1 (2001) 778–786.

[30] Z.P. Xu, H.C. Zeng, Interconversion of brucite-like and hydrotalcite-like phases in cobalt hydroxide compounds, Chem. Mater. 11 (1999) 67–74. doi:Doi 10.1021/Cm980420b.

[31] and H.-Y.W. Zhong-Ai Hu,* Yu-Long Xie, Yao-Xian Wang, Li-Jing Xie, Guo-Rui Fu, Xiao-Qing Jin, Zi-Yu Zhang, Yu-Ying Yang, Synthesis of a-cobalt hydroxides with different intercalated anions and effects of intercalated anions, J. Phys. Chem. C. 113 (2009) 12502–12508.

[32] H. Yuan, D. Dubbink, R. Besselink, J.E. Ten Elshof, The Rapid Exfoliation and Subsequent Restacking of Layered Titanates Driven by an Acid-Base Reaction, Angew. Chemie - Int. Ed. 54 (2015) 9239–9243. doi:10.1002/anie.201502539.

[33] Y. Ishijima, M. Okaniwa, Y. Oaki, H. Imai, Two exfoliation approaches for organic layered compounds: hydrophilic and hydrophobic polydiacetylene nanosheets, Chem. Sci. 8 (2017) 647–653. doi:10.1039/C6SC03350D.

[34] C. Faure, C. Delmas, M. Fouassier, P. Willmann, Preparation and characterization of cobalt-substituted α-nickel hydroxides stable in KOH medium Part I. α′-hydroxide with an ordered packing, J. Power Sources. 35 (1991) 249–261. doi:http://dx.doi.org/10.1016/0378-7753(91)80110-J.

[35] J.-H. Zhong, A.-L. Wang, G.-R. Li, J.-W. Wang, Y.-N. Ou, Y.-X. Tong, Co3O4/Ni(OH)2 composite mesoporous nanosheet networks as a promising electrode for supercapacitor applications, J. Mater. Chem. 22 (2012) 5656. doi:10.1039/c2jm15863a.

[36] O. Diaz-Morales, D. Ferrus-Suspedra, M.T.M. Koper, The importance of nickel oxyhydroxide deprotonation on its activity towards electrochemical water oxidation, Chem. Sci. 7 (2016) 2639–2645. doi:10.1039/C5SC04486C.

[37] P.L. Bourgault, B.E. Conway, The Electrochemical Behavior of the Nickel Oxide Electrode: Part II. Quasi-Equilibrium Behavior, Can. J. Chem. 38 (1960) 1557–1575. doi:10.1139/v60-216.

[38] V. Srinivasan, B.C. Cornilsen, J.W. Weidner, A nonstoichiometric structural model to characterize changes in the nickel hydroxide electrode during cycling, J. Solid State Electrochem. 9 (2005) 61–76.

[39] R. Barnard, C.F. Randell, F.L. Tye, Studies concerning charged nickel hydroxide electrodes IV. Reversible potentials in LiOH, NaOH, RbOH and CsOH, J. Appl. Electrochem. 11 (1981) 517–523. doi:10.1007/BF01132440.

[40] E.J. Rubin, R. Baboian, A Correlation of the Solution Properties and the Electrochemical Behavior of the Nickel Hydroxide Electrode in Binary Aqueous Alkali Hydroxides, J. Electrochem. Soc. 118 (1971) 428. doi:10.1149/1.2408074.

[41] Y.M. Cai, Z.Y. Qin, L. Chen, Effect of electrolytes on electrochemical properties of graphene sheet covered with polypyrrole thin layer, Prog. Nat. Sci. Mater. Int. 21 (2011) 460–466. doi:10.1016/S1002-0071(12)60083-5.

[42] C. Xu, C. Wei, B. Li, F. Kang, Z. Guan, Charge storage mechanism of manganese dioxide for capacitor application: Effect of the mild electrolytes containing alkaline and alkaline-earth metal cations, J. Power Sources. 196 (2011) 7854–7859. doi:10.1016/j.jpowsour.2011.04.052.

[43] J. Zhu, Y. Xu, J. Wang, J. Lin, X. Sun, S. Mao, The effect of various electrolyte cations on electrochemical performance of polypyrrole/RGO based supercapacitors, Phys. Chem. Chem. Phys. 17 (2015) 28666–28673. doi:10.1039/c5cp04080a.

[44] C. Zhong, W. Hu, Y. Deng, D. Sun, X. Han, J. Qiao, J. Zhang, Electrolytes for Electrochemical Supercapacitors, CRC Press, 2016. doi:10.1201/b21497-3.

[45] A.I. Inamdar, Y.S. Kim, S.M. Pawar, J.H. Kim, H. Im, H. Kim, Chemically grown, porous, nickel oxide thin-film for electrochemical supercapacitors., J. Power Sources. 196 (2011) 2393–2397. doi:10.1016/j.jpowsour.2010.09.052.

[46] L. Soserov, T. Boyadzhieva, V. Koleva, C. Girginov, A. Stoyanova, R. Stoyanova, Effect of the Electrolyte Alkaline Ions on the Electrochemical Performance of α-Ni(OH)2/Activated Carbon Composites in the Hybrid Supercapacitor Cell, ChemistrySelect. 2 (2017) 6693–6698. doi:10.1002/slct.201701579.

[47] J.W. Lee, J.M. Ko, J.D. Kim, Hierarchical microspheres based on alpha-Ni(OH)2 nanosheets intercalated with different anions: Synthesis, anion exchange, and effect of intercalated anions on electrochemical capacitance, J. Phys. Chem. C. 115 (2011) 19445–19454. doi:10.1021/jp206379h.

Conclusions and outlook

4. Conclusions

The main goal of this work was to synthesize new nanostructured nickel-cobalt based materials, in combination with reduced graphene oxide, for application as electrodes in electrochemical energy storage devices. This chapter summarizes the most important achievements obtained in this dissertation, and its relevance in the current state of the art. As discussed, the increased development of new nanostructured materials has led to unexpected electrochemical performances, inducing the need to clearly identify the nature of their reactions. Therefore, establishing the right framework of work is essential for the correct evaluation of the electrochemical performance of the materials synthesized.

When nanostructured, certain metal oxides display a pseudo-capacitive behaviour, in which charge storage is not dependent on phase transformations [1,2]. Consequently, material charging is no longer controlled by diffusion of species, and the power-response of the material increases. This has been one of the main limitations of batteries and recent advances on material science are focused on producing electrodes for high-energy density and high-power density devices. Nickel-cobalt hydroxides and oxides have well-known battery-like behaviour in their bulky form. In the work here presented for nanostructured nickel-cobalt (hydr)oxides, phase transformations were not inhibited and, therefore, there is still a faradaic-dominated electrochemical response. Nonetheless, the main objective is analogous to pseudocapacitive materials: to limit diffusion-controlled processes by confining reactivity to the surface of the material, hence increasing power capabilities. When the material is nanostructured, the diffusion paths are shortened and, diffusion-controlled processes, therefore, lose relevance in the electrochemical response of the material. Moreover, the intention behind the synthesis of these metal oxides and hydroxides is to combine them with graphene-based materials, in particular, reduced graphene oxide (rGO) to form hybrid composites in which the properties of both materials intertwine, for enhanced electrochemical performances. Thus, the reasoning to define the materials here developed as a high-rate energy storage material, internal parallel hybrid or hybrid composite is two-fold: (i) nanostructured materials with surface-confined reactivity (high-rate properties) are synthesized and (ii) the combination of faradaic materials with graphene, a carbon-based material with supercapacitive properties is presented.

These materials have been obtained by two different synthetic strategies, namely, electrodeposition and exfoliation and re-stacking. Electrodeposition was chosen as a simple, one-step route that enables deposition of nickel-cobalt hydroxide in controlled ratios directly on top of the current collector, this is, without the need of binders or additional additives. This technique facilitates an intimate contact between the current collector and the active material, reducing the overall resistance of the system. Moreover, different phases or morphologies can be obtained by applying different deposition conditions. As consequence of the absence of external reactants or binders, electrodeposition is also generally used in studies concerning the mechanisms of materials [3,4]. Finally, it is worth mentioning that electrodeposition is a technique generally used in industry, therefore, the materials synthesized by electrodeposition can be, potentially up-scaled.

On the other hand, exfoliation is a promising technique in the nano-structuration of lamellar materials. Although in its early stages, when compared to electrodeposition, many materials have been prepared by different delamination routes, specially LDH lamellar materials [5]. Delamination is a promising technique to increase active surface

area and, therefore, its potential application in energy storage is of great interest. Moreover, apart from enabling the production of few-layer nanoslabs, it also serves as a precursor strategy to combine materials with different properties. Although this line of work was not explored, due to time constraints, the combination of nickel-cobalt oxyhydroxide or hydroxides with other metal oxides like manganese oxide, or 2D structures such as graphene, can bring synergistic effects that are worth exploring.

The first experimental work reported was based on the electrodeposition of nickel and cobalt hydroxide as electrode material, and the impact that reduced graphene oxide has on its performance. A similar synthesis strategy and electrochemical analysis was performed for nickel-cobalt oxide, obtained by electrodeposition and thermal treatment. Moreover, an in-depth study by means of electrochemical impedance spectroscopy was performed to evaluate the main mechanisms of degradation of these materials. Results highlight several important contributions to the state-of-the-art of these materials.

First, α phases of nickel-cobalt hydroxides, in ratios 2:1 and 1:2, displayed only ~30 $mA \cdot h \cdot g^{-1}$ in 1M KOH at $1A \cdot g^{-1}$ in the -0.2V to 0.45V potential range, while nickel-cobalt oxide, only studied in a 2:1 ratio, displayed 113 $mA \cdot h \cdot g^{-1}$. It is worth mentioning the much lower capacity value obtained for nickel-cobalt hydroxide, especially when compared to literature. Since electrodeposition conditions displayed similar mass for both materials, the increase of capacity due to thermal treatment suggests that the lower results for the hydroxide material may be caused by a poor electrode-electrolyte interaction. In fact, when SEM images are evaluated, presented in Fig. 4.1, it is possible to observe that the hydroxide thin-film, despite presenting several nanoflake-like features, displays a much smoother surface underneath, while nickel-cobalt oxide exhibits a relatively porous morphology. Any region not accessible by the electrolyte becomes "dead mass", this is, electrochemically inactive deposit. Due to the nature of the thin-film, in which small weight differences can translate in very different results (this is seen in the form of overestimation of *capacitance* in literature), this phenomenon has a very detrimental impact in the overall capacity of the material. In the case of nickel-cobalt oxide, the thin-film seems to be formed by small aggregated areas, formed to better accommodate strain during the thermal treatment. It is possible that this induces an increased porosity of the film, promoting the electrode-electrolyte interaction and displaying more active sites, with the consequent increase of capacity.

On the other hand, when reduced graphene oxide (Er-GO) is introduced, Ni-$Co(OH)_2$(2:1)/Er-GO displayed 77 $mA \cdot h \cdot g^{-1}$ while 96 $mA \cdot h \cdot g^{-1}$ were obtained for Ni-$Co(OH)_2$(1:2)/Er-GO (~250% capacity increase) and 180 $mA \cdot h \cdot g^{-1}$ for $Ni_{1-x}Co_xO_y$/Er-GO (~159% capacity increase). When nickel-cobalt hydroxide is deposited on top of Er-GO, a similar effect to thermal treatment, in which aggregation is avoided, is observed, thus unravelling increased capacity for the hydroxide material. Moreover, it may also improve faradaic charge-transfer, increase the number of active sites and enhance overall conductivity. Thus, Er-GO still improves the performance of nickel-cobalt oxide but in a more moderate rate when compared to nickel-cobalt hydroxide.

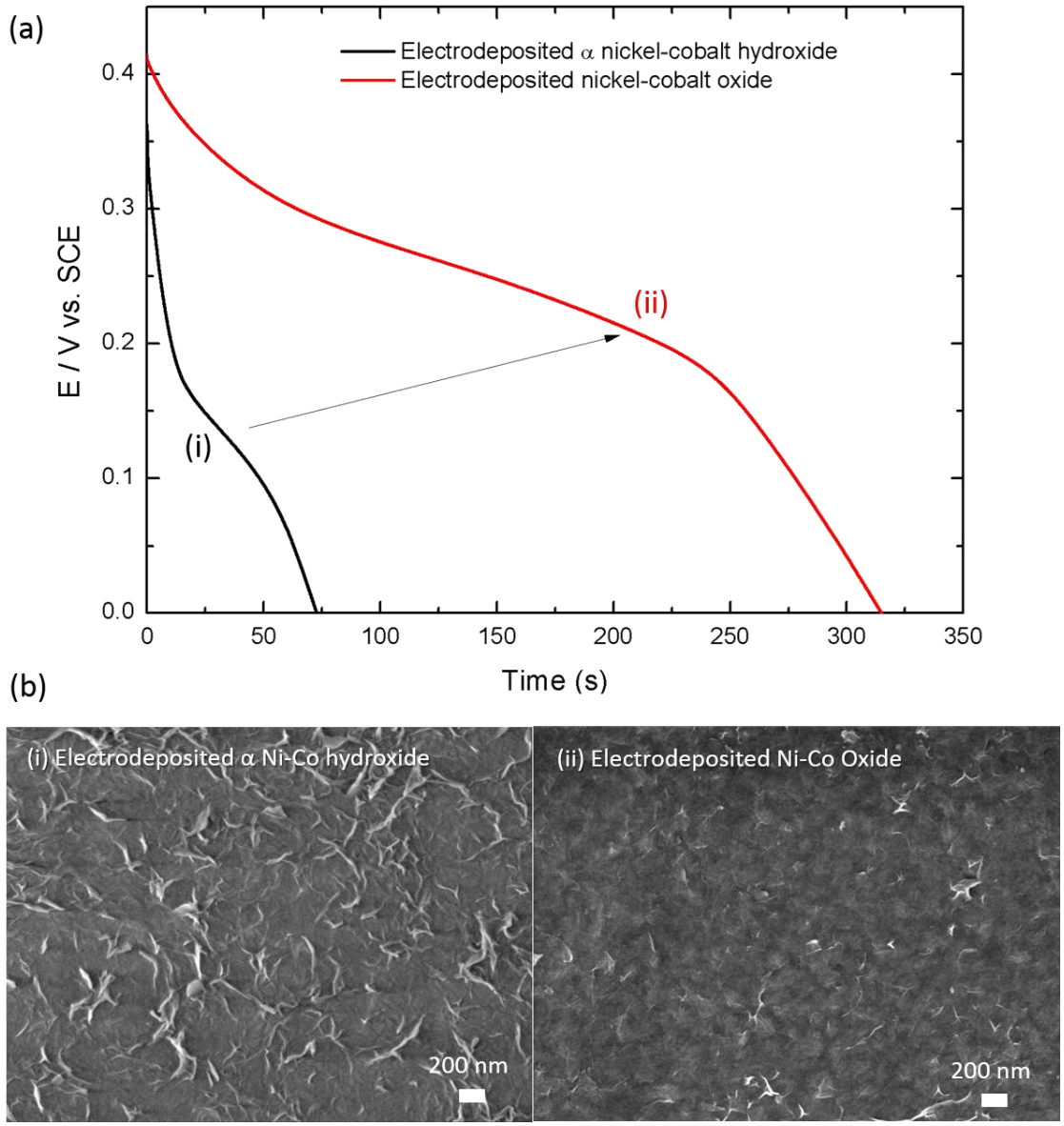

Fig. 4.1. (a) Galvanostatic discharge curves of nickel-cobalt (i) hydroxide and (ii) oxide with (b) their corresponding SEM images

Furthermore, cycling stability after 5000 cycles was improved in any case in approximately 20% when Er-GO was incorporated. The carbon-based material acted as conductive matrix that enhanced the faradaic reaction rate and provided more anchoring sites than stainless steel, thus increasing the active surface area and avoiding aggregation of both graphene layers and nickel-cobalt (hydr)oxides.

These materials also presented an interesting characteristic that is usually not reported for faradaic-dominated electrode materials: they could be scanned at a rate up to 1500 $mV \cdot s^{-1}$ without major loss of peak definition in cyclic voltammetry. Diffusion controlled battery-like materials can usually be evaluated only in the 1-20 $mV \cdot s^{-1}$ scan rate range. This exemplifies enhanced power capabilities and potential applicability to devices that require relatively high power and capacity. In this case, it could be considered that there was a trade-off of between high capacity values and high-power capabilities.

Moreover, an interpretation of the degradation mechanisms of nickel-cobalt (hydr)oxide during cycling stability tests was performed. In fact, many reports focus on different synthesis strategies for nickel-cobalt hydroxides and oxides, nonetheless, very few of them do an in-depth evaluation of the mechanisms that cause degradation. In the present manuscript, a combination of electrochemical impedance spectroscopy with scanning electron microscopy and cyclic voltammetry, enabled the elucidation of the possible degradation mechanisms, which were: (i) α to β phase transformation, (ii) micro-structural cracking due to volume changes and (iii) effect of parasitic reactions, especially, oxygen evolution reaction (OER) during charge of the sample, as exemplified in Fig. 4.2. When Er-GO was introduced, the overall resistance of the system was reduced while the parasitic reactions, α→β phase transformation and OER were inhibited. When nickel-cobalt (hydr)oxide was deposited on top of the graphene flakes, it stabilized the (hydr)oxide phase and inhibited volume changes during charge-discharge. It is worth pointing out that issues such as OER and α→β transformation have been one of the main challenges of nickel hydroxide electrodes in the past, thus, the work here presented may have an impact on future hybrid devices and hybrid composites but may also affect nickel hydroxide electrodes in nickel-based batteries.

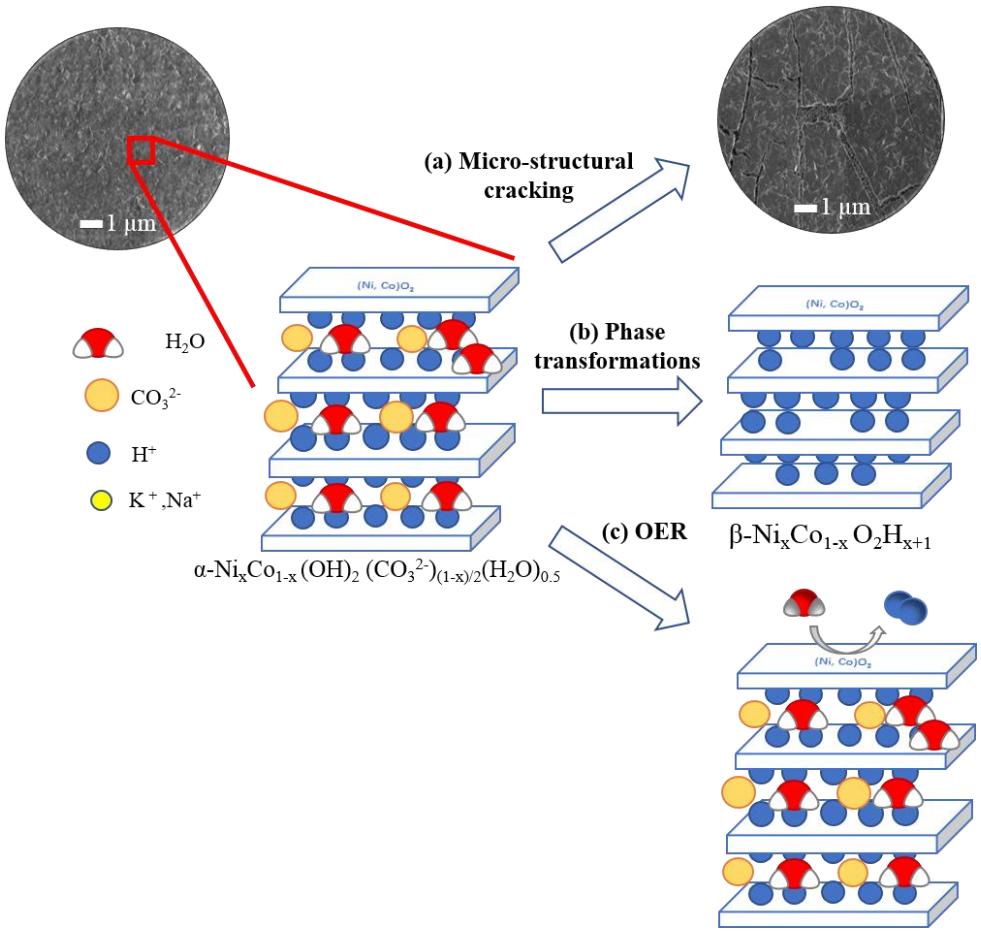

Fig. 4.2. Schematic representation of the main degradation phenomena reported in this thesis, exemplified in an α phase of nickel-cobalt hydroxide.

As final remark concerning electrodeposition, it is worth mentioning that this technique enabled a single-step synthesis of reduced graphene oxide-metal (hydr)oxide composite electrode, with Er-GO as part of the active material. Most of the literature concerning reduced graphene oxide composite materials tend to be based on rather complicated, multiple-step synthesis strategies and, in many cases, graphene derivatives are used as

substrate and not active material when combined with metal oxides. In this case, although Er-GO also serves as a conductive matrix, it plays an important role in the electrochemical activity of the material.

As far as exfoliation is concerned, the delamination of nickel-cobalt hydroxide was performed by means of lactate intercalation while the delamination of nickel-cobalt oxyhydroxide was performed by the intercalation of tetrabutylammonium cations in aqueous media. Although the delamination of nickel-cobalt hydroxides by lactate intercalation had already been reported in literature [6], the exfoliation of nickel-cobalt oxyhydroxide is here reported, to the best of the author's knowledge, for the first time in aqueous media. This route had already been applied to delaminate other materials, such as manganese oxide by Sasaki et al. [7], or cobalt oxyhydroxide by Tang et al. [8], however, from an energy storage perspective, it is interesting to evaluate the performance of delaminated nickel-cobalt oxyhydroxide, which are expected to deliver more energy density than pure cobalt pure oxyhydroxide.

Moreover, a complete evaluation of the electrochemical performance of the materials involved in these synthesis is here presented. It is worth pointing out that, although some cyclic voltammetry studies in 1M KOH were done for the lactate intercalation route, as presented in the introductory chapter, no in-depth evaluation of the electrochemical performance of these materials had been reported. In addition, the work presented in this thesis exemplified the importance of careful design of synthetical routes for energy storage applications, and the implications that these routes have on the ultimate performance of the materials. Lactate intercalation led to surface blockage, caused by the poor ionic conductivity of the organic molecules attached to the surface of the active material, whereas nickel-cobalt oxyhydroxide exfoliated in tetrabutylammonium led, in comparison, to an enhanced electrochemical performance. Non-exfoliated nickel-cobalt oxyhydroxide exhibited 112 $mA \cdot h \cdot g^{-1}$ in 1M LiOH, the material displayed 165 $mA \cdot h \cdot g^{-1}$ after delamination. This was assigned to increased active surface area and better electrode-electrolyte interaction that led to enhanced faradaic charge-transfer phenomena.

It is interesting to compare the enhanced behaviour that the material displays when nanostructured, as opposed to its bulk behaviour. Although the performance of the nanostructured material was faradaic dominated, the contribution to charge storage was slightly expanded to a wider potential range. While the non-exfoliated material presented most of the charge stored in the 0.0V to 0.1V vs. SCE potential range, the delaminated material discharge curve displayed a more relevant contribution in the potential range from 0.1V to 0.5V vs. SCE. Moreover, nanostructuring the material led to better ionic pathways and chemical and physical activation, this is, higher number of active sites. The difference between bulk and nano- structures is more evident when the materials obtained by electrodeposition and co-precipitation are compared. If the discharge curve of hydroxides and oxides obtained by electrodeposition, Fig. 4.1, are compared to the curves obtained by coprecipitation (and oxidation), Fig. 4.3, the latter present a more evident plateau, with most charge stored in a limited potential range, while the nanostructured materials have a more distributed charge storage mechanism in the potential range in which they are active.

It is interesting to compare the fundamental difference between these two techniques: while electrodeposition can be considered as a bottom-up strategy, delamination is a top-down approach. Interestingly, they result in different trade-offs when used in energy storage. On the one hand, the capacity of nickel-cobalt oxide and hydroxide obtained by electrodeposition is not as high as in some other cases, but they can reach much higher

scan rates without the appearance of resistive diffusion-controlled phenomena. On the other hand, exfoliated nickel-cobalt oxides and hydroxides cannot reach such fast scan rates, with a maximum of 20 $mV \cdot s^{-1}$, a common value for battery-like materials, while their capacities are considerably higher in the case of hydroxides. This perfectly exemplifies how the same material, under different synthesis strategies, morphologies and structures can lead to very different results in similar conditions (1M KOH and using stainless steel as current collector). This ratifies the reasoning behind exploring different synthesis routes for the same material. Thus, depending upon final application, not only the materials under use shall be considered but also the synthesis strategies undertaken.

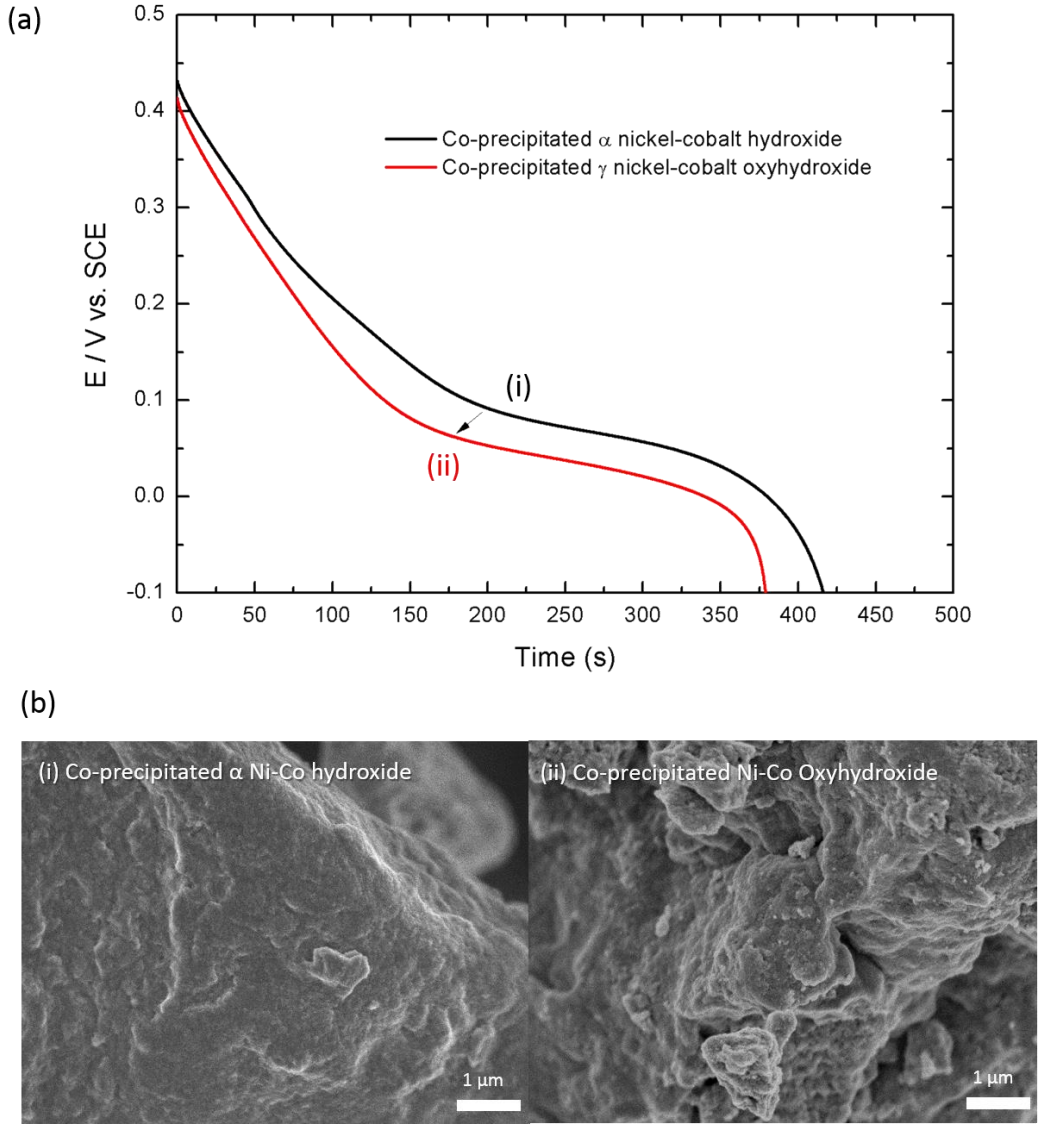

Fig. 4.3. (a) Galvanostatic discharge curves of nickel-cobalt (i) hydroxide and (ii) oxyhydroxide with (b) their corresponding SEM images.

Another comparison arises between oxide and hydroxide materials. Although the different response due to an activation process for electrodeposited materials in the hydroxide to oxide transformation has already been discussed, and since the response obtained by the two delamination strategies are not comparable (due to the different nature of the synthetic routes), the different results obtained for nickel-cobalt hydroxide and oxyhydroxide prepared by co-precipitation are also discussed (Fig. 4.3). In this case, the variation of capacity observed is opposed to results by electrodeposition. Both

materials present very similar morphology. Nonetheless, there seems to be a diminution of the particle size. Consequently, very similar results are obtained for both materials and the decrease in capacity is associated to lower number of exchanged electrons, due to stabilization of higher average oxidation states for cobalt, with a mixture of Co(III)/Co(IV) and Ni(III)/Ni(IV) [9].

In conclusion, different nanostructured nickel-cobalt based materials have been successfully synthesized and their electrochemical properties for energy storage applications investigated, fulfilling the initial goal of this work. A summary of the most illustrative results for the different materials studied in this work is included in table 4.1.

Additionally, two fundamental studies of nickel-cobalt hydroxide by means of micro-potentiometry and the application of the Mott-Schottky model have been done. It is of vital importance to fully understand the underlaying phenomena that enables charge storage to correctly interpret the results obtained. This is, as it has been seen, crucial for correct EIS interpretation, but also to develop materials in a conscious well-planned manner. In fact, part of the confusion regarding electrochemical charge storage arises from the limited understanding of the electrode-electrolyte interface, and phenomena within, that occurs during charge and discharge. Here, we report two novel approaches to investigate said interface.

On the one hand, the Mott-Schottky model has brought further understanding of nickel-cobalt hydroxide at the interface with KOH. EIS is a very powerful technique that is usually used to evaluate the electrode-electrolyte interaction and provides information about resistance and charge-transfer phenomena. However, it is sometimes misused or incorrectly performed. Thus, the work here presented has a triple purpose in the context of electrochemical energy storage: (i) Brings to light the need to select an adequate potential to perform EIS and proposes the Mott-Schottky model to help in that process, (ii) helps in better understanding, from an electrochemical point of view, the electrode-electrolyte interface and (iii) aids unravelling the changes in conductivity of the studied material, this is, the bending of conductive bands in relation to the Fermi level. Nickel-cobalt hydroxide is a well-known system. However, the results here presented may have a great impact if applied to other less-known materials.

On the other hand, in-situ localized micro-potentiometry (SIET) is also used to understand the electrode-electrolyte interface of nickel-cobalt hydroxide with Na_2SO_4 by measuring the pH, pNa and dissolved O_2 at a quasi-constant micro-distance over the active surface. Most studies concerning the charge-discharge mechanism are based on either solid-state characterization or electrochemical quartz micro-balance combined with probe laser beam. While the former strategy investigates the evolution of the electrode material and not the interface, the latter, based on quantification of mass changes and measure of the ionic flux, is not ion-selective and, to elucidate and separate the contribution from cations, anions and solvent molecules has been proven to be rather difficult. SIET, as an ion-selective technique, has provided useful information in understanding the charge-discharge mechanism of β-Ni-$Co(OH)_2$, which has been under study since 1966 [10]. Therefore, the work presented in this manuscript introduces SIET as a useful technique for energy storage applications, that can be easily used in other systems, and collaborates in understanding the charge-discharge mechanism of nickel-cobalt hydroxide. Hydrogen transport is pin-pointed as the most plausible charge mechanism of β-Ni-$Co(OH)_2$, as opposed to hydroxide transport models. Moreover, the role of sodium ions in maintaining surface electroneutrality and the influence of OER during charge-discharge have been confirmed.

Table 4.1
Summary of the main results obtained for the different materials synthesized and presented in the course of this manuscript.

Material	Morphology	Synthesis	Capacity ($mA \cdot h \cdot g^{-1}$)	Current density	Electrolyte	Potential window vs. SCE (V)	Capacity retention (number cycles)
$Ni_{0.67}Co_{0.33}(OH)_2$	Nanoflakes	Electrodeposition	35	1 $A \cdot g^{-1}$	1M KOH	-0.2 - 0.45	42% (5000)
$Ni_{0.67}Co_{0.33}(OH)_2$/Er-GO	Nanoflakes on top of Er-GO sheets	Electrodeposition	75	1 $A \cdot g^{-1}$	1M KOH	-0.2 - 0.45	64% (5000)
$Ni_{0.33}Co_{0.67}(OH)_2$	Nanoflakes	Electrodeposition	30	1 $A \cdot g^{-1}$	1M KOH	-0.2 - 0.45	48% (5000)
$Ni_{0.33}Co_{0.67}(OH)_2$/Er-GO	Nanoflakes on top of Er-GO sheets	Electrodeposition	96	1 $A \cdot g^{-1}$	1M KOH	-0.2 - 0.45	60% (5000)
$Ni_{0.63}Co_{0.37}O_y$	Nanoparticles	Electrodeposition and thermal treatment	113	1 $A \cdot g^{-1}$	1M KOH	0.0 - 0.45	58% (5000)
$Ni_{0.68}Co_{0.32}O_y$/Er-GO	Nanoflakes on top of Er-GO sheets	Electrodeposition and thermal treatment	180	1 $A \cdot g^{-1}$	1M KOH	0.0 - 0.45	83% (5000)
DS-intercalated $Ni_{0.27}Co_{0.73}(OH)_2$	Hexagonal nanoplatelets	Hydrothermal synthesis	60	1 $A \cdot g^{-1}$	1M KOH	-0.2 - 0.46	44% (5000)
Delaminated $Ni_{0.27}Co_{0.73}(OH)_2$	Hexagonal nanoplatelets	Exfoliation by lactate intercalation	21	1 $A \cdot g^{-1}$	1M KOH	-0.2 - 0.46	75% (5000)
DS-intercalated $Ni_{0.27}Co_{0.73}(OH)_2$	Hexagonal nanoplatelets	Hydrothermal synthesis	81	1 $A \cdot g^{-1}$	1M LiOH	-0.2 – 0.52	51% (5000)
Delaminated $Ni_{0.27}Co_{0.73}(OH)_2$	Hexagonal nanoplatelets	Exfoliation by lactate intercalation	28	1 $A \cdot g^{-1}$	1M LiOH	-0.2 – 0.52	75% (5000)
$Ni_{0.65}Co_{0.35}(OH)_2$	Bulk	Co-precipitation	120	1 $A \cdot g^{-1}$	1M KOH	-0.2 - 0.45	53% (5000)
$Ni_{0.65}Co_{0.35}O_2 \cdot (H, Na, K)_y$	Bulk	Co-precipitation and oxidation	105	1 $A \cdot g^{-1}$	M KOH	-0.2 - 0.45	62% (5000)
Delaminated $Ni_{0.65}Co_{0.35}O_2$	Nanoparticles	Exfoliation by TBA^+ intercalation	115	1 $A \cdot g^{-1}$	1M KOH	-0.2 - 0.45	113% (5000)
$Ni_{0.65}Co_{0.35}(OH)_2$	Bulk	Co-precipitation	160	1 $A \cdot g^{-1}$	1M LiOH	-0.2 - 0.5	56% (5000)
$Ni_{0.65}Co_{0.35}O_2 \cdot (H, Na, K)_y$	Bulk	Co-precipitation and oxidation	112	1 $A \cdot g^{-1}$	1M LiOH	-0.2 - 0.5	38% (5000)
Delaminated $Ni_{0.65}Co_{0.35}O_2$	Nanoparticles	Exfoliation by TBA^+ intercalation	165	1 $A \cdot g^{-1}$	1M LiOH	-0.2 - 0.5	60% (5000)

4.1 Outlook and future work

Both lines of work, electrodeposition and exfoliation, have very exciting opportunities of study ahead. On the one hand, the electrodeposition of reduced graphene oxide shall be optimized. The performance of reduced graphene oxide in supercapacitor applications is yet to meet the standards of commercialized carbon-based materials. It faces several challenges, such as morphology optimization (single layer electrodeposition, development of different 3D structures with controlled porosity and inhibition of agglomeration), enhanced attachment to the conductive substrate, control of carbon to oxygen ratio or electrodeposition of transparent reduced graphene oxide with good conductivity are some of them.

Moreover, its combination with different materials is being studied. In this case, the response obtained from the composite had the typical response of a battery-like faradaic material. An interesting line of research may be focused towards increased capacitance contribution. It would be interesting if, by controlling the ratio of metal oxide – reduced graphene oxide by electrodeposition, different electrochemical responses would be achieved and tuned to satisfy the energetic demand of different applications. Other applications of reduced graphene oxide obtained by electrodeposition, such as their use in lithium-ion batteries, photosensors or in catalysis are yet to be explored.

Regarding exfoliation, despite the promising results obtained for the delamination of oxyhydroxide in aqueous media, there are still many challenges to overcome. First of all, the resulting material is obtained in very low-yield, therefore, the exfoliation route has to be optimized to increase the amount of product obtained. Another challenge, and therefore opportunity for improvement, is the limited power performance of these materials. Unfortunately, due to limit constraints, the combination of exfoliated nickel-cobalt oxyhydroxide with other delaminated materials could not be performed. However, this is a very exciting and promising strategy to combine materials with very different properties. If combined with materials such as manganese oxide, cobalt oxide or exfoliated graphene, all lines of work conducted at the ICMCB - University of Bordeaux, different electrochemical performances can be achieved. By tuning the ratio between different materials, a more power-oriented or capacity-oriented response may be obtained. Therefore, exfoliation routes may greatly influence the future of energy storage composite materials, and, due to their recent exploration, fascinating results are certainly yet to come. Furthermore, although delamination by lactate intercalation did not yield excellent results, it is worth highlighting that, if other purification routes are achieved, in which the active surface of the material is restored, it may also be a promising route for energy storage applications. Otherwise, the study of aqueous delamination of hydroxide materials is still an interesting field of work and this route may be modified, and lactates substituted by good ionic and electronic conductive materials instead, yielding better results. An interesting approach to this problem would be to include computational simulations to evaluate the impact of the intercalated materials and select, from experimental studies, the best possible material within a confined range of potentially good candidates. In any case, the work reported by Lang et al. [6] serves as base line to further investigate this material. Finally, this route, as well as exfoliation by tetrabutylammonium intercalation, may be useful in other applications, and the fact that their synthesis has been achieved shall not be overlooked.

Finally, local micro-potentiometry and the application of the Mott-Schottky model have resulted in useful information about the nickel-cobalt hydroxide/KOH (Na_2SO_4) interface. Thus, these techniques may be applied to other materials beyond the mixed

metal hydroxide. Understanding the transport of ions, electron transport and surface reactivity is a challenging task [11]. In the present manuscript some light has been shed on the nickel-cobalt hydroxide system by means of these techniques. Hopefully, some additional reports concerning SIET and Mott-Schottky will increase our knowledge on other systems as well. Furthermore, other important aspects beyond charge-discharge, such as the effect of oxygen evolution reaction on current efficiency, self-discharge or the evolution of the pH gradient and its effect on degradation of the electrode can also be studied. In addition, it would be very interesting to evaluate EIS results alongside the Mott-Schottky model and SIET results for nickel-cobalt hydroxide, results that are currently under investigation, for the first time, in our team at Instituto Superior Técnico.

To summarize, different research lines are involved in the work presented in this manuscript, which hopes to aid in the production of optimized next-generation energy storage devices and better understand the electrode-electrolyte interface. Undoubtedly, exciting opportunities of improvement in the field of energy storage lie ahead and, hopefully, they will translate in a sustainable future with satisfied energetic needs and increased quality of life.

Chapter 4 References

[1] M. Salanne, B. Rotenberg, K. Naoi, K. Kaneko, P.L. Taberna, C.P. Grey, B. Dunn, P. Simon, Efficient storage mechanisms for building better supercapacitors, Nat. Energy. 1 (2016). doi:10.1038/nenergy.2016.70.

[2] Y. Wang, Y. Song, Y. Xia, Electrochemical capacitors: mechanism, materials, systems, characterization and applications, Chem. Soc. Rev. 45 (2016) 5925–5950. doi:10.1039/C5CS00580A.

[3] H.M. French, M.J. Henderson, A.R. Hillman, E. Vieil, Ion and solvent transfer discrimination at a nickel hydroxide film exposed to LiOH by combined electrochemical quartz crystal microbalance (EQCM) and probe beam deflection (PBD) techniques, J. Electroanal. Chem. 500 (2001) 192–207. doi:10.1016/S0022-0728(00)00373-9.

[4] M. Wehrens-Dijksma, P.H.L. Notten, Electrochemical Quartz Microbalance characterization of Ni(OH)2-based thin film electrodes, Electrochim. Acta. 51 (2006) 3609–3621. doi:10.1016/j.electacta.2005.10.022.

[5] R. Ma, Z. Liu, L. Li, N. Iyi, T. Sasaki, Exfoliating layered double hydroxides in formamide : a method to obtain positively charged nanosheets, (2006) 3809–3813. doi:10.1039/b605422f.

[6] B. Schneiderová, J. Demel, A. Zhigunov, J. Bohuslav, H. Tarábková, P. Janda, K. Lang, Nickel-cobalt hydroxide nanosheets : Synthesis , morphology and electrochemical properties, J. Colloid Interface Sci. 499 (2017) 138–144. doi:10.1016/j.jcis.2017.03.096.

[7] Y. Omomo, T. Sasaki, L. Wang, M. Watanabe, Redoxable nanosheet crystallites of MnO2 derived via delamination of a layered manganese oxide, J. Am. Chem. Soc. 125 (2003) 3568–3575. doi:10.1021/ja021364p.

[8] C. Tang, Exfoliation and restacking of manganese and cobalt based lamellar oxides for supercapacitor electrodes, Université de Bordeaux, 2017. doi:HAL Id: tel-01696266.

[9] C. Delmas, Y. Borthomieu, C. Faure, Nickel hydroxide and derived phases obtained by chimie douce from NaNiO2, Solid State Ionics. 33 (1989) 104–111. doi:10.1016/0167-2738(89)90209-9.

[10] H. Bode, K. Dehmelt, J. Witte, Zur Kenntnis der Nickelhydroxidelektrode - I. Über das Nickel(II)-Hydroxidhydrat, Electrochim. Acta. 11 (1966) 1079–1087. doi:10.1016/0013-4686(66)80045-2.

[11] C. Taviot-Guého, P. Vialat, F. Leroux, F. Razzaghi, H. Perrot, O. Sel, N.D. Jensen, U.G. Nielsen, S. Peulon, E. Elkaim, C. Mousty, Dynamic Characterization of Inter- and Intralamellar Domains of Cobalt-Based Layered Double Hydroxides upon Electrochemical Oxidation, Chem. Mater. 28 (2016) 7793–7806. doi:10.1021/acs.chemmater.6b03061.

Experimental results

Annex. Résumé étendu en français

La demande croissante d'énergie dans le transport, le secteur résidentiel et l'industrie, ainsi que la prolifération de sources d'énergie renouvelable nécessitent des dispositifs plus efficaces de stockage de l'énergie. Les récents efforts en ingénierie des matériaux sont axés sur le développement de matériaux nanostructurés susceptibles de faire face à ces besoins, tant en termes de densité énergétique (quantité totale d'énergie stockée par unité de masse ou de volume), de densité de puissance (puissance qui peut être transférée par unité de temps,de masse ou de volume), que de stabilité en cyclage, qui correspond à la dégradation des dispositifs en utilisation continue. De nombreux matériaux sont actuellement étudiés en tant que candidats potentiels pour le stockage d'énergie au sein des batteries, condensateurs, supercondensateurs (dispositifs pouvant stocker beaucoup plus d'énergie que les condensateurs tout en conservant une densité de puissance élevée) ou pseudocondensateurs. L'objectif de ce travail est d'élaborer des matériaux destinés à être utilisés dans des électrodes hybrides avec une réponse électrochimique intermédiaire par rapport à celles observées dans un supercondensateur et une batterie. Dans ce contexte, les (hydr)oxydes de nickel et de cobalt ont été choisis en raison de leur activité électrochimique élevée et de leur faible coût et ont été combinés avec des dérivés de graphène, qui présentent une conductivité et une surface active élevées. Ce travail concerne plus précisément la synthèse par deux voies, l'électrodéposition et l'exfoliation, d' hydroxydes et oxydes de nickel-cobalt nanostructurés, et leur combinaison avec l'oxyde de graphène réduit. Ces deux stratégies, du point de vue de l'ingénierie des nanomatériaux, sont de nature opposée. Alors que l'électrodéposition est une approche *bottom-up* dans la production de films minces, l'exfoliation est une technique *top-down*, après reconstitution, qui donne un matériau nanostructuré. L'accent a été mis sur la caractérisation physico-chimique et électrochimique pour les applications de stockage de l'énergie.

Tout d'abord, l'électrodéposition d'une phase α d'hydroxyde de nickel-cobalt et sa combinaison avec de l'oxyde de graphène réduit électrochimiquement (Er-GO) sur des supports d'acier inoxydable a été explorée. Les résultats mettent en évidence une réponse électrochimique améliorée avec une capacité, un comportement en puissance et une stabilité en cyclage accrus lorsque l'oxyde de graphène réduit est incorporé. Le matériau composite présente une capacité de 96 $mA \cdot h \cdot g^{-1}$ et une rétention de capacité de 62% après 5000 cycles. De plus, des vitesses de balayage allant jusqu'à 2 $V \cdot s^{-1}$ ont pu être appliquées

sans distorsion de la réponse électrochimique du matériau, prouvant l'excellent comportement en puissance de ce matériau. Enfin, la dégradation du matériau a été étudiée en détails au moyen de la spectroscopie d'impédance électrochimique (EIS), de la microscopie électronique à balayage (MEB) et de la voltampérométrie cyclique. Après cyclage, la MEB a montré la dégradation mécanique que le matériau subit en cyclage, tandis que la EIS a révélé la formation d'une phase secondaire, probablement de type β qui est connue pour apparaître en raison de l'instabilité connue de la phase α. En comparaison, lorsque Er-GO est introduit, il sert de matrice qui inhibe la déformation mécanique et stabilise la phase α, avec une amélioration de la stabilité du matériau.

L'oxyde de nickel-cobalt a été obtenu par électrodéposition de l'hydroxyde de nickel-cobalt suivie d'un traitement thermique postérieur. Dans ce cas, le matériau présente une capacité de 77 $mA \cdot h \cdot g^{-1}$ et une rétention de capacité de 58% après 5000 cycles de charge-décharge. Cependant, lorsque Er-GO a été introduit, formant un matériau composite, le matériau affiche 130 $mA \cdot h \cdot g^{-1}$ et 83% de rétention de la capacité. Ainsi, comme dans le cas de l'hydroxyde de nickel-cobalt, l'introduction d'Er-GO a considérablement amélioré les propriétés électrochimiques du matériau. Les phénomènes de dégradation ont également été étudiés par MEB, EIS et voltammétrie cyclique. Encore une fois, les mécanismes de dégradation, et la décroissance de capacité qui en découle, sont attribués à des contraintes mécaniques qui induisent la formation d'une phase parasitaire, susceptible d'être de l'hydroxyde de nickel-cobalt, ainsi qu'un « broyage » de la microstructure entraînant une perte de matière qui déplace les potentiels de réaction et favorise le dégagement d'oxygène.

En ce qui concerne la voie top-down, l'(hydr)oxyde de nickel-cobalt est exfolié dans des milieux aqueux. Ceci est réalisé via l'intercalation d'entités lactate pour les hydroxydes et de cations tétrabutylammonium pour l'exfoliation des oxyhydroxydes. Les hydroxydes et les oxyhydroxydes de nickel-cobalt sont des matériaux lamellaires et, par conséquent, peuvent être en feuillets par intercalation de molécules volumineuses dans un solvant dans des conditions adéquates. Ensuite, les réponses électrochimiques des deux matériaux sont évaluées dans différents électrolytes après délamination et ré-empilement. Les résultats révèlent l'influence primordiale des espèces intercalées lors du processus d'exfoliation, lactate et tétrabutylammonium,: la nature des espèces intercalées ainsi que les forces d''interaction avec le matériau actif doivent être considérées préalablement pour éviter le blocage de la surface et l'inhibition de l'interaction électrode-électrolyte. Les résultats

corroborent que l'exfoliation est une voie prometteuse pour augmenter la surface active des matériaux, mais constitue néanmoins un paramètre critique dans la performance électrochimique des matériaux d'électrode.

Par exemple, pour l' oxyhydroxyde de nickel-cobalt γ réempilé après exfoliation en milieu TBAOH, une capacité de 117 $mA \cdot h \cdot g^{-1}$ avec une rétention de capacité> 100% a été obtenue dans KOH 1 M, alors que les matériaux non-exfoliées affichent seulement 106 $mA \cdot h \cdot g^{-1}$ et une rétention de capacité de 62% après 5000 cycles de charge-décharge. Cependant, dans le cas des hydroxydes exfoliés en milieu lactate et réempilés, bien que les matériaux présentent une capacité, la capacité, bien que plus élevée que celle du matériau initial non exfolié, est beaucoup plus faible que pour l'hydroxyde de nickel-cobalt intercalé avec du dodécylsulfate de sodium. Ceci est probablement dû à la forte interaction des molécules de lactate avec les nanofeuillets d'hydroxyde, qui bloquent les sites actifs du matériau et inhibent l'interaction électrode-électrolyte. Il est également à noter qu'une étape d'activation est observée lors des premiers cycles électrochimiques pour les matériaux exfoliés. Ceci suggère que la purification est également une étape critique dans la préparation de matériaux exfoliés pour le stockage d'énergie.

Enfin, la dernière partie s'inscrit dans l'investigation du mécanisme de charge-décharge de l'hydroxyde de nickel-cobalt, qui n'était pas encore complètement compris à ce jour. L'appréhension de ce mécanisme est une étape critique pour l'optimisation des performances et la conception de futurs dispositifs de stockage de l'énergie basés sur ce matériau. Afin d' éclairer les processus de charge, le modèle de Mott-Schottky a été utilisé en combinaison avec la EIS tandis que la micropotentiométrie locale a été mise en œuvre pour évaluer les variations de pH, de pNa et d'oxygène dissous à la proximité de l'interface.

La spectroscopie d'impédance électrochimique est un outil très puissant qui fournit des informations détaillées sur la résistance, la porosité, la dégradation et les phénomènes de transport de charge d'un système. Cependant, les résultats sont souvent difficiles à interpréter, et soulignent l'importance du potentiel appliqué lors de l'acquisition des données de spectroscopie d'impédance électrochimique dans l'optique d'une interprétation correcte.. Le modèle de Mott-Schottky a été utilisé pour expliquer l'évolution des bandes électroniques et des niveaux de Fermi à l'interface de l'hydroxyde de nickel-cobalt dans les milieux alcalins et pour sélectionner de façon critique un potentiel adéquat pour réaliser l'EIS. En outre, il aide à la compréhension des

changements de conductivité, lorsque l'on passe pendant le processus de charge d'un semi-conducteur de type p, l'hydroxyde de nickel-cobalt, à un matériau conducteur, l'oxyhydroxyde de nickel-cobalt.

De plus, la micro-potentiométrie locale in situ (SIET) et de microcapteur à fibre optique ont été appliqués à l'interface de l'hydroxyde de nickel-cobalt avec des milieux sulfate de sodium et de potassium pour obtenir des informations sur les gradients de pH, pNa et d'oxygène dissous pendant la charge et la décharge de ce matériau. Bien que largement mis en œuvre dans d'autres domaines tels que la biologie ou la corrosion, la SIET ne l'a pas été à notre connaissance pour étudier les matériaux de stockage d'énergie. Nous l'avons donc utilisé pour tenter d'éclairer le mécanisme de charge-décharge de l'hydroxyde de nickel-cobalt. Ce mécanisme a été étudié dès 1966, lorsque Bode et al.[1] ont proposé un diagramme avec les transformations de phase possibles de l'hydroxyde de nickel pendant la charge-décharge. Depuis lors, deux principaux mécanismes possibles ont été rapportés dans la littérature, mettant en jeu des modèles de transport de protons ou d'hydroxyle. Par la suite, différentes contributions d'ions alcalins ont été mises en évidence au moyen de différentes techniques de caractérisation. Au moyen de la SIET, la contribution des ions alcalins dans l'hydroxyde de nickel-cobalt β a été étudiée en même temps que la variation du pH à l'interface du matériau. Sur la base des résultats obtenus, le transport de protons a été désigné comme le mécanisme le plus probable pendant la charge et la décharge de l'hydroxyde de nickel-cobalt, tandis que les ions sodium étaient uniquement impliqués dans la compensation de charge.

En conclusion, les techniques d'exfoliation / réempilement à partir de matériaux lamellaires et d'électrodéposition sont des voies efficaces pour la synthèse d'hydroxydes, d'oxyhydroxydes et d'oxydes de nickel-cobalt nanostructurés, qui sont des candidats potentiels pour des dispositifs de stockage de l'énergie. De plus, la combinaison de ces matériaux avec de l'oxyde de graphène réduit est une voie prometteuse pour l'amélioration de la réponse électrochimique. La spectroscopie d'impédance électrochimique s'est révélée comme une technique utile dans l'évaluation des phénomènes de dégradation des matériaux actifs. L'application du modèle de Mott-Schottky est un excellent outil pour sélectionner les potentiels adéquats pour l' évaluation du matériau et pour mieux comprendre les variations de conductivité du matériau. Finalement, la SIET a été identifiée comme une technique prometteuse pour étudier l'interface électrode-électrolyte dans le cadre des applications de stockage de l'énergie et a permis de comprendre, à un

niveau fondamental, les processus impliqués dans la charge-décharge de l'hydroxyde de nickel-cobalt.

Référence:

[1] H. Bode, J. Witte, K. Dehmelt, Zur Kenntnis der Nickelhydroxidelektrode - I. Über das Nickel (II)-Hydroxidhydrat, Electrochim. Acta. 11 (1966) 1079–1087.